



Lawton, Lorreta (2011) *Structure property relationships in Prussian Blue analogues and hydrogen bond mediated metal complexes*. PhD thesis.

<http://theses.gla.ac.uk/2426/>

Copyright and moral rights for this thesis are retained by the author

A copy can be downloaded for personal non-commercial research or study, without prior permission or charge

This thesis cannot be reproduced or quoted extensively from without first obtaining permission in writing from the Author

The content must not be changed in any way or sold commercially in any format or medium without the formal permission of the Author

When referring to this work, full bibliographic details including the author, title, awarding institution and date of the thesis must be given

# **Structure Property Relationships in Prussian Blue Analogues and Hydrogen Bond Mediated Metal Complexes**

Lorreta Lawton

Thesis submitted to the University of Glasgow  
for the degree of Doctor of Philosophy

School of Chemistry

Submitted September 2010

Lorreta Lawton, September 2010

## Abstract

Within this work the effects of metal identity are investigated on the magnetic properties of a range of materials, in which different transition metals are shown to produce significantly different calculated magnetic coupling values when incorporated into the same structure. The model structures composed of transition metals mediated by hydrogen halide ligands of the form  $\text{FHF}^-$ ,  $\text{ClHCl}^-$  and  $\text{FHCl}^-$  enable the calculation of magnetic coupling values via hydrogen bonds (HBs), providing insight into a scarcely studied topic. The employment of the well known HF=35% functional, provides results anticipated to represent potential experimental trends. Interesting results are also reported which indicate a relationship between the binding energy of the atom and the level of coupling displayed. The quantum nature of the H atom, often difficult to localise, are also accounted for by use of a shooting algorithm in order to solve the one dimensional Schrödinger equation in relation to the hydrogen positions within the isotropic lattice. Hydrogen positions were fixed during geometry optimisations in order to obtain the  $E(x)$  potential energy curve required to allow this to be achieved. Both the  $\langle J \rangle$  in which proton motion is incorporated and J coupling values from the optimised ground state structures, in which the atomic positions including the H positions underwent a full geometry optimisation, are presented.

The electronic effects of incorporating different group one and group two metals into the related Prussian Blue (PB), Prussian Yellow (PY) and Prussian White (PW) model lattices are also presented. More specifically band gaps within these complexes are calculated from projected density of state (DOS) plots of the electrons within the atomic orbitals from a converged calculation in which the B3LYP functional (HF=20%) is employed. This functional has previously been shown to provide band gap energies in good agreement with experimental values. The results obtained confirm that the value of  $\sim 3\text{eV}$ , associated with an absorption in the yellow region, lies within the PY band gap range, indicated by the HOMO and LUMO orbitals within the DOS plot. Band gaps calculated directly from SCF energy differences do not agree well with experimental values or trends for the various group one PB complexes.

A number of related metal containing bromanilic acid (BA) and chloranilic acid (CA) complexes are synthesised, crystallised and their structures, as determined by X-ray single crystal diffraction, reported. The structural packing of the molecules is analysed by defining a number or recurring unit within the structures in order to obtain key similarities. The structures are also broken down in to lower dimensional units composed of the individual components within the asymmetric unit and built up into higher

dimensional units such as clusters, chains and planes that all intersect with one another in order to produce the overall three dimensional structures. In most cases the point of intersection is on a key symmetry element such as an inversion centre.

Particularly short M-M contact distances are observed in a number of the complexes. This proves interesting within the related isomorphous complexes in which the main effect of incorporating a larger metal cation into the same structure is in the ionic repulsions between the metals. This is particularly interesting in more extended structures in which the metals exist in chains or planes that run along a particular direction of the unit cell. The specific increase in cell parameter can in most cases be explained as a consequence of the repulsion between the shortest M-M contacts. The effect is also observed in structures in which the metals exist as isolated clusters, and also displays some interesting consequential effects on other interactions.

A variable pressure neutron single crystal diffraction experiment on a short asymmetric HB is also reported, in which one lattice is compressed significantly more than the other two, an effect that is explained by the change in contact distances with pressure.

## **Declaration**

This thesis has been written in accordance with the University and all work presented is original and performed by the author unless otherwise stated and referenced in the text.

Lorreta Lawton

## Acknowledgements

First and foremost I would like to thank Prof. Chick Wilson for being everything a person could possibly want in a supervisor. I will always be grateful for his hands off approach during the course of the PhD which enabled me to grow as a student, and for the very much hands on approach at the end when I let things slip. The man is nothing short of a miracle worker.

I would also like to thank both Lynne and Derek from the bottom of my heart for all the computational and crystallography help and guidance over the past few years and all the last minute reading and correcting to get things finished on time. I never seem to learn and will be eternally indebted to you both.

Naturally I would like to acknowledge all past and present members of the group who I have enjoyed working alongside - especially the guys in the down office for making the working day both fun and stimulating, except during the topic of last night's game ...'but why?!', also the Damiano dialogues' that will never fail to raise a smile. Redbull and tea are also worth mentioning, although more as caffeine containing drinks as supposed to crystal growing solvents - maadam! :)

I would of course also like to thank my mum and dad for all the encouragement and support, both moral and financial throughout the whole higher education journey. Even through all the hard times you always tried to help any way that you could, I'm so grateful to have you both as parents. Mum's continual enquiries and badgering on thesis progress, while at the same time trying to get me to go to bingo, and Dad's laid back 'just do your best' and 'whatever will be will be' helped to keep focused while remaining sane.

I would also like to thank my little brother Cameron just for being him. He's one of the most grounded level headed people I know and he knows just what to say in a moment of worry to bring you back down to earth. If only he'd realise himself how special he really is one day and start taking his own advice.

I would like to say thank you to Jackie and Bob for having me for the past year, hopefully not too big a price to pay for having their son back for a bit. From mountains of snow to eagerly awaited days of sun out the back with a few drinks and a barbie, not that the weather ever stops anything.

Last and certainly not least I would like to thank my husband Craig for standing by and encouraging me all these years. I could not have done this without you. All your supportive nagging and putting up with notes and papers scattered all over the bedroom and tidying them away back into their organised clumps has finally paid off. I love you so much and can't wait for our next little adventure to finally begin - bring on scuba in the sun! x



2.2.1.4.2	Direct Methods.....	52
2.2.1.5	Structure Refinement.....	53
2.2.2	Neutron Diffraction.....	54
2.2.3	Sample Preparation.....	57
2.2.3.1	Crystallisation.....	57
2.2.3.2	Characterisation and Screening.....	59
2.3	Ab Initio Calculations.....	60
2.3.1	Simulation of condensed Matter.....	60
2.3.2	The Hartree-Fock (HF) Theory for Solids.....	61
2.3.3	Density Functional Theory (DFT) for Solids.....	65
2.3.4	Hybrid Hartree Fock-Density Functional Hamiltonians - and their Implementation in the CRYSTAL06 Code.....	68
2.3.5	Electronic Structure.....	70
2.3.6	Magnetic Coupling.....	73
<b>3.</b>	<b>Prussian Blue Analogues (PBAs)</b>	<b>77</b>
3.1	Structures and Computational Methods.....	78
3.2	Calculation of Band Gaps.....	82
3.2.1	SCF Calculations.....	82
3.2.2	DOS Calculations.....	89
3.2.2.1	Prussian Yellow (PY).....	89
3.2.2.2	Prussian Blue.....	92
3.2.2.3	Prussian White.....	95
3.2.2.4	Effects of Metal Identity on PW and PB Band Gaps.....	98
3.3	Discussion and Conclusions.....	101
<b>4.</b>	<b>Transition Metal Hydrogen Halides (TMHHs)</b>	<b>103</b>
4.1	Computational Methods.....	104
4.2	Cu Hydrogen Halide (CuHH).....	110
4.3	V and Ni Static Calculations.....	115
4.4	Effects of Quantum Motion in the $\text{HF}_2^-$ , $\text{HCl}_2^-$ , and $\text{HFCl}^-$ Ions.....	119
4.5	Quantum Motion Effects.....	127
4.6	Conclusions and Outlook.....	132

<b>5.</b>	<b>Metal Complexes with Bromanilic and Chloranilic Acid</b>	<b>134</b>
5.1	Systematic Studies of Metal Complexes.....	134
5.1.1	Classification of the Crystal Packing.....	137
5.1.2	CSD Survey of M-M and X-X Interactions.....	143
5.2	Potassium-containing Bromanilic Acid Complexes.....	144
5.2.1	Anhydrous Tautomeric Polymorphs.....	144
5.2.1.1	Form I Structure Determination and Analysis.....	145
5.2.1.2	Form II Structure Determination and Analysis.....	149
5.2.1.3	Structural Comparison of the Two Anhydrous Tautomeric Polymorphs.....	157
5.2.2	Hydrated Polymorphs.....	158
5.2.2.1	Form I.....	158
5.2.2.2	Form II.....	170
5.2.2.3	Form III.....	175
5.2.2.4	Comparison of the Structural Packing of the Three Hydrated Polymorphs.....	179
5.3	Isomorphous Chloranilic Acid and Bromanilic Acid Complexes.....	188
5.3.1	2:1 Metal-Bromanilic Acid Dihydrate Complexes.....	188
5.3.2	2:1 Metal-Chloranilic Acid Monohydrate Complexes.....	195
5.3.3	1:1 Metal - Chloranilic Acid Dihydrate Complexes.....	204
5.3.4	2:3 Metal - Chloranilic Acid Hexahydrate Complexes.....	218
5.4	Additional Group One Metals Complexes.....	233
5.4.1	Lithium Complexes.....	233
5.4.1.1	Lithium CA Monohydrate Complex.....	233
5.4.1.2	2:1 Lithium CA/BA Monohydrate Complex.....	238
5.4.1.3	1:1 Lithium CA dihydrate Complex.....	241
5.4.2	Sodium Complexes.....	248
5.4.2.1	2:1 Sodium BA tetrahydrate Complex.....	248
5.4.2.2	2:1 Sodium CA trihydrate Complex.....	255
5.5	Conclusions.....	269

<b>6.</b>	<b>Variable Pressure Neutron Diffraction Study of Potassium Hydrogen Dicrotonate (KHDC)</b>	<b>271</b>
6.1	Potassium Hydrogen Dicrotonate.....	271
6.2	Experimental.....	272
6.3	The Crystal Structure of KHDC.....	273
6.4	The Effect of Pressure on the Crystal Structure of KHDC.....	277
<b>7.</b>	<b>Conclusions and Forward Look</b>	<b>284</b>
7.1	Prussian Blue Analogues.....	284
7.2	Transition Metal Hydrogen Halides.....	286
7.3	Metal Containing BA and CA complexes.....	288
7.4	Future Potential.....	290
	<b>References</b>	<b>292</b>

## LIST OF SCHEMES AND FIGURES

<b>Scheme 1-1:</b>	Ionisation of PB to reduced and oxidised forms; PY and PW respectively	9
<b>Scheme 1-2:</b>	Redox activity associated with different quinone ligands	21
<b>Scheme 1-3:</b>	Potential resonance forms of chloranilic acid	27
<b>Scheme 1-4:</b>	Formation of various ligand architectures using CA.	28
<b>Scheme 1-5:</b>	Packing arrangements in metal chloranilate salts.	29
<b>Scheme 1-6:</b>	Packing of monomeric $M(CA)_2$ units.	33
<b>Scheme 5-1</b>	Substitution reaction scheme for $Cl^-$ anion with BA	23
<b>Figure 1-1:</b>	Notation for a typical $D-H\cdots A$ HB, showing the geometric parameters	4
<b>Figure 1-2:</b>	Examples of BHBs (i) One donor, one H atom and two acceptor atoms (DHAA), (also referred to as three-centred in the literature) (ii) Two donors, two H atoms and one acceptor atom (DDHHA) (iii) Two donors, with two H atoms between and no acceptor atoms (DHHD) (iv) One donor, two H atoms and one acceptor atom (DHHA)	4
<b>Figure 1-3:</b>	Geometry of BHB (i) symmetric (ii) asymmetric	5
<b>Figure 1-4:</b>	Typical potential well for a moderate HB, with one potential proton site of significantly lower energy than the other	6
<b>Figure 1-5:</b>	Types of broadened potential wells in shorter HBs	6
<b>Figure 1-6:</b>	The ideal crystal structure for IPB	8
<b>Figure 1-7:</b>	The ideal crystal structure for sPB	9
<b>Figure 1-8:</b>	(i) The two interpenetrating sublattices of A and B, (ii) Ferromagnetic (FM) (iii) Antiferromagnetic (AF) and Ferrimagnetic Coupling (FI)	14
<b>Figure 1-9:</b>	Dinuclear Cu complex.	18
<b>Figure 1-10:</b>	Crystal structure of $[Cu(HF_2)(pyz)_2]BF_4$ ; strong magnetic coupling via pyrazine in the xy plane and weak magnetic coupling via $FHF^-$ along the z axis. Cu positioned at (0,0,0). Pyrazine H atoms and $BF_4^-$ anions have been omitted for clarity. Figure from reference 82	19
<b>Figure 1-11:</b>	Anilic acid or Benzoquinone family of compounds	22
<b>Figure 1-12:</b>	(i) Bromanilic acid (BA) and (ii) chloranilic acid (CA)	22
<b>Figure 1-13:</b>	The three observed forms and adopted notations of bromanilic and chloranilic acid; neutral, fully protonated $H_2BA$ and $H_2CA$ ; partially deprotonated $HBA^-$ and $HCA^-$ (monoanions); and fully deprotonated $BA^{2-}$ and $CA^{2-}$ (dianions)	23
<b>Figure 1-14:</b>	Bond lengths in the neutral $H_2XA$ molecules (i) CA (ii) BA	24
<b>Figure 1-15:</b>	$HCA^-$ molecule bond lengths from (i) $MoHCA^-$ complex (ii) average structures	25
<b>Figure 1-16:</b>	$HBA^-$ molecule bond lengths from (i) $FeHBA^-$ complex (ii) average structures, obtained using Vista	26
<b>Figure 1-17:</b>	Average bond lengths found using Vista of (i) $CA^{2-}$ and (i) $BA^{2-}$	27
<b>Figure 1-18:</b>	Observed architectures in metal-CA complexes	31
<b>Figure 1-19:</b>	Lanthanide sheet structures (i) $Ce_2(C_6O_4H_2)^{2-}_3 \cdot 24H_2O$ (ii) $Pr_2(CA^{2-})_3 \cdot 18H_2O$ (iii) $Y_2(CA^{2-})_3 \cdot 16H_2O$ (iv) $Ce_2(CA^{2-})_3 \cdot 18H_2O$ (v) $Pr_2(CA^{2-})_3 \cdot 8CH_3CH_2OH$ (vi) $Y_2(CA^{2-})_3 \cdot 12H_2O$ (vii) $La_2(CA^{2-})_3 \cdot 13H_2O$ and extended structure for (viii) $Y_2(CA^{2-})_3$ network	32

<b>Figure 1-20:</b>	Two dimensional extended structures in La CA complexes	33
<b>Figure 1-21:</b>	(i) $M^{2+}(C_6O_4X_2)^{2-} \cdot 4H_2O$ , (M = Ca, Sr, X= Cl, Br), polymorph of (ii) $Ba^{2+}(C_6O_4Cl_2)^{2-} \cdot 3H_2O$	35
<b>Figure 1-22:</b>	(i) $2Na^+ CA^{2-} \cdot 3H_2O$ complex, <sup>148</sup> (ii) $2Na^+ (phen)_2 CA^{2-} \cdot 2H_2O$ complex	36
<b>Figure 2-2:</b>	Crystal unit cell, parallelepiped enclosed by eight lattice points.	39
<b>Figure 2-2:</b>	The Wigner-Seitz cell shows volume associated with one lattice point	39
<b>Figure 2-3:</b>	(i) number of possible primitive unit cells in a lattice (ii) cell 3 is an example of a centred lattice	40
<b>Figure 2-4:</b>	Illustration of the fourteen Bravais lattices	41
<b>Figure 2-5:</b>	Laue cone construction for diffraction geometry	45
<b>Figure 2-6:</b>	Geometric construction for the derivation of Bragg's Law	46
<b>Figure 2-7:</b>	Illustration of the (2 2 2) Miller index plane in a unit cell	47
<b>Figure 2-8:</b>	Sets of lattice planes leading to diffraction spots	47
<b>Figure 2-9:</b>	Form factor fall-off of X-ray scattering factors for three atom types. The fall-off in scattering with angle is further emphasised by thermal vibrations	49
<b>Figure 2-10:</b>	Neutron scattering lengths and comparison with X-ray scattering factor variation with Z	55
<b>Figure 2-11:</b>	Neutron scattering shows no form factor fall-off with scattering angle, unlike with X-rays, illustrated here for two typical light atoms	56
<b>Figure 2-12:</b>	The ReactArray Microvate, a device designed to allow temperature programmable crystallisation regimes	58
<b>Figure 2-13:</b>	Superexchange pathway in different orbital overlaps	76
<b>Figure 3-1:</b>	(i) PY model structure, LS $Fe^{3+}$ (black) and HS $Fe^{3+}$ (blue), no charge balancing cation, space group Fm-3m; (ii) PB, LS $Fe^{2+}$ (black) and HS $Fe^{3+}$ (blue), $2^+$ cation (green), space group Pn-3m; (iii) PB model structure, LS $Fe^{2+}$ (black) and HS $Fe^{3+}$ (blue), $1^+$ cation (green) and PW model structure, LS $Fe^{2+}$ (black) and HS $Fe^{2+}$ (blue), $2^+$ cation (green), space group F-43m; (iv) PW model structure, LS $Fe^{2+}$ (black) and HS $Fe^{2+}$ (blue), $1^+$ cation, space group Fm-3m. The electron seeking nitrogen is coloured yellow and less reactive carbon red in all cases	79
<b>Figure 3-2:</b>	Ground state electron arrangements of the (i) PB, (ii) PY and (iii) PW d orbitals implemented in the input file of the CRYSTAL06 code	81
<b>Figure 3-3:</b>	Dependence of ground $E_0$ and excited $E_1$ state energy profiles on a notational nuclear reaction coordinate.	83
<b>Figure 3-4:</b>	PB $t_{2g} \beta$ to $t_{2g} \beta e^-$ transfer between the LS $Fe^{2+}$ and HS $Fe^{3+}$ ions	83
<b>Figure 3-5:</b>	PB SCF band gap energies modelled (i) by movement of the excited electron between the ground state allocation of Fe basis sets and (ii) by switching of Fe basis sets between ground and excited states.	85
<b>Figure 3-6:</b>	Comparison of the band gaps obtained by the two methods of excitation at (i) 20% HF, (ii) 30% HF, (iii) 40% HF and (iv) 60% HF	86
<b>Figure 3-7:</b>	PB Comparison of band gaps obtained using uhf and 100%HF with experiment	87
<b>Figure 3-8:</b>	Atom projected PY DOS plot showing total N (yellow) and C (red) and $Fe^{3+}$ low spin (blue) and high spin (black) contributions, the latter two further split into $t_{2g}$ (dashed) and $e_g$ (solid) orbital contributions. The positive and negative y-axes denote $\alpha$ and $\beta$ spins respectively, where $\alpha$ denotes the majority spin alignment of the lattice. The Fermi energy is -0.28 Hartrees.	90

<b>Figure 3-9:</b>	PY electron arrangement of d orbitals in ground and excited state	91
<b>Figure 3-10:</b>	PB DOS populations of total N (yellow) and C (red) orbitals, Fe <sup>2+</sup> low spin (blue) and Fe <sup>3+</sup> high spin (black) t <sub>2g</sub> (dashed) and e <sub>g</sub> (solid) orbitals respectively. The positive and negative y-axes denote α and β spins respectively. The Fermi energy is -0.223 Hartrees	92
<b>Figure 3-11:</b>	DOS plot band gap between HOMO and LUMO	93
<b>Figure 3-12:</b>	PB Comparison of band gaps from incorporation of different M <sup>+</sup> ions	94
<b>Figure 3-13:</b>	PB Band gap dependence on type of interstitial cation, comparison of SCF; 100%HF and uhf, DOS; difference in most populated states (DOS MP) and highest HOMO and lowest LUMO (DOS H-L), and experiment	95
<b>Figure 3-14:</b>	KPW DOS populations of total N (yellow) and C (red) orbitals, Fe <sup>2+</sup> low spin (blue) and high spin (black) t <sub>2g</sub> (dashed) and e <sub>g</sub> (solid) orbitals respectively. The positive and negative y-axes denote α and β spins respectively. The Fermi energy is -0.15 Hartrees	96
<b>Figure 3-15:</b>	PW electron arrangement of d orbitals in ground and excited state	97
<b>Figure 3-16:</b>	CaPW DOS populations of total N (yellow) and C (red) orbitals, Ca <sup>2+</sup> (green) orbitals, Fe <sup>2+</sup> low spin (blue) and high spin (black) t <sub>2g</sub> (dashed) and e <sub>g</sub> (solid) orbitals respectively. The positive and negative y-axes denote α and β spins respectively. The Fermi energy is -0.15 Hartrees	97
<b>Figure 4-1:</b>	Primitive M XHX unit cell	105
<b>Figure 4-2:</b>	Two magnetic sublattices required to calculate FM (TM <sub>A</sub> and TM <sub>B</sub> both have same spin) and AF (TM <sub>A</sub> and TM <sub>B</sub> both have opposite spins) magnetic states	106
<b>Figure 4-3:</b>	Cu <sup>2+</sup> d <sup>9</sup> configuration in Octahedral (O <sub>h</sub> ) and Jahn-Teller distorted (D <sub>8</sub> ) ligand field	108
<b>Figure 4-4:</b>	Model 2K <sup>+</sup> [4Cu <sup>2+</sup> (XHX <sup>-</sup> ) <sub>6</sub> ] structure	108
<b>Figure 4-5:</b>	Magnetic Coupling (J) values for TM = V <sup>2+</sup> , Ni <sup>2+</sup> , and XFX <sup>-</sup> = FHF <sup>-</sup> , ClHCl <sup>-</sup> and FHCl	116
<b>Figure 4-6:</b>	NiFHF potential energy profile E(x) and magnetic coupling constant J <sub>FHF</sub> (x) as a function of proton position x along the FHF bond	120
<b>Figure 4-7:</b>	NiClHCl potential energy profile E(x) and magnetic coupling constant J <sub>ClHCl</sub> (x) as a function of proton position x along the ClHCl bond	121
<b>Figure 4-8:</b>	NiFHCl potential energy profile E(x) and magnetic coupling constant J <sub>FHCl</sub> (x) as a function of proton position x along the FHCl bond	122
<b>Figure 4-9:</b>	FHCl <sup>-</sup> ligand; F–H / H–Cl Ratio with lattice expansion	125
<b>Figure 4-10:</b>	FHF (i) optimised structure with single potential well (ii) formation of double potential well in +2.5% expanded HB structure. Potential (black), wavefunction (red), solid line energy relative to the minimum (E <sub>rel</sub> ), dotted line first excited state energy. The first excited state energy magnitude is so large in comparison to calculated critical temperatures that it is assumed to have no effect on low temperature magnetic ordering	128
<b>Figure 4-11:</b>	(i) FHF (ii)ClHCl (iii) FHCl comparison of <J> (blue) and J (pink) values from optimised structure (centre) and structures in which HB compressed and expanded	130
<b>Figure 5-1</b>	Samples of solutions containing: (a) H <sub>2</sub> CA (neutral CA, very low pH), (b) HCA <sup>-</sup> (mono anions, neutral pH) and (c) CA <sup>2-</sup> (dianion, high pH). Crystals of CA dihydrate are red (d), crystals of HCA <sup>-</sup> salts are dark violet and opaque (e), and crystals of CA <sup>2-</sup> salts are violet and transparent (f).	136

<b>Figure 5-2</b>	Units depicting: M to XA ligand coordination; XA ligand to M coordination; M to M coordinating atoms, and HB motifs, see Table 5-2.	139
<b>Figure 5-3</b>	Examples and notation of combined XA ligand to M coordinating units.	140
<b>Figure 5-4</b>	Example and notation for BA ligands coordinating to M. There are 5 coordinating BA ligands in total. One of these coordinates in the bidentate halide carbonyl A2 form, two in the bidentate carbonyl carbonyl B2 form and two in the monodentate C1 form.	141
<b>Figure 5-5</b>	XA ligand and M ions form MXA chains linked by (i) 2(A2) units (ii) 2(B2) units (iii) B2 and E1 units	142
<b>Figure 5-6</b>	(i) M...M chain composed of alternating D4 units (ii) two M...M chains composed of D1 units HB together (iii) four M cluster composed of alternating D2 units (iv) M...M chain composed of alternating D2 and D4 units.	143
<b>Figure 5-7</b>	$K^+(C_6O_4Br_2H)^-$ environment of (i) half protonated $HBA^-$ molecule (ii) $K^+$ ion.	145
	Figure 5-8 $K^+(C_6O_4Br_2H)^-$ . Intersection of the two identical sets of planes along the diagonals of the unit cell (red and blue), Viewed along the a-axis.	146
<b>Figure 5-9</b>	Angle at which the carbon ring of the $HBA^-$ molecule cuts the plane along the diagonal of the unit cell.	147
<b>Figure 5-10</b>	$K^+(C_6O_4Br_2H)^-$ viewed (i) perpendicular to and (ii) along the two identical planes. The two planes intersect along the $K^+$ chains; so that on one $HBA^-$ plane the $K^+$ chains are enclosed by the hydroxyl groups and on the other the $O^-$ atoms.	147
<b>Figure 5-11</b>	$K...K$ chains showing the oxygen coordination and hydrogen bonding.	148
<b>Figure 5-12</b>	$K^+(C_6O_4Br_2H)^-$ HB and oxygen-oxygen interactions.	149
<b>Figure 5-13</b>	$2K^+(C_6O_4Br_2H_2)(C_6O_4Br_2)^{2-}$ environment of (i) fully deprotonated $BA^{2-}$ molecule (ii) fully protonated $H_2BA$ molecule (iii) $K^+$ ion	150
<b>Figure 5-14</b>	$2K^+(C_6O_4Br_2H_2)(C_6O_4Br_2)^{2-}$ Intersection of two identical sets of $H_2BA$ planes along the diagonals of the unit cell, (red and blue), plus additional intersecting $BA^{2-}$ plane (yellow). Viewed along c-axis.	151
<b>Figure 5-15</b>	$2K^+(C_6O_4Br_2H_2)(C_6O_4Br_2)^{2-}$ The carbon rings of the (i) $H_2BA$ and (ii) identical intersecting $H_2BA$ planes, (iii) intersecting $BA^{2-}$ plane, cut the planes along the symmetry element.	152
<b>Figure 5-16</b>	$2K^+(C_6O_4Br_2H_2)(C_6O_4Br_2)^{2-}$ Intersecting (i) blue, (ii) red and (iii) yellow planes as viewed along the b-axis.	152
<b>Figure 5-17</b>	$2K^+(C_6O_4Br_2H_2)(C_6O_4Br_2)^{2-}$ . The $BA^{2-}$ plane as viewed along the c-axis (left) and perpendicular to the c-axis (right).	153
<b>Figure 5-18</b>	$2K^+(C_6O_4Br_2H_2)(C_6O_4Br_2)^{2-}$ . Out of phase waves representing the $H_2BA$ plane.	153
<b>Figure 5-19</b>	$2K^+(C_6O_4Br_2H_2)(C_6O_4Br_2)^{2-}$ (i) Out of phase waves, (ii) $BA^{2-}$ plane.	154
<b>Figure 5-20</b>	$2K^+(C_6O_4Br_2H_2)(C_6O_4Br_2)^{2-}$ . The short $K...K$ distances and HBs.	155
<b>Figure 5-21</b>	$2K^+(C_6O_4Br_2H_2)(C_6O_4Br_2)^{2-}$ HB and halogen interactions.	156
<b>Figure 5-22</b>	$2K^+(C_6O_4Br_2H_2)(C_6O_4Br_2)^{2-}$ structure (i) viewed along b axis (ii) staggered alignment of $BA^{2-}$ molecules.	157
<b>Figure 5-23</b>	$2K^+(C_6O_4Br_2)^{2-} \cdot 2H_2O$ Form I, environment of (i) $BA^{1-}$ and (ii) $BA^{2-}$ .	159
<b>Figure 5-24</b>	$2K^+(C_6O_4Br_2)^{2-} \cdot 2H_2O$ form I BHBs (i) single donor double acceptor DHAA (ii) double donor and single acceptor DDHHA.	159

<b>Figure 5-25.</b>	$2K^+(C_6O_4Br_2)^{2-} \cdot 2H_2O$ Form I BHBs (i) single donor double acceptor DHAA (ii) double donor and single acceptor DDHHA.	160
<b>Figure 5-26</b>	$2K^+(C_6O_4Br_2)^{2-} \cdot 2H_2O$ Form I, environment of (i) $K1^+$ (ii) $K2^+$ (iii) $K3^+$ and (iv) $K4^+$ .161	
<b>Figure 5-27</b>	$K^+(C_6O_4Br_2)^{2-} \cdot 2H_2O$ structure viewed along (i) <i>a</i> -axis (ii) <i>b</i> -axis and (iii) <i>a</i> -diagonal.	162
<b>Figure 5-28</b>	$2K^+(C_6O_4Br_2)^{2-} \cdot 2H_2O$ composed of an extended cluster of two $BA1^{2-}$ and two $BA2^{2-}$ molecules centred around two $K1^+$ ions.	163
<b>Figure 5-29</b>	The $2K^+(C_6O_4Br_2)^{2-} \cdot 2H_2O$ , extended cluster can be split into two symmetry equivalent and identical planes. $K^+$ ions and H atoms omitted for clarity.	163
<b>Figure 5-30</b>	The $2K^+(C_6O_4Br_2)^{2-} \cdot 2H_2O$ , form I extended cluster can be split into two symmetry equivalent and identical planes. H atoms omitted for clarity.	164
<b>Figure 5-31</b>	$2K^+(C_6O_4Br_2)^{2-} \cdot 2H_2O$ form I, angles at which the $BA1^{2-}$ (red) and $BA2^{2-}$ (blue) molecules cross the same plane.	165
<b>Figure 5-32</b>	$2K^+(C_6O_4Br_2)^{2-} \cdot 2H_2O$ form I, (i) $K1 \cdots K1$ chain and (ii) $K2 \cdots K4$ chain.	165
<b>Figure 5-33</b>	$2K^+(C_6O_4Br_2)^{2-} \cdot 2H_2O$ form I (i) intersection of $K1 \cdots K1$ and $K2 \cdots K4$ chains (ii) points of interaction (iii) via $O10 \cdots O9$ HBs and $K1 \cdots K4$ interactions.	166
<b>Figure 5-34</b>	$2K^+(C_6O_4Br_2)^{2-} \cdot 2H_2O$ form I $K3 \cdots K3$ chain, and interaction with other $K3 \cdots K3$ chains via the $O12 \cdots O11$ , and potential $O12 \cdots O7$ HBs of the water molecules in between the chains, and an additional $K3 \cdots K3$ interaction of 5.406Å.	167
<b>Figure 5-35</b>	$2K^+(C_6O_4Br_2)^{2-} \cdot 2H_2O$ form I, (i) Interaction of $K2 \cdots K4$ and $K3 \cdots K3$ chains along the <i>c</i> axis via (ii) potential $O12 \cdots O7$ HB interaction (blue dashed), the $O \cdots O$ and $O \cdots O$ HBs and further $K2 \cdots K3$ and $K3 \cdots K4$ interactions.	168
<b>Figure 5-36</b>	Intersection of $K1 \cdots K1$ and $K2 \cdots K4$ chains along (i) <i>a</i> - (ii) <i>b</i> - and (iii) <i>c</i> - axes.	169
<b>Figure 5-37</b>	Intersection of $K2 \cdots K4$ and $K3 \cdots K3$ chains along (i) <i>a</i> - (ii) <i>b</i> - and (iii) <i>c</i> - axes.	169
<b>Figure 5-38</b>	Intersection of $K3 \cdots K3$ with adjacent $K3 \cdots K3$ chains along (i) <i>a</i> - (ii) <i>b</i> - and (iii) <i>c</i> - axes.	169
<b>Figure 5-39</b>	Superimposed interactions and intersections of $K1 \cdots K1$ and $K2 \cdots K4$ chains, $K2 \cdots K4$ and $K3 \cdots K3$ chains and $K3 \cdots K3$ and adjacent $K3 \cdots K3$ chains, along (i) <i>a</i> - (ii) <i>b</i> - and (iii) <i>c</i> - axes.	170
<b>Figure 5-40</b>	$2K^+(C_6O_4Br_2)^{2-} \cdot 2H_2O$ form I, along (i) <i>a</i> - (ii) <i>b</i> - and (iii) <i>c</i> - axes.	170
<b>Figure 5-41</b>	$2K^+(C_6O_4Br_2)^{2-} \cdot 2H_2O$ Form II. Images from the data collection showing strong diffuse scattering.	171
<b>Figure 5-42</b>	$2K^+(C_6O_4Br_2)^{2-} \cdot 2H_2O$ Form II. Environments of the (i) $BA^{2-}$ and (ii) $K^+$ ion.	172
<b>Figure 5-43</b>	$2K^+(C_6O_4Br_2)^{2-} \cdot 2H_2O$ Form II. Structure viewed along (i) <i>a</i> - (ii) <i>b</i> - and (iii) <i>c</i> - axes.	173
<b>Figure 5-44</b>	$2K^+(C_6O_4Br_2)^{2-} \cdot 2H_2O$ Form II Two identical stacking planes, viewed (i) perpendicular and (ii) along planes.	174
<b>Figure 5-45</b>	$2K^+(C_6O_4Br_2)^{2-} \cdot 2H_2O$ Form II Potentially significant Interaction bond lengths.	174
<b>Figure 5-46</b>	$2K^+(C_6O_4Br_2)^{2-} \cdot 2H_2O$ Form II $K \cdots K$ chains composed of alternating D4 and D2 units, connected by further $K \cdots K$ D1 unit to form double chains that run through <i>c</i> axis.	175
<b>Figure 5-47</b>	$2K^+(C_6O_4Br_2)^{2-} \cdot 2H_2O$ Form III Environments of (i) $BA^{2-}$ molecule (ii) $K^+$ ion.	175

<b>Figure 5-48.</b>	$2K^+.(C_6O_4Br_2)^{2-} \cdot 2H_2O$ Form III Structure viewed along (i) <i>a</i> - (ii) <i>b</i> - and (iii) <i>c</i> - axes.	176
<b>Figure 5-49</b>	$2K^+.(C_6O_4Br_2)^{2-} \cdot 2H_2O$ Form III BA planes composed of alternating chains of BA molecules and $K^+$ ion connected by water molecules.	177
<b>Figure 5-50</b>	$2K^+.(C_6O_4Br_2)^{2-} \cdot 2H_2O$ Form III $Br \cdots Br$ interactions.	177
<b>Figure 5-51</b>	$2K^+.(C_6O_4Br_2)^{2-} \cdot 2H_2O$ Form III. Every second BA chain cuts the plane at the same angle however a different orientation to the preceding chain.	178
<b>Figure 5-52</b>	$2K^+.(C_6O_4Br_2)^{2-} \cdot 2H_2O$ Form III. $K \cdots K$ chains.	178
<b>Figure 5-53</b>	$BA^{2-}$ and $K^+$ planes point of intersection.	179
<b>Figure 5-54</b>	Comparison of $BA^{2-}$ environments and interaction distances in (i) KBA and RbBA and (ii) RbBA and CsBA complexes. KBA (black), RbBA (red), CsBA (blue).	190
<b>Figure 5-55</b>	Comparison of $M^+$ environments and interaction distances in (i) KBA and RbBA and (ii) RbBA and CsBA complexes. KBA (black), RbBA (red), CsBA (blue).	191
<b>Figure 5-56</b>	$2M^+(C_6O_4Cl_2)^{2-} \cdot H_2O$ Isomorphous structures ( $M = K, Rb$ ); environment of (i) $CA^{2-}$ molecule and (ii) $M^+$ ion.	195
<b>Figure 5-57</b>	$2M^+(C_6O_4Cl_2)^{2-} \cdot H_2O$ Isomorphous structures ( $M = K, Rb$ ), viewed along (i) <i>a</i> - (ii) <i>b</i> - and (iii) <i>c</i> - axes.	196
<b>Figure 5-58</b>	$2M^+(C_6O_4Cl_2)^{2-} \cdot H_2O$ Isomorphous structures ( $M = K, Rb$ ), $CA^{2-}$ plane viewed along (i) <i>a</i> - (ii) <i>b</i> - and (iii) <i>c</i> - axes. $M^+$ ions and water molecules excluded for clarity.	197
<b>Figure 5-59</b>	$2M^+(C_6O_4Cl_2)^{2-} \cdot H_2O$ isomorphous structures ( $M = K, Rb$ ), Two alternating $CA^{2-}$ planes viewed along (i) <i>a</i> - (ii) <i>b</i> - and (iii) <i>c</i> - axes. $M^+$ ions and water molecules excluded for clarity.	198
<b>Figure 5-60</b>	$2M^+(C_6O_4Cl_2)^{2-} \cdot H_2O$ isomorphous structures ( $M = K, Rb$ ), (i) D4 and D2 + 2HB units comprising (ii) $M^+$ chains, joined to adjacent chains via the two additional D1 + HB and D1 M-M interactions.	198
<b>Figure 5-61</b>	$2M^+(C_6O_4Cl_2)^{2-} \cdot H_2O$ isomorphous structures ( $M = K, Rb$ ), composed of intersection of two alternating $CA^{2-}$ planes (red and blue) and $M^+$ planes , and viewed along (i) <i>a</i> - (ii) <i>b</i> - and (iii) <i>c</i> - axes.	199
<b>Figure 5-62</b>	$2M^+(C_6O_4Cl_2)^{2-} \cdot H_2O$ isomorphous structures ( $M = K, Rb$ ), illustration of the O3–H1...O2 HBs between the two differently (red and blue) orientated columns of $CA^{2-}$ molecules within the CA planes.	200
<b>Figure 5-63</b>	$2M^+(C_6O_4Cl_2)^{2-} \cdot H_2O$ Isomorphous structures ( $M = K, Rb$ ), Comparison of KCA (black) and RbCA (red) complexes; overlay of (i) $CA^{2-}$ molecules (ii) $M^+$ planes connected by the O3w HBs and (iii) two $CA^{2-}$ molecules connected by the O3w HBs.	202
<b>Figure 5-64</b>	$M^+(C_6O_4Cl_2H)^- \cdot 2H_2O$ ( $M = Rb, Cs$ ) isomorphous structures; environment of (i) $HCA^-$ molecule and (ii) $M^+$ ion.	204
<b>Figure 5-65</b>	$M^+(C_6O_4Cl_2H)^- \cdot 2H_2O$ ( $M = Rb, Cs$ ) isomorphous structures, bifurcated HB.	205
<b>Figure 5-66</b>	$M^+(C_6O_4Cl_2H)^- \cdot 2H_2O$ ( $M = Rb, Cs$ ) isomorphous structures, viewed along <i>a</i> -, <i>b</i> -, and <i>c</i> - axes.	206
<b>Figure 5-67</b>	$M^+(C_6O_4Cl_2H)^- \cdot 2H_2O$ ( $M = Rb, Cs$ ) isostructures, $HCA^-$ planes viewed along the (i) <i>a</i> -, (ii) <i>b</i> - and (iii) <i>c</i> - axes. $M^+$ ions excluded for clarity. Significant $Cl \cdots Cl$ , $Cl \cdots O$ and $O \cdots O$ interactions are indicated.	207
<b>Figure 5-68</b>	$M^+(C_6O_4Cl_2H)^- \cdot 2H_2O$ ( $M = Rb, Cs$ ) isomorphous structures, $HCA^-$ planes with connecting $M^+$ ions, viewed along (i) <i>a</i> -, (ii) <i>b</i> - and (iii) <i>c</i> - axes.	208

<b>Figure 5-69</b>	$M^+(C_6O_4Cl_2H)^- \cdot 2H_2O$ (M = Rb, Cs) isomorphous structures, inversely related alternating HCA <sup>-</sup> planes (red and blue) viewed along (i) <i>a</i> -, (ii) <i>b</i> - and (iii) <i>c</i> - axes. M <sup>+</sup> ions excluded for clarity.	208
<b>Figure 5-70</b>	$M^+(C_6O_4Cl_2H)^- \cdot 2H_2O$ (M = Rb, Cs) isostructures, M <sup>+</sup> ions planes, viewed along (i) <i>a</i> -, (ii) <i>b</i> - and (iii) <i>c</i> - axes.	209
<b>Figure 5-71</b>	$M^+(C_6O_4Cl_2H)^- \cdot 2H_2O$ (M = Rb, Cs) isomorphous structures, (i) M <sup>+</sup> chains composed of a D2 +2HB and a 2HB unit, (ii) joined together via a HB and 2HB unit to make M <sup>+</sup> planes.	210
<b>Figure 5-72</b>	$M^+(C_6O_4Cl_2H)^- \cdot 2H_2O$ (M = Rb, Cs) isomorphous structures, M <sup>+</sup> and HCA <sup>-</sup> repeating cluster unit (i) point of intersection for two inversely orientated HCA <sup>-</sup> planes (red, blue) (ii) comprised of two M <sup>+</sup> ions and two HCA <sup>-</sup> molecules related by inversion centre.	211
<b>Figure 5-73</b>	$M^+(C_6O_4Cl_2H)^- \cdot 2H_2O$ (M = Rb, Cs) isomorphous structures, M <sup>+</sup> and HCA <sup>-</sup> repeating cluster unit viewed along (i) <i>a</i> -, (ii) <i>b</i> - and (iii) <i>c</i> - axes.	212
<b>Figure 5-74</b>	$M^+(C_6O_4Cl_2H)^- \cdot 2H_2O$ (M = Rb, Cs) isomorphous structures, interactions between repeating cluster unit (i) at point of intersection for two inversely orientated HCA <sup>-</sup> planes (red, blue) (ii) comprised of two HCA <sup>-</sup> molecules and significant interactions related by inversion centre.	212
<b>Figure 5-75</b>	$M^+(C_6O_4Cl_2H)^- \cdot 2H_2O$ (M = Rb, Cs) isomorphous structures; interactions between repeating cluster unit as viewed along (i) <i>a</i> -, (ii) <i>b</i> -, and (iii) <i>c</i> - axes.	213
<b>Figure 5-76</b>	$M^+(C_6O_4Cl_2H)^- \cdot 2H_2O$ (M = Rb, Cs) isomorphous structures, inversely related alternating HCA <sup>-</sup> planes (red and blue) viewed along (i) <i>a</i> -, (ii) <i>b</i> - and (iii) <i>c</i> - axes.	213
<b>Figure 5-77</b>	$M^+(C_6O_4Cl_2H)^- \cdot 2H_2O$ (M = Rb, Cs) isomorphous structures. Comparison of RbCA (red) and CsCA (blue) complexes; overlay of (i) HCA <sup>-</sup> molecules (ii) M <sup>+</sup> and HCA <sup>-</sup> clusters, and (iii) interactions between M <sup>+</sup> and HCA <sup>-</sup> clusters.	215
<b>Figure 5-78</b>	$2M^+ 2(C_6O_4Cl_2H)^- (C_6O_4Cl_2H_2) 6H_2O$ (M= Rb, Cs) isomorphous structures; environments of the (i) H <sub>2</sub> CA molecule with inversion centre, (ii) HCA <sup>-</sup> molecule and (iii) M <sup>+</sup> ion.	218
<b>Figure 5-79</b>	$2M^+ 2(C_6O_4Cl_2H)^- (C_6O_4Cl_2H_2) 6H_2O$ (M= Rb, Cs) isomorphous structures, viewed along (i) <i>a</i> -, (ii) <i>b</i> - and (iii) <i>c</i> - axes.	220
<b>Figure 5-80</b>	$2M^+ 2(C_6O_4Cl_2H)^- (C_6O_4Cl_2H_2) 6H_2O$ (M= Rb, Cs) isomorphous structures; three alternating CA planes of the form ABCABC... (red, blue, green), viewed along (i) <i>a</i> -, (ii) <i>b</i> - and (iii) <i>c</i> - axes.	220
<b>Figure 5-81</b>	$2M^+ 2(C_6O_4Cl_2H)^- (C_6O_4Cl_2H_2) 6H_2O$ (M= Rb, Cs) isomorphous structures; interactions within two identical HCA <sup>-</sup> planes (blue), inversely related through symmetry, viewed along (i) <i>c</i> -, (ii) <i>a</i> - and (iii) <i>b</i> - axes.	221
<b>Figure 5-82</b>	$2M^+ 2(C_6O_4Cl_2H)^- (C_6O_4Cl_2H_2) 6H_2O$ (M= Rb, Cs) isomorphous structures; interactions within two identical HCA <sup>-</sup> planes (red), inversely related through symmetry, viewed along (i) <i>c</i> -, (ii) <i>a</i> - and (iii) <i>b</i> - axes.	222
<b>Figure 5-83</b>	$2M^+ 2(C_6O_4Cl_2H)^- (C_6O_4Cl_2H_2) 6H_2O$ (M= Rb, Cs) isomorphous structures, three alternating CA planes of the form ABCABC... (red, blue, green), and M <sup>+</sup> chains, viewed along (i) <i>a</i> -, (ii) <i>b</i> - and (iii) <i>c</i> - axes.	222
<b>Figure 5-84</b>	$2M^+ 2(C_6O_4Cl_2H)^- (C_6O_4Cl_2H_2) 6H_2O$ (M= Rb, Cs) isomorphous structures; (i) D2 + 2HB and 4HB M-M units, (ii) plus O5-O6 interaction, comprising (ii) M <sup>+</sup> chains.	223

<b>Figure 5-85</b>	$2M^+ 2(C_6O_4Cl_2H)^- (C_6O_4Cl_2H_2) 6H_2O$ (M= Rb, Cs) isomorphous structures, $M^+$ and $HCA^-$ repeating cluster unit (i) point of intersection for two inversely orientated $HCA^-$ planes (red, blue) (ii) comprised of two $M^+$ ions and two $HCA^-$ molecules related by inversion centre.	224
<b>Figure 5-86</b>	$2M^+ 2(C_6O_4Cl_2H)^- (C_6O_4Cl_2H_2) 6H_2O$ (M= Rb, Cs) isostructures, $H_2CA$ planes (green) viewed along (i) $c^-$ , (ii) $a^-$ and (iii) $b^-$ axes.	225
<b>Figure 5-87</b>	$2M^+ 2(C_6O_4Cl_2H)^- (C_6O_4Cl_2H_2) 6H_2O$ (M= Rb, Cs) isomorphous structures, $H_2CA$ planes (green) viewed along (i) $c^-$ , (ii) $a^-$ and (iii) $b^-$ axes.	226
<b>Figure 5-88</b>	$2M^+ 2(C_6O_4Cl_2H)^- (C_6O_4Cl_2H_2) 6H_2O$ (M= Rb, Cs) isomorphous structures, $H_2CA$ planes (green) viewed along (i) $c^-$ , (ii) $a^-$ and (iii) $b^-$ axes.	227
<b>Figure 5-89</b>	$2M^+ 2(C_6O_4Cl_2H)^- (C_6O_4Cl_2H_2) 6H_2O$ (M= Rb, Cs) isostructures, $H_2CA$ planes (green) viewed along (i) $c^-$ , (ii) $a^-$ and (iii) $b^-$ axes.	227
<b>Figure 5-90</b>	$2Li^+ (C_6O_4Cl_2)^{2-} H_2O$ environment of (i) $CA^{2-}$ molecule and (ii) $Li^+$ ion.	233
<b>Figure 5-91</b>	$2Li^+ (C_6O_4Cl_2)^{2-} H_2O$ and $2Li^+ (C_6O_4Br_{1.25}Cl_{0.75})^{2-} H_2O$ $CA^{2-}$ planes viewed (i) perpendicular to $bc$ plane and at angles at which plane cuts the (ii) $b^-$ and (iii) $c^-$ axes.	234
<b>Figure 5-92</b>	$2Li^+ (C_6O_4Cl_2)^{2-} H_2O$ and $2Li^+ (C_6O_4Br_{1.25}Cl_{0.75})^{2-} H_2O$ angle at which $CA^{2-}$ molecules cut the plane.	235
<b>Figure 5-93</b>	$2Li^+ (C_6O_4Cl_2)^{2-} H_2O$ and $2Li^+ (C_6O_4Br_{1.25}Cl_{0.75})^{2-} H_2O$ alternating $CA^{2-}$ planes, rotated $180^\circ$ along $b^-$ axis with respect to one another.	236
<b>Figure 5-94</b>	$2Li^+ (C_6O_4Cl_2)^{2-} H_2O$ (i) D1 + HB units (ii) $Li^+$ chains in individual $CA^{2-}$ planes, joined together via (iii) short D1 unit and 2HB unit to form larger $Li^+$ chain that coordinates two alternating $CA^{2-}$ planes.	237
<b>Figure 5-95</b>	$2Li^+ (C_6O_4Cl_2)^{2-} H_2O$ . Large $Li^+$ chains that coordinate two alternating $CA^{2-}$ planes, as viewed along the (i) $a^-$ , (ii) $b^-$ and (iii) $c^-$ axes.	237
<b>Figure 5-96</b>	$2Li^+ (C_6O_4Cl_2)^{2-} H_2O$ . Point of intersection between $CA^{2-}$ planes and $Li^+$ chains.	238
<b>Figure 5-97</b>	$2Li^+ (C_6O_4Cl_2)^{2-} (C_6O_4Cl_2H_2) 2H_2O$ environment of (i) $CA^{2-}$ molecule (ii) $H_2CA$ molecule and (iii) $Li^+$ ion.	241
<b>Figure 5-98</b>	$2Li^+ (C_6O_4Cl_2)^{2-} (C_6O_4Cl_2H_2) 2H_2O$ structure viewed along (i) $a^-$ (ii) $b^-$ and $c^-$ axis.	242
<b>Figure 5-99</b>	$2Li^+ (C_6O_4Cl_2)^{2-} (C_6O_4Cl_2H_2) 2H_2O$ structure viewed (i) perpendicular to plane and as it cuts the (ii) $b^-$ and (iii) $c^-$ axes.	243
<b>Figure 5-100</b>	$2Li^+ (C_6O_4Cl_2)^{2-} (C_6O_4Cl_2H_2) 2H_2O$ angles at which $CA^{2-}$ and $H_2CA$ molecules cut the plane.	243
<b>Figure 5-101</b>	$2Li^+ (C_6O_4Cl_2)^{2-} (C_6O_4Cl_2H_2) 2H_2O$ , $CA$ planes viewed in terms of interconnecting wavy chains (orange and black).	244
<b>Figure 5-102</b>	$2Li^+ (C_6O_4Cl_2)^{2-} (C_6O_4Cl_2H_2) 2H_2O$ , Interactions within and between interconnecting wavy chains (orange and black) in $CA$ planes.	244
<b>Figure 5-103</b>	$2Li^+ (C_6O_4Cl_2)^{2-} (C_6O_4Cl_2H_2) 2H_2O$ , (i) D1 $Li \cdots Li$ chains and (ii) 2HB $Li \cdots Li$ units comprising (iii) interacting D1 chains.	245
<b>Figure 5-104</b>	$2Li^+ (C_6O_4Cl_2)^{2-} (C_6O_4Cl_2H_2) 2H_2O$ , interaction of $CA^{2-}$ molecules within $CA$ rows and adjacent planes via the interacting $Li^+$ chains.	246
<b>Figure 5-105</b>	$2Na^+ (C_6O_4Br_2)^{2-} 4H_2O$ environment of (i) $BA^{2-}$ (ii) $Na^{1+}$ ion and (ii) $Na^{2+}$ ion.	248
<b>Figure 5-106</b>	$2Na^+ (C_6O_4Br_2)^{2-} 4H_2O$ structure as viewed along the (i) $a^-$ , (ii) $b^-$ , and (iii) $c^-$ axes.	249

<b>Figure 5-107</b>	$2\text{Na}^+(\text{C}_6\text{O}_4\text{Br}_2)^{2-} \cdot 4\text{H}_2\text{O}$ structure composed of $\text{BA}^{2-}$ planes that lie along the ac plane, as viewed along the (i) <i>a</i> -, (ii) <i>b</i> -, and (iii) <i>c</i> -axes.	250
<b>Figure 5-108</b>	$2\text{Na}^+(\text{C}_6\text{O}_4\text{Br}_2)^{2-} \cdot 4\text{H}_2\text{O}$ structure composed of $\text{Na}^+$ chains that lie along the ac plane, as viewed along the (i) <i>a</i> -, (ii) <i>b</i> -, and (iii) <i>c</i> -axes.	250
<b>Figure 5-109</b>	$2\text{Na}^+(\text{C}_6\text{O}_4\text{Br}_2)^{2-} \cdot 4\text{H}_2\text{O}$ $\text{BA}^{2-}$ planes viewed (i) perpendicular to the plane and the angle at which the plane cuts the (ii) <i>b</i> - and (iii) <i>c</i> -axes.	251
<b>Figure 5-110</b>	$2\text{Na}^+(\text{C}_6\text{O}_4\text{Br}_2)^{2-} \cdot 4\text{H}_2\text{O}$ $\text{BA}^{2-}$ planes composed of rows of $\text{BA}^{2-}$ molecules (orange and black) connected to one another by $\text{Na}^+$ ions.	251
<b>Figure 5-111</b>	$2\text{Na}^+(\text{C}_6\text{O}_4\text{Br}_2)^{2-} \cdot 4\text{H}_2\text{O}$ Interactions between rows of $\text{BA}^{2-}$ molecules (orange and black) within $\text{BA}^{2-}$ planes.	252
<b>Figure 5-112</b>	$2\text{Na}^+(\text{C}_6\text{O}_4\text{Br}_2)^{2-} \cdot 4\text{H}_2\text{O}$ (i) $\text{D}_2 + \text{HB Na}_1 \cdots \text{Na}_2$ (ii) $\text{D}_2 + 2\text{HB Na}_2 \cdots \text{Na}_2$ and (iii) $4\text{HB Na}_1 \cdots \text{Na}_1$ units that comprise (iv) $\text{Na}^+$ chains.	253
<b>Figure 5-113</b>	$2\text{Na}^+(\text{C}_6\text{O}_4\text{Br}_2)^{2-} \cdot 4\text{H}_2\text{O}$ alternating $\text{Na}^+$ chains flipped $180^\circ$ with respect to one another in order to interact and form $\text{Na}^+$ planes.	254
<b>Figure 5-114</b>	$2\text{Na}^+(\text{C}_6\text{O}_4\text{Br}_2)^{2-} \cdot 4\text{H}_2\text{O}$ (i) interaction point of alternating $\text{Na}^+$ chains (ii) split into repeating units within which are two inversion centres (iii) between two $4\text{HB Na}_1 \cdots \text{Na}_2$ units and (iv) and between the $\text{Na}^+$ ions within a $\text{Na}_1 \cdots \text{Na}_1$ $4\text{HB}$ unit.	254
<b>Figure 5-115</b>	$2\text{Na}^+(\text{C}_6\text{O}_4\text{Br}_2)^{2-} \cdot 4\text{H}_2\text{O}$ Planes of $\text{BA}^{2-}$ molecules connected by (i) the two $4\text{HB Na}_1 \cdots \text{Na}_2$ units and (ii) the $\text{Na}^+$ ions within a $\text{Na}_1 \cdots \text{Na}_1$ $4\text{HB}$ unit.	255
<b>Figure 5-116</b>	$2\text{Na}^+(\text{C}_6\text{O}_4\text{Cl}_2)^{2-} \cdot 3\text{H}_2\text{O}$ environment of (i) $\text{CA}^{2-}$ molecule (ii) $\text{Na}^+$ ion and (iii) $\text{Na}_2^+$ ion.	256
<b>Figure 5-117</b>	$2\text{Na}^+(\text{C}_6\text{O}_4\text{Cl}_2)^{2-} \cdot 3\text{H}_2\text{O}$ structure as viewed along the (i) <i>a</i> - (ii) <i>b</i> - and <i>c</i> - axes.	257
<b>Figure 5-118</b>	$2\text{Na}^+(\text{C}_6\text{O}_4\text{Cl}_2)^{2-} \cdot 3\text{H}_2\text{O}$ structure $\text{CA}^{2-}$ planes as viewed along the (i) <i>a</i> - (ii) <i>b</i> - and <i>c</i> - axes.	258
<b>Figure 5-119</b>	$2\text{Na}^+(\text{C}_6\text{O}_4\text{Cl}_2)^{2-} \cdot 3\text{H}_2\text{O}$ structure $\text{Na}^+$ planes as viewed along the (i) <i>a</i> - (ii) <i>b</i> - and <i>c</i> - axes.	258
<b>Figure 5-120</b>	$2\text{Na}^+(\text{C}_6\text{O}_4\text{Cl}_2)^{2-} \cdot 3\text{H}_2\text{O}$ $\text{CA}^{2-}$ planes viewed along (i) <i>a</i> -axis which is perpendicular to plane and angle at which cuts the (ii) <i>b</i> - and <i>c</i> - axes.	259
<b>Figure 5-121</b>	$2\text{Na}^+(\text{C}_6\text{O}_4\text{Cl}_2)^{2-} \cdot 3\text{H}_2\text{O}$ rows of $\text{CA}^{2-}$ molecules (orange and black) within $\text{CA}^{2-}$ planes.	259
<b>Figure 5-122</b>	$2\text{Na}^+(\text{C}_6\text{O}_4\text{Cl}_2)^{2-} \cdot 3\text{H}_2\text{O}$ interactions between rows of $\text{CA}^{2-}$ molecules (orange and black) within $\text{CA}^{2-}$ planes.	260
<b>Figure 5-123</b>	$2\text{Na}^+(\text{C}_6\text{O}_4\text{Cl}_2)^{2-} \cdot 3\text{H}_2\text{O}$ (i) $\text{D}_2 + 2\text{HB}$ , (ii) $\text{D}_2 + \text{HB}$ (iii) $\text{D}_2 + 2\text{HB Na-Na}$ interaction units arranged in ABACAB fashion to form (iv) $\text{Na}^+$ chains.	261
<b>Figure 5-124</b>	$2\text{Na}^+(\text{C}_6\text{O}_4\text{Cl}_2)^{2-} \cdot 3\text{H}_2\text{O}$ $\text{Na}^+$ ion chains interact to form $\text{Na}^+$ ion planes that run along ac plane, as viewed along (i) <i>a</i> - (ii) <i>b</i> - (iii) and <i>c</i> axes.	262
<b>Figure 5-125</b>	$2\text{Na}^+(\text{C}_6\text{O}_4\text{Cl}_2)^{2-} \cdot 3\text{H}_2\text{O}$ interactions between adjacent $\text{Na}^+$ ion chains (red and blue).	262
<b>Figure 5-126</b>	$2\text{Na}^+(\text{C}_6\text{O}_4\text{Cl}_2)^{2-} \cdot 3\text{H}_2\text{O}$ (i) Additional $\text{Na} \cdots \text{Na}$ interactions between adjacent $\text{Na}^+$ ion chains (ii) highlighted in black (iii) $\text{Na}_1 \cdots \text{Na}_1$ $2\text{HB}$ unit and (iv) $\text{Na}_2 \cdots \text{Na}_2$ $2\text{HB}$ unit. Both units have a centre of inversion in the middle of the $\text{Na} \cdots \text{Na}$ contact distance.	263
<b>Figure 5-127</b>	$2\text{Na}^+(\text{C}_6\text{O}_4\text{Cl}_2)^{2-} \cdot 3\text{H}_2\text{O}$ Points of intersection of the alternating/reversed $\text{CA}^{2-}$ planes and $\text{Na}^+$ chains at (i) $\text{Na}_1 \cdots \text{Na}_1$ $2\text{HB}$ unit and (ii) $\text{Na}_2 \cdots \text{Na}_2$ $2\text{HB}$ unit.	264

<b>Figure 6-1</b>	(i) Stereoscopic views of the HDC <sup>-</sup> anion; <sup>195</sup> (J) and (M) refer to the two non equivalent crotonate residues (ii) K <sup>+</sup> coordination and HDC <sup>-</sup> contacts: HB (dotted lines) and ionic contacts (broken lines). The authors have identified some centres of inversion by asterisks.	272
<b>Figure 6-2</b>	KHDC at 40 K and ambient pressure showing (i) HDC <sup>-</sup> anion and (ii) K <sup>+</sup> ion coordinated to blue HDC <sup>-</sup> by O2 and O4, red by O1 and O3, green by O3 and yellow by O4.	273
<b>Figure 6-3</b>	The packing of KHDC at 40 K and ambient pressure, (i) view perpendicular to HDC <sup>-</sup> plane and viewed along (ii) a- and (iii) b- axes.	274
<b>Figure 6-4</b>	KHDC, HDC <sup>-</sup> planes viewed along the (i) a- (ii) b- and (iii) c -axes.	275
<b>Figure 6-5</b>	The K <sup>+</sup> ion coordination in KDHC; (i) chains composed of alternating D2 units; (ii) coordination to adjacent chains via the asymmetric O2-H1...O3 HB; and (iii) point of intersection of HDC <sup>-</sup> and K <sup>+</sup> ions planes.	275
<b>Figure 6-6</b>	KHDC, K <sup>+</sup> planes viewed along the (i) a- (ii) b- and (iii) c -axes.	276
<b>Figure 6-7</b>	KHDC, superimposed HDC <sup>-</sup> and K <sup>+</sup> planes viewed along the (i) a- (ii) b- and (iii) c- axes to produce resulting KHDC structure in three dimensions.	276
<b>Figure 6-3</b>	Comparison of HDC <sup>-</sup> anion and surrounding K <sup>+</sup> ions at 40 K; (i) 0 and 2.4 kbar; (ii) 2.4 and 4.8 kbar; (iii) 0 and 4.8 kbar; and (iv) 0, 2.4 and 4.8 kbar. <u>Key</u> : 0kbar (black), 2.4kbar (red), 4.8kbar (blue).	280
<b>Figure 6-9</b>	Comparison of K <sup>+</sup> ion chains at 40 K; (i) 0 and 2.4 kbar; (ii) 2.4 and 4.8 kbar; (iii) 0 and 4.8 kbar; and (iv) 0, 2.4 and 4.8 kbar. <u>Key</u> : 0 kbar (black), 2.4 kbar (red), 4.8 kbar (blue).	281
<b>Figure 6-10</b>	K <sup>+</sup> ion chains, at 40 K and 0, 2.4 and 4.8 kbar, viewed along (i) a- (ii) b- and (iii) c- axes. <u>Key</u> : 0 kbar (black), 2.4 kbar (red), 4.8 kbar (blue).	281

## LIST OF TABLES

<b>Table 1-1:</b>	Classification of HB's into strong, moderate and weak	3
<b>Table 2-1:</b>	The seven crystal systems and fourteen Bravais lattices	40
<b>Table 2-2:</b>	Interband Coulomb and exchange interactions. $U'$ and $J$ as a function of d-orbitals, $\gamma$ and $\gamma$ and expressed in terms of the Racah A, B and C parameters	73
<b>Table 3-1:</b>	PB band gaps obtained for incorporated group one metals, using a range of hybrid functionals by direct SCF calculations. Electron excitation modelled by both movement of $e^-$ between the LS and HS Fe basis sets and also complete switching of basis sets. Band gaps are calculated for $e^-$ movement from the ground state $E_g$ to excited state using ground state coordinates, $E_{ex}$ , ( $E_{ex}-E_g$ ), and also from the ground state $E_g$ to excited state in which the modelled excited state converged after a full geometry optimisation to represent the relaxed excitation state $E_{rel}$ , ( $E_{rel}-E_g$ )	88
<b>Table 3-2:</b>	PY Energy of highest HOMO to lowest LUMO, most populated HOMO to most populated LUMO and lowest HOMO to highest LUMO	91
<b>Table 3-3:</b>	PB Comparison of band gaps from incorporation of different $M^+$ ions	93
<b>Table 3-4:</b>	Band gaps of PY, PB and PW complexes and associated lattice parameters, atom spins and atom Charges	100
<b>Table 4-1:</b>	Effective ionic radii for $TM^{2+}$ ions, as presented in the data of Shannon.	105
<b>Table 4-2:</b>	Experimental and calculated HB binding energies and distances for the isolated $FHF^-$ , $FHCl^-$ and $ClHCl^-$ ligands	105
<b>Table 4-3:</b>	$M^{2+}$ ion FM and AF spin alignments and energies obtained using the nearest neighbour Ising Hamiltonian and two magnetic states	107
<b>Table 4-3:</b>	Cu ion spin alignments and energies obtained using the nearest neighbours Ising Hamiltonian for the four magnetic states	109
<b>Table 4-4:</b>	$J_1$ and $J_2$ values, inclusive of $ \sigma ^2$ , obtained for a range of hybrid functionals using the nearest-neighbour Ising Hamiltonian. Converged wavefunctions were not obtained for $F_0 = 0$	110
<b>Table 4-5:</b>	Cu ion spin alignments and energies obtained using the nearest neighbours Ising Hamiltonian for the four magnetic states	111
<b>Table 4-6:</b>	Full set of J values, inclusive of $ \sigma ^2$ , obtained from a range of hybrid functional within both the nn and nnn Ising Hamiltonians	112
<b>Table 4-7:</b>	Optimised structural parameters ( $\text{\AA}$ ) and J values, inclusive of $ \sigma ^2$ , for model $2K^+[4Cu^{2+}(XHX^-)_6]$ structure and comparable experimental and theoretical Values	114
<b>Table 4-9:</b>	Selected optimised structural parameters ( $\text{\AA}$ ), J values (K) and associated $T_C/T(\chi_{max})$ values for $F_0=100$	118
<b>Table 4-8:</b>	Selected optimised structural parameters ( $\text{\AA}$ ), J values (K) and associated $T_C/T(\chi_{max})$ values for $F_0=70$	118
<b>Table 4-9:</b>	Selected optimised structural parameters ( $\text{\AA}$ ), J values (K) and associated $T_C/T(\chi_{max})$ values for $F_0=50$	118
<b>Table 4-10:</b>	Selected optimised structural parameters ( $\text{\AA}$ ), J values (K) and associated $T_C/T(\chi_{max})$ values for $F_0=30$	118
<b>Table 4-11:</b>	HB Parameters ( $\text{\AA}$ ) and associated J values for optimised, extended and contracted lattice $E(x)$ minima	124

<b>Table 4-12:</b>	Comparison of static J values which do not incorporate proton motion and $\langle J \rangle$ values, and associated eigenstate energies relative to the minimum of the respective potential, for the ground and first excited vibrational states, which do incorporate proton motion	131
<b>Table 5-1</b>	Van der Waals radii of Li, Na and K metal cations and partially negatively charged O, N, Cl and Br anions. No Van der Waals radii quoted for larger Rb, Cs and Ca metals	137
<b>Table 5-2.</b>	Classification of the different coordination motifs.	138
<b>Table 5-3</b>	M...M and X...X Short Contact Distances found in the CSD	144
<b>Table 5-4</b>	Experimental Information for anhydrous KBA complexes	181
<b>Table 5-5</b>	Crystallographic Information for KBA complexes	182
<b>Table 5-6</b>	HB parameters and significant interactions for anhydrous tautomeric KBA	183
<b>Table 5-7</b>	K <sup>+</sup> interactions for anhydrous tautomeric KBA polymorphs.	183
<b>Table 5-8</b>	Significant carbon contact distances for anhydrous tautomeric KBA polymorphs	184
<b>Table 5-9</b>	HB Parameters and Significant Interactions for Hydrated KBA polymorphs	184
<b>Table 5-10</b>	Carbon Contact Distances for Hydrated KBA Complex BA <sup>2-</sup> molecules	185
<b>Table 5-11</b>	M Distances for Hydrated KBA Complex BA <sup>2-</sup> molecules	186
<b>Table 5-12</b>	M Distances for Hydrated KBA Complex BA <sup>2-</sup> molecules	187
<b>Table 0-13</b>	HB parameters and significant interactions for 2M <sup>+</sup> (C <sub>6</sub> O <sub>4</sub> Br <sub>2</sub> ) <sup>2-</sup> 2H <sub>2</sub> O isomorphous structures (M = K, Rb, Cs).	193
<b>Table 0-14</b>	Intra-molecular bond lengths for 2M <sup>+</sup> (C <sub>6</sub> O <sub>4</sub> Br <sub>2</sub> ) <sup>2-</sup> 2H <sub>2</sub> O isomorphous structures (M = K, Rb, Cs).	193
<b>Table 5-15</b>	M Distances for 2M <sup>+</sup> (C <sub>6</sub> O <sub>4</sub> Br <sub>2</sub> ) <sup>2-</sup> 2H <sub>2</sub> O isomorphous structures (M = K, Rb, Cs)	194
<b>Table 5-16</b>	M Distances for 2M <sup>+</sup> (C <sub>6</sub> O <sub>4</sub> Cl <sub>2</sub> ) <sup>2-</sup> H <sub>2</sub> O isomorphous structures (M = K, Rb)	201
<b>Table 5-17</b>	HB parameters and significant interactions for 2M <sup>+</sup> (C <sub>6</sub> O <sub>4</sub> Cl <sub>2</sub> ) <sup>2-</sup> H <sub>2</sub> O isomorphous structures (M = K, Rb).	203
<b>Table 5-18</b>	Intra-molecular bond lengths for 2M <sup>+</sup> (C <sub>6</sub> O <sub>4</sub> Cl <sub>2</sub> ) <sup>2-</sup> H <sub>2</sub> O isomorphous structures (M = K, Rb).	203
<b>Table 5-19</b>	M distances for M <sup>+</sup> (C <sub>6</sub> O <sub>4</sub> Cl <sub>2</sub> H) <sup>-</sup> 2H <sub>2</sub> O (M = Rb, Cs) isomorphous structures	216
<b>Table 5-20</b>	HB parameters and significant interactions for 2M <sup>+</sup> (C <sub>6</sub> O <sub>4</sub> Cl <sub>2</sub> ) <sup>2-</sup> H <sub>2</sub> O isomorphous structures (M = K, Rb).	217
<b>Table 5-21</b>	Intra-molecular bond lengths for 2M <sup>+</sup> (C <sub>6</sub> O <sub>4</sub> Cl <sub>2</sub> ) <sup>2-</sup> H <sub>2</sub> O isostructures (M = K, Rb)	217
<b>Table 5-22</b>	M interaction distances in 2M <sup>+</sup> 2(C <sub>6</sub> O <sub>4</sub> Cl <sub>2</sub> H) <sup>-</sup> (C <sub>6</sub> O <sub>4</sub> Cl <sub>2</sub> H <sub>2</sub> ) 6H <sub>2</sub> O (M = Rb, Cs) Isomorphous structures.	229
<b>Table 5-23</b>	Intra-molecular bond lengths for 2M <sup>+</sup> 2(C <sub>6</sub> O <sub>4</sub> Cl <sub>2</sub> H) <sup>-</sup> (C <sub>6</sub> O <sub>4</sub> Cl <sub>2</sub> H <sub>2</sub> ) 6H <sub>2</sub> O (M = Rb, Cs) Isomorphous structures.	229
<b>Table 5-24</b>	HBs and significant distances for 2M <sup>+</sup> 2(C <sub>6</sub> O <sub>4</sub> Cl <sub>2</sub> H) <sup>-</sup> (C <sub>6</sub> O <sub>4</sub> Cl <sub>2</sub> H <sub>2</sub> ) 6H <sub>2</sub> O (M = Rb, Cs) Isomorphous structures.	230
<b>Table 5-25</b>	Crystallographic data for Isomorphous Structures	231
<b>Table 5-26</b>	Experimental Details for Isomorphous Structures.	232
<b>Table 5-27</b>	M Distances for 2Li <sup>+</sup> (C <sub>6</sub> O <sub>4</sub> X <sub>2</sub> ) <sup>2-</sup> H <sub>2</sub> O (X=Cl, Br)	240
<b>Table 5-28</b>	Intra-molecular bond lengths for 2Li <sup>+</sup> (C <sub>6</sub> O <sub>4</sub> X <sub>2</sub> ) <sup>2-</sup> H <sub>2</sub> O (X=Cl, Br)	240

<b>Table 5-29</b>	HB Parameters and Significant Interactions for $2\text{Li}^+ (\text{C}_6\text{O}_4\text{X}_2)^{2-} \text{H}_2\text{O}$ (X=Cl, Br)	240
<b>Table 5-30.</b>	HB Parameters and Significant Interactions for $2\text{Li}^+ (\text{C}_6\text{O}_4\text{Cl}_2)^{2-}(\text{C}_6\text{O}_4\text{Cl}_2\text{H}_2) 2\text{H}_2\text{O}$	247
<b>Table 5-31</b>	M interactions for $2\text{Li}^+ (\text{C}_6\text{O}_4\text{Cl}_2)^{2-}(\text{C}_6\text{O}_4\text{Cl}_2\text{H}_2) 2\text{H}_2\text{O}$	247
<b>Table 5-32.</b>	Intra-molecular distances for $2\text{Li}^+ (\text{C}_6\text{O}_4\text{Cl}_2)^{2-}(\text{C}_6\text{O}_4\text{Cl}_2\text{H}_2) 2\text{H}_2\text{O}$	247
<b>Table 5-33</b>	M distances for $2\text{Na}^+ (\text{C}_6\text{O}_4\text{Br}_2)^{2-} 4\text{H}_2\text{O}$ and $2\text{Na}^+ (\text{C}_6\text{O}_4\text{Cl}_2)^{2-} 3\text{H}_2\text{O}$ complexes	265
<b>Table 5-34</b>	HB and significant interaction distances for $2\text{Na}^+ (\text{C}_6\text{O}_4\text{Br}_2)^{2-} 4\text{H}_2\text{O}$ and $2\text{Na}^+ (\text{C}_6\text{O}_4\text{Cl}_2)^{2-} 3\text{H}_2\text{O}$ complexes.	266
<b>Table 5-35</b>	Intra-molecular distances for $2\text{Na}^+ (\text{C}_6\text{O}_4\text{Br}_2)^{2-} 4\text{H}_2\text{O}$ and $2\text{Na}^+ (\text{C}_6\text{O}_4\text{Cl}_2)^{2-} 3\text{H}_2\text{O}$ complexes.	266
<b>Table 5-36</b>	Crystallographic details for additional group one metal complexes	267
<b>Table 5-37</b>	Experimental details for additional $\text{M}^+$ complexes.	268
<b>Table 6-1</b>	Distances (Å), angles ( $^\circ$ ) and standard deviations ( ) in crotonate residues	282
<b>Table 6-2</b>	KHDC $\text{K}^+$ ion interactions (Å) and associated van der Waals radii (Å).	283
<b>Table 6-3</b>	Crystallographic Information for KHDC at Varied Pressure	283

# 1 Introduction

## 1.1 Studies of the Solid State

Many studies of the solid state, both theoretical and practical, utilise materials of interest that are in their solid crystalline forms. The regular periodic arrangement of atoms in their crystalline form eases experimental investigations and theoretical treatment and is a significant influence upon behaviour and properties. There are many fields and well known systems reported in the literature in which it has been possible to meet or discover new practical applications by tuning the properties of a solid crystalline material by altering certain parameters.

The objective of this work was to complete a series of systematic investigations on a range of metal-containing materials and to document the effects on the properties of interest. This chapter will introduce the materials explored and the properties studied in later chapters. This includes a range of computational investigations on Prussian Blue, associated derivatives and analogues, and also a series of related transition metal hydrogen halides. Structural characterisations and comparisons of a range of synthesised metal containing organic complexes will also be reported.

## 1.2 Review of Materials of Interest

The presence of a metal ion is responsible for interesting and useful properties in many materials. Examples include the magnetic properties associated with materials containing transition metals, or the crucial role played by  $\text{Li}^+$  ions in lithium batteries. It is this significant presence of metal which ties together all of the materials studied in this work. By changing either the identity of the metal itself or its coordination sphere, it is possible to examine the effect on magnetic, electronic or structural properties.

### 1.2.1 Hydrogen Bonding

Although the term Hydrogen Bond (HB) was originally coined by Pauling in 1931 <sup>1</sup>, the concept started to emerge in the literature as far back as the 1920's. In 1920 Latimer and Rodebush <sup>2</sup> stated that

*'the ionization of acids, or indeed extreme polarity of any compounds involving hydrogen, must be interpreted as due to the transfer of a hydrogen nucleus from one molecule to another, thus forming a complex ion'*.

The formation of this complex ion was then later described in 1922 by Huggins <sup>3</sup> in regard to his own work as

*'the reaction of a positively charged kernel containing no electrons in its valence shell with an atom containing a lone valence pair'*

In both cases, the great significance of these interactions can be seen in crystal formation, collectively shaping structures and in the formation of polymers and molecular aggregates. Indeed the HB is one of the most important intermolecular interactions in which the strengths of forces and magnitudes of energies involved may range from those of very weak van der Waals and dispersive nature, rising close to an almost covalent nature. The energy involved in a HB interaction can range from as little as 0.2 to as much as 40 kcal/mol, (compared to the typical energy of a covalent C–C single bond of ~80 kcal/mol), and its presence can play a role in determining the structure and influencing the physical and chemical properties of a wide range of materials <sup>4</sup>.

A number of techniques can be used to study HBs, the existence of which was originally confirmed by infrared spectroscopy (IR) <sup>5</sup>. By examining the vibrational modes of a HB donor molecule both before and after the formation of a HB, the interaction effects can be measured by the shift in the OH absorption band. HBs can also be confirmed and measured by the presence of a lower resonance shift in solid state nuclear magnetic resonance (NMR). Techniques such as X-ray and neutron diffraction can however give a direct image of the average atom positions

within a crystalline structure, from which it is therefore possible, with a good dataset, to measure a number of structural HB parameters. Computationally it is also possible to obtain a one-dimensional potential energy curve or a three-dimensional surface by altering the proton position with respect to the rest of the stationary unit cell.

HBs have been classified into three types by Jeffrey<sup>4</sup>: strong, moderate and weak. This classification is dependent on a number of parameters defined in Table-1-1, and has been adopted in discussions of the complexes within this work.

**Table 1-1 Classification of HB's into strong, moderate and weak<sup>4</sup>.**

	Strong	Moderate	Weak
X-H...A interaction	covalent	electrostatic	electrostatic/dispersive
Bond lengths	D-H $\approx$ H...A	D-H < H...A	D-H $\ll$ H...A
H...A (Å)	1.2-1.5	1.5-2.2	2.2-3.2
D...A (Å)	2.2-2.5	2.5-3.2	3.2-4.0
Lengthening of D-H (Å)	0.08-0.25	0.02-0.08	<0.02
Bond angles (°)	175-180	130-180	90-150
Bond energy (kJ mol <sup>-1</sup> )	>60	15-60	<15
Relative IR shift $\Delta V_{\text{AH}}$ (cm <sup>-1</sup> )	25%	10-25%	<10%
H <sup>1</sup> downfield shift (ppm)	14-22	<14	

The HBs presented in this work are represented in the form D–H...A, where D–H is the HB donor group and A is the acceptor. The associated HB distance,  $d$ , and angle are represented in Figure 1-1.

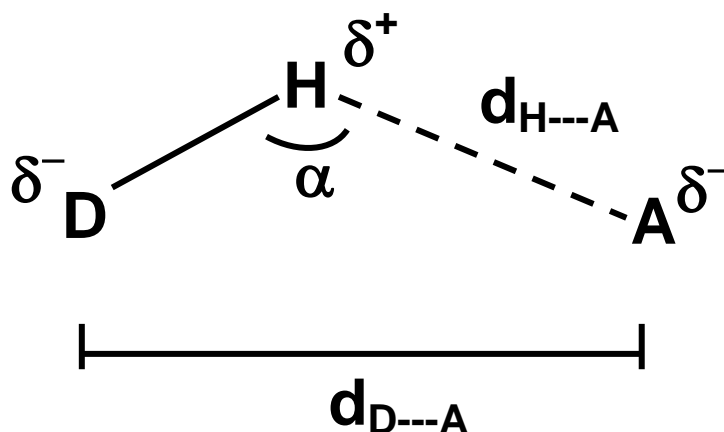


Figure 1-1 Notation for a typical D–H...A HB, showing the geometric parameters.

HBs are long range and directional interactions. It is not uncommon for the HB donor group to be bonded to more than one acceptor group at the same time. This is referred to a bifurcated HB (BHB) of which there can be a number of forms, illustrated in Figure 1-2.

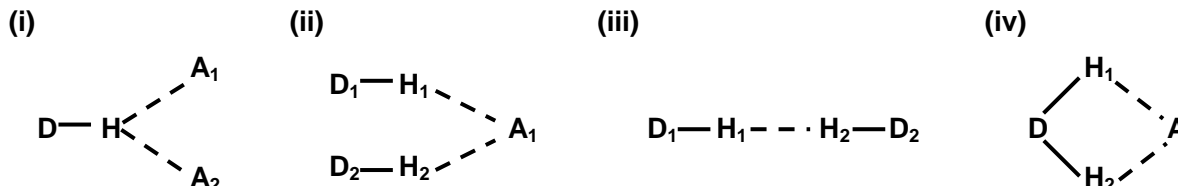


Figure 1-2 Examples of BHBs (i) One donor, one H atom and two acceptor atoms (DHAA), (also referred to as three- centred in the literature) (ii) Two donors, two H atoms and one acceptor atom (DDHHA) (iii) Two donors, with two H atoms between and no acceptor atoms (DHHD) (iv) One donor, two H atoms and one acceptor atom (DHHA).

Examples of BHBs include the superficially simple case of how water molecules assemble, while BHBs are not uncommon in organometallic systems, in which organic ligands with electron rich sites are specifically chosen to form interesting three-dimensional networks with the metals, and also weaker HBs which are consequently less direction specific.

A bifurcated HB tends to be denoted D–H...A1(A2) (Figure 1-3) <sup>4</sup>, in which A1 signifies the dominant HB interaction, distinguished by its shorter bond distance

and angle closer to  $180^\circ$ , and A2 the weaker HB interaction which is often ignored. It is unusual for the proton to lie equidistant from the two acceptor atoms.

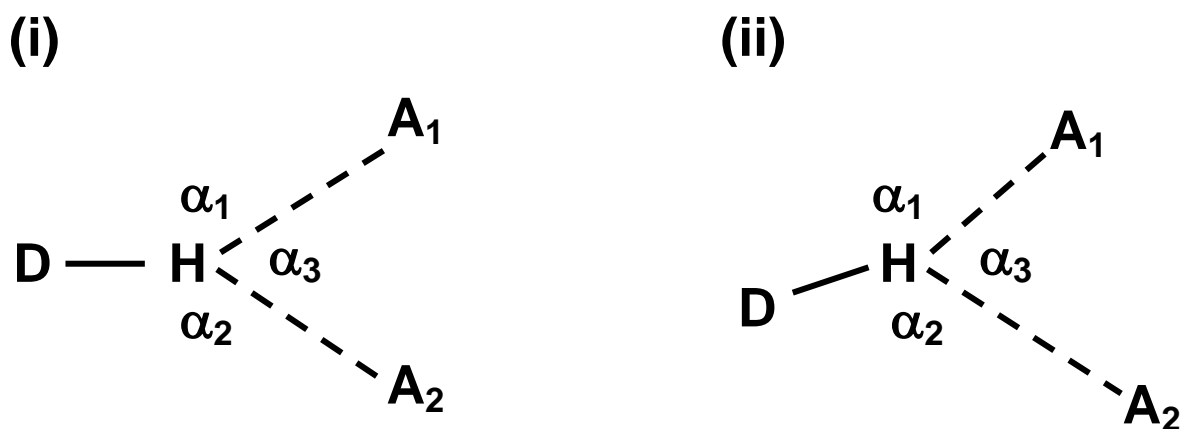
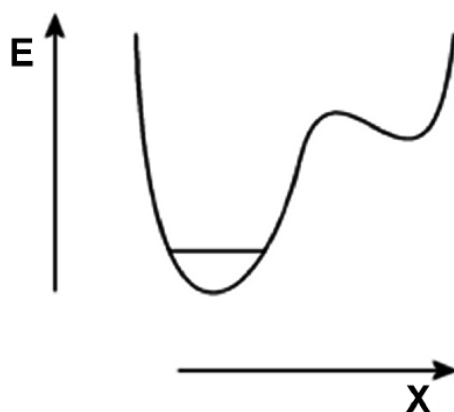


Figure 1-3 Geometry of BHB (i) symmetric (ii) asymmetric.

As mentioned above, the HB potential energy profile, obtained as the proton is transferred along the HB path, is also of interest in this work. In our theoretical studies, this potential energy curve can be used to calculate a corresponding magnetic coupling profile with a comparison of the two profiles yielding the magnetic coupling and energy cost incurred at a particular state.

In the more common (moderate) HB, the energy potential profile tends to possess two energy minima; one of lower and one of significantly higher energy. The energy gap between the two states will be so large that the proton will remain stationary in the lower energy state, Figure 1-4.



Common (moderate) HB

Figure 1-4 Typical potential well for a moderate HB, with one potential proton site of significantly lower energy than the other.

It is well known that reducing the distance between the two hydrogen bonded atoms tends, in the limit, to yield a broader energy profile with no energy barrier for proton transfer<sup>6</sup>. This is called a single well HB (SWHB), Figure 1-5.

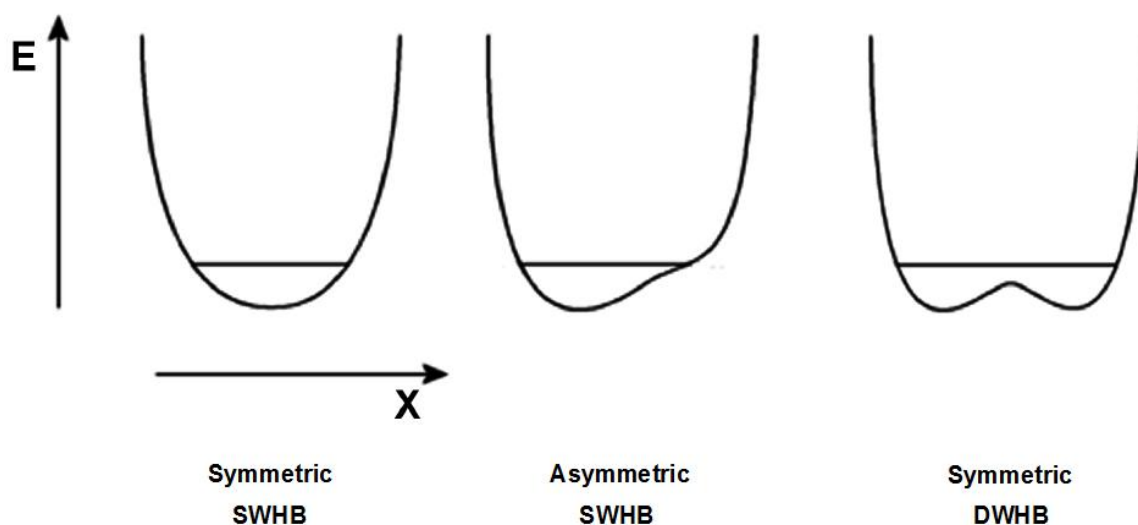


Figure 1-5 Types of broadened potential wells in shorter HBs.

In a shortened HB in general, the minima tend to become less separated, more similar in energy, and the energy barrier is lowered. This type of double well potential energy curve with a low energy barrier in which the proton may readily interchange between the two energy states is called a double well HB (DWHB), Figure 1-5.

In addition to the D---A separation distance, the identity of the two hydrogen bonded atoms can also affect the shape of the potential energy curve. When the two atoms are identical, for example FHF<sup>-</sup> and ClHCl<sup>-</sup>, the curve tends to be symmetrical and the proton positioned centred between the donor and acceptor. When the two atoms are different, such as in FHCl<sup>-</sup>, the curve is usually asymmetrical and the proton positioned off centre.

### 1.2.2 Prussian Blue (PB)

Initially produced as a blue dye in 1704<sup>7</sup> Prussian Blue (PB) has been used by artists and manufacturers ever since. The name 'Prussian' Blue originated from its use to colour Prussian military uniforms, and today PB dyes and paint are still readily available to buy.

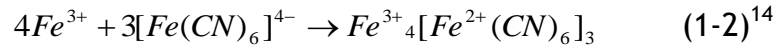
PB has a three dimensional cubic structure of Fe<sup>2+</sup> and Fe<sup>3+</sup> transition metal ions that interact through intermediate CN<sup>-</sup> ligands. The Fe centres are present in either a low or high spin configuration depending on which side of the CN<sup>-</sup> bridge they inhabit. Due to the nature of the CN<sup>-</sup> ion, this will be high spin if the iron ion is positioned next to the electron seeking nitrogen atom, and low spin if positioned next to the carbon atom.<sup>8,9</sup>

The band gap of the material corresponds to the intervalence Fe<sup>2+</sup>-Fe<sup>3+</sup> charge transfer (CT) transition, (1-1), which has a maximum wavelength of approximately 700nm.



This corresponds to energy in the red region of the visible spectrum, thus explaining the characteristic blue colour of the material.

PB can be synthesized electrochemically on a variety of substrates, including graphite,<sup>8,11,12</sup> Pt,<sup>9,13,14</sup> Ge,<sup>15</sup> Indium tin oxide (ITO) glass<sup>10,16-18</sup> electrodes or plates by the reduction of a solution containing both metalcyanide and free metal ions, as shown in (1-2).



Two stoichiometries have been proposed for PB, the insoluble form above (IPB)  $Fe^{3+}_4[Fe^{2+}(CN)_6]_3 (H_2O)_n$  and the soluble form (SPB)  $KFe^{3+}Fe^{2+}(CN)_6 (H_2O)_n$ . The ideal crystal structure for IPB<sup>19</sup> (Figure 1-6), which assumes an ordered face centered unit cell, shows the vacancies which are located in the centre of  $\frac{1}{4}$  of the unit cells in place of  $Fe^{2+}$  sites, surrounded by 6 coordinated water molecules. The cell also shows uncoordinated interstitial zeolitic water molecules.

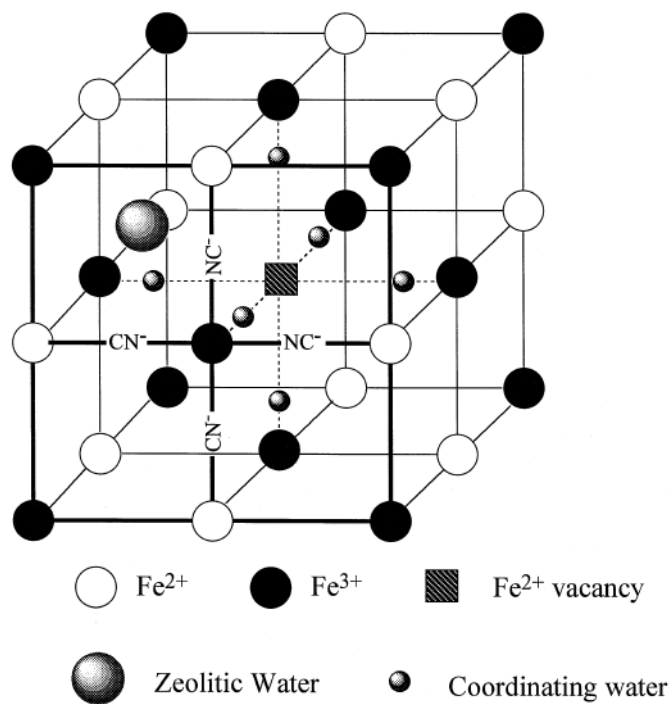


Figure 1-6 The ideal crystal structure for IPB<sup>19</sup>

SPB is formed during the potential cycling of the resultant IPB films in aqueous KCl. The ideal structure of SPB<sup>12</sup> (Figure 1-7), has no  $Fe^{2+}$  vacancies or coordinated or zeolitic water molecules, but instead possesses an ordered cubic structure of alternating  $Fe^{2+}$  and  $Fe^{3+}$  ions bridged by  $CN^-$  ligands and charge balancing metal  $K^+$  cations.

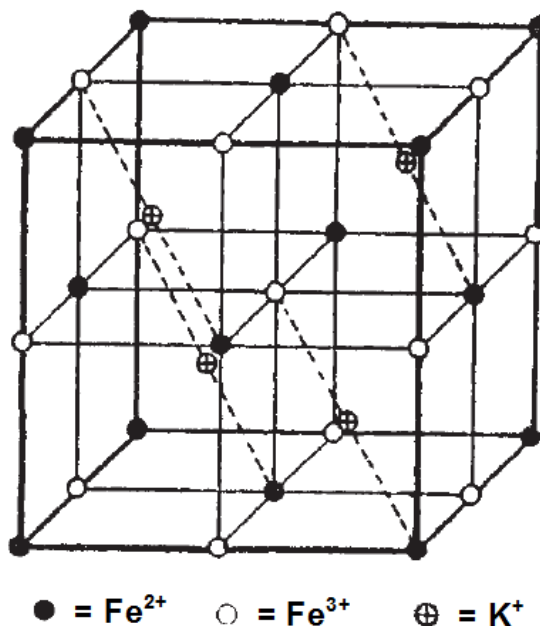


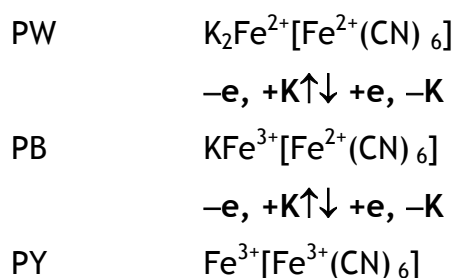
Figure 1-7 The ideal crystal structure for SPB<sup>12</sup>

In reality, most PB complexes are disordered, the degree of which depends on preparation procedures, and the structural formulae will lie somewhere between the two extreme forms.

### 1.2.3 Ionisation of PB

The two closest derivatives to PB are Prussian Yellow (PY) and Prussian White<sup>13</sup> (PW); the latter is also commonly referred to as Everitt's Salt (ES) in the literature. Only Fe<sup>3+</sup> ions are present in PY and only Fe<sup>2+</sup> in PW, both of which can be obtained from PB by electrochemical oxidation and reduction respectively.<sup>8-11, 14-17</sup> The relationship between the PW, PB and PY structures is illustrated in Scheme 1-1.

Scheme 1-1



PW has been shown to reduce to PB and in turn PY via electrochemical means in which a voltage is applied to a solution of cations and the initial substance.<sup>8-11, 14-17</sup> The procedure is also reversible - the reduced substance can be oxidised back. It is possible to identify which PB derivatives are present by measuring the vibrational modes in the CN<sup>-</sup> stretching region using Fourier transform infrared attenuated total reflection (FT-IR/ATR) spectroscopy. A peak at 2075cm<sup>-1</sup> indicates the presence of IPB, whereas peaks at 2106, 2080 and 2175 cm<sup>-1</sup> have been shown to identify the presence of SPB, PW and PY respectively.<sup>9</sup> An intermediate mixture, Berlin Green (BG),<sup>15</sup> has also been observed in which not all PB present is reduced to PY, leaving a PB:2PY mixture ( $\{KFe^{3+}[Fe^{2+}(CN)_6]\}_{1/3}\{Fe^{3+}[Fe^{3+}(CN)_6]\}_{2/3}$ ). This was determined by the presence of two peaks at 2106 and 2175 cm<sup>-1</sup> in the FT-IR spectrum during potential cycling, the second of which was double the intensity of the first.

#### **1.2.4 Effects of Metal Cation Identity**

Due to the large open frameworks of PB and its derivatives, which possess unit cells of approximately 10 Å<sup>3</sup>,<sup>20</sup> these materials are able to allow a range of small hydrated ions to pass through the structure and interchange with one another through electrochemical means. This has so far been exploited in applications such as radioactive waste removal,<sup>21</sup> ion-sensitive membranes for determination of alkaline cations<sup>22</sup> and nanosieving of cations.<sup>23</sup> The porous frameworks and reversible redox property of PB has also been of use in applications such as catalytic activity towards the reduction of hydrogen peroxide in electrochemical bio- and immunosensors,<sup>24</sup> solid state rechargeable batteries and their components,<sup>19, 25</sup> and electrochromic displays and sensors.<sup>26</sup>

Consequently, other PB complexes also obtained by this means have been reported in the literature in which other group one metals have been interchanged in place of the K<sup>+</sup> ion. One example allowed the authors to conclude that the PW lattice contracts on oxidation to PB which again expands on further oxidation to PY.<sup>27</sup> This was after obtaining an RbPW complex in which one of the Rb<sup>+</sup> ions became irreversibly bonded due to this contraction. On further oxidation the Rb<sup>+</sup> ions

could not diffuse through the PB channels. This prevented the formation of PY due to its inability to conduct ions. This was also the case for a TIPW complex.<sup>27</sup> A comparison of IR spectra for NaPB and KPB<sup>6</sup> has shown both complexes to possess a strong absorbance for the CN<sup>-</sup> group in the range 2060-2070cm<sup>-1</sup> and also the presence of water at the characteristic peaks of 1650cm<sup>-1</sup> and 3500cm<sup>-1</sup>. Significant differences between the two complexes were only observed in the far infrared region (667-10cm<sup>-1</sup>) which is sensitive to metal-carbon and metal-nitrogen bending vibrations.<sup>28</sup> The identity of the charge balancing metal cation has also been shown to alter the electronic structure of PB which in turn affects the PB band gap<sup>10, 29-30</sup>, a trend which has also been shown to occur in other related complexes<sup>31</sup>.

Experimental studies have shown a relationship between the identity of the charge balancing metal cation and the CT band gap of the material, suggesting that it is possible to tune the electronic structure of a material by the careful selection of a counter-cation. Rosseinsky *et al.*, have demonstrated that the CT band gap in Prussian Blue (PB) is dependent on the interstitial cation and lattice energy framework interaction.<sup>10</sup> Different alkali metals were introduced into the structure by means of electrochemical voltammetric cycling and microgravimetry and solubility correlation results showed that the intercalated cation could potentially influence band gaps. The PB band shift energies quoted for the inclusion of Na<sup>+</sup>, K<sup>+</sup>, Rb<sup>+</sup> and Cs<sup>+</sup> in the structure were 703, 686, 691 and 703nm respectively. The study also concluded that for PB, a stronger interaction between the cation and framework gave a greater stabilisation of the CT ground state between the Fe centres and hence a bigger gap.

The cation-induced spectral shifts were then reproduced theoretically in 2006 by Wojdeł and Bromley<sup>29</sup> using a technique previously found to be successful in describing the properties of PB and its analogues.<sup>30</sup> The technique involved mixing different parameterisations of ultrasoft pseudopotentials ( see Chapter 2), in order to obtain USPPs for use in fully periodic calculations of real materials. However, due to the instability of the charged infinite system, it was not possible to remove all the cations from the material in order to calculate their absolute interaction

energy with the framework. Therefore by modelling the motions of different cations through the system and comparing total energy, structure and band gap differences, it was found that in addition to the cation type and position, the CT band gap was also heavily influenced by the specific cation-induced distortion on the lattice.

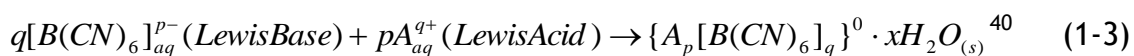
Although PB is structurally interesting in terms of hosting guest cations, the electronically rich Fe metal framework also gives rise to the possibility of interesting magnetic properties. The ability to tune the magnetic and optical properties of these materials by careful selection of ions of specific valence is well known with applications of PB in magnetic materials,<sup>32</sup> optical sensors,<sup>33</sup> electrocatalysis,<sup>34</sup> and other applications on the nanoscale including use in nanowires,<sup>32</sup> nanotubes,<sup>35</sup> nanoparticles<sup>24, 36</sup> and nanofilms.<sup>37</sup> This link between electronic/magnetic and optical properties has also led to the synthesis of a new range of PB analogue materials with potential electro-optical device application.<sup>38</sup> For a fixed choice of metal centre, PB and its derivatives can be influenced by changes in stoichiometry, type of interstitial cation and incorporation of water molecules.<sup>10, 39</sup>

It is therefore no surprise that PB, the oldest coordination compound reported,<sup>13</sup> has a large number of related structures and derivatives in the literature in which numerous structural parameters and atom identities have been altered in order to obtain brand new complexes. These so called analogues have in many cases been tuned in order to obtain interesting properties.

### **1.2.5 Prussian Blue Analogues (PBAs)**

Prussian Blue Analogues (PBAs) possess the general formula  $M_nA_p[B(CN)_6]_q \cdot xH_2O$  in which A and B are transition metal ions and M is a monovalent counter cation. The PBA structure, like that of PB from which it is derived, is a three-dimensional cubic lattice of TM ions that interact through intermediate  $CN^-$  ligands. TM A is positioned next to the nitrogen atom and consequently has a high spin crystal field, and TM B, positioned next to the less reactive C atom, is usually more stable

and has a low spin crystal field. The usual means by which a neutral solid complex is obtained is by a simple Lewis acid-base reaction (1-3):<sup>40</sup>



The most common structures have either

- a 1:1 A/B stoichiometry, in which the coordinations of A and B are  $\{A(NC)_6\}$  and  $\{B(CN)_6\}$  respectively and each has six A(B) or B(A) neighbours;
- the same 1:1 A/B stoichiometry with M cations present in the interstitial sites;
- or a 3:2 A/B stoichiometry in which one third of the  $[B^{III}(CN)_6]$  vacancies are filled with water molecules. Consequently, in this case although the B coordination is the same as before, the A coordination sphere is now  $\{A(NC)_4(H_2O)_2\}$  and the mean number of B neighbours has been reduced to four.

In many cases, the TMs possess different oxidation states that enable electron-to-electron transfer due to an energy perturbation. As with the parent PBs, this has led to the formation of many interesting complexes exhibiting a diverse range of magnetic,<sup>41</sup> optical<sup>42</sup> and electrochemical<sup>43</sup> properties. They also have potential for device applications such as molecular magnets,<sup>44</sup> nanowires,<sup>45</sup> electrodes<sup>46</sup> and rechargeable batteries.<sup>47</sup> There are examples of high transition temperature PBA magnets,<sup>48</sup> magnetic pole reversal,<sup>49-50</sup> spin glass behaviour,<sup>51</sup> photo induced magnetic transitions,<sup>49, 52</sup> photo<sup>53</sup> and pressure induced<sup>54</sup> electron transfers and room temperature magnetic phases.<sup>55</sup>

The structure-directing property of the cyanide ligands and the flexibility of the structure also allow the TM ions to be specifically tailored in terms of spin and oxidation states so that exchange interactions behave as predicted from fundamental orbital interaction rules. The magnetic properties of PBAs are particularly sensitive to such alterations. The magnetic coupling (J) value is a measure of the interaction between the unpaired electrons of the TMs present in a complex. This is dependent on a number of conditions such as the identity,

oxidation state and crystal field spin splitting of the interacting TMs and also a number of other parameters that can influence the long range order.

This can be explained by means of an ordered cubic PBA structure with two interacting TMs, A and B (Figure 1-8).

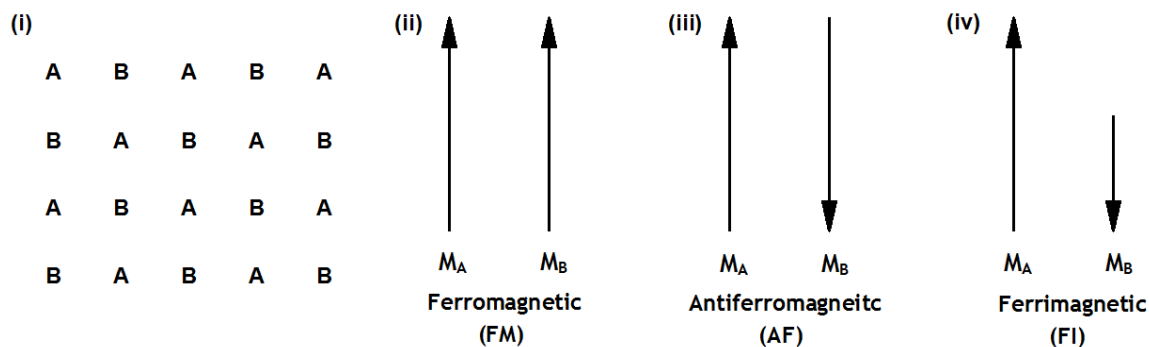


**Figure 1-8 (i) The two interpenetrating sublattices of A and B, (ii) ferromagnetic (FM) (iii) antiferromagnetic (AF) and ferrimagnetic coupling (FI).**

If the spin-containing orbitals of A and B possess the same symmetry they will couple antiferromagnetically (AF), whereas if the orbitals are orthogonal they will couple ferromagnetically (FM).<sup>40</sup> If the orbitals couple AF and do not have equal spins then this is referred to as ferrimagnetism (FI). As each equivalent magnetic ion is separated by approximately 10 Å, a distance too large for direct orbital interactions, the magnetic exchange present in these materials is referred to as superexchange.

The large number of possible combinations of ions and oxidation states give rise to many competing orbital interactions, which will cause the structure to reach an overall order; either FM, AF or FI. There are many examples in the literature in which the overall order of the system has been changed by external conditions. For example the material  $KMn^{II}Mn^{III}[Fe^{II}Fe^{III}]$ <sup>56</sup> has both strong AF and weak FM interactions leading to two different magnetic transitions at two different temperatures; a thermally induced phase transition by charge transfer. Therefore the properties of materials of this nature can be tuned by external perturbations, such as fine tuning of the magnetic moment by adsorption of light or electrical current.

Magnetic coupling constants are also very sensitive to exchange pathways. Due to the strong relationship between magnetic coupling and unit cell volume, there have been a significant number of experimental studies of compounds displaying both magnetic and structural changes induced by pressure. These include the switching of magnetisation in cobalt-iron cyanide by both pressure and photo irradiation,<sup>57</sup> the use of pressure to tune the bulk magnetisation and linkage isomerism in iron (II) hexacyanochromate,<sup>58</sup> and more recently to induce a series of magnetic pole inversions in  $\text{Rb}_{0.64}\text{Ni}_{0.31}\text{Mn}_{0.87} [\text{Fe}(\text{CN})_6] \cdot 2.8\text{H}_2\text{O}$ .<sup>59</sup>

The latter example is one of many experimentally synthesised trimetallic PBAs with competing magnetic interactions that display magnetic pole inversions in response to external perturbations. Here, pressures as low as 0.2 kbar depending on experimental conditions, were used to switch the magnetisation from positive to negative and back to positive, whereas moderate pressures induced an internal charge transfer causing a crossover from ferri- to ferromagnetic ordering. Pressure has also been used to increase the transition temperature for the ferrimagnetic  $\text{Mn}_3^{\text{II}}[\text{Mn}^{\text{III}}(\text{CN})_6]_2 \cdot 2\text{H}_2\text{O} \cdot 1.7(\text{CH}_3\text{OH})$ <sup>60</sup> structure from 29 to 40 K, the dependence of which was interpreted in terms of the shrinkage of the Mn-CN-Mn superexchange pathway.

Experimentally the structure and properties of these materials have been tuned by both external perturbations and the ratio of the metallic components, by doping. For example it is possible to vary the saturation magnetisation and compensation temperature ( $T_c$ ) by changing the composition factor  $x$ , and for  $x \sim 0.4$  a switch from a FM to FI magnetic ordering was observed in the family of the mixed ferro-antiferromagnets  $\text{Ni}_x^{\text{II}}\text{Mn}_{x-1}^{\text{II}}[\text{Cr}^{\text{III}}(\text{CN})_6] n\text{H}_2\text{O}$ .<sup>61</sup> This change in magnetisation has also been observed in similar studies involving humidity and light irradiation.<sup>62</sup> Hashimoto and various colleagues have also induced magnetic phase transitions by controlled electrochemical and optical induction.<sup>63</sup>

There are also many computational studies reported in the literature that have been performed on theoretical PBA model complexes in which the disordered water molecules have been replaced by charge equivalent cations.<sup>29,30,60,64-65</sup> These models, used with an appropriate calculation functional, have been shown

to successfully reproduce experimental measurements. Although Chapter 2 will provide more detail on functionals in regard to this work, the B3LYP<sup>59</sup> functional with electron correlation was shown to give accurate coupling values in PBA systems and to yield magnetic phase transition temperatures that were linearly correlated with experimental values.<sup>67</sup>

The B3LYP hybrid functional has also successfully reproduced experimental measurements for electronic properties in PBA materials<sup>64,65,68,69</sup>. This functional was also used with a dinuclear model in which protons were attached to the cyano groups to simulate the missing metal atoms of the extended structure and decrease the overall negative charge. This estimated that transition temperatures as high as 552K for a Mo<sup>III</sup>V<sup>II</sup> system could be obtained.<sup>70</sup> However, the coupling constants in these models were significantly higher than experimental values and the basis sets, when compared to those used by Nishino *et al*,<sup>71</sup> gave coupling constant values 40-50% greater.<sup>70</sup> This deviation of coupling values from experimental results suggest that that the coefficients, especially the weight coefficient representing the percentage of the Hartree Fock (HF) exchange functional, are not the optimal set of parameters for studying magnetic properties of materials.

A related hybrid density functional with 35% HF<sup>72</sup> exchange has been shown to predict ground states correctly, as well as providing far better coupling constants for a range of magnetic materials with different structures and spin orderings than B3LYP, with 20% HF. B3LYP is, however, still favoured to obtain more accurate energy gaps. In order to study specific properties theoretically, hybrid density functionals with different percentages of HF exchange may be required. For studies of thermodynamic and magnetic properties, success has been obtained with the B3LYP and the 35%HF exchange hybrids respectively.<sup>64,65</sup>

Although this is a useful means by which trends can be obtained, caution should be applied when selecting an appropriate functional and when interpreting individual results during computational studies. Due to the large numbers of water molecules and the resulting low crystal symmetry of most experimental PBAs, a problem when theoretically modelling the crystal and electronic structures of these

materials accurately, most systematic computational investigations of PBAs use charge balancing cations in place of the disordered water molecules. Studies have shown that the water content in PBAs can affect properties such as  $J$ , which has been shown to decrease with increasing water content.<sup>65</sup> This is however not a problem when comparing experimental results with those of the anhydrous models in which the presence of water is easily accounted for. Although the synthesis of anhydrous PBAs would allow a direct comparison of theory and experiment, at present the approach outlined seems to be the best means of comparison between experimental and model complexes. This is due to the fact that experimentally, PBAs in general are disordered and difficult to obtain<sup>73-74</sup> and anhydrous PBAs of a specific composition would be even more so.

Linkage isomerism, in which the positions of the C and N atoms in the  $CN^-$  bond exchange places, have been noted in experimentally obtained complexes<sup>74</sup>. The energy values obtained from simulations of modelled derivatives of these complexes also indicate the likely presence of the effect.<sup>65</sup>

### **1.2.6 Hydrogen Bond Mediated Magnetic Coupling Systems**

In the previous section, a number of studies were shown to employ the PBA model structure in order to investigate various effects on magnetic coupling. The PBA system in combination with optimised hybrid functionals was shown to produce values and trends in good agreement with experiment. Metal organic structures containing hydrogen bonds (HBs) are also known to display complex magnetic behaviour at low temperatures but there are a fewer number of these reported in the literature.

The literature is rich in organometallic complexes in which TM coupling via HBs has been observed.<sup>75-77</sup> For example this is found in the structure  $\text{pipzH}_2 [\text{MnF}_4(\text{HF}_2)]$ <sup>76</sup> (pipz = piperazine) which is made up of anionic chains of planar  $[\text{Mn}^{3+}\text{F}_4]$  connected by bridging FHF ligands in the  $a$  direction. The unit cell includes eight  $\text{Mn}^{3+}$  ions on the outer corners and central pipz hydrogen bonded to the planes by  $\text{N-H}\cdots\text{F-H}$  bonds; this material orders AF below 1.8 K. However a systematic search based on

these types of systems would contain a large number of parameters and be computationally expensive.

In one study the B3LYP functional has been used in combination with a dinuclear Cu complex (Figure 1-9)<sup>78</sup> in order to investigate the effect of altering the HB distance and angle. The Cu atoms are mediated by two O–H---O HB interactions and although there are a few discrepancies,<sup>79-80</sup> overall the computed coupling values obtained for specific HB distances are in good agreement with those in the experimental results.<sup>79, 81</sup>

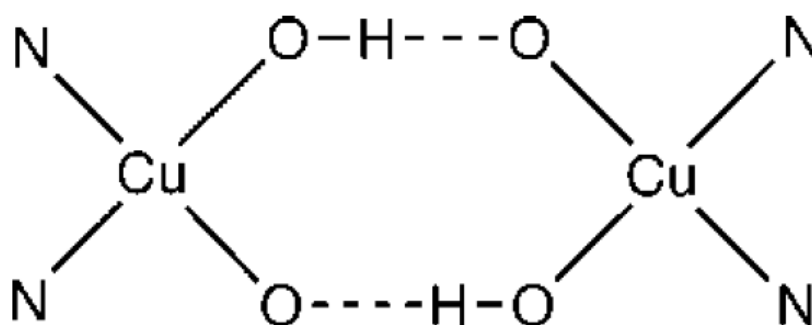
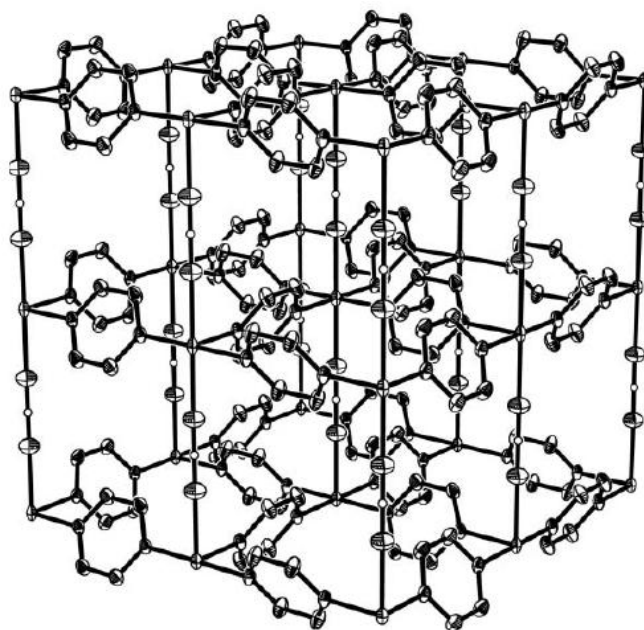


Figure 1-9 Dinuclear Cu complex<sup>78</sup>

This study employed the ‘cluster approach’ in which the Cu ions have been coordinated to two N atoms in order to simulate any external interactions which may be present in experimentally comparable complexes. This approach has a complex magnetic analysis unlike a solid state structure which would also guarantee that the long range electrostatic effects of the interaction are present.

The  $[\text{Cu}^{\text{II}}(\text{HF}_2)(\text{pyz})_2]\text{BF}_4$  complex, obtained and studied experimentally,<sup>82</sup> was observed to possess strong and weak magnetic coupling via pyrazine (pyz) and  $\text{FHF}^-$  ligands, respectively (Figure 1-10).



**Figure 1-10** Crystal structure of  $[\text{Cu}(\text{HF}_2)(\text{pyz})_2]\text{BF}_4$ <sup>82</sup>; strong magnetic coupling via pyrazine in the xy plane and weak magnetic coupling via  $\text{FHF}^-$  along the z axis. Cu positioned at (0,0,0). Pyrazine H atoms and  $\text{BF}_4^-$  anions have been omitted for clarity.

The magnetic and electronic structure of this complex was further investigated using solid state hybrid functionals.<sup>83</sup> Theoretical approaches of this sort have proven useful previously in application to related materials,<sup>84</sup> and to inorganic solids in general.<sup>85</sup> The coupling values obtained with the 35% HF functional were in good agreement with those from the experimental complex although the  $J_{\text{FHF}}/J_{\text{pyz}}$  ratio of 0.0065 was below the experimental value of 0.0105. This has been suggested to be due to contributions from higher order spin interactions. Also the presence of small amounts of spin density on the F atoms of the  $\text{FHF}^-$  ligand and the sensitive relationship between coupling and the position of the H atom suggested the presence of spin polarisation influencing the coupling due to the  $\text{pyz}(\text{HF})$  overlap. However the  $\text{FHF}^-$  ligand has in this case demonstrated effectiveness in mediating magnetic exchange interactions.

Other effects thought to affect the  $\text{FHF}^-$  interaction in other complexes include: weakening of the HB interaction due to a strong F–Mo interaction;<sup>86</sup> magnetic coupling which was initially thought to mediate through  $\text{FHF}^-$  ligands but this was found not to be the case due to the very low Mn–F---H angle of  $112^\circ$ ;<sup>76</sup> how the F---

F distance affects the sign and magnitude of the coupling.<sup>77</sup> Although there are reported studies of  $\text{FHF}^-$ , the related  $\text{FHCl}^-$  and  $\text{ClHCl}^-$  anion themselves,<sup>87</sup> and on molecules into which they have been incorporated,<sup>88</sup> there are very few examples of complexes which display hydrogen halide mediated magnetic coupling despite the fact that they seem suitable ligands to study systematically in an ordered TM system.

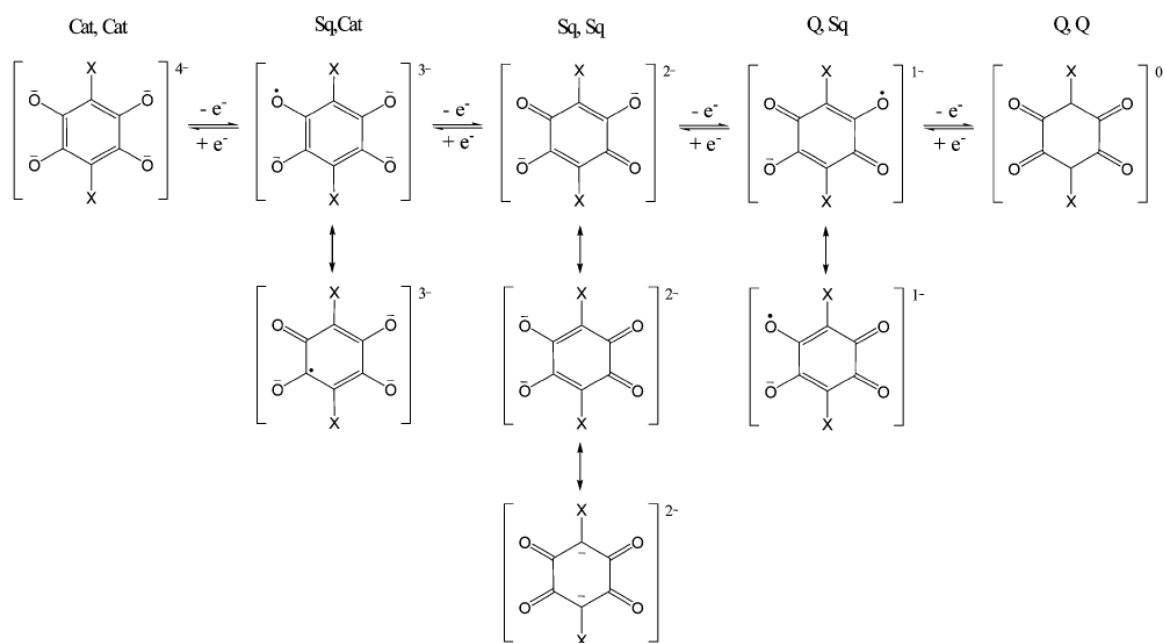
### **1.2.7 Metal-Organic Complexes**

The combination of metal ions and organic ligands can result in the formation of metal organic complexes. The use of specially selected organic molecules with functional groups that will interact with the other components in a complex in a predetermined fashion can result in the design of extended structures in one, two and three dimensions. These structures may be composed of lower dimensional units such as clusters, chains or planes and utilise a range of interactions. The types of interactions can be of an ionic metal nature through to weaker non-covalent intermolecular forces such as van der Waals, halogen-halogen and, most significantly, hydrogen bonding.

#### **1.2.7.1 The Quinone Ligand**

Metal-quinone complexes have been widely reported in the literature due to their range of possible interactions and the potential for interesting electronic behaviour. These ligands have been combined with a variety of proton acceptors in order to give organic molecular complexes with predictable supramolecular architectures. The possible electron exchange and redox activity associated with the quinone ligand is illustrated in Scheme 1-2,<sup>89</sup>. Each half of the ligand is represented by one of three notations: Cat which represents the fully reduced aromatic form; Sq, the semi quinone; and Q, a tetraoxolene.

**Scheme 1-2 Redox activity associated with different quinone ligands.** <sup>89</sup>



The combination of these ligands with metals has attracted much interest recently due to their ability to form interesting metal organic frameworks (MOFs). The metal-semiquinone complexes are probably the most interesting due to the radical nature of the semiquinone ligand, especially in the cases of transition metals in which unusual magnetic and optical properties have been observed <sup>90-92</sup>. This is due to the combination of unpaired electrons on the TM centre and the charge transferring ability of these ligands, also aided by the potential to adopt different arrangements of the C-C bond lengths in the carbon ring.

The anilic acid or benzoquinone family of compounds (Figure 1-11), is an example of a semiquinone ligand which has itself already been present in a significant number of studies.

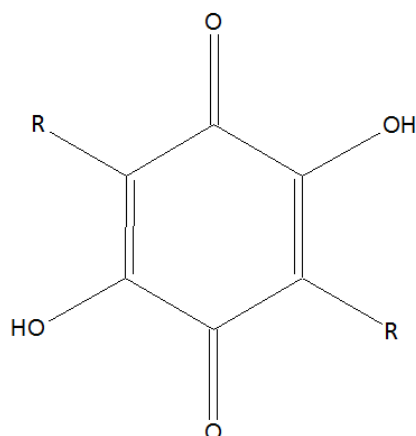


Figure 1-11 Anilic acid or Benzoquinone family of compounds.

The R group can take a number of forms, for example H, OH, CN. Our own work has focused on R=X, a halogen atom. The crystal structures of X=Cl and Br were determined in 1987 by Andersen <sup>93</sup> and Robl <sup>94</sup>, respectively; the structures of the compounds with X=F <sup>95</sup> and X=I <sup>96</sup> were also reported. However due to the difficult synthesis, and the hazards associated with the halogen chemistry of the latter two, we chose to carry out our investigations only on the compounds bromanilic acid (2,5-dibromo-3,6-dihydroxy-*p*-benzoquinone) (BA) and chloranilic acid (2,5-dichloro-3,6-dihydroxy-*p*-benzoquinone) (CA) (Figure 1-12), two commercially available compounds, denoted in general terms as haloanilic acids (XA).

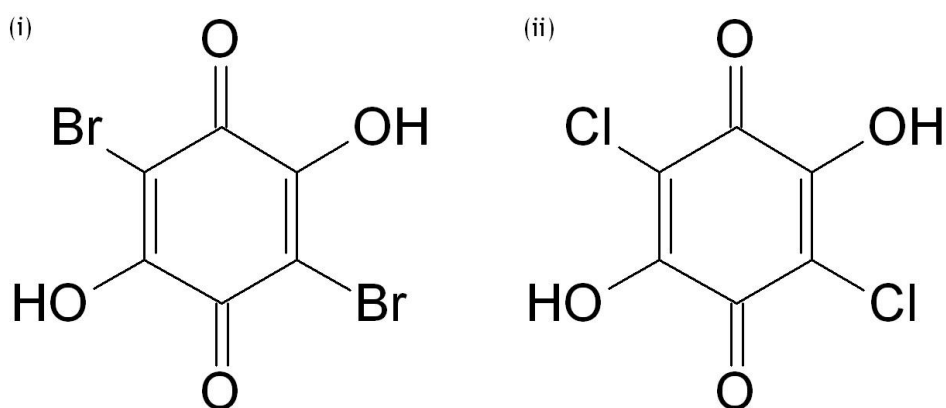
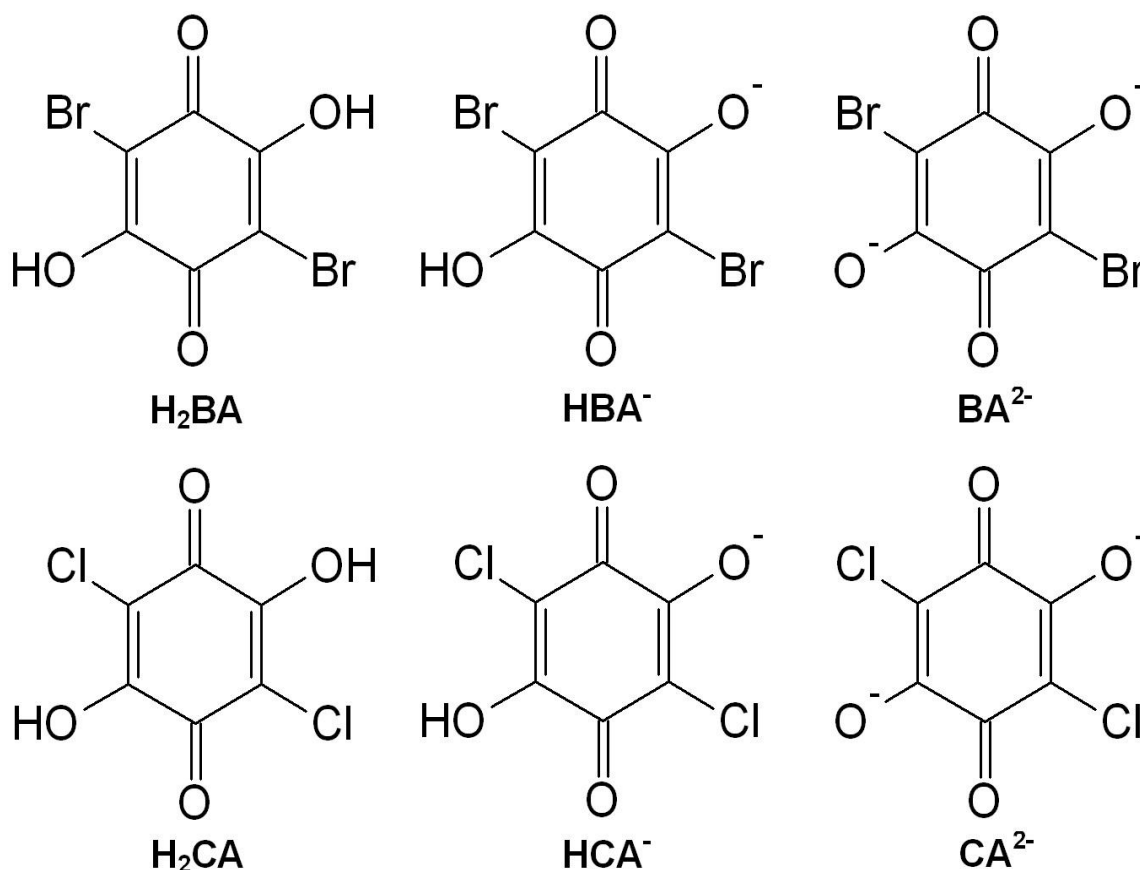


Figure 1-12 (i) Bromanilic acid (BA) and (ii) chloranilic acid (CA)

Due to the proton-donating properties of the hydroxyl groups, which can either lose or retain their protons, the ligands can exist in one of three different levels of protonation: fully protonated, singly deprotonated, and doubly deprotonated (Figure 1-13).



**Figure 1-13** The three observed forms and adopted notations of bromanilic and chloranilic acid; neutral, fully protonated H<sub>2</sub>BA and H<sub>2</sub>CA; partially deprotonated HBA<sup>-</sup> and HCA<sup>-</sup> (monoanions); and fully deprotonated BA<sup>2-</sup> and CA<sup>2-</sup> (dianions).

Although both BA and CA metal-anilic acid complexes are present in the literature, there are significantly more of the latter. A search using the Cambridge Structural Database (CSD)<sup>97</sup> located 145 CA containing metal complexes and only 7 for BA. The main focus of the literature is therefore on metal-CA complexes.

### 1.2.7.2 Chloranilic Acid and Bromanilic Acid

First prepared in its dihydrate form in 1891 by Graebe<sup>98</sup>, the crystal structures of CA<sup>93</sup>, its dehydrate<sup>99</sup>, and ammonium chloranilate monohydrate<sup>100</sup> were later

reported by Anderson. Although all of these complexes are very water soluble, CA also forms many complexes, particularly salts, which are not soluble in water<sup>101</sup> and therefore has many uses in analytical chemistry. Uses of CA include the determination of Mg(II) with flame atomic absorption spectroscopy (FAAS)<sup>102</sup>, construction of electrode membranes<sup>103</sup>, and kinetic determination of formaldehyde<sup>104</sup> and Mn(II)<sup>105</sup>.

The structure of pure CA is constructed from neutral H<sub>2</sub>CA molecules in which there are three types of bond in the carbon ring; two C=C double bonds of length 1.3464(4) Å, two C–C single bonds of length 1.5007(2) Å and two intermediate C–C/C=C bonds of length 1.4451(2) Å<sup>93</sup>. These are almost identical to those in the BA carbon ring<sup>94</sup> (Figure 1-14). The carbonyl and hydroxyl bond lengths for the two ligands are also very similar, and the C-Cl and C-Br bonds are also of characteristic length. In both cases there is hydrogen bonding between the proton donating hydroxyl groups and the proton accepting carbonyl groups. The HB parameters are 2.7690(7) Å, 157.541(1)° and 2.781(4) Å, 148(5)° for the CA and BA structures respectively. In both cases there are also strong halogen-halogen interactions between the Cl and Br atoms of different molecules of length 3.347(8) Å and 3.434(1) Å respectively, compared to the significantly larger sum of the van der Waals radii of 3.5 Å and 3.7 Å.

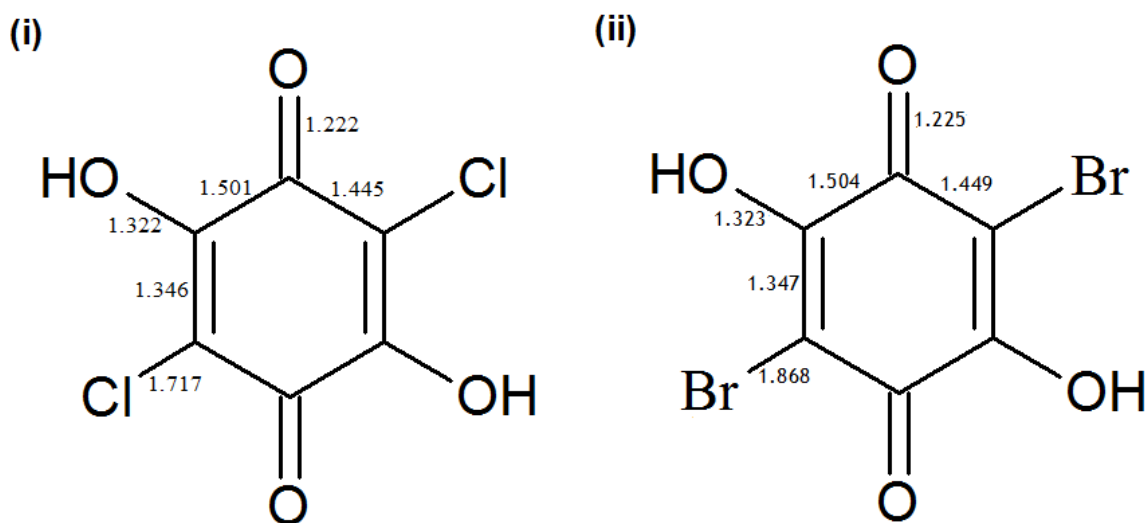


Figure 1-14 Bond lengths in the neutral H<sub>2</sub>XA molecules (i) CA<sup>93</sup> (ii) BA<sup>94</sup>

There are also molecular complexes in the literature in which the partially deprotonated HCA<sup>-</sup> molecule is present, most of which are comprised of the HCA<sup>-</sup> molecule itself and another small organic molecule<sup>106,107</sup>. The majority of cases are salts in which a proton has migrated from the proton donating H<sub>2</sub>CA to the co-molecule. In a few of the cases the authors have also managed to obtain the related structure in which the H<sub>2</sub>CA and co-molecule remain neutral<sup>107</sup>.

### 1.2.7.3 Metal anilic acid complexes

A search using the CSD gave 32 hits of structures in which the HCA<sup>-</sup> ligand was present, only two of which contained a metal, Fe<sup>108</sup> and Mo<sup>109</sup>, the latter to which the ligand was directly bound. Using the programme Vista<sup>110</sup> it was possible to obtain mean bond lengths for the HCA<sup>-</sup> ligand, which were found to be very similar to those in the Fe complex but different to those of the Mo complex in which the ligand was bound to the metal, Figure 1-15.

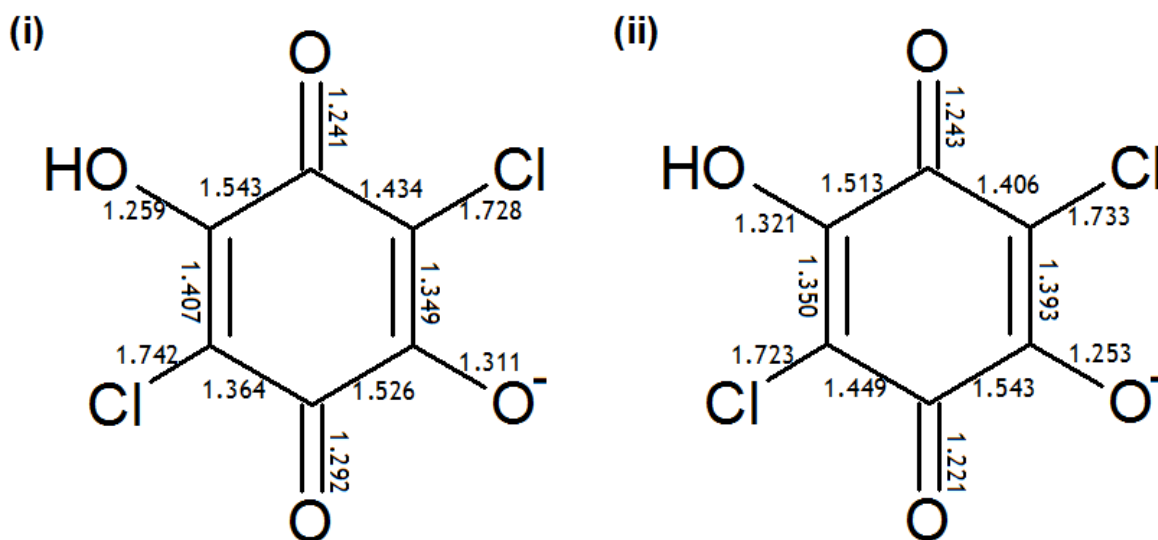


Figure 1-15 HCA<sup>-</sup> molecule bond lengths from (i) MoHCA<sup>-</sup> complex<sup>109</sup> (ii) average structures.

The HCA<sup>-</sup> molecule was joined to a Mo ion in bidentate fashion via the deprotonated hydroxyl group and adjacent carbonyl group in the metal complex. The influence of this is reflected in the bond lengths of the molecule - elongation of the C–O bond lengths of the coordinated oxygen atoms and the switched

positions of the intermediate and double bonds forming an electronic rearrangement in the carbon ring.

This electron exchange was also observed in Scheme 1-2 for the  $1^-$  Q,Sq quinones. A similar search and comparison was carried out using the CSD on the 5 structures found to contain the  $\text{HBA}^-$  molecule, one of which also contained Fe <sup>108</sup>. A comparison of the mean  $\text{HBA}^-$  bond lengths to those in the Fe complex is illustrated in Figure 1-16. As the  $\text{HBA}^-$  ligand was not bound to the Fe, it is more similar to the average  $\text{HBA}^-$  structure, unlike in the case of the  $\text{MoHCA}^-$  complex above.

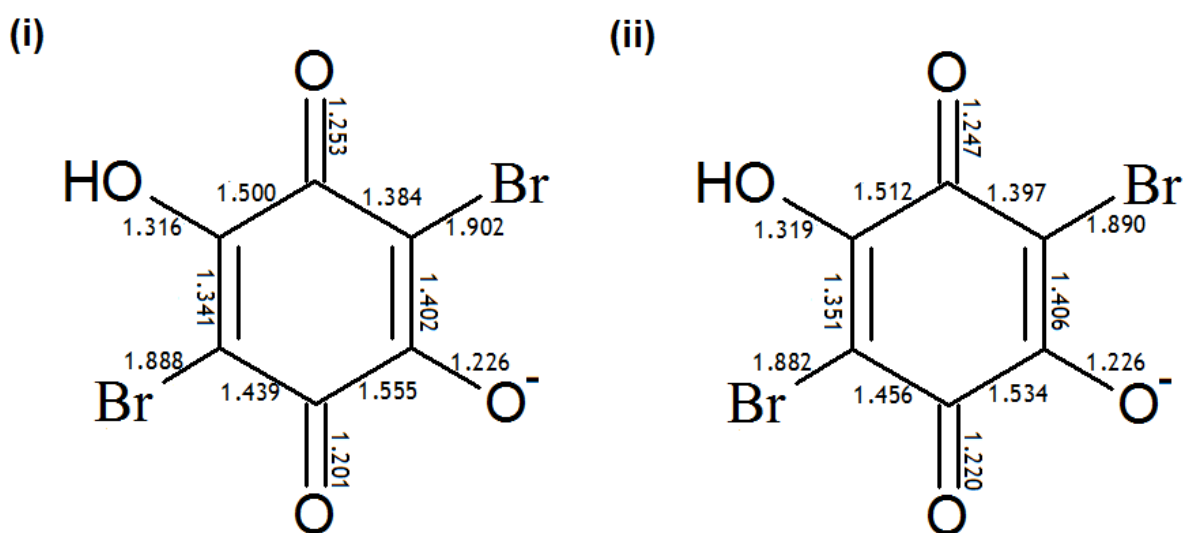


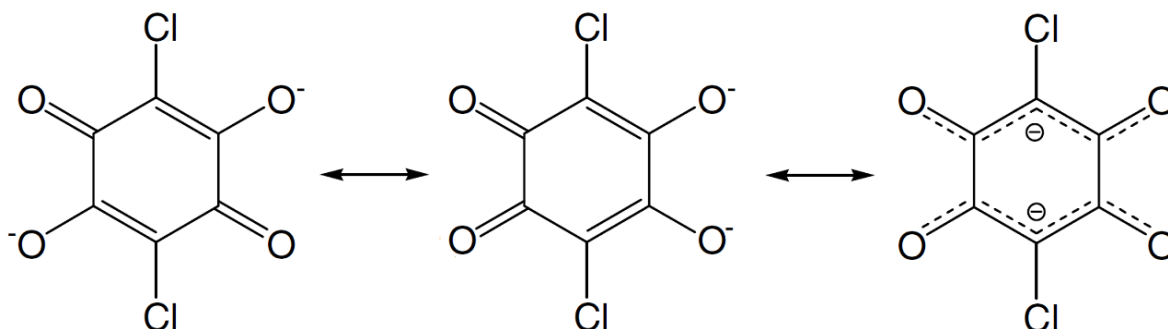
Figure 1-16  $\text{HBA}^-$  molecule bond lengths from (i)  $\text{FeHBA}^-$  complex <sup>108</sup> (ii) average structures, obtained using Vista <sup>110</sup>.

In both partially deprotonated ligands there are slight discrepancies on comparison to the neutral  $\text{H}_2\text{CA}$  molecule; the deprotonated C–O bond is shorter to compensate for the loss of a proton; and the adjacent double and intermediate C–C bonds to the halogen have become more equal, which may suggest the possibility of a delocalisation around the halogen carbon.

The most common form of the XA ligand is the completely deprotonated  $\text{XA}^{2-}$  dianion which can act as either a bridging, terminal bidentate ligand or bridging bisbidentate ligand. With the exception of a few cases in the literature, the most

common arrangement of the  $\text{XA}^{2-}$  carbon ring is the delocalised case shown in Scheme 1-3.

**Scheme 1-3 Potential resonance forms of chloranilic acid**



This is also confirmed by the calculated average bond lengths of the metal anilic acid complexes found in the CSD, Figure 1-17, in which the average structure of the  $\text{XA}^{2-}$  dianion has a characteristic structure of four intermediate C–C bonds of approximately the same length, and two single C–C bonds.

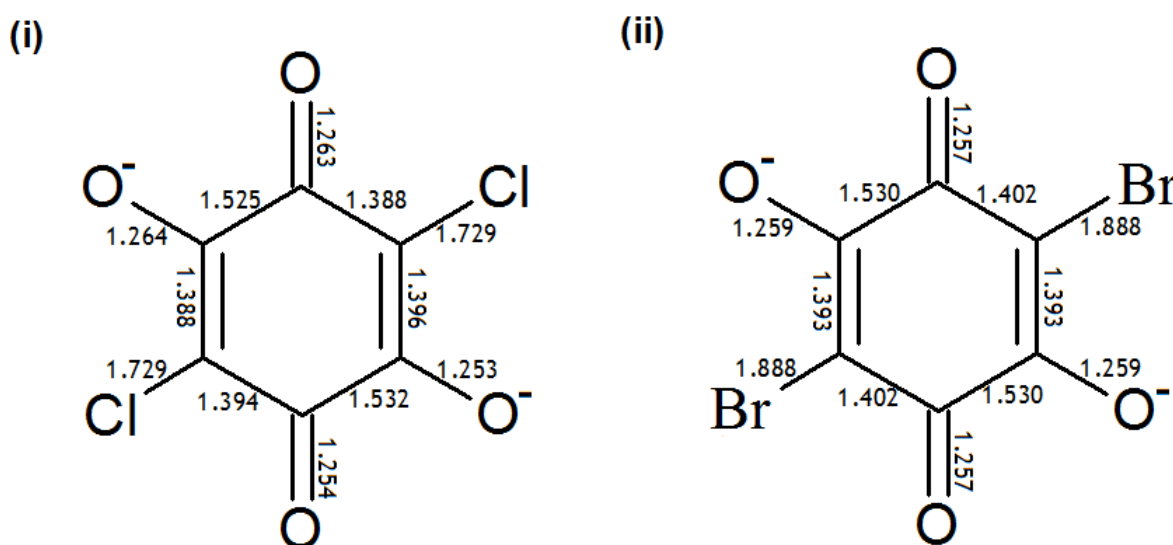


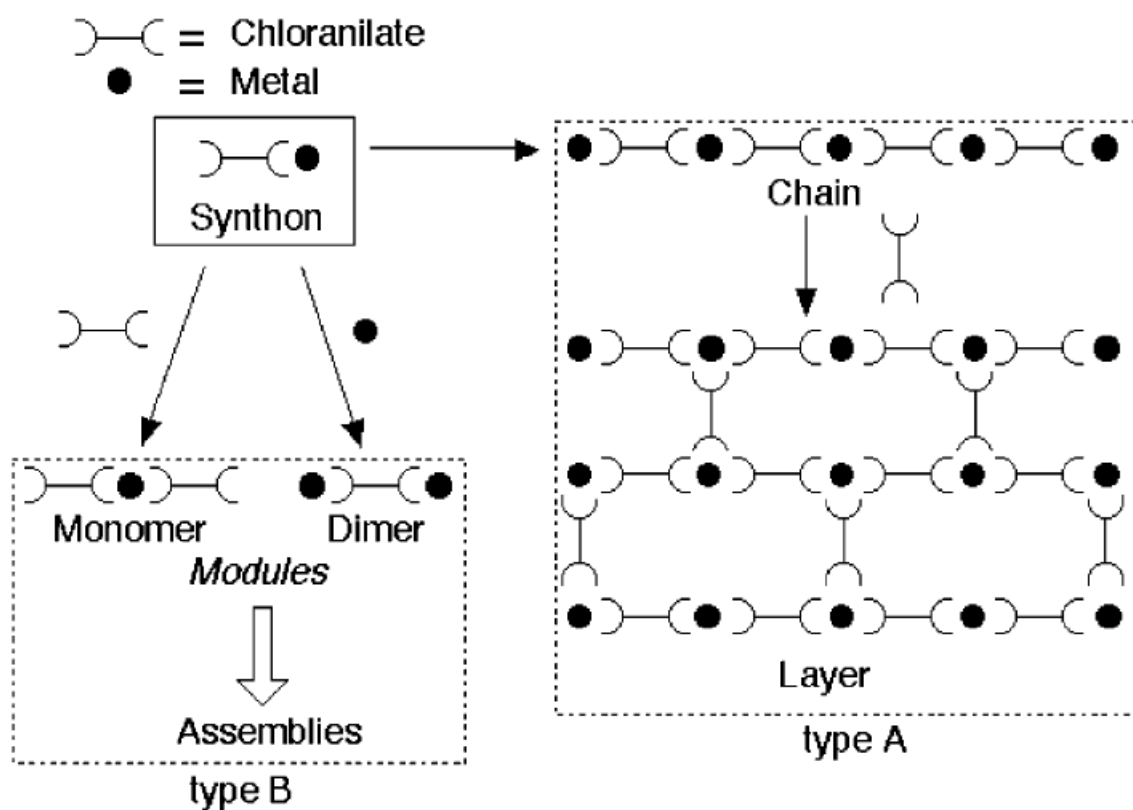
**Figure 1-17 Average bond lengths found using Vista<sup>110</sup> of (i)  $\text{CA}^{2-}$  and (ii)  $\text{BA}^{2-}$**

Due to the significantly greater number of CA metal complexes, the slight discrepancies in the average bond lengths of the  $\text{CA}^{2-}$  dianion may reflect the different levels of electron delocalisation in the  $\text{MCA}^{2-}$  complexes. As there are

only five  $\text{MBA}^{2-}$  complexes known, all of which are bound to the metal as a bridging bisbidentate ligand, and possess the delocalised structure, this is not observed in the average  $\text{BA}^{2-}$  bond lengths which average out symmetrically. However, from both cases it is clear to see that the delocalised form is dominant.

The different levels of deprotonation allows XA to act as a monodentate, bidentate or bisbidentate ligand, and the formation of dimers, one-dimensional (1D) chains, and two-dimensional (2D) layers have been observed, depicted in Scheme 1-4 <sup>111</sup>.

Scheme 1-4 <sup>111</sup> Formation of various ligand architectures using CA

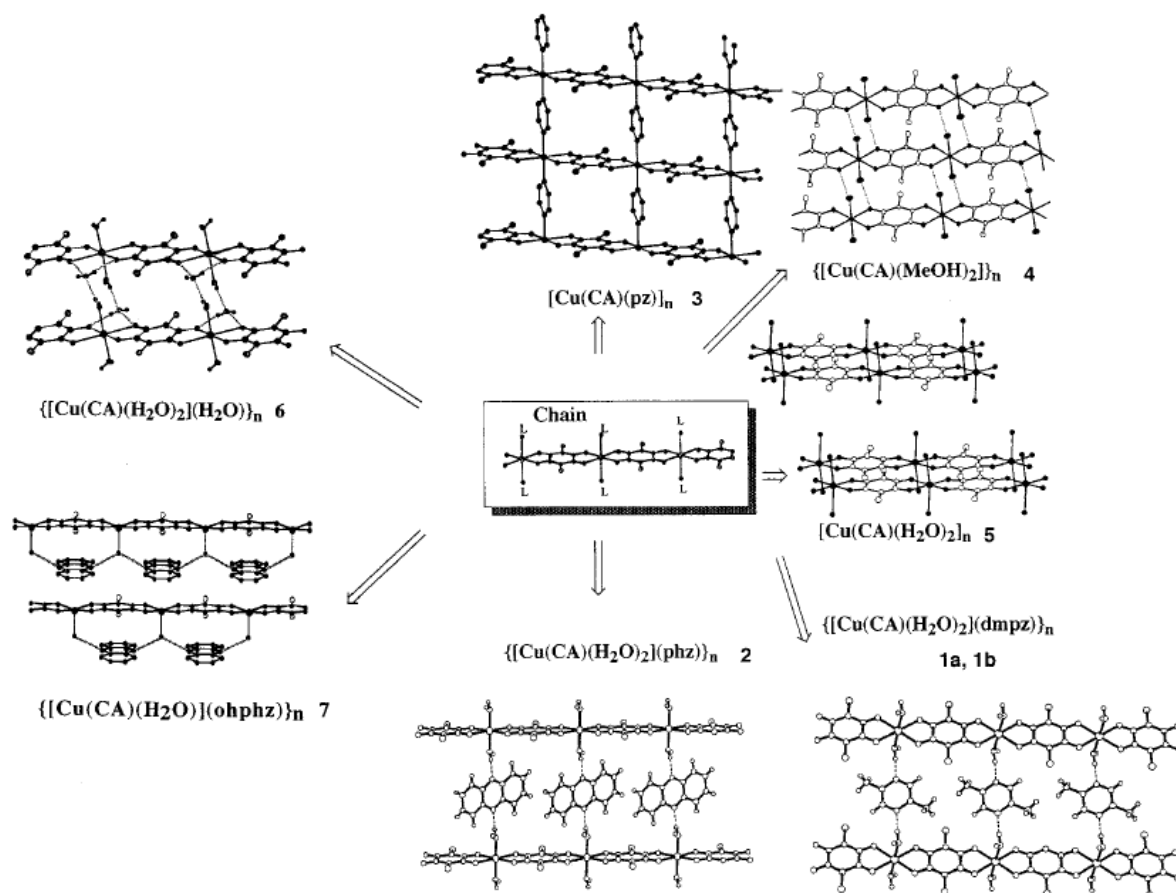


All of these entities can and have been built up to higher dimensional structures by intermolecular interactions such as hydrogen-bonding (HB) <sup>112,113</sup>,  $\pi$ - $\pi$  interactions <sup>112-115</sup>,  $\pi$ -X interactions <sup>113</sup>,  $\pi$ -M interactions <sup>113</sup>, X-X interactions <sup>116,117</sup>, M-M <sup>112, 118</sup> and ionic interactions <sup>119</sup>. The interactions studied most extensively in the literature are HB and M-ligand complexation, particularly in crystal engineering as these are directional and significantly stronger than the other interactions, with the exception of ionic <sup>120,121</sup>.

In most of the examples in the literature the metal is a TM: Cu,<sup>110,113,126,127</sup> Fe,<sup>128-131</sup> Co,<sup>114,125,127,128,132</sup> Mo<sup>109,133,134</sup> and Mn,<sup>127,128,135,136</sup> and the ligand is in its dianion form. This potential coordination of paramagnetic TM ions through delocalised CA<sup>2-</sup> bridges gives the possibility of both interesting structures and electronic behaviour, particularly those of a magnetic nature<sup>89,111, 114,123-124, 127-133,135-136</sup>. The fact that the TM, in principle, as well as the ligand can exist in different oxidation states, also adds a degree of flexibility to these systems.

The CA<sup>2-</sup> dianion most commonly acts as a bis-bidentate ligand bridging itself between two metal centres and forming one-dimensional MCA chains. Usually the M has an octahedral or a slightly distorted octahedral environment in which two water molecules<sup>128</sup> or another mono/ bidentate ligand(s)<sup>126-128</sup> completes the coordination, giving a wide range of possible packing arrangements, as illustrated in Scheme 1-5.

**Scheme 1-5**<sup>126</sup> Packing arrangements in metal chloraninate salts



A number of studies in the literature have used a series of other large organic ligands to form complexes in which it is possible to control the layer-gap sizes between these MCA chains<sup>126,128</sup>. Similar combinations have also formed grids of MCA chains coordinated to such ligands resulting in sturdy frameworks.<sup>127,128,137</sup> Due to the ability of the CA ligand to form bifurcated bonds with molecules such as pyridine with sufficient reliability it has become supported by a number of groups for use in crystal engineering. Others feel that the dimensionality of the crystal structures of the metal-assembled compounds can be designed by the proper choice of the organic ligands and that the use of mixed organic ligands can help to get predictable molecular architecture.<sup>125</sup>

By varying the size and identity of the additional ligand it is also possible to control the pore shapes and sizes of the frameworks<sup>128,137</sup> and one current application of these types of structures is as supra-molecular metallacyclic hosts with inner cavities for guest inclusion,<sup>137-138</sup> in particular those in which the frameworks possess rectangular pores<sup>137</sup> and therefore a lower symmetry, which has the potential of greater selectivity and binding, especially for planar aromatic guests.<sup>139</sup> Other potential properties are redox activity, magnetic behaviour, photo- and electrochemical sensing, and catalysis.<sup>138</sup>

The metal CA chains are not always linear and can also take the form of a wave or zig-zag chain (Figure 1-18). This is particularly the case when the other coordinating molecule(s), in addition to the two bisbidentate CA molecules, are two water molecules which are not directly opposite one another,<sup>129,131</sup> another CA molecule<sup>140</sup> (which would place the metal in an oxidation state of 3<sup>+</sup>), or a completely different large bidentate ligand<sup>130,136,141</sup>. These zig-zag chains again may also form sheets or planes of higher dimensions through intermolecular interactions. The overall structure also takes the form of a honeycomb sheet,<sup>136</sup> this is particularly common in the case of the lanthanide anilic acid complexes (Figure 1-18),<sup>142</sup> which tend to possess an oxidation state of 3<sup>+</sup>.

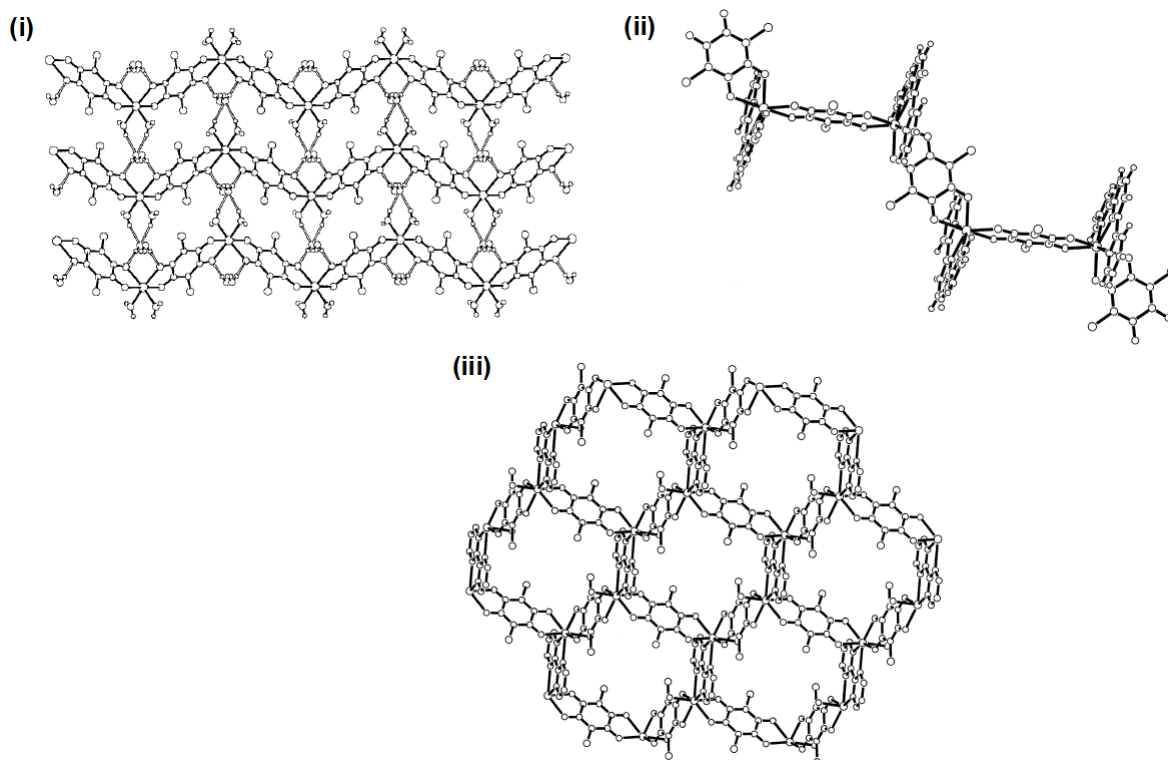


**Figure 1-18 Observed architectures in metal-CA complexes** <sup>131,136</sup>

The larger the radius, and hence coordination sphere of a lanthanide, the higher the potential coordination of CA ligands; the structures can therefore be described as composed of 2-dimensional sheets, <sup>112,138,142</sup> instead of one-dimensional chains (Figure 1-19).

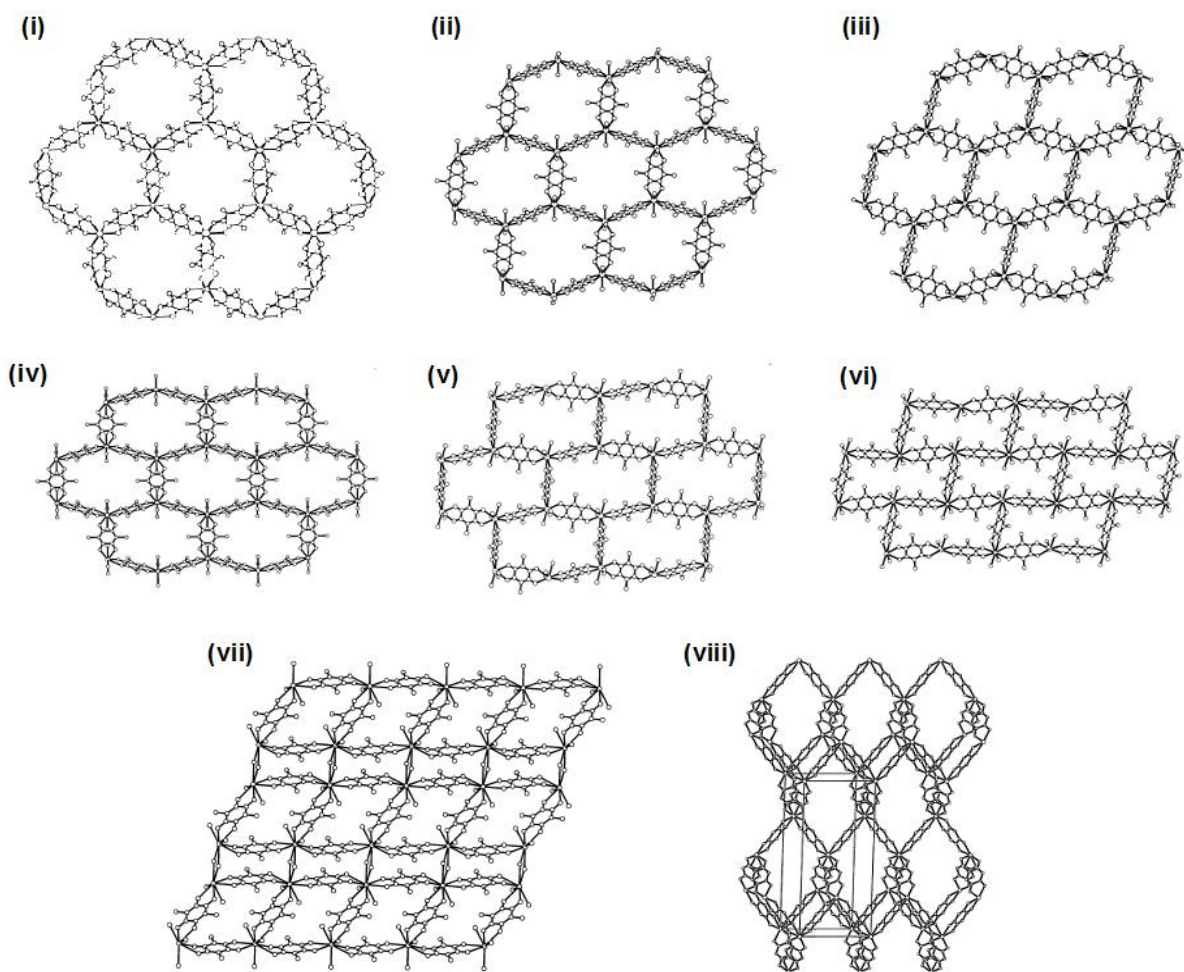


**Figure 1-19 Lanthanide sheet structures (i)  $\text{Ce}_2(\text{C}_6\text{O}_4\text{H}_2)_3 \cdot 24\text{H}_2\text{O}$  (ii)  $\text{Pr}_2(\text{CA}^{2-})_3 \cdot 18\text{H}_2\text{O}$  (iii)  $\text{Y}_2(\text{CA}^{2-})_3 \cdot 16\text{H}_2\text{O}$  (iv)  $\text{Ce}_2(\text{CA}^{2-})_3 \cdot 18\text{H}_2\text{O}$  (v)  $\text{Pr}_2(\text{CA}^{2-})_3 \cdot 8\text{CH}_3\text{CH}_2\text{OH}$  (vi)  $\text{Y}_2(\text{CA}^{2-})_3 \cdot 12\text{H}_2\text{O}$  (vii)  $\text{La}_2(\text{CA}^{2-})_3 \cdot 13\text{H}_2\text{O}$  and extended structure for (viii)  $\text{Y}_2(\text{CA}^{2-})_3$  network.<sup>142</sup>**

Lanthanides and CA as a bis-bidentate ligand have also been used in the synthesis of two-dimensional organometallic rectangles (Figure 1-20)<sup>138</sup>. The authors believe it will soon be possible to synthesise supramolecules with prism or cubic frameworks following their general strategy.

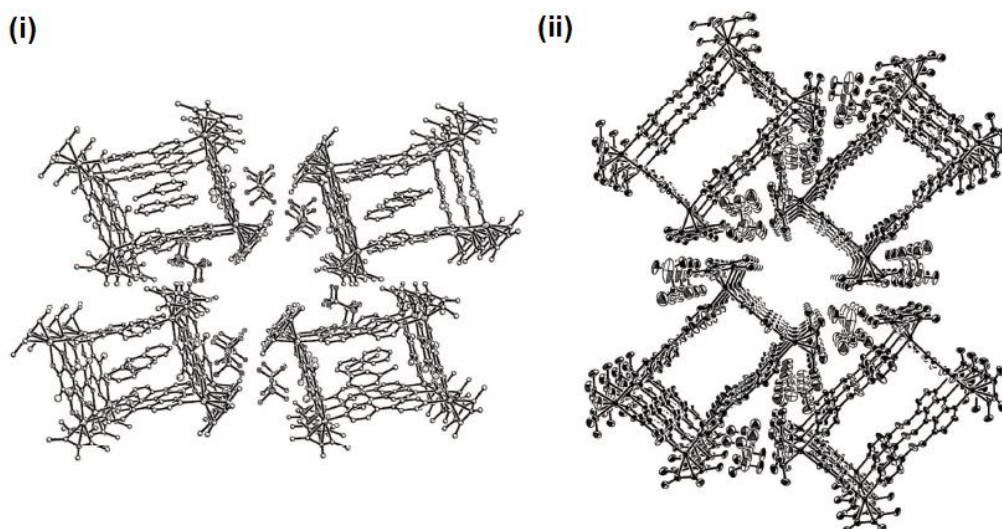
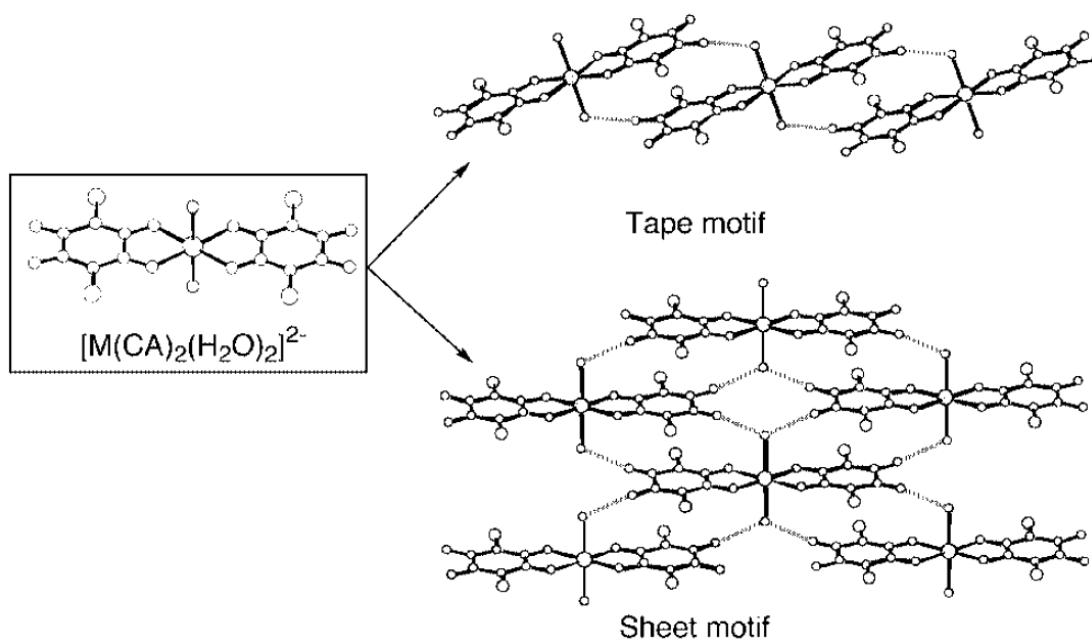


Figure 1-20 Two dimensional extended structures in La CA complexes <sup>138</sup>

#### 1.2.7.4 Monomeric metal complexes

There are also a number of monomeric structures in the literature in which a metal is bound by one, <sup>113,143</sup> or more <sup>109,125,129</sup> terminal CA ligands forming unitary constituents which are held together by intermolecular interactions. Scheme 1-6 illustrates the types of packing from monomeric units composed of a metal with the same octahedral environment of two terminal bidentate CA ligands and two water molecules repeated in the chains and present in a number of complexes. <sup>125</sup>

Scheme 1-6 Packing of monomeric  $M(CA)_2$  units <sup>125</sup>



There are also monomeric units in which metal has a distorted octahedral environment. In this case the carbon rings of the CA molecules are not in the same plane and can be at as much as a 90° angle to one another, around which the other coordinating ligands are fitted. In some cases this had led the monomeric unit to combine with another unit and two ethanol molecules forming a structure composed of dimers.<sup>143</sup>

Another example of a monomeric unit is the case in which a bis bidentate ligand connects two metal centres. The metals are then also connected either to another large multi dentate ligand,<sup>111,114,132</sup> multiple smaller monodentate ligands,<sup>134,144</sup> or in some cases both.<sup>124</sup> These individual monomeric units may also be held together by a number of intermolecular interactions, yielding the overall structure. There are also examples in the literature of complexes that are composed of two or more different monomers held together by intermolecular interactions,<sup>111</sup> and also of monomers and other guest organic cations.<sup>129</sup>

#### 1.2.7.5 Group 1 and 2 Metal Complexes

Although most of the metal anilic acid complexes found in the literature contain TMs, our own work has focused on the combination of the BA and CA ligands with group 1 metals, although group 2 metal complexes are also of potential interest. A literature search has identified isostructural complexes of (1)  $M^{2+}(C_6O_4X_2)^{2-} \cdot 4H_2O$ , ( $M = Ca, Sr, X = Cl, Br$ ),<sup>145</sup> (2)  $Ba^{2+}(C_6O_4X_2)^{2-} \cdot 3H_2O$ , ( $X = Cl, Br$ ),<sup>146</sup> and also a polymorph (3)  $Ba^{2+}(C_6O_4Cl_2)^{2-} \cdot 3H_2O$ <sup>116</sup> of the latter. In each case, the metal ion had a coordination of 8. Complex 1 possesses MXA chains in which M is coordinated to two bridging  $XA^{2-}$  ligands and four water molecules which also connect the chains (Figure 1-21(i)). Complex 2 instead coordinates to only 2 water molecules and 2 oxygen atoms on different XA molecules on the chain below. Complex 3 (Figure 1-21(ii)) the polymorph of 2, also possesses the MXA chain, however each metal ion is only coordinated to three of the bridging  $CA^{2-}$  oxygen atoms and in addition it coordinates to one of the CA oxygens in the chain below, and four water molecules; short  $Cl \cdots Cl$  and  $O \cdots O$  contacts between CA ligands and water molecules were also observed.

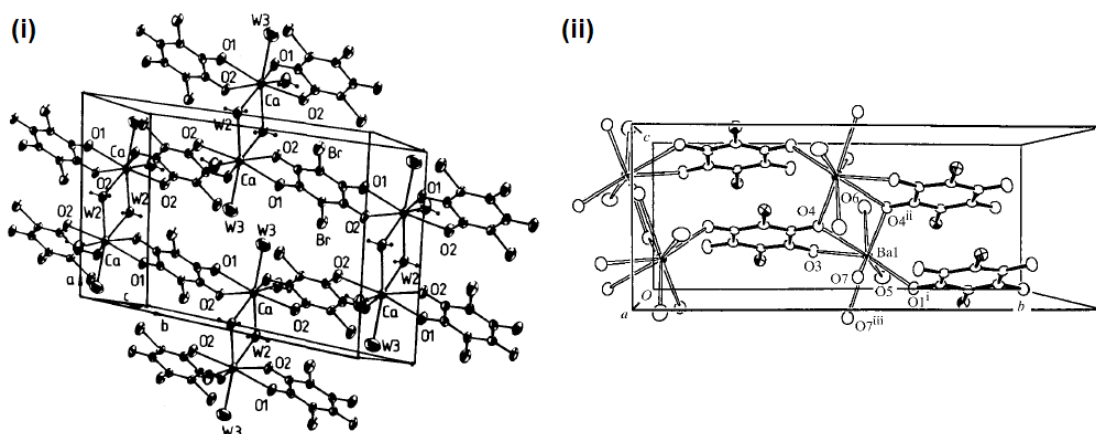


Figure 1-21 (i)  $M^{2+}(C_6O_4X_2)^{2-} \cdot 4H_2O$ , ( $M = Ca, Sr, X = Cl, Br$ ), <sup>145</sup> polymorph of (ii)  $Ba^{2+}(C_6O_4Cl_2)^{2-} \cdot 3H_2O$  <sup>116</sup>

Our main focus, group 1 metals, has very few relevant structures reported in the literature. Crystal data for the hydrated K, Rb, and Cs CA complexes were reported by Herstein and Kaftor in 1972, <sup>147</sup> however there was no detailed structural analysis. To date only NaCA complexes have been analysed, namely the  $2Na^+ CA^{2-} \cdot 3H_2O$  complex by Savariault and Benchekroun <sup>148</sup> and the  $2Na^+ (phen)_2 CA^{2-} \cdot 2H_2O$  complex studied by Papadimitriou et al. <sup>149</sup> both of which possess 2:1 Na to CA ratios, and have 2 different  $Na^+$  environments.

In the  $2Na^+ CA^{2-} \cdot 3H_2O$  complex, (Figure 1-22(i)) both  $Na^+$  ions have a distorted octahedral environment, denoted by the authors as NA1 [ $Na(1)O_5Cl$ ] and NA2 [ $Na(2)O_6$ ]. Na2 connects two  $CA^{2-}$  anions of the same layer in mono and bidentate fashion to form a chain, and also bridges in a monodentate fashion to another  $CA^{2-}$  anion in the second layer. A Na1 ion is also connected to each  $CA^{2-}$  anion in a bidentate fashion by O and Cl. A HB network also connects the water molecules to the O atoms of the  $CA^{2-}$  ions.

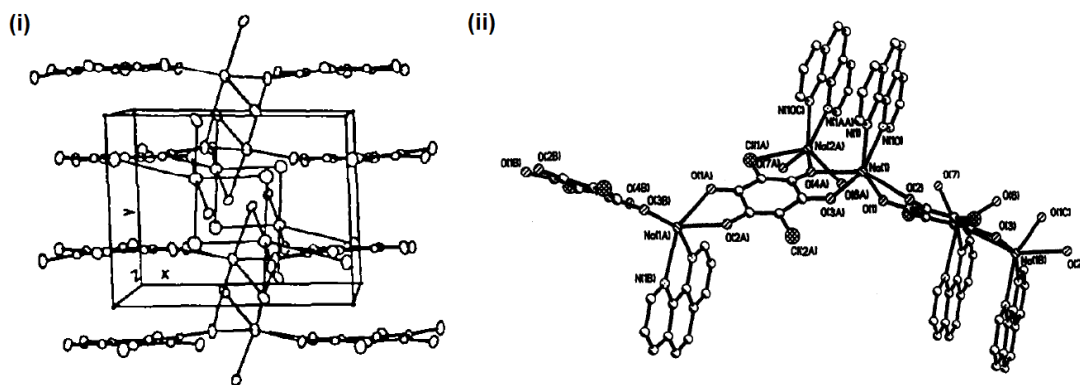


Figure 1-22 (i)  $2\text{Na}^+ \text{CA}^{2-} 3\text{H}_2\text{O}$  complex,<sup>148</sup> (ii)  $2\text{Na}^+ (\text{phen})_2 \text{CA}^{2-} 2\text{H}_2\text{O}$  complex.<sup>149</sup>

The  $2\text{Na}^+ (\text{phen})_2 \text{CA}^{2-} 2\text{H}_2\text{O}$  complex (Figure 1-22(ii)), also has two Na environments. The Na(1) ions possess a disordered octahedral environment, forming a twisted Na(1) chain bridged by bisbidentate  $\text{CA}^{2-}$  dianions, with the additional coordination of the bidentate phen ligand to the Na(1) ion. Each  $\text{CA}^{2-}$  is also bound to a Na(2) in a bidentate fashion by a Cl and adjacent O, the Na(2) also coordinates to 2 water molecules and another bidentate phen ligand.

### 1.3 Applicable Techniques

An ever expanding range of methods are available with which to investigate materials in their solid form both experimentally and computationally. The choice depends on the nature of the material and the property under analysis.

In this work computational methods, deemed appropriate from previous studies of a similar nature, have been used to establish trends in our own materials and properties of interest. All calculations in this work were carried out using the Crystal06 code, in which both Hartree Fock (HF) and Density Functional Theory (DFT) were combined in the form of hybrid calculations, as accounted in the following chapter.

Experimental methods were used in this work to produce and study new complexes, not possible to predict computationally. Although it is common for the two techniques to be used to complement one another, this has not been appropriate in this work, as the development of computational and experimental

approaches for the various families of compounds are not developed to the same extent. For example computational studies of substituted PBAs and HB-bridged metal-metal magnetic couplings are convenient to carry out, while the corresponding syntheses are not so straightforward. In contrast, experimental measurements of more complex metal-organic framework structures are relatively easy to carry out while detailed computational work on these rather complex hydrogen-bonded crystalline materials is less tractable at present.

These techniques are described fully in the following chapter which begins by introducing the concept of a crystalline solid and goes on to provide an explanation of how it is possible by single crystal diffraction to find the positions of the atoms in the smallest repeating unit of a sample in relation to one another by use of the methods of X-ray crystallography. A brief overview of powder and neutron diffraction methods to the extent required in this work is also provided.

The underlying principles for both HF and DFT methods used to calculate the ground state energy for a known structure are also presented. Also discussed are some of the successful approximations within these theories, made and used by others, in order to obtain a successfully converged ground state and their application in the CRYSTAL06 code. The easy manner in which this code allows the use of hybrid HF and DFT functionals based on the format of the successful B3LYP functional is explained and the models used in order to obtain band gaps, magnetic coupling and ordering temperatures from the energies obtained from these calculations presented.

The succeeding chapters three and four provide an analysis of the theoretical results obtained on the electronic band gaps of PB and its derivatives and on magnetic coupling values in a range of transition metal hydrogen halides (TMHs) respectively. Chapter five examines the structural properties of a number of related crystalline architectures synthesised in the lab and chapter six uses neutron diffraction to examine the effect of applied pressure on the  $\text{KH}(\text{C}_4\text{H}_5\text{O}_2)_2$  complex which contains a short asymmetric HB. The main findings of this work including those linked to metal identities are pulled together in a concluding summary in chapter seven.

## 2 Theory and Methodology

The aims of the work presented here were to probe the structural and physical properties of materials in the crystalline solid-state, with a focus on metal-organic materials in which hydrogen bonding might play a significant role, and on related model systems. To this end, a variety of methods and techniques suitable for the solid-state have been utilised. Experimentally, crystallisation and diffraction techniques were used to produce and determine the structures of a series of related metal organic complexes. Other techniques such as X-ray Powder Diffraction (XRPD), Differential Scanning Calorimetry (DSC) and Thermogravimetric Analysis (TGA) were also used to aid in the characterisation of the materials. Computationally, CRYSTAL06,<sup>150</sup> a quantum chemical code designed to study materials in the solid-state and in particular to evaluate their physical properties, was used to calculate the total energies of materials under various conditions of pressure and temperature, and the energy differences inserted into theoretical models to examine the effect of these on physical properties such as magnetic coupling.

### 2.1 Crystalline Solids

#### 2.1.1 Crystal Lattices

A crystalline solid, or crystal, is a three dimensional periodic arrangement of atoms. Each arbitrary repeating unit in space can be represented as a lattice point, and when combined by translation these points constitute the crystal lattice. The volume associated with a single lattice point is known as the primitive unit cell and is usually illustrated in the form of a parallelepiped. The eight vertical lattice points are all shared between eight other cells so each parallelepiped contains only one lattice point. The unit cell is defined by six lattice parameters; three lattice constants,  $a$ ,  $b$ ,  $c$  and three angles  $\alpha$ ,  $\beta$ ,  $\gamma$  (Figure 2-1).

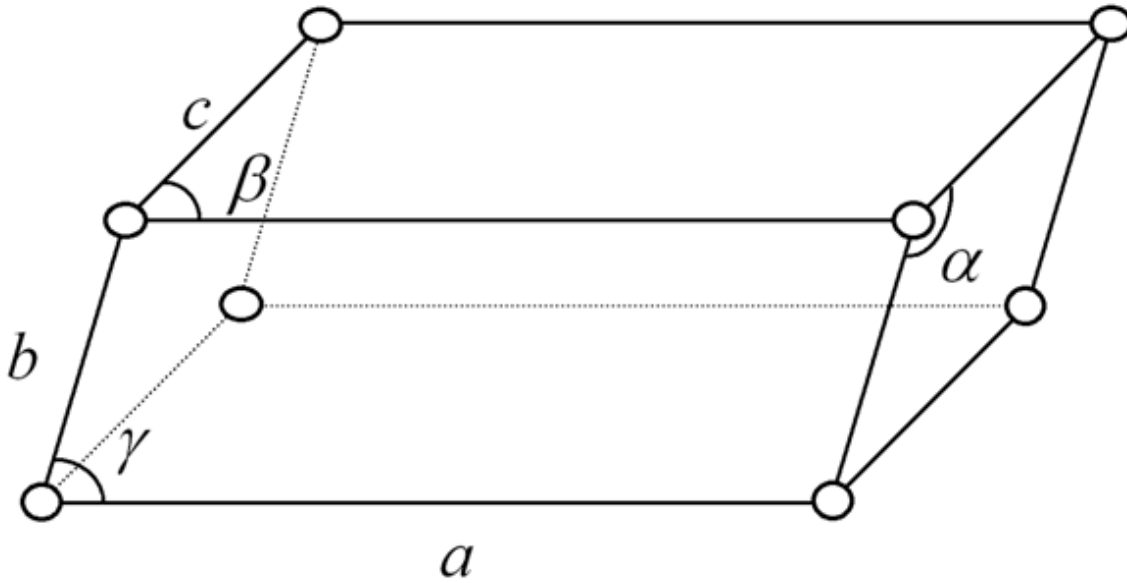


Figure 2-1 Crystal unit cell, parallelepiped enclosed by eight lattice points. <sup>151</sup>

In some cases, referred to later, it is more useful to express the primitive unit cell for each lattice point in the form of the Wigner-Seitz cell (Figure 2-2). In this case the lattice point is fixed to the centre of the unit cell, and the cell is determined by the perpendicular bisectors of the lines joining neighbouring points.

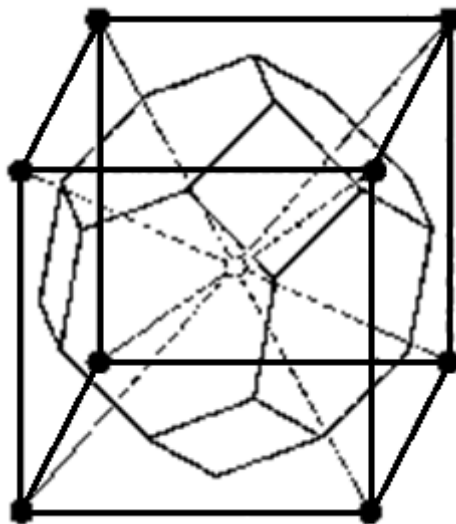


Figure 2-2 The Wigner-Seitz cell shows volume associated with one lattice point.

The lattice can often be expressed in terms of a number of possible unit cells (Figure 2-3(i)) some of which will contain more than one lattice point leading to centred unit cells (C,I,F,R) (Figure 2-3(ii)). Usually the cell with angles closest to 90° is chosen to take most advantage of crystal symmetry.

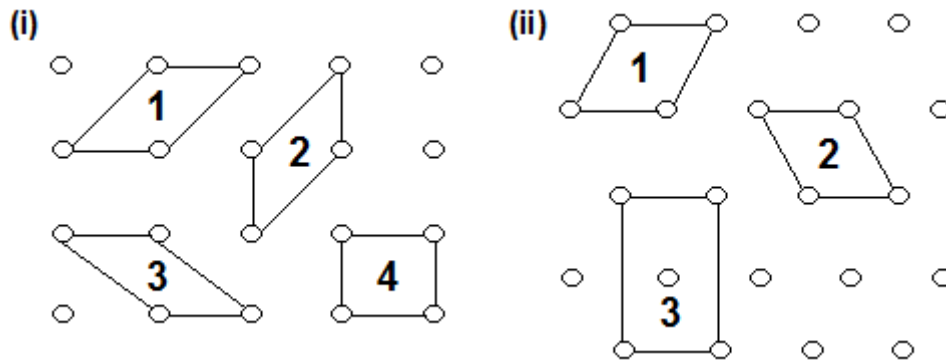


Figure 2-3 (i) number of possible primitive unit cells in a lattice (ii) cell 3 is an example of a centred lattice<sup>152</sup>

Once the unit cell most appropriate for describing the crystal is established, the six lattice parameters and the number of lattice points contained within the cell will determine to which of the seven crystal systems and fourteen possible Bravais lattices the crystal belongs, Table 2-1, Figure 2-4.

Table 2-1 The seven crystal systems and fourteen Bravais lattices.

Crystal System	Restrictions in cell dimensions	Bravais Lattices	
	$a, b, c$	$\alpha, \beta, \gamma$	
Triclinic	None	None	P
Monoclinic	None	$\alpha = \gamma = 90^\circ$	P, C
Orthorhombic	None	$\alpha = \beta = \gamma = 90^\circ$	P, C, I, F
Tetragonal	$a = b$	$\alpha = \beta = \gamma = 90^\circ$	P, I
Cubic	$a = b = c$	$\alpha = \beta = \gamma = 90^\circ$	P, I, F
Trigonal	$a = b = c$	$\alpha = \beta = \gamma < 120^\circ$	
	$a = b$	$\alpha = \beta = 90^\circ, \gamma = 120^\circ$	R
Hexagonal	$a = b$	$\alpha = \beta = 90^\circ, \gamma = 120^\circ$	P

P = primitive, C = centred, I = body-centred, F = face-centred, R = rhombohedral

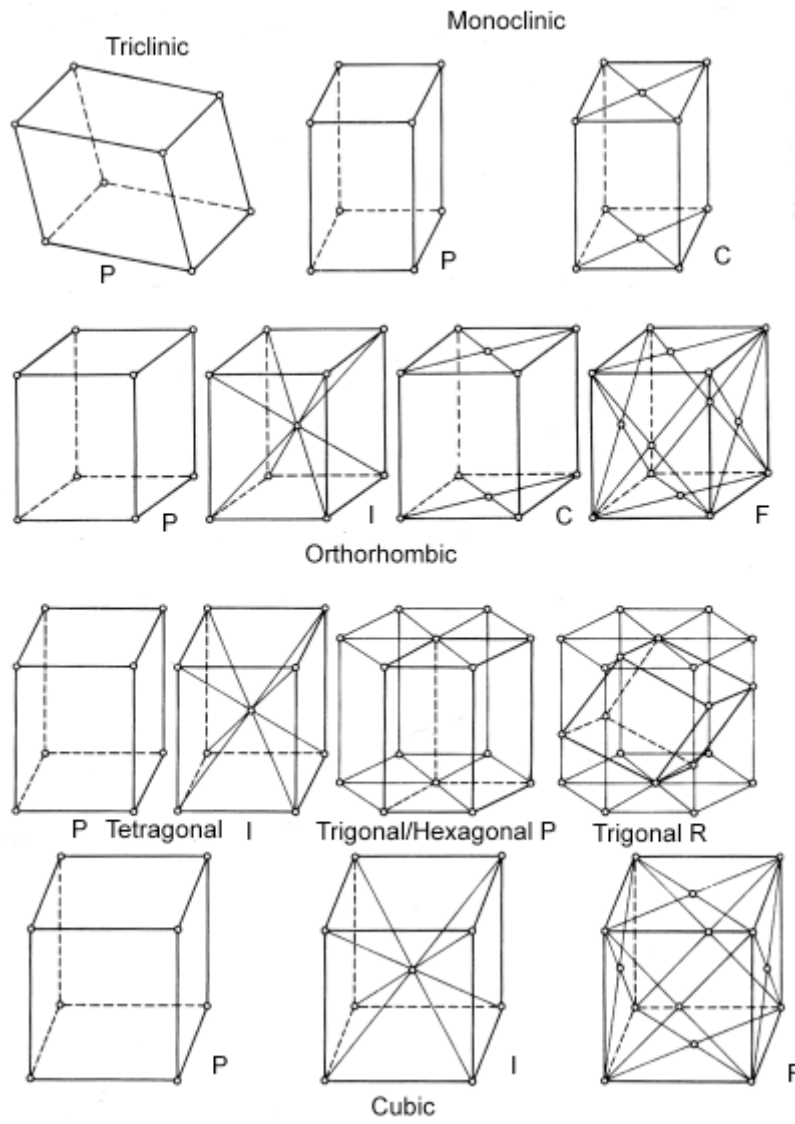


**Figure 2-4 Illustration of the fourteen Bravais lattices**

Lattice points are related only by translation and the smallest repeating group of atoms within the structure and related by symmetry is called the basis. The crystal structure is therefore the combination of two quantities; a lattice of points and a basis. In crystallography terms, the basis is more commonly referred to as the asymmetric unit and is the smallest repeating unit in the structure. Having used the lattice points to identify the most appropriate unit cell and Bravais lattice, combining the internal rotation and reflection elements with the Bravais lattice will associate the crystal with one of a possible 32 point groups.

The further consideration of internal translational symmetry elements within the cell, including screw axes and glide planes, will then determine to which of the 230 space groups the crystal belongs. By identifying the correct space group and applying the associated symmetry operations to the basis, it is therefore possible to reproduce the entire contents of the unit cell and hence the entire crystal. The atom positions within the unit cell are usually given in terms of fractional coordinates  $(x, y, z)$ , which are fractions of the lattice constants  $a$ ,  $b$  and  $c$  respectively.

### **2.1.2 Crystal Symmetry**

There are two types of symmetry in a crystal structure: point symmetry within the unit cell and translational symmetry both within and between unit cells. Point symmetry includes rotations, reflections and inversions, while combining these with internal translational symmetry produces glide planes and screw axes. Pure translational symmetry in the crystal structure relates lattice points to one another. The internal symmetry inside the unit cell introduces relationships between the unit cell contents and can comprise inversion centres ( $\bar{1}$ ), mirror planes ( $m$ ) and glide planes, rotation axes (2-, 3-, 4-, 6-) and screw axes, and rotoinversion axes ( $\bar{4}$ , etc), in which the inversion centre and rotation axis symmetry elements are coupled.

## **2.2 Diffraction Techniques**

The basis of all diffraction techniques is the same: a sample is bombarded with a form of electromagnetic radiation or matter which will interact with the sample in a way which allows the structure to be probed. The types of diffraction used in this project include both powder and single crystal diffraction, in which the sample is either a finely ground powder or a single crystalline solid, respectively, and both X-ray and neutron diffraction experiments. The three-dimensional periodic translation in a crystal allows the interacting waves or matter to produce a three-dimensional diffraction pattern of spots which can be Fourier transformed to reproduce the crystal structure. In the case of powder diffraction, there are many

different unit cell orientations contained within the sample, so that instead of spots, a pattern of concentric rings is produced. When viewed along the plane of concentric rings, a one-dimensional pattern is observed. Although the use of powder diffraction during this work was limited to the attempted characterisation of a few samples it is also possible to reproduce a crystal structure from a powder diffraction pattern. However the procedure is not always straightforward and often requires a good starting model. The benefits of powder diffraction include its less stringent sample requirements: it is possible to obtain a powder pattern in 15-60 minutes from as little as a few milligrams of sample whereas the size of single-crystal required ranges from 0.1-0.5mm<sup>3</sup>, in the case of X-rays, to 1-100mm<sup>3</sup> for neutrons, and data collection can take from a few hours to a few days.

### **2.2.1 X-ray Diffraction**

The main uses of single-crystal X-ray diffraction are to identify unknown compounds, to determine stereochemistry and molecular packing in the solid state and to give accurate measurements of the angles and bond lengths in the unit cell of the crystal. The three-dimensional regular repeating unit cell in a crystal allows the symmetry present to be used to classify the crystal type, to determine the unit cell parameters and to define the geometry required for the collection of diffraction data.

#### **2.2.1.1 Production of X-Rays**

X-rays are produced when charged particles such as electrons, are accelerated at high speed (and hence with high energy) to collide with matter. In most laboratory diffractometers, the electrons are accelerated through a potential of around 30 kV, and collide with readily available metals, usually Cu or Mo which yields X-rays of characteristic wavelengths of order 1 Å, comparable to the separation between the atoms in a crystalline structure.

The accelerated electrons have enough energy to ionise some of the target metal *1s* electrons, causing a vacancy into which outer shell *2p* or *3p* electrons can drop down, releasing energy in the form of X-ray radiation. These transition energies

have discrete values and a spectrum of characteristic X-rays results for each metal. For Cu and Mo the  $K_{\alpha}$  ( $2p-1s$ ) and  $K_{\beta}$  ( $3p-1s$ ) transitions have wavelengths of 1.5406 Å and 1.3922 Å, and 0.709 Å and 0.632 Å, respectively. The transition causing the  $K_{\alpha}$  line occurs more frequently and as the more intense of the two is normally used in diffraction experiments. The spectrum will also display a broad background of white radiation, caused when electrons are slowed or stopped by collisions and energy is converted into other wavelengths. For most diffraction experiments a monochromatic beam is required and all other wavelengths are filtered out. For Cu radiation, for example, a Ni filter is used to absorb the  $K_{\beta}$  and most of the white radiation, leaving a monochromatic beam of  $K_{\alpha}$ . Once produced, the X-rays leave the tube through beryllium windows, interact with the sample material and a diffraction pattern is produced.

#### **2.2.1.2 Interaction with Matter, Lattice Planes and Diffraction Geometry**

X-rays are a form of electromagnetic radiation with wavelengths of similar magnitudes to those of inter-atomic distances. This and the fact that the atoms in a crystalline sample are highly ordered and periodic in nature allow the scattered X-rays, by their wave nature, to interact and produce a diffraction pattern consisting of discrete spots of varying intensity due to the interference of different parts of the waves that meet at the observation point by different paths.

The spots produced on a diffraction pattern are a result of the waves scattered by a sample interacting constructively with one another. In order for this to occur the path differences of the interacting scattered waves must be equal to an integer number of wave lengths,  $n\lambda$ . In order to produce a diffraction pattern the crystalline sample and the incoming X-ray beam must therefore be aligned in a specific way to one another so that this condition is met.

The relationship between lattice parameters for constructive interference can be observed mathematically in terms of the Laue equations (2-1). This is a very restricting condition which show how the path difference between the waves scattered by neighbouring points are related by the angle of incidence  $\mu$  and the

angle of scattering  $\nu$ . In order to observe diffraction spots, all three of these conditions must apply at the same time in the three dimensions.

$$\begin{aligned} a(\cos \mu_a + \cos \nu_a) &= n_1 \lambda \\ b(\cos \mu_b + \cos \nu_b) &= n_2 \lambda \\ c(\cos \mu_c + \cos \nu_c) &= n_3 \lambda \end{aligned} \quad (2-1)$$

If this condition is met in the one dimensional case, the resulting scattering from a lattice point can be illustrated by a Laue cone, Figure 2-5. If this condition is met in the case of the three dimensional crystal lattice, three Laue cones, one from each dimension, will intersect one another in a single line. This is the condition for constructive interference; scattering in all other directions will result in destructive interference.

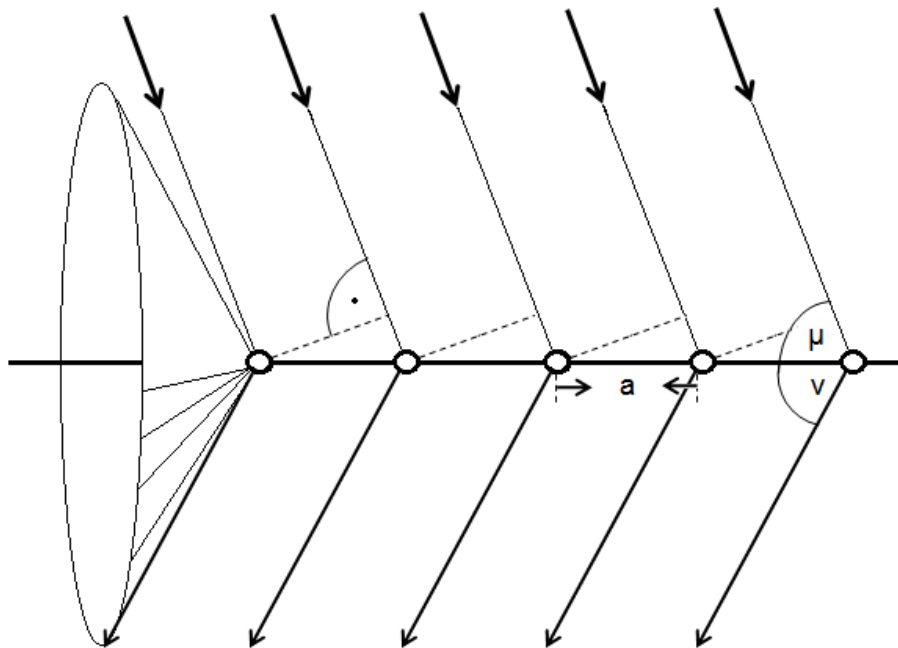


Figure 2-5 Laue cone construction for diffraction geometry <sup>152</sup>

This condition can also more usefully be illustrated using sets of parallel lattice planes with interplanar spacing  $d$ , as shown in Figure 2-6.

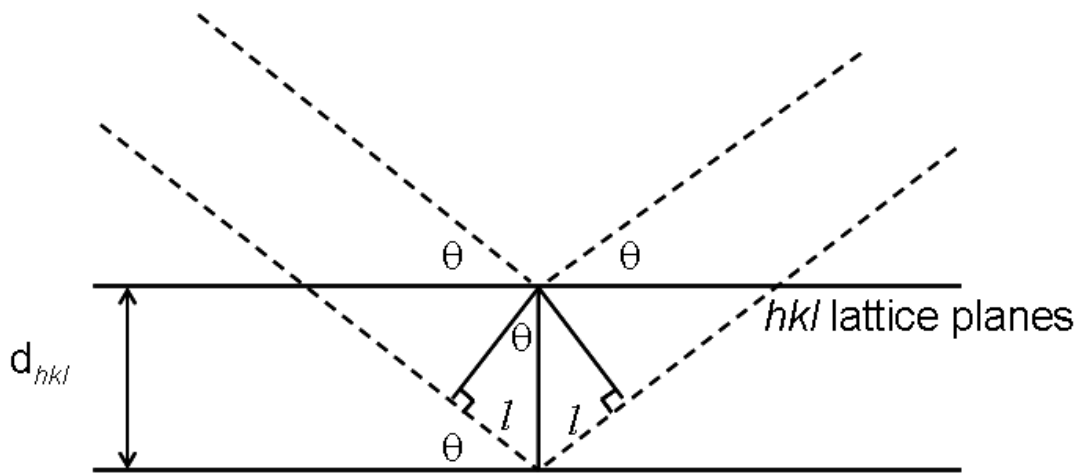


Figure 2-6 Geometric construction for the derivation of Bragg's Law

In order to interfere constructively the waves that are incident at an angle  $\theta$  must be reflected from these planes and the resulting path difference between the scattered waves  $l + l$  must therefore equal  $n\lambda$ . This condition defines Bragg's law, equation 2-2

$$l + l = 2d \sin \theta = n\lambda \quad (2-2)$$

Each set of planes is related to the unit cell and characterised in terms of Miller indices ( $hkl$ ) and the inter-planar spacing,  $d_{hkl}$ . The Miller indices are established by examining the plane nearest, but not passing through, the origin (Figure 2-7) and determining the intercepts on the  $a$ ,  $b$  and  $c$  axes of the unit cell which will be  $a/h$ ,  $b/k$ , and  $c/l$  respectively.

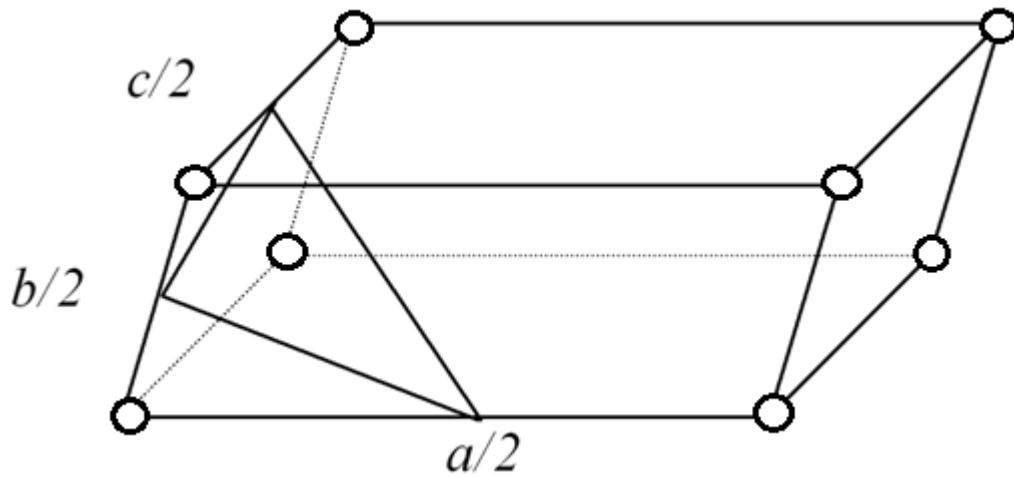


Figure 2-7 Illustration of the (2 2 2) Miller index plane in a unit cell

In order to determine a structure a series of diffracted intensities must be collected. Each diffraction intensity corresponds to the spots produced by the alignment of the incident radiation and one possible set of intersecting planes, which meet the conditions of Bragg's law. Only by collecting images from a large number of the possible sets of planes (Figure 2-8) is it possible to gather enough information to determine a structure.

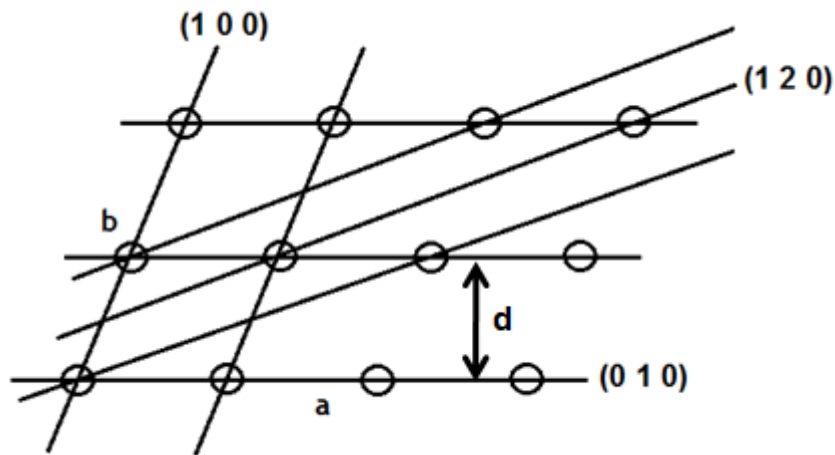


Figure 2-8 Sets of lattice planes leading to diffraction spots <sup>152</sup>

### 2.2.1.3 Structure Factors

The intensities  $I_{hkl}$  of the scattered beams reflected from the  $hkl$  planes (spots in the diffraction pattern), are measured during a diffraction experiment. After processing, the intensities and associated errors are written into a .hkl file alongside their associated Miller indices. From this it is possible to construct a reciprocal unit cell which can be mathematically transformed into a model of the electron density,  $\rho$ , of the real space unit cell by the use of a Fourier transform.

Each spot, therefore position in reciprocal space, has an associated structure factor  $F_{hkl}$  which is directly proportional to the measured intensity ( $I \propto |F_{hkl}|^2$ ).

$$|F_{hkl}| \approx \sqrt{I_{hkl}} \quad (2-3)$$

The structure factor  $F_{hkl}$ , the magnitude of which can be approximated to the square root of the intensity, equation 2-3, reflects the unit cell contents and represents the waves scattered by one unit cell during Bragg reflection from a particular set of lattice planes. As not all atoms positions lie on a plane, therefore scattering in phase, each atom  $j$  has an associated phase shift  $\phi$  which is dependent on the distance from the plane  $hkl$  and therefore its fractional coordinates  $x_j, y_j, z_j$

$$\phi_j = 2\pi(hx_j + ky_j + lz_j) \quad (2-4)$$

The structure factor is therefore an expression of the amplitude and phase of each scattered wave, and is also related to the types and positions of the atoms within the unit cell, through equation 2-5

$$F_{hkl} = \sum_{j=1}^N f_j e^{2\pi i(hx_j + ky_j + lz_j)} \quad (2-5)$$

The summation is over  $N$  atoms in the unit cell, and  $x_j, y_j, z_j$  are the fractional coordinates of atom  $j$ . The scattering factor  $f_j$ , depends on a number of factors, including the scattering angle  $\theta$ , and falls off with  $\sin\theta/\lambda$  (Figure 2-9), the types of

atoms present in the unit cell; heavier atoms scatter the X-rays to a greater degree. The scattering is also weakened by the atomic vibrations summarised by the Debye Waller temperature effect which accounts for an additional reduction in scattered intensity depending on the scattering angle.

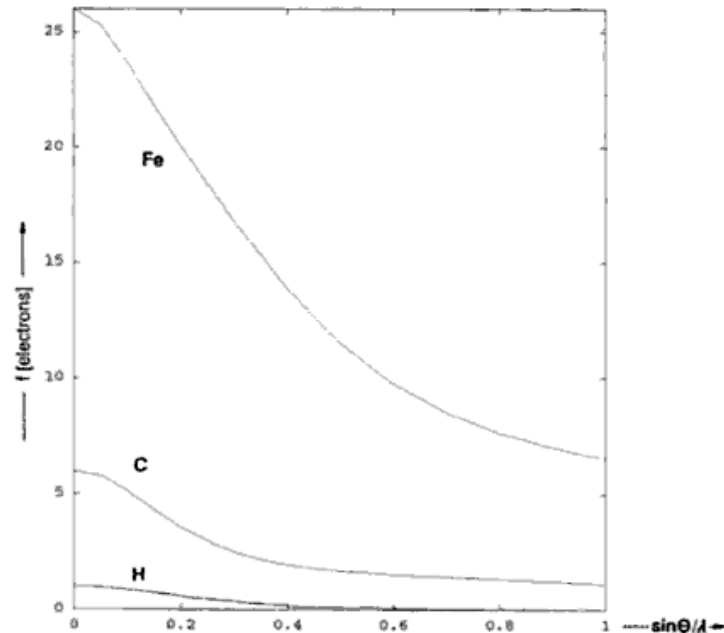


Figure 2-9 Form factor fall-off of X-ray scattering factors for three atom types. The fall-off in scattering with angle is further emphasised by thermal vibrations

These factors can be summarised in the following expression

$$f_j = f \cdot e^{\{-2\pi)^2 U d^2\}} \quad (2-6)$$

In which  $U$  is the atomic displacement factor,  $f$  is the scattering factor for a particular atom type. This can be rewritten as

$$f_j = f \cdot e^{\left\{-B \frac{\sin^2 \theta}{\lambda^2}\right\}} \quad (2-7)$$

where  $B$  is the Debye-Waller factor.

Due to the phase shift the scattered wave may be expressed as a complex quantity in the form of either an exponential with an imaginary part

$$F_{hkl} = \sum_j f_j \exp(hx_j + ky_j + lz_j) \quad (2-8)$$

or, from the Euler formalism, as the sum of a cosine (real part A) and sine (imaginary part B)

$$F_{hkl} = \sum_j f_j [\cos 2\pi(hx_j + ky_j + lz_j) + i \sin 2\pi(hx_j + ky_j + lz_j)] = A_j + iB_j \quad (2-9)$$

$$(A_j = f_j \cos \phi_j, \quad B_j = f_j \sin \phi_j) \quad (2-9a)$$

For an individual scattering wave the relation of the real and imaginary parts form to combine the scattering amplitude and its associated phase

$$|F_{hkl}| = \sqrt{A_j^2 + B_j^2} \quad \phi_j = \arctan \frac{B}{A} \quad (2-10)$$

The idea of structure solution in crystallography arises from this - it is not possible to measure directly the phases  $\phi_j$  and thus it is necessary to utilise methods of solving this “phase problem”.

This can be simplified in many cases. A large majority of structures are centrosymmetric and therefore possess an inversion centre, such that any atom at position (x, y, z) will also possess an associated atom at (-x, -y, -z). In relation to equation 2-9, as  $\sin \phi = \sin -\phi = 0$ , the imaginary terms in the structure factor will cancel out yielding

$$F_{hkl} = \sum_j f_j \cos 2\pi(hx_j + ky_j + lz_j) \quad (2-11)$$

This reduces the phase problem to a sign problem, with  $\phi = 0$  or  $\pi$ . However, in general phases can take any value and structure solution methods must address this.

The importance of the structure factors can be emphasised by their relationship with the electron density

$$F_{hkl} = \int_V \rho_{xyz} e^{2\pi i(hx+ky+lz)} dV \quad (2-12)$$

where the integration is over the whole volume of the unit cell.

By the associated inverse Fourier transform, it is also possible to obtain the electron density for a point  $(x, y, z)$  in the unit cell from a knowledge of the structure factors (both magnitude and phase)

$$\rho_{xyz} = \frac{1}{V} \sum_{hkl} F_{hkl} e^{-2\pi i(hx+ky+lz)} \quad (2-13)$$

and this expression thus relates the “measurable” quantities  $F_{hkl}$  to the electron density, but recognising that we can only measure  $|F_{hkl}|$  and must obtain the phase information by other routes.

As it is only possible to measure intensities during a diffraction experiment where all phase information is lost there are other methods by which an initial model structure can be calculated based on the intensities alone before the calculation of Fourier difference maps.

#### 2.2.1.4 Structure Solution

In order to solve a crystal structure, the structure factors which contain both the intensity and phase information of the diffracted reflections, must be determined

$$F_{hkl} = |F_{hkl}| \exp(i\phi_{hkl}) \quad (2-14)$$

As only intensities are measured during a diffraction experiment, it is not possible to solve the structure (produce an electron density map) by the simple application of an inverse Fourier transform. This is known as the phase problem and a number of methods exist by which to get around this problem.

#### 2.2.1.4.1 Patterson Methods

The Patterson method is of most use in cases where there are a few atoms heavier in comparison to the other atoms within the structure. It uses a method analogous to the Fourier transform of the electron density, equation 2-12, in order to calculate all the interatomic distances between atoms within the unit cell directly from the measured intensities  $F_{obs}^2$ , producing a map of interatomic vectors that must be deconvoluted to produce atomic coordinates.

The origin of a Patterson map corresponds to the position at which each atom in the unit cell is at a distance 0 to itself, this will therefore always be the highest peak and will have a height in proportion to the sum of the squares of all the atomic numbers of the atoms in the cell. The intensity of each vector is proportional to the sum of electrons in the related atoms. Making use of the heavy atom method thus is valuable as the vectors between the heavier atoms will have very high intensity.

#### 2.2.1.4.2 Direct Methods

This is probably the most common structure solution technique and gets its name by its link from the relationships of the reflection intensities directly to the phases themselves. Direct methods make use of the Sayre rule, which assumes that electron density is always positive and concentrated in well defined maxima. The simplest relationship between reflection intensities used in direct methods is the triplet relationship. For a triplet relationship, if the sum of the  $(hkl)$  indices of three strong reflections equals  $(000)$  then the sum of their phases is likely to equal zero with a probability that this is true being calculable from the data. Direct methods approaches use automatic generation of sets of phases based on many such relationships, to produce most probable sets of estimated phases.

Once a suitable set of phases is available, a structural model can be calculated from equation 2-13, using one of the methods above, in which coordinates are given in relation to the origin of a space group and model structural factors can be calculated.

### 2.2.1.5 Structure Refinement

Once a suitable structure model with sufficiently determined phases has been established, this can be used to calculate structure factors  $F_{calc}$  that can be compared with the observed values. These values can also be used to refine the model, allowing an improved set of calculated structure factors to be obtained, and this model can then be refined to give the best fit to experimental data.

As it is not possible to measure an infinite set of  $hkl$  values required to provide the total electron density for the unit cell, and since initial structure solution often does not reveal all atoms, late in a structural analysis an electron density difference map is plotted by applying a difference Fourier transform

$$\Delta\rho_{xyz} = \frac{1}{V} \sum_{hkl} (F_{hkl}^{obs} - F_{hkl}^{calc}) e^{-2\pi(hx+ky+lz)} \quad (2-15)$$

By subtracting the calculated structure factor magnitudes  $|F_{hkl}^{calc}|$  from the observed  $|F_{hkl}^{obs}|$  (experimentally measured) structure factors only the electron density not yet determined in the model structure solution is observed thus serving as a means by which to determine the location of any missing atoms.

In addition to Fourier difference maps which can be used to allocate any remaining electron density, parameters associated with atom positions and thermal displacement are also refined by the method of least squares. This involves refining the parameters against either the structure factors  $|F_{obs}|$  or the structure factors squared  $F_{obs}^2$ . In either case the weaker reflections are less reliable than stronger reflections and the structure factors are weighted to allow for this fact.

The R-factors used to measure the agreement between the observed  $|F_{obs}|$  and calculated  $|F_{calc}|$  structural amplitudes are calculated using equations 2-16. The lower these values the better the agreement.

$$R = \frac{\sum_{hkl} \left| |F_{obs}| - |F_{calc}| \right|}{\sum_{hkl} |F_{obs}|} \quad (2-16a)$$

$$wR_2 = \sqrt{\frac{\sum_{hkl} w(F_{obs}^2 - F_{calc}^2)^2}{\sum_{hkl} w(F_{obs})^2}} \quad (2-16b)$$

### 2.2.2 Neutron Diffraction

Due to the concept of wave/particle duality, beams of particles can also be used to probe the structure of crystalline solids assuming, as in the case of X-rays, the wavelength of the particle is of the same magnitude of the inter-atomic distances. Electron and neutron diffraction are the most common application of particle diffraction in structure determination. In the case of electron diffraction the electrons are scattered by the electrons in the sample, are easily absorbed and therefore do not travel very far into the material. This technique is used more to probe the surface of a material.

In the case of neutron diffraction the neutrons are scattered by the atomic nuclei and not the electrons. Neutrons also possess a magnetic spin and are also scattered by the atomic spins, making it possible to probe the magnetic structure of a material. The scattering factors (referred as scattering lengths,  $b$ ), and hence the measured intensities, for neutrons are therefore not directly proportional to the atomic number  $Z$  as in the case of X-rays, Figure 2-10.

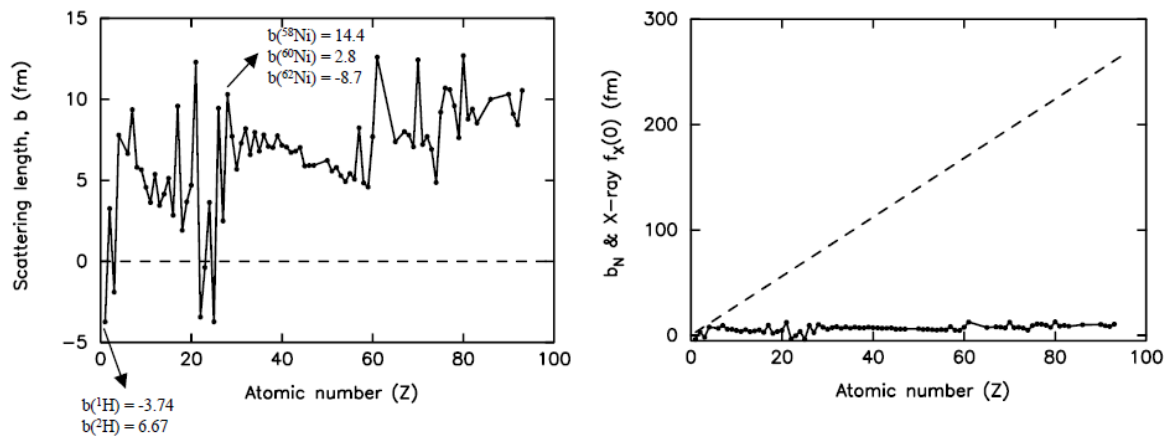


**Figure 2-10 Neutron scattering lengths and comparison with X-ray scattering factor variation with  $Z^{151}$**

The scattering length can take both positive and negative values and does not vary monotonically across the periodic table as shown in Figure 2-10. It can therefore vary significantly for neighbouring elements and even for isotopes of the same element, unlike in the case of X-ray diffraction where such elements are difficult to distinguish. For example in the study of H and D which have negative and positive scattering factors respectively. e.g.  $^1\text{H}$  -3.74,  $^2\text{H}$  +6.67 fm.

The fact that neutrons scatter from the atomic nuclei also means that there is no decrease in scattering factor as a function of scattering angle (which happens for X-ray scattering due to the diffuse electrons), Figure 2-11. This enables structures to be studied at high resolution.

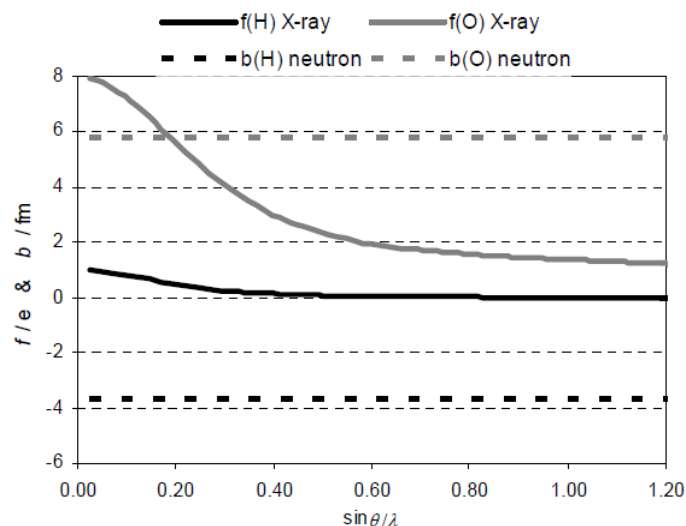


**Figure 2-11 Neutron scattering shows no form factor fall-off with scattering angle, unlike with X-rays, illustrated here for two typical light atoms <sup>151</sup>**

As neutrons interact very weakly with matter this is a suitable technique for probing the bulk of a material without damaging the sample. This however requires larger sample sizes and collection time. As neutrons possess energies similar to those associated with molecular translations, rotations and vibrations, the dynamics of the structure can also be studied.

One of the main uses of neutron diffraction, and its use in this investigation, is the location and study of H atoms. As most elements scatter to the same order of magnitude lighter elements such as H are easier to see, unlike in X-ray diffraction where they cannot be determined accurately or even at all in for example the presence of heavy atoms.

Neutron diffraction is thus a technique that complements X-ray diffraction very well, particularly in the study of H atoms. Unfortunately access to neutron sources is limited due to the few locations available and the high running costs. Neutrons are produced from either reactor or spallation sources. Reactors are steady state sources from which the neutrons are produced by nuclear fission e.g. ILL, Grenoble. In spallation sources (e.g. ISIS at RAL in Oxfordshire) the neutrons are produced by hitting a heavy metal target with a pulse of high energy charged particles in a controlled manner. These are pulsed sources using time-of-flight to determine wavelength; the time taken for a neutron produced at the initiation of

the pulse, when the proton beam hits the heavy metal target,  $t$ , is related to the velocity of the neutron and hence its energy and wavelength. The time-of-flight is thus a direct measure of the wavelength of the detected neutron. This allows the full white beam of neutrons to be used in the diffraction pattern. In both cases, the neutrons produced initially have energies that are too high for their intended use. They are thus cooled down to energies of the order of 1eV (or less, a 1Å neutron has energy ~81 meV) by passing through a hydrogen-containing moderator. The extent to which the neutrons are slowed down depends on the temperature and also the size and shape of the moderator which to an extent governs the number of collisions. The desired characteristics of the moderator are dependent on the neutron source.

### **2.2.3 Sample Preparation**

A reliable crystal structure is dependent on a good quality data set which in turn depends very much on the quality of the sample. Care is therefore required throughout each stage of sample preparation: growth, selection of a good quality crystal, and mounting on the diffractometer.

#### **2.2.3.1 Crystallisation**

There are many techniques by which single crystals of small organic molecules and their complexes have been formed. All crystals reported in this study were produced using the solvent evaporation method in which two starting materials were dissolved separately, combined into a small 7mm<sup>3</sup> glass vial, and left to evaporate. In order to slow evaporation, and therefore crystal growth, to obtain better crystals, the vials were covered with parafilm, pierced with a needle and placed in a location free of vibrations.

As there is no way to predict optimum conditions for crystal growth, particularly for new combinations of materials, it is only possible to alter conditions such as concentration of substances, temperature and pH of solutions which are known to affect nucleation and crystal growth. This can be achieved by varying the quantity and stoichiometric ratios of the starting materials used, the solvents in which the

starting materials are dissolved and the temperatures at which the solvents are left to evaporate.

The most common solvents used in this work were methanol, ethanol, acetone, acetonitrile, isopropanol, dimethylformamide, acetic acid, water and their combinations. By repeating the same crystallisations in a range of solvents it is possible that new complexes (in different stoichiometric ratios) or polymorphs will be formed. It is also possible that some solvents become incorporated into the crystal structure, the most common example being water in the formation of hydrates.

The temperature of crystallisation is also very important. In most cases slow crystal growth, at lower temperatures, will produce larger more ordered single crystals. This is not always the case and it is therefore advantageous for any system to explore a range of temperatures under which crystallisation is undertaken, also increasing the likelihood of detecting new and/or less stable complexes or polymorphs. As temperature gradients can also affect crystal quality, it is also advantageous to maintain a constant temperature during crystallisation. This was achieved here by placing vials in a cold-room, on a hotplate held at a specific temperature, or in devices such as the ReactArray Microvate (Figure 2-12) which can be programmed to maintain a specific temperature for a specific time or to carry out a tailored heating and cooling programme.



**Figure 2-12 The ReactArray Microvate, a device designed to allow temperature programmable crystallisation regimes**

The timescales involved in the process of single-crystal formation can vary from a few days to many months, and it is therefore essential to check progress regularly to prevent samples decomposing or drying out. Powder samples on the other hand require to be fully dried prior to grinding finely and filling a capillary.

### **2.2.3.2 Characterisation and Screening**

On the successful formation of a single crystal it must then be established whether the crystal is of a good enough quality for diffraction measurements and if so whether or not the structure has already been determined. The most common way is to determine the unit cell of the crystal and compare with the Cambridge Structural Database (CSD), <sup>97</sup> a large online database of compounds of which the structures have already been identified.

The quality of a crystal is best judged by use of a polarising microscope which can identify the presence of multiple or cracked crystals. These should be discarded or cut carefully with a scalpel to remove the unwanted areas. Once a single-crystal of the required size, free from defects and debris, is located, this can be mounted to a thin glass fibre, attached to a goniometer head. Usually the crystal is coated in an inert oil which solidifies on cooling to low temperatures and is usually enough to hold it on the thin glass fibre of the goniometer head which is itself is attached to a mount on the diffractometer. In total three single crystal X-ray diffractometers were used in this work: a Bruker Nonius Kappa CCD diffractometer, Bruker APEX II CCD diffractometer and a Rigaku R-axis/RAPID image plate diffractometer.

The unit cell and the space group can be determined by collecting a small selection of images from different crystal orientations representing different regions of reciprocal space. This preliminary unit cell can then be compared to entries contained within the CSD to determine whether or not the structure has already been determined. From the quality of these images it is also possible to tell if the crystal is of sufficient quality to run a full data collection, including factors such as the crystal mosaicity and its effect on the diffraction peaks.

As a single-crystal is not necessarily representative of the solid material throughout the whole vial, and it is possible for multiple product materials to co-exist, it is necessary to repeat the above procedure a number of times to ensure that nothing has been missed. As a more comprehensive screening check, a sample of the products can be ground into a fine powder and used to obtain a powder diffraction pattern representative of the bulk sample. Consistent results are not always guaranteed as grinding may cause structural changes thus potentially altering the initial products of the experiment, as was found to be the case in some examples in this work.

## **2.3 *Ab Initio* Calculations**

### **2.3.1 *Simulation of Condensed Matter***

Ab initio computational methods are intended to take the chemical constitution and crystal structure of a periodic system and calculate both chemical and physical properties as accurately as possible. For a truly accurate picture, a Quantum Mechanical (QM) description for each individual electron and nucleus in the system is required, however due to the large number of particles present it is unfeasible to accurately account for each individual interaction. This is simplified, slightly, by the Born-Oppenheimer approximation, which states that the nuclei can be treated as stationary and that the behaviour of the significantly lighter electrons can be traced back to any change in nuclear positions. Also due to the translation invariance of the crystal lattice the potential energy is also a periodic function, with the same periodicity of the lattice, so for a translation by any direct lattice vector  $\mathbf{g}$ , the potential energy is the same.

$$V(\mathbf{r} - \mathbf{g}; k) = V(\mathbf{r}; k) \quad (2-17)$$

Symmetry considerations mean that the Schrodinger equation must also be translation invariant and that a translation by any direct lattice vector  $\mathbf{g}$  results in a coincidence of the two sets of solutions.

$$\hat{H}(r;k)\Psi(r;k) = E\Psi(r;k) \quad (2-18)$$

$$\hat{H}(r-g;k)\Psi(r-g;k) = E\Psi(r-g;k) \quad (2-19)$$

Bloch's theorem states that eigenfunctions representative of this periodic potential can be expressed in the following form:

$$\Phi(r+g;k) = e^{ik \cdot g} \Phi(r;k) \quad (2-20)$$

Assuming that  $\hat{H}$  is the one-electron electrostatic Hamiltonian based on the Born-Oppenheimer approximation, the solutions 2-20 to the Schrodinger equation 2-21 are called crystalline orbitals, and are linear combinations of one-electron Bloch functions with coefficients  $c_{jn}$ .

$$\Psi_n(r;k) = \sum_j c_{jn}(k) \Phi_j(r;k) \quad (2-21)$$

These Bloch functions are constructed from atomic functions, appropriate for the structure under study, by application of the translational symmetry of the lattice. The two most common exchange approximations for periodic systems are the Hartree-Fock (HF) approximation and Density Functional Theory (DFT).

### **2.3.2 The Hartree-Fock (HF) Theory for Solids**

The HF approximation neglects all electron-electron correlations except those required by the Pauli Exclusion Principle which states that electrons are fermions, and so must possess a wavefunction that is antisymmetric with respect to the interchange of particle coordinates. The simplest antisymmetric form for the N-electron wavefunction is the Slater determinant composed of the spin orbitals

$\phi_a, \phi_b, \dots$

$$\psi_{(1,2,\dots,N)} = \left(\frac{1}{N!}\right)^{\frac{1}{2}} \begin{vmatrix} \phi_a(1) & \phi_b(1) & \cdots & \phi_z(1) \\ \phi_a(2) & \phi_b(2) & \cdots & \phi_z(2) \\ \vdots & \vdots & \cdots & \vdots \\ \phi_a(N) & \phi_b(N) & \cdots & \phi_z(N) \end{vmatrix} \quad (2-22)$$

The Slater determinant naturally incorporates the requirement of the exclusion principle that no two electrons have exactly the same state; if this were to occur, the determinant would be equal to zero. The determinant is usually summarised by its principal diagonal

$$\psi_{(1,2,\dots,N)} = \left(\frac{1}{N!}\right)^{\frac{1}{2}} \det|\phi_a(1)\phi_b(2)\dots\phi_z(N)| \quad (2-23)$$

For such an approximation to be of use, a set of atom centred basis functions is required in which to expand the determinant. Although Slater-type orbitals, which are the natural solutions of the hydrogen model, seem ideal, Gaussian-type functions are preferred as they are more easily manipulated mathematically. In practice, it is more convenient to use a linear combination of a few Gaussian functions (or primitives) to ‘fit’ the form of a Slater-type orbital.

The HF approach takes the single Slater determinant as a complete electron wavefunction, and treats the electron-electron repulsions in an average way. Each electron is considered as moving in the field of the nuclei and the average field of the other  $N-1$  electrons. The spin orbitals that give the best  $N$  electron wavefunction are found by minimising the ratio

$$\varepsilon = \frac{\int \psi_{trial}^*(x; R) H \psi(x; R) dx}{\int \psi_{trial}^*(x; R) \psi(x; R) dx} \quad (2-24)$$

where the variational principle states that  $\varepsilon \geq E_0$  for any  $\psi_{trial}$ , and that the equality holds only if the trial function is identical to the true ground state wavefunction. The HF equations for the individual spin orbitals are then of the form

$$f_1 \phi_a(1) = \varepsilon_a \phi_a(1) \quad (2-25)$$

where  $\phi_a(1)$  denotes the orbital occupied by electron 1,  $\varepsilon_a$  is the orbital energy, and  $f_1$  is the Fock operator:

$$f_1 = h_1 + \sum_u \{J_u(1) - K_u(1)\} \quad (2-26)$$

Here  $h_1$  is the core Hamiltonian for electron 1, which includes the kinetic energy and the interaction with the nuclei,  $u = a, b \dots z$  denotes a sum over all orbitals, and the Coulomb,  $J_u$ , and exchange,  $K_u$ , operators are defined as follows:

$$J_u(1)\phi_a(1) = \left\{ \int \phi_u^*(2) \left( \frac{e^2}{4\pi\varepsilon_0 r_{12}} \right) \phi_u(2) dx_2 \right\} \phi_a(1) \quad (2-27)$$

$$K_u(1)\phi_a(1) = \left\{ \int \phi_u^*(2) \left( \frac{e^2}{4\pi\varepsilon_0 r_{12}} \right) \phi_a(2) dx_2 \right\} \phi_u(1) \quad (2-28)$$

$J_u$  accounts for the Coulombic repulsion between the electrons and  $K_u$  is a purely quantum mechanical term which emerges from the effects of electron exchange. Electron exchange accounts for the fact that two electrons with the same spin cannot occupy the same space within a wavefunction.

In 2-26, the sum represents the average potential energy of electron 1 due to the other  $n-1$  electrons. Now, the spin orbital for each electron is dependent on  $f_1$  which, from 2-26, requires the predetermination of all other electron spin orbitals, and at this stage, these are also unknown. The solution to this problem is to employ a self-consistent field (SCF) procedure, in which a trial set of spin orbitals are chosen, usually from the unmodified atomic ground states, and used to devise  $f_1$ . The HF equations are then solved to obtain a new set of spin orbitals from which a new  $f_1$  emerges. This cycle is then repeated until self-consistency is

achieved, or where, in practice, the required convergence in total energy is achieved.

The various HF methods appropriate for systems with fully spin paired and unpaired electrons must now be discussed. The first, for an even number of electrons and hence closed shell states, is the Restricted Hartree-Fock (RHF) approach. Here the spatial components of the spin orbitals are assumed identical for each pair of electrons and there are  $N/2$  spatial orbitals of the form  $\psi_a(r_1)$ . The wavefunction is therefore composed of a determinant in which all the orbitals are doubly occupied.

In the case of unpaired electrons and open shell states, there are two possible procedures. The first is the restricted open (ROHF) formation in which the electrons, excluding those in open-shell orbitals, are forced to occupy doubly occupied spatial orbitals. The drawback of this method is that all unpaired electrons are constrained to have parallel spins, which make the representation of antiferromagnetic (AF) states impossible. The second is the unrestricted open shell Hartree-Fock (UHF) method, in which no constraint is placed upon the spin orbitals, and so the spatial and spin parts are formally separate, and the method can produce AF solutions.

As mentioned earlier, especially in the case of partially filled d-shells, the overall energy of the system can usually be lowered by electron rearrangement, which is less constrained in the UHF theory. However although lower total energy is possible using this method, there is the disadvantage that, unlike the RHF case, the UHF solutions are not acceptable eigenfunctions of the  $S^2$  operator, which can lead to a problem known as 'spin contamination'. In practice, due to the lower energies achieved, the UHF wavefunction is favoured, and the degree of spin contamination can be tested by comparison of calculated properties with experiment.

The more obvious and major imperfection associated with this method is that the HF SCF atomic orbitals are rooted in the single-particle approximation, and hence are based on an average form of the potential for each electron, whereas the true wavefunction depends on the separations of the individual electrons. The incorporation of the separations  $r_{12}$  explicitly in the wavefunction begins to account

for the presence of correlations in the electron motion beyond those imposed by a single Slater determinant. Another route to improvement is to use the Dirac equation for the calculation rather than the non-relativistic Schrodinger equation as relativistic effects become more significant for heavier atoms and account for various properties of the elements such as the lanthanide contraction. The correlation energy can be defined as

$$E_{\text{Correlation}} = E_{\text{True}} - E_{\text{Hartree-Fock}} - E_{\text{Relativistic}} \quad (2-29)$$

### **2.3.3 Density Functional Theory (DFT) for Solids**

Another popular method used to obtain atomic orbitals is Density Functional Theory (DFT). Unlike HF, DFT takes the electron correlation into account, if only in an approximate way, and is less computationally demanding. Also for systems involving *d*-block metals, such as those to be studied here, the results are very frequently in better agreement with experiment than those obtained in the HF approach.

Instead of taking a wavefunction-based approach to calculate the energy of an electronic system, this method instead centres on the use of the electron probability density. For a system of *N* electrons,  $\rho(r)$  represents the total electron density at a point *r* in space, and the energy due to electron-electron interactions comes into the theory as a functional of the density, denoted  $E[\rho]$ . Therefore, for a given function  $\rho(r)$  there is a single corresponding energy. However wavefunctions must still be used to calculate the kinetic energy as before, as there is no functional for that term.

Under the same assumption made in the RHF theory, that the paired electrons have the same spatial one-electron orbitals, Kohn and Sham showed that the exact ground state electronic energy of an *n*-electron system could be written

$$E[\rho] = -\frac{\hbar^2}{2m_e} \sum_{i=1}^n \int \varphi_i^*(r_1) \nabla_1^2 \varphi_i(r_1) dr_1 - \sum_{I=1}^N \int \frac{Z_I e^2}{4\pi\epsilon_0 r_{I1}} \rho(r_1) dr_1 + \frac{1}{2} \int \frac{\rho(r_1)\rho(r_2)e^2}{4\pi\epsilon_0 r_{12}} dr_1 dr_2 + E_{xc}[\rho] \quad (2-30)$$

Where the one electron spatial orbitals  $\psi_i$  ( $i=1,2,\dots,n$ ) are the Kohn-Sham orbitals, found by solving the Kohn-Sham equations. The first term represents the kinetic energy of the electrons. The second term represents the electron-nucleus attraction with the sum over all  $N$  nuclei with index  $I$ , and atomic number  $Z_I$ . The third term represents the Coulomb interaction between the total charge distribution summed over  $r_1$  and  $r_2$ . The final term is the exchange correlation energy, which tries to incorporate all the many body electron-electron interactions of the system, and is a functional of the density. It is not yet known how to precisely obtain this term, and therefore only approximate forms exist.

The Kohn-Sham equations have the form

$$\left\{ -\frac{\hbar^2}{2m_e} \nabla_1^2 - \sum_{I=1}^N \frac{Z_I e^2}{4\pi\epsilon_0 r_{I1}} + \int \frac{\rho(r_2)e^2}{4\pi\epsilon_0 r_{12}} dr_2 + V_{xc}(r_1) \right\} \varphi_i(r_1) = \epsilon_i \varphi_i(r_1) \quad (2-31)$$

Where the  $\epsilon_i$  values are the Kohn-Sham eigen-energies and the exchange correlation potential  $V_{xc}$  is the functional derivative of the exchange-correlation energy:

$$V_{xc}[\rho] = \frac{\delta E_{xc}[\rho]}{\delta \rho} \quad (2-32)$$

The exact ground state charge density  $\rho$ , at a location  $r$  is given by the modulus-squared of the Kohn-Sham orbitals, in the usual way

$$\rho(r) = \sum_{i=1}^n |\varphi_i(r)|^2 \quad (2-33)$$

Where the sum is over all the occupied Kohn-Sham orbitals and is known once they have been computed.

The Kohn-Sham equations are solved by use of an SCF procedure as detailed above, and the initial charge density is usually obtained from a superposition of atomic densities. The initial set of Kohn-Sham orbitals, obtained by solving the Kohn-Sham equations, is then used to compute an improved density. This process is repeated until the density and total energy have converged to within the required tolerance.

The exchange correlation energy  $E_{xc}$  is therefore dependent only on the electron density, which is obtained by solving the Schrodinger equation. Once the electron density is known,  $E_{xc}$  can be calculated, with limitations depending on the applied functional. The two most common are the local density approximation (LDA), in which  $E_{xc}$  is a function of the local density only and depends only on the value of the electron density at each point in space, and the generalised gradient approximation (GGA) which also includes the density gradient thus also takes into account the gradient of the electron density at the same point in space. There is also the option to mix  $E_{xc}$  with the exact exchange of HF in the form of hybrid functionals.

However, whereas the self interaction terms are exactly cancelled by corresponding negative terms in the exchange sum in HF theory, this is not the case for the inexact exchange present in DFT. Hybrid functionals clearly incorporate some varying degree of self interaction, depending upon how much Fock exchange we include. The main effect of self interaction is to artificially increase the single particle energies of highly localised states, which makes sense if the self interaction is thought of as the overlap of an electron's eigenfunction with itself. This is a real problem for *d*-electron states.

In pure DFT approaches, the electronic structure is often calculated using sets of plane waves (PW) to describe only the outer valence orbital electrons, and so is uncoupled from the atomic nuclei. The plane waves obey periodic boundary conditions and so the resulting electron density can be pictured as a linear combination of the plane waves. However, in order to model the high electron densities and gradients near the atomic nuclei a large number of plane waves would be required; this is computationally expensive. Pseudopotentials, consisting of the atomic nuclei and core electrons are therefore additionally employed.

These exert an effective Coulomb potential upon the valence electrons, modelled by the plane waves, which consequently only have to represent the comparably low valence electron density, thus saving computational time.

As an alternative to plane waves, the electronic structure can also be calculated by the atomic orbital (AO) approach in which the electron density is described in terms of atom centred orbitals ( $s$ ,  $p$ ,  $d$ ,  $f$ , etc.). Each atomic orbital, is composed of sets of Gaussian or Slater type functions (basis sets), which have to be assembled in order to accurately describe the system under study. The Linear Combination of Atomic Orbitals (LCAO) then provides a complete portrayal of the electron density of a single atom.

#### ***2.3.4 Hybrid Hartree Fock – Density Functional Hamiltonians and their Implementation in the CRYSTAL06 Code***

The CRYSTAL06 <sup>150</sup> linear combination of atomic orbitals (LCAO) electronic structure package allows the use of both the HF and DFT approximations under periodic boundary conditions, and also the use of hybrid-exchange calculations required for accurate magnetic interaction energies of correlated, many-body systems. The input of the crystal geometry and structural information such as the space group, cell parameters and fractional coordinates of the atoms in the cell are initially required.

A basis set for each element is then used for the expansion of the crystalline orbitals. The Gaussian primitives of these sets are expressed as the product of Cartesian angular and radial functions; these are then built up into fixed contractions, characterised by a series of radial exponents and expansion coefficients. The geometrical options available allow easy manipulation of structures. Options include the creation of defects, cell distortions, the creation of super cells and the removal of atoms and molecules from the bulk. For a given compound, CRYSTAL06 calculates the theoretical ground state energy, structure and lattice constants. Options available include the optimisation of atomic structure alone, of cell and atomic positions, and optimisation to a fixed volume. Usually the superposition of spin polarised charge densities are enough to give an

adequately accurate initial spin density in order to converge the self-consistent-field solutions for different magnetic orderings. However due to convergence problems it is sometimes necessary to directly control the spin patterns in the initial wavefunction by locking the total spin of the cell to a desired value, and by shifting the initial eigenvalues of the Fock matrix to favour a distinct pattern of transition metal *d*-orbital occupation. The calculations within CRYSTAL06 are done in reciprocal space. It is possible to set the mesh within the reciprocal grid to a higher or lower value in order to obtain the best possible converged state. For arduous calculations a parallelised, replicated, data version of the code has been employed, split over a variable number of nodes on the local computing cluster.

It is well known that pure HF to give results that underestimates magnetic properties such as coupling constants (*J*), by around 30-50%, and overestimate electronic properties such as band gaps. On the other hand pure spin polarized DFT calculations tend to overestimate magnetic properties and underestimate electronic properties.

The B3LYP hybrid function adiabatic connection formula<sup>59</sup> states that 20% HF exchange density is mixed into the total energy functional of the exchange correlation GGA energy. The weights for the gradient correlation energy, local exchange energy and non local HF were determined by a linear least squares fitting of the atomization energies, ionisation potentials, proton affinities, and total atomic energies of a selection of experimental atoms and molecules. Also, the gradient-corrected correlation used in the original work by Becke<sup>153</sup> is replaced by the Lee-Yang-Parr correlation energy.<sup>154</sup> The mixing of non local HF exchange reduced the self interaction in the LDA and GGA approximations to density functional theory, allowing B3LYP to correctly predict ground states of, for example, strongly correlated electronic AF materials for which LDA and GGA would give non magnetic ground states.

The CRYSTAL06 code can implement hybrid exchange functional of the form

$$f^{xc} = \frac{100-F_0}{100} (f_{\text{LSDA}}^x + 0.9\Delta f_{\text{B88}}^x) + \frac{F_0}{100} f_{\text{HF}}^x + 0.81f_{\text{LYP}}^c + 0.19f_{\text{VWN}}^c \quad (2-34)$$

in which  $x$  and  $c$  signify the exchange and correlation contributions respectively; LSDA, B88 and HF signify the local spin density, Becke88<sup>153</sup> and Hartree-Fock exchange potentials, and LYP and VWN signify the Lee, Yang and Parr<sup>154</sup>, and Vosko, Wilk and Nusair, correlation functionals.

The common B3LYP function can therefore be obtained by fixing the  $F_0$  parameter equal to 20%. This functional is well known in its use for modelling electronic properties and has been shown to produce band gaps in good agreement with experimental data.<sup>156-157</sup> A similar hybrid functional, in which the  $F_0$  parameter has been set to 35%, has been shown to produce experimentally comparable magnetic properties such as coupling values for a number of TM compounds.<sup>64-65,158-159</sup>

There are two options when using the CRYSTAL06 code to calculate properties. The first option is to perform an optimisation based on the parameters contained in the input file, which is edited by the user. This contains the crystal geometry and structural information such as the space group, cell parameters and fractional coordinates of the atoms in the cell and also the functional. The optimised wavefunction can then be used by Properties06, a complementary code used to calculate further properties such as density of states, from the optimised ground state. The other option is to calculate the total energies for two structures, one in the ground state and one in the excited state, both set using the input file, and to use the energy difference in order to calculate the property of interest. The main properties of interest in this work are those associated with electronic excitations: bands and band gaps, and those associated with the interacting unpaired electrons on the TMs.

### **2.3.5 Electronic Structure**

The concept of electronic structure began in the 1890s; when the electron was recognised as a particle - a fundamental constituent of matter<sup>160</sup>. Since then a number of theories have been developed to try and understand the electronic behaviour of materials and hence their resulting properties. There are the two extremes: the ionic model that neglects all bonding interactions and only accounts for the electrostatic charge due to the extended lattice at each site; and band

theory in which each electron is considered as part of the infinite periodic structure. No one theory is able to reproduce all observed behaviours.

A knowledge of the energy difference between the higher energy  $e_g$  and lower energy  $t_{2g}$  orbitals in an octahedral metal complex is significant in determining the specific transitions that take place and any resulting Jahn-Teller distortions of the local environments of ions with particular d-electron configurations. Crystal field theory (CFT) relates the electrostatic interaction between the positively charged metal cation and the negative charge on the non-bonding electrons of the ligand. Although the theory considers the energy changes of the five degenerate  $d$ -orbitals, it neglects the orbital overlap between cation and neighbouring anion states and is therefore unable to reproduce experimental values for the crystal field splitting energy for TM systems.

The  $d-d$  electron excitations that give rise to band gaps are forbidden by the Laporte selection rule, and tend to appear with weak intensity in optical absorption.

In the present work, band gaps were calculated from electronic structures by two different techniques using the Crystal06 code. The first involved calculating the energy difference between the total energy of the ground state and the total energy of the excited state. The second involved the use of the wavefunction from the ground state calculation and the Properties06 code to generate a plot of energy versus the density of states (DOS). This is an illustration of the number of states at each energy level that are available to be occupied. A high DOS at a specific energy indicates that there are many states available for occupation. A DOS of zero energy indicates that no states can be occupied at that energy level. By referring to the output from the ground state energy calculation the user can choose to plot the electron density associated with the different atom, group of atoms or atom orbital separately, and on calculation of a DOS plot the Fermi energy is also provided. These allow a clear observation of the path of the excited electron(s).

In addition to *ab initio* calculations, the positions of the electrons in the *d* orbitals have been calculated from first principles, using the Kanamori Crystal Field Hamiltonian (KCFH).<sup>170</sup> The underlying theory is based on CFT but also incorporates ligand field theory that accounts for bonding interactions.<sup>171</sup> This<sup>171</sup> has been used in order to map out the *d-d* excitations in a number of TM complexes in the literature.<sup>65,172-173</sup>

For each isolated metal site, the KCFH takes the following form

$$\hat{H}_{CF} = \hat{H}_{CF}^0 + \frac{1}{2} \sum_{\bar{\gamma}} \sum_{\bar{\sigma}} C(1,2) a_{\gamma_1\sigma_1}^\dagger a_{\gamma_2\sigma_2}^\dagger a_{\gamma_2\sigma_2} a_{\gamma_1\sigma_1} \quad (2-35)$$

in which  $\bar{\gamma} = \gamma_1\gamma_2\gamma_1'\gamma_2'$  and  $\bar{\sigma} = \sigma_1\sigma_2\sigma_1'\sigma_2'$ . The integrals of the two-electron interactions are

$$C(1,2) = \left\langle \gamma_1\sigma_1, \gamma_2\sigma_2 \left| \frac{e^2}{r_{12}} \right| \gamma_1'\sigma_1', \gamma_2'\sigma_2' \right\rangle \quad (2-36)$$

where  $\gamma$  and  $\gamma'$  refer to the type of *d* orbital, and  $\sigma$  and  $\sigma'$  to the electron spin.

The three possible types of *d-d* interaction can be identified as:

- (i) intraband Coulomb terms  $U = \langle \gamma\sigma, \gamma\sigma' | \gamma\sigma, \gamma\sigma' \rangle$  with  $\sigma \neq \sigma'$
- (ii) interband Coulomb terms  $U' = \langle \gamma\sigma, \gamma'\sigma' | \gamma\sigma, \gamma'\sigma' \rangle$  with  $\gamma \neq \gamma'$
- (iii) interband exchange terms  $J = \langle \gamma\sigma, \gamma'\sigma' | \gamma'\sigma, \gamma\sigma' \rangle$  with  $\gamma \neq \gamma'$

These can be written in terms of the Racah parameters *A*, *B* and *C*, of atomic spectroscopy<sup>174</sup>, for which the orbital independent value for *U* can be expressed as  $U = A+4B+3C$ . The orbital dependent *U'* and *J* values are as shown in Table-2-2.

**Table 2-2 Interband Coulomb and exchange interactions.  $U'$  and  $J$  as a function of  $d$ -orbitals,  $\gamma$  and  $\gamma'$  and expressed in terms of the Racah  $A$ ,  $B$  and  $C$  parameters.**

$\gamma$	$\gamma'$	$U'$	$J$
$xy, yz, xz$	$xy, yz, xz$	$A - 2B + C$	$3B + C$
$x^2-y^2, z^2$	$x^2-y^2, z^2$	$A - 4B + C$	$4B + C$
$xy$	$x^2-y^2$	$A + 4B + C$	$C$
$xy$	$z^2$	$A - 4B + C$	$4B + C$
$yz, xz$	$x^2-y^2$	$A - 2B + C$	$3B + C$
$yz, xz$	$z^2$	$A + 2B + C$	$B + C$

Although for simplicity  $U'$  and  $J$  may be averaged over the  $d$  orbitals in order to obtain the orbital ( $\gamma$ ) and spin ( $\sigma$ ) independent expressions

$$\begin{aligned}
 U' &= A - B + C \\
 J &= \frac{5}{2}B + C
 \end{aligned}
 \tag{2-37}$$

By respecting the orbital dependence of the interactions in Table 2-2, and mapping the ground, spin-allowed, and Laporte spin forbidden  $d-d$  excited states onto the KCFH, a set of energies can be obtained from which values can be assigned to each of the Racah parameters and to the  $e_g-t_{2g}$  crystal field splitting  $\Delta_{CF}$ .

However the Racah  $A$  parameter is not involved in the energies of the  $d \rightarrow d$  excitations and appears only when the number of electrons in the  $d$  orbital is altered. In addition  $B$ ,  $C$  and  $\Delta_{CF}$  are often seen as adjustable parameters when fitting experimental spectra, and the energies of the crystal field states interpreted using a Tanabe-Sugano diagram. This tends to give a fixed ratio of  $C/B \approx 4.5$  and a standard value of  $\Delta_{CF} = 10Dq$ .<sup>175</sup>

### 2.3.6 Magnetic Coupling

TM complexes are well known in their ability to display magnetic properties. This arises from interactions between the unpaired electrons contained in the  $d$  orbitals

of the TMs. The magnetic exchange is said to be indirect if the interaction is between non-neighbouring magnetic TM ions mediated by a non-magnetic ion. This is referred to as superexchange and is the type of interaction present in the materials studied in this work. The magnetic coupling ( $J$ ) value, indicative of the strength of this interaction, can be calculated using the model Ising Hamiltonian of the form:

$$\hat{H}_{\text{Ising}} = + \frac{J_{se(AB)}}{2} \sum_{i \in A, j \in B}^{nnn} \sigma_i \sigma_j \quad (2-38)$$

where A and B denote different metal centres,  $J_{se}$  is the superexchange coupling constant, and  $\sigma_i$  and  $\sigma_j$  are the projections of the spin moments, constrained to point up or down only at sites  $i$  and  $j$  on the axis of quantisation, and the summations run over  $nnn$  next nearest neighbours.

The energies per metal site of various states of magnetic order may be expressed in terms of combinations of  $J$ -values, and compared with the energy differences emerging from calculation, permitting the extraction of the magnitudes of the coupling constants. The values can then be used in various models of the ordering behaviour. Of these, the mean field model perhaps strikes the best balance between acceptable accuracy and simplicity and has been applied to many different types of phase transition. It assumes that all spins feel an identical average exchange field, proportional to the magnetisation, produced by all their neighbours. However this method is known to overestimate the critical temperature of the system as fluctuations or deviations from the average are not taken into consideration. In spite of this drawback, this approximation is still widely used and it is easily related, by a known correction factor of 0.75<sup>176</sup>, to the results of accurate Monte Carlo simulations for the same Ising-type Hamiltonians, in which fluctuations are naturally incorporated.

The energies per TM site of the ferromagnetic (FM), ferromagnetic (FI) and antiferromagnetic (AF) states may be derived from the nearest-neighbour Ising Hamiltonian as

$$E[FM] = E_0 + 3JS_A S_B \quad (2-39)$$

$$E[AF, FI] = E_0 - 3JS_A S_B ()$$

$E_0$  is the energy of the non-magnetic lattice and  $S_A$  and  $S_B$  are the spin moments assumed by the interacting  $TM_A$  and  $TM_B$  sublattices respectively. The sign convention employed means a positive  $J$  value indicates an AF (or FI) ground state and a negative  $J$  value a FM ground state.

The  $J$  values can be derived from the energy difference obtained from the respective total energies of the FO and AF (or FI) states, calculated from the CRYSTAL06 code, by

$$J = \frac{E[FM] - E[AF, FM]}{zS_A S_B} \quad (2-40)$$

in which  $z$  is the number of *nnn* next nearest neighbours. From the  $J$  values obtained it is possible to calculate the type of long range magnetic order of a material by estimating the critical temperature ( $T_C/T_N$ ) for the transition from spin order to paramagnetism, as in previous cluster<sup>177</sup> and solid state calculations<sup>64,65</sup> on related materials within the mean field approach of Langevin, Weiss and Néel<sup>178</sup>

$$T_C / T_N = \frac{6|J_{se}|S_A S_B}{3k_B} \quad (2-41)$$

Factors that can influence  $J$  include the identities, oxidation numbers and spin states (e.g. whether a low or high spin crystal field) of the interacting TMs, and the nature of the mediating ligand. The superexchange interaction is also strongly dependent on the bond angle of the metal-ligand-metal bond, Figure 2-13.

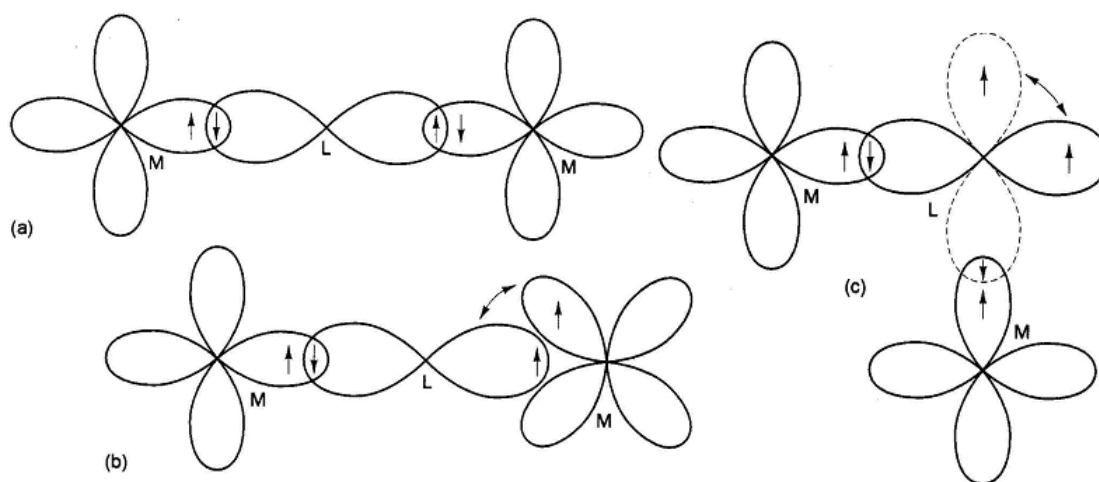


**Figure 2-13 Superexchange pathway in different orbital overlaps.**

An angle of  $180^\circ$  between two identical  $e_g$  orbitals on two transition metals overlapping with a ligand  $p$ -orbital leads to AF coupling, while coupling between orthogonal orbitals, for example  $e_g$  and  $t_{2g}$  orbitals, is FM and the unpaired electrons tend to align with parallel spins. However for a bond angle of  $90^\circ$ , the interaction pathway includes two ligand  $p$ -orbitals, for which the interaction becomes exchange-stabilised and the unpaired electrons also align in parallel, leading to FM coupling. It is very difficult to observe this FM experimentally, however, as for angles only a few degrees away from  $90^\circ$  the interaction becomes AF. It is possible with careful choice of metal ions and bridging ligands to set up an orthogonal pathway so that FM occurs, but in most cases there will exist at least one dominant AF pathway, rendering the design of large molecules with FM exchange difficult. This is not an issue in this work as the model complexes employed ensure  $180^\circ$  angles between the interacting d orbitals of the TM ions.

### 3 Prussian Blue Analogues

A number of theoretical studies have been previously carried out on Prussian blue (PB) and analogous materials, but there have been very few studies of a similar nature on the Prussian Yellow (PY) and Prussian White (PW) derivatives of PB.

This chapter begins by comparing the PB band gap values obtained using different functionals and calculation methods to those obtained experimentally. The method and functional shown to yield PB band gaps most comparable to experimental values is then used to calculate band gaps for the PY and PW derivatives.

Chapter one established the possibility of the electrochemical production of PY and PW by the reduction and oxidation of PB, respectively, and also discussed the nature of the charge balancing metal cations within these complexes. A previous study by Rosseinsky *et al*<sup>10</sup> has shown that the identity of the charge balancing metal cation can affect the electronic band gap in the PB structure; incorporation of Na<sup>+</sup>, K<sup>+</sup>, Rb<sup>+</sup> and Cs<sup>+</sup> ions producing optical absorptions at 703, 686, 691 and 703nm, respectively. The peak at 686 nm in the K<sup>+</sup>-doped PB corresponds to an excitation energy of 1.81 eV.

A theoretical investigation by Wojdeł and Bromley<sup>29-30</sup> also examined the band gap variations arising from the substitution of a range of alkali metal cations in PB. Although the lattice constants and metal-ligand bond lengths obtained were in good agreement with experimental values, the limited transferability of the ultrasoft pseudopotential lead to difficulties in the accurate representation both of Fe<sup>2+</sup> and Fe<sup>3+</sup> oxidation states by application of a single potential. Furthermore the use of the pure PW91 functional led to the systematic underestimation of the gap widths and, in particular, to a narrower KPB band gap of 1.15 eV in width.

A recent solid state hybrid functional study of KPB<sup>65</sup> provided a band gap of width 3.87 eV at F<sub>0</sub>=35%, representing a clear overestimation of the experimental value. The B3LYP (F<sub>0</sub>=20%) functional, for which the previous study was unable to obtain a converged ground state, has been shown to provide band gaps in good agreement

with experiment in a wide range of materials<sup>156-157</sup> and has also, on this basis, been used to predict band gaps for other related PBAs.<sup>64-65</sup>

Here, a range of hybrid functionals have been employed to study the effects of substitution of a range of group 1 and 2 metals on the band gaps of PB and PW. The structural models and computational methods used are detailed first, followed by discussion of the results of SCF calculations on PB at different  $F_0$  values. The B3LYP ( $F_0=20\%$ ) functional is then used to examine the density of states in PB and PW complexes in which different metals have been incorporated, and also for the PY complex. In this manner, information relating to the electronic structure and band gaps comparable with relevant experimental data are obtained. The electronic structure results are then related to the associated calculated cell parameters, bond lengths, atomic charges, and spin moments.

### **3.1 Structures and Computational Methods**

The calculations employ model anhydrous structures of PB, PY and PW, as shown in Figure 3-1.

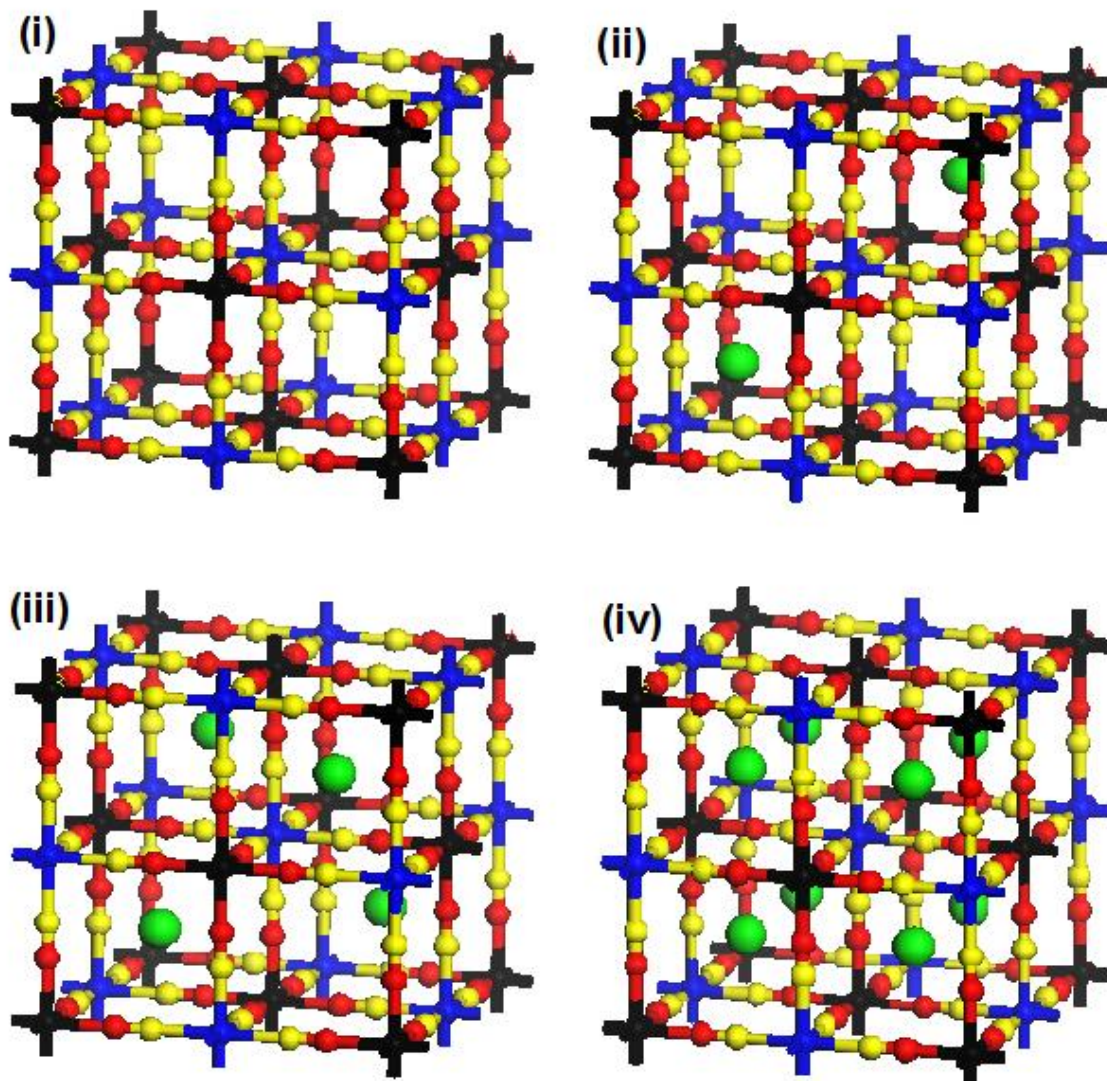


Figure 3-1 (i) PY model structure, LS  $\text{Fe}^{3+}$  (black) and HS  $\text{Fe}^{3+}$  (blue), no charge balancing cation, space group  $Fm\text{-}3m$  ; (ii) PB, LS  $\text{Fe}^{2+}$  (black) and HS  $\text{Fe}^{3+}$  (blue),  $2^+$  cation (green), space group  $Pn\text{-}3m$ ; (iii) PB model structure, LS  $\text{Fe}^{2+}$  (black) and HS  $\text{Fe}^{3+}$  (blue),  $1^+$  cation (green) and PW model structure, LS  $\text{Fe}^{2+}$  (black) and HS  $\text{Fe}^{2+}$  (blue),  $2^+$  cation (green), space group  $F\text{-}43m$ ; (iv) PW model structure, LS  $\text{Fe}^{2+}$  (black) and HS  $\text{Fe}^{2+}$  (blue),  $1^+$  cation, space group  $Fm\text{-}3m$ . The electron seeking nitrogen is coloured yellow and less reactive carbon red in all cases.

In the conventional group 1 metal PB structure model, the TM sublattices are fully occupied and the charge balancing  $M^+$  ions are placed in half of the available green sublattice sites, resulting in a lattice of  $F4\text{-}3m$  symmetry. This same model structure has been used in other computational investigations of PB<sup>29-30, 65</sup> and is a close approximation of the SPB structure (see Figure 1-7).

This same model structure has been used to model PW incorporating group 2 metals. In the PB model structures, incorporating group 2 metals, only two out of

the eight sublattice and therefore only half of the tetrahedral sites will be occupied, which is expected to alter the electronic structure and therefore the band gap of the material, resulting in a lattice of  $Pn-3m$  symmetry. In the PW model structures incorporating group 1 metals, all eight of the sublattice sites are occupied, resulting in a lattice of  $Fm-3m$  symmetry. The incorporation of tetrahedral site metals into the PY structure would result in a charge imbalance, and so studies of this effect have been restricted to PB and PW. In the PY structure employed, none of the sublattice sites are occupied, resulting in a lattice also of  $Fm-3m$  symmetry.

In all materials the ground state structure was obtained by allowing all atom positions and cell parameters to optimise fully. In the KPB complex, a lattice parameter of 10.13 Å, as obtained from the neutron diffraction study of the dehydrated  $Fe^{3+}_4 [Fe^{2+} (CN)_6]_3$ <sup>179</sup> is not an appropriate choice due to the lack of  $[Fe^{2+} (CN)_6]$  vacancies within the models employed. A lattice constant of 10.28 Å was instead used as a starting value, as in the related solid state hybrid functional study of PB<sup>65</sup>. This value was also derived from the associated experimental  $Fe^{2+}-C$ ,  $Fe^{3+}-N$ , and  $C-N$  bond lengths of 1.94, 2.06, and 1.14 Å, respectively<sup>179</sup> and corresponds to that proposed by Verdaguer and Girolami.<sup>180</sup> The study by Wojdeł and Bromley<sup>29-30</sup> also adopted identical experimental bond lengths in order to compare with their own calculated structures. The lattice constants obtained by Wojdeł and Bromley for the KPB, RbPB and CsPB model complexes are 10.20, 10.19 and 10.20 Å, respectively and those for the calculated NaPB NaPW and PY model complexes are 10.16, 10.19 and 10.13 Å. The small changes in lattice anticipated across the range of substituted group one metals and PB derivatives are not so significant that they will not be reached by starting from the initial structure just described.

All calculations have been carried out within the CRYSTAL06 code.<sup>150</sup> The code uses atom-centred basis sets that can be obtained from the CRYSTAL home page,<sup>181</sup> which consist of linear combinations of Gaussian functions to expand the crystalline orbitals. For C and N, the 6-311G\* basis sets were re-optimised by iterative variation in the valence shell exponents and contraction coefficients in UHF calculations within the crystalline environment. These sets were also used in

the related studies of PB,<sup>65</sup> the VCr, CrMn, and CrNi PBAs,<sup>64</sup> and a Mn<sup>2+</sup>Cr<sup>3+</sup> PBA.<sup>60</sup> The Fe<sup>2+</sup> and Fe<sup>3+</sup> ions were represented by 8-6411d41G sets (featuring a 3d<sup>5</sup> configuration for Fe<sup>3+</sup> and a 3d<sup>6</sup> configuration for Fe<sup>2+</sup>), previously optimised for the correct charge. The group one metals were represented by: Li<sup>+</sup> 61-1G; Na<sup>+</sup> 8-511G; K<sup>+</sup> 8-6511G; Rb<sup>+</sup> SC HAYWSC-31; and Cs<sup>+</sup> SC HAYWSC-31G basis. The group 2 metals were represented by: Be<sup>2+</sup> 5-11G; Mg<sup>2+</sup> 8-511G; Ca<sup>2+</sup> 86-511d3G; Sr<sup>2+</sup> SC HAYWSC-31(3d)G; and Ba<sup>2+</sup> SC HAYWSC-31G basis sets, the latter two sets employing small core effective pseudopotentials.

Adequate convergence of the total energy was ensured by application of a Monkhorst-Pack reciprocal space sampling with a shrinking factor of 8, truncation thresholds for bielectronic integrals have been set at 7,7,7,7 and 14 as described in the CRYSTAL06 documentation. Calculations with strict convergence criteria were pursued, so as to allow detection of the changes in electronic structure arising out of variations in the nature of the cation present.

A range of hybrid functionals were applied in order to calculate band gap energies via the direct SCF approach, in which convergence of the electronic structure into the minimum associated with the first excited state is sought and the excitation energy calculated directly from the difference in the total energies of the ground and excited states. Clearly, the method is founded upon the local stability of the electronic structure in the excited state, but this condition is often met, particularly in excitations associated with variations in the occupation numbers of strongly localised TM 3d orbitals. The spins of the Fe ions were set according to the orbital occupancies shown, Figure 3-2.

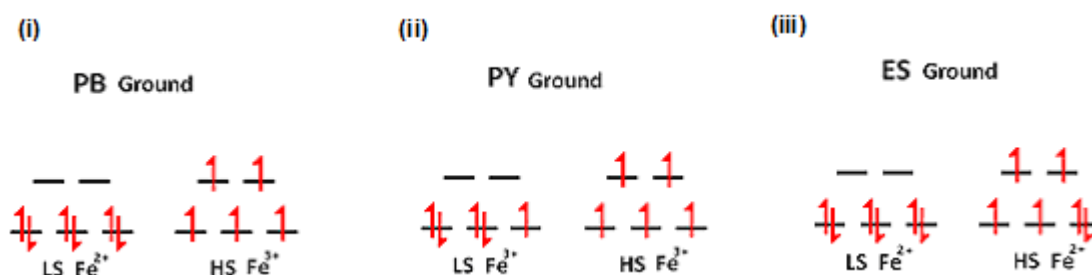


**Figure 3-2** Ground state electron arrangements of the (i) PB, (ii) PY and (iii) PW d orbitals implemented in the input file of the CRYSTAL06 code.

Only ferromagnetic alignments of the TM moments were considered. Symmetry breaking along the z-axis was included for the PY and PW materials; so as to allow for the lifting of the degeneracy in the  $t_{2g}$  orbital configuration should this be variationally favoured. Initial excited state geometries and wavefunctions for lower  $F_0$  value calculations were taken from converged runs at higher  $F_0$  values. Also, for the Li and Cs calculations, successful convergences had to be re-run at specific geometries in order to obtain suitable wavefunctions. Such wavefunctions being secured, properties of interest such as densities of states (DOS) plots were obtained by application of the PROPERTIES06 code forming part of the CRYSTAL06 package.

## **3.2 Calculation of Band Gaps**

### ***3.2.1 SCF Calculations***

Band gaps in PB were obtained for a range of group one metals using various hybrid functionals by direct SCF calculations, as described above. Optimised ground states were obtained for each case and the optimised ground state geometries were then used to obtain excited state energies, the energy differences yielding the charge transfer (CT) energy gap on absorption at the Franck-Condon limit, i.e. assuming a 'vertical' transition within which the electronic structure rearranges essentially instantaneously relative to the atomic positions. Optimisation of the excited state lattice and corresponding calculation of the ground state energy in the same lattice will provide the CT transition energy on photon emission (phosphorescence assuming relaxation in the excited state with sufficiently long life time). The dependence of the ground and excited state energy profiles of a notational nuclear reaction coordinate are illustrated in Figure 3-3. The emission energy is typically smaller than the absorption energy.

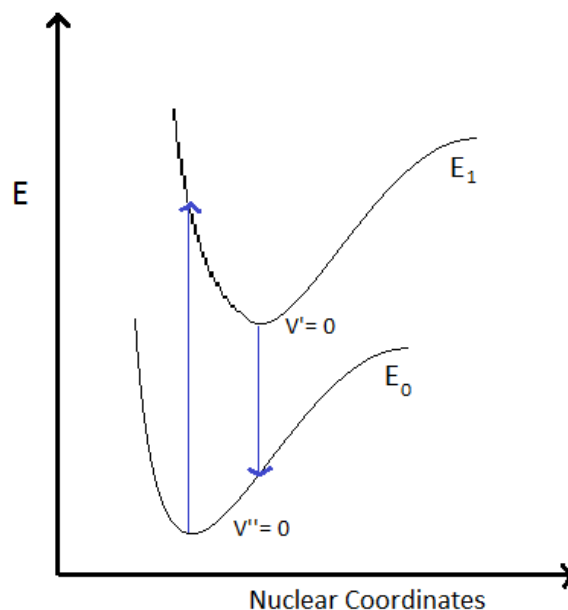


Figure 3-3 Dependence of ground  $E_0$  and excited  $E_1$  state energy profiles on a notational nuclear reaction coordinate.

The PB band gap has a  $t_{2g} \beta$  to  $t_{2g} \beta e^-$  transfer between the LS  $\text{Fe}^{2+}$  and HS  $\text{Fe}^{3+}$  ions, via the intermediate  $\text{CN}^-$  ligand, as illustrated in Figure 3-4.

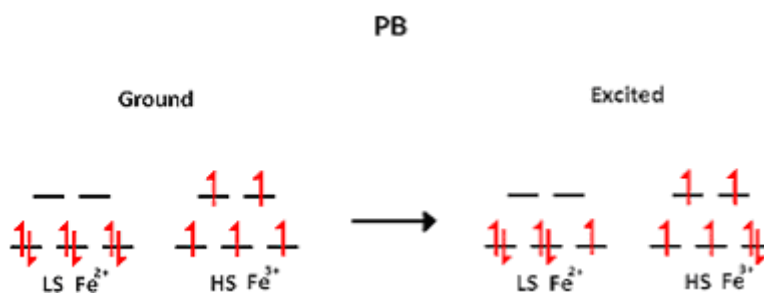


Figure 3-4 PB  $t_{2g} \beta$  to  $t_{2g} \beta e^-$  transfer between the LS  $\text{Fe}^{2+}$  and HS  $\text{Fe}^{3+}$  ions.

It is noted that there is no *a priori* reason to expect that any of the Hamiltonians used will perform significantly better than any other in reproducing the experimental energy of this excitation. While UHF calculations omit the effects of electron correlation entirely, it is clear that contributions from such interactions should be minimal, given that the ground and excited states share the same number of spin-paired electrons.

The excited states were modelled in two ways: first the electron is transferred from the LS to HS Fe ions preserving the basis sets appropriate for the ground state configuration. Second the two Fe sets were switched consistent with the corresponding oxidation states of the Fe ions in the excited state. While this seems a purely technical distinction, it is important to test the dependence of the excitation energy upon such methodological issues. The resulting band gap energies are presented in Table 3-1, and shown graphically in Figure 3-5

Comparing the excitation energies obtained from the two methods outlined above, it is clear that slightly larger band gaps emerge from the method involving basis set switching. The differences however, are generally not significant, particularly at high  $F_0$  values, and the two methods can be concluded to produce excitation energies of similar magnitudes.

The increase in the different excitation energies as  $F_0$  falls is likely to be due to increasing delocalisation and corresponding variations in the extent to which the ground and excited cation state interact with the ligand orbitals.

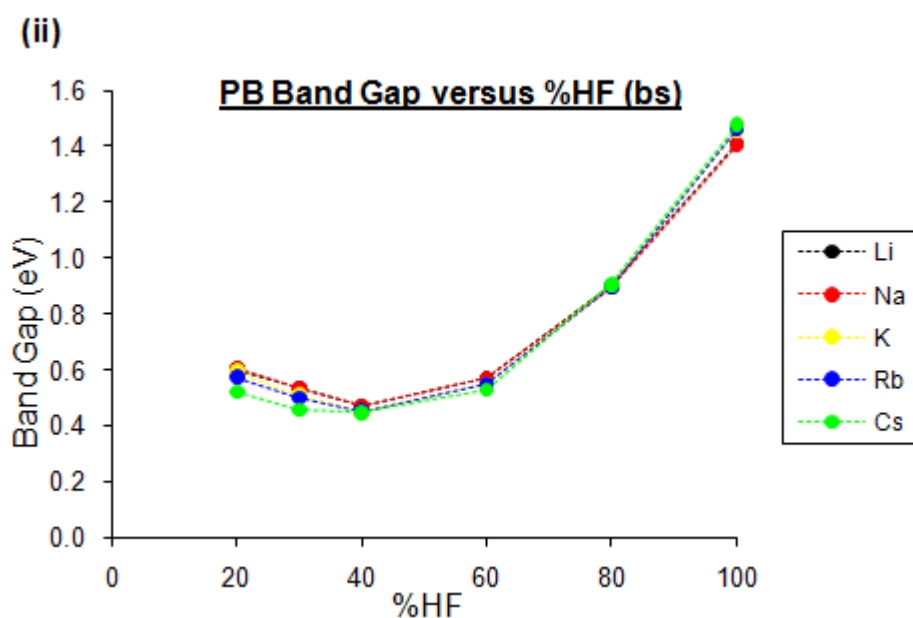
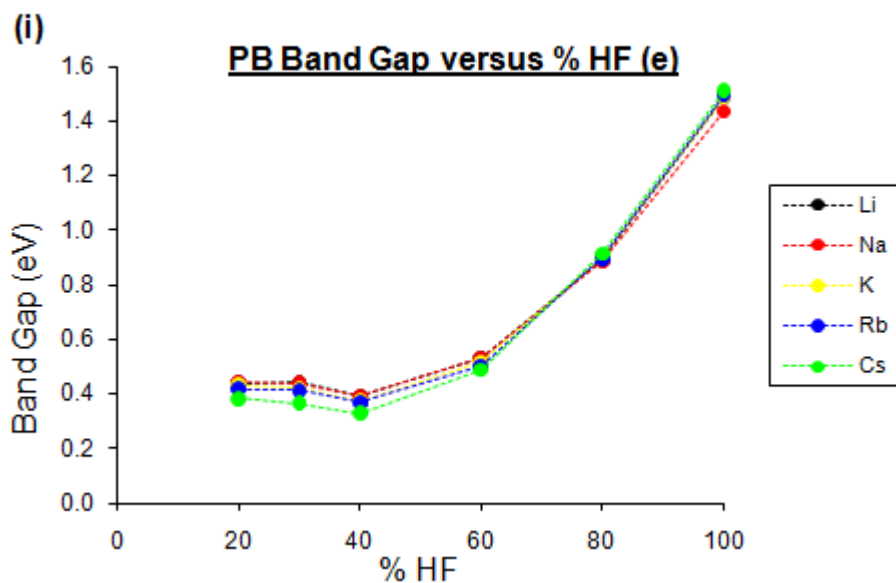
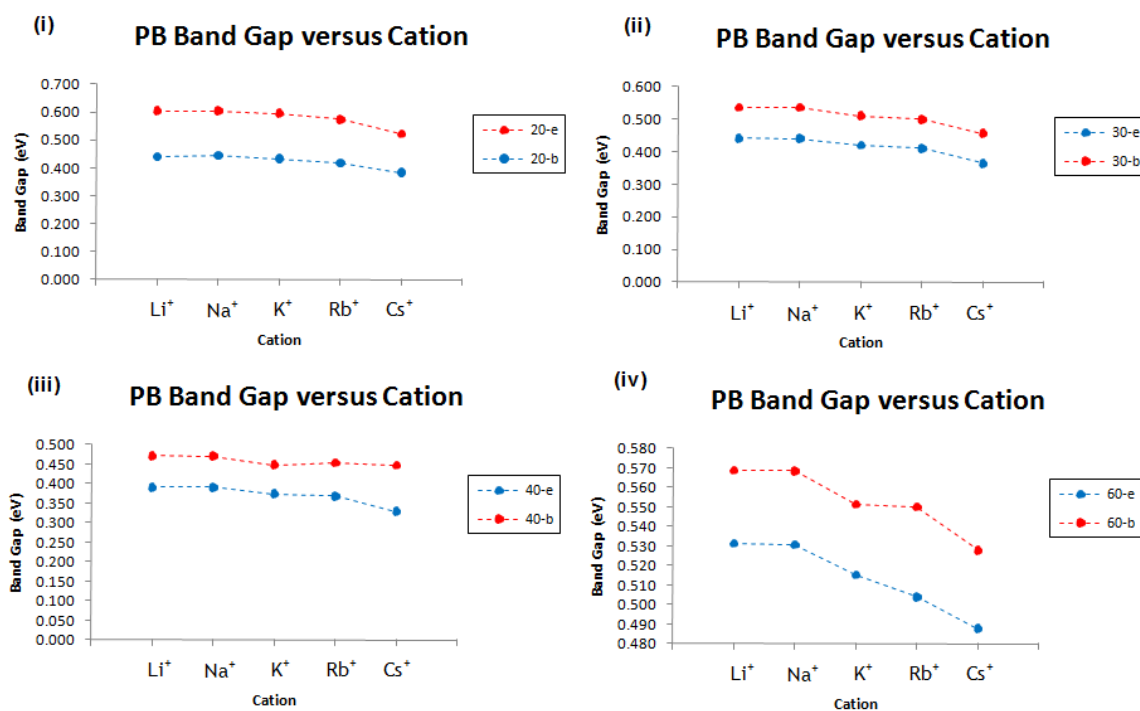


Figure 3-5 PB SCF band gap energies modelled (i) by movement of the excited electron between the ground state allocation of Fe basis sets and (ii) by switching of Fe basis sets between ground and excited states.

The B3LYP band gaps obtained with the basis switching method increase marginally significantly in comparison with the  $F_0=35\%$  values, while in the electron shifting calculations the B3LYP band gaps decreased slightly. These discrepancies between the two methods appear at the level of HF mixing at which quantitatively comparable electronic information is expected to be derived, assuming band gaps are obtained directly from the electronic structure (as in DOS plots). There is however no real evidence in the literature to indicate that directly calculated

excitation energies of this type above are any better at lower  $F_0$ . From these results UHF values seem to be the best overall.

A comparison of the band gaps obtained using 60, 40, 30 and 20% HF, is shown in Figure 3-6.



**Figure 3-6 Comparison of the band gaps obtained by the two methods of excitation; electron shifting denoted by (e) and basis switching denoted by (b) at (i) 20% HF, (ii) 30% HF, (iii) 40% HF and (iv) 60% HF.**

A comparison of the band gaps with respect to the incorporated metals continues to show the same trend between the two methods.

Comparing the band gap values obtained using the B3LYP hybrid functional to those obtained experimentally, shows that the experimental values are significantly underestimated. This is true for band gap values obtained by all hybrid functionals including 100% HF (which is significantly closer than lower  $F_0$  values). The values obtained using the uhf functional, usually known to overestimate band gap energies, were as expected; high in comparison to the experimental values although in comparison to the other functionals provided values most comparable to experiment. Again findings in the literature are true only for band gaps

estimated from the single particle eigenvalues and there is nothing discussing how the quality of calculated excitation energy in the direct approach used above varies as a function of  $F_0$ . A comparison of the band gaps obtained using the uhf and 100% HF functional with those obtained by experiment is illustrated in Figure 3-7.

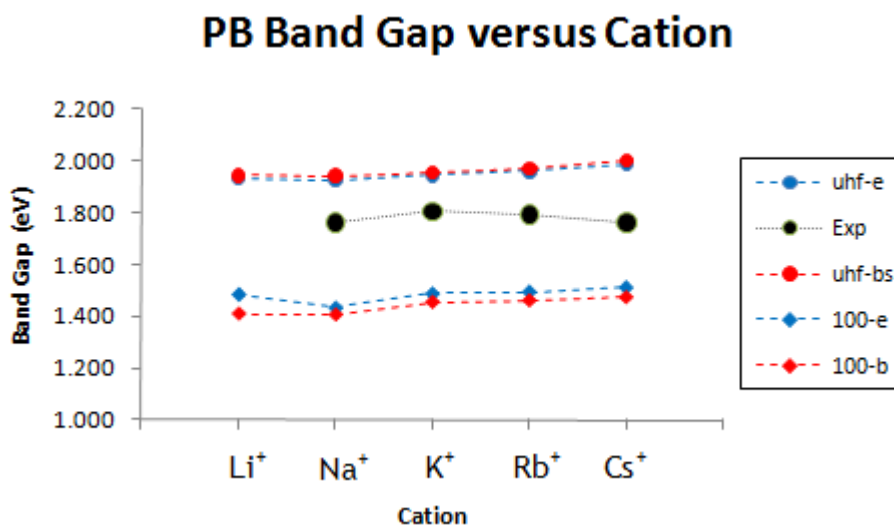


Figure 3-7 PB Comparison of band gaps obtained using uhf and 100%HF with experiment.

Although the UHF band gap values are more similar in magnitude in comparison to the other hybrid functionals, the trend with regard to variation of the alkali metal is not followed (Figure 3-7). Also shown are UHF band gaps, which show trends that may appear as more comparable to those experimentally determined. In conclusion the general magnitudes of the energy differences obtained by direct SCF calculations are well described at around  $F_0=100%$  to UHF, but the finer scale variations with change of metal species are not so well described. Accounting for this would be a difficult task in which the difference in electronic structure involved in the CT excitation would have to be described at an equal level of fidelity accounting for the small variations in lattice constant arising from the different substituted metal species.

**Table 3-1 PB band gaps obtained for incorporated group one metals, using a range of hybrid functionals by direct SCF calculations. Electron excitation modelled by both movement of  $e^-$  between the LS and HS Fe basis sets and also complete switching of basis sets. Band gaps are calculated for  $e^-$  movement from the ground state  $E_g$  to excited state using ground state coordinates,  $E_{ex}$ , ( $E_{ex}-E_g$ ), and also from the ground state  $E_g$  to excited state in which the modelled excited state converged after a full geometry optimisation to represent the relaxed excitation state  $E_{rel}$ , ( $E_{rel}-E_g$ ).**

	<i>Li</i>				<i>Na</i>				<i>K</i>				<i>Rb</i>				<i>Cs</i>			
	Excited $e^-$		Basis set		Excited $e^-$		Basis set		Excited $e^-$		Basis set		Excited $e^-$		Basis set		Excited $e^-$		Basis set	
	$E_{ex}-E_g$	$E_{rel}-E_g$	$E_{ex}-E_g$	$E_{rel}-E_g$	$E_{ex}-E_g$	$E_{rel}-E_g$	$E_{ex}-E_g$	$E_{rel}-E_g$	$E_{ex}-E_g$	$E_{rel}-E_g$	$E_{ex}-E_g$	$E_{rel}-E_g$	$E_{ex}-E_g$	$E_{rel}-E_g$	$E_{ex}-E_g$	$E_{ex}-E_g$	$E_{rel}-E_g$	$E_{ex}-E_g$	$E_{rel}-E_g$	$E_{rel}-E_g$
20	0.440	-	0.604	0.395	0.445	-	0.604	0.402	0.433	-	0.595	0.377	0.418	0.575	0.353	0.384	0.522	0.277		
30	0.442	-	0.536	0.229	0.440	-	0.537	0.236	0.419	-	0.510	0.209	0.411	0.500	0.184	0.365	0.456	0.126		
40	0.391	-	0.471	0.116	0.391	-	0.471	0.123	0.374	-	0.448	0.101	0.368	0.454	0.088	0.328	0.447	0.031		
60	0.531	0.110	0.569	0.133	0.531	0.115	0.569	0.142	0.515	0.098	0.551	0.118	0.504	0.085	0.550	0.104	0.488	0.055	0.528	0.059
80	0.891	0.337	0.898	0.360	0.888	0.340	0.896	0.364	0.899	0.336	0.899	0.355	0.897	0.326	0.896	0.345	0.913	0.313	0.906	0.326
100	1.485	-	1.410	-	1.434	-	1.406	-	1.488	-	1.457	-	1.495	-	1.464	-	1.511	-	1.476	-
uhf	1.933	1.012	1.946	0.905	1.929	1.011	1.942	0.908	1.946	1.008	1.956	0.901	1.962	1.005	1.972	0.895	1.991	0.990	2.003	0.875

### **3.2.2 Density of States (DOS) Calculations**

Optimised ground state structure calculations were found to converge successfully for hybrid functionals as low as  $F_0=20\%$  (B3LYP), in which the correct occupancies were maintained. Densities of states plots were calculated for each of the different metal-substituted species using the converged ground state wavefunctions obtained at  $F_0=20\%$  (B3LYP), well known for its ability to reproduce experimental band gaps.<sup>64-65, 156-157</sup>

#### **3.2.2.1 Prussian Yellow (PY)**

The observed yellow colour of the PY complex indicates an energy absorption at wavelengths of approximately 420-430 nm, which corresponds to an electron excitation band gap in the electronic structure of 2.89-2.96 eV. The PY structure differs from that of PB in that instead of a  $\text{CN}^-$  bridged  $\text{Fe}^{2+}$  (low spin) and  $\text{Fe}^{3+}$  (high spin) there are two  $\text{Fe}^{3+}$  ions (one low spin and the other high spin). The TM-ligand framework in this material is innately neutral, so that there is no need to introduce charge-balancing cations at tetrahedral sites. The DOS plot of the electronic structure of PY is illustrated in Figure 3-8.

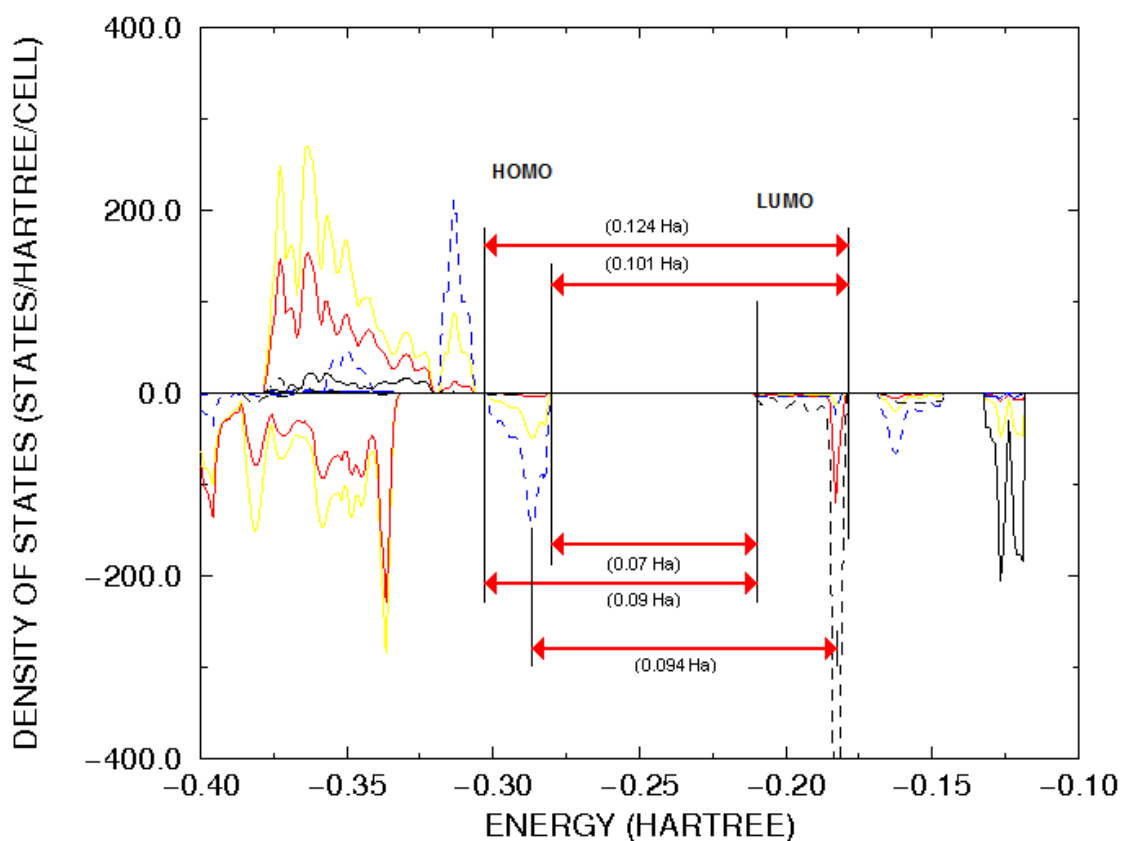


Figure 3-8 Atom projected PY DOS plot showing total N (yellow) and C (red) and Fe<sup>3+</sup> low spin (blue) and high spin (black) contributions, the latter two further split into  $t_{2g}$  (dashed) and  $e_g$  (solid) orbital contributions. The positive and negative y-axes denote  $\alpha$  and  $\beta$  spins respectively, where  $\alpha$  denotes the majority spin alignment of the lattice. The Fermi energy is -0.28 Hartrees.

The Fermi energy occurs at  $-0.28$  Hartrees, so that the HOMO comprises LS  $t_{2g}$  Fe<sup>3+</sup>  $\beta$  states with a small admixture of  $N_{\pi}$   $\beta$  states, and the LUMO HS  $t_{2g}$  Fe<sup>3+</sup>  $\beta$  states with a small admixture of  $C_{\pi}$   $\beta$  states. Inspection of the DOS plots above, obtained from B3LYP ground state calculations shows that both the valence band (VB) and conduction band (CB) edge are metal dominated, suggesting a metal-to-metal CT transition. The main indicative  $e^{-}$  transition between the LS and HS Fe<sup>3+</sup> ions is a  $t_{2g}$ - $t_{2g}$ ,  $\beta$ - $\beta$   $e^{-}$  transition. This is illustrated in Figure 3-9.

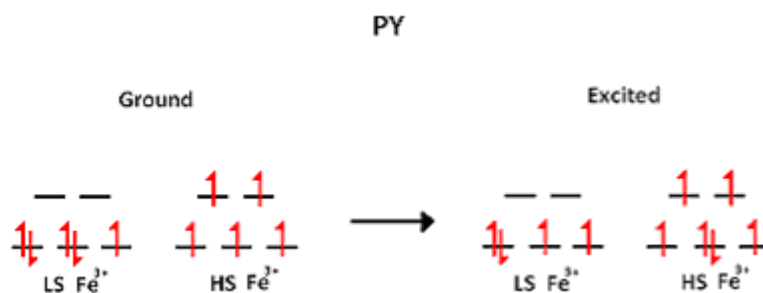


Figure 3-9 PY electron arrangement of d orbitals in ground and excited state.

An  $e^-$  transition between the highest HOMO and lowest LUMO state is equal to a band gap of 0.07 Ha; this is equivalent to 1.905 eV, significantly lower than the range of 2.89-2.96 eV associated with a yellow absorption spectrum. Other energy differences indicated between the HOMO and LUMO states include the energy band from the lowest HOMO to highest LUMO of 0.124 Ha to provide a range of 0.07 - 0.124 Ha that spans the whole of the HOMO and LUMO energy states, and also the difference between the most occupied states. These are converted to eV and compared in Table 3-2.

**Table 3-2 PY Energy of highest HOMO to lowest LUMO, most populated HOMO to most populated LUMO and lowest HOMO to highest LUMO**

	Ha	eV
Highest HOMO to lowest LUMO	0.07	1.905
Most Pop. HOMO to most pop. LUMO	0.094	2.585
Lowest HOMO to highest LUMO	0.124	3.374

The range of 2.89-2.96 eV associated with a yellow absorption clearly lies within the 1.905-3.374 range between the HOMO and LUMO states. Therefore the ~3 eV (0.11 Ha) energy gap required to explain the yellow colour of the complex is only available when the whole conduction and valence band range is taken into consideration. It is also worth noting that the ligand composition in the VB and CB is significantly larger in PY in comparison to PB. This may be better explained on the successful convergence of an excited state, which was not successfully obtained in this work.

### 3.2.2.2 Prussian Blue

The DOS plot obtained for KPB is illustrated in Figure 3-10, and with the exception of the MgPB for which a converged wavefunction was not obtained, is representative of those obtained for all group one and group two metals.

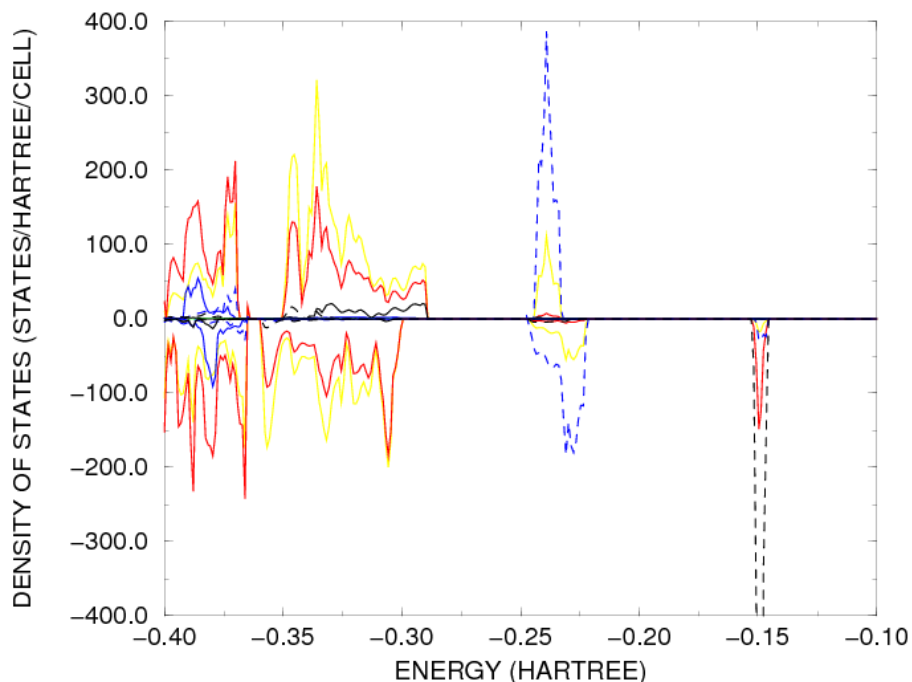


**Figure 3-10** PB DOS populations of total N (yellow) and C (red) orbitals, Fe<sup>2+</sup> low spin (blue) and Fe<sup>3+</sup> high spin (black)  $t_{2g}$  (dashed) and  $e_g$  (solid) orbitals respectively. The positive and negative y-axes denote  $\alpha$  and  $\beta$  spins respectively. The Fermi energy is -0.223 Hartrees.

The Fermi energy occurs at  $-0.223$  Hartrees so that the HOMO comprises LS  $t_{2g}$  Fe<sup>2+</sup>  $\beta$  states with a small admixture of  $N_{\pi}$   $\beta$  states, and the LUMO by HS  $t_{2g}$  Fe<sup>3+</sup>  $\beta$  states with a small admixture of  $C_{\pi}$   $\beta$  states. This is the LS Fe<sup>2+</sup> to HS Fe<sup>3+</sup>,  $t_{2g}$ - $t_{2g}$ ,  $\beta$ - $\beta$   $e^{-}$  transition between the ions expected as obtained previously<sup>3</sup> and as modelled in the above SCF excited states. The  $d$ - $d$   $e^{-}$  excitation is therefore illustrated in the  $d$  orbital electron arrangements for the ground and excited Fe ions in Figure 3-4.

A comparison of the band gaps resulting from different group one metals being incorporated into the PB lattice is presented in Table 3-3.

**Table 3-3 PB Comparison of band gaps from incorporation of different M<sup>+</sup> ions.**

	<i>a</i>	<i>Highest HOMO - lowest LUMO (eV)</i>	<i>Most Pop HOMO - Most Pop LUMO (eV)</i>	<i>Lowest HOMO- highest LUMO (eV)</i>	<i>Exp (eV)</i>
Li	10.29	1.905	2.129	2.818	-
Na	10.29	1.904	2.169	2.780	1.763
K	10.31	1.890	2.176	2.772	1.807
Rb	10.32	1.871	2.130	2.748	1.794
Cs	10.36	1.834	2.074	2.690	1.763

The highest HOMO - lowest LUMO, most populated HOMO - most populated LUMO and lowest HOMO- highest LUMO descriptions refer to the energy differences obtained from the points illustrated in Figure 3-11.

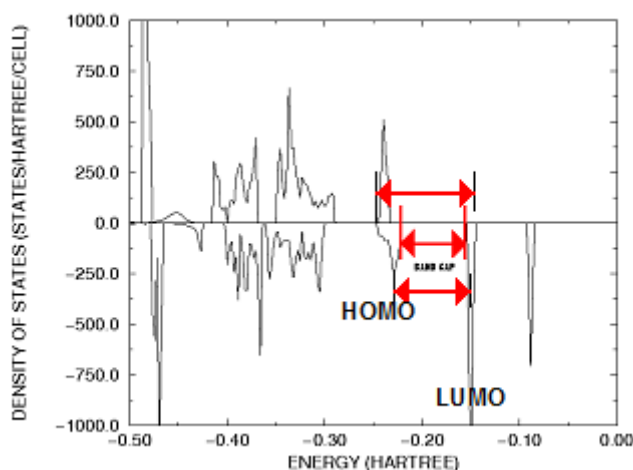


**Figure 3-11 DOS plot band gap between HOMO and LUMO**

The Fermi energy lies at the HOMO of highest energy. The band gap quoted is usually the energy difference between the Fermi energy (or highest HOMO) and the LUMO of lowest energy. As this is comparatively small in comparison to an energy difference between the most populated HOMO and LUMO states, which was more comparable to the energy gap expected in the PY complex, both energy differences have been compared to the experimental band gap values. The energy difference between the lowest HOMO and highest LUMO, which spans the whole VB-CB range,

has also been used in this comparison as in the PY case above. The results presented in Table 3-3 are illustrated in Figure 3-12.

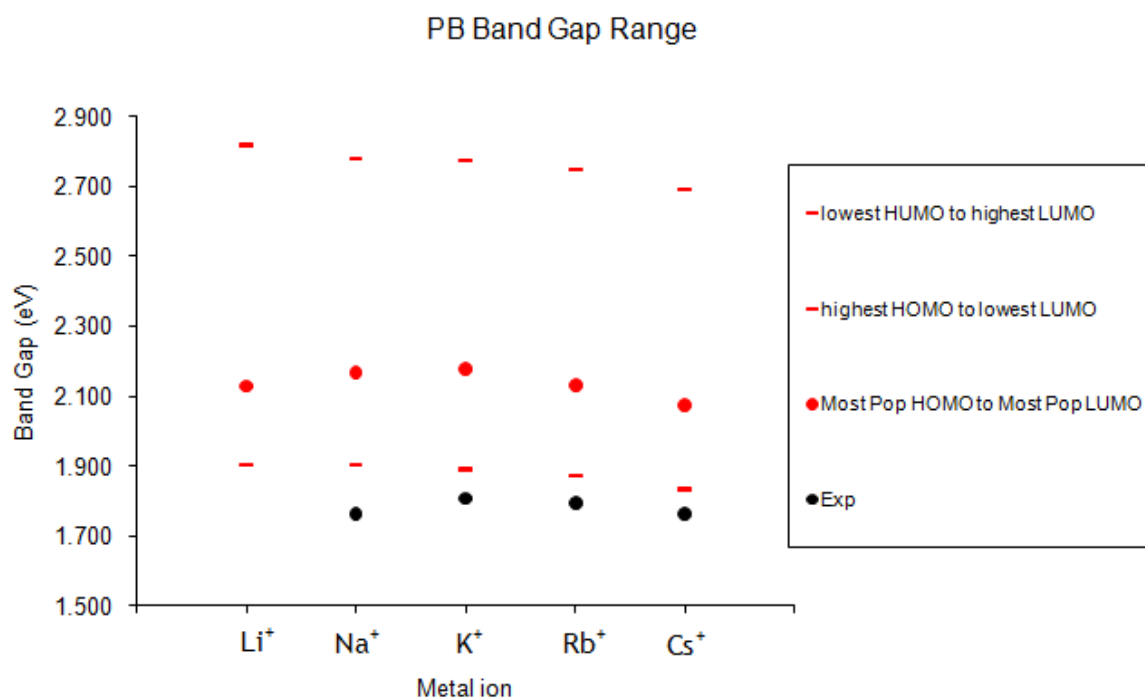


**Figure 3-12 PB Comparison of band gaps from incorporation of different M<sup>+</sup> ions.**

The band gaps calculated from the DOS populations, by use of the B3LYP functional, are also shown to overestimate the band gap energies as obtained by experiment. However when compared to the band gaps obtained from the 100%HF and uhf calculations, are significantly more comparable (Figure 3-13).

## PB Band Gap versus Cation

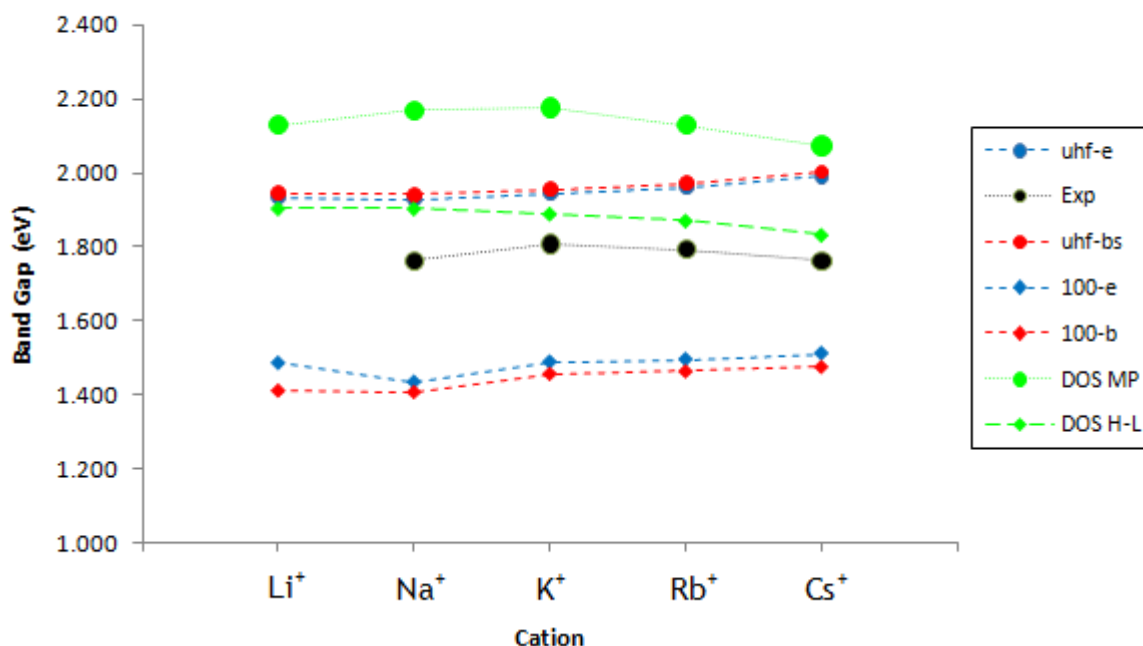
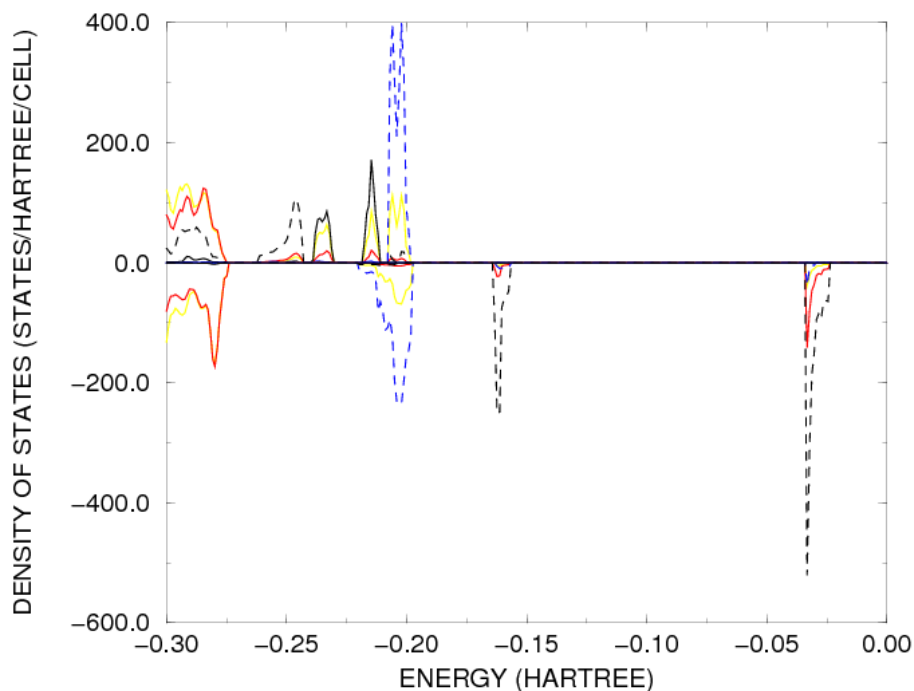


Figure 3-13 PB Band gap dependence on type of interstitial cation, comparison of SCF; 100%HF and uhf, DOS; difference in most populated states (DOS MP) and highest HOMO and lowest LUMO (DOS H-L), and experiment.

The energy difference between the most populated state in the HOMO and LUMO also fits the trend displayed by the incorporation of different metal cations in the experimental values. The use of DOS projections from the B3LYP hybrid functional in order to determine band gaps is more comparable than direct energy differences from SCF calculations.

### 3.2.2.3 Prussian White (PW)

The DOS plot obtained for KPW is illustrated in Figure 3-14.



**Figure 3-14** KPW DOS populations of total N (yellow) and C (red) orbitals, Fe<sup>2+</sup> low spin (blue) and high spin (black)  $t_{2g}$  (dashed) and  $e_g$  (solid) orbitals respectively. The positive and negative y-axes denote  $\alpha$  and  $\beta$  spins respectively. The Fermi energy is -0.15 Hartrees.

This DOS plot is representative of those calculated for all incorporated group 1 and group 2 metals, except for Ca<sup>2+</sup>PW (an explanation for which will follow) and Mg<sup>2+</sup> for which a converged B3LYP wavefunction was not obtained.

The Fermi energy occurs at -0.15 Hartrees, so that the HOMO comprises HS  $t_{2g}$  Fe<sup>2+</sup>  $\beta$  states, with a small admixture of  $C_{\pi}$   $\beta$  states, and the LUMO also comprises HS  $t_{2g}$  Fe<sup>2+</sup>  $\beta$  states with a small admixture of  $C_{\pi}$   $\beta$  states. As expected due to the lack of colour in this system, the PW DOS plot produced a band gap of 3.332 eV in the UV energy range. The associated HOMO and LUMO are both high spin Fe  $t_{2g}$  orbitals suggesting that upon excitation the  $\beta$  electron in the orbital containing the electron pair moves between the degenerate high spin Fe  $t_{2g}$  orbitals. This is illustrated in Figure 3-15.

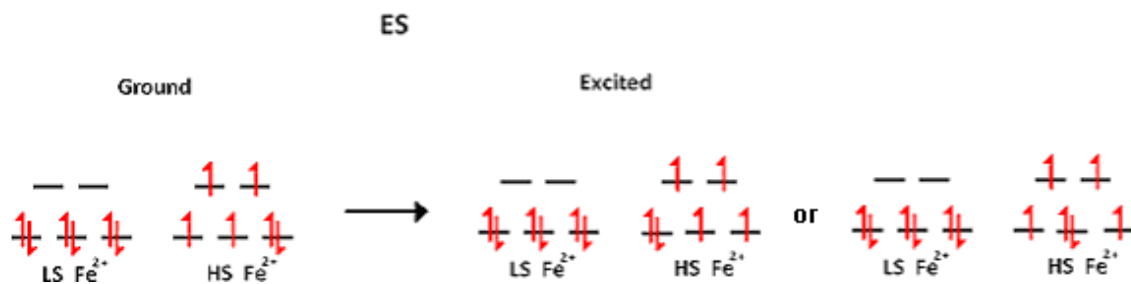


Figure 3-15 PW electron arrangement of d orbitals in ground and excited state

The DOS plot obtained for Ca<sup>2+</sup>PW, is illustrated in Figure 3-16

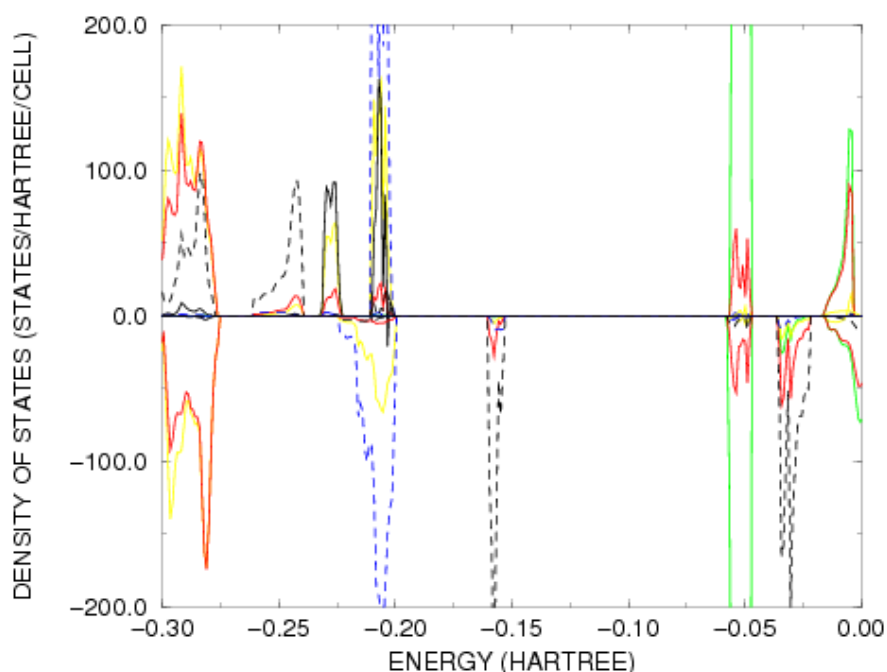


Figure 3-16 CaPW DOS populations of total N (yellow) and C (red) orbitals, Ca<sup>2+</sup> (green) orbitals, Fe<sup>2+</sup> low spin (blue) and high spin (black)  $t_{2g}$  (dashed) and  $e_g$  (solid) orbitals respectively. The positive and negative y-axes denote  $\alpha$  and  $\beta$  spins respectively. The Fermi energy is -0.15 Hartrees.

As in the KPW complex, above the Fermi energy of -0.15 Hartrees, the HOMO is occupied by HS  $t_{2g}$  Fe<sup>2+</sup>  $\beta$  electrons, and there is also a presence of  $C_{\pi}$   $\beta$  electrons. However the LUMO appears in this case to be occupied by the Ca<sup>2+</sup> orbitals and  $C_{\pi}$   $\beta$  electrons, suggesting the possibility of metal-ligand excitation.

### 3.2.2.4 Effects of Metal Identity on PB and PW Band Gaps

The band gaps obtained from the DOS plots of the B3LYP functional for the PY, PB and PW complexes along with the associated calculated cell parameters, bond lengths, atomic charges, and spin moments are presented in Table 3-4.

Successfully converged ground states were obtained for all the metal PB and PW complexes, using the B3LYP functional, with the exception of the  $Mg^{2+}$  complexes. As in the  $Ca^{2+}$  complex this may be due to the presence of  $Mg^{2+}$  orbitals around the Fermi level.

In the PB group 1 metal complexes, the lattice constant is shown to increase and the obtained band gap is shown to decrease as the size of the incorporated metal increases. This appears to be a linear relationship (Table 3-4), emphasised by the comparably larger change in both the lattice constant and band gap from the Rb to Cs ion. The LS  $Fe^{2+}$ -C and HS  $Fe^{3+}$ -N distances also increase accordingly with an increase in metal cation and the lattice constant, and as expected the C-N distances remain the same at approximately 1.163 Å. The same trends are present in the PB group 2 metal complexes although not as significantly. Also, only the HS  $Fe^{3+}$ -N distance, onto which an electron is transferred to the  $t_{2g}$  orbital, appears to increase with the small increase in lattice constant due to the increased metal cation size.

In both the group 1 and group 2 PB complexes, neither the C or N or the LS  $Fe^{2+}$  and HS  $Fe^{3+}$  spins are affected by cation identity. The charges on the LS  $Fe^{2+}$  and HS  $Fe^{3+}$  both increase linearly with increased cation size, although the charges on the C and N atoms also change there is no apparent trend. It is also worth noting that whereas the group 1 PB complexes contain a charge balancing cation in four of the eight sub-lattice positions, the group 2 PB complexes only contain two.

Due to the induced reduced symmetry in the PW complexes to allow for the unpaired electron in the  $d_{xy}$  orbital in order to obtain a converged ground state, both the resulting  $a$  and  $c$  lattice coordinates are presented, as are both distance, spin and charge values concerning both sets of C and N atoms. In the case of the

group 1 PW complexes, the lattice constant is again shown to increase as the size of the incorporated metal is increased; however the band gap obtained is also shown to increase, unlike in the group 1 PB complexes where it is shown to decrease. The relationship does appear linear.

Again, as for the PB complexes, the same trends are also present in the PW group 2 metal complexes although not as significantly for group 1, and again the HS  $\text{Fe}^{3+}$ -N distance, through which an excited electron may transfer between either of the three degenerate  $t_{2g}$  orbitals, appears most affected by the increase in lattice constant due to the increased metal cation size. In the case of BaPW, compared to SrPW however, the lattice constant only increased from 10.41 to 10.42 Å and instead of the expected increase, the band gap decreased from 3.22 to 3.209 eV.

The spins on the C, N and  $\text{Fe}^{2+}$  LS ions are not affected by the cation identity in either the group 1 or group 2 metals. However, the  $\text{Fe}^{2+}$  HS ion spin increases as the size of metal is increased. Again in both group 1 and group 2 PW complexes, similarly to the PB complexes, the charge on both the  $\text{Fe}^{2+}$  LS and  $\text{Fe}^{2+}$  HS ions increases linearly with increasing cation size and although the charge on the C and N atoms also changes there is no apparent pattern.

**Table 3-4 Band gaps of PY, PB and PW complexes and associated lattice parameters, atom spins and atom charges\*.**

PY	Lattice Parameters					Spins				Charges					Band
	a	c	Fe <sup>3+</sup> LS-C	C-N	N-Fe <sup>3+</sup> HS	Fe <sup>3+</sup> LS	C	N	Fe <sup>3+</sup> HS	Fe <sup>2+</sup> LS	C	N	Fe <sup>3+</sup> HS	M	Gap
	10.37	10.29	1.949	1.155	2.082	4.375	-0.016	0.111	1.097	+2.259	-0.089	-0.558	+1.688	-	1.905
			1.932	1.157	2.055		-0.014	0.059			-0.091	-0.588			2.585**
PB	a		Fe <sup>2+</sup> LS-C	CN	N-Fe <sup>3+</sup> HS	Fe <sup>2+</sup> LS	C	N	Fe <sup>3+</sup> HS	Fe <sup>2+</sup> LS	C	N	Fe <sup>3+</sup> HS	M	
Li	10.29		1.916	1.163	2.069	0.142	0.027	0.058	4.347	1.198	-0.135	-0.605	2.244	+0.998	1.905
Na	10.29		1.915	1.163	2.069	0.142	0.027	0.058	4.348	1.198	-0.127	-0.609	2.244	+0.976	1.904
K	10.31		1.919	1.164	2.073	0.141	0.026	0.059	4.349	1.204	-0.123	-0.614	2.245	+0.972	1.890
Rb	10.32		1.922	1.164	2.076	0.142	0.026	0.059	4.349	1.207	-0.135	-0.610	2.246	+0.983	1.871
Cs	10.36		1.930	1.164	2.084	0.0143	0.025	0.059	4.351	1.217	-0.130	-0.613	2.248	+0.991	1.834
Be	10.24		1.900	1.163	2.064	0.126	0.027	0.060	4.351	1.186	-0.123	-0.615	2.247	+1.984	1.895
Mg	-		-	-	-	-	-	-	-	-	-	-	-	-	-
Ca	10.25		1.900	1.163	2.066	0.131	0.026	0.060	4.351	1.186	-0.107	-0.620	2.247	+1.862	1.910
Sr	10.26		1.903	1.163	2.068	0.133	0.026	0.060	4.351	1.189	-0.117	-0.619	2.248	+1.964	1.903
Ba	10.27		1.906	1.163	2.070	0.133	0.026	0.060	4.352	1.192	-0.113	-0.621	2.248	+1.923	1.901
PW	a	c	Fe <sup>2+</sup> LS-C	C-N	N-Fe <sup>2+</sup> HS	Fe <sup>2+</sup> LS	C	N	Fe <sup>3+</sup> HS	Fe <sup>2+</sup> LS	C	N	Fe <sup>2+</sup> HS	M	
Li	10.48	10.42	1.920/1.906	1.163/1.164	2.157/2.141	0.025	-0.001	0.029	3.772	1.184	-0.285	-0.535	1.738	0.998	3.276
							0.025	0.021			-0.260	-0.558			
Na	10.48	10.41	1.918/1.905	1.164/1.164	2.157/2.139	0.030	-0.001	0.028	3.772	1.183	-0.272	-0.541	1.736	0.976	3.279
							0.026	0.020			-0.247	-0.554			
K	10.51	10.45	1.924/1.911	1.164/1.164	2.170/2.150	0.024	-0.001	0.028	3.777	1.193	-0.263	-0.550	1.740	0.971	3.332
							0.024	0.021			-0.239	-0.572			
Rb	10.54	10.48	1.930/1.920	1.164/1.164	2.177/2.156	0.023	-0.001	0.028	3.780	1.197	-0.285	-0.545	1.742	0.980	3.352
							0.024	0.020			-0.259	-0.565			
Cs	10.62	10.55	1.942/1.933	1.165/1.165	2.202/2.176	0.023	0.000	0.026	3.789	1.214	-0.272	-0.553	1.749	0.989	3.402
							0.023	0.019			-0.248	-0.572			
Be	10.39	10.34	1.902/1.892	1.162/1.162	2.132/2.119	0.032	-0.001	0.029	3.761	1.173	-0.286	-0.532	1.730	1.989	3.162
							0.027	0.020			-0.257	-0.553			-
Mg	-		-	-	-	-	-	-	-	-	-	-	-	-	-
Ca	10.38	10.34	1.900/1.890	1.163/1.163	2.131/2.119	0.030	-0.001	0.029	3.762	1.170	-0.260	-0.540	1.173	1.890	3.177
							0.027	0.021			-0.232	-0.562			
Sr	10.41	10.37	1.905/1.895	1.162/1.163	2.139/2.125	0.031	-0.001	0.028	3.764	1.176	-0.278	-0.538	1.173	1.974	3.222
							0.027	0.020			-0.249	-0.560			
Ba	10.42	10.38	1.907/1.897	1.163/1.163	2.145/2.130	0.031	-0.001	0.028	3.767	1.179	-0.268	-0.544	1.734	1.941	3.209
							0.027	0.020			-0.240	-0.565			

\*Broken symmetry invoked in PY and PW complexes resulted in differing a and c lattice parameters and two sets of CN data. \*\*HOMO Most Pop - LUMO Most Pop

### 3.3 Discussion and Conclusions

The effect of the metal identity on the band gap in PB and related complexes has been investigated by means of both SCF calculations and density of state plots. The band gap energies obtained from direct SCF calculations using a range of hybrid functionals did not compare well with experimental values. The band gap values obtained using the B3LYP functional were significantly lower in comparison to the experimental values. This was also the case when all other hybrid functionals, including HF=100%, were applied.

The values obtained using the UHF functional, usually known to overestimate band gap energies, were as expected, high in comparison to the experimental values, although in comparison to the other functionals, provided values most comparable to experiment. In addition, the means by which the excited electron was modelled had little to no effect on either the band gap energy or the trend of the energies in relation to one another. Slight discrepancies do however begin to appear around 20% HF mixing at which it is predicted that the electronic findings are qualitatively comparable to experiment.

The band gaps calculated from the DOS plots, by use of the B3LYP functional, were also shown to overestimate the experimentally obtained band gap energies. These did, however, give values significantly better in comparison to those obtained by direct energy differences from SCF calculations. Interestingly, the energy difference between the most populated states in the HOMO and LUMO also appeared to fit the trend in band gaps with respect to the identity of the metal cation incorporated into the lattice.

A comparison of the PB, PY and PW DOS plots has produced some interesting observations. As expected the PB HOMO and LUMO were identified as the low spin Fe  $t_{2g}$  orbital and high spin Fe  $t_{2g}$  orbital respectively, in which the  $e^-$  transition was  $\beta$ - $\beta$ . The PY HOMO and LUMO were identified as the low spin Fe  $t_{2g}$  orbital and high spin  $t_{2g}$  orbital respectively, again in which the  $e^-$  transition was  $\beta$ - $\beta$ . Although the energy difference of 1.905 eV between the VB and CB was significantly lower than the expected value for yellow absorption spectra in the 2.89-2.96 eV range, this

range was well within the 1.905 - 3.374 eV value spanning the lowest HOMO to lowest LUMO. Also as expected, due to lack of colour in PY, the PW DOS plot produced a band gap in the UV energy range. The associated HOMO and LUMO are both high spin Fe  $t_{2g}$  orbitals suggesting that upon excitation, the  $\beta$  electron in the orbital containing the electron pair moves between the degenerate high spin Fe  $t_{2g}$  orbitals.

A significant effect on band gap resulting from the identity of the included cation has been noted. In the PB complexes, a linear relationship was found between the increased lattice constant and decreased band gap upon the incorporation of a larger cation, although the effect was not as significant in group two complexes. In the PW complexes, a linear relationship was also noted between the increased lattice constant and increased band gap upon the incorporation of a larger cation, with the exception of Cs, although again, the effect was not as significant in group two complexes. The effect in group two complexes was however more so than that in the PB complexes, suggesting the possibility that the number of metals within the eight available charge balancing sites may also influence the lattice constant and therefore band gap.

In all complexes, an increase in the Fe ion charges are observed with increased cation size, suggesting the change in band gap is due to both the resulting increase in lattice parameter with the increasing cation size, but also the increase in the interaction between the Fe ions and the metal cation. This confirms the claim by Wojdeł and Bromley<sup>29-30</sup>. The subtle differences observed suggest that by altering metal identity it is possible to make small changes in the obtained band gap.

In the future DOS plots in which the densities of states of the individual  $d$  orbitals are plotted may provide more information on whether the excitations are specific to any of the degenerate one in for example the case of PW. Also the Kalimori method, outlined in Chapter 2, could also be used to derive expressions for any  $d$ -electron configuration of the systems in terms of Racah parameters. This may be of use in allowing the order of each state to be visualised in terms of total energy. It is then possible to determine the total energy for all of the excited states by the successful convergence of a limited few.

## 4 Transition Metal Hydrogen Halides (TMHH)

Hybrid organic-inorganic transition metal (TM) bearing structures, in which the TMs are bridged by organic ligands, have been shown to display a wide range of properties associated with the presence of unpaired 3d or 4d-shell electrons. However, the intermolecular hydrogen bonds and other weak interactions binding the TM complexes in the solid state have also been shown to affect the long-range order of these systems, at the critical ordering temperature.

Previous computational studies have provided computed geometries, spin transition energies and magnetic coupling constants ( $J$ ) in good agreement with the available experimental data for PB and related analogues (PBA).<sup>64-65</sup> The model structures discussed in this chapter comprise the same cubic TM framework and charge balancing  $K^+$  ion occurring in the PBAs; however, in place of the interlinking  $CN^-$  ligands, we substitute bridging HBs of the form  $X\cdots H-X$ , where  $X$  denotes a halide anion. While the model structures adopted must be considered as entirely theoretical, the simple periodic structures they provide not only aid the analyses of the magnetic coupling strengths, but also ensure that the proper ionic charges and long range electrostatic interactions are conserved. In regard to the latter point, consider that isolated cluster models of solids often encounter difficulties in relation to the preservation of the correct charge state of the constituent ions and finite size effects.

The following investigations are split into two sections. The first section systematically examines the effects of altering the TM (V, Ni, Cu) and HB halide linker (FHF, FHCl, ClHCl) species, and also the composition of the hybrid functional [specifically the exact exchange content, denoted here as  $F_0(\%)$ ]. The optimised ground state structures obtained, in which the protons occupy the minima of the HB potential energy profiles, will yield coupling values in the static limit. The second section examines the effects of quantum motion within the HB interactions by varying halide-halide distances and proton positions. A hybrid functional  $F_0=50\%$  is used, and, for reasons of computational tractability, only Ni is used. Such calculations will yield coupling constants which take account of the postulated

strongly quantum mechanical nature of such bonds. A further aim is to provide guidance as to the HB lengths and strengths required to affect a given magnetic coupling, with a view to the future engineering and post-rationalisation of the interactions between TM complexes in the solid state.

## 4.1 Computational Methods

The *ab initio* calculations have been carried out using the CRYSTAL06 code.<sup>150</sup> A range of hybrid functionals were used (2-34), in which  $F_0$  was varied from 0 to 100% in steps of 10% have been employed, so as to provide further insight into the variations in  $J$  with  $F_0$ , seeking consistent trends with variation of other parameters such as HB geometry, and the identity of the TM species. The calculated total energies were obtained using basis sets obtained from the CRYSTAL online repository,<sup>181</sup> of the specific form

Cl 86-311G, F 7-311G, H 6-311G\*\*,  
Potassium K\_86-511G (without *d*-functions),  
Vanadium 86-411G, Nickel 86-411G and Copper 86-4111G.

Where the notation used in defining these basis sets denotes the number of Gaussian primitives used for each shell type, for example 86-311G means that the basis set used for Cl is of the specific form 1s(8)2sp(6)3sp(3)4sp(1)5sp(1). Adequate convergence of the total energy was obtained in all cases by use of a Monkhorst-Pack reciprocal space mesh with a shrinking factor of 8. The truncation thresholds for bielectronic integrals were set at 7,7,7,7 and 14, as further described in the CRYSTAL06 documentation.<sup>150</sup> Initial geometry optimisations of the ground state were performed with set SCF tolerances, at which the total energy convergence was set to  $10^{-7}$  au. This was then lowered to  $10^{-9}$  au, so as to obtain sufficient convergence in  $J$  values. RMS (maximum) gradient and displacement tolerances of 0.00050 (0.0005) and 0.0010 (0.001) au respectively were also implemented.

The bond lengths used in the initial CRYSTAL06 input file were derived by combining the effective ionic radii of the  $TM^{2+}$  ions in six-fold coordination

presented by Shannon, <sup>182</sup> see Table 4-1, with previously calculated HB distances, see Table 4-2. Binding energies relevant to the preferred dissociation channels;  $[XHY]^- \rightarrow HX + Y^-$ , <sup>183</sup> are also presented.

**Table 4-1 Effective ionic radii for TM<sup>2+</sup> ions, as presented in the data of Shannon.** <sup>182</sup>

TM	Crystal Radius
V <sup>2+</sup>	93
Ni <sup>2+</sup>	83
Cu <sup>2+</sup>	71

**Table 4-2 Experimental and calculated HB binding energies and distances for the isolated FHF<sup>-</sup>, FHCl<sup>-</sup> and ClHCl<sup>-</sup> ligands.** <sup>183</sup>

X <sub>1</sub> -H-X <sub>2</sub>	Exp				Theory			
	E kcal mol <sup>-1</sup>	X <sub>1</sub> -X <sub>2</sub> (Å)	X <sub>1</sub> -H (Å)	H-X <sub>2</sub> (Å)	E kcal mol <sup>-1</sup>	X <sub>1</sub> -X <sub>2</sub> (Å)	X <sub>1</sub> -H (Å)	H-X <sub>2</sub> (Å)
FHF <sup>-</sup>	38.6	2.2778	1.1389	1.1389	45.0	2.288	1.144	1.144
ClHCl <sup>-</sup>	23.1	3.1466	1.5733	1.5733	22.4	3.126	1.563	1.563
FHCl <sup>-</sup>	21.8				20.0	2.887	0.963	1.924

The rhombohedral primitive unit cell contains two TM centres, six bridging XHX<sup>-</sup> anions and two K<sup>+</sup> counterions, as shown in Figure 4-1. The same cell was used for all subsequent calculations of *J* at structural equilibrium, and as a function of variation in HB geometry.

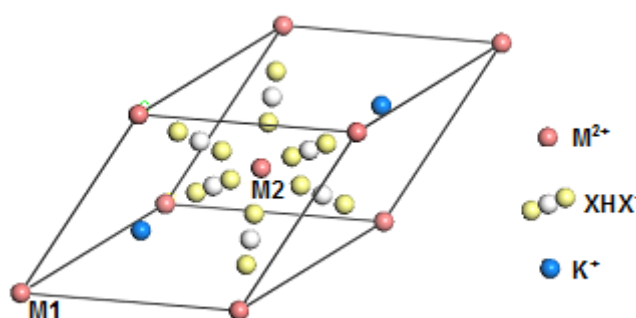


**Figure 4-1 Primitive M XHX unit cell**

The  $J$  values linking the interacting unpaired electrons on  $M^{2+}$  ions ( $M = \text{Cu}, \text{V}, \text{Ni}$ ), as mediated by the bridging  $\text{XHX}^-$  ( $= \text{FHF}, \text{FHCl}, \text{ClHCl}$ ) anions, were obtained from the calculated total energies of the FM and AF magnetic states. The two magnetic sublattices are shown in Figure 4-2, where in the AF state, any given TM site neighbours exclusively sites bearing spin density of the opposite sign. The representation of magnetic states is limited here to an Ising-like model, in that only collinear or anticollinear spin alignments are permitted.

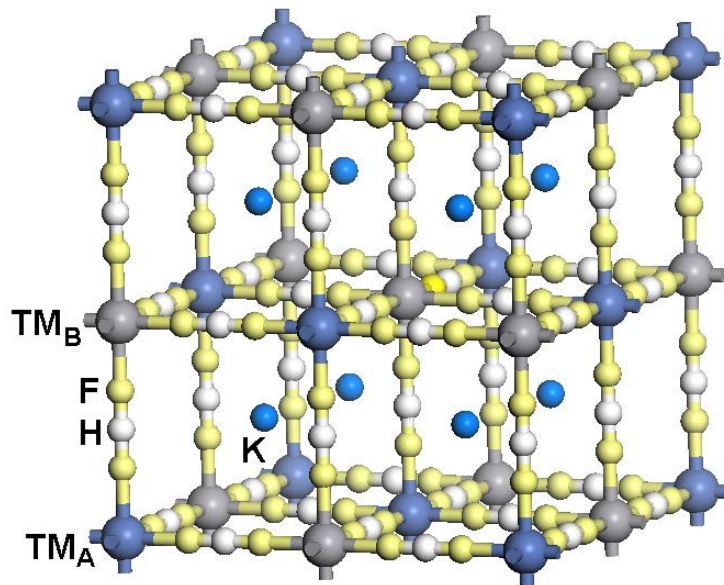


**Figure 4-2 Two magnetic sublattices required to calculate FM ( $\text{TM}_A$  and  $\text{TM}_B$  both have same spin) and AF ( $\text{TM}_A$  and  $\text{TM}_B$  both have opposite spins) magnetic states.**

The energy operator corresponding to the previously defined Ising Hamiltonian (Equation 2-38) is

$$\hat{E} = E_0 + \frac{J}{2} \sum_{ij}^{nn} \sigma_i \sigma_j \quad (4-1)$$

where  $J$  is the superexchange coupling constant, and  $\sigma_i$  and  $\sigma_j$  are the projections of the spin moments, constrained to point up or down only at sites  $i$  and  $j$  on the axis of quantisation, and the summations run over  $nn$  next nearest neighbours. This was employed, yielding expressions for the total energies of the FM and AF states in terms of  $J$ , from which the latter are easily obtained, all as presented in Table 4-3.

**Table 4-3  $M^{2+}$  ion FM and AF spin alignments and energies obtained using the nearest neighbour Ising Hamiltonian and two magnetic states.**

Magnetic State (S)	$M^{2+}$ Spins		Energy (E) per $M^{2+}$ ion
	$M_1$	$M_2$	
$S_{FM}$	↑	↑	$E_{FM} = E_0 + 3J \sigma ^2$
$S_{AF}$	↑	↓	$E_{AF} = E_0 - 3J \sigma ^2$

An optimisation in which this model structure was used in the CuFHF complex resulted in shortening of the  $a$  and  $b$ , and lengthening of the  $c$  lattice constants - indicative of the Jahn-Teller (JT) effect common in  $Cu^{2+}$  systems. Consequently a larger unit cell in which the symmetry was manually broken was used to model this complex instead, see below. In an undistorted octahedral environment the  $e_g$  ( $z^2$  and  $x^2-y^2$ ) and  $t_{2g}$  ( $xz$ ,  $yz$  and  $xy$ ) orbital subsets are each two- and three-fold degenerate, respectively. With Jahn-Teller distortion of the type found here (equatorial Cu-O bonds contracted and axial elongated) the  $x^2-y^2$  and  $xy$  orbitals overlaps more strongly with  $\sigma$  and  $\pi$  orbitals, respectively, on the neighbouring anions leading to increase in energy, and vice-versa for  $z^2$ ,  $xz$  and  $yz$  orbitals; and also a decrease in the total energy of a system. The effect on the Cu  $d$ -orbitals is illustrated in Figure 4-3.

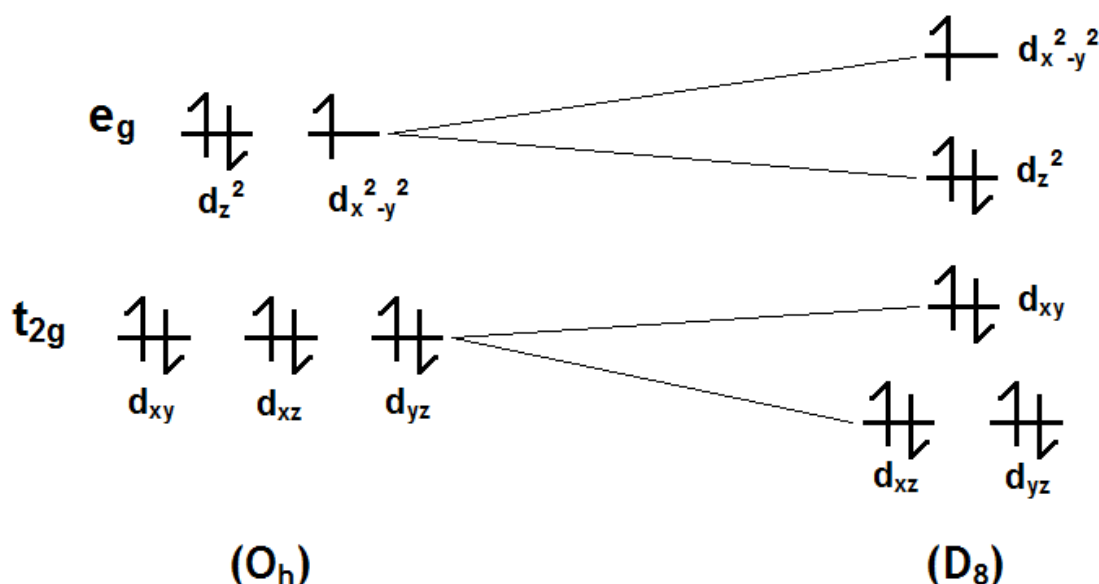


**Figure 4-3  $Cu^{2+}$   $d^9$  configuration in Octahedral ( $O_h$ ) and Jahn-Teller distorted ( $D_8$ ) ligand field.**

As a consequence of the JT distortion, the magnetic couplings in the  $xy$ -plane (now denoted  $J_1$ ) could conceivably differ from that along the  $z$ -axis ( $J_2$ ), and so their calculation requires the use of a larger supercell. The resulting  $2K^+[4Cu^{2+}(XHX^-)_6]$  supercell is illustrated in Figure 4-4.

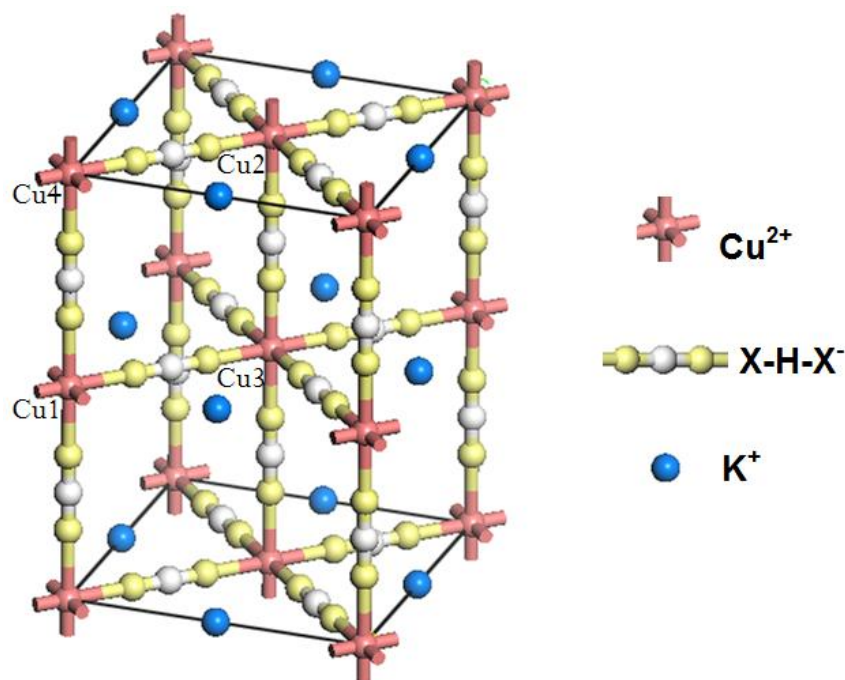


Figure 4-4 Model  $2K^+[4Cu^{2+}(XHX^-)_6]$  structure.

Also shown are the four spin-bearing  $Cu^{2+}$  ions, which may potentially bear different spin alignments. To account for the two  $J$  values a slightly modified Ising Hamiltonian of the form (4-2) was employed.

$$\hat{E} = E_0 - \frac{J_1}{2} \sum_{ij}^{nn_{xy}} \sigma_i \sigma_j - \frac{J_2}{2} \sum_{ij}^{nn_z} \sigma_i \sigma_j \quad (4-2)$$

The four magnetic states and corresponding energy expressions used to obtain  $J_1$  and  $J_2$  values are shown in Table 4-4.

**Table 4-4 Cu ion spin alignments and energies obtained using the nearest neighbours Ising Hamiltonian for the four magnetic states.**

Magnetic State (S)	$Cu^{2+}$ Spins				Energy (E) per $Cu^{2+}$ ion
	Cu <sub>1</sub>	Cu <sub>2</sub>	Cu <sub>3</sub>	Cu <sub>4</sub>	
S1	↑	↑	↑	↑	$E_1 = E_0 - 2J_1 \sigma ^2 - J_2 \sigma ^2$
S2	↑	↓	↓	↑	$E_2 = E_0 + 2J_1 \sigma ^2 - J_2 \sigma ^2$
S3	↑	↓	↑	↓	$E_3 = E_0 - 2J_1 \sigma ^2 + J_2 \sigma ^2$
S4	↑	↑	↓	↓	$E_4 = E_0 + 2J_1 \sigma ^2 + J_2 \sigma ^2$

The spin alignments correspond to the FM state (S1) and three AF states (S2-S4). The total energies ( $E_1$ - $E_4$ ), obtained using CRYSTAL06 were used to derive the coupling values  $J_1$  and  $J_2$ . In order to test the numerical accuracy and consistency of the results, both couplings were obtained separately twice from different combinations of the total energies as shown below (4-3).

$$J_1 = \frac{E_2 - E_1}{4} = \frac{E_4 - E_3}{4}$$

$$J_2 = \frac{E_3 - E_1}{2} = \frac{E_4 - E_2}{2} \quad (4-3)$$

## 4.2 Cu Hydrogen Halide (CuHH)

The resulting  $J$  values obtained using a variety of hybrid functionals in the CuFHF system are presented in Table 4-5, in which the factor  $|\sigma|^2$  is included. The negative  $J$  values are indicative of an overall AF ground state.

**Table 4-5  $J_1$  and  $J_2$  values, inclusive of  $|\sigma|^2$ , obtained for a range of hybrid functionals using the nearest-neighbour Ising Hamiltonian. Converged wavefunctions were not obtained for  $F_0 = 0$ .**

$F_0$	$J_1 / k_B$ (K)		$J_2 / k_B$ (K)	
	E2-E1	E4-E3	E3-E1	E4-E2
100	-5.54	-5.54	-0.023	-0.025
90	-6.45	-6.45	-0.025	-0.028
80	-7.71	-7.71	-0.028	-0.031
70	-9.51	-9.51	-0.031	-0.036
60	-12.14	-12.14	-0.035	-0.043
50	-16.28	-16.29	-0.039	-0.053
40	-23.25	-23.26	-0.042	-0.068
30	-35.98	-36.01	-0.036	-0.099
20	-61.14	-61.26	0.029	-0.207
10	-108.16	-109.63	1.335	-1.613

For all values of  $F_0$ , the two  $J_1$  values appear to be consistent in both magnitude and antiferromagnetic state. The  $J_2$  values on the other hand, although similar at larger  $F_0$  representative of higher HF mixing, become significantly less comparable upon lowering  $F_0$ . Clearly the  $J_2$  values are significantly weaker in comparison with  $J_1$ , in keeping with the understanding that the JT split orbital occupation confines most of the unpaired spin density to lie within the  $xy$ -plane. Thus, it is likely that coupling along the  $z$ -axis proceeds only by the  $\delta$ -type overlap of the singly occupied  $x^2-y^2$  orbitals. Seeking to resolve the inconsistency of the  $J_2$  values, a Hamiltonian in which the effects of the next nearest neighbours (termed the  $nnn$  Hamiltonian) are included (4-4) was also used to model the same magnetic states.

$$\hat{E} = E_0 - \frac{J_1}{2} \sum_{ij}^{nn-xy} \sigma_i \sigma_j - \frac{J_2}{2} \sum_{ij}^{nn-z} \sigma_i \sigma_j - \frac{J_3}{2} \sum_{ij}^{nnn-xy} \sigma_i \sigma_j - \frac{J_4}{2} \sum_{ij}^{nnn-z} \sigma_i \sigma_j \quad (4-4)$$

From this it was possible to establish whether the extra couplings included in the  $nnn$  Hamiltonian were sufficient to lie at the root of the discrepancies noted above. The four  $J$  values in the  $nnn$  Hamiltonian correspond to  $J_1$  and  $J_2$  as previously defined, along with the couplings between a Cu ion and the 4 Cu  $nnn$  in

the same  $xy$ -plane ( $J_3$ ), and the 8 Cu  $nnn$  in the neighbouring  $xy$ -planes above and below ( $J_4$ ). The corresponding energies ( $E_1^*$ - $E_4^*$ ) per  $\text{Cu}^{2+}$  ion as derived from the  $nnn$  Hamiltonian (4-4) are shown in Table 4-6.

**Table 4-6 Cu ion spin alignments and energies obtained using the nearest neighbours Ising Hamiltonian for the four magnetic states.**

Magnetic State (S)	$\text{Cu}^{2+}$ Spins				Energy ( $E^*$ ) per $\text{Cu}^{2+}$ ion
	$\text{Cu}_1$	$\text{Cu}_2$	$\text{Cu}_3$	$\text{Cu}_4$	
S1	↑	↑	↑	↑	$E_1^* = E_0 - 2J_1 - J_2 - 2J_3 - 4J_4$
S2	↑	↓	↓	↑	$E_2^* = E_0 + 2J_1 - J_2 - 2J_3 + 4J_4$
S3	↑	↓	↑	↓	$E_3^* = E_0 - 2J_1 + J_2 - 2J_3 + 4J_4$
S4	↑	↑	↓	↓	$E_4^* = E_0 + 2J_1 + J_2 - 2J_3 - 4J_4$

By solving the resulting  $nnn$  simultaneous equations it is possible to obtain  $J_1$ ,  $J_2$  and  $J_4$  values, using (4-5).

$$\begin{aligned}
 J_1 &= \frac{[E_4^* - E_3^*] + [E_2^* - E_1^*]}{8} \\
 J_2 &= \frac{[E_4^* - E_1^*] + [E_3^* - E_2^*]}{4} \\
 J_4 &= \frac{[E_3^* - E_4^*] + [E_2^* - E_1^*]}{16}
 \end{aligned}
 \tag{4-5}$$

Note that  $J_3$  cannot be accessed from calculations within the present supercell; a larger supercell incorporating twice as many Cu ions would be required. Moreover, it is no longer possible to obtain each coupling constant separately twice, as before. A comparison of the  $J$  values obtained using both the  $nn$  and  $nnn$  Ising models is given in Table 4-7.

**Table 4-7 Full set of J values, inclusive of  $|\sigma|^2$ , obtained from a range of hybrid functional within both the nn and nnn Ising Hamiltonians.**

$F_0$	$J_1 / k_B$ (K)			$J_2 / k_B$ (K)			$J_4 / k_B$ (K)	
	nn model		nnn model	nn model		nnn model	nnn model	
%	E2-E1	E4-E3		E3-E1	E4-E2	average		
100	-5.54					-0.024		
90		-5.54	-5.54	-0.023	-0.025		-0.024	0.00024
80	-6.45	-6.45	-6.45	-0.025	-0.028	-0.027	-0.026	0.00034
70	-7.71	-7.71	-7.71	-0.028	-0.031	-0.030	-0.030	0.00043
60	-9.51	-9.51	-9.51	-0.031	-0.036	-0.034	-0.034	0.00067
50	-12.14	-12.14	-12.14	-0.035	-0.043	-0.039	-0.039	0.00105
40	-16.28	-16.29	-16.28	-0.039	-0.053	-0.046	-0.046	0.00172
30	-23.25	-23.26	-23.25	-0.042	-0.068	-0.055	-0.055	0.00326
20	-35.98	-36.01	-35.99	-0.036	-0.099	-0.068	-0.068	0.00781
10	-61.14	-61.26	-61.20	0.029	-0.207	-0.089	-0.089	0.02944
	-	-				-0.139		
	108.16	109.63	-108.90	1.335	-1.613		-0.140	0.36861

The  $J_1$  values obtained in both models are consistent. Comparing the averages of the two inconsistent  $J_2$  values within the *nn* Hamiltonian with the  $J_2$  values obtained using the *nnn* Hamiltonian, it is clear that the values are now consistent across the full  $F_0$  range. The  $J_4$  *nnn* out-of-plane couplings are very weak, as expected, but become more significant as  $F_0$  decreases. At  $F_0=100\%$   $J_4$  amounts to only 1% of  $J_2$ , but this proportion increases to 10% at approximately  $F_0=30\%$ , to 33% at  $F_0=20\%$ , with the final result that  $J_4$  is approximately three times larger than  $J_2$  at  $F_0=10\%$ . However, it is well known that the B3LYP functional ( $F_0=20\%$ ) overestimates  $J$  values so this is not surprising; the  $J$  values obtained below  $F_0=30\%$  can likely be considered as physically unrepresentative. Nevertheless, the variations in  $J$  values with  $F_0$  demonstrate the well-known trend whereby spin

density increasingly delocalises, and orbitals become more diffuse as the HF exchange content of the functional is reduced.<sup>184</sup>

The optimised structural parameters (Å), *nnn* *J* and associated  $T(\chi_{max})$  values from these calculations, and comparable experimental and theoretical values are presented in Table 4-8.  $\chi(T)$  plots in which broad peaks in susceptibility, due to short range 2D ordering, are the domineering feature, are often a good indication of a quality 2D antiferromagnet.  $T(\chi_{max})$  values were calculated, (4-6), using the larger  $J_1$  values and assuming isolated 2D planes of spin density. This same method, that estimates the temperature associated with the maximum in  $\chi$  within a mean-field approach<sup>185</sup> was also employed in the calculation of  $T(\chi_{max})$  in pseudo cubic  $[\text{Cu}^{\text{II}}(\text{HF}_2)(\text{pyz})_2]\text{BF}_4$  (pyz = pyrazine) coordination polymer<sup>82</sup>. *S* refers to the number of unpaired electrons.

$$T(\chi_{\max}) = \frac{2.53J_1S(S+1)}{k_B} \quad (4-6)^{82}$$

**Table 4-8 Optimised structural parameters (Å) and J values, inclusive of  $|\sigma|^2$ , for model  $2K^+[4Cu^{2+}(XHX^-)_6]$  structure and comparable experimental and theoretical values.**

$F_0$ (%)	a=b (Å)	Cu-Cu(Å)	Cu-F(Å)	F-F (Å)	F-H (Å)	$J_1$ (K)	$T(\chi_{max})$	c (Å)	Cu-Cu (Å)	Cu-F(Å)	F-F (Å)	F-H (Å)	$J_2$ (K)
100	8.5610	4.2805	1.372	1.536	0.768	-5.54	10.52	12.6348	6.3174	2.056	2.206	1.103	-0.024
90	8.5841	4.2920	1.376	1.541	0.770	-6.45	12.24	12.6766	6.3383	2.063	2.213	1.107	-0.026
80	8.6073	4.3036	1.379	1.546	0.773	-7.71	14.64	12.7198	6.3599	2.069	2.221	1.110	-0.030
70	8.6305	4.3153	1.382	1.552	0.776	-9.51	18.05	12.7649	6.3824	2.077	2.229	1.115	-0.034
60	8.6537	4.3269	1.385	1.558	0.779	-12.14	23.04	12.8126	6.4063	2.084	2.238	1.119	-0.039
50	8.6770	4.3385	1.387	1.564	0.782	-16.28	30.90	12.8625	6.4312	2.092	2.247	1.124	-0.046
40	8.7004	4.3502	1.390	1.570	0.785	-23.25	44.13	12.9158	6.4579	2.101	2.257	1.128	-0.055
30	8.7244	4.3622	1.393	1.577	0.788	-35.99	68.30	12.9728	6.4864	2.110	2.267	1.134	-0.068
20	8.7503	4.3751	1.396	1.584	0.792	-61.20	116.13	13.0348	6.5174	2.120	2.278	1.139	-0.089
10	8.7813	4.3907	1.400	1.591	0.795	-108.90	206.63	13.0977	6.5489	2.129	2.290	1.145	-0.140
Theory <sup>1</sup>								6.6201	6.6201	2.189	2.242	1.121	-0.0190
Exp <sup>RLE<sup>+</sup></sup>									6.6193(4)	2.208	2.204	1.102	-0.03

\*Note in cases of multiple J values  $T(\chi_{max})$  is determined using largest, in this case  $J_1$

As %HF is reduced the electron exchange becomes increasingly less orbital dependent so that the electrons' ability to avoid one another is reduced and in order to lower energy the electron distribution must expand in space. Therefore the lattice constants and internal bond lengths within the  $2K^+[4Cu^{2+}(FHF^-)_6]$  complex are increased with decreasing  $F_0$ . Despite the strong HB nature of the FHF HB, the F–H distances increase in a similar manner as the F–Cu distances.

From the literature, it seems that the F–F distance for the isolated  $FHF^-$  ligand is approximately 2.28 Å.<sup>183</sup> In addition F–F bond lengths of 2.21 and 2.24 Å were obtained for the coordinated Cu–FHF–Cu in the pseudo cubic  $[Cu^{II}(HF_2)(pyz)_2]BF_4$  (pyz = pyrazine) coordination polymer<sup>82</sup> and the related computational model<sup>83</sup> respectively. This suggests that the F–F distances obtained in the  $2K^+[4Cu^{2+}(FHF^-)_6]$  complex above, ranging between 1.536 and 1.591 Å, on the xy axis, are unrealistic and further comparisons will utilise only the Cu–FHF–Cu exchange pathway and associated  $J_2$  values along the z axis.

The Cu-Cu distances obtained for the  $2K^+[4Cu^{2+}(FHF^-)_6]$  complex are significantly smaller than in the experimental and theoretical  $[Cu^{II}(HF_2)(pyz)_2]BF_4$  complexes. The  $F_0=35$  hybrid functional has been shown to provide J values in good agreement with experiment.<sup>64-65,158-159</sup> Approximating the  $F_0=35\%$  values as averages of the values obtained at  $F_0=30$  and 40% leads to estimated Cu-Cu, Cu–F, F–F, F–H and J parameters of 6.4722 Å, 2.106 Å, 2.262 Å, 1.131 Å and –0.062K respectively. Comparing with the equivalent experimental Cu-Cu, Cu–F, F–F, F–H and J values of 6.6193(4) Å, 2.208 Å, 2.204 Å, 1.102 Å and –0.03 respectively, a significantly larger F–F distance is observed. It is later shown during the quantum analysis that increase in the FHF distance tends to result in a larger J value, consistent with the present comparison. Although not conclusive the results estimated for  $F_0=35$  may still be comparable to experiment.

### 4.3 V and Ni Static Calculations

The J values calculated for V and Ni materials as a function of  $F_0$  value and HB comprising species are shown in Figure 4-5. Note now that the higher symmetry

structures obtained for these materials (lacking JT distortion) lead to a much simpler magnetic Hamiltonian comprising only one coupling constant.

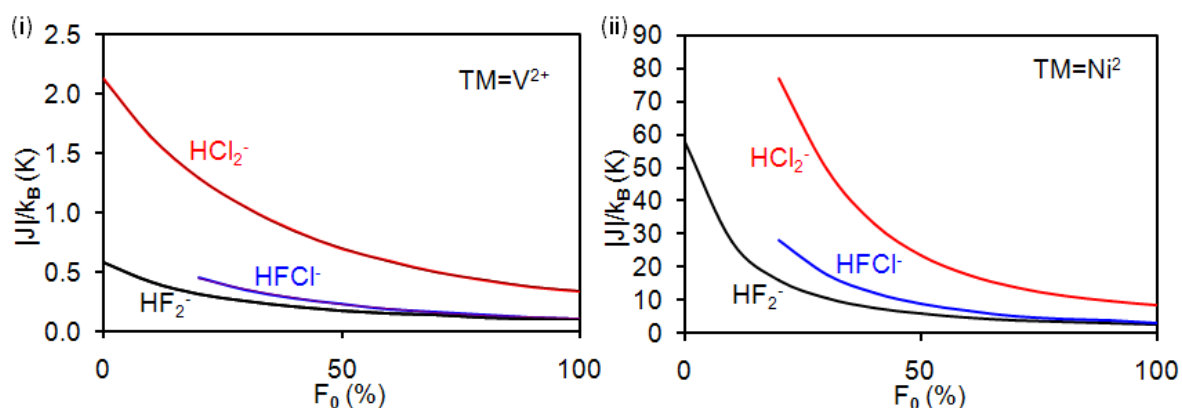


Figure 4-5 Magnetic Coupling ( $J$ ) values for  $TM = V^{2+}$ ,  $Ni^{2+}$ , and  $XFX^- = FHF^-$ ,  $ClHCl^-$  and  $FHCl^-$ .

First, in keeping with the Cu-bearing material, the V and Ni compounds both manifest an AF ground state. This is as expected due to the interaction between d-orbitals of the same symmetry type ( $e_g-e_g$  for  $Ni^{2+}$ ,  $t_{2g}-t_{2g}$  for  $V^{2+}$ ).<sup>186-187</sup> Again, the  $J$  values also increase with decrease in  $F_0$ . The coupling linking  $Ni^{2+}$  ions is significantly stronger, likely due to the effects of  $e_g-p_\sigma$  overlap as opposed to the  $t_{2g}-p_\pi$  overlap operating for  $V^{2+}$  ions. In both TM complexes, the different HBs behave in a similar manner in terms of  $J$ . In both cases, the coupling values present in the order  $ClHCl \gg FHCl > FHF$ . This is interesting when compared to the HB strengths derived for the isolated molecules, Table 4-2, which fall in the order  $FHF \gg ClHCl > FHCl$ , with experimental values of 38.6, 23.1 and 21.8 kcal mol<sup>-1</sup> respectively. As the  $ClHCl^-$  coupling is significantly larger than both the  $FHF^-$  and  $FHCl^-$  ions, it seems that it may be the way in which the H is bound to the halides that affects the coupling, rather than the overall HB energy, i.e. the tighter bound H in an H-F bond is less able to participate in the coupling exchange interaction.

Selected optimised structural parameters (Å),  $J$  values (K) and associated  $T(\chi_{max})$  values obtained from the V, Ni and Cu calculations within the  $F_0 = 100, 70, 50$  and 30% functionals are presented in Tables 4-9 to 4-12 respectively.  $T(\chi_{max})$  values for Cu complex, presented as above, Table 4-8, and  $T_c$  values in V and Ni

complexes, estimated within the mean field approach, as detailed in chapter 2 (2-41).

**Table 4-9 Selected optimised structural parameters (Å), J values (K) and associated  $T_c/T(\chi_{max})$  values for  $F_0=100\%$**

M	$X_1HX_2$	a/c(Å)	M-M(Å)	M- $X_1$ (Å)	$X_1$ -H(Å)	H- $X_2$ (Å)	$X_1$ - $X_2$ (Å)	$X_2$ -M(Å)	$J_{HXH}$ (K)	$T_c/T(\chi_{max})$
V	FHF	12.58	6.29	2.054	1.092	1.092	2.184	2.054	-0.098	0.93
	FHCl	14.67	7.34	2.045	0.962	1.751	2.714	2.577	-0.105	1.00
	ClHCl	16.35	8.18	2.563	1.527	1.527	3.052	2.563	-0.335	3.18
Ni	FHF	12.26	6.13	1.973	1.091	1.091	2.182	1.973	-2.402	12.15
	FHCl	14.33	7.17	1.961	0.964	1.745	2.708	2.496	-3.079	15.58
	ClHCl	16.03	8.02	2.483	1.524	1.524	3.049	2.483	-8.328	42.09
Cu	FHF	12.63	6.32	2.056	1.103	1.103	2.206	2.056	-0.024	0.045

**Table 4-10 Selected optimised structural parameters (Å), J values (K) and associated  $T_c/T(\chi_{max})$  values for  $F_0=70\%$**

M	$X_1-H-X_2$	a/c(Å)	M-M(Å)	M- $X_1$ (Å)	$X_1$ -H(Å)	H- $X_2$ (Å)	$X_1$ - $X_2$ (Å)	$X_2$ -M(Å)	$J_{HXH}$ (K)	$T_c/T(\chi_{max})$
V	FHF	12.68	6.34	2.068	1.103	1.103	2.207	2.068	-0.134	1.27
	FHCl	14.72	7.36	2.059	0.980	1.741	2.721	2.582	-0.159	1.51
	ClHCl	16.43	8.22	2.573	1.535	1.536	3.071	2.573	-0.497	4.71
Ni	FHF	12.36	6.18	1.987	1.102	1.102	2.204	1.987	-3.733	18.89
	FHCl	14.38	7.19	1.975	0.981	1.734	2.715	2.499	-5.150	26.06
	ClHCl	16.09	8.04	2.489	1.533	1.533	3.065	2.489	-13.760	69.63
Cu	FHF	12.76	6.38	2.077	1.115	1.115	2.229	2.077	-0.034	0.064

**Table 4-11 Selected optimised structural parameters (Å), J values (K) and associated  $T_c/T(\chi_{max})$  values for  $F_0=50\%$**

M	$X_1-H-X_2$	a/c(Å)	M-M(Å)	M- $X_1$ (Å)	$X_1$ -H(Å)	H- $X_2$ (Å)	$X_1$ - $X_2$ (Å)	$X_2$ -M(Å)	$J_{HXH}$ (K)	$T_c/T(\chi_{max})$
V	FHF	12.75	6.38	2.077	1.112	1.112	2.223	2.077	-0.175	1.66
	FHCl	14.75	7.38	2.068	0.993	1.732	2.726	2.585	-0.227	2.15
	ClHCl	16.47	8.24	2.576	1.543	1.543	3.085	2.576	-0.698	6.62
Ni	FHF	12.43	6.21	1.996	1.110	1.110	2.220	1.996	-5.711	28.90
	FHCl	14.41	7.20	1.984	0.995	1.725	2.719	2.501	-8.586	43.44
	ClHCl	16.12	8.06	2.491	1.539	1.539	3.078	2.491	-23.509	118.96
Cu	FHF	12.86	6.43	2.092	1.124	1.124	2.248	2.092	-0.046	0.087

**Table 4-12 Selected optimised structural parameters (Å), J values (K) and associated  $T_c/T(\chi_{max})$  values for  $F_0=30\%$**

M	$X_1-H-X_2$	a/c(Å)	M-M(Å)	M- $X_1$ (Å)	$X_1$ -H(Å)	H- $X_2$ (Å)	$X_1$ - $X_2$ (Å)	$X_2$ -M(Å)	$J_{HXH}$ (K)	$T_c/T(\chi_{max})$
V	FHF	12.82	6.41	2.085	1.121	1.121	2.242	2.085	-0.252	2.39
	FHCl	14.79	7.39	2.077	1.010	1.722	2.732	2.586	-0.350	3.32
	ClHCl	16.52	8.26	2.579	1.550	1.551	3.101	2.579	-1.040	9.87
Ni	FHF	12.50	6.25	2.006	1.120	1.120	2.240	2.006	-10.542	53.3
	FHCl	14.44	7.22	1.994	1.011	1.715	2.726	2.502	-17.608	89.10
	ClHCl	16.16	8.08	2.494	1.547	1.547	3.094	2.494	-49.473	250.33
Cu	FHF	12.97	6.49	2.110	1.134	1.134	2.268	2.110	-0.068	0.128

As expected, all the distance parameters;  $a$ ,  $M-M$ ,  $M-X_1$ ,  $X_1-H$ ,  $H-X_2$ ,  $X_1-X_2$  and  $X_2-M(\text{\AA})$  increase with decreasing  $F_0$ , independent of TM and X identity as before. The  $J$  and  $T_C/T(\chi_{max})$  values also increase with decreasing  $F_0$ . The  $M-F-H-F-M$  and  $M-Cl-H-Cl-M$  distances remain symmetric and equidistant on both sides of the H atom in all calculations.

The F-H distance in the FHF ligand is approximately 10% larger than in the FHCl ligand within both the V- and Ni-bearing materials for each  $F_0$  value. This is in keeping with the larger electronegativity of the F atom as compared with the Cl atom. The tight binding of the H atom by the F atoms in both the FHF and FHCl ligands may explain the significantly lower  $J$  values. The consequence of this is that the H atom is in comparison loosely bound to the Cl atom in the FHCl ligand with a significantly larger H-Cl distance. Clearly it is not this factor that reduces  $J$  in the FHCl anions, given that the H-Cl distances are of a similar magnitude in the ClHCl ligands which in comparison yield large  $J$  values. The position of the H atom therefore appears to significantly affect the  $J$  value obtained. This is studied in more detail in the following section.

#### 4.4 Effects of Quantum Motion in the $HF_2^-$ , $HCl_2^-$ , and $HFCl^-$ Ions

The optimised calculations in the previous section have assumed the HB proton as static and positioned at the optimised equilibrium position. Clearly this is a poor approximation for many hydrogen bonded materials, wherein the protons undergo significant zero point quantum motion governed by potential energy profiles with forms varying from flat-bottomed wells with single minima for short and strong HBs, to degenerate double wells for longer XHX bonds, to asymmetric double wells for XHY bonds. A simple strategy accounting for such effects is outlined below, where we now use only Ni TMs due to the significantly larger  $J$  values, and to the fact that stronger couplings are likely more faithfully represented by the present DFT approach. The proton position was systematically varied along the X-H-X axis in the three NiFHF, NiFHCl and NiClHCl materials within at a fixed functional  $F_0 =$

50%. The HB lengths were also altered by compressing and expanding the lattice constants of the previously optimised structures by  $\pm 2.5$ ,  $\pm 5$  and  $\pm 7.5\%$ .

The energy potentials and associated  $J$  values obtained by altering the proton position in both the optimised, contracted and expanded structures are shown in Figures 4-6 to 4-8 for the NiFHF, NiClHCl and NiFHCl materials respectively.

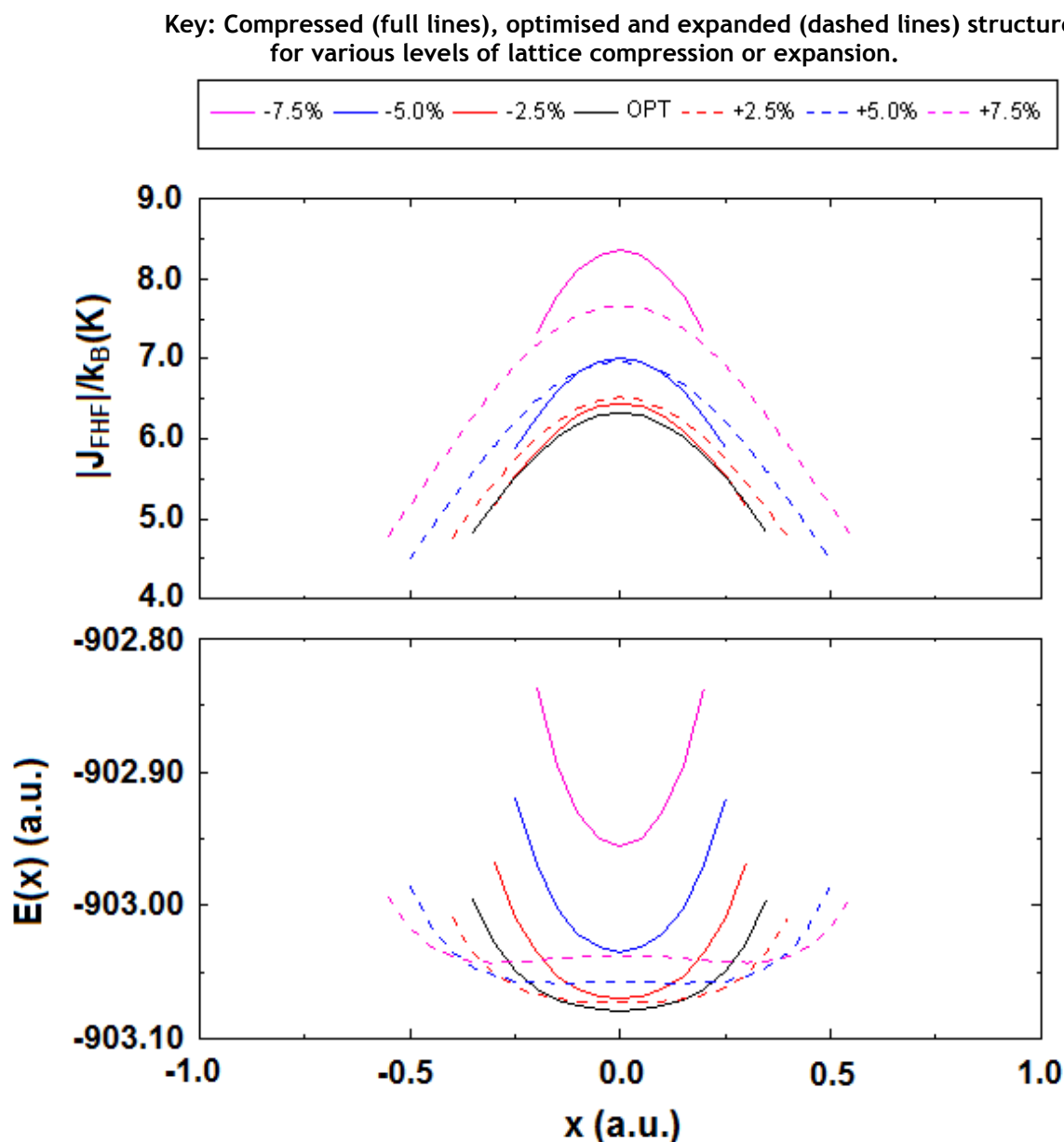


Figure 4-6 NiFHF potential energy profile  $E(x)$  and magnetic coupling constant  $J_{\text{FHF}}(x)$  as a function of proton position  $x$  along the FHF bond.

Key: Compressed (full lines), optimised and expanded (dashed lines) structures, for various levels of lattice compression or expansion.

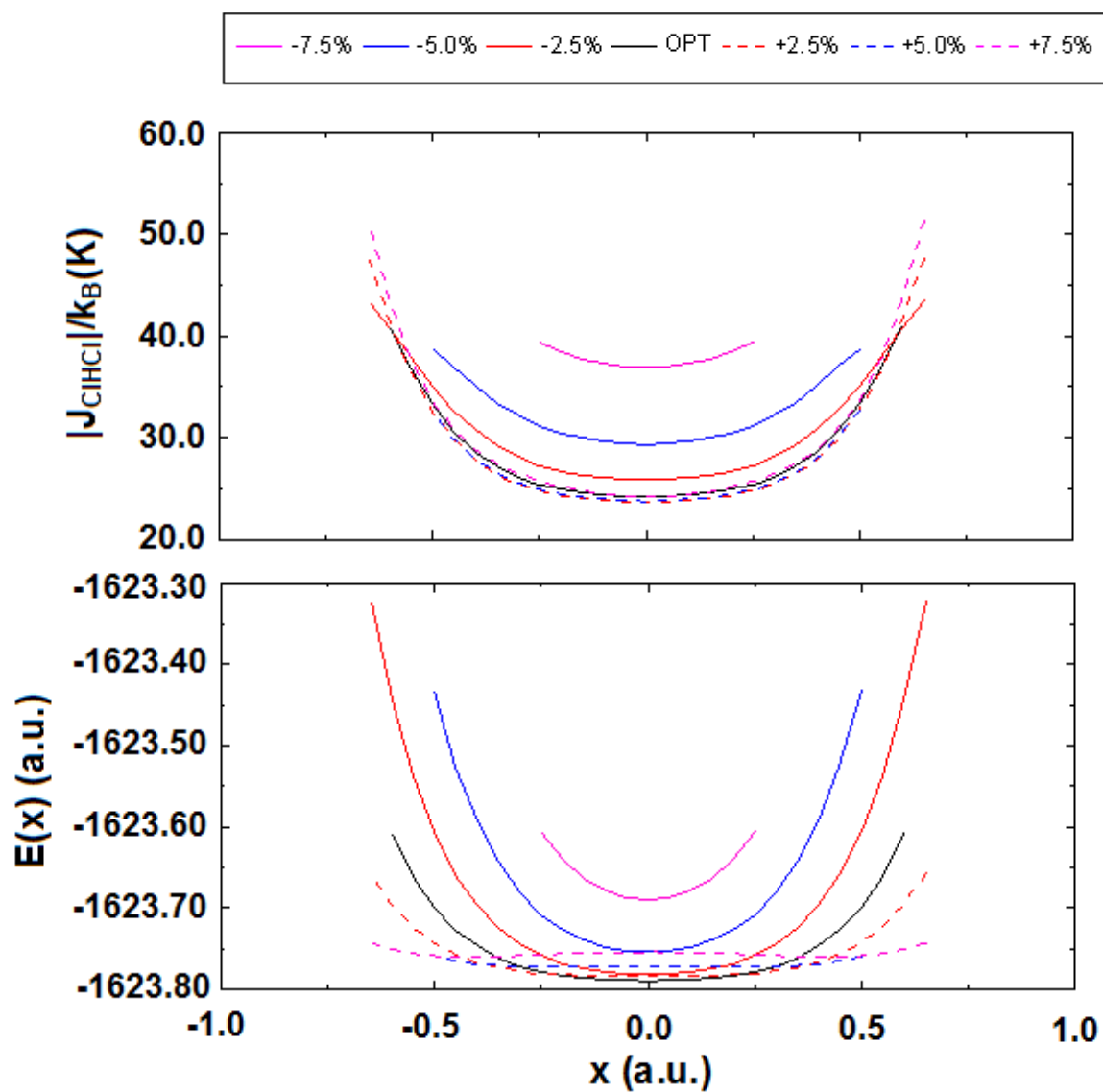


Figure 4-7 NiClHCl potential energy profile  $E(x)$  and magnetic coupling constant  $J_{\text{ClHCl}}(x)$  as a function of proton position  $x$  along the ClHCl bond.

Key: Compressed (full lines), optimised and expanded (dashed lines) structures, for various levels of lattice compression or expansion.

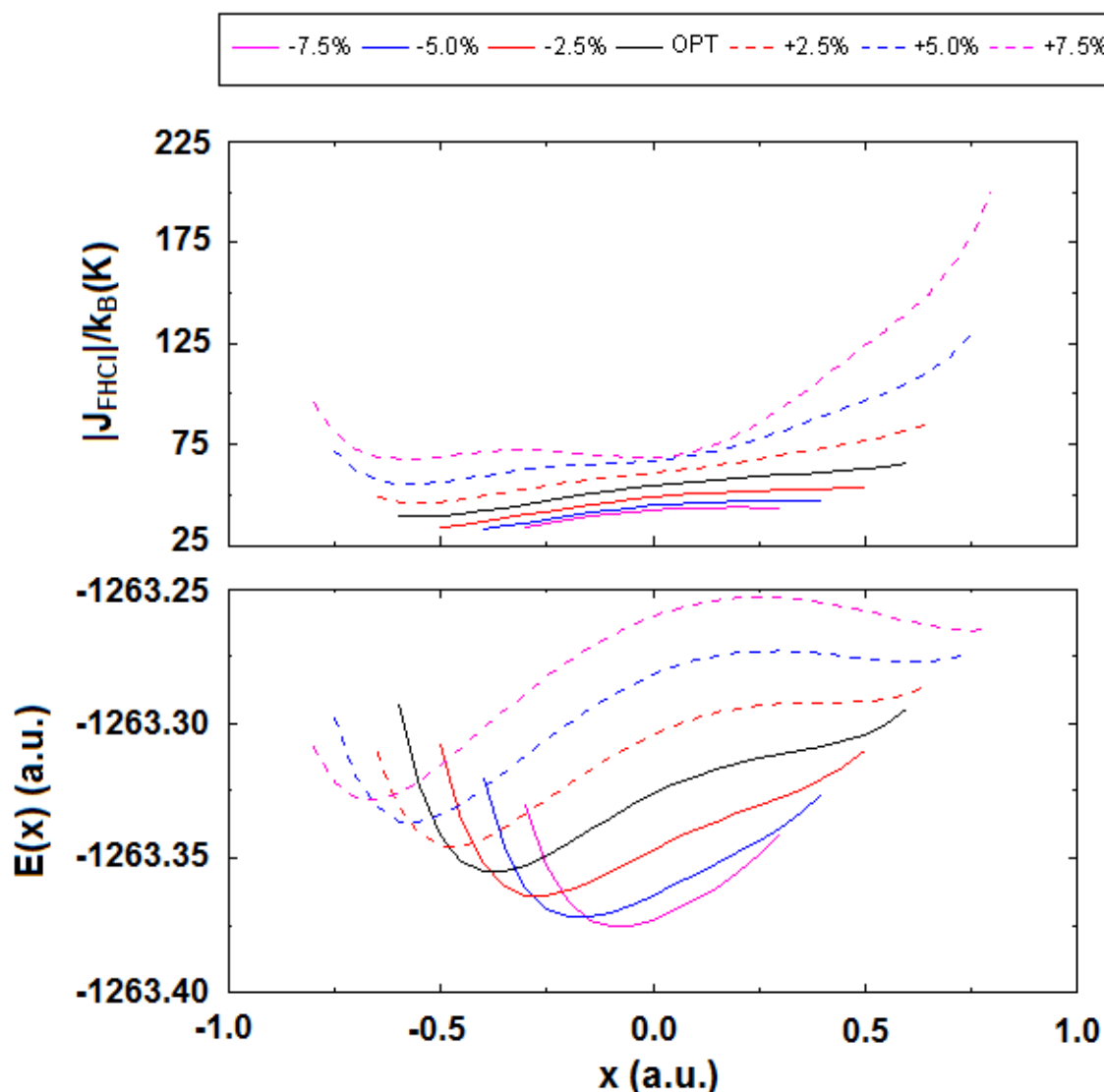


Figure 4-8 NiFHCI potential energy profile  $E(x)$  and magnetic coupling constant  $J_{\text{FHCl}}(x)$  as a function of proton position  $x$  along the FHCl bond.

As expected, all potential and  $J$  coupling curves obtained by altering the proton position and halogen-halogen distance in the NiFHF and NiClHCl structures are symmetrical about the bond midpoint. The expansion and contraction of both these structures from the optimum ground state structure results, as expected, in higher potential energies, and therefore higher energy profiles. The larger the lattice distortion, the higher in energy the potential profile. Most of the energy profiles are single well potentials (SWHB), however for both ligands the structures expanded by +5 and +7.5% form double well potentials, in which the preferred

proton position shifts away from the bond midpoint to lie in degenerate minima at either side.

Due to the higher electronegativity of the F atom in the FHCl ligand, the energy profile is asymmetric and the energy minimum in the optimised equilibrium, expanded and contracted structures corresponds to the H atom being significantly closer to the F atom. Also, an expansion of the lattice, introducing a larger F–Cl distance, yields a higher energy minimum and associated profile, whereas a contraction, introducing a shorter F–Cl distance, yields a lower energy minimum and associated profile. Most of the energy profiles are asymmetric SWHB potentials, however the structures expanded by +5 and +7.5% may start to form a second shallow well at an energy state much higher than the minimum. Due to the significantly higher energy state of the higher well this cannot be classed as a typical DWHB potential, and the preferred proton position always remains significantly closer to the F atom.

The lowest energy points of each of the optimised, contracted, and expanded curves have been presented along with the associated coupling values in Table 4-13.

In the single well curves, the minimum energy point lies in the centre of the HB. In the double wells, there are two minimum energy points equidistant from the centre of the HB. In the asymmetric FHCl curves, a plot of the ratio of the F–H and H–Cl distances at the energy minima (Figure 4-9), reveals a linear relationship with lattice expansion.

**Table 4-13 HB Parameters (Å) and associated J values for optimised, extended and contracted lattice E(x) minima**

Expansion / contraction %	FHF				ClHCl				FHCl				
	F-H(Å)	F-F(Å)	E(x)(a.u.)	J <sub>FHF</sub> (K)	Cl-H(Å)	Cl-Cl(Å)	E(x)(a.u.)	J <sub>ClHCl</sub> (K)	F-H(Å)	H-Cl(Å)	F-Cl(Å)	E(x)(a.u.)	J <sub>FHCl</sub> (K)
-7.5	0.877	1.754	-902.956	-8.36	1.237	2.475	-1623.690	-38.88	0.989	1.189	2.178	-1263.375	-40.32
-5.0	0.955	1.910	-903.035	-7.01	1.338	2.676	-1623.753	-29.33	1.029	1.329	2.357	-1263.372	-41.16
-2.5	1.032	2.065	-903.070	-6.44	1.438	2.877	-1623.782	-25.83	1.019	1.519	2.537	-1263.364	-41.77
0	1.110	2.220	-903.079	-6.32	1.539	3.078	-1623.789	-24.25	1.009	1.709	2.717	-1263.355	-43.73
+2.5	1.188	2.375	-903.073	-6.52	1.640	3.279	-1623.784	-23.71	0.998	1.898	2.897	-1263.346	-47.78
+5.0	1.115 <sup>*</sup>	2.530	-903.058	-6.68	1.490 <sup>*</sup>	3.480	-1623.772	-24.91	0.988	2.088	3.077	-1263.337	-55.29
+7.5	1.043 <sup>*</sup>	2.685	-903.043	-6.61	1.441 <sup>*</sup>	3.681	-1623.760	-28.82	0.978	2.278	3.257	-1263.328	-68.79

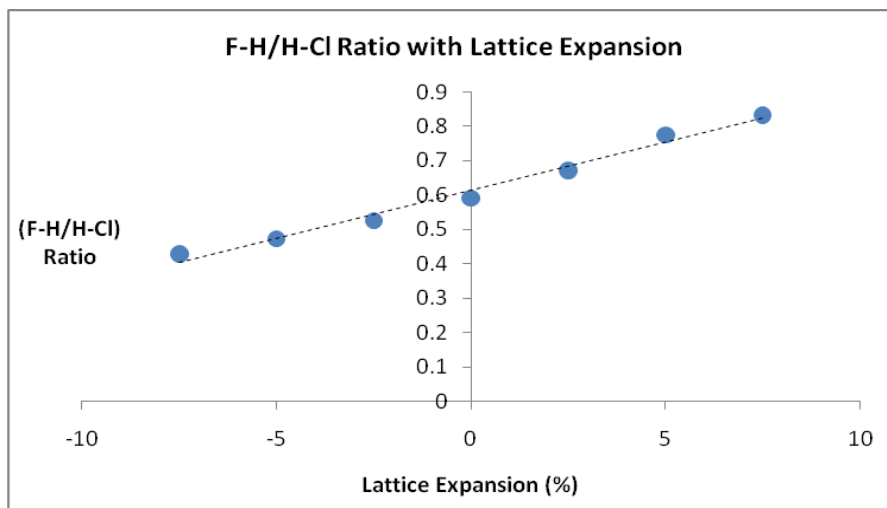


**Figure 4-9**  $\text{FHCl}^-$  ligand; F–H / H–Cl Ratio with lattice expansion

Having established the minimum energy points in each profile, and hence the preferred H atom location, it is now possible to determine the effect of proton position and HB length on magnetic coupling.

Like the energy profiles for the FHF and ClHCl structures, the coupling profiles with respect to the proton position are also symmetric. In the FHF case, the coupling maximum occurs when the proton is positioned in the centre of the HB. The further from the centre of the HB the proton is positioned, the lower the  $J$  value, again fitting with the idea that the coupling is only as strong as the weakest overlap. Therefore in the SWHB potentials the lowest energy proton position corresponds to the position yielding the highest  $J$ , while in the DWHB potentials, the lowest energy positions at either side of the bond midpoint yield  $J$  values significantly lower than those obtained for the proton positioned at the centre of the HB, a significantly higher energy state, again fitting with the ‘weakest link’ model.

Interestingly, the overall lowest lying potential energy profile obtained at equilibrium yields the lowest profile of coupling values. Expansion and contraction of the F-F distance both result in significantly higher couplings. A comparison of  $J$  values obtained at the energy minimum and preferred proton position, in the

expanded and contracted structures, Table 4-23, are of a similar magnitude to those obtained in the optimised structures, only when the F–F distances become significantly short (under 1Å) does the coupling significantly increase. The energy minimum obtained for the optimised structure is the lowest, and although interesting comparisons can be made, all other energy minima occur at states too high to be thermally populated at these ordering temperatures.

In the ClHCl case, the coupling minimum occurs when the proton is positioned in the centre of the HB, and  $J$  increases as the proton is moved further from the centre of the HB. This is the inverse trend to that found in the FHF structures. Therefore in the SWHB potentials the lowest energy corresponds to the lowest  $J$ , and in the DWHB potentials the lowest energy corresponds to  $J$  values higher than those obtained for the proton positioned at the centre of the HB.

The optimised lattice, with lowest potential energy profile, has coupling value profiles of similar magnitudes for those of the expanded lattices in which an increased Cl–Cl distance has been introduced. The coupling values associated with the energy minimum of the optimum and expanded SWHB potential are therefore very similar, whereas the coupling values associated with the energy minimum of the expanded DWHB potential are slightly higher, Table 4-13. The contracted lattices, introducing a decreased Cl–Cl length, have both significantly higher potential energy profiles and  $J$  coupling profiles. It therefore follows that the coupling values associated with the energy minimum of the contracted SWHB potentials are significantly higher. As for the FHF case, the energy minimum obtained for the optimised structure is the lowest and although interesting comparisons can be made, all other energy minima occur at states too high to be thermally populated at the ordering temperatures obtained for the static complexes above in which the proton position was optimised.

In the case of the FHCl bonds, the energy minimum occurs when the proton is positioned closer to the F atom than the Cl atom, the F-H/H-Cl ratio with respect to the FHCl HB length, as shown above, is a linear relationship. If the lattice is expanded, introducing a larger F–Cl distance, the energy minimum, associated  $J$  value, and energy and  $J$  profiles are increased. If however the lattice is

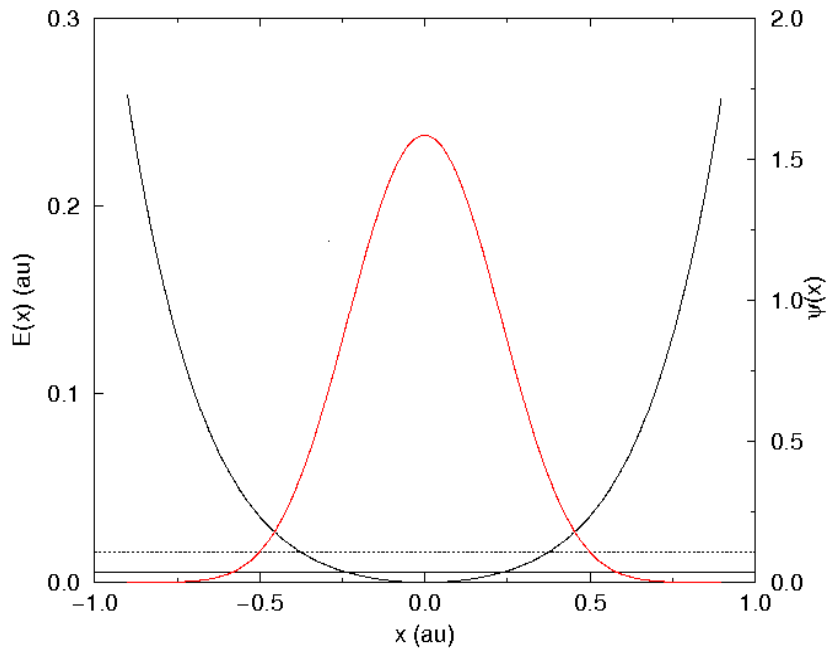
contracted, forcing an artificially short F–Cl distance, the energy minimum, associated  $J$  value, and energy and  $J$  profiles are decreased. It should be noted that this is not likely to be a physically attainable situation under normal conditions. In all cases, the  $J$  coupling value shows a decrease when the H atom position is moved closer to the F atom and an increase when the H atom is moved closer to the Cl atom. This would appear to make sense as in the FHF case,  $J$  coupling decreases when the H atom is moved from the centre and closer to one F atom than the other and in the ClHCl case increased when it is moved from the centre closer to one Cl atom than the other.

## 4.5 Quantum Motion Effects

Having established the dependence of the potential energy and  $J$  values on the proton position, it was possible to use these  $E(x)$  and  $J(x)$  functions in order to solve the Schrodinger equation and obtain expectation values  $\langle J \rangle$  accounting for the change in H position. This is carried out by solving the 1D Schrodinger equation with the predetermined potential  $E(x)$ , and then calculating the expectation value  $\langle J \rangle$  by combining the normalised ground state vibrational wavefunction  $\psi(x)$  with the predetermined function  $J(x)$ .

The 1D potential energy curves obtained by altering the proton position within the fixed HB were fitted using even, sixth-order polynomials in the symmetric FHF and ClHCl structures and additional non-even polynomials in the asymmetric FHCl structure. The resulting functions were used to solve the 1D Schrodinger equation by combining a shooting algorithm with fifth-order numerical integration. The normalised wavefunctions obtained represent the motion of the proton within the HB potential. The wavefunction profiles obtained for the single and double well energy potentials for FHF-containing material is illustrated in Figure 4-10.

(i)



(ii)

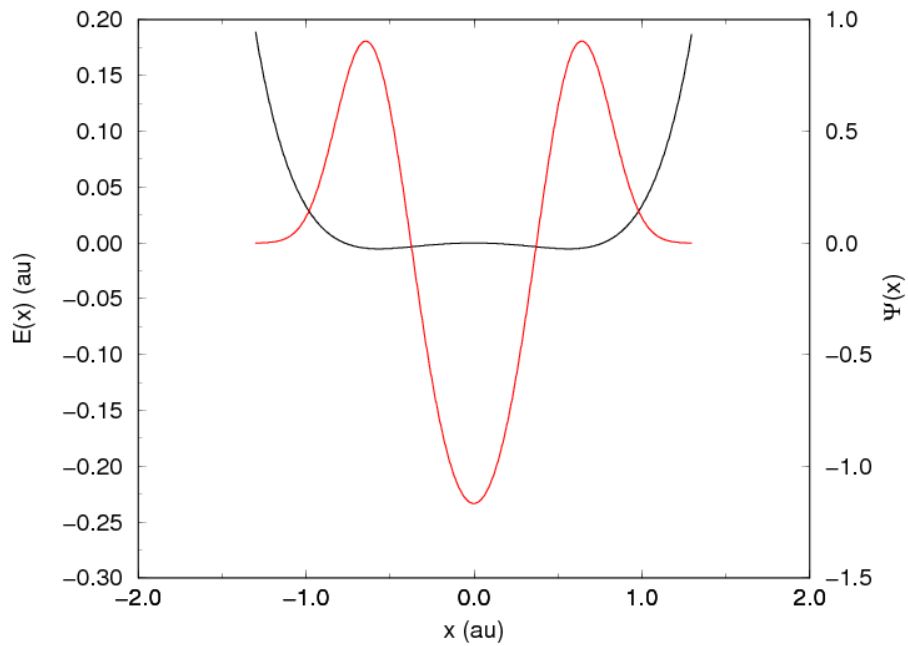


**Figure 4-10 FHF (i) optimised structure with single potential well (ii) formation of double potential well in +2.5% expanded HB structure. Potential (black), wavefunction (red), solid line energy relative to the minimum ( $E_{rel}$ ), dotted line first excited state energy. The first excited state energy magnitude is so large in comparison to calculated critical temperatures that it is assumed to have no effect on low temperature magnetic ordering.**

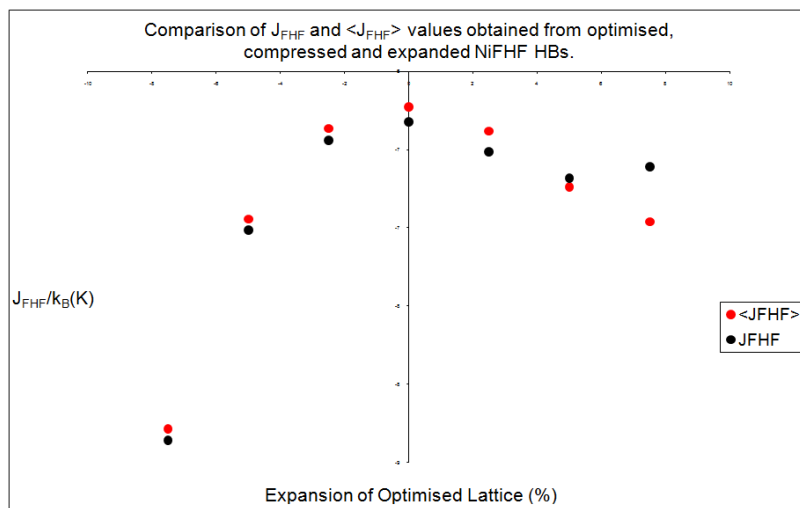
Expectation values  $\langle J \rangle$  for the coupling strengths, naturally incorporating the effects of the proton quantum motion, were then obtained from the normalised ground and first excited state wavefunctions using equation (4-7) in which the  $\pm x_0$  limits were set to lie well within the classically-forbidden region.

$$\langle J \rangle = \int_{-x_0}^{x_0} \psi^2(x) J(x) dx \quad (4-7)$$

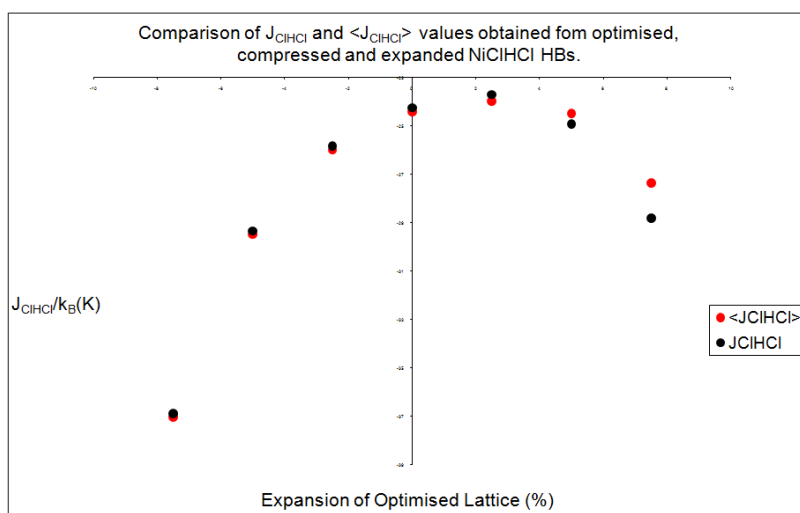
A comparison of the  $\langle J \rangle$  (ground and first excited vibrational states) and static  $J$  values for each of the FHF, ClHCl and FHCl ligands over different HB length is illustrated in Figure 4-11. The  $\langle J \rangle$  expectation values were very similar to the static  $J$  values, except in those wherein the proton moves in a DWHB potential. In the latter case the  $\langle J \rangle$  values fall in a range  $\pm 6\%$  of the  $J$  values not incorporating quantum motion.

The static  $J$  values, which do not account for proton motion, are also presented, along with the  $\langle J \rangle$  values for the ground and first excited states, in which proton motion has been incorporated with the associated eigenstate energies (Table 4-14). The first excited state energy magnitude is so large in comparison to calculated critical temperatures that it is assumed to have no effect on low temperature magnetic ordering.

(i)



(ii)



(iii)

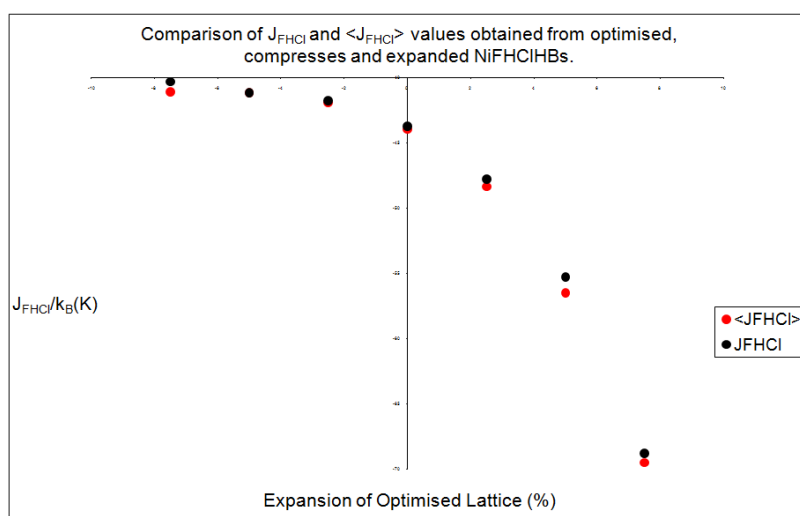


Figure 4-11 (i) FHF (ii) CIHCl (iii) FHCl comparison of  $\langle J \rangle$  (blue) and  $J$  (pink) values from optimised structure (centre) and structures in which HB compressed and expanded.

**Table 4-14 Comparison of static J values which do not incorporate proton motion and <J> values, and associated eigenstate energies relative to the minimum of the respective potential, for the ground and first excited vibrational states, which do incorporate proton motion.**

HB	Vibrational State	-7.5*		-5.0*		-2.5*		0*		2.5*		5*		7.5*	
		E(mHa)	J/k <sub>B</sub> (K)	Energy	J/k <sub>B</sub> (K)										
FHF	Static	-	-8.36	-	-7.01	-	-6.44	-	-6.32	-	-6.52	-	-6.68	-	-6.61
	Ground	13.79	-8.29	10.32	-6.94	7.47	-6.37	5.20	-6.23	3.20	-6.38	1.21	-6.74	4.27	-6.96
	1 <sup>st</sup> Excited	42.03	-8.15	-	-	-	-	16.33	-6.06	-	-	-	-	9.28	-6.73
FHCl	Static	-	-40.32	-	-41.16	-	-41.77	-	-43.73	-	-47.78	-	-55.29	-	-68.79
	Ground	3.4	-41.07	-2.68	-41.15	-11.41	-41.89	-22.43	-43.96	-34.81	-48.36	-47.82	-56.47	-51.88	-69.50
	1 <sup>st</sup> Excited	14.69	-41.43	-	-	-	-	-8.71	-47.09	-	-	-	-	-39.06	-72.84
ClHCl	Static	-	-36.88	-	-29.33	-	-25.83	-	-24.25	-	-23.71	-	-24.91	-	-28.82
	Ground	9.36	-37.02	6.90	-29.48	5.06	-25.99	3.39	-24.41	1.97	-23.97	0.30	-24.49	1.11	-27.37
	1 <sup>st</sup> Excited	28.4	-37.30	-	-	-	-	10.66	-24.73	-	-	-	-	3.57	-29.60

\* Percentage expansion or contraction of lattice

## 4.6 Conclusions and Outlook

The present investigation, in which TMHH structures have been used to study the effects of a number of parameters on the magnetic coupling interactions borne by FHF, ClHCl and FHCl HBs has produced a number of interesting findings:

- (i) Related work in the literature has shown that the  $F_0=35\%$  hybrid functional yields  $J$  coupling values in good agreement with experiment. The estimated  $F_0=35\%$   $J_2$  value of  $-0.062$  obtained from our CuFHF material by averaging of the  $F_0 = 30$  and  $40\%$  values was significantly larger than the values of  $\sim 0.03$  and  $0.0190$  quoted for the experimental<sup>82</sup> and theoretical<sup>83</sup>  $[\text{Cu}^{\text{II}}(\text{HF}_2)(\text{pyz})_2]\text{BF}_4$  (pyz = pyrazine) coordination polymers respectively. This could, however, be due to the significantly shorter Cu–Cu, Cu–F, F–H distances in the present material;
- (ii) In cases of the very weak couplings along the  $z$ -axis ( $J_2$ ) in the Cu material, the  $nn$  Ising Hamiltonian incorporating only  $J_1$  and  $J_2$  couplings did not produce consistent  $J_2$  values when comparing couplings obtained separately from two sets of magnetic energy differences. Interestingly, the average  $J_2$  values computed over the two inconsistent results was identical to the  $J_2$  values calculated using an extended Ising Hamiltonian in which further  $z$ -axis  $nnn$  couplings ( $J_4$ ) were included. It was clear from this that in cases of weak out-of-plane coupling in JT-distorted structures, the additional  $nnn$  interactions can be as significant as the weak  $nn$  couplings. However, it is clear that the magnetic interactions in this antiferromagnetic material are highly anisotropic: strong in-plane order (associated with the singly occupied JT split  $x^2-y^2$  orbitals) being anticipated on the basis of the large  $J_1$  couplings, along with a much weaker tendency to form a long-range 3D ordered state at low temperature driven by the small  $J_2$  couplings;
- (iii) A number of full atom and geometry optimisation calculations were carried in order to obtain the static ground state structures for materials in which the identity of the TM and X-H-X' ligand, and the  $F_0$  value were altered. This revealed that the magnetic coupling increases with decreased  $F_0$ , and is

affected by both the identity of the interacting TM ions and HB halide linkers, the coupling constants emerging in the order Ni >> V > Cu and ClHCl > FHCl > FHF.

- (iv) The effect of altering the HB lengths, introduced by expanding and contracting the lattice, and altering the proton position along the one dimensional HB was also examined.
- (v) The HB potential energy and J coupling profiles were then used to obtain quantum mechanical expectation values  $\langle J \rangle$  which incorporated the proton motion.

Many of the weak intermolecular HBs in the literature are  $\text{OHO}^{3-}$  ligands. Due to the 3- charge on the OHO ligand, studies using the present structures are not possible, for the reason that a charge neutral cell cannot be easily created. Similar investigations using cluster models are therefore of future interest.

## 5 Metal Complexes with Bromanilic and Chloranilic Acid

As illustrated in previous chapters, metal identity can affect a wide variety of properties for a given material. The materials described so far have demonstrated this effect on magnetic, electronic and vibrational properties. This chapter reports the results of investigations exploring the effect of metal identities on the packing arrangements obtained for a range of closely related materials synthesised using ligands with hydrogen bonding capabilities.

Our aim was therefore to expand the series of group 1 and group 2 metals and anilic acid containing complexes and observe and analyse the different types of structures and packing arrangements obtained under a variety of conditions. By focusing on group 1 complexes we hoped to see a variation in the protonation state of the ligand, and a variation in the metal to ligand ratios in our complexes, and consequently different types of associated packing. Although metal identity has been shown to play a role in the tuning of magnetic and electronic properties of related complexes, in this work we wished to examine the effects of this on the structural properties only.

A systematic investigation was carried out in which two starting materials, one a metal containing salt and the other either the BA or CA ligand were combined with the aim of generating potentially interesting three-dimensional metal-organic frameworks. Compounds were synthesised by the solvent evaporation method and the effects of varying the metal identity were then explored.

### 5.1 Systematic Studies of Metal Complexes

Previously reported systematic investigations have also incorporated different metals<sup>89,125,128,145</sup>, halogens<sup>127,145</sup> and solvent molecules<sup>113,135</sup> into the structure. Due to the associated ionic radii the metal identity has been shown to influence chain type, hydrogen bond distances<sup>128</sup> and coordination sphere<sup>145</sup> in a number of isostructural complexes suggesting that it may be possible to delicately tune these

properties.<sup>128</sup> Different metals introduced under the same conditions have also produced different structures; in one example a Cu-containing complex incorporated an organic cation into a cage as a dimer whereas the related Co-complex had the organic cations stacked, forming a segregated columnar structure between the  $[\text{MCA}_2(\text{H}_2\text{O})_2]_2$  layers.<sup>125</sup>

In the isostructural CA and BA complexes,<sup>145</sup> the presence of the larger Br in the BA complex tends to restrict the freedom of nearby water molecules. In a hydrated Y complex<sup>140</sup> the author states the CA and BA complexes were in principle isostructural with a minor difference concerning one water molecule not bound to  $\text{Y}^{3+}$ . The CA complex had slightly higher water content than the Y-BA complex although the other structural features were rather similar pointing to negligible structural influences of the larger Br substituent in comparison with Cl.

Solvents have been shown to act both in intercalation compounds, where removal whilst retaining the metal ligand framework is possible,<sup>112</sup> and as an incorporated part of the structure in which the solvent molecule plays a role in holding it together.<sup>113</sup> For such solvent containing complexes many authors in the literature have observed high thermal parameters for the solvent atom which has been interpreted as disorder<sup>136,138,145</sup> and have in some cases excluded them from the structures completely.<sup>136,138</sup> In many cases attempts to either grind<sup>112</sup> or dehydrate<sup>140,145</sup> has resulted in the decomposition of the compound or a destruction of the crystallinity.

Although secondary interactions in a structure are weak in comparison to more significant interactions such as HBs, a collective stabilization of these forces may still be susceptible to external perturbations such as a change in temperature of the same reaction mixture or the participation of the solvent during crystallisation.

188-189

The pH of a solution has in general been shown to influence the outcome of crystallisations, particularly in metal-organic architectures.<sup>190</sup> The pH can affect the presence of specific ligand forms which are dependent on the degree of protonation and the generation of a hydroxo ligand.<sup>120</sup> An analysis of a number of

salts and co-crystals of CA with organic bases, by Molcanov and Kojic-Prodi <sup>191</sup> has suggested that it may be possible to predict which level of protonation is present by the colour of a solution before crystallisation (Figure 5-1). It has been shown that altering pH can also allow the formation of new ligand forms different from the originals, and the ability to control reaction kinetics. <sup>120</sup>

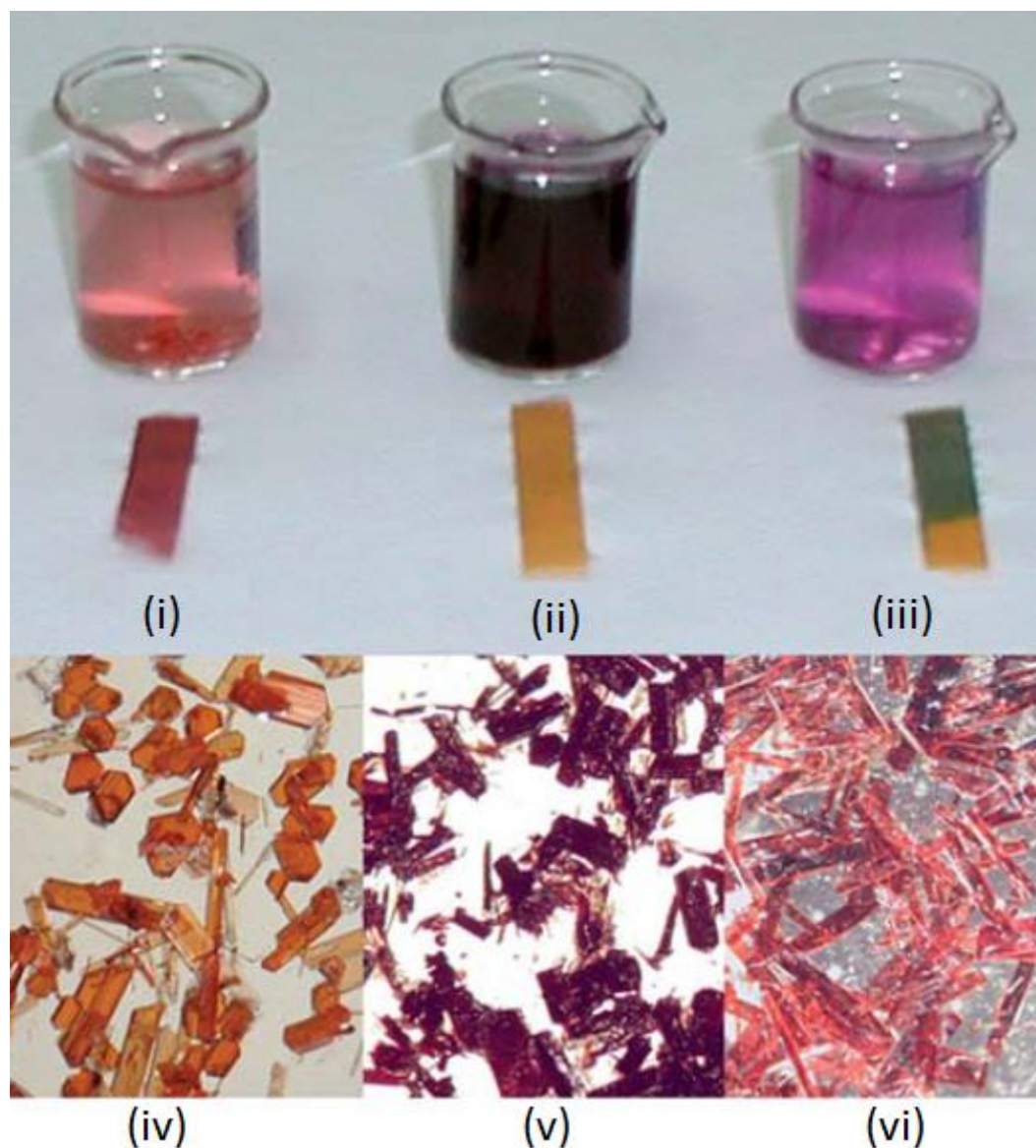


Figure 5-1 Samples of solutions containing: (a)  $\text{H}_2\text{CA}$  (neutral CA, very low pH), (b)  $\text{HCA}^-$  (mono anions, neutral pH) and (c)  $\text{CA}^{2-}$  (dianion, high pH). Crystals of CA dihydrate are red (d), crystals of  $\text{HCA}^-$  salts are dark violet and opaque (e), and crystals of  $\text{CA}^{2-}$  salts are violet and transparent (f). <sup>191</sup>

### 5.1.1 Classification of the Crystal Packing

In order to analyse a number of related metal organic complexes it is necessary to measure the strength of the various interactions that may be observed. Section 1.2.1 has given a detailed account of the classification of a HB interaction based on the HB distances and HB angles.

All other non covalent interactions present in the complexes within this work will all be classified with respect to the sum of the van der Waals radii of two atoms, Table 5-1.

**Table 5-1 Van der Waals radii of Li, Na and K metal cations and partially negatively charged O, N, Cl and Br anions. No Van der Waals radii quoted for larger Rb, Cs and Ca metals.** <sup>193</sup>

Metal cation	Van der Waals radius (Å)	Partial anions	Van der Waals radius (Å)
Li	1.82	O	1.52
Na	2.27	N	1.55
K	2.75	Cl	1.75
		Br	1.85

If two atoms are close enough for a potential interaction to arise, the distance between the two atoms can be measured and compared to the sum of the van der Waals radii of the two atoms. If the van der Waals radii of two atoms overlap, a coordination interaction is said to occur, the strength of which will depend on the distance. As it is the sum of all these interactions that give rise to the overall packing arrangement of the atoms within a complex, some interactions may dominate over others.

In order to describe and compare the structural packing of complexes a set of units have been predefined (Figure 5-2) and arranged into groups (Table 5-2), in order to aid comparison of the different types of coordination and motifs regularly observed in the complexes obtained, and also to show how those units are related in order to obtain the whole structure.

The same units are present in complexes containing the different ligand forms and group E contains a distinct HB motif that was regularly observed within the complexes. The motif consists of a 7 atom ring which includes the halide carbonyl, the carbonyl oxygen or the carbonyl hydroxyl unit, a coordinated metal which is also coordinated to another O atom and the H atom in the HB (group E, Figure 5-2). Depending on the level of deprotonation of the ligand the XA hydroxyl group acts as either the proton acceptor or proton donor to and from a nearby oxygen atom or hydroxyl group of another ligand.

**Table 5-2. Classification of the different coordination motifs.**

<i>Type of coordination</i>	<i>M to XA ligand</i>		<i>XA ligand to M</i>		<i>M to M</i>	<i>XA ligand to M to external O</i>
	Halide-carbonyl	Carbonyl-carbonyl	Mono-dentate	Bi-dentate	Coordinating atoms	HB
Type of unit	Halide-carbonyl	Carbonyl-carbonyl	Mono-dentate	Bi-dentate	Coordinating atoms	HB
Group	Group A	Group B	Group C	A2 B2	Group D	Group E

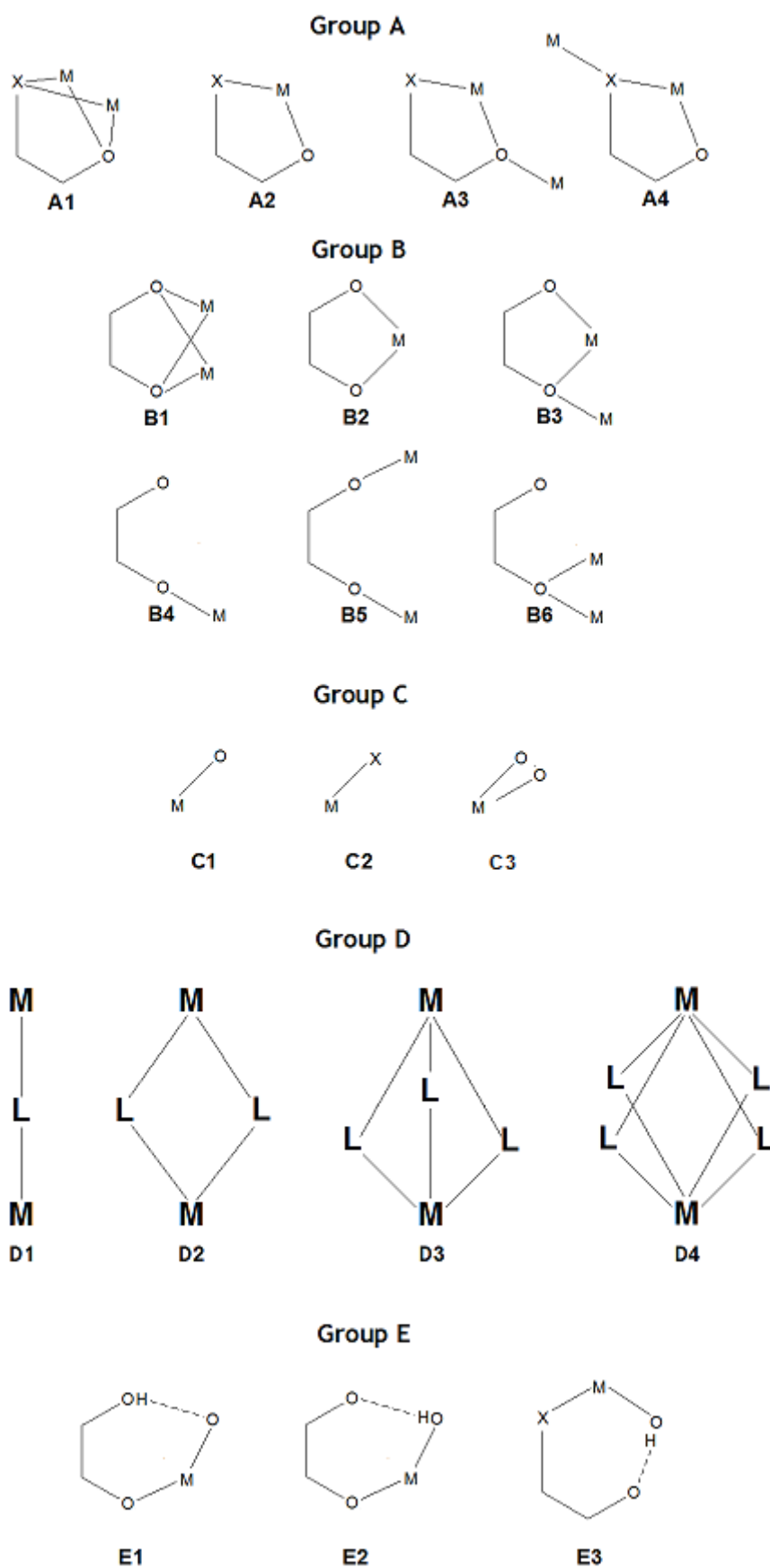


Figure 5-2 Units depicting: M to XA ligand coordination; XA ligand to M coordination; M to M coordinating atoms, and HB motifs, see Table 5-2.

The units in group A and group B can be used alone or combined in order to describe the metal coordination of the whole ligand, as illustrated by the examples and notation in Figure 5-3. In cases of very complex packing, one ligand may require as many as 4 units from group A and 2 units from group B to describe its coordination.

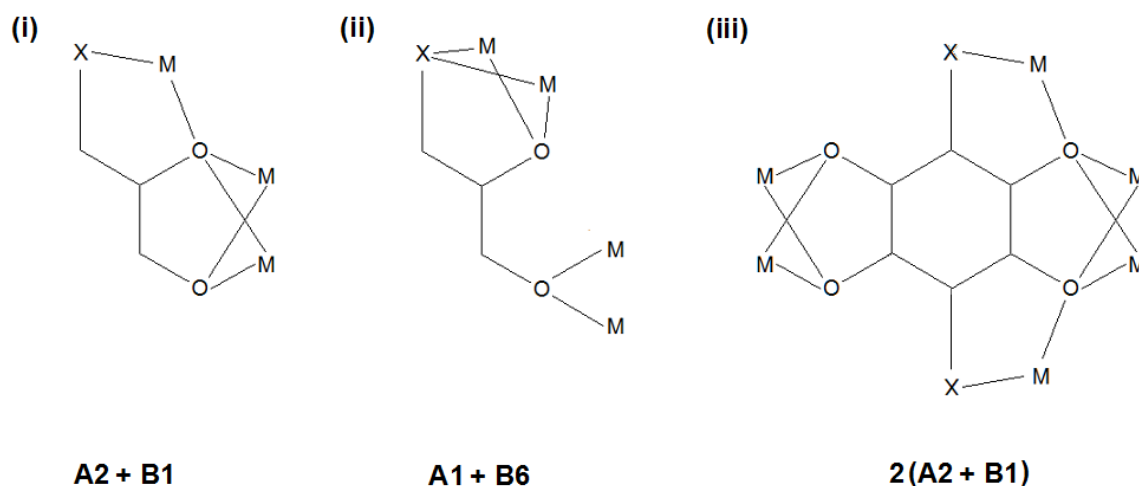
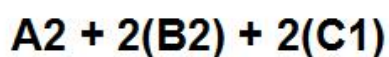
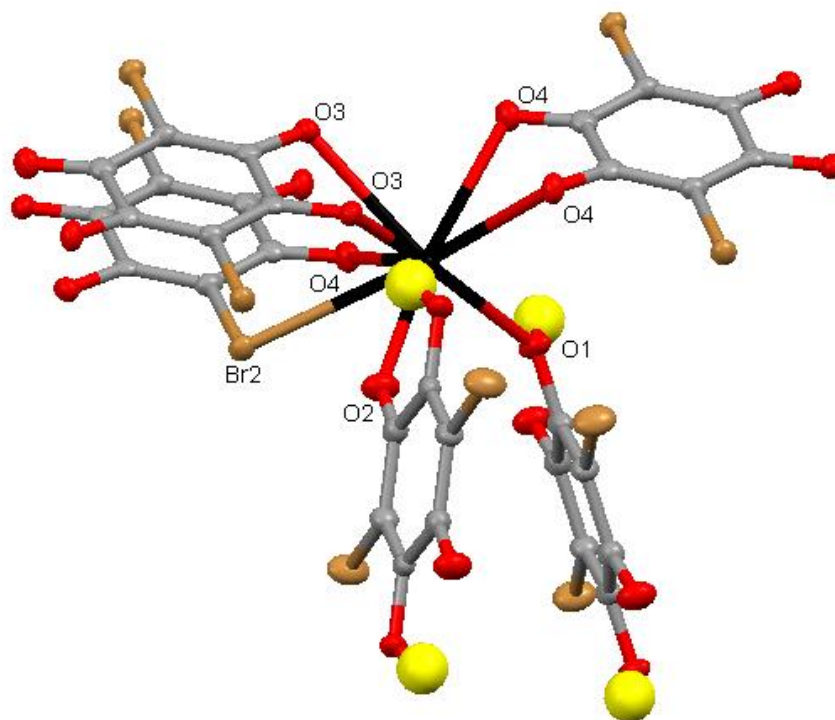


Figure 5-3 Examples and notation of combined XA ligand to M coordinating units.

In the complexes examined, the ligands tend to coordinate to an individual metal in a mono, group C, or bidentate, A2 or B2, fashion. The same principle can therefore be applied to the way in which the surrounding ligand(s) coordinate to an individual metal, as shown in Figure 5-4.



**Figure 5-4 Example and notation for BA ligands coordinating to M. There are 5 coordinating BA ligands in total. One of these coordinates in the bidentate halide carbonyl A2 form, two in the bidentate carbonyl carbonyl B2 form and two in the monodentate C1 form.**

The number of atoms coordinating the incorporated metal varies between 4 and 10 in the complexes examined in this work. Each individual metal is usually coordinated to multiple ligands and it is common to observe MXA chains within the structures that can also be broken down into the units previously defined (Figure 5-5).

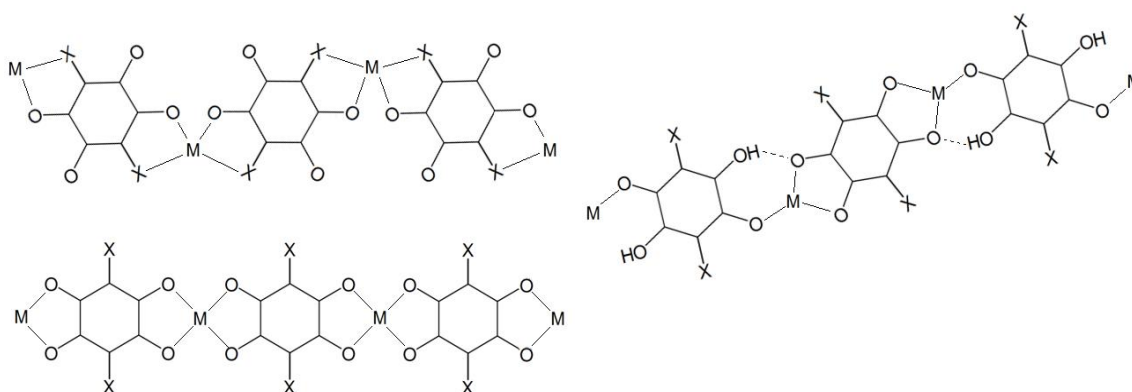


**Figure 5-5** XA ligand and M ions form MXA chains linked by (i) 2(A2) units (ii) 2(B2) units (iii) B2 and E1 units

These chains may in some cases, using additional units between the chains, be built up into higher dimensions such as planes and sheets by which to describe the three-dimensional structure.

Most of the structures studied in this work possess short  $M \cdots M$  interactions. These interactions tend to form characteristic metal clusters, existing by themselves or making up extended clusters in the form of chains or planes of chains connected by the halide and oxygen atoms of the XA ligands or the oxygen atoms of surrounding water molecules. In addition to the close proximity of the two interacting metals, compared to the sum of the van der Waals radii, the metals were usually connected in one or more of the forms illustrated in group D. Examples of the metal clusters or multiple alternating units that make a periodic chain are illustrated in Figure 5-6. There are also cases in which one of the coordinating O atoms has an H atom attached, which gives the addition of a HB along the chain.

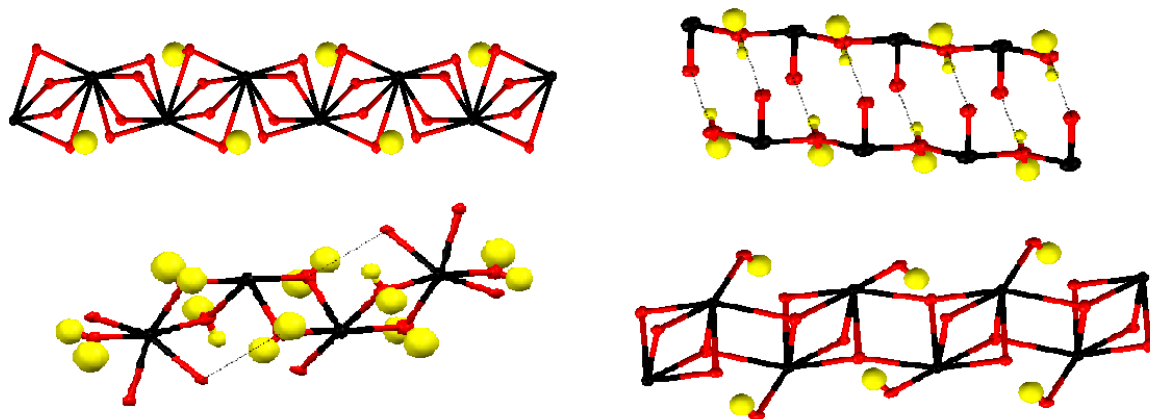


Figure 5-6 (i) M...M chain composed of alternating D4 units (ii) two M...M chains composed of D1 units HB together (iii) four M cluster composed of alternating D2 units (iv) M...M chain composed of alternating D2 and D4 units.

These recurrent units, which can be combined in a number of ways, will allow comparison of multiple aspects of the structures observed in this work.

### 5.1.2 CSD survey of Metal -Metal and Halogen - Halogen Interactions

There is very little in the literature in terms of comparing M...M and X...X interactions within MOFs. Therefore in order to compare the M...M distances obtained within this investigation with those in other comparable complexes the CSD<sup>97</sup> was searched for structures containing non bonded M...M distances (M = Li, Na, K, Rb, Cs and Ca) within the sum of the van der Waals radii. The search was restricted to non disordered complexes with 3D coordinates determined and R factors  $\leq 0.05$ . The results were viewed using Vista<sup>110</sup> and Mercury<sup>192</sup> in order to obtain the mean, median and range in M...M distances. Any anomalous structures with implausible short contacts or structures corresponding to very different metal frameworks were systematically removed from the results. The results are presented in Table 5-3.

**Table 5-3 M...M and X...X Short Contact Distances found in the CSD <sup>97</sup>**

		Range (Å)	Mean (Å)	Median (Å)	No of Refcodes	No of fragments
M	Li	2.224-3.632	3.008	3.019	146	274
	Na	2.987-4.539	3.695	3.621	812	1703
	K	3.330-5.499	4.434	4.359	970	3052
	Rb	3.413-3.996	3.870	3.896	29	43
	Cs	3.821-3.997	3.946	3.962	11	14
	Ca	3.483-3.997	3.868	3.918	75	98
X	Cl	3.028-3.500	3.387	3.408	819	1052
	Br	3.267-3.700	3.570	3.585	154	190

A comparison of X...X close contacts (X=Cl or Br) was also obtained in a similar manner. In order to obtain the most relevant interactions, the search was restricted to X...X contacts for structures in which at least one metal was also present and each X atom was bonded to at least one carbon atom. A consequence of this is that a significant number of short X...X distances obtained were due to the interactions between small coordinated or intercalated organic molecules within the metal complexes.

## 5.2 Potassium-containing Bromanilic Acid Complexes

A total of five crystal forms were identified for the syntheses using potassium salts with bromanilic acid (BA) as the ligand, giving the most diverse set of packing arrangements; this family is therefore the most studied in this work. The complexes obtained include both anhydrous and hydrated forms, and both 1:1 and 2:1 potassium to BA ratios.

### 5.2.1 Anhydrous Tautomeric Polymorphs

In recently coined nomenclature, two definitions tautomer and polymorph have been combined in the single term 'tautomeric polymorph' to define the existence of structural isomers which differ only in the position of a hydrogen atom or proton. To date this term has been used only to refer to the presence of different tautomeric equilibria in the same crystal structure <sup>194</sup> and not, as in this case, different tautomeric forms in different crystal structures.

The two anhydrous potassium - bromanilic acid (KBA) complexes synthesised were found to crystallise in a 1:1 K to BA ratio giving the tautomeric polymorphs:



Dark red crystals of both forms were obtained, simultaneously, as described in Table 5-4. In addition to single crystals large multiple crystals of these two forms grew together, which could be cut apart into diffracting segments. Crystallographic data for the two complexes are provided in Table 5-5.

### 5.2.1.1 Form 1 Structure Determination and Analysis

The asymmetric unit contains one  $\text{HBA}^-$  molecule, and one  $\text{K}^+$  ion (Figure 5-7).

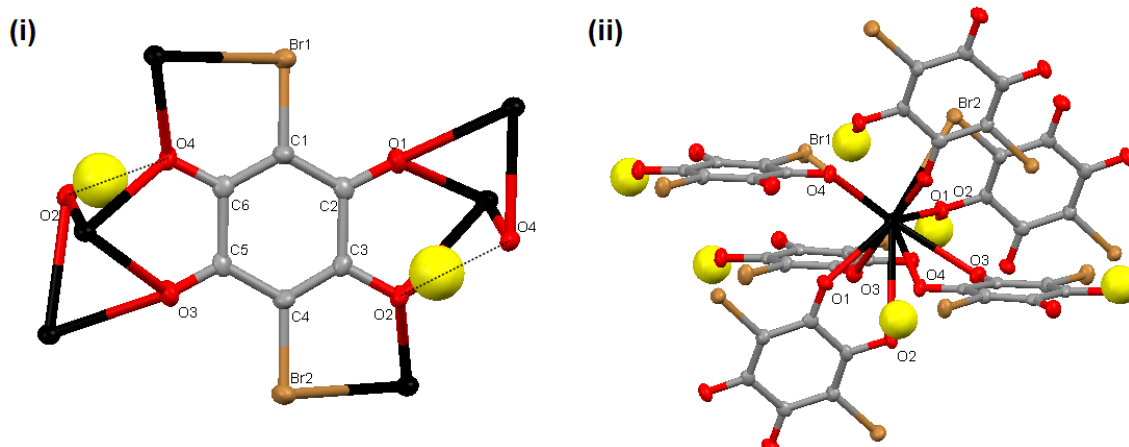


Figure 5-7  $\text{K}^+(\text{C}_6\text{O}_4\text{Br}_2\text{H})^-$  environment of (i) half protonated  $\text{HBA}^-$  molecule (ii)  $\text{K}^+$  ion

Although the  $\text{HBA}^-$  molecule has no inversion centre it can be viewed as two halves that have the same two metal coordinating units giving overall two distinct bidentate (A2 +B3 in the definition provided earlier) coordinations. The carboxylic acid unit possesses the E1 HB motif and the deprotonated carboxylate unit the E2 HB motif.

Each  $\text{K}^+$  ion is coordinated to 6  $\text{HBA}^-$  molecules; two monodentate C1, two bidentate B2 and two bidentate A2. Each  $\text{K}^+$  ion is hence coordinated to 10 other atoms in total: eight oxygen atoms, the bond lengths of which range from

2.6825(11) - 3.3611(12) Å, and two bromine atoms, with bond lengths 3.4450(4) Å and 3.5780(4) Å.

Half of the coordinated  $\text{HBA}^-$  molecules are orientated in one direction and half in another. These two groups of three ligands are from two identical sets of planes, each of which pass through two diagonals of the unit cell, and intersect in the middle at an angle of  $68.99^\circ$  (Figure 5-8). The angle at which the six-membered ring of the  $\text{HBA}^-$  molecule cuts these intersecting planes can be seen in Figure 5-9.

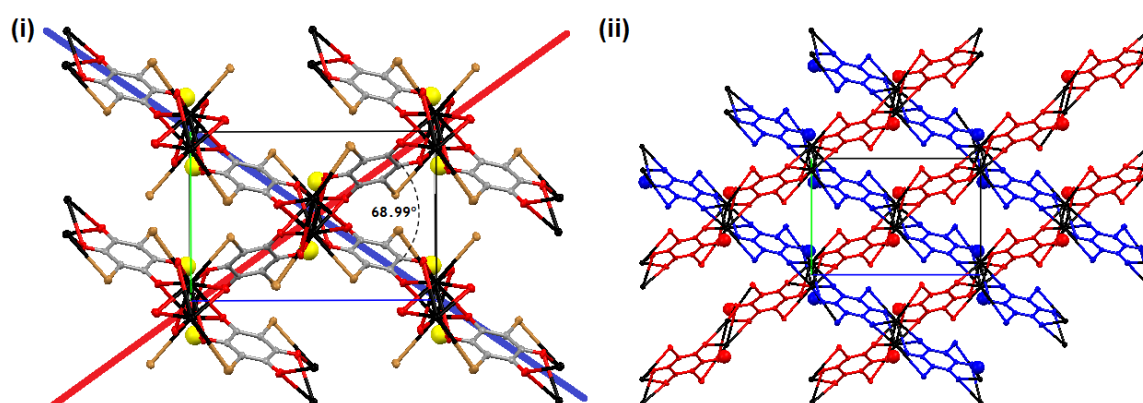


Figure 5-8  $\text{K}^+(\text{C}_6\text{O}_4\text{Br}_2\text{H})^-$ . Intersection of the two identical sets of planes along the diagonals of the unit cell (red and blue), Viewed along the  $a$ -axis.

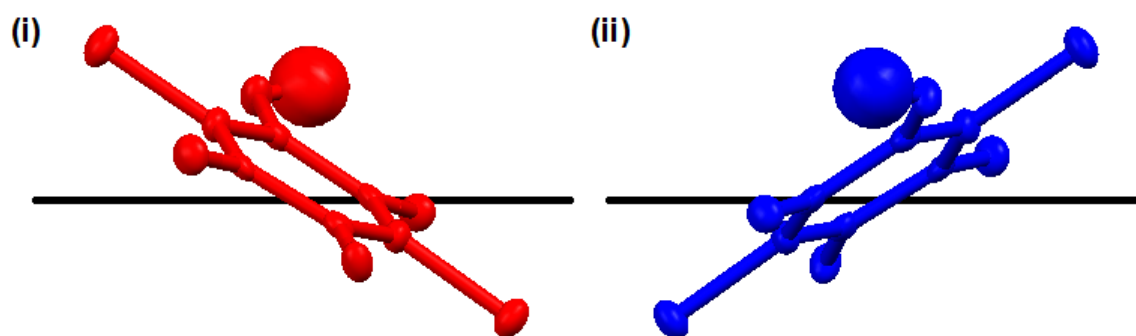
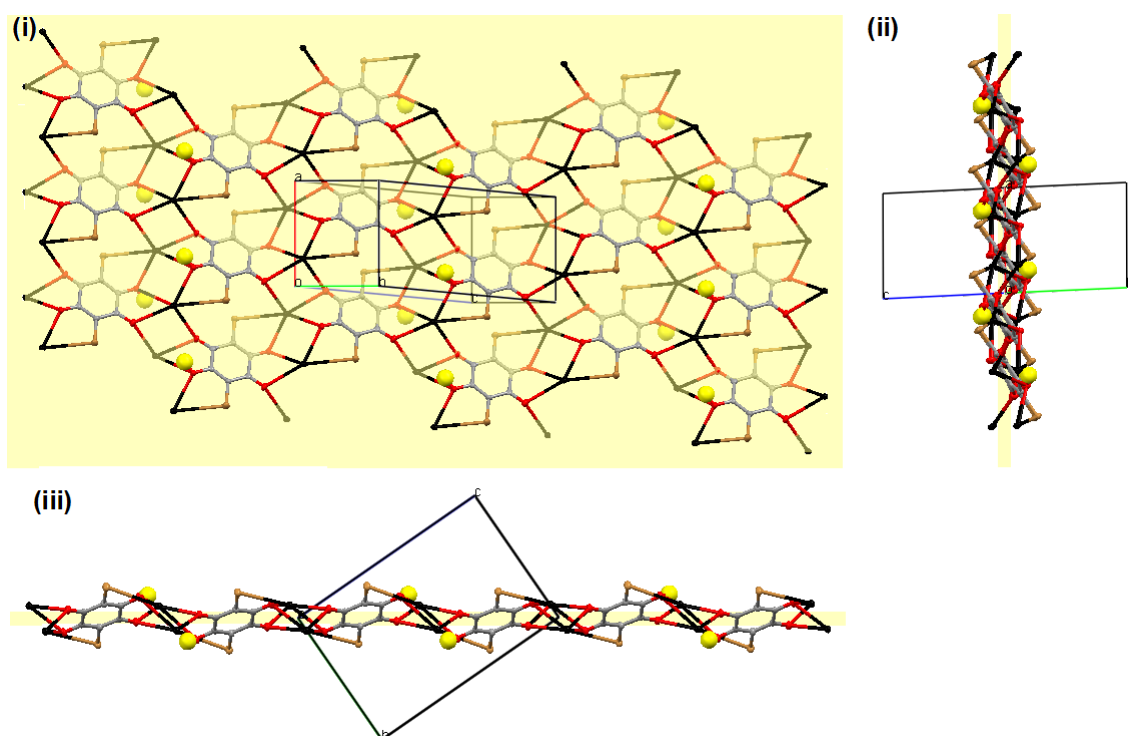


Figure 5-9 Angle at which the carbon ring of the  $\text{HBA}^-$  molecule cuts the plane along the diagonal of the unit cell.

At each point of intersection there is also a cluster of  $\text{K}^+$  ions. A perpendicular view of the intersecting planes shows that these  $\text{K}^+$  ion clusters are actually  $\text{K}^+$  ion chains that run along the  $a$ -axis, Figure 5-10, and are connected in the  $b$  and  $c$

directions by linking  $\text{HBA}^-$  molecules. There are two independent  $\text{K}^+$  chains within each plane, one enclosed by the hydroxyl groups and one by the deprotonated  $\text{O}^-$ .



**Figure 5-10**  $\text{K}^+(\text{C}_6\text{O}_4\text{Br}_2\text{H})^-$  viewed (i) perpendicular to and (ii) along the two identical planes. The two planes intersect along the  $\text{K}^+$  chains; so that on one  $\text{HBA}^-$  plane the  $\text{K}^+$  chains are enclosed by the hydroxyl groups and on the other the  $\text{O}^-$  atoms.

Along the  $\text{K}^+$  chain, at the point at which the two planes intersect one plane provides the surrounding hydroxyl groups and the other the surrounding  $\text{O}^-$  ions. A closer inspection reveals that the  $\text{K}^+$  chains are composed of two short K-K interactions of lengths  $3.7496(5) \text{ \AA}$  and  $3.9963(5) \text{ \AA}$ , compared to the sum of the van der Waals radii of  $5.5 \text{ \AA}$ .

Four linking oxygen atoms that make the overall shape of a D4 diamond unit also strengthen each  $\text{K}\cdots\text{K}$  interaction Figure 5-11. The two alternating D4 units make up the  $\text{K}^+$  chain. Due to the presence of a hydrogen atom on one of the linking oxygen atoms, one of the diamonds is slightly distorted and forms a HB with one of the oxygen atoms on the other diamond.

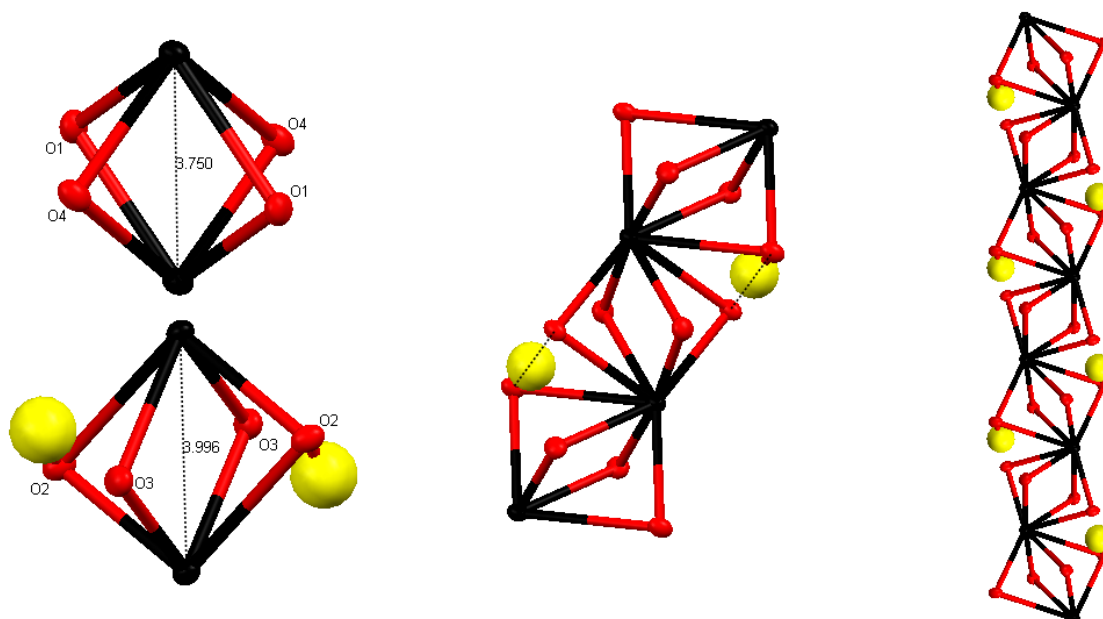


**Figure 5-11 K...K chains showing the oxygen coordination and hydrogen bonding.**

Figure 5-12 shows that this HB links the hydroxyl group of a  $\text{HBA}^-$  molecule in one plane to the  $\text{O}^-$  atom of a  $\text{HBA}^-$  molecule on the other plane. Three of these HB interactions can be observed within the six  $\text{HBA}^-$  molecules surrounding each  $\text{K}^+$  ion.

In addition to HBs, intermolecular oxygen–oxygen interactions are also present along the chain at these points of intersection, the parameters of which can be found in Table 5-4. It is not clear whether these interactions contribute significantly to stabilising the overall packing arrangement of the structure or whether the oxygen atoms are forced into close contact by the stronger interactions present, which can also be observed in Table 5-4. The result is a three-dimensional porous structure with pores that run along the  $a$ -axis, 4 Å in length along the  $b$ -axis and 6 Å in length along the  $c$ -axis.

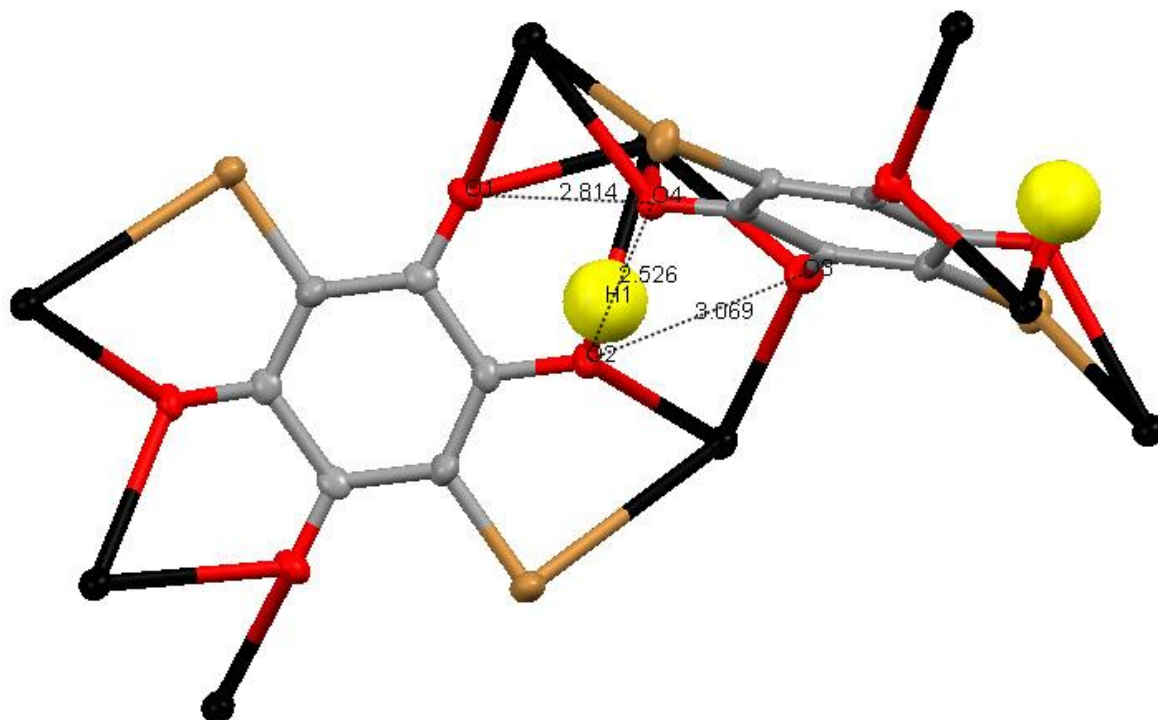


Figure 5-12  $K^+(C_6O_4Br_2H)^-$  HB and oxygen-oxygen interactions

### 5.2.1.2 Form II Structure Determination and Analysis

The asymmetric unit contains one half  $H_2BA$  molecule, one half  $BA^{2-}$  molecule and one  $K^+$  ion environment (Figure 5-13).

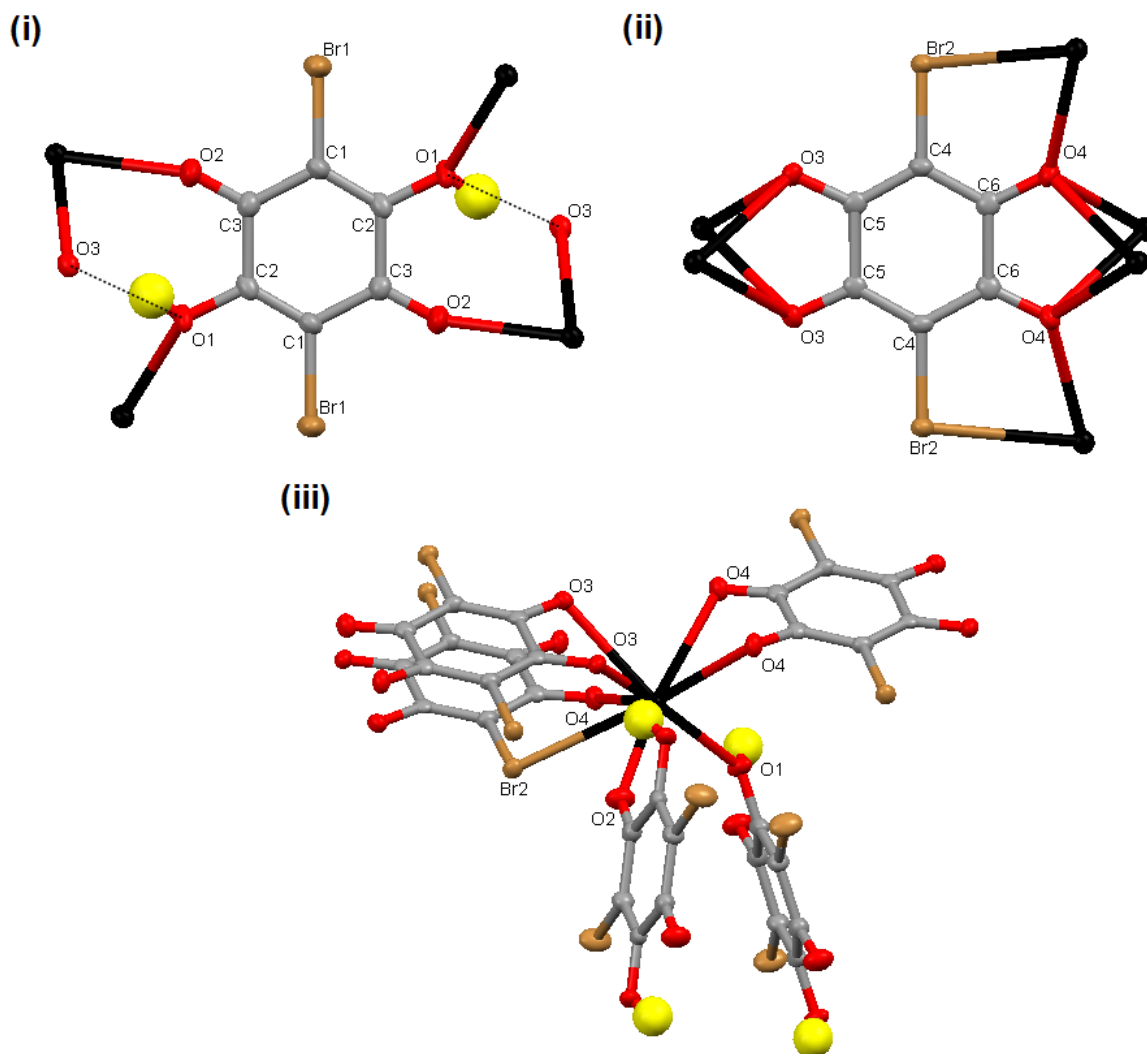


Figure 5-13  $2K^+(C_6O_4Br_2H_2)(C_6O_4Br_2)^{2-}$  environment of (i) fully deprotonated  $BA^{2-}$  molecule (ii) fully protonated  $H_2BA$  molecule (iii)  $K^+$  ion

The  $H_2BA$  has an inversion centre and therefore has 2(B5) metal coordination units, in addition to 2(E1) HB motifs. The  $BA^{2-}$  molecule has a mirror plane that passes through the two carbonyl units. This is unusual in the sense that it has not been seen in any of the other complexes in our investigation or the literature. It is then not surprising that this particular  $BA^{2-}$  molecule has an unusual 2(A2 + B1) metal coordination.

Each  $K^+$  ion is coordinated to only 2  $H_2BA$  molecules; both monodentate C1, one by the hydroxyl oxygen and the other the carbonyl oxygen, and 3  $BA^{2-}$  molecules; one bidentate A2 and two bidentate B2. Each  $K^+$  ion is therefore coordinated to 8 other

atoms; seven oxygen atoms, the metal-oxygen bond lengths of which range from 2.7277(18) - 2.8788(16) Å and one bromine atom with bond length 3.3169(6) Å.

In a similar fashion to form I, two identical sets of planes, containing the H<sub>2</sub>BA molecules, each pass through two diagonals of the unit cell, and intersect in the middle, this time however at a lower angle of 40.59°, Figure 5-14. This leaves room for an additional plane, containing the BA<sup>2-</sup> molecules, which also intersects these two identical H<sub>2</sub>BA planes. Again similar to form 1, the K<sup>+</sup> ions are clustered at the point at which the three planes intersect.

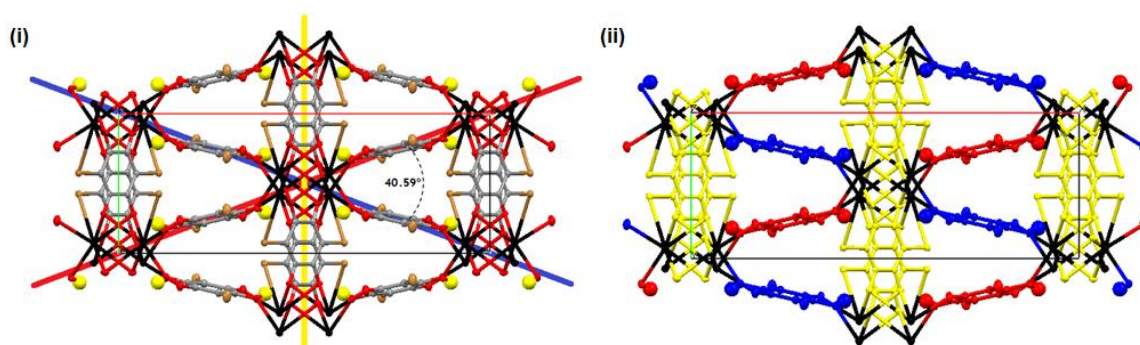


**Figure 5-14**  $2\text{K}^+(\text{C}_6\text{O}_4\text{Br}_2\text{H}_2)(\text{C}_6\text{O}_4\text{Br}_2)^{2-}$  Intersection of two identical sets of H<sub>2</sub>BA planes along the diagonals of the unit cell, (red and blue), plus additional intersecting BA<sup>2-</sup> plane (yellow). Viewed along c-axis.

The carbon rings of each BA molecule cut their associated planes in an interesting manner. The symmetry element associated with each molecule lies on the plane; the inversion centre in case of the H<sub>2</sub>BA molecule, and the mirror plane in case of the BA<sup>2-</sup> molecule so that in each case half of the molecule lies on one side of the intersecting plane and the other half on the other side of the intersecting plane. Figure 5-15 illustrates each intersecting plane as viewed along the *b*-axis.

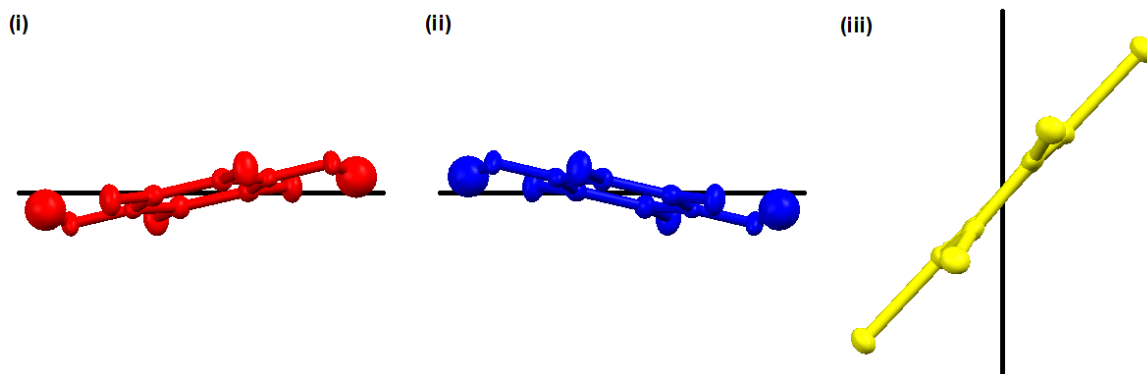


Figure 5-15  $2K^+(C_6O_4Br_2H_2)(C_6O_4Br_2)^{2-}$  The carbon rings of the (i)  $H_2BA$  and (ii) identical intersecting  $H_2BA$  planes, (iii) intersecting  $BA^{2-}$  plane, cut the planes along the symmetry element.

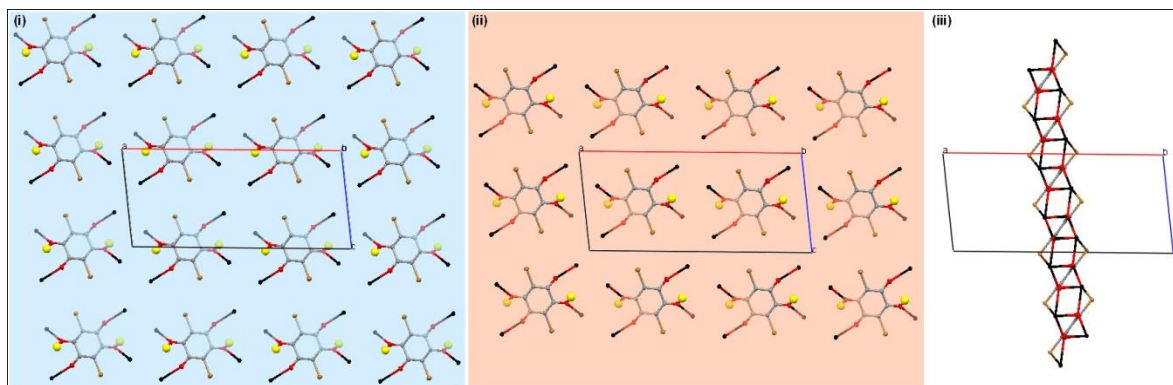


Figure 5-16  $2K^+(C_6O_4Br_2H_2)(C_6O_4Br_2)^{2-}$  Intersecting (i) blue, (ii) red and (iii) yellow planes as viewed along the b-axis.

Independently the two identical intersecting planes consist of isolated  $H_2BA$  molecules and their coordinating  $K^+$  ions. The additional intersecting plane of  $BA^{2-}$  molecules shows how these same  $K^+$  ions are also coordinated to the  $BA^{2-}$  molecules.

Unlike the molecules in the  $H_2BA$  planes, a perpendicular view of the intersecting  $BA^{2-}$  plane indicates that the  $BA^{2-}$  molecules interact with surrounding  $BA^{2-}$  molecules via  $K^+$  interactions, Figure 5-17.

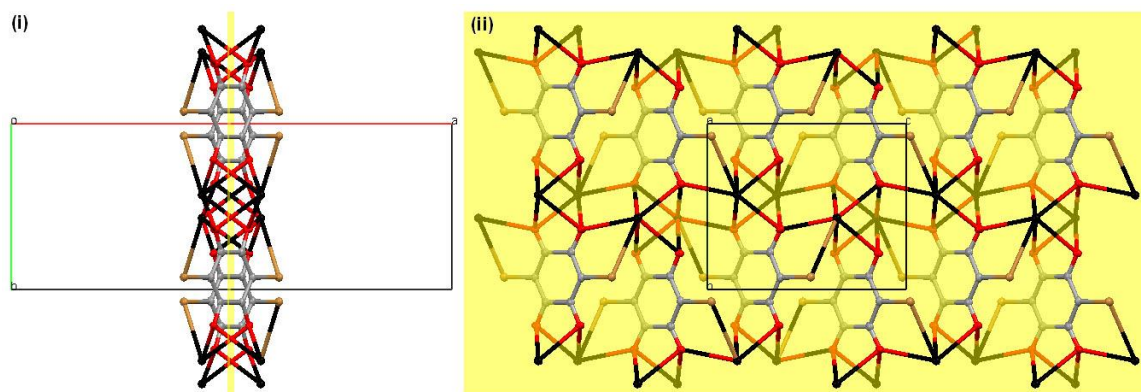


Figure 5-17  $2K^+(C_6O_4Br_2H_2)(C_6O_4Br_2)^{2-}$ . The  $BA^{2-}$  plane as viewed along the  $c$ -axis (left) and perpendicular to the  $c$ -axis (right).

The plane is composed of alternating chains of  $K^+$  ions and staggered  $BA^{2-}$  molecules, held together by strong oxygen and halogen interactions. In terms of comparing form I and form II, this depiction of planes is probably more useful, however the structure can also be viewed more simply in terms of only two sets of planes, the first being the  $BA^{2-}$  plane already illustrated, Figure 5-17, and secondly a set of out of phase waves, describing the  $H_2BA$  plane, Figure 5-18.

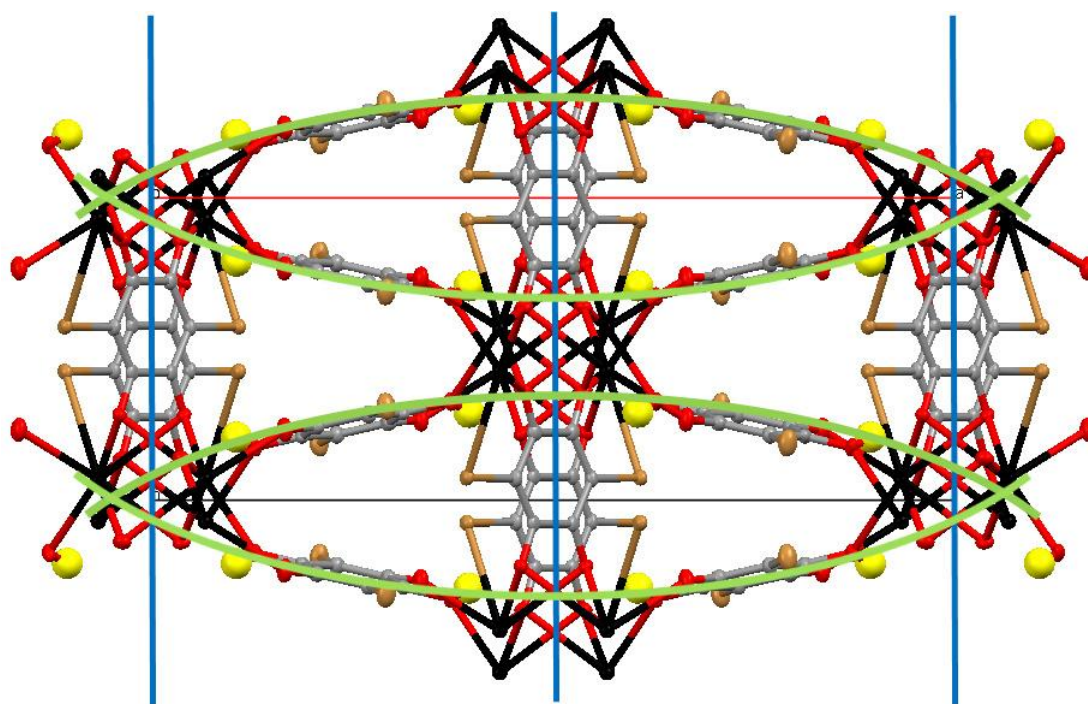


Figure 5-18  $2K^+(C_6O_4Br_2H_2)(C_6O_4Br_2)^{2-}$ . Out of phase waves representing the  $H_2BA$  plane.

The chain of  $K^+$  ions at the peak and the trough of the waves are the same  $K^+$  ion chains within the  $BA^{2-}$  planes and act as a point of intersection between the two planes (Figure 5-19).

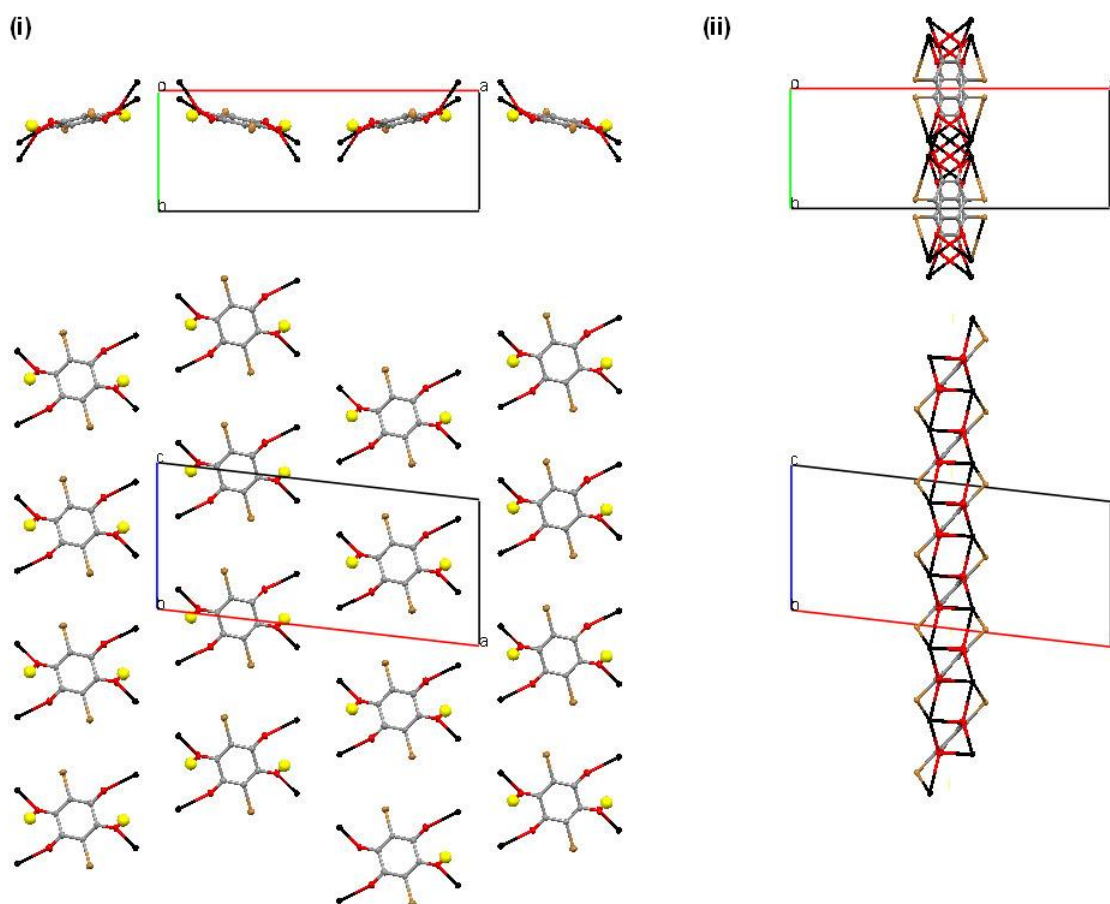


Figure 5-19  $2K^+(C_6O_4Br_2H_2)(C_6O_4Br_2)^{2-}$  (i) Out of phase waves, (ii)  $BA^{2-}$  plane.

Similarly to the two identical intersecting  $H_2BA$  planes, the  $H_2BA$  wave planes are composed of the same isolated  $H_2BA$  molecules coordinated to  $K^+$  ions as described previously.

Significantly in both depictions the  $K^+$  ion chain is the point of intersection for the three intersecting planes. A closer inspection reveals that the  $K^+$  chains are composed of two short  $K\cdots K$  interactions of lengths 3.6793(9) Å and 4.0576(8) Å, compared to the sum of van der Waals radii of 5.5 Å (Figure 5-20).

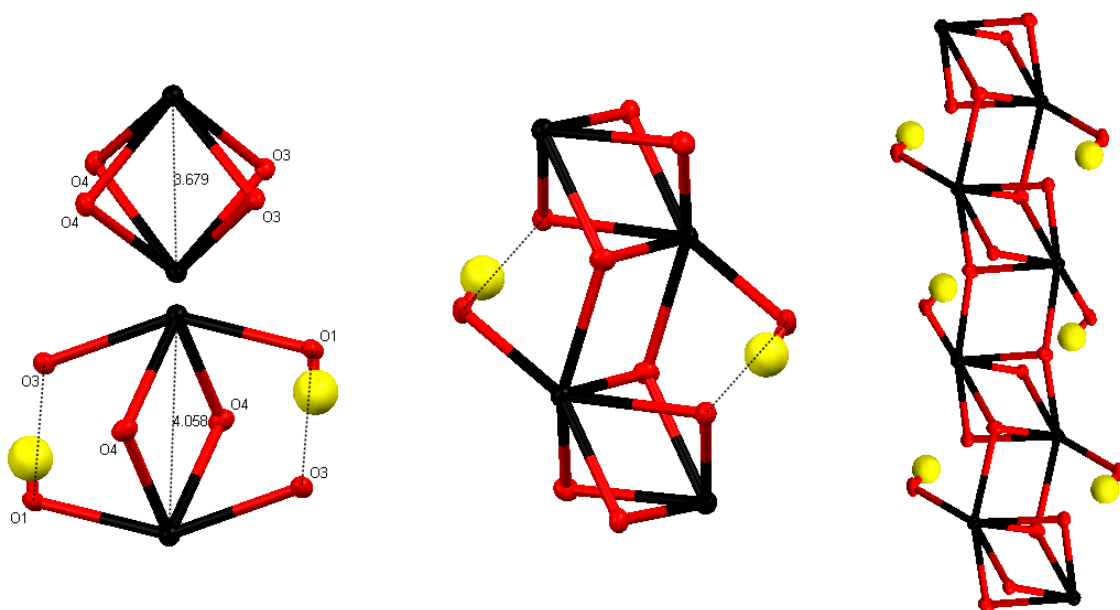


Figure 5-20  $2K^+(C_6O_4Br_2H_2)(C_6O_4Br_2)^{2-}$ . The short  $K\cdots K$  distances and HBs

The shorter of the two  $K\cdots K$  contacts is strengthened by four linking oxygen atoms which make the overall shape of a D4 diamond unit, and the other by a two linking oxygen D2 unit and coordinated hydroxyl oxygen which HBs to an oxygen of the D4 unit. The alternating D4 and D2 units, plus the HB make up the  $K^+$  chain. The HB and halogen interactions are illustrated in Figure 5-21.

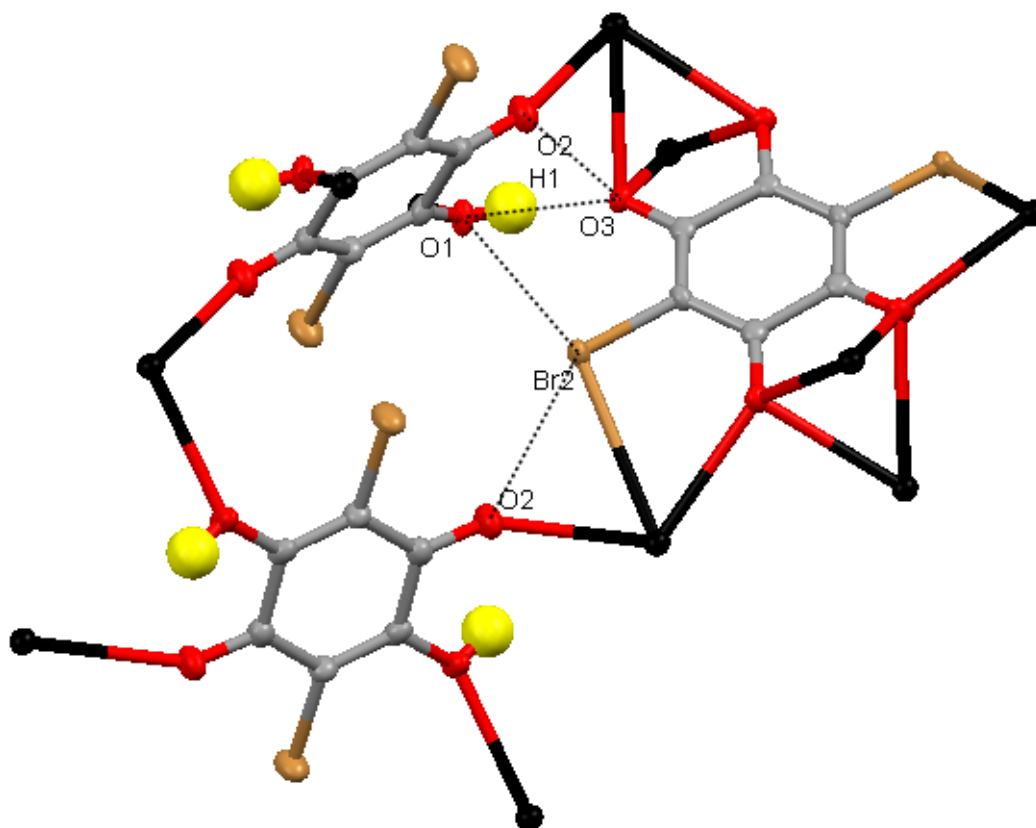


Figure 5-21  $2K^+(C_6O_4Br_2H_2)(C_6O_4Br_2)^{2-}$  HB and halogen interactions

Although  $H_2BA$  molecules do not interact with other  $H_2BA$  molecules on the same plane, they do interact with  $H_2BA$  molecules on the identical intersecting plane via  $K^+$  ions, at the point of intersection. Although the Br atoms on the  $H_2BA$  molecules do not have any significant interactions, each Br atom on a  $BA^{2-}$  molecule interacts directly with the hydroxyl oxygen of a  $H_2BA$  molecule in one of the identical intersecting plane and with the carbonyl group of a  $H_2BA$  molecule on the other identical intersecting plane.

The HB and other weaker intermolecular interaction parameters can be found in Table 5-6. As in form I, it is not clear whether these weaker interactions contribute significantly to the overall packing arrangement of the structure or whether the short contacts are forced by the stronger interactions present within the structure.

Due to the symmetric nature of both molecules these interactions also occur in the second halves of the molecules in the same manner. The overall result is a

complex three dimensional porous structure (Figure 5-22) with pores that run along the c- axis; 5 Å in length along the b- axis and 7 Å in length along the a- axis.

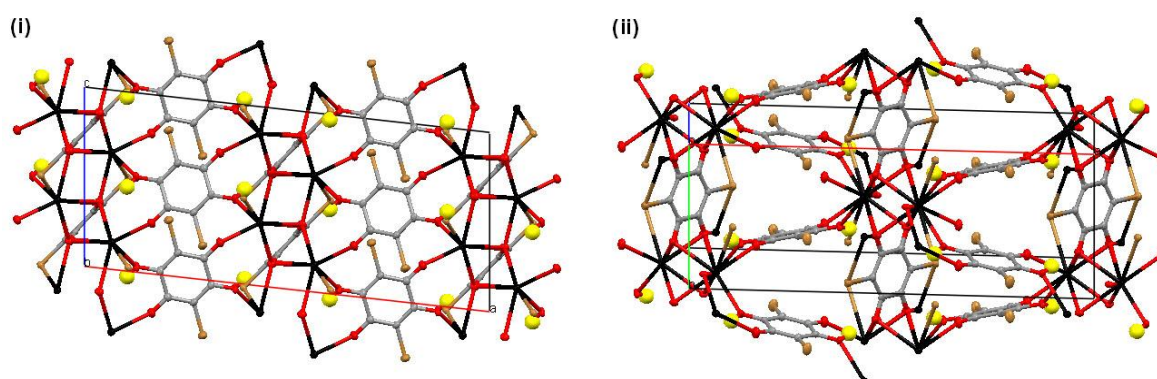


Figure 5-22  $2K^+(C_6O_4Br_2H_2)(C_6O_4Br_2)^{2-}$  structure (i) viewed along b axis (ii) staggered alignment of  $BA^{2-}$  molecules

### 5.2.1.3 Structural Comparison of the Two Anhydrous Tautomeric Polymorphs

The syntheses of potassium bromanilic acid complexes have produced two anhydrous tautomeric polymorphs: form I composed of  $K^+$  ions and  $HBA^-$  molecules, and form II composed of  $K^+$  ions,  $H_2BA$  molecules and  $BA^{2-}$  molecules. All bond lengths and placements of the single and double bonds in both the  $HBA^-$  and the  $H_2BA$  molecules, Table 5-8, match well with those in the average structures defined in Chapter 1. The  $BA^{2-}$  molecule, however, possesses a mirror plane that cuts across the two single C–C bonds in the carbon ring. This is unlike the average  $BA^{2-}$  molecule, which usually possesses a centre of symmetry. The resulting bond lengths and pattern of the single and double bonds are therefore unusual (Table 5-8). This incorporation of BA molecules of different protonation states is the fundamental difference between the two polymorphs.

Interestingly both complexes can be broken down into planes that intersect along a  $K^+$  ion chain. However at the points of intersection in form I one  $HBA^-$  molecule from each plane acts as either the HB donor or the HB acceptor, resulting in two independent  $K^+$  chains within each plane. This is unlike form II in which the symmetric nature of the  $H_2BA$  molecules means that each  $H_2BA$  equally contributes a proton at each point of intersection, and the symmetric nature of the  $H_2BA$

molecules dictates that the second halves of the molecules also coordinate to another  $K^+$  ion in the same manner. This results in very different  $K^+$  chains.

In conclusion, two anhydrous tautomeric polymorphs of potassium bromanilic acid complexes have been obtained with significantly different packing arrangements. By analysing the two complexes in terms of planes it is possible to compare the two forms and associate major differences with the different protonation states present in the two structures. By considering the individual environments of these different protonation states it is also possible to explain the differences in conjugations and bond lengths of the  $BA^{2-}$  molecule from the average.

### **5.2.2 Hydrated Polymorphs**

In addition to two anhydrous tautomeric polymorphs, the syntheses involving K and BA has also produced three hydrated polymers which possess the same structural formula;  $2K^+(C_6O_4Br_2)^{2-} \cdot 2H_2O$  and the same 2:1 K to BA ratio. The experimental details and crystallographic data can be found in Tables 5-4 and 5-5 respectively.

#### **5.2.2.1 Form I**

Although stoichiometrically the structural formula for this complex is  $2K^+(C_6O_4Br_2)^{2-} \cdot 2H_2O$ , a more accurate description may be  $4K^+ \cdot 2(C_6O_4Br_2)^{2-} \cdot 4H_2O$  due to the fact that the asymmetric unit contains two  $BA^{2-}$  molecules and four distinct  $K^+$  ion environments (Figure 5-23).

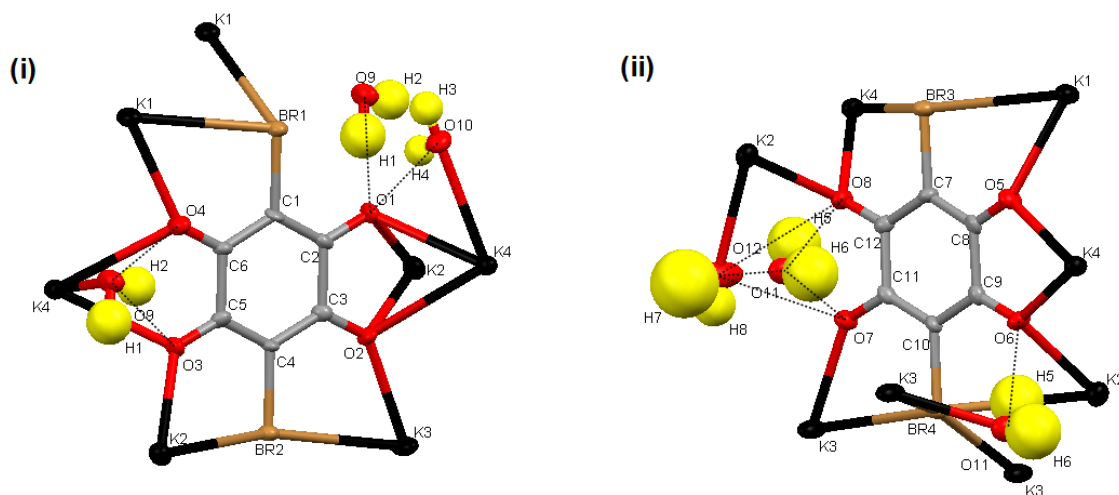


Figure 5-23  $2K^+(C_6O_4Br_2)^{2-} \cdot 2H_2O$  Form I, environment of (i)  $BA1^{2-}$  and (ii)  $BA2^{2-}$

The first  $BA^{2-}$  molecule, which we term  $BA1^{2-}$ , has  $(2A1 + A4 + B1 + B2)$  metal coordination, HBs to three water molecules, and both carbonyl units possess the E2 HB motif and are examples of BHBs. The first is of the single donor double acceptor DHAA form and the second the double donor single acceptor DDHHA form both illustrated in Figure 5-24.

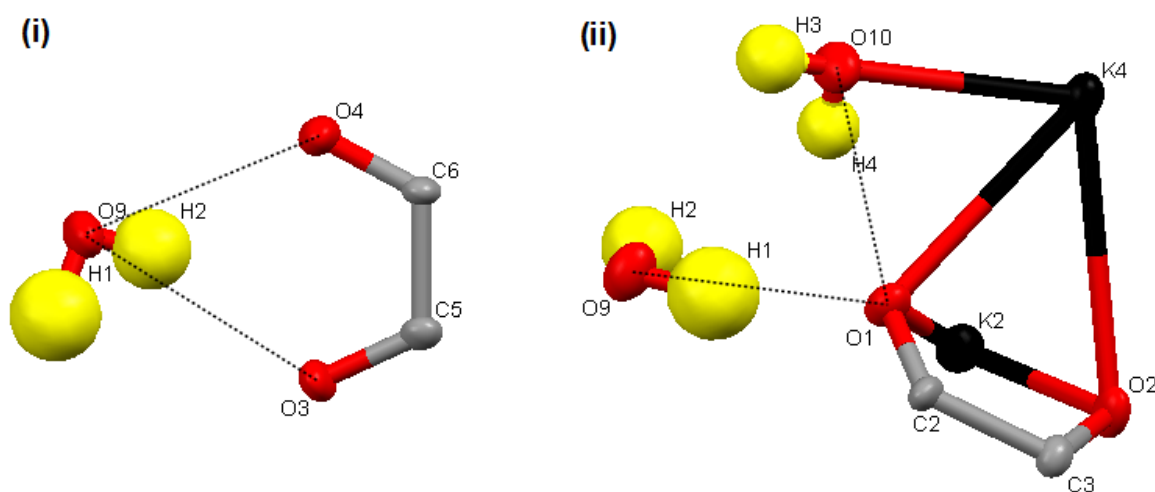
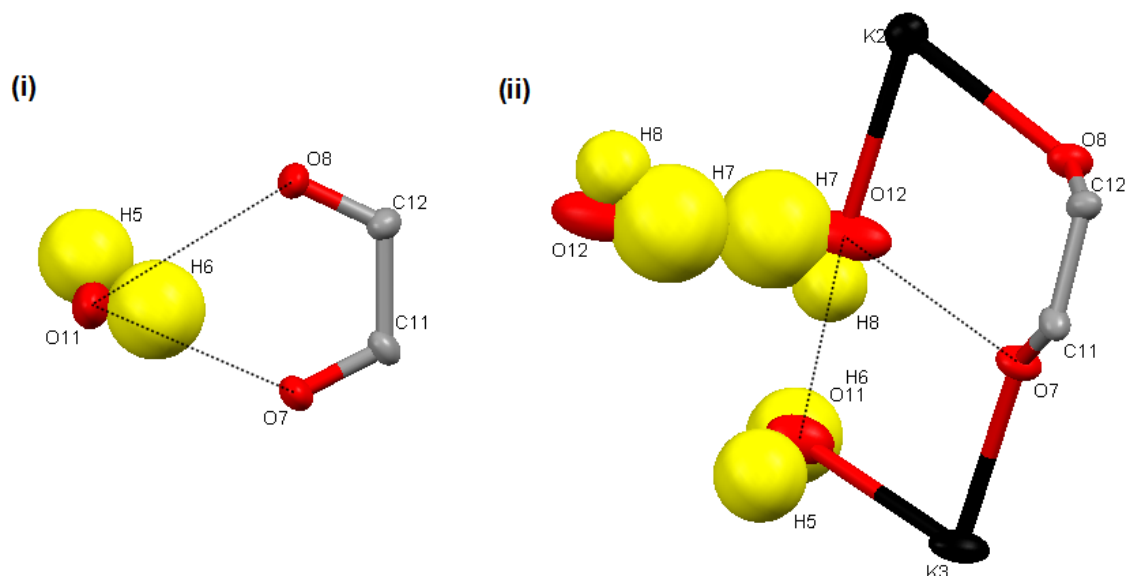


Figure 5-24  $2K^+(C_6O_4Br_2)^{2-} \cdot 2H_2O$  form I BHBs (i) single donor double acceptor DHAA (ii) double donor and single acceptor DDHHA

The second  $BA^{2-}$  molecule  $BA2^{2-}$  has  $(A2 + A3 + 2A4 + B2)$  metal coordination, also HBs to three water molecules, and the halide carbonyl unit has the E3 HB motif. The coordinated water O12 atom has large thermal parameters and distinctly oval

ellipsoids suggesting the presence of disorder which may have affected the riding H7 atom. Although the H7 thermal parameters and ellipsoids are also large the atom position does remain stable during refinement. The present positions for this hydrogen mean there are a further two BHBs in the structure: another of the single donor double acceptor DHAA form and also a double donor and zero acceptor DHHX form both illustrated in Figure 5-25.



**Figure 5-25**  $2K^+(C_6O_4Br_2)^{2-} \cdot 2H_2O$  Form I BHBs (i) single donor double acceptor DHAA  
(ii) double donor and single acceptor DDHHA

The positions of surrounding O atoms and the HB of the H8 atom also situated on the O12 atom does give rise to the possibility that the H7 could potentially HB to the O7 atom; this would also give rise to an additional carbonyl carbonyl E2 HB motif.

The four  $K^+$  ion environments present in the complex are very different, suggesting that the complex has been described in the correct space group and does not demonstrate higher symmetry (Figure 5-26).

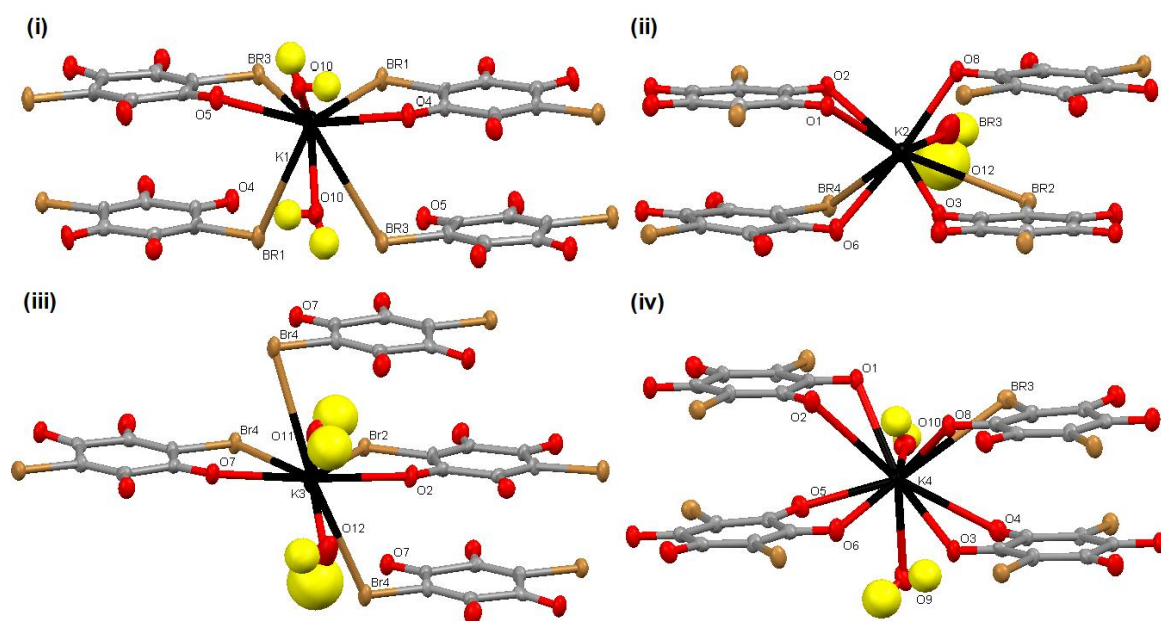


Figure 5-26  $2\text{K}^+(\text{C}_6\text{O}_4\text{Br}_2)^{2-} \cdot 2\text{H}_2\text{O}$  Form I, environment of (i)  $\text{K1}^+$  (ii)  $\text{K2}^+$  (iii)  $\text{K3}^+$  and (iv)  $\text{K4}^+$

The  $\text{K1}^+$  ion is coordinated to four  $\text{BA}^{2-}$  molecules (two  $\text{BA1}^{2-}$ ; a monodentate C2 and a bidentate A2, and two  $\text{BA2}^{2-}$ , also a monodentate C2 and a bidentate A2) and two symmetrically equivalent water molecules. This  $\text{K}^+$  ion is therefore coordinated to 8 other atoms in total: four oxygen atoms, the bond lengths of which range from 2.6693(28) - 2.8769(37) Å and four bromine atoms, the bond lengths of which range from 3.5439(18) - 3.7358(14) Å.

The  $\text{K2}^+$  ion is coordinated to four  $\text{BA}^{2-}$  molecules (two  $\text{BA1}^{2-}$ , a bidentate A2 and a bidentate B2, and two  $\text{BA2}^{2-}$ , a monodentate C1 and a bidentate A2) and one water molecule. This  $\text{K}^+$  ion is therefore also coordinated to 8 other atoms in total: six oxygen atoms, the bond lengths of which range from 2.6500(33) - 2.9181(25) Å and two bromine atoms of bond length 3.5468(15) and 3.6345(20) Å.

The  $\text{K3}^+$  ion is coordinated to four  $\text{BA}^{2-}$  molecules (one  $\text{BA1}^{2-}$ ; a bidentate A2, and three  $\text{BA2}^{2-}$ ; two monodentate C2 and a bidentate A2) and two symmetrically inequivalent water molecules. This  $\text{K}^+$  ion is therefore again coordinated to 8 other atoms in total: four oxygen atoms, the bond lengths of which range from 2.6597(28) - 2.7968(38) Å and four bromine atoms, the bond lengths of which range from 3.4387(18) - 3.7487(28) Å.

The  $K^+$  ion is coordinated to 4  $BA^{2-}$  molecules (two  $BA1^{2-}$ ; two bidentate B2, and two  $BA2^{2-}$ ; a bidentate A2 and a bidentate B2) and two symmetrically inequivalent water molecules. This  $K^+$  ion is therefore coordinated to 10 other atoms in total: nine oxygen atoms, the bond lengths of which range from 2.6724(25) - 3.3539(33) Å and one bromine atom of bond length 3.6333(18) Å.

The resulting structure is the complex and porous three-dimensional framework, illustrated in Figure 5-27.

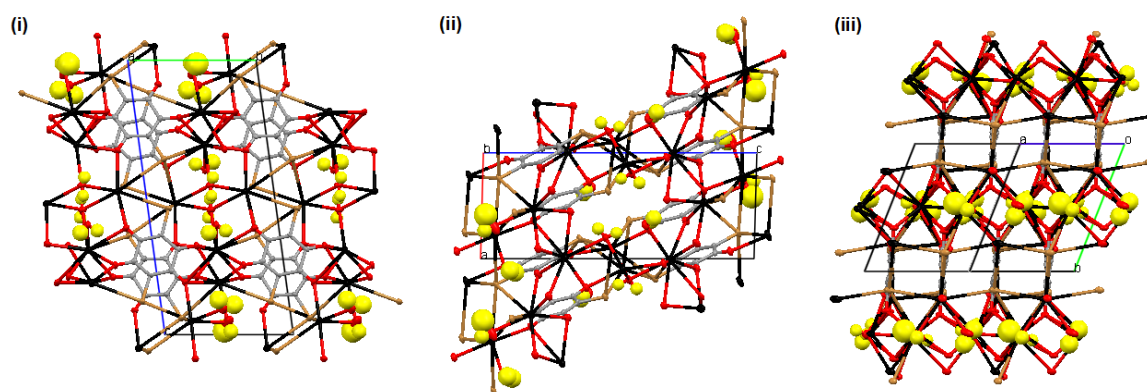


Figure 5-27  $K^+(C_6O_4Br_2)^{2-} \cdot 2H_2O$  structure viewed along (i) *a*-axis (ii) *b*-axis and (iii) *ac*-diagonal

The structure can be described as being composed of extended clusters of two  $BA1^{2-}$  and two  $BA2^{2-}$  molecules centred around two  $K1^+$  ions (Figure 5-28).

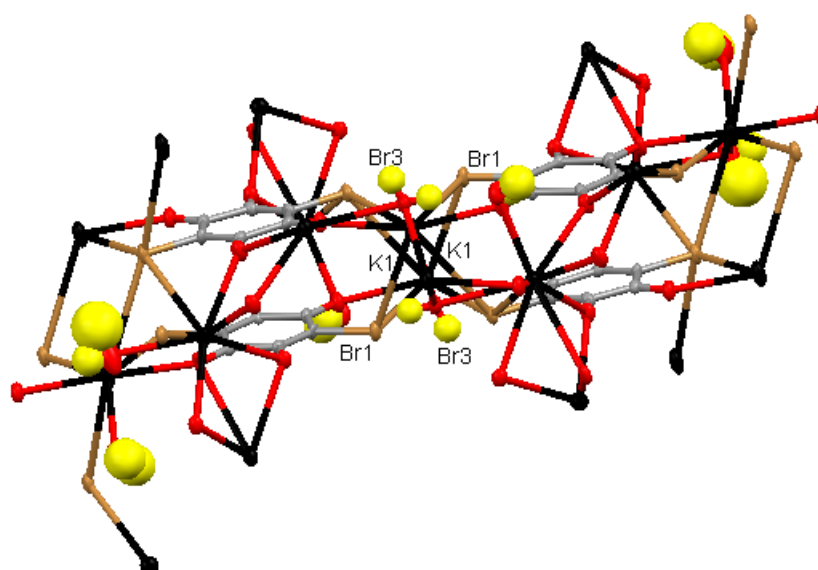
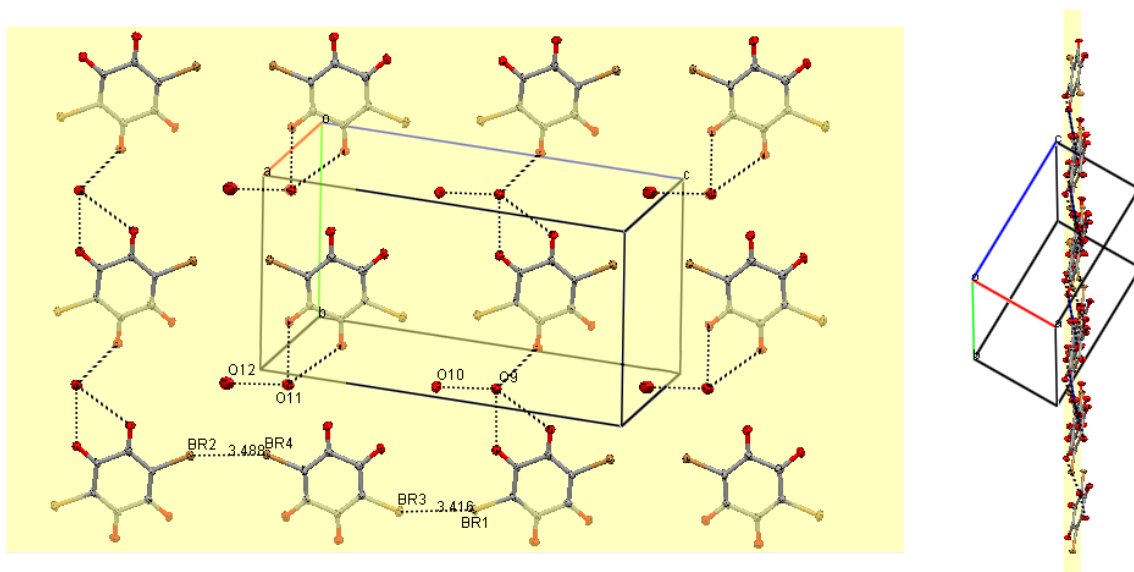


Figure 5-28  $2K^+(C_6O_4Br_2)^{2-} \cdot 2H_2O$  composed of an extended cluster of two  $BA1^{2-}$  and two  $BA2^{2-}$  molecules centred around two  $K1^+$  ions.

Each  $\text{BA}^{2-}$  molecule coordinates to one  $\text{K}^+$  ion by A2 coordination and to the other  $\text{K}^+$  ion by C2 coordination. In terms of the  $\text{BA}^{2-}$  molecules, the extended cluster can be split into two symmetry equivalent and identical planes. Figure 5-29 illustrates the positions of the BA molecules in each plane, and how they connect with one another on the plane via  $\text{Br}\cdots\text{Br}$  interactions and HBs from water molecules.



**Figure 5-29** The  $2\text{K}^+(\text{C}_6\text{O}_4\text{Br}_2)^{2-} \cdot 2\text{H}_2\text{O}$ , extended cluster can be split into two symmetry equivalent and identical planes.  $\text{K}^+$  ions and H atoms omitted for clarity.

Figure 5-30 illustrates how the  $\text{BA}^{2-}$  molecules, within the plane, further interact with one another via  $\text{K}^+$  ions and water molecules.

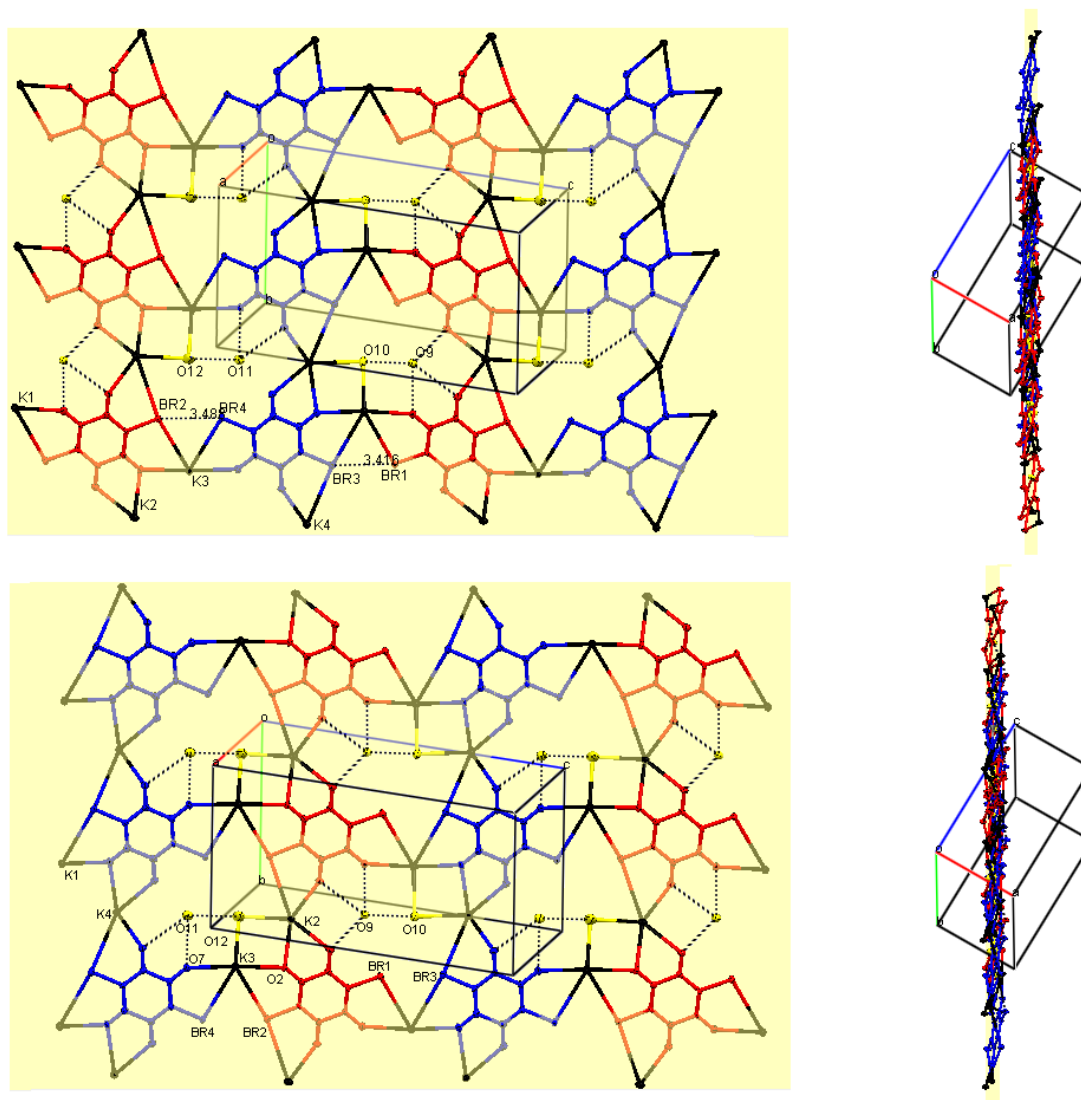


Figure 5-30 The  $2\text{K}^+(\text{C}_6\text{O}_4\text{Br}_2)^{2-} \cdot 2\text{H}_2\text{O}$ , form I extended cluster can be split into two symmetry equivalent and identical planes. H atoms omitted for clarity.

The way in which the two planes align with respect to one another is also illustrated, as are the alternating rows of BA1<sup>2-</sup> and BA2<sup>2-</sup> molecules. The angles at which the BA<sup>2-</sup> molecule cut the planes are illustrated in Figure 5-31.

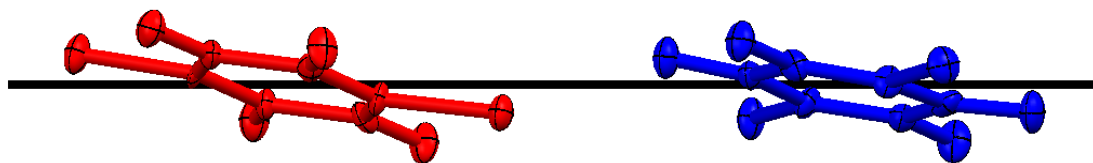


Figure 5-31  $2K^+(C_6O_4Br_2)^{2-} \cdot 2H_2O$  form I, angles at which the BA1<sup>2-</sup> (red) and BA2<sup>2-</sup> (blue) molecules cross the same plane

Due to the nature of this structure and the four K<sup>+</sup> environments, there are many different K...K interactions. The whole structure can be viewed as built up of three sets of K chains that connect to one another via HBs and through further K...K interactions. The first two are illustrated in Figure 5-32.

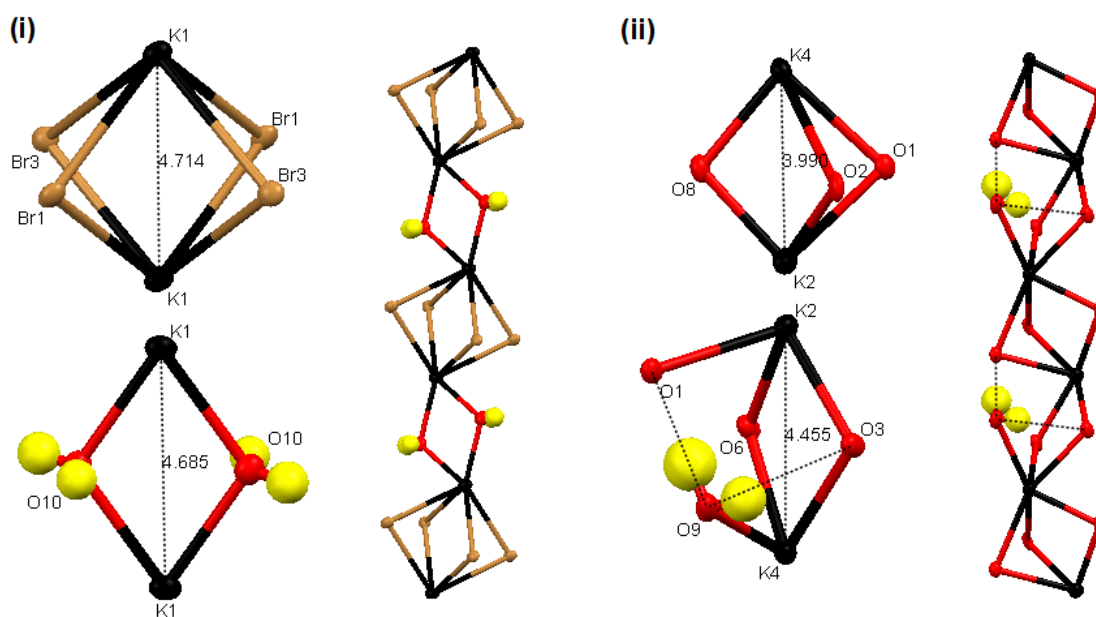
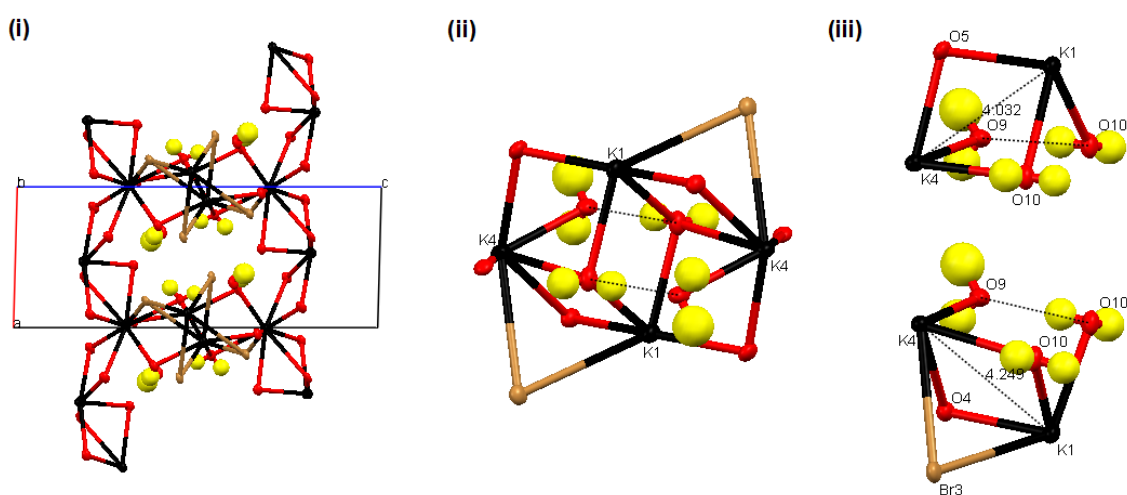


Figure 5-32  $2K^+(C_6O_4Br_2)^{2-} \cdot 2H_2O$  form I, (i) K1...K1 chain and (ii) K2...K4 chain

The K1...K1 chain that runs along the *b*-axis is composed of two alternating units; a D4 diamond unit, of four Br atoms, and a D2 unit of two O<sub>w</sub> (water molecule)

atoms. The K1...K1 distances are 4.7140(30) and 4.6847(32) Å respectively. The K2...K4 chain that runs along the c axis is also composed of two alternating units: a D3 unit, of three O atoms, and a D2 unit, of two O atoms. The K2...K4 lengths are 3.9902(22) and 4.4550(30) Å respectively

The chain is further supported by two HBs due to an incorporated water molecule. The two chains intersect one another in the unit cell and also interact with one another via the O10...O9 HBs and also by a further two K1...K4 interaction units. One is a D2 unit, of O and Ow, and the other a D3 unit, of Br, O and Ow atoms. Each unit has K1...K4 distances of 4.0324(16) and 4.2492(16) Å respectively and is further supported by the O10...O9 HB, as illustrated in Figure 5-33. Neither of these two chains interacts with another of the same chain.



**Figure 5-33**  $2\text{K}^+(\text{C}_6\text{O}_4\text{Br}_2)^{2-} \cdot 2\text{H}_2\text{O}$  form I (i) intersection of K1...K1 and K2...K4 chains (ii) points of interaction (iii) via O10...O9 HBs and K1...K4 interactions.

The third, K3...K3 chain, that also runs along the c axis is composed of two alternating D2 units; both of two Br atoms, and with K3...K3 distances of 4.7283() and 5.891(3) Å (Figure 5-34), the latter of which is significantly larger than the sum of van der Waals radii of 5.5 Å. The K3...K3 chains interact with one another via the O12...O11, and potential O12...O7 HBs of the water molecules in between the chains, and also an additional K3...K3 interaction of 5.406(3) Å. Although the two  $\text{K}^+$

ions in the K3...K3 unit do interact directly via an interlinking atom they do interact via two of the O12...O11 and one of the potential O12...O7 HBs.

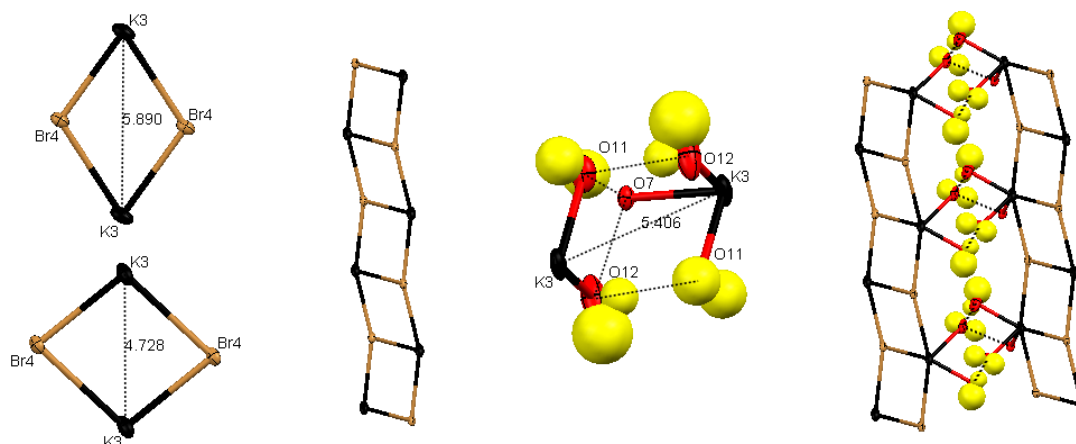


**Figure 5-34**  $2K^+(C_6O_4Br_2)^{2-} \cdot 2H_2O$  form I K3...K3 chain, and interaction with other K3...K3 chains via the O12...O11, and potential O12...O7 HBs of the water molecules in between the chains, and an additional K3...K3 interaction of 5.406Å.

Both the K2...K4 and K3...K3 chains run along the *c*-axis and interact with one another via the potential O12...O7 HB interaction, the O...O and O...O HBs and two further K2...K3 and K3...K4 interactions of 4.033(2) and 4.937(2) Å as illustrated in Figure 5-35. The K2...K3 unit is a D2 unit composed of an O and an Ow atom; it is also further supported by the potential O12...O7 HB s. The K3...K4 unit is a D1 unit composed of an O atom and is also supported by the potential O12...O7 HB and the O...O HB.

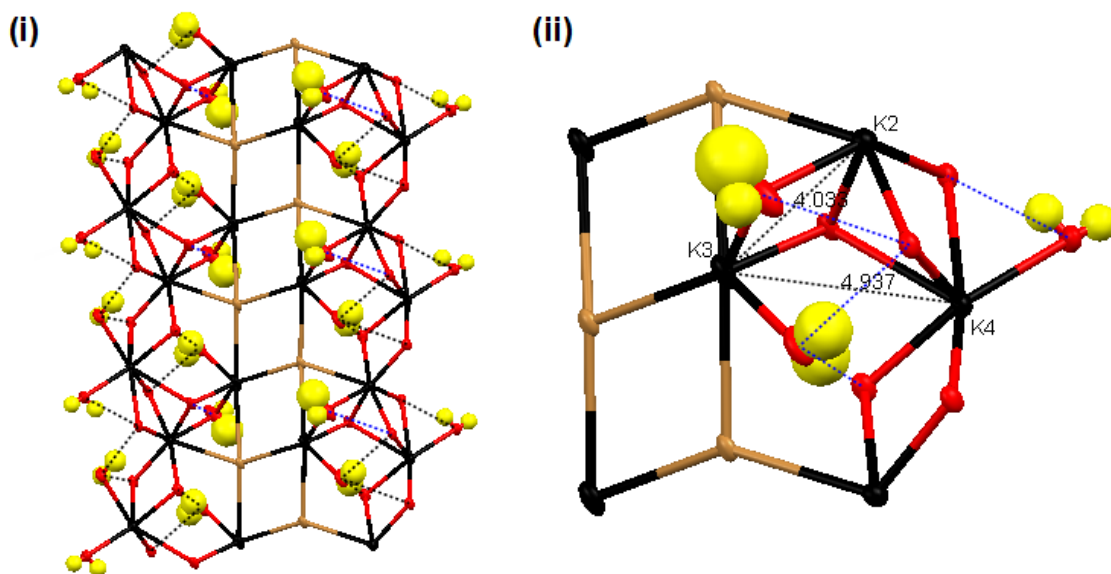


Figure 5-35  $2K^+(C_6O_4Br_2)^{2-} \cdot 2H_2O$  form I, (i) Interaction of K2...K4 and K3...K3 chains along the *c* axis via (ii) potential O12...O7 HB interaction (blue dashed), the O...O and O...O HBs and further K2...K3 and K3...K4 interactions.

Having identified the two dimensional BA molecule planes and the one dimensional K1...K1, K2...K4 and K3...K3 chains and the manners in which they interact with one another, it is now possible to illustrate how the whole three-dimensional structure can be seen as built up from these components.

Figures 5-36, 5-37 and 5-38 illustrate the interactions and intersections of the K1...K1 and K2...K4 chains, K2...K4 and K3...K3 chains and the K3...K3 and adjacent K3-K3 chains respectively, along each of the axes *a*, *b* and *c*. In Figure 5-39 each of the three interactions are superimposed on each of the axes *a*, *b* and *c* from which, with the previous understanding, it is now possible to relate the whole three-dimensional arrangement, from which the carbon rings have been removed. The carbon rings, BA molecule planes defined earlier are then added to this in Figure 5-40.

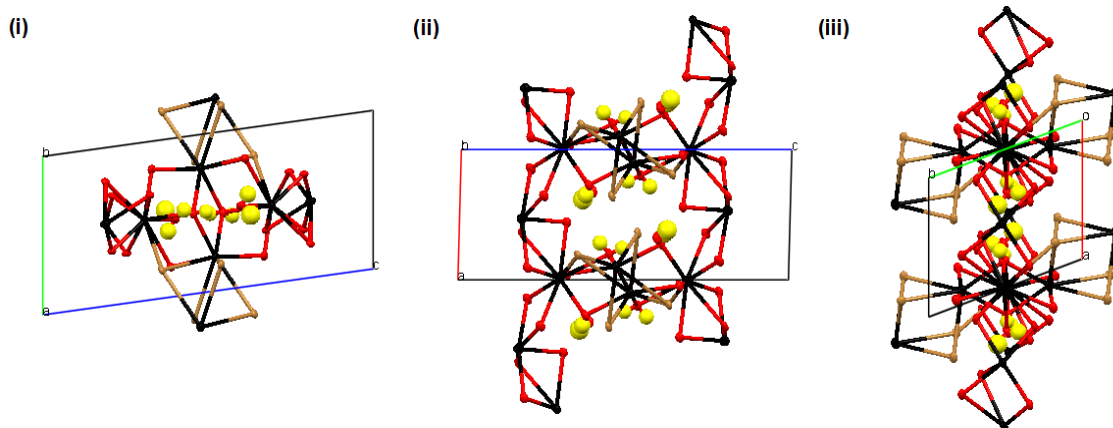


Figure 5-36 Intersection of K1...K1 and K2...K4 chains along (i) *a*- (ii) *b*- and (iii) *c*- axes.

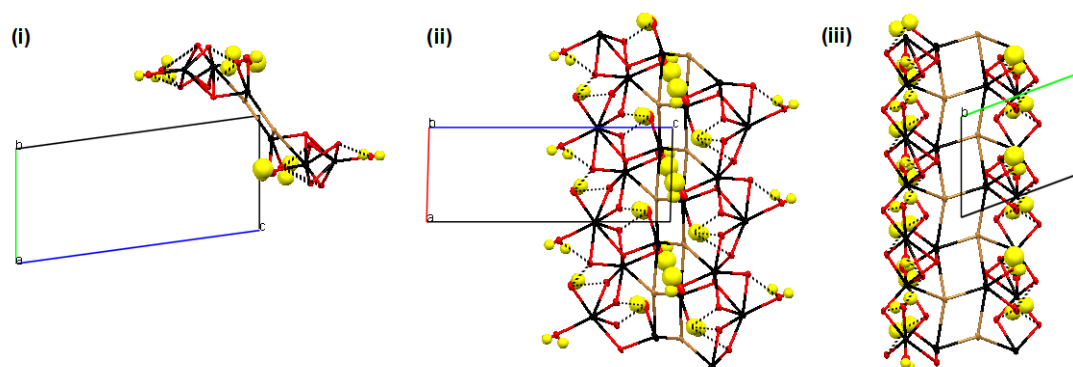


Figure 5-37 Intersection of K2...K4 and K3...K3 chains along (i) *a*- (ii) *b*- and (iii) *c*- axes.

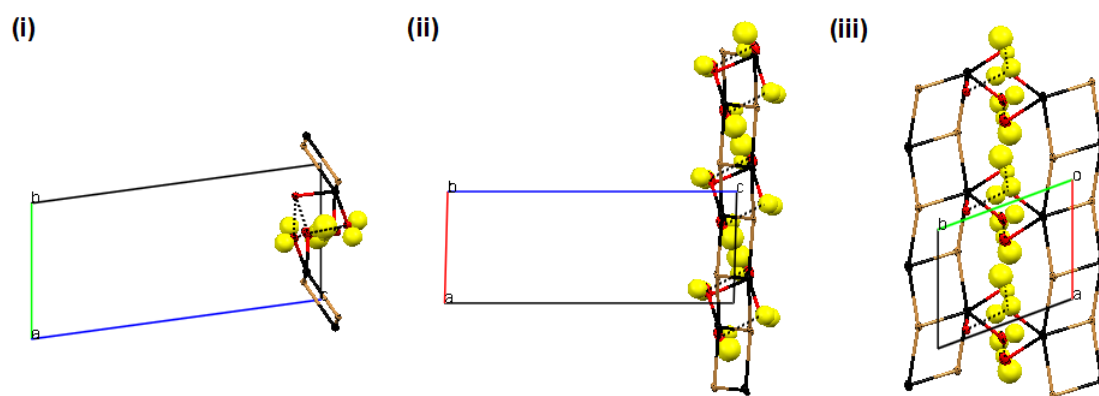


Figure 5-38 Intersection of K3...K3 with adjacent K3...K3 chains along (i) *a*- (ii) *b*- and (iii) *c*- axes.

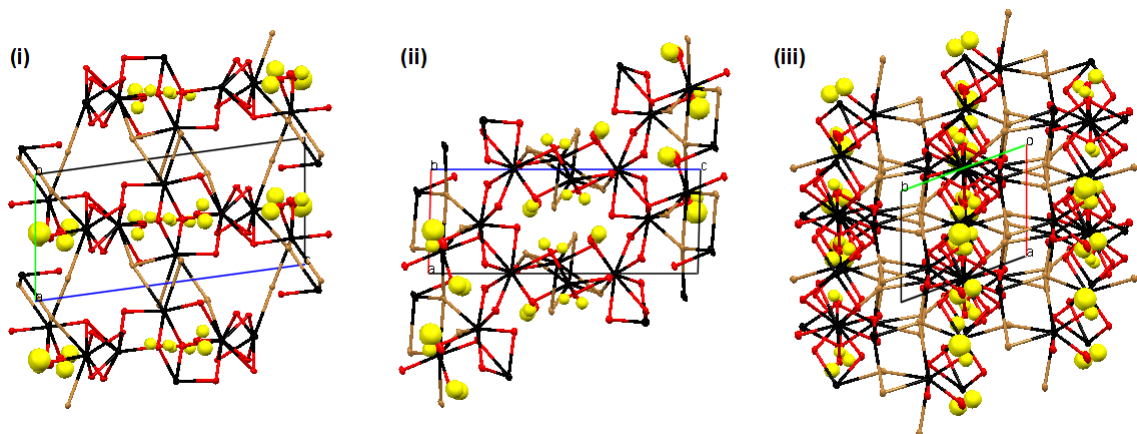


Figure 5-39 Superimposed interactions and intersections of K1...K1 and K2...K4 chains, K2...K4 and K3...K3 chains and K3...K3 and adjacent K3...K3 chains, along (i) *a*- (ii) *b*- and (iii) *c*- axes.

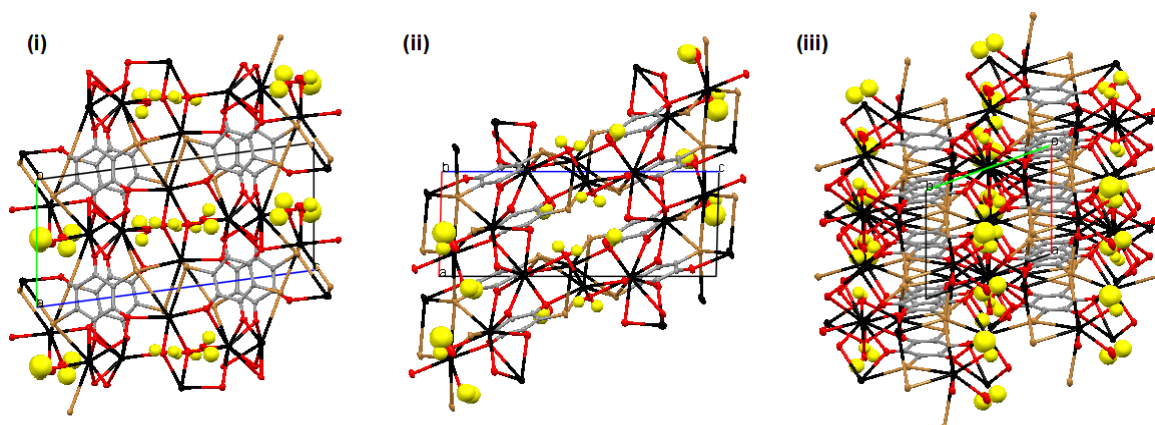
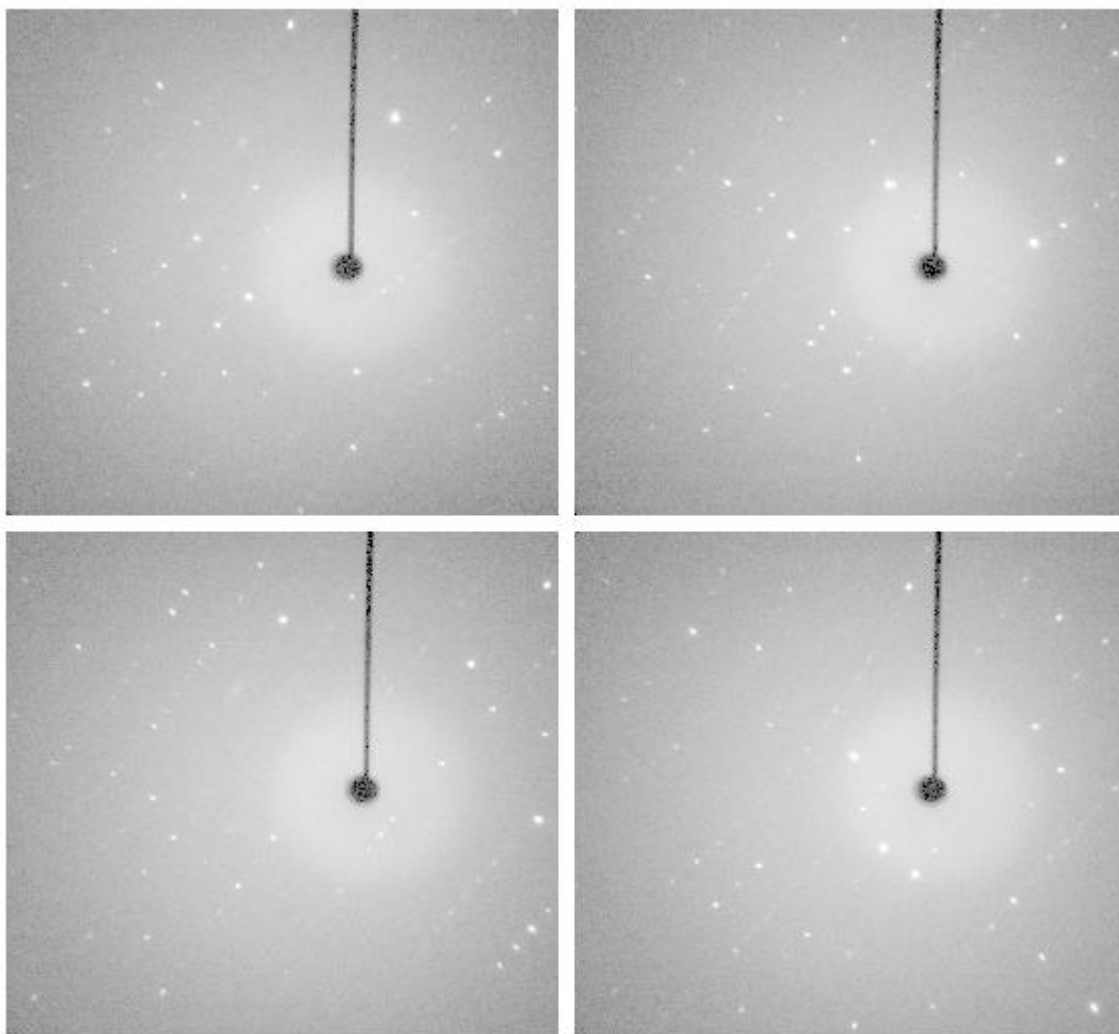


Figure 5-40  $2K^+(C_6O_4Br_2)^{2-} \cdot 2H_2O$  form I, along (i) *a*- (ii) *b*- and (iii) *c*- axes.

### 5.2.2.2 Form II

The images taken during data collection for form II of  $2K^+ \cdot (C_6O_4Br_2)^{2-} \cdot 2H_2O$  showed significant diffuse scattering (Figure 5-41).



**Figure 5-41  $2\text{K}^+(\text{C}_6\text{O}_4\text{Br}_2)^{2-} \cdot 2\text{H}_2\text{O}$  Form II. Images from the data collection showing strong diffuse scattering**

This may explain the difficulty, despite the application of constraints, in obtaining a model in which hydrogen positions were reliably determined. There are two water molecules present in the asymmetric unit, the associated oxygen atoms O3 and O4 possess normal and flat oval shaped ellipsoids respectively, and in accordance with the associated molecular formula, the residual electron density map suggested the presence of two hydrogen atoms with each water oxygen atom. However on fixing these hydrogen positions it is unclear whether the resulting four hydrogen atoms per water oxygen atom is a consequence of incorrect symmetry due to an incorrectly assigned space group or whether this is a consequence of water disorder in the structure as possibly indicated by the diffuse scattering and water oxygen ellipsoid.

The best model obtained, without hydrogen atoms, from the data yielded an asymmetric unit containing half a  $\text{BA}^{2-}$  molecule with an inversion centre, and one  $\text{K}^+$  ion (Figure 5-42).

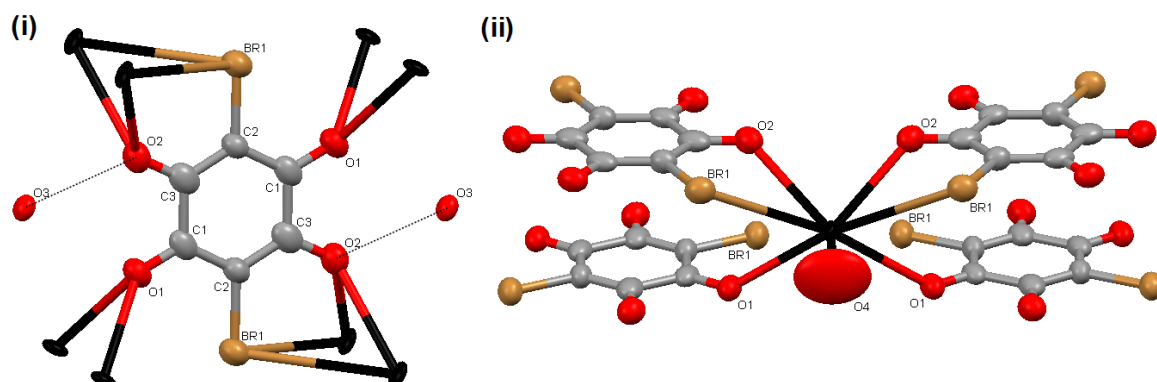


Figure 5-42  $2\text{K}^+(\text{C}_6\text{O}_4\text{Br}_2)^{2-} \cdot 2\text{H}_2\text{O}$  Form II. Environments of the (i)  $\text{BA}^{2-}$  and (ii)  $\text{K}^+$  ion.

Due to the inversion centre, both identical halves of the  $\text{BA}^{2-}$  molecule have the same two metal coordinating units giving an overall 2 (A1 +B6) coordination. The  $\text{BA}^{2-}$  molecule does not seem to possess any of the HB motifs and due the fact that H positions were not determined, possible HB to a nearby water molecule can only be speculated upon.

Each  $\text{K}^+$  ion coordinates to 4  $\text{BA}^{2-}$  molecules; two monodentate C1 and two bidentate A2, and also to a disordered water molecule. In total each  $\text{K}^+$  ion is therefore coordinated to 7 other atoms: five oxygen atoms, the bond lengths of which range from 2.8719(49) - 3.0107(52) Å and two bromine atoms of bond length 3.7052(11) Å.

The resulting three-dimensional structure is presented in projections along the  $a$ -,  $b$ - and  $c$ - axes in Figure 5-43.

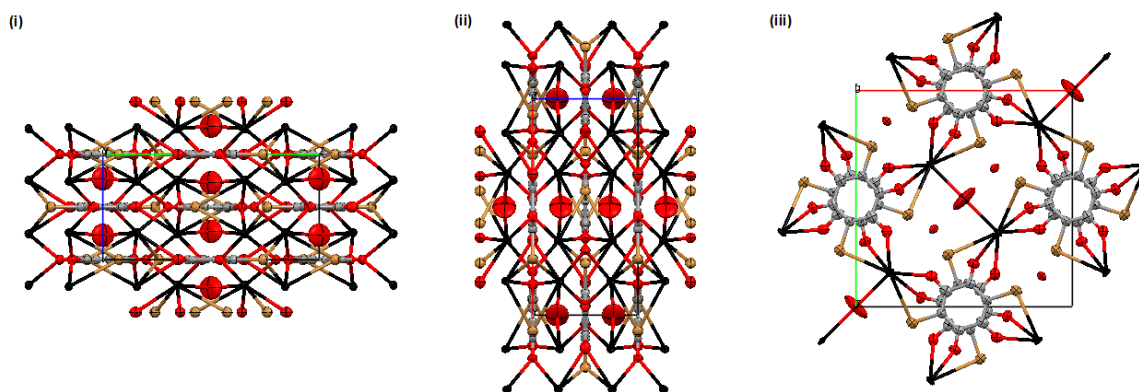


Figure 5-43  $2\text{K}^+(\text{C}_6\text{O}_4\text{Br}_2)^{2-} \cdot 2\text{H}_2\text{O}$  Form II. Structure viewed along (i) *a*- (ii) *b*- and (iii) *c*-axes.

From the identical *a* and *b* axis projections it is clear that the structure can be broken down into  $\text{BA}^{2-}$  planes. By further considering the columns of  $\text{BA}^{2-}$  molecules in the *c* orientation, in which every alternating carbon ring is orientated  $90^\circ$  to the one preceding, the structure can be visualised as being composed of two identical stacking planes along the *c*-axis, Figure 5-44.

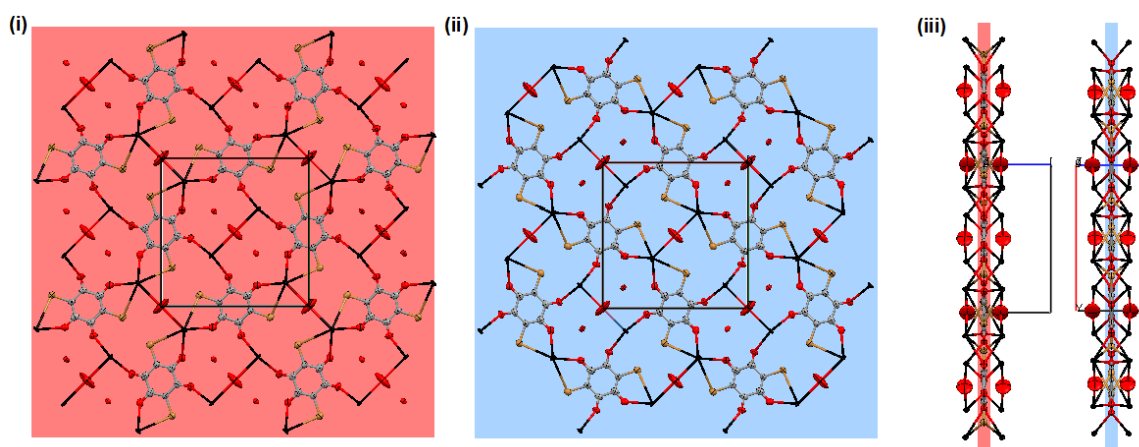


Figure 5-44  $2\text{K}^+(\text{C}_6\text{O}_4\text{Br}_2)^{2-} \cdot 2\text{H}_2\text{O}$  Form II Two identical stacking planes, viewed (i) perpendicular and (ii) along planes.

Although only the  $\text{BA}^{2-}$  molecules and the O3 water molecules lie on the planes, the planes are connected by the  $\text{K}^+$  ions and O4 water molecule interactions, both of which have also been illustrated. The  $\text{BA}^{2-}$  molecules, which lie on each individual plane, are orientated  $60^\circ$  to their four neighbouring  $\text{BA}^{2-}$  molecules so that each plane is composed of rows of alternating  $\text{BA}^{2-}$  molecules. The result is the

presence of clusters of either bromine or oxygen atoms that surround the interplanar connecting O4 water molecules.

Due to the inability to fix the locations of the water molecule hydrogen atoms it is not possible to comment on the degree to which hydrogen bonding within the structure contributes to the overall packing arrangement. The short O...O distances within the structure, which seem most likely to HB, along with a short O...Br interaction, have been illustrated in Figure 5-45.

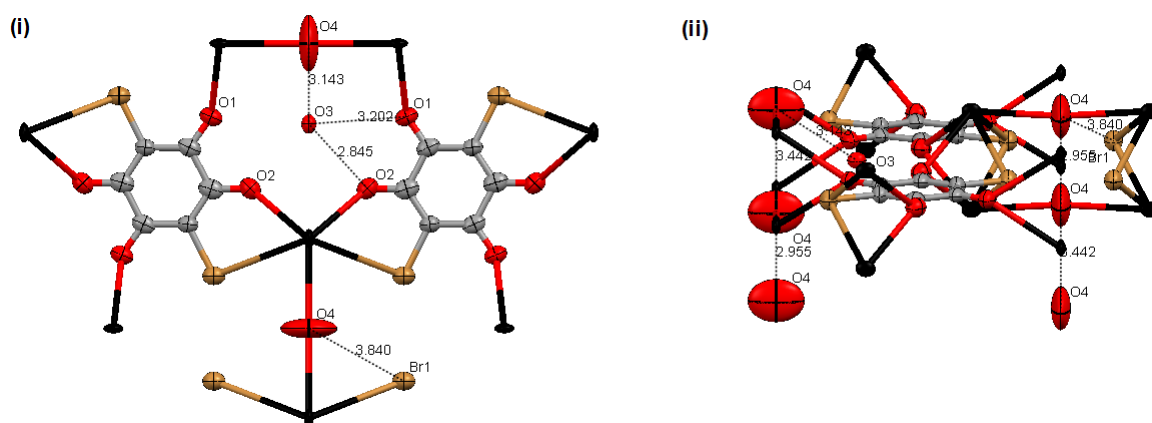


Figure 5-45  $2\text{K}^+(\text{C}_6\text{O}_4\text{Br}_2)^{2-} \cdot 2\text{H}_2\text{O}$  Form II Potentially significant Interaction bond lengths

There is clear structured diffuse scattering present, suggesting some type of short-range order associated with the water/hydrogen positions. This may be due to the fact that the closest contacts to the O4 atom are four Br atoms at 3.840(7) Å and another two O4 atoms at 3.44(0) and 2.96(3) Å, the first two are both outside the sum of the van der Waals radii of 3.04 and 3.37 Å, respectively. As the waters in this space have such little interaction with the rest of the structure this may explain the disorder.

In addition to the BA planes, there are also  $\text{K}^+$  ion chains that run along the c axis, and intersect the planes. As the planes are alternating in terms of BA orientation, the  $\text{K}^+$  chains are composed of two alternating units: one D4 unit of two Br atoms and two O atoms, and one D2 unit of two O atoms. The associated  $\text{K}^+\cdots\text{K}^+$  distances are 3.277(3) and 3.120(3) Å respectively Figure 5-46.

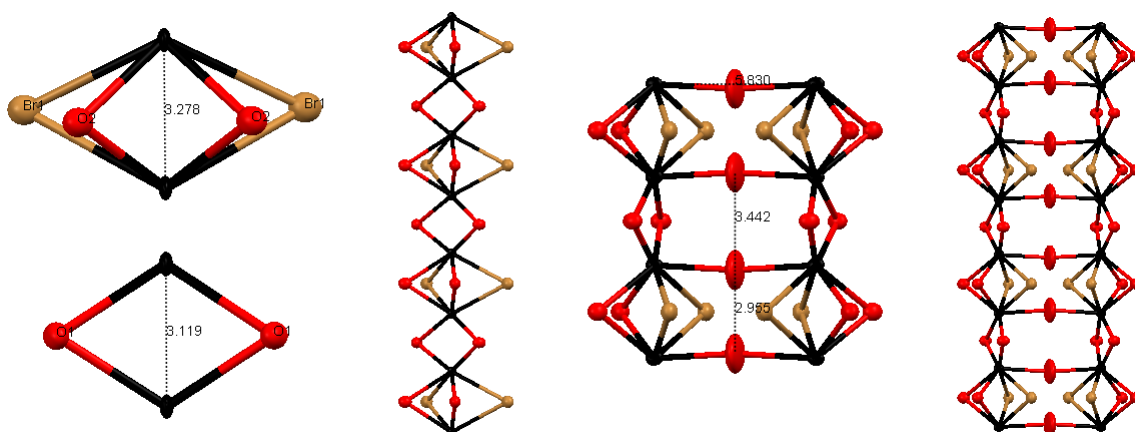


Figure 5-46  $2K^+(C_6O_4Br_2)^{2-} \cdot 2H_2O$  Form II  $K \cdots K$  chains composed of alternating D4 and D2 units, connected by further  $K \cdots K$  D1 unit to form double chains that run through c axis.

Each  $K^+$  chain also coordinates to another adjacent  $K^+$  chain forming a double chain that runs along the c-axis. This  $K \cdots K$  interaction is a D1 unit comprised of a O4 atom and is  $5.830(1) \text{ \AA}$ , outside the  $5.5 \text{ \AA}$  sum of the van der Waals radii. The overall structure is therefore composed of alternate BA planes intersected by an alternating double  $K^+$  chain.

### 5.2.2.3 Form III

The asymmetric unit of Form III contains half a  $BA^{2-}$  molecule with an inversion centre, one  $K^+$  ion, and a water molecule (Figure 5-47).

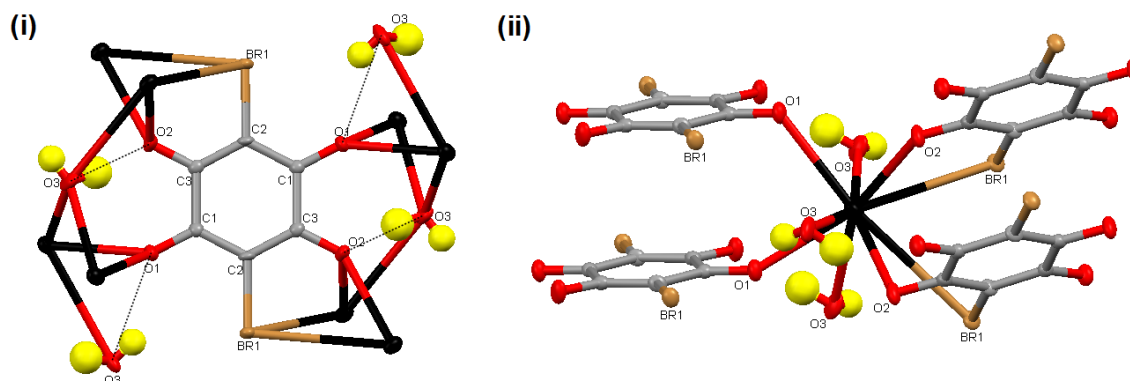


Figure 5-47  $2K^+(C_6O_4Br_2)^{2-} \cdot 2H_2O$  Form III Environments of (i)  $BA^{2-}$  molecule (ii)  $K^+$  ion

Due to the inversion centre both identical halves of the  $\text{BA}^{2-}$  molecule have the same two metal coordinating units giving an overall 2 (A1 + B6) metal coordination. Both of the identical halves also possess the E2 HB motif.

Each  $\text{K}^+$  ion is coordinated to 4  $\text{BA}^{2-}$  molecules; two monodentate C1 and two bidentate A2, and also to three water molecules. In total each  $\text{K}^+$  ion is therefore coordinated to 9 other atoms: seven oxygen atoms, the bond lengths of which range from 2.6849(13) - 3.2778(13) Å and two bromine atoms of bond lengths 3.6201(4) and 3.7999(4) Å. The  $\text{K}^+$  ion is coordinated to three water molecules, two of which are planar to one another, and four  $\text{BA}^{2-}$  molecules; two sets of pairs that are planar to one another.

The resulting three dimensional porous structure is presented in the *a*-, *b*- and *c*-axes projections in Figure 5-48.

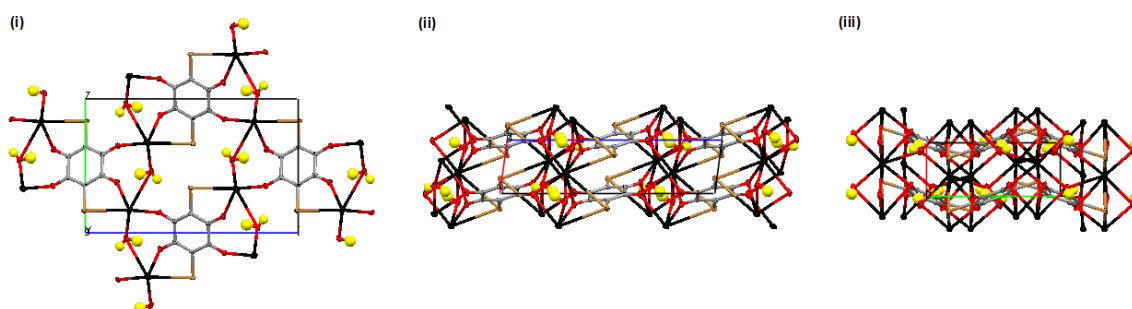


Figure 5-48  $2\text{K}^+(\text{C}_6\text{O}_4\text{Br}_2)^{2-} \cdot 2\text{H}_2\text{O}$  Form III Structure viewed along (i) *a*- (ii) *b*- and (iii) *c*-axes.

From this it can be seen that the overall structure is composed of BA planes that run along the *bc* plane and  $\text{K}^+$  planes that run along the *ab* plane. The BA planes are composed of alternating chains of BA molecules and  $\text{K}^+$  ions connected by water molecules (Figure 5-49).

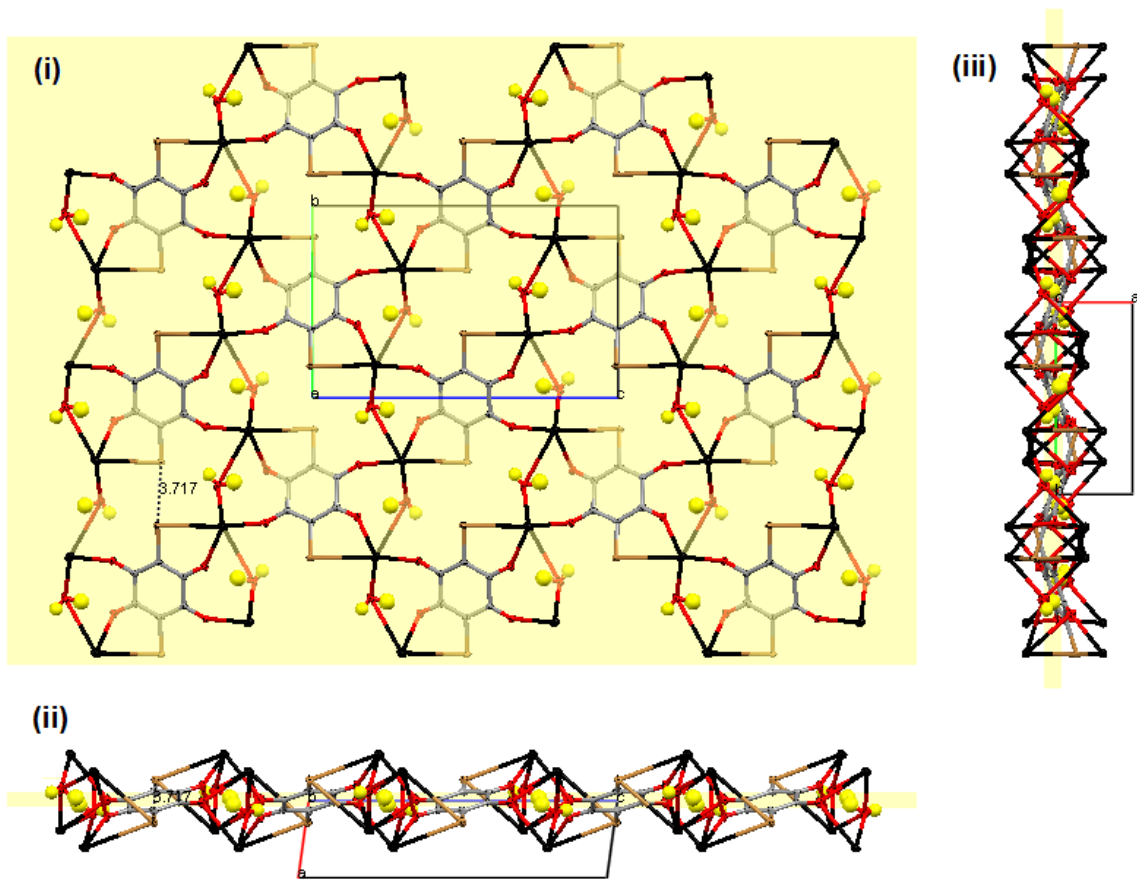


Figure 5-49  $2K^+ \cdot (C_6O_4Br_2)^{2-} \cdot 2H_2O$  Form III BA planes composed of alternating chains of BA molecules and  $K^+$  ion connected by water molecules.

Other interactions within the plane include  $Br \cdots Br$  interactions between adjacent BA molecules, and HB interactions from the connecting water molecules.

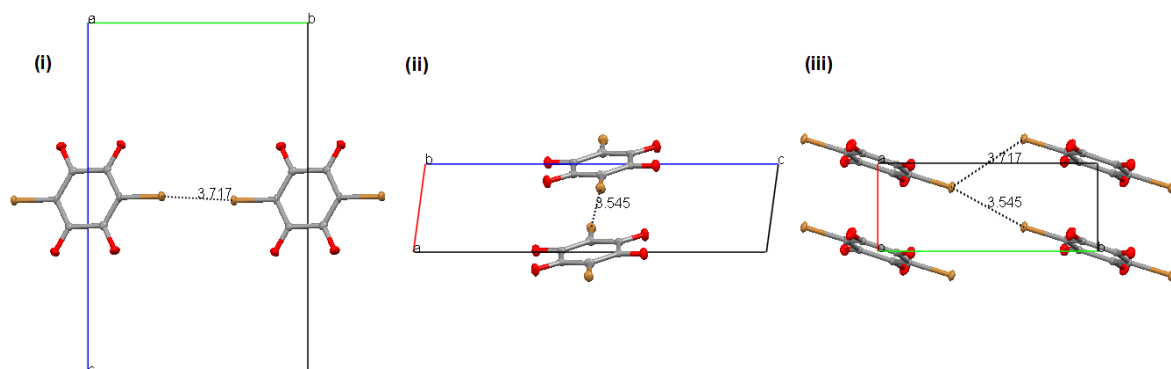


Figure 5-50  $2K^+ \cdot (C_6O_4Br_2)^{2-} \cdot 2H_2O$  Form III  $Br \cdots Br$  interactions.

Every second BA chain cuts the plane at the same angle however at a different orientation to the preceding chain, Figure 5-51.

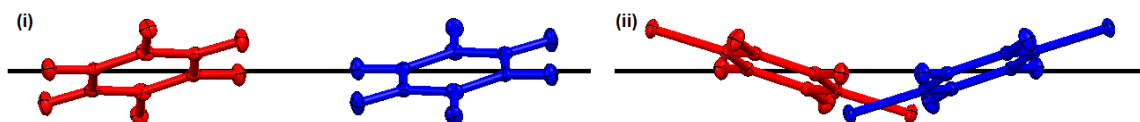


Figure 5-51  $2\text{K}^+(\text{C}_6\text{O}_4\text{Br}_2)^{2-} \cdot 2\text{H}_2\text{O}$  Form III. Every second BA chain cuts the plane at the same angle however a different orientation to the preceding chain.

The  $\text{K}^+$  plane is composed of  $\text{K}^+$  chains that run along the  $a$  axis and are joined together into a plane by coordinating water molecules (Figure 5-52).

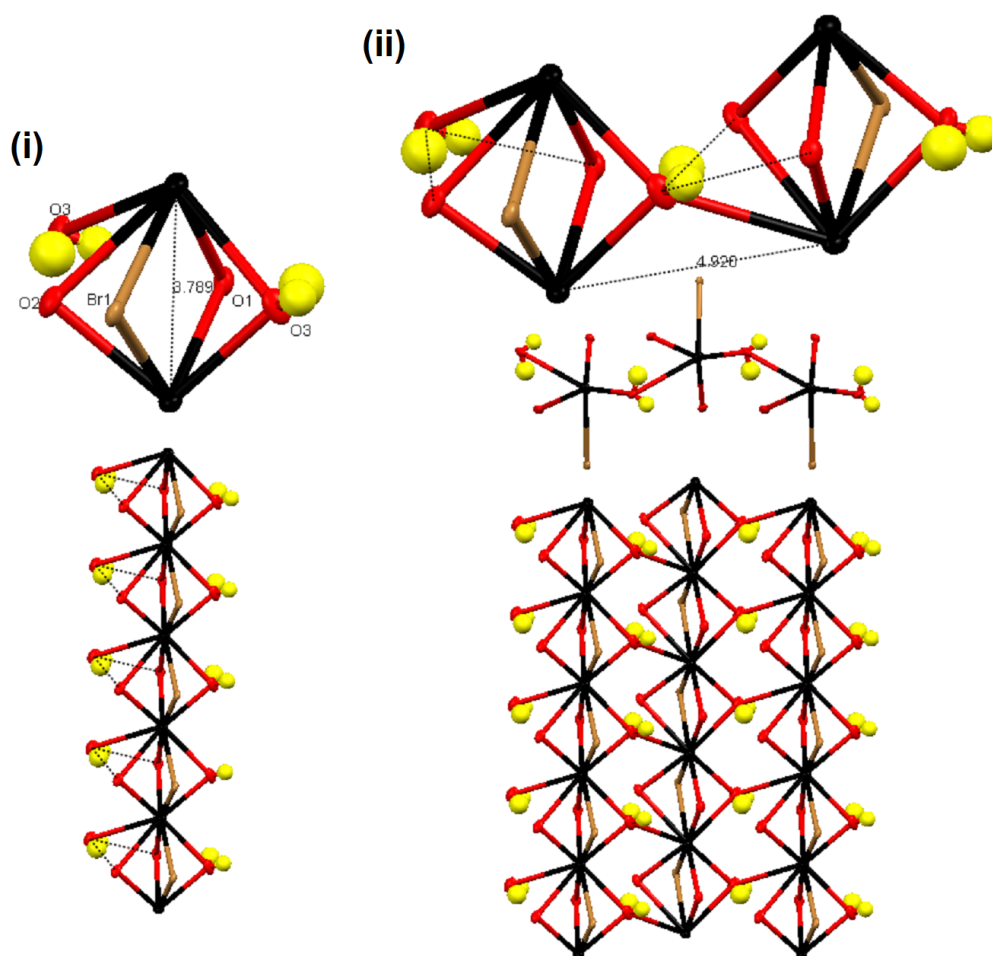


Figure 5-52  $2\text{K}^+(\text{C}_6\text{O}_4\text{Br}_2)^{2-} \cdot 2\text{H}_2\text{O}$  Form III.  $\text{K}\cdots\text{K}$  chains.

Each chain is composed of one repeating  $\text{K}\cdots\text{K}$  D4 interaction unit of one Br, two O, one  $\text{O}_w$  atoms and also supported by the hydrogen bonding interactions of an additional water molecule which HBs to the two O atoms. The  $\text{K}\cdots\text{K}$  distance of

the chain is 3.7885(4) Å, and each chain connects to the adjacent chain by a further K $\cdots$ K distance of 4.9201(4) Å, and by a D1 Ow unit.

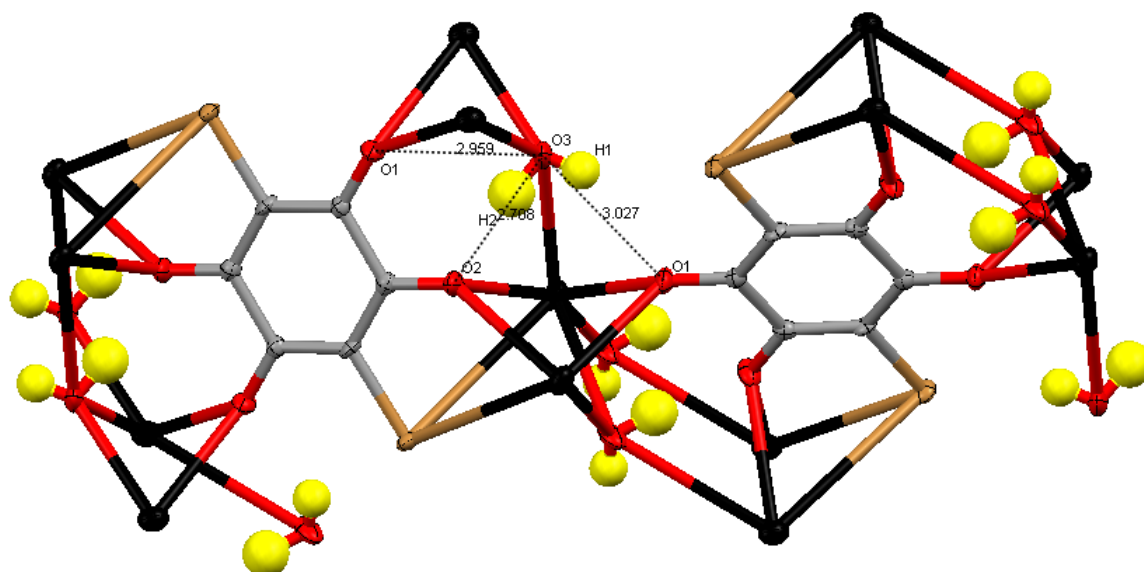


Figure 5-53 BA $^{2-}$  and K $^{+}$  planes point of intersection

The point at which the BA and K $^{+}$  planes intersect is illustrated in Figure 5-53. As a K $^{+}$  plane intersects the BA plane in between the rows of the two differently orientated BA molecules, the BA molecules on each side of the K $^{+}$  plane are of opposite orientation. The BA molecules on each side of the plane interact with one another via the two O atoms in the D4 K $\cdots$ K unit, both of which HB to the Ow atom. Due to the symmetric nature of the BA molecules these interactions also occur in the second halves of the molecules in the same manner.

#### 5.2.2.4 Comparison of the Structural Packing of the Three Hydrated Polymorphs

The syntheses of potassium bromanilic acid complexes has produced three very different hydrated complexes, each of which have been interpreted by use of BA planes and K $^{+}$  chains, built up into higher dimensions, in order to describe the full three-dimensional packing in the structure.

Each complex has the same stoichiometric ratio of 2K: BA: 2H $_2$ O molecules and all BA molecules are in the deprotonated BA $^{2-}$  form. Each complex was obtained by

very different means (Table 5-4). Form I was obtained from starting materials in which the K:BA ratio was 1:1 whereas in form II and III the ratio was 2:1. In addition the synthesis using potassium salts  $\text{KCO}_3$  and  $\text{KOH}$  in water solution yield form I and II respectively whereas Form II results from the reaction of  $\text{KOH}$  and BA in methanol. It therefore seems that it is not possible to predict the structural outcome in these systems from the identity of and ratio of starting materials, but that the solvent also plays a role. Crystals of these same three materials were also formed under a number of other conditions.

A comparison of the BA molecule bond lengths in each of the forms is presented in Table 5-10. There are very few complexes containing the  $\text{BA}^{2-}$  bond lengths in the literature, in comparison to the data available for  $\text{H}_2\text{BA}$  lengths. In the average structure from the literature, although the C–C distance between the two C–O bonds remained at a single C–C bond length, the double C=C and intermediate tended to become larger and smaller in length respectively to reach similar lengths of around  $1.402\text{\AA}$ . Although this is true for form I and form III, the form II seems to have retained the C–C bond lengths characteristic of a  $\text{H}_2\text{BA}$  molecule. The average  $\text{BA}^{2-}$  bond lengths, obtained from the literature also indicated an increase in the C=O bond length and decrease in the C–OH bond length, both to around  $1.25\text{\AA}$  upon deprotonation. Again this occurs in both form I and form III, however the bond lengths of  $1.2284(97)$  and  $1.2781(102)\text{\AA}$  respectively in form II are more characteristic of those in a fully protonated  $\text{H}_2\text{BA}$  molecule.

An inspection of coordinating compounds reveals that in each of the three forms it is typical for each O and Br atom on the  $\text{BA}^{2-}$  molecule to coordinate to two  $\text{K}^+$  ions and in some cases also to form a HB with a water molecule. An examination of the short contact distances (Table 5-9) does reveal these to be weaker in form II in comparison to those of forms I and III, although the  $\text{K}\cdots\text{K}$  interactions appear of similar distances to form I and III. It is therefore not clear why the bond distances of the  $\text{BA}^{2-}$  molecule in form II seem to retain the  $\text{H}_2\text{BA}$  character.

**Table 5-4 Experimental Information for anhydrous KBA complexes**

	FORM I	FORM II	FORM III
$K^+(C_6O_4Br_2H)^- / 2K^+(C_6O_4Br_2)^{2-} (C_6O_4Br_2H_2)$	Dark red crystalline needles obtained, simultaneously with form II, from a 1:1 molar ratio ( $6.7 \times 10^{-5}$ mol) of BA (0.020g) and KOH (0.008g), both dissolved in MeOH, combined, and left to evaporate at room temperature.	Dark red crystalline blocks and plates obtained, simultaneously with form I, from a 1:1 molar ratio ( $6.7 \times 10^{-5}$ mol) of BA (0.020g) and KOH (0.008g), both dissolved in MeOH, combined, and left to evaporate at room temperature.	n/a
$2K^+(C_6O_4Br_2)^{2-} \cdot 2H_2O$	Red rectangular crystalline blocks obtained from a 1:1 molar ratio ( $6.7 \times 10^{-5}$ mol) of BA (0.02g), dissolved in IPA and $K_2CO_3$ (0.010g), dissolved in water, combined, and left to evaporate at room temperature.	Dark red crystalline needles obtained from a 1:2 molar ratio ( $6.7 \times 10^{-5}$ mol, $1.34 \times 10^{-4}$ mol) of BA (0.02g), dissolved in MeCN, and KOH (0.016g), dissolved in water, combined, and left to evaporate at room temperature.	Dark red crystalline needles obtained from a 1:2 molar ratio ( $3.35 \times 10^{-5}$ mol, $6.7 \times 10^{-5}$ mol) of BA (0.01g), and KOH (0.004g), both dissolved in methanol, combined, and left to evaporate at 50°.

**Table 5-5 Crystallographic Information for KBA complexes**

	Anhydrous		Hydrated		
	$K^+(C_6O_4Br_2H)^-$	$2K^+(C_6O_4Br_2)^{2-} \cdot (C_6O_4Br_2H_2)$	$2K^+(C_6O_4Br_2)^{2-} \cdot 2H_2O$	$2K^+(C_6O_4Br_2)^{2-} \cdot 2H_2O$	$2K^+(C_6O_4Br_2)^{2-} \cdot 2H_2O$
Diffractometer	Kappa	Rigaku	Kappa	Kappa	Kappa
Crystal size/mm <sup>3</sup>	0.1 x 0.2 x 0.4	0.1 x 0.1 x 0.05	0.1 x 0.3 x 0.5	0.2 x 0.2 x 0.5	0.1 x 0.1 x 0.3
M/g mol <sup>-1</sup>	335.99	671.98	410.11	410.11	410.11
T/K	100	100	100	100	100
Space group	P21/c	C2/c	P-1	P42/mnm	P21/c
a/Å	6.71490(10)	21.760(5)	7.290(5)	13.146	3.78850(10)
b/Å	9.4152(2)	8.1204(12)	8.863(5)	13.146	9.4016(2)
c/Å	13.7537(3)	9.8192(19)	17.874(5)	6.397	15.0979(4)
$\alpha$ /°	90	90	82.292(5)	90	90
$\beta$ /°	94.2930(10)	96.557(7)	88.760(5)	90	97.7420(10)
$\gamma$ /°	90	90	69.725(5)	90	90
V/Å <sup>3</sup>	867.10(3)	1723.7(6)	1073.1(10)	1105.4	532.85(2)
Z	4	9	4	2	2
Pcalc/g cm <sup>-3</sup>	2.574	2.589	2.526	2.464	2.556
$\mu$ /mm <sup>-1</sup>	0.9803	0.9862	8.336	8.093	8.395
$\theta$ range/°	2.62 - 27.57	3.33 - 27.48	2.3 - 27.86	2.19 - 27.46	2.56 - 27.5
Reflections					
Collected	20635	14729	22086	35195	12533
Independent	1978	1981	3116	732	1197
Observed (>2 $\sigma$ (I))	1866	1875	2751	696	1175
Solved using	Sir97	Shelxs97	Superflip	Sir92	Sir92
Rint	0.0279	0.0594	0.0383	0.0325	0.021
Completeness/%	99.1	99.8	60.8	99.7	98.8
Parameters	122	122	289	51	81
GOOF	1.098	1.086	1.173	1.16	1.189
R1 (observed)	0.0145	0.0226	0.0293	0.0490	0.0146
R1 (all)	0.0167	0.0243	0.0365	0.0505	0.0149
wR2 (all)	0.0331	0.0512	0.074	0.1661	0.0374
pmax, min/eÅ <sup>3</sup>	0.358 -0.421	0.571 -0.817	0.68 -0.528	2.423 -1.241	0.413 -0.662

**Table 5-6 HB parameters and significant interactions for anhydrous tautomeric KBA.**

	<i>D-H</i> / Å	<i>H---A</i> / Å	<i>D---A</i> / Å	$\angle DHA$ / °	sum of van der Waals radii / Å	
Form I	O1-----O4	-	-	2.814(2)	-	3.04
	O2-H1---O4	0.90(3)	1.64(3)	2.5261(16)	171(3)	3.04
Form II	O1-H1---O3	0.79(4)	1.78(4)	2.553(2)	166(4)	3.04
	O1-----Br2	-	-	3.282(2)	-	3.37
	O2-----O3	-	-	2.940(2)	-	3.04
	O2-----Br2	-	-	3.144(2)	-	3.37

**Table 5-7 K<sup>+</sup> interactions for anhydrous tautomeric KBA polymorphs.**

	<i>D---A</i>	<i>D---A</i> / Å	Sum of van der Waals radii / Å	
Form I	D4	K1-----K1	3.7496(5)	5.5
	D4	K1-----K1	3.9963(5)	5.5
	C1 HBA <sup>-</sup>	K1-----O1	2.7693(2)	3.27
	C1 HBA <sup>-</sup>	K1-----O3	2.8546(3)	3.27
	B2 HBA <sup>-</sup>	K1-----O1	2.8734(1)	3.27
		K1-----O2	3.3611(1)	3.27
	B2 HBA <sup>-</sup>	K1-----O3	2.8861(2)	3.27
		K1-----O4	2.9018(1)	3.27
	A2 HBA <sup>-</sup>	K1-----O2	2.7823(4)	3.27
		K1-----Br2	3.5780(1)	4.6
	A2 HBA <sup>-</sup>	K1-----O4	2.6825(1)	3.27
		K1-----Br1	3.4450(1)	4.6
Form II	D2	K1-----K1	3.6793(9)	5.5
	D4	K1-----K1	4.0576(8)	5.5
	C1 H <sub>2</sub> BA	K1-----O1	2.732(2)	3.27
	C1 H <sub>2</sub> BA	K1-----O2	2.728(2)	3.27
	B2 BA <sup>2-</sup>	K1-----O3	2.784(2)	3.27
		K1-----O3	2.879(2)	3.27
	B2 BA <sup>2-</sup>	K1-----O4	2.807(2)	3.27
		K1-----O4	2.857(2)	3.27
	A2 BA <sup>2-</sup>	K1-----O4	2.826(2)	3.27
		K1-----Br2	3.3168(6)	4.6

**Table 5-8 Significant carbon contact distances for anhydrous tautomeric KBA polymorphs.**

	C-C Distances		C-O and C-Br Distances	
Form I			HBA <sup>-</sup>	
	C1-C2	1.4215(22)	C1-Br1	1.8935(15)
	C2-C3	1.5206(22)	C2-O1	1.2343(19)
	C3-C4	1.3511(22)	C3-O2 (H1)	1.3222(18)
	C4-C5	1.4488(21)	C4-Br2	1.8844(15)
	C5-C6	1.5371(22)	C5-O3	1.2304(19)
	C6-C1	1.3745(22)	C6-O4	1.2718(18)
Form II			BA <sup>2-</sup>	
	C4-C5	1.388(3)	C4-Br2	1.8972(22)
	C4-C6	1.408(3)	C5-O3	1.2691(25)
	C5-C5	1.542(4)	C6-O4	1.2516(26)
	C6-C6	1.548(4)		
			H <sub>2</sub> BA	
	C1-C2	1.343(3)	C1-Br1	1.8860(20)
	C1-C3	1.453(3)	C2-O1 (H1)	1.3261(27)
	C2-C3	1.524(3)	C3-O2	1.2206(27)

**Table 5-9 HB Parameters and Significant Interactions for Hydrated KBA polymorphs.**

	<i>D-H</i> / Å	<i>H---A</i> / Å	<i>D---A</i> / Å	<i>&lt;DHA</i> / °	<i>Sum of the van der waals radii</i> / Å	
Form I	O9-H1---O1	0.94(7)	1.95(7)	2.875(4)	168(6)	3.04
	O9-H2---O4	0.74(7)	2.26(8)	2.822(5)	135(6)	3.04
	O9-H2---O3	0.74(7)	2.53(6)	3.178(4)	147(6)	3.04
	O10-H3---O9	0.80(6)	1.94(6)	2.723(4)	170(5)	3.04
	O10-H4---O1	0.7401(3)	2.1600(5)	2.8535(8)	156.36	3.04
	O11-H5---O6	0.66(7)	2.16(8)	2.798(4)	164(10)	3.04
	O11-H6---O7	0.83(9)	2.16(8)	2.872(4)	145(7)	3.04
	O11-O8	0.83(9)	2.490	3.099(4)	131.24	3.04
	O11-Br4			3.397(2)		3.37
	O12-H8---O11	0.85(11)	1.99(11)	2.805(5)	160(10)	3.04
	O12-O7			3.029(7)		3.04
	Br1-Br3			3.4158(9)		3.7
	Br2-Br4			3.4876(9)		3.7
	Form II	O3---O1		3.202(8)		3.04
		O3---O2		2.845(7)		3.04
		O3---O4		3.14(1)		3.04
O4---O4			2.96(3)		3.04	
O4---O4			3.44(3)		3.04	
O4---Br1			3.840(7)		3.37	
Form III	O1---O3		2.959(2)		3.04	
	O3-H1---O1	0.71(3)	2.41(3)	3.0269(16)	146(2)	3.04
	O3-H2---O2	0.85(3)	1.86(3)	2.7076(16)	173(3)	3.04

**Table 5-10 Carbon Contact Distances for Hydrated KBA Complex BA<sup>2-</sup> molecules**

	C-C Distances		C-O and C-Br Distances	
Form I			1_BA <sup>2-</sup>	
	C1-C2	1.387(5)		C1-BR1 1.904(4)
	C2-C3	1.551(5)		C2-O1 1.262(5)
	C3-C4	1.413(5)		C3-O2 1.244(4)
	C4-C5	1.393(5)		C4-BR2 1.902(3)
	C5-C6	1.543(5)		C5-O3 1.241(5)
	C6-C1	1.422(5)		C6-O4 1.236(4)
			2_BA <sup>2-</sup>	
	C7-C8	1.418(5)		C7-BR3 1.906(3)
	C8-C9	1.547(5)		C8-O5 1.239(4)
	C9-C10	1.393(5)		C9-O6 1.251(5)
	C10-C11	1.405(5)		C10-Br4 1.903(4)
C11-C12	1.544(5)		C11-O7 1.241(4)	
C12-C7	1.383(5)		C12-O8 1.262(5)	
Form II			BA <sup>2-</sup>	
	C1-C2	1.441(1)		C2-Br1 1.8803(79)
	C1-C3	1.527(12)		C1-O1 1.2284(97)
C2-C3	1.377(12)		C3-O2 1.2781(102)	
Form III			BA <sup>2-</sup>	
	C1-C2	1.410(2)		C2-Br1 1.8939(15)
	C1-C3	1.550(2)		C1-O1 1.2447(18)
C2-C3	1.390(2)		C3-O2 1.2587(17)	

**Table 5-11 M Distances for Hydrated KBA Complex BA<sup>2-</sup> molecules**

	<i>D</i> --- <i>A</i>	<i>D</i> --- <i>A</i> / Å	<i>Sum of the van der Waals radii</i> /Å
<b>Form I</b>			
D2	K1-----K1	4.685(3)	5.5
D4	K1-----K1	4.714(3)	5.5
D2 + HB	K1-----K4	4.0324(16)	5.5
D3 + HB	K1-----K4	4.2492(16)	5.5
D2 + PHB	K2-----K3	4.0328(17)	5.5
D3	K2-----K4	3.990(2)	5.5
D2 + 2HB	K2-----K4	4.455(3)	5.5
D2	K3-----K3	4.728(3)	5.5
- + 2HB + PHB	K3-----K3	5.406(3)	5.5
D2	K3-----K3	5.890(3)	5.5
D1 + HB + PHB	K3-----K4	4.937(2)	5.5
C1 H <sub>2</sub> O	K1-----O10	2.830(3)	3.27
C1 H <sub>2</sub> O	K1-----O10	2.877(4)	3.27
C2 BA1 <sup>2-</sup>	K1-----Br1	3.551(2)	4.6
C2 BA2 <sup>2-</sup>	K1-----Br3	3.736(1)	4.6
A2 BA1 <sup>2-</sup>	K1-----O4	2.683(3)	3.27
	K1-----Br1	3.544(2)	4.6
A2 BA2 <sup>2-</sup>	K1-----O5	2.669(3)	3.27
	K1-----Br3	3.675(2)	4.6
C1 H <sub>2</sub> O	K2-----O12	2.827(4)	3.27
C1 BA2 <sup>2-</sup>	K2-----O8	2.650(3)	3.27
B2 BA1 <sup>2-</sup>	K2-----O1	2.918(3)	3.27
	K2-----O2	2.777(3)	3.27
A2 BA1 <sup>2-</sup>	K2-----O3	2.686(3)	3.27
	K2-----Br2	3.635(2)	4.6
A2 BA2 <sup>2-</sup>	K2-----O6	2.734(3)	3.27
	K2-----Br4	3.5468(15)	4.6
C1 H <sub>2</sub> O	K3-----O11	2.755(4)	3.27
C1 H <sub>2</sub> O	K3-----O12	2.797(4)	3.27
C2 BA2 <sup>2-</sup>	K3-----Br4	3.659(2)	4.6
C2 BA2 <sup>2-</sup>	K3-----Br4	3.749(3)	4.6
A2 BA1 <sup>2-</sup>	K3-----O2	2.682(3)	3.27
	K3-----Br2	3.439(2)	4.6
A2 BA2 <sup>2-</sup>	K3-----O7	2.660(3)	3.27
	K3-----Br4	3.488(2)	4.6
C1 H <sub>2</sub> O	K4-----O9	2.880(3)	3.27
C1 H <sub>2</sub> O	K4-----O10	2.939(3)	3.27
B2 BA1 <sup>2-</sup>	K4-----O1	2.988(3)	3.27
	K4-----O2	3.354(3)	3.27
B2 BA1 <sup>2-</sup>	K4-----O3	2.866(3)	3.27
	K4-----O4	3.050(3)	3.27
B2 BA2 <sup>2-</sup>	K4-----O5	2.760(3)	3.27
	K4-----O6	2.687(3)	3.27
A2 BA2 <sup>2-</sup>	K1-----O8	2.672(3)	3.27
	K1-----Br3	3.633(2)	4.6

**Table 5-12 M Distances for Hydrated KBA Complex BA<sup>2-</sup> molecules**

	<i>D</i> --- <i>A</i>	<i>D</i> --- <i>A</i> / Å	<i>Van Der waals</i> <i>radii</i> / Å
Form II			
D2	K1-----K1	3.120(3)	5.5
D4	K1-----K1	3.277(3)	5.5
D1	K1-----K1	5.830(1)	5.5
C1 H <sub>2</sub> O	K1-----O4	2.919(2)	3.27
C1 BA <sup>2-</sup>	K1-----O1	2.872(2)	3.27
A2 BA <sup>2-</sup>	K1-----O2	3.011(5)	3.27
	K1-----Br1	3.7052(11)	4.6
A2 BA <sup>2-</sup>	K1-----O2	3.011(5)	3.27
	K1-----Br1	3.7052(11)	4.6
Form III			
D4	K1-----K1	3.7885(1)	5.5
D1	K1-----K1	4.9201(4)	5.5
C1 H <sub>2</sub> O	K1-----O3	2.6849(13)	3.27
C1 H <sub>2</sub> O	K1-----O3	2.8520(13)	3.27
C1 H <sub>2</sub> O	K1-----O3	3.2778(13)	3.27
C1 BA <sup>2-</sup>	K1-----O1	2.7706(11)	3.27
C1 BA <sup>2-</sup>	K1-----O1	2.8802(12)	3.27
A2 BA <sup>2-</sup>	K1-----O2	2.7278(11)	3.27
	K1-----Br1	3.6201(4)	4.6
A2 BA <sup>2-</sup>	K1-----O2	2.9977(12)	3.27
	K1-----Br1	3.7999(4)	4.6

## 5.3 Isomorphous Chloranilic acid and Bromanilic Acid Complexes

In addition to potassium, other group 1 metals were crystallised alongside CA and BA in attempts to obtain other MXA complexes. A number of isomorphous complexes, were obtained, differing in the identity of the metal ion incorporated into the structure.

The following section presents the four sets of isomorphous structures obtained during this investigation. Each set contains at least two complexes containing the metal ions,  $K^+$ ,  $Rb^+$  and  $Cs^+$ . The first set contains three MBA complexes and the remaining three sets contain two CA complexes. The subtle effects of the metal identity on structural packing are discussed.

### 5.3.1 2:1 Metal-Bromanilic Acid Dihydrate Complexes

In the previous section, a structural analysis of hydrated KBA polymorph form I was presented. Crystals were also obtained for the related Rb and Cs isomorphous complexes. The experimental conditions under which the three related complexes were obtained is presented in Table 5-26. As in the hydrated KBA polymorphs the conditions under which the various complexes were obtained were found to vary. The KBA complex was obtained using a 1:2 starting material ratio of BA to metal-containing salt at 50°C, whereas the RbBA and CsBA complexes were obtained from a reaction mixture of 1:1 at room temperature. The RbBA and CsBA complexes were obtained using water to dissolve the metal carbonate and ethanol and methanol, respectively, to dissolve the BA, whereas KBA was obtained from a solution of KOH and BA both dissolved in water. Screening of single crystals of samples obtained under other conditions also indicated the presence of these complexes. Due to the structural similarity of the three complexes more work is required to document the specific conditions under which particular complexes appear. The crystallographic data for the three complexes are presented in Table 5-25. As expected the three lattice constants  $a$ ,  $b$ , and  $c$  show a systematic increase with increased size of metal. A comparison of the  $BA^{2-}$  and  $K^+$  ion

environments of the KBA and RbBA complexes and the RbBA and CsBA complexes are illustrated in Figure 5-54 and 5-55.

In both cases the overlay of the BA molecules is very similar; the main differences seem to occur around the  $M \cdots M$  chain. This suggests, perhaps as would be expected, that the effect of incorporating a larger metal ion gives rise to an increase in distance between the  $M^+$  ions, thus affecting the M interactions most. In the previous section the  $K \cdots K$  distances observed in these complexes were shown to be short and therefore more significant in comparison to other MOFs; an increase in M size would therefore cause an increased repulsion and thus an increase in  $M \cdots M$  distances.

A comparison of the intra-molecular bond lengths within the  $BA^{2-}$  molecules are presented in Table 5-14. The distances of the  $M \cdots M$ ,  $M \cdots O$  and  $M \cdots Br$  interactions, Table 5-15, the distances of the HB,  $O \cdots O$  and  $Br \cdots Br$  interactions, Table 5-13. The crystallographic data are provided in Table 5-25.

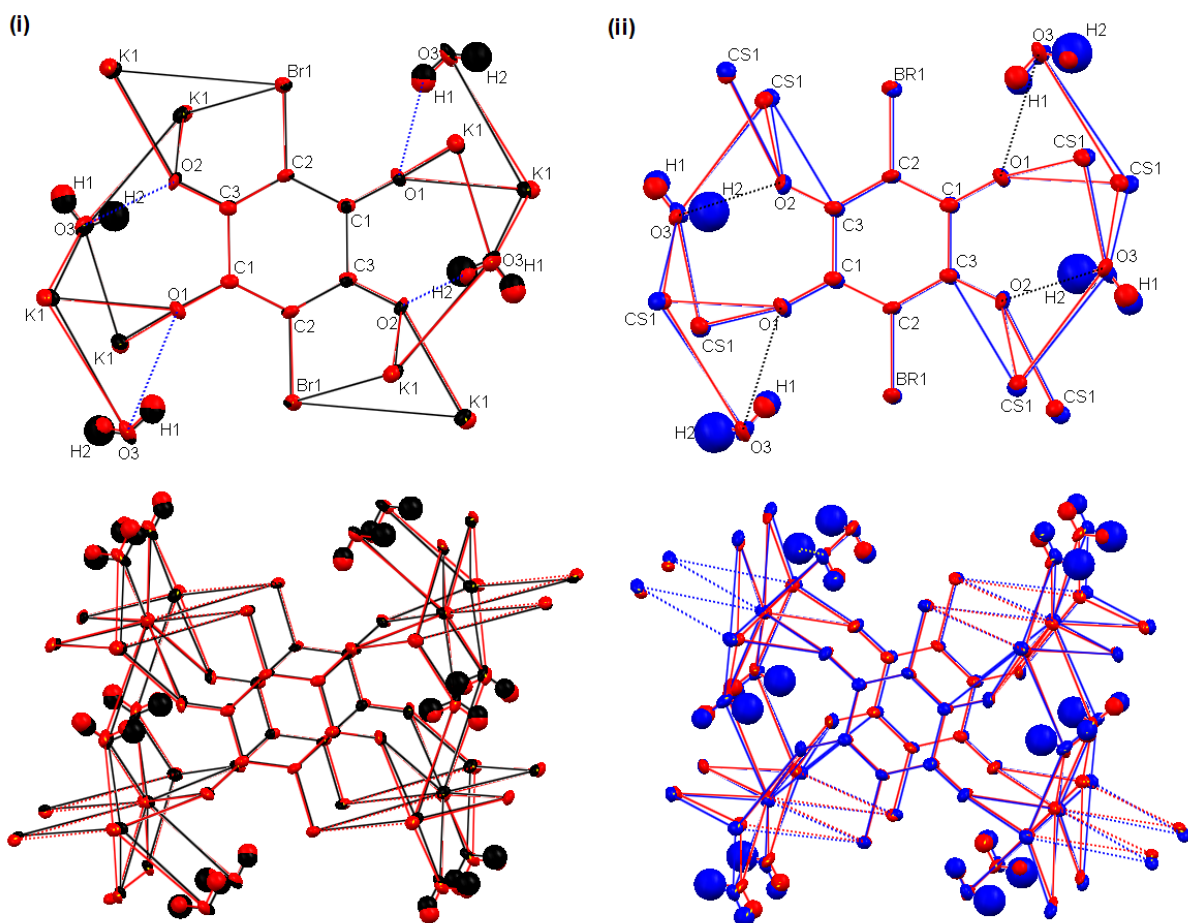


**Figure 5-54 Comparison of BA<sup>2-</sup> environments and interaction distances in (i) KBA and RbBA and (ii) RbBA and CsBA complexes. KBA (black), RbBA (red), CsBA (blue).**

The intra-molecular distances for the BA<sup>2-</sup> molecules (Table 5-14) clearly show that each complex contains the delocalised BA<sup>2-</sup> arrangement discussed elsewhere. Although the lengths of the C–Br, and four C–O delocalised bonds display characteristic values of approximately 1.90 and 1.25 Å in the K and Cs complexes, in the Rb complex the C–Br distance was 1.933(13) Å and the unusually uneven C–O distances were 1.239(14) and 1.276(15) Å, all the C–C bonds in the delocalised carbon ring were also noticeably shorter than usual.

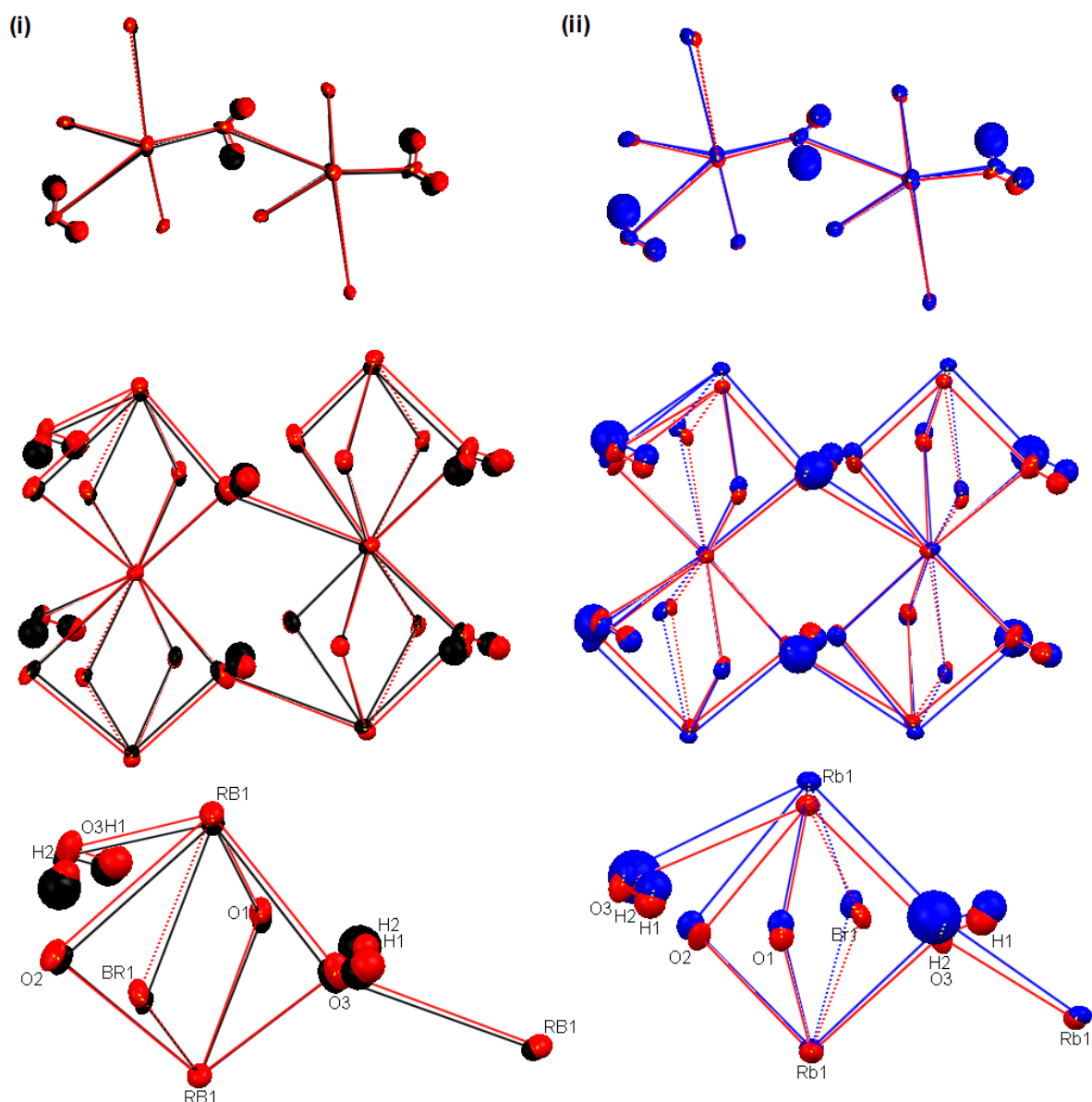


**Figure 5-55 Comparison of  $M^+$  environments and interaction distances in (i) KBA and RbBA and (ii) RbBA and CsBA complexes. KBA (black), RbBA (red), CsBA (blue).**

The HB parameters and significant Interactions within the complexes are compared in Table 5-15. As the size of the incorporated metal is increased, the distance between the two interacting  $Br \cdots Br$  and  $O1 \cdots O3$  atoms is also increased. These interactions were previously illustrated in Figure 5-25. The shorter and more significant of the two  $Br \cdots Br$  interactions increases from 3.5450(2) Å in the KBA complex, to 3.7039(5) Å in RbBA to 3.9628(4) Å in CsBA. This is also the case for the  $O1 \cdots O3$  interaction, the length of which increases from 2.959(2) to 3.070(4) to 3.1486(1) Å. In each case the interaction goes from a significant to a non-significant interaction when compared with the associated sum of the van der

Waals radii of 3.7 and 3.04Å, respectively. This is a consequence of the increased distance, along the a-axis, of the short M-M interaction distance due to the increased repulsion from increased size of ion. There is one water molecule in the asymmetric unit for this isomorphous series of complexes, and two resulting HB interactions within each structure. As the size of the incorporated metal is increased the O3-H1...O1 HB interaction becomes more significant, i.e. shorter in length and with D-H--A angle nearer to 180°, and the O3-H1...O2 HB interaction becomes less significant, i.e. the angle decreases and length increases.

An examination of the metal interactions within each complex (Table 5-15), shows that all M...M, M...O and interactions increase in length as the size of the incorporated metal is increased. The van der Waals radii are not available for Rb and Cs, however it can be remarked that the M...M interactions for all three complexes remain within those associated with the K<sup>+</sup> ion. A comparison of the change in the M...M distances between the KBA and RbBA complexes and between the RbBA and CsBA complexes on increasing the size of the incorporated metal is also presented. The change in the latter is significantly greater, also reflected in the earlier comparisons of the structure overlays (Figures 5-54 and 5-55).

The most significant change is in the length of the comparatively shorter D4 M...M interaction distance which provides the backbone of the M<sup>+</sup> chain, along the a - axis. This has consequently affected the other atoms contributing to the D4 unit. The longer D2 M...M interaction and associated M-O3 interactions are affected less by the inclusion of a larger M in the structure. The D4 M...M chain also includes two M-Br interactions. It has therefore been established that the length of the shorter, stronger M...M interactions increase most significantly when a larger group 1 metal is incorporated into the structure, thus affecting surrounding M interactions. The change in the HBs and significant interactions mentioned above can therefore also be understood as a consequence of the increase in M...M distance.

**Table 5-13 HB parameters and significant interactions for  $2M^+(C_6O_4Br_2)^{2-} \cdot 2H_2O$  isomorphous structures (M = K, Rb, Cs).**

D-----A	KBA				RbBA				CsBA				Sum of van der Waals radii / Å
	D-H/ Å	H---A/ Å	D---A/ Å	<DHA/ °	D-H/ Å	H---A/ Å	D---A/ Å	<DHA/ °	D-H/ Å	H---A/ Å	D---A/ Å	<DHA/ °	
O3-H1---O1	0.71(3)	2.41(3)	3.027(2)	146(2)	0.76(4)	2.28(5)	2.951(4)	149(4)	0.77(5)	2.21(5)	2.907(4)	151(5)	3.04
O3-H2---O2	0.85(3)	1.86(3)	2.708(2)	173(3)	0.75(4)	1.98(4)	2.720(4)	174(4)	0.69(6)	2.08(6)	2.737(3)	159(7)	3.04
O1-----O3			2.959(2)				3.070(4)				3.1486(1)		3.04
Br1-----Br1			3.5450(2)				3.7039(5)				3.9628(4)		3.7
Br1-----Br1			3.7168(2)				3.8121(5)				4.0744(4)		3.7

**Table 5-14 Intra-molecular bond lengths for  $2M^+(C_6O_4Br_2)^{2-} \cdot 2H_2O$  isomorphous structures (M = K, Rb, Cs).**

	KBA	RbBA	CsBA
<i>C-C Distances</i>			
C1-C2	1.410(2)	1.393(18)	1.405(4)
C2-C3	1.390(2)	1.381(19)	1.397(4)
C3-C1	1.550(2)	1.528(18)	1.549(4)
<i>C-O and C-Br Distances</i>			
C1-O1	1.245(2)	1.239(15)	1.249(4)
C2-Br1	1.894(2)	1.933(13)	1.902(3)
C3-O2	1.259(2)	1.276(15)	1.258(4)

**Table 5-15 M Distances for  $2M^+(C_6O_4Br_2)^{2-} \cdot 2H_2O$  isomorphous structures (M = K, Rb, Cs).**

<i>D-----A</i>		<i>KBA</i>	<i>Sum of van der waals radii / Å</i>	<i>RbBA</i>	<i>Sum of van der waals radii / Å</i>	<i>CsBA</i>	<i>Sum of van der waals radii / Å</i>	<i>K/RbBA M-M change / Å</i>	<i>Rb/CsBA M-M change / Å</i>
D4 + 2HB	M1-----M1	3.7885(5)	5.5	3.9514(2)	-	4.2582(3)	-	0.1629	0.3068
D1 + 2HB	M1-----M1	4.9201(4)	5.5	5.0005(3)	-	5.1191(3)	-	0.0804	0.1186
C1 H <sub>2</sub> O	M1-----O3	2.6849(13)	3.27	2.814(3)	-	2.999(2)	-	0.1289	0.1855
C1 H <sub>2</sub> O	M1-----O3	2.8520(13)	3.27	2.971(3)	-	3.134(3)	-	0.1188	0.1634
C1 H <sub>2</sub> O	M1-----O3	3.2778(13)	3.27	3.291(3)	-	3.3794(3)	-	0.0136	0.088
C1 BA <sup>2-</sup>	M1-----O1	2.7706(11)	3.27	2.914(2)	-	3.120(2)	-	0.1433	0.206
C1 BA <sup>2-</sup>	M1-----O1	2.8802(12)	3.27	2.981(2)	-	3.125(2)	-	0.1007	0.1391
A2 BA <sup>2-</sup>	M1-----O2	2.7278(11)	3.27	2.851(2)	-	3.025(2)	-	0.1231	0.1736
	M1-----Br1	3.6201(4)	4.6	3.6838(05)	-	3.8021(4)	-	0.0637	0.1183
A2 BA <sup>2-</sup>	M1-----O2	2.9977(12)	3.27	3.132(3)	-	3.35(2)	-	0.134	0.2184
	M1-----Br1	3.7999(4)	4.6	3.7586(5)	-	3.8456(4)	-	-0.0413	0.087

### 5.3.2 2:1 metal – chloranilic acid monohydrate complexes



An isomorphous pair of K and Rb 2:1 CA monohydrate complexes were obtained as described in Table 5-26. The synthesis and recrystallisation conditions were identical with the exception of the identity of the anion in the metal containing starting materials, which were KOH and RbCO<sub>3</sub>. Although the structures for both these complexes were previously solved in 1972 by Herbstein and Kaftory,<sup>147</sup> no structural analysis was given. The following analysis was carried out using data collected on a Rigaku R-axis/RAPID and a Bruker Nonius Kappa CCD diffractometer, respectively, at 100K.

The asymmetric unit, for both complexes, contains half of a CA<sup>2-</sup> molecule, with an inversion centre located in the centre of the carbon ring, one M<sup>+</sup> ion, and one water molecule (Figure 5-56).

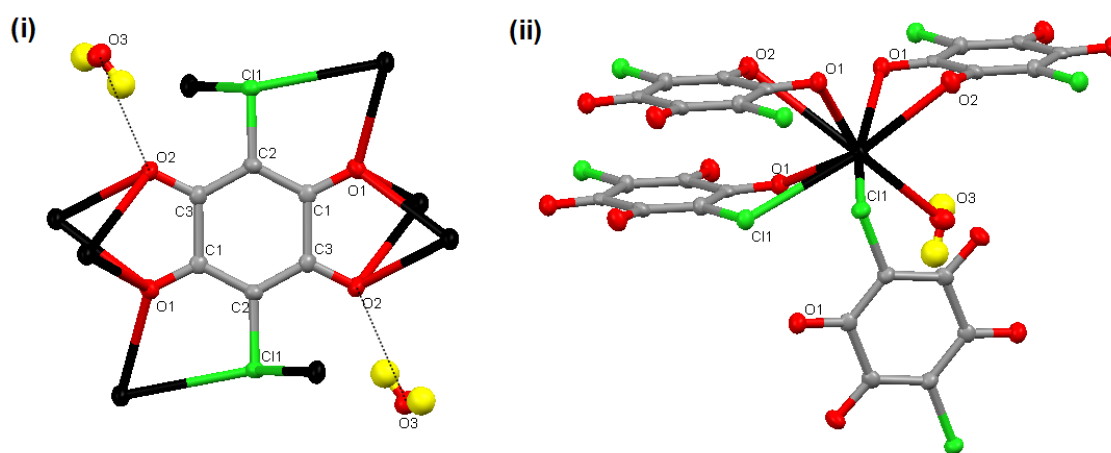


Figure 5-56  $2M^+(C_6O_4Cl_2)^{2-} \cdot H_2O$  Isomorphous structures ( $M = K, Rb$ ); environment of (i)  $CA^{2-}$  molecule and (ii)  $M^+$  ion.

Due to the inversion centre, each identical half of the CA<sup>2-</sup> molecule has the same two metal coordinating units giving an overall coordination of two (A4 +B1). In each structure, the deprotonated carbonyl group (identified by the longest C-O distance) acts as a proton acceptor in the two symmetry equivalent moderate O3w–H1···O2 HBs with the nearby water molecule.

Each  $M^+$  ion is coordinated to four  $CA^{2-}$  molecules: one monodentate C2, two bidentate B2 and one bidentate A2, and to one water molecule. The carbon rings of the three coordinated bidentate molecules are co-planar with one another. Each  $M^+$  ion is hence coordinated to 8 other atoms in total: six oxygen atoms and two chlorine atoms. In the KCA complex, the K–O bond lengths range from 2.6913(6) - 3.2026(6) Å, with the two K–Cl bond lengths of 3.1734(8) Å and 3.3044(7) Å. In the RbCA complex, the Rb–O bond lengths range from 2.8265(9) - 3.381(1) Å with two Rb–Cl bond lengths of 3.288(1) Å and 3.350(1) Å. As expected, due to the larger radii the bond lengths between the metal and coordinating atoms are larger in the RbCA complex.

The resulting structure is a three dimensional network (Figure 5-57), which like the previous structures reported in this work can be broken down into  $CA^{2-}$  and  $M^+$  planes.

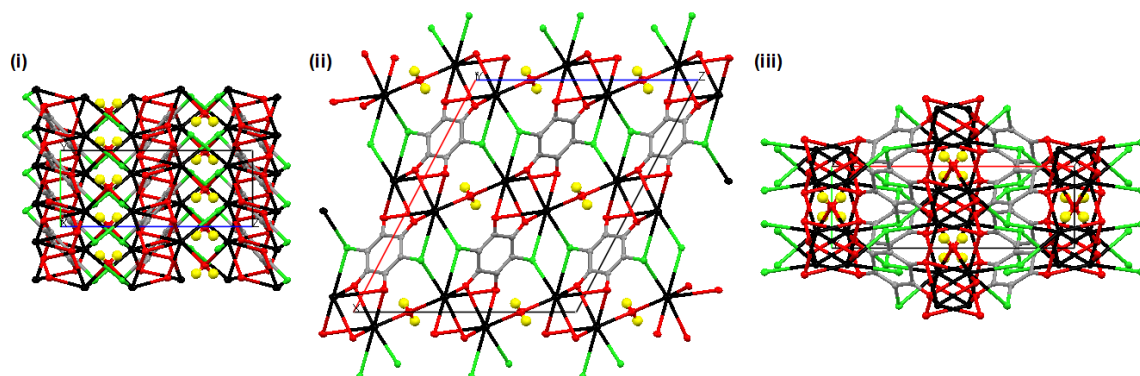
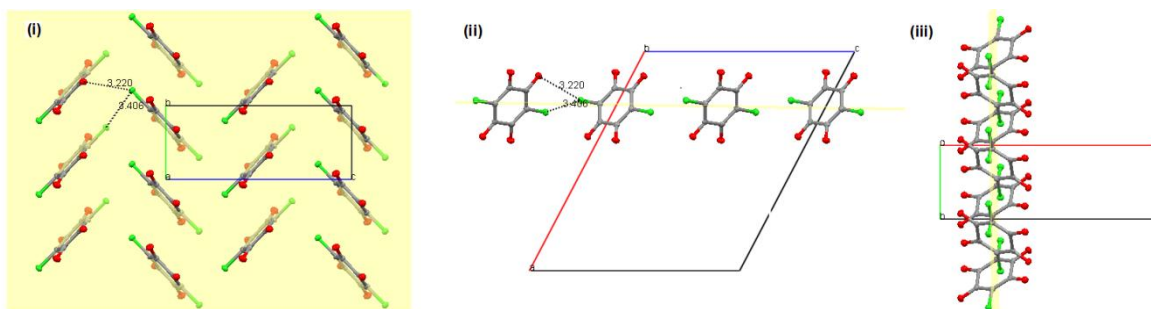


Figure 5-57  $2M^+(C_6O_4Cl_2)^{2-} \cdot H_2O$  Isomorphous structures ( $M = K, Rb$ ), viewed along (i)  $a$ - (ii)  $b$ - and (iii)  $c$ - axes.

The  $CA^{2-}$  plane, as viewed along the  $a$ -,  $b$ -, and  $c$ - axes, is illustrated in Figure 5-58.



**Figure 5-58**  $2M^+(C_6O_4Cl_2)^{2-} \cdot H_2O$  Isomorphous structures ( $M = K, Rb$ ),  $CA^{2-}$  plane viewed along (i)  $a$ - (ii)  $b$ - and (iii)  $c$ -axes.  $M^+$  ions and water molecules excluded for clarity.

The plane cuts down the centre of the  $CA^{2-}$  molecules so that the two symmetry related Cl atoms lie on the plane. Within the planes, there are  $O1 \cdots Cl1$  and  $Cl1 \cdots Cl1$  interactions, Table 5-17. The  $O1 \cdots Cl1$  distances are 3.2199(8) and 3.288(2) Å, and the  $Cl1 \cdots Cl1$  distances are 3.4056(5) and 3.479(2) Å in the KCA and RbCA complexes, respectively. Both interaction distances increase on the incorporation of a larger metal, although all values remain significant in comparison with the sum of the van der Waals radii of 3.27 and 3.5 Å for the  $O \cdots Cl$  and  $Cl \cdots Cl$  interactions respectively. The  $CA^{2-}$  molecules are also connected to one another via coordination to  $K^+$  ions, which have been excluded for clarity in Figure 5-59.

The  $CA^{2-}$  planes lie along the  $bc$  plane, and are stacked along the  $a$  axis in an alternate ABAB manner, where each alternate plane is orientated inversely to the one preceding, due to the inversion centre. This is illustrated in Figure 5-59 in which the  $CA^{2-}$  molecules within the inversely stacked A and B planes are denoted by red and blue.

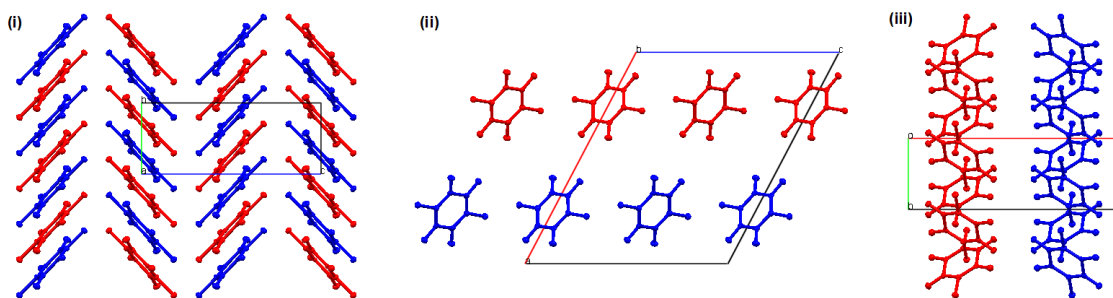


Figure 5-59  $2M^+(C_6O_4Cl_2)^{2-} \cdot H_2O$  isomorphous structures ( $M = K, Rb$ ), Two alternating  $CA^{2-}$  planes viewed along (i)  $a$ - (ii)  $b$ - and (iii)  $c$ - axes.  $M^+$  ions and water molecules excluded for clarity

The  $M^+$  planes are composed of  $M^+$  chains that run along the  $b$  axis, joined along the  $c$  axis into a plane by coordinating water molecules (Figure 5-60).

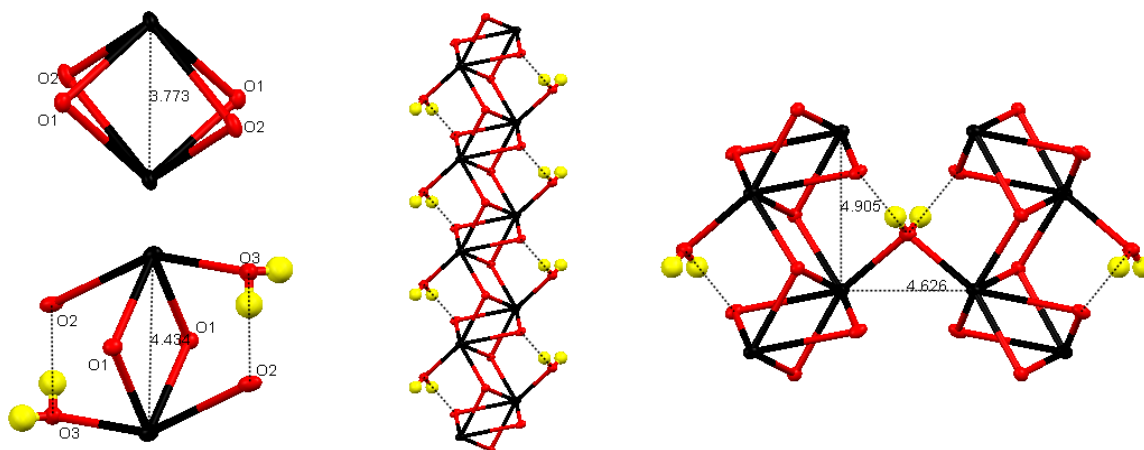


Figure 5-60  $2M^+(C_6O_4Cl_2)^{2-} \cdot H_2O$  isomorphous structures ( $M = K, Rb$ ), (i) D4 and D2 + 2HB units comprising (ii)  $M^+$  chains, joined to adjacent chains via the two additional D1 + HB and D1 M-M interactions.

Each chain is composed of two alternating D4 and D2 + 2HB  $M \cdots M$  interactions, both of which have an inversion centre in the middle. The D4 unit is composed of four O atoms, two O1 and two O2, from two symmetry related B2  $CA^{2-}$  molecules, and a D2 unit composed of two O1 atoms, from two symmetry related A2  $CA^{2-}$  molecules, and is also supported by two symmetry related O3w-H1 $\cdots$ O2 HBs. As the O2 atoms are part of both the D4 unit and the D2 HBs, the result is a particularly robust chain. The  $M \cdots M$  distances are 3.6292(2) and 3.773(1) Å for the particularly short D4 interaction, and 4.2299(9) and 4.434(2) in the D2 interaction in the KCA and RbCA complexes, respectively. Each chain connects to adjacent

chains by a two further D1 and D1 + HB units of distances 4.7070(10) and 4.7800(10) Å in the KCA complex and 4.626(1) and 4.905(5) Å in the RbCA complex.

The incorporation of the larger Rb<sup>+</sup> ion causes an increase in all M···M interaction distances with the exception of the D1 unit which decreases by 0.081Å (Table 5-16). The M···M distance most affected is the D2 +2HB unit in the M<sup>+</sup> chain, whereas the affect on the D4 and D1 + HB units is similar. All M–O interaction distances, also presented in Table 5-16, are shown to increase by a similar amount when the larger Rb<sup>+</sup> ion is incorporated into the structure.

The way in which the alternating CA<sup>2-</sup> and M<sup>+</sup> planes intersect one another in order to produce the whole structure is illustrated in Figure 5-61.

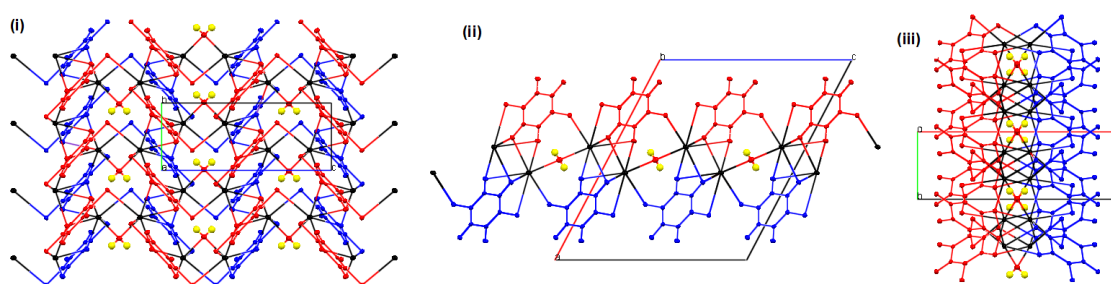


**Figure 5-61**  $2M^+(C_6O_4Cl_2)^{2-} \cdot H_2O$  isomorphous structures ( $M = K, Rb$ ), composed of intersection of two alternating  $CA^{2-}$  planes (red and blue) and  $M^+$  planes, and viewed along (i) *a*- (ii) *b*- and (iii) *c*- axes.

At these points of intersection, each  $CA^{2-}$  molecule interacts with two other  $CA^{2-}$  molecules, of opposite orientation, from the  $CA^{2-}$  planes above and below via the two  $O3w-H1 \cdots O2$  HBs (Figure 5-62). The two HBs are identical and symmetry related due to the centre of inversion within the  $CA^{2-}$  molecules and on the O3 atom.

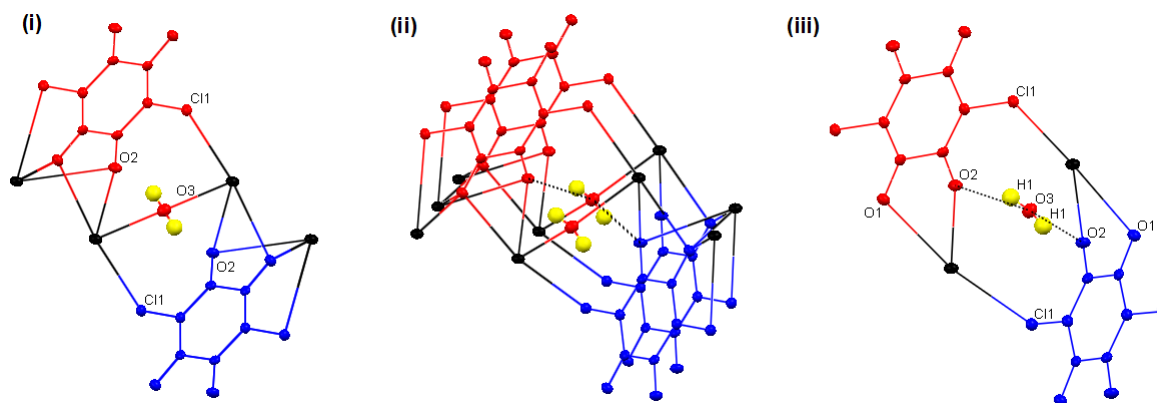


**Figure 5-62**  $2M^+(C_6O_4Cl_2)^{2-} \cdot H_2O$  isomorphous structures ( $M = K, Rb$ ), illustration of the  $O3-H1 \cdots O2$  HBs between the two differently (red and blue) orientated columns of  $CA^{2-}$  molecules within the CA planes.

The  $O \cdots O$  HB distances are 2.8368(19) and 2.797(2) Å, and the HB angles are 161.1 and 166(2)° in the KCA and RbCA complexes, respectively (Table 5-17). The H atom does not show any indication of moving across the HB but the interaction appears to become more significant with the incorporation of the larger  $Rb^+$  ion.

Also illustrated in Figure 5-62 are the A2 and C2  $M1-Cl1$  interactions (Table 5-16). The A2  $M1-Cl1$  interaction increases in distance by a similar amount to the  $M-O$  interactions when the larger  $Rb^+$  ion is incorporated into the structure, whereas the C2 interaction distance is affected significantly less.

A comparison of the KCA and RbCA complexes has been carried using the structure overlay tool in Mercury<sup>192</sup> (Figure 5-63). Overall, this shows that there are no significant differences in the positions of the atoms due to the incorporation of the larger metal. An overlay of the  $CA^{2-}$  molecules suggests that the intra-molecular  $CA^{2-}$  bond lengths are very similar. This is confirmed in Table 5-18 which shows that both complexes contain the delocalised  $CA^{2-}$  structure. Table 5-18 also suggests, in accordance with the overlays of the  $M^+$  planes connected by the O3w HBs, and the two  $CA^{2-}$  molecules connected by the O3w HBs, as in earlier findings that the main effect of the increased  $Rb^+$  ion size was in the  $M \cdots M$  and  $M-O$  distances and that all other effects are in turn a consequence of these.

The most affected  $M\cdots M$  interactions were as in the previous isomorphous series, those comprising the  $M^+$  chain; the D2 and short D4 interactions, thus in turn affecting the associated  $M-O$  coordination distances. Interestingly the D1  $M\cdots M$  interactions connecting the  $M^+$  chains via O3w molecules, were shown to decrease in length, the accumulated effect of which strengthened the O3w–H1 $\cdots$ O2 HBs.

On incorporating a larger metal into the structure, the shorter  $M\cdots M$  interactions have been shown to increase in length, most likely due to the larger repulsion felt by the two interacting metals. In this series the longer  $M\cdots M$  distance has also been shown to decrease on the incorporation of a larger metal. Although this may be another consequence of the more significant D4 and D2  $M-M$  repulsion interaction caused by a larger metal, it may also be due to an attraction due to the larger interacting ions. The incorporation of specific metals may enable the tuning of specific interactions to have increased or decreased length.

**Table 5-16 M Distances for  $2M^+(C_6O_4Cl_2)^{2-} \cdot H_2O$  isomorphous structures (M = K, Rb).**

		KCA	Sum of the van der Waals radii / Å	RbCA	Sum of the van der Waals radii / Å	Rb/CsCA M-M change / Å
D4	M1-----M1	3.6292(2)	5.5	3.773(1)	-	0.1438
D2 + 2HB	M1-----M1	4.2299(9)	5.5	4.434(2)	-	0.2041
D2	M1-----M1	4.7070(10)	5.5	4.626(1)	-	-0.081
D1 + HB	M1-----M1	4.7800(10)	5.5	4.905(5)	-	0.125
C1 H <sub>2</sub> O	M1-----O3	2.7909(4)	3.27	2.8977(16)	-	0.1068
C2 CA <sup>2-</sup>	M1-----Cl1	3.3044(7)	4.5	3.3500(14)	-	0.0456
B2 CA <sup>2-</sup>	M1-----O1	2.8937(5)	3.27	3.0552(25)	-	0.1615
	M1-----O2	3.2026(6)	3.27	3.3808(16)	-	0.1782
B2 CA <sup>2-</sup>	M1-----O1	2.8370(8)	3.27	3.0041(13)	-	0.1671
	M1-----O2	2.6913(6)	3.27	2.8265(14)	-	0.1352
A2 CA <sup>2-</sup>	M1-----O1	2.7082(4)	3.27	2.8422(22)	-	0.134
	M1-----Cl1	3.1734(8)	4.5	3.2875(11)	-	0.1141

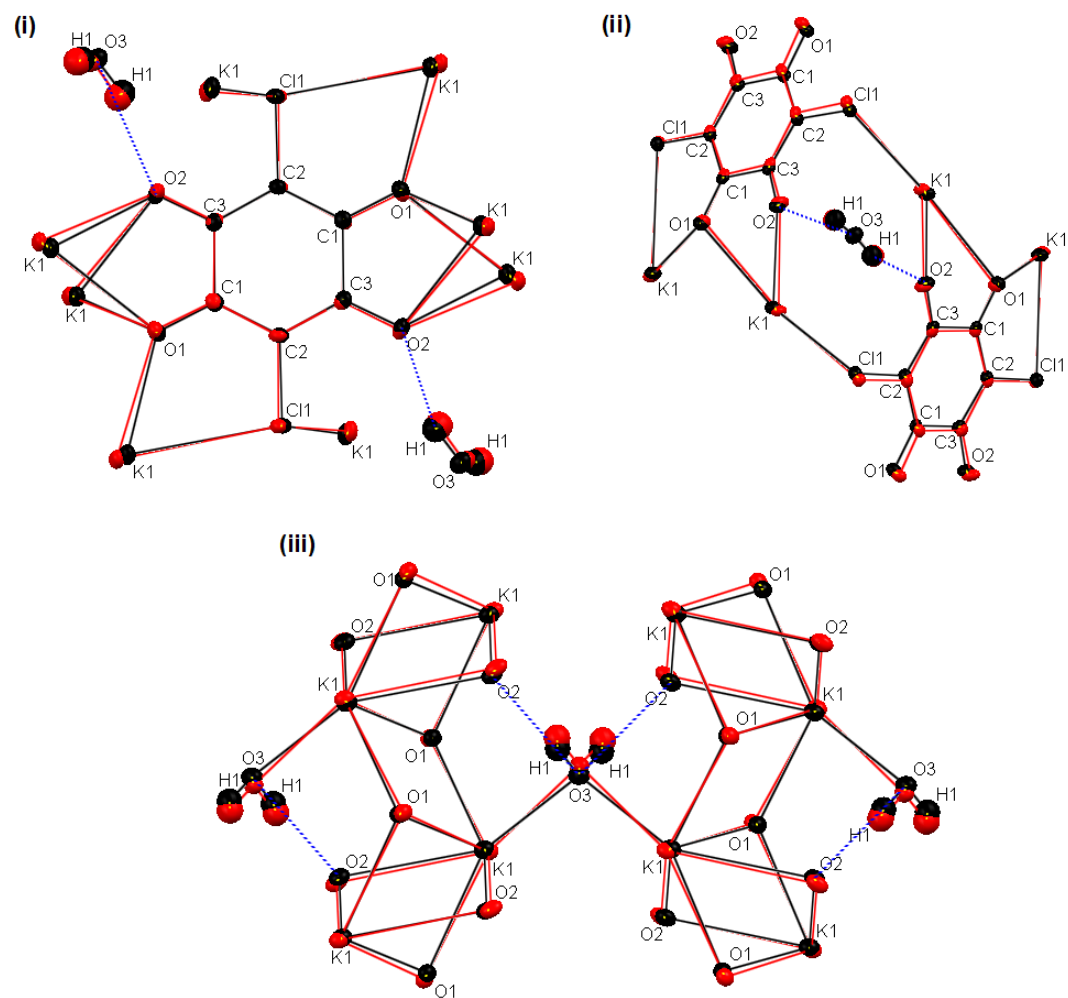


Figure 5-63  $2M^+(C_6O_4Cl_2)^{2-} \cdot H_2O$  Isomorphous structures ( $M = K, Rb$ ), Comparison of KCA (black) and RbCA (red) complexes; overlay of (i)  $CA^{2-}$  molecules (ii)  $M^+$  planes connected by the O3w HBs and (iii) two  $CA^{2-}$  molecules connected by the O3w HBs.

**Table 5-17 HB parameters and significant interactions for  $2M^+(C_6O_4Cl_2)^{2-}$  H<sub>2</sub>O isomorphous structures (M = K, Rb).**

D-----A	KCA				RbCA				Sum of van der waals radii / Å
	D-H/ Å	H---A/ Å	D---A/ Å	<DHA/ °	D-H/ Å	H---A/ Å	D---A/ Å	<DHA/ °	
O1---Cl1			3.2199(8)				3.288(2)		3.27
O3-H1---O2	0.82	2.05	2.8368(19)	161.1	0.84(2)	1.97(2)	2.797(2)	166(2)	3.04
Cl1---Cl1			3.4056(5)				3.479(2)		3.5

**Table 5-18 Intra-molecular bond lengths for  $2M^+(C_6O_4Cl_2)^{2-}$  H<sub>2</sub>O isomorphous structures (M = K, Rb).**

	KCA	RbCA
<i>C-C Distances / Å</i>		
C1-C2	1.3979(24)	1.4063(21)
C2-C3	1.4036(24)	1.3983(21)
C3-C1	1.5451(24)	1.5477(22)
<i>C-O and C-Cl Distances / Å</i>		
C1-O1	1.2473(21)	1.2463(19)
C2-Cl1	1.7433(18)	1.7478(18)
C3-O2	1.2491(22)	1.2517(19)

### 5.3.3 1:1 metal – chloranilic acid dihydrate complexes $M^+(C_6O_4Cl_2H)^- 2H_2O$

An isomorphous pair of Rb and Cs 1:1 CA dihydrate complexes were obtained as described in Table 5-26. The only difference in the otherwise identical conditions under which the two complexes were obtained was the temperature at which crystallisation occurred; 40 and 50°C for the RbCA and CsCA complexes respectively.

The asymmetric unit, for both complexes, contains one  $HCA^-$  molecule, one  $M^+$  ion and two water molecules (Figure 5-64).

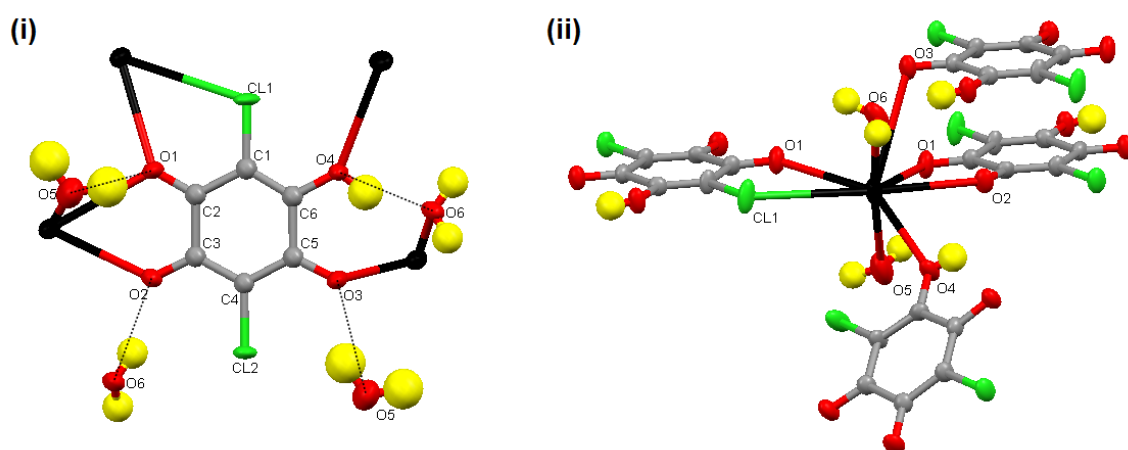


Figure 5-64  $M^+(C_6O_4Cl_2H)^- 2H_2O$  ( $M = Rb, Cs$ ) isomorphous structures; environment of (i)  $HCA^-$  molecule and (ii)  $M^+$  ion.

In both the RbCA and CsCA complexes, the H atom on the  $HCA^-$  molecule was located and refined freely, following its identification from a peak in the electron density difference Fourier map. However it was not possible to obtain a stable refinement of the two O5w and two O6w H atoms. Constraints were therefore used to fix the O–H distances to 0.9 Å. The H atoms treated in this manner produced sensible HB angles and distances.

The  $HCA^-$  molecule has no inversion centre and in total possesses three of the previously defined metal coordinating units giving an overall (A2 + B2 + B5)

coordination. The O2 and O3 carbonyls act as proton acceptors in the O5w–H4···O3 and O6w–H3···O2 HB interactions with the nearby water molecules. The hydroxyl carbonyl unit possesses the E1 HB motif and the carbonyl on the other side of the adjacent halide unit the E2 HB motif, although interaction distances and angles (Table 5-20) suggest that this is an example of a BHB in which the E2 motif is the less dominant interaction. This is illustrated in Figure 5-65 in which both the O5w H4 and H5 atoms are directed towards two O3 atoms resulting in O5w–O1, O5w–H4···O3 and O5w–H5···O3 interactions.

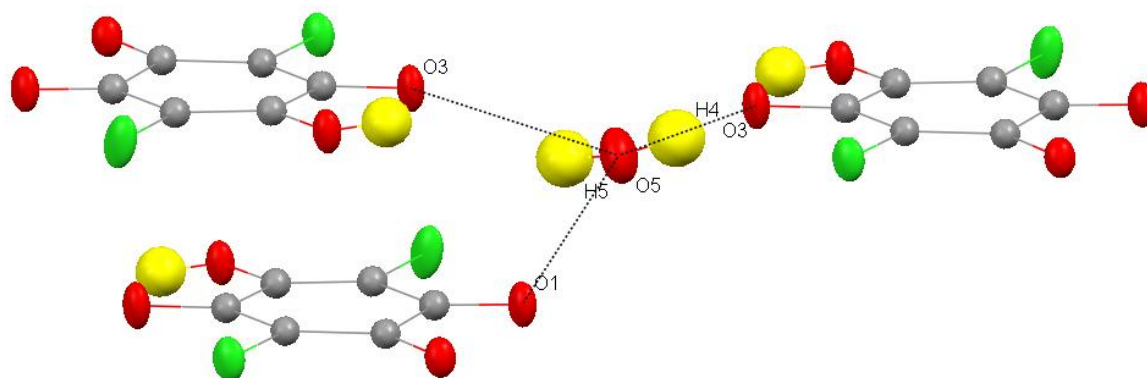


Figure 5-65  $M^+(C_6O_4Cl_2H)^- \cdot 2H_2O$  ( $M = Rb, Cs$ ) isomorphous structures, bifurcated HB.

On the incorporation of the larger  $Cs^+$  ion, the O5w–H4···O3 O···O HB distance decreases from 2.965 to 2.907 Å and the HB angle increases from 156(6) to 166(6)° in the RbCA and CsCA complexes, respectively. In comparison to the other two interactions within the BHB, this remains the most significant primary interaction.

Bearing in mind that the positions of the H atoms were fixed before refinement, the more dominant secondary O5–H5···O3 interaction distance increases from 3.077 to 3.211 Å and the angle decreases from 133.40 to 121.93° in the RbCA and CACA complexes, respectively. The less significant secondary O5–H5···O1 interaction distance increases to a far lesser extent, from 3.014 to only 3.043 Å, while the angle increases from 121.72 to 130.87° in the RbCA and CsCA complexes, respectively. This suggests that the incorporation of the larger  $Cs^+$  ion causes a

switch between which of the two secondary interactions is more dominant in the BHB.

Each  $M^+$  ion is coordinated to four  $CA^{2-}$  molecules; two monodentate C2, one bidentate B2 and one bidentate A2, and two water molecules. Each  $M^+$  ion is hence coordinated to eight other atoms in total: seven oxygen atoms and one chlorine atom. In the RbCA complex the Rb–O distances range from 2.8570 to 3.4408 Å and the Rb–Cl1 is 3.4597 Å. In the CsCA complex Cs–O distances range from 3.021(3) to 3.433(3) Å and the Rb–Cl distance is 3.605(2) Å. The van der Waals radii for the  $Rb^+$  and  $Cs^+$  ions are not available, but as these distances are within those for the sum of van der Waals radii values for K–O and K–Cl, of 3.27 and 4.5 Å, respectively, these interactions can be considered to be significant. As expected due to the increased radii of the larger ions, the distances between the  $M^+$  ions and coordinating atoms are larger in the CsCA complex (Table 5-19). The exception is the C1 M–O3 distance in which the increase is so slight it is insignificant.

The resulting three dimensional structure is presented in Figure 5-66, as viewed along the  $a$ -,  $b$ - and  $c$ - axes, and like previous structures can be broken down into  $HCA^-$  and  $M^+$  planes.

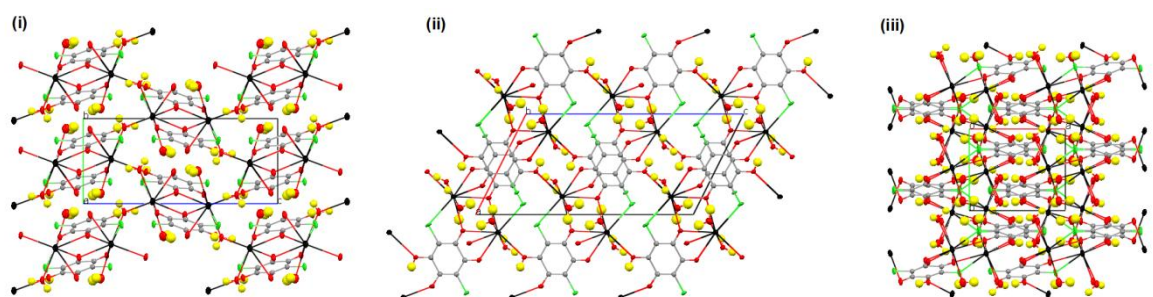


**Figure 5-66**  $M^+(C_6O_4Cl_2H)^- 2H_2O$  ( $M = Rb, Cs$ ) isomorphous structures, viewed along  $a$ -,  $b$ -, and  $c$ - axes.

The  $HCA^-$  plane, as viewed along the  $a$ -,  $b$ -, and  $c$ - axes, is illustrated in Figure 5-67, in which all other identical planes and interacting  $M^+$  ions have been excluded for clarity.

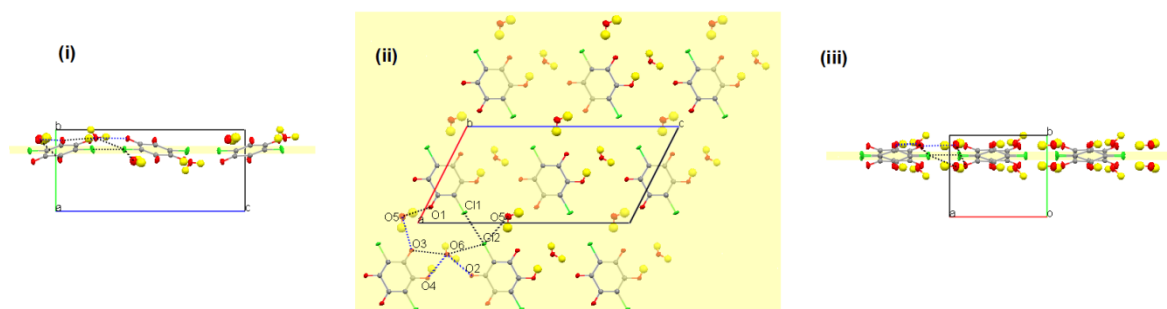


**Figure 5-67**  $M^+(C_6O_4Cl_2H)^- \cdot 2H_2O$  ( $M = Rb, Cs$ ) isostructures,  $HCA^-$  planes viewed along the (i)  $a$ -, (ii)  $b$ - and (iii)  $c$ - axes.  $M^+$  ions excluded for clarity. Significant  $Cl \cdots Cl$ ,  $Cl \cdots O$  and  $O \cdots O$  interactions are indicated.

The  $HCA^-$  planes are composed of alternating rows of  $HCA^-$  molecules that cut the plane as illustrated in Figure 5-67(i). The interactions present within the planes include the previously defined  $O5w \cdots O1$  and  $O5w-H4 \cdots O3$  interactions. The  $O6$  water atom, situated between the two alternating  $HCA^-$  rows, acts as proton acceptor for the  $HCA^-$  hydroxyl H atom in the  $O4-H1 \cdots O6$  HB, and also as proton donor in the  $O6-H3 \cdots O2$  HB on the  $HCA^-$  plane; the interaction distances and angles are similar in both the  $RbCA$  and  $CsCA$  complexes. Additional interactions present include the  $O6w \cdots O3$ , and  $O6w \cdots Cl2$ ,  $Cl2 \cdots O5w$   $Cl1 \cdots Cl2$  halogen interactions, all of which increase in distance on the incorporation of the larger  $Cs^+$  ion. The last of these is a particularly significant  $Cl \cdots Cl$  interaction of distance 3.0866(8) and 3.160(1) Å in the  $RbCA$  and  $CsCA$  complexes, respectively, well below the average of 3.387 Å and comparable to the shortest, 3.028 Å, observed in the CSD [F. H. Allen, *Acta Cryst.*, B58, 380-388, 2002].

All interactions are illustrated in Figure 5-67(ii) in which black represents  $Cl \cdots Cl$ ,  $Cl \cdots O$  and  $O \cdots O$  interactions and blue represents HB interactions, and are significant in comparison to the sum of the van der Waals radii (Table 5-20). The  $HCA^-$  molecules possess no internal symmetry although the way in which one side of the molecule interacts with another is identical to the way in which another molecule interacts with it.

Within each plane the HCA<sup>-</sup> molecules also interact via Rb<sup>+</sup> or Cs<sup>+</sup> ions, as illustrated in Figure 5-68.

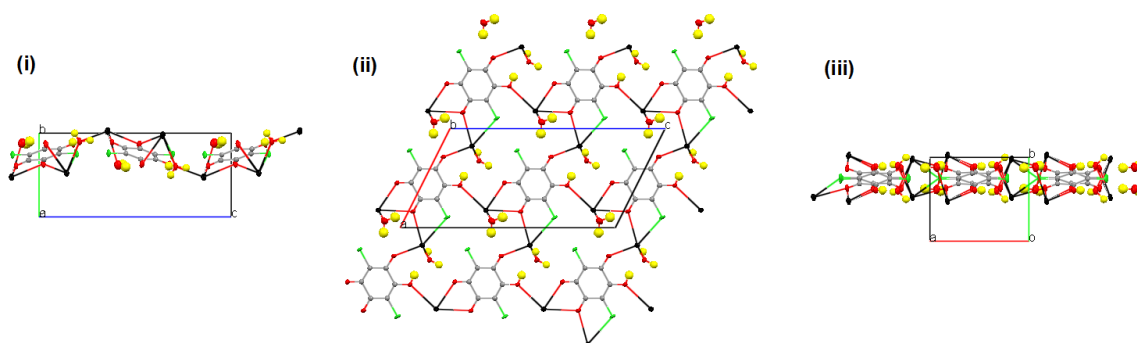


**Figure 5-68** M<sup>+</sup>(C<sub>6</sub>O<sub>4</sub>Cl<sub>2</sub>H)<sup>-</sup> 2H<sub>2</sub>O (M = Rb, Cs) isomorphous structures, HCA<sup>-</sup> planes with connecting M<sup>+</sup> ions, viewed along (i) *a*-, (ii) *b*- and (iii) *c*- axes.

These M<sup>+</sup> ions also allow the HCA<sup>-</sup> molecules to interact with HCA<sup>-</sup> molecules on other planes. The structure is composed of alternating planes inversely related to one another. This is illustrated in Figure 5-69, in which the alternate planes are coloured red and blue, and M<sup>+</sup> ions are excluded for clarity.

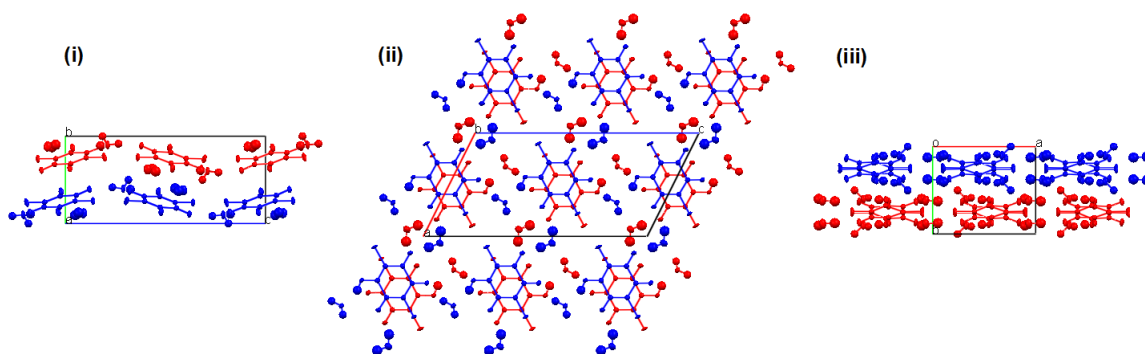


**Figure 5-69** M<sup>+</sup>(C<sub>6</sub>O<sub>4</sub>Cl<sub>2</sub>H)<sup>-</sup> 2H<sub>2</sub>O (M = Rb, Cs) isomorphous structures, inversely related alternating HCA<sup>-</sup> planes (red and blue) viewed along (i) *a*-, (ii) *b*- and (iii) *c*- axes. M<sup>+</sup> ions excluded for clarity.

As in previous structures the M<sup>+</sup> ions can be viewed as planes, this is illustrated as viewed along the *a*-, *b*-, and *c*- axes in Figure 5-70.

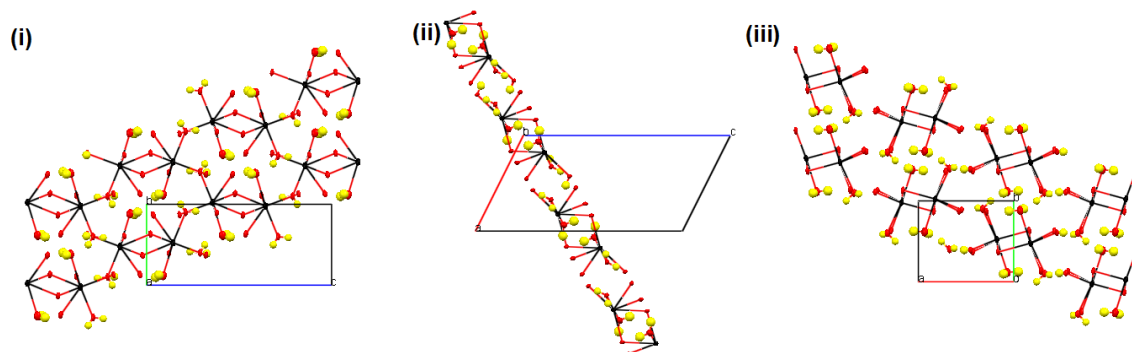


**Figure 5-70**  $M^+(C_6O_4Cl_2H)^- \cdot 2H_2O$  ( $M = Rb, Cs$ ) isostructures,  $M^+$  ions planes, viewed along (i) *a*-, (ii) *b*- and (iii) *c*- axes.

Unlike previous structures, the planes do not run along the points of intersection between the inversely orientated  $HCA^-$  planes. However by the previously defined notation, the planes are composed of  $M^+$  chains, joined to adjacent chains via many HB and significant  $O \cdots O$  interactions (Figure 5-71).

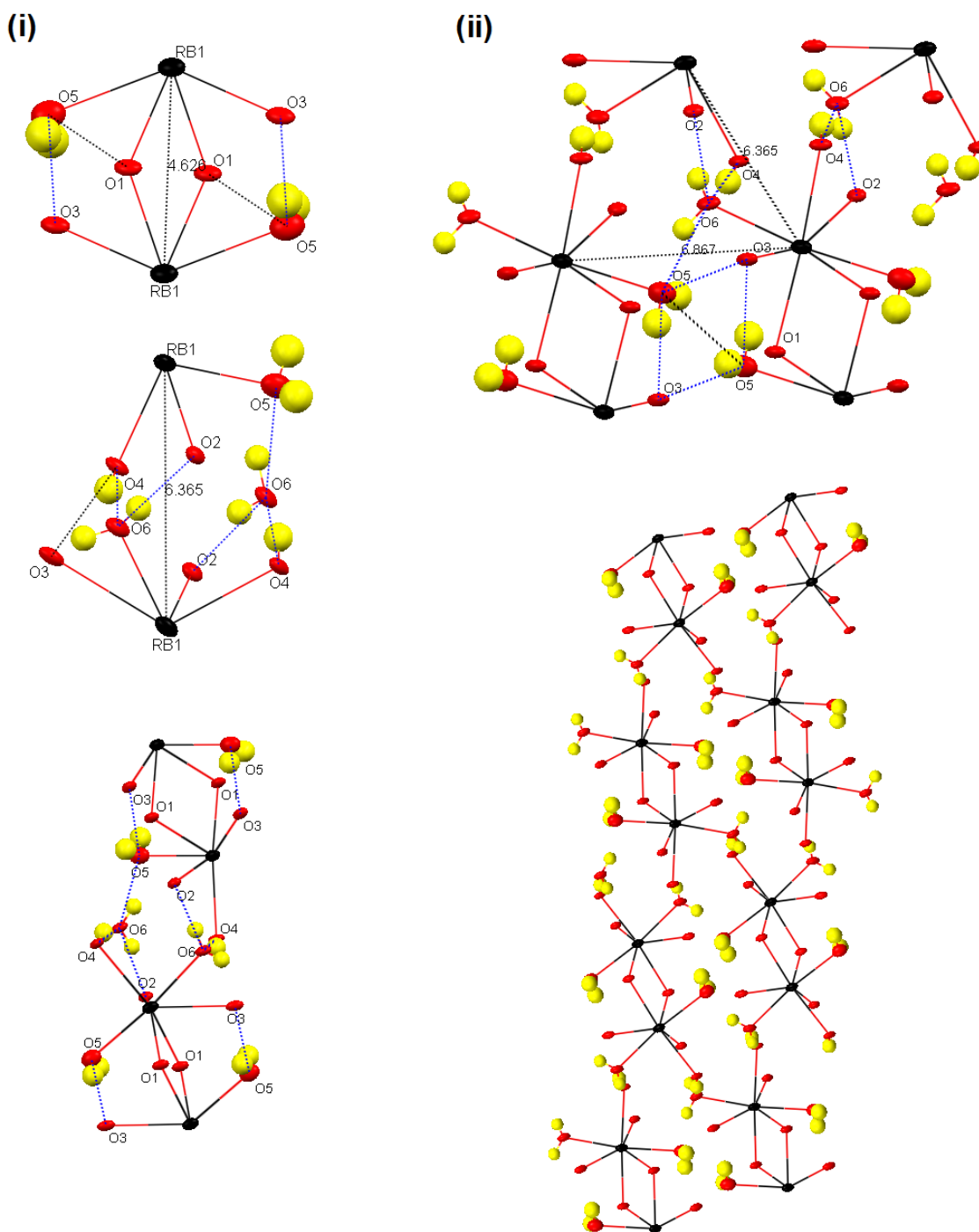


**Figure 5-71**  $M^+(C_6O_4Cl_2H)^- \cdot 2H_2O$  ( $M = Rb, Cs$ ) isomorphous structures, (i)  $M^+$  chains composed of a D2 + 2HB and a 2HB unit, (ii) joined together via a HB and 2HB unit to make  $M^+$  planes

Each chain is composed of two alternating  $M \cdots M$  interactions; a D2 + 2HB  $M$ - $M$  unit of 4.626(3) and 4.741(2) Å, and an  $M \cdots M$  interaction, in which the  $M^+$  ions also interact via two HBs, and have resulting  $M \cdots M$  distances of 6.365(1) and 6.413(3) Å in the RbCA and CsCA complexes respectively. Although there is no quoted value for the Rb or Cs van der Waals radii the latter two  $M$ - $M$  distances are significantly

larger than that of the  $K^+$  ion. The chains also interact with one another via another symmetry related  $M \cdots M$  interaction via 2HB of the same length and a larger  $M \cdots M$  interaction via one HB of 6.875(3) and 6.984(5) Å in the RbCA and CsCA complexes respectively.

With the exception of the D2 + 2HB unit, the  $M \cdots M$  distances are large and most likely insignificant in comparison to the sum of the van der Waals radii. Instead of  $M^+$  planes or indeed chains, it may therefore be more appropriate to break this structure down into  $M \cdots M$  clusters composed of the D2 + 2HB unit above. In this interpretation, the repeating cluster unit comprised of two  $M^+$  ions and two  $HCA^-$  molecules, inversely related by symmetry in terms of the two alternating planes, extended into three dimensions is illustrated in Figure 5-72. This is the point at which the two inversely orientated  $HCA^-$  planes intersect.

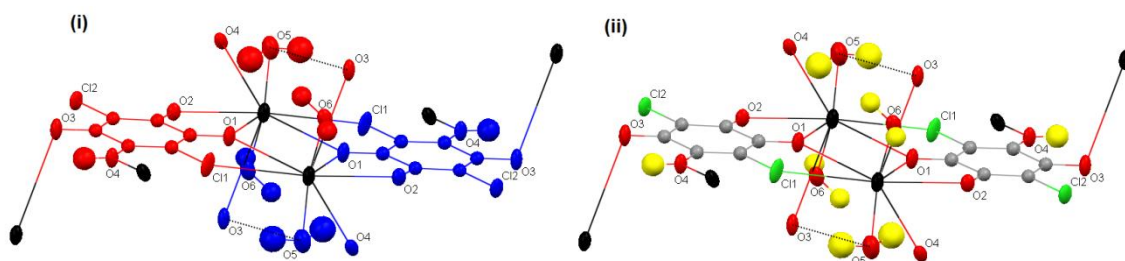


**Figure 5-72**  $M^+(C_6O_4Cl_2H)^- 2H_2O$  ( $M = Rb, Cs$ ) isomorphous structures,  $M^+$  and  $HCA^-$  repeating cluster unit (i) point of intersection for two inversely orientated  $HCA^-$  planes (red, blue) (ii) comprised of two  $M^+$  ions and two  $HCA^-$  molecules related by inversion centre.

The two  $HCA^-$  molecules are both coordinated to the two  $M$  ions by A2 + B2 coordination. An inversion centre is present in the middle of the two  $M^+$  ions which interact via a D2  $M \cdots M$  interaction unit, comprised of two symmetry related O1 atoms and further strengthened by 2 symmetry related O5–H4 $\cdots$ O3 HBs. As mentioned above the D2 unit is 4.626(3) and 4.741(2) Å in the RbCA and CsCA complexes respectively. The orientation of the cluster along the  $a$ -,  $b$ -, and  $c$ - axes is illustrated in Figure 5-73.

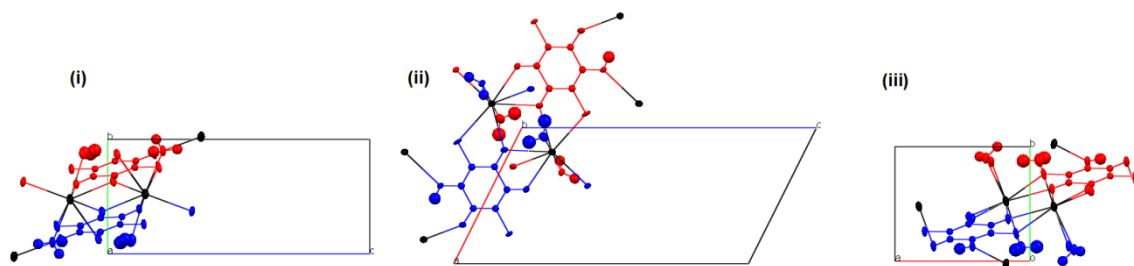


Figure 5-73  $M^+(C_6O_4Cl_2H)^- 2H_2O$  ( $M = Rb, Cs$ ) isomorphous structures,  $M^+$  and  $HCA^-$  repeating cluster unit viewed along (i)  $a$ -, (ii)  $b$ - and (iii)  $c$ - axes.

The  $HCA^-$  molecules themselves do not possess an inversion centre and the coordination is therefore not identical on both sides. By extending out the cluster above it is possible to observe the interactions that occur at the other side of the  $HCA^-$  molecules, which all participate in holding the clusters together, Figure 5-74.

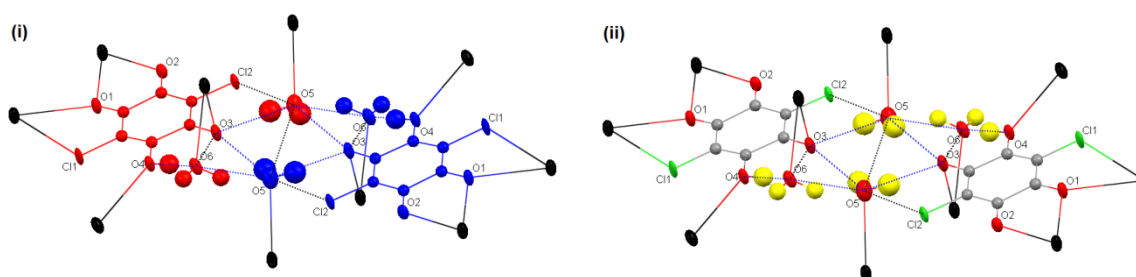
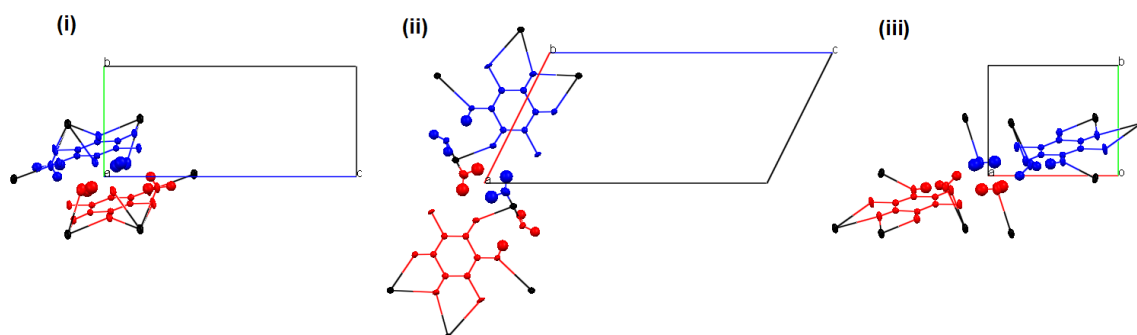


Figure 5-74  $M^+(C_6O_4Cl_2H)^- 2H_2O$  ( $M = Rb, Cs$ ) isomorphous structures, interactions between repeating cluster unit (i) at point of intersection for two inversely orientated  $HCA^-$  planes (red, blue) (ii) comprised of two  $HCA^-$  molecules and significant interactions related by inversion centre.

There are many significant HB and close contact interactions between the clusters, in comparison to the sum of the van der Waals radii. The  $HCA^-$  molecules are again related by a centre of inversion between the symmetry related O3 atoms of each molecule. The inversion centre is also in the middle of two inversely related O5w molecules, that interact with one another in a  $O5 \cdots O5$  interaction which decreases in length on incorporation of the larger  $Cs^+$  ion. The O5w atoms also HB to the O3 atoms via two symmetry related  $O5w-H4 \cdots O3$  and  $O5w-H5 \cdots O3$  interactions, the latter of which switches from the more to less prominent of the two secondary HBs within the previously illustrated BHB, on the incorporation of a larger cation. In addition to the inter-planar interactions mentioned above, an additional

interaction between the two inversely related  $\text{HCA}^-$  planes is the  $\text{O6-H2}\cdots\text{O5}$  HB in which the  $\text{O5w}$  atom acts as a proton acceptor; this is not significantly affected by the larger  $\text{Cs}^+$  ion incorporation. All of the above interaction distances are presented and compared for the RbCA and CsCA complexes in Table 5-20, and the interactions between the clusters are further illustrated along the  $a$ -,  $b$ -, and  $c$ -axes, Figure 5-75.



**Figure 5-75**  $\text{M}^+(\text{C}_6\text{O}_4\text{Cl}_2\text{H})^- \cdot 2\text{H}_2\text{O}$  ( $\text{M} = \text{Rb}, \text{Cs}$ ) isomorphous structures; interactions between repeating cluster unit as viewed along (i)  $a$ -, (ii)  $b$ -, and (iii)  $c$ -axes.

The way in which the structure is built up from the two inversely related  $\text{HCA}^-$  planes and the  $\text{M}^+$  ion clusters is illustrated in Figure 5-76 along the  $a$ -,  $b$ -, and  $c$ -axes.

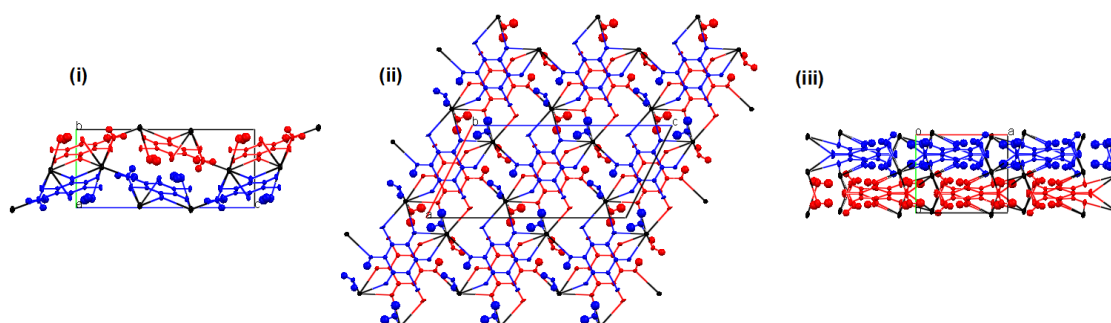


**Figure 5-76**  $\text{M}^+(\text{C}_6\text{O}_4\text{Cl}_2\text{H})^- \cdot 2\text{H}_2\text{O}$  ( $\text{M} = \text{Rb}, \text{Cs}$ ) isomorphous structures, inversely related alternating  $\text{HCA}^-$  planes (red and blue) viewed along (i)  $a$ -, (ii)  $b$ - and (iii)  $c$ -axes.

A comparison of the RbCA (red) and CsCA (blue) complexes has been carried using the structure overlay tool in Mercury<sup>192</sup> (Figure 5-77). As in other isomorphous structures this shows that the positions of the atoms remain the same in the two

complexes, although there are slight differences due to the effects of the different metal size.

An overlay of the  $\text{HCA}^-$  molecules suggests that the intra-molecular  $\text{CA}^{2-}$  bond lengths are very similar. This is confirmed in Table 5-21 which shows that both complexes contain bond lengths characteristic of those of an average  $\text{HCA}^-$  structure, presented earlier in chapter one. Overlays of the  $\text{M}^+$  and  $\text{HCA}^-$  clusters show that the O1 atoms in the D2  $\text{M}\cdots\text{M}$  interaction unit are at longer distances in CsCA than in RbCA due to the larger size of the  $\text{Cs}^+$  ions.

This would also explain the effect of the O5w HBs on the other side of the  $\text{HCA}^-$  molecules, also illustrated in Figure 5-77, an overlay of the interaction between the two clusters. This is also reflected in the  $\text{M}\cdots\text{M}$ ,  $\text{M}-\text{O}$  and  $\text{M}-\text{Cl}$  distances presented in Table 5-20. The distances most affected by the incorporation of a larger metal are those involved in the D2 unit, including the HB interactions. Those least affected are the C1  $\text{M1}-\text{O3}$  and  $\text{M1}-\text{O4}$  interactions which connect the  $\text{M}^+$  ions in one cluster to the  $\text{HCA}^-$  molecules in another.

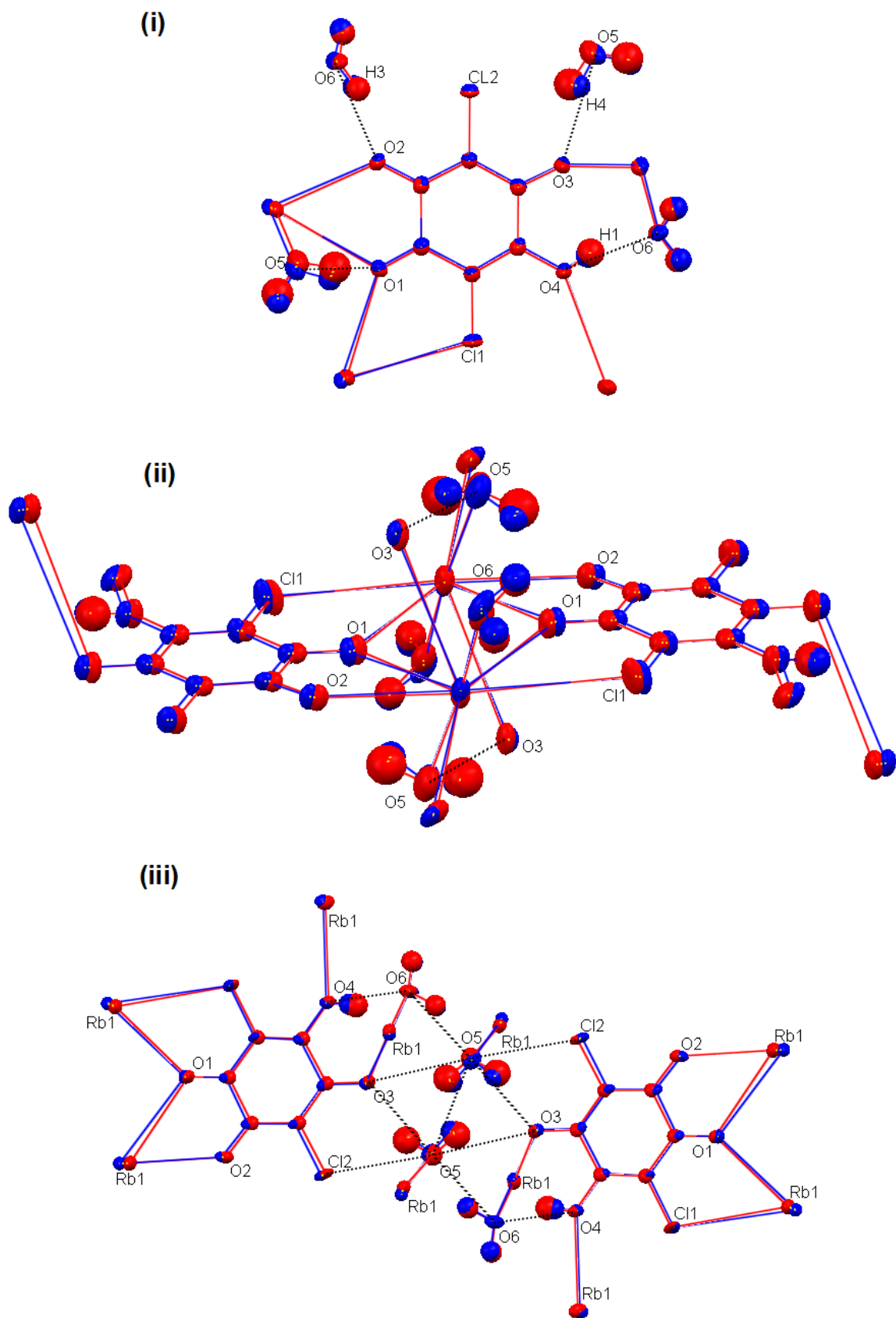


Figure 5-77  $M^+(C_6O_4Cl_2H)^- \cdot 2H_2O$  ( $M = Rb, Cs$ ) isomorphous structures. Comparison of RbCA (red) and CsCA (blue) complexes; overlay of (i)  $HCA^-$  molecules (ii)  $M^+$  and  $HCA^-$  clusters, and (iii) interactions between  $M^+$  and  $HCA^-$  clusters.

**Table 5-19 M distances for  $M^+(C_6O_4Cl_2H)^- \cdot 2H_2O$  (M = Rb, Cs) isomorphous structures.**

		<i>RbCA</i>	<i>CsCA</i>	<i>K<sup>+</sup> sum of the van der Waals radii / Å</i>	<i>Rb/CsCA M-M change / Å</i>
D2 + 2HB	M1-----M1	4.6266(4)	4.741(2)	5.5	0.115
2HB	M1-----M1	6.3653(4)	6.413(3)	5.5	0.048
1HB	M1-----M1	6.8753(5)	6.984(5)	5.5	0.109
C1 H <sub>2</sub> O	M1-----O5	2.969(3)	3.196(4)	3.27	0.2093
C1 H <sub>2</sub> O	M1-----O6	2.915(3)	3.095(3)	3.27	0.18
C1 HCA <sup>-</sup>	M1-----O3	3.440(3)	3.433(3)	3.27	-0.0078
C1 HCA <sup>-</sup>	M1-----O4	3.124(2)	3.195(2)	3.27	0.0717
B2 HCA <sup>-</sup>	M1-----O1	3.048(2)	3.190(3)	3.27	0.1423
	M1-----O2	2.857(2)	3.021(3)	3.27	0.164
A2 HCA <sup>-</sup>	M1-----O1	2.961(2)	3.132(3)	3.27	0.1707
	M1-----Cl1	3.460(1)	3.605(2)	4.5	0.1453

**Table 5-20 HB parameters and significant interactions for  $2M^+(C_6O_4Cl_2)^{2-} \cdot H_2O$  isomorphous structures (M = K, Rb).**

D-----A	RbCA				CsCA				Van der waals radii / Å
	D-H/ Å	H---A/ Å	D---A/ Å	<DHA/ °	D-H/ Å	H---A/ Å	D---A/ Å	<DHA/ °	
O4-H1---O6	0.84(4)	1.77(4)	2.561(3)	157(5)	0.71(5)	1.87(5)	2.573(1)	166(6)	3.04
O5-H4---O3	-	-	2.964(3)	153(3)	-	-	2.907(4)	155.53	3.04
O5-H5 --O1	-	-	3.014(1)	128(5)	-	-	3.042(3)	130.87	3.04
O5-H5---O3	-	-	3.077(2)	133(4)	-	-	3.211(1)	121.93	3.04
O5-----O5	-	-	3.258(4)	-	-	-	3.1731(9)	121.75	3.04
O5-----Cl2	-	-	3.223(6)	-	-	-	3.321(3)	116.86	3.27
O6-H2---O5	-	-	2.800(3)	152(3)	-	-	2.786(1)	152.77	3.04
O6-H3---O2	-	-	2.754(2)	156(6)	-	-	2.7553(9)	154.26	3.04
O6-----O3	-	-	2.944(3)	-	-	-	2.995(1)	-	3.04
O6-----Cl2	-	-	3.374(5)	-	-	-	3.507(3)	-	3.27
Cl1-----Cl2	-	-	3.087(8)	-	-	-	3.160(1)	-	3.5

**Table 5-21 Intra-molecular bond lengths for  $2M^+(C_6O_4Cl_2)^{2-} \cdot H_2O$  isostructures (M = K, Rb).**

	RbCA	CsCA		RbCA	CsCA
C-C Distances / Å			C-O and C-Cl Distances / Å		
C1-C2	1.447(4)	1.450(4)	C1-Cl1	1.729(3)	1.729(3)
C2-C3	1.549(4)	1.546(4)	C2-O1	1.226(4)	1.227(4)
C3-C4	1.396(4)	1.398(4)	C3-O2	1.251(4)	1.244(4)
C4-C5	1.409(4)	1.413(4)	C4-Cl2	1.730(3)	1.735(3)
C5-C6	1.520(4)	1.510(4)	C5-O3	1.244(4)	1.248(4)
C6-C1	1.347(4)	1.349(5)	C6-O4 (H1)	1.318(4)	1.317(4)

### 5.3.4 2:3 metal – chloranilic acid hexahydrate complexes $2M^+$



An isomorphous structural pair of Rb and Cs 2:3 CA hexahydrate complexes were obtained as described in Table 5-26. The only difference in the otherwise identical conditions under which the two complexes were obtained was the temperature at which crystallisation occurred, room temperature for the Rb complex and 40°C for the Cs complex.

The asymmetric unit, for both complexes, contains half a  $H_2CA$  molecule, one  $HCA^-$  molecule, one  $M^+$  ion and three water molecules, Figure 5-78.

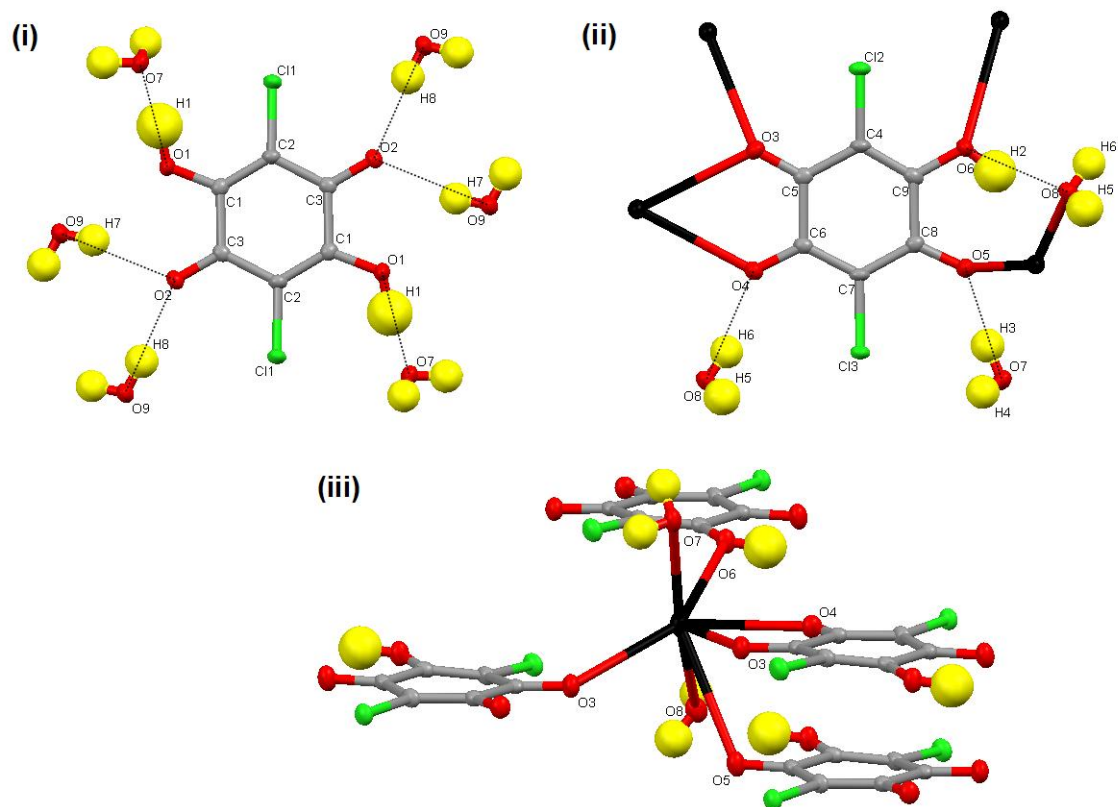


Figure 5-78  $2M^+ 2(C_6O_4Cl_2H)^- (C_6O_4Cl_2H_2) 6H_2O$  ( $M = Rb, Cs$ ) isomorphous structures; environments of the (i)  $H_2CA$  molecule with inversion centre, (ii)  $HCA^-$  molecule and (iii)  $M^+$  ion.

The  $H_2CA$  molecule has an inversion centre and does not coordinate to any metal ions within the complex. The two symmetry equivalent hydroxyl carbonyls, related by the inversion centre, act as proton donors in  $O1-H1 \cdots O7w$  HB interactions.

Although the distance of these interactions is the same in both the RbCA and CsCA complexes the angle decreases from 174(3) to 164(5)° in the latter. The two symmetry related carbonyls act as the proton acceptor, in a DHHAA bifurcated HB, for two incoming HBs; the O9w–H7···O2 and O9w–H8···O2 interactions.

The HCA<sup>-</sup> molecule has no inversion centre and possesses two of the previously defined metal coordinating units giving an overall (B3 + B5) coordination. The hydroxyl carbonyl unit possesses the E1 HB motif, and acts as proton donor in O6–H2···O8w HB interaction, and the deprotonated carbonyl and the carbonyl on the other side of the adjacent halide unit both act as acceptors in the O8w–H6···O4 and O7w–H3···O5 HB interactions respectively.

Each M<sup>+</sup> ion is coordinated to four HCA<sup>-</sup> molecules; three monodentate C1, one bidentate B2, and two water molecules. Each M<sup>+</sup> ion is hence coordinated to 7 other atoms in total: seven oxygen atoms the interaction distances range from 2.922(1) - 3.333(1) Å and 3.0589(2) - 3.079(2) Å in the RbCA and CsCA complexes, respectively, and as expected due to the larger radii of the larger ion, the bond lengths between the metal and coordinating atoms are longer in the CsCA complex. There are no M-Cl interactions with this material.

The resulting three-dimensional structure contains pores along the c axis (Figure 5-79).

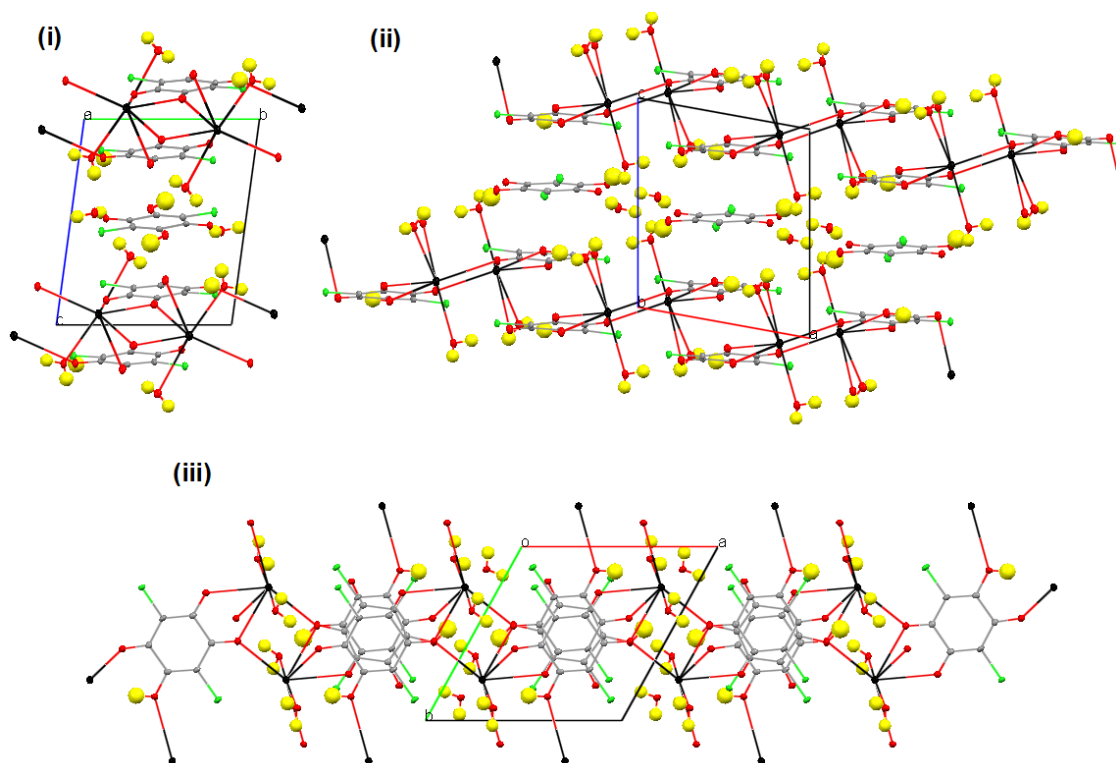


Figure 5-79  $2M^+ 2(C_6O_4Cl_2H)^- (C_6O_4Cl_2H_2) 6H_2O$  ( $M= Rb, Cs$ ) isomorphous structures, viewed along (i)  $a$ -, (ii)  $b$ - and (iii)  $c$ - axes.

The structure can be broken down into three alternating CA planes, that lie on the  $ab$  plane and  $M \cdots M$  chains that run along the  $b$ -axis. The three CA planes on which the carbon rings lie, are stacked perpendicular to the  $c$ -axis and are illustrated in Figure 5-80, in which the  $M^+$  ions have been excluded for clarity.

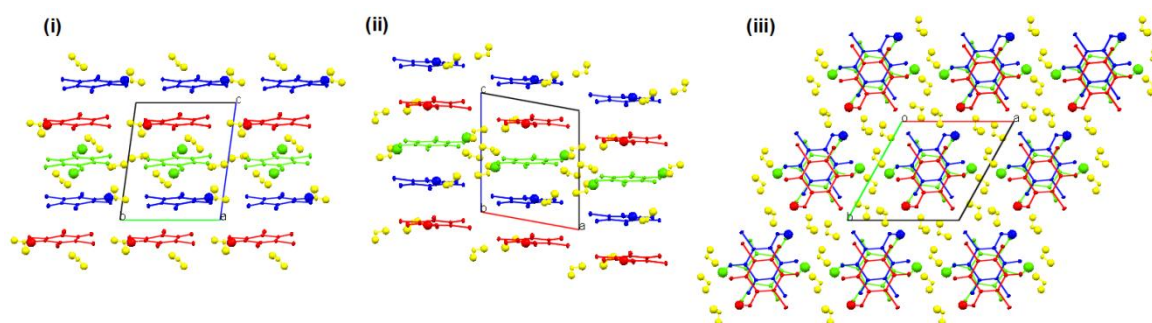
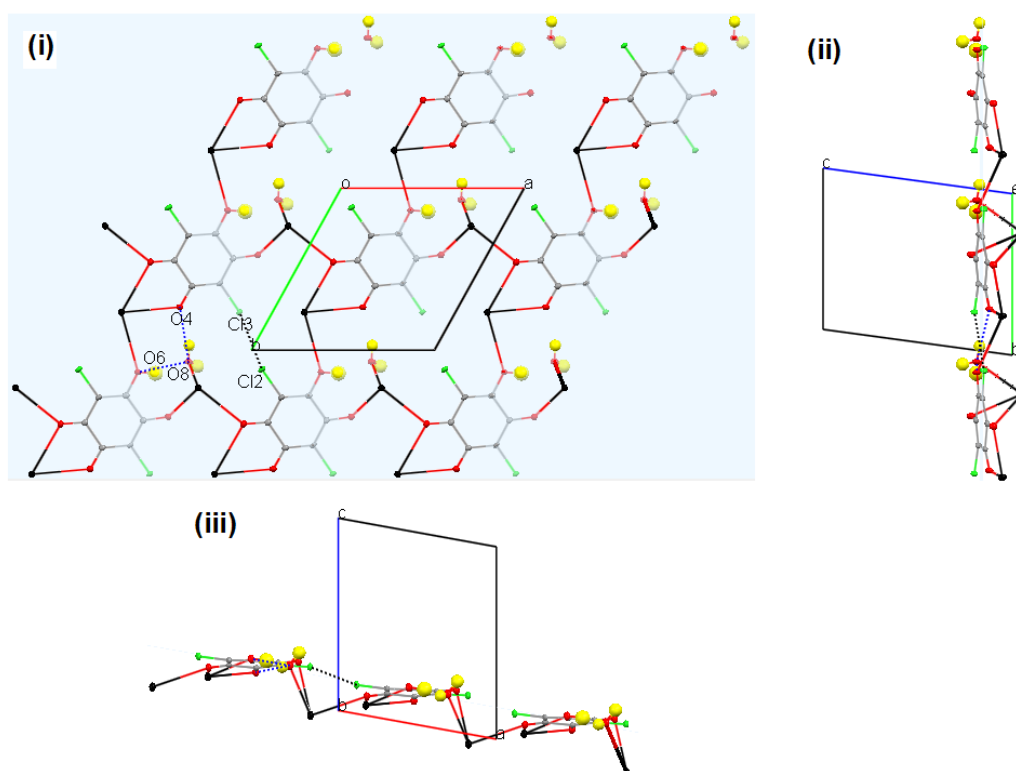


Figure 5-80  $2M^+ 2(C_6O_4Cl_2H)^- (C_6O_4Cl_2H_2) 6H_2O$  ( $M= Rb, Cs$ ) isomorphous structures; three alternating CA planes of the form ABCABC... (red, blue, green), viewed along (i)  $a$ -, (ii)  $b$ - and (iii)  $c$ - axes.

The identical blue and red planes are composed of  $\text{HCA}^-$  molecules, and are inversely related through symmetry, Figures 5-81 and 5-82. Within the  $\text{HCA}^-$  planes the planar  $\text{HCA}^-$  molecules are arranged in columns and interact directly with one another via  $\text{Cl2}\cdots\text{Cl3}$  interactions of 3.2150(1) and 3.278(1) Å in the RbCA and CsCA complexes, respectively. These are short in comparison to the average of 3.387 Å obtained from the CSD and the sum of the van der Waals radii of 3.5 Å. The  $\text{HCA}^-$  columns are coordinated to one another via  $M^+$  chains and  $\text{O6-H2}\cdots\text{O8w}$  and  $\text{O8w-H6}\cdots\text{O4}$  HB interactions to make up the two dimensional plane. These interactions are also illustrated within the two identical planes in Figure 5-81, and interaction distances for both the RbCA and CsCA complexes are presented in Table 5-24.



**Figure 5-81**  $2M^+ 2(\text{C}_6\text{O}_4\text{Cl}_2\text{H})^- (\text{C}_6\text{O}_4\text{Cl}_2\text{H}_2) 6\text{H}_2\text{O}$  ( $M = \text{Rb}, \text{Cs}$ ) isomorphous structures; interactions within two identical  $\text{HCA}^-$  planes (blue), inversely related through symmetry, viewed along (i)  $c$ -, (ii)  $a$ - and (iii)  $b$ - axes.

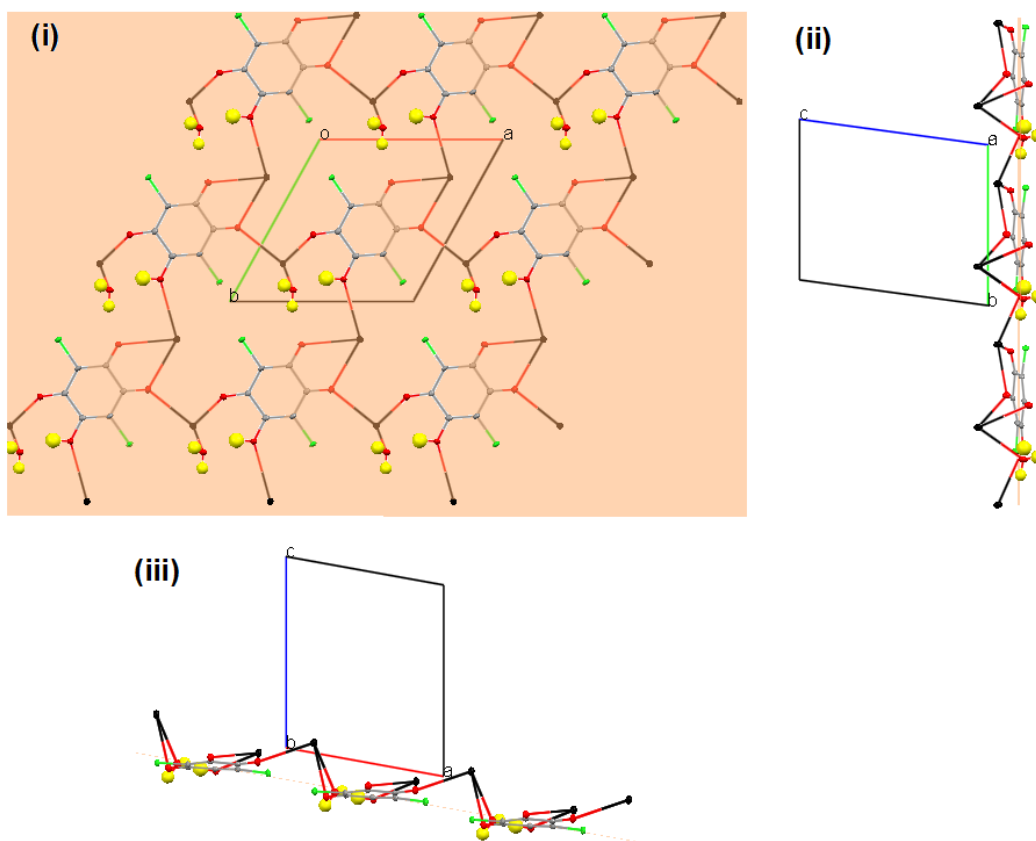


Figure 5-82  $2M^+ 2(C_6O_4Cl_2H)^- (C_6O_4Cl_2H_2) 6H_2O$  ( $M= Rb, Cs$ ) isomorphous structures; interactions within two identical  $HCA^-$  planes (red), inversely related through symmetry, viewed along (i)  $c$ -, (ii)  $a$ - and (iii)  $b$ - axes.

The two identical planes coordinate to one another via  $M^+$  ions, as illustrated in Figure 5-83 in which the  $M^+$  ions have been included.

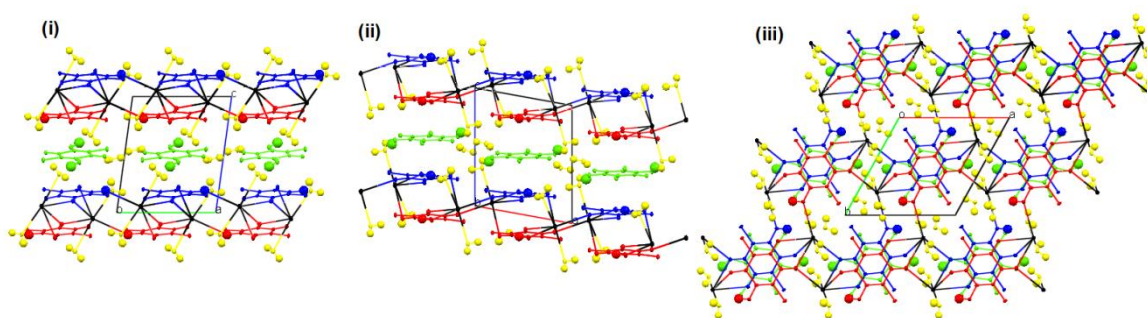
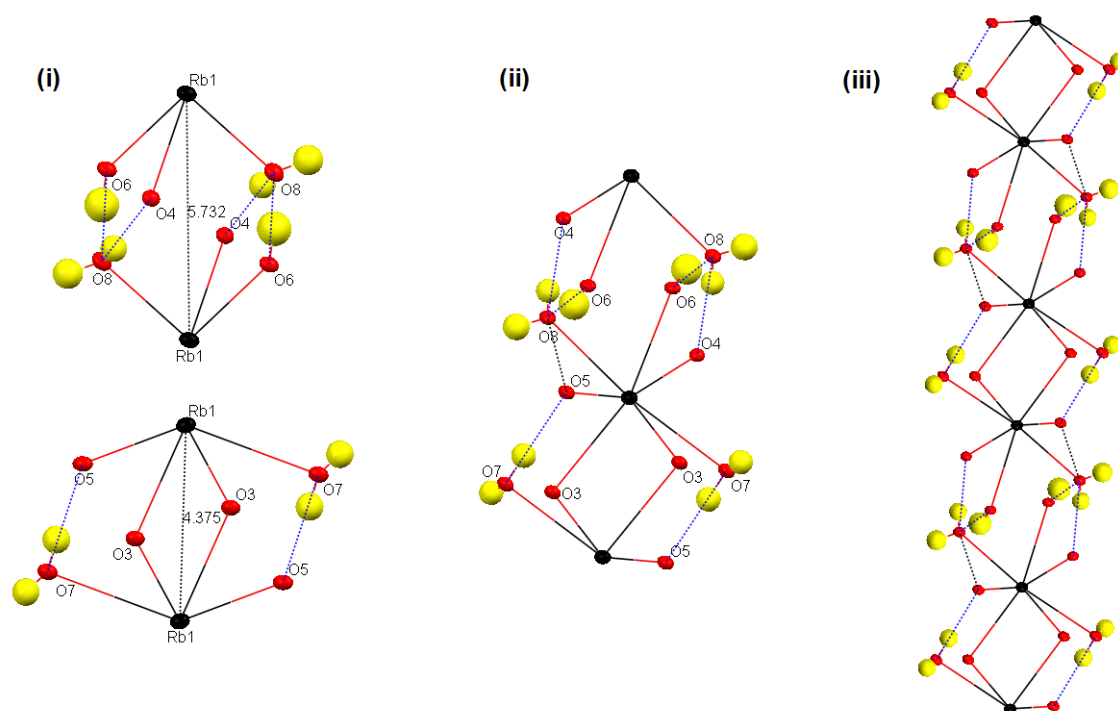


Figure 5-83  $2M^+ 2(C_6O_4Cl_2H)^- (C_6O_4Cl_2H_2) 6H_2O$  ( $M= Rb, Cs$ ) isomorphous structures, three alternating CA planes of the form ABCABC... (red, blue, green), and  $M^+$  chains, viewed along (i)  $a$ -, (ii)  $b$ - and (iii)  $c$ - axes.

The point of intersection between the two related planes is the  $M \cdots M$  ion chain illustrated in Figure 5-84.



**Figure 5-84**  $2M^+ 2(C_6O_4Cl_2H)^- (C_6O_4Cl_2H_2) 6H_2O$  ( $M = Rb, Cs$ ) isomorphous structures; (i) D2 + 2HB and 4HB  $M \cdots M$  units, (ii) plus O5-O6 interaction, comprising (ii)  $M^+$  chains.

Each chain is composed of two alternating D2 + HB, and 4HB  $M \cdots M$  interaction units, both of which have an inversion centre in the middle. The D2 + HB unit is comprised of two O3 atoms, from two symmetry related  $CA^{2-}$  molecules that coordinate to the two interacting metals in B3 fashion. The 4HB unit is comprised of two hydroxyl O6 atoms, from two symmetry related  $CA^{2-}$  molecules that coordinate to the two interacting metals in B5 fashion, two O4 atoms, from two symmetry related  $CA^{2-}$  molecules, each of which coordinates to one of the interacting metals in B2 fashion, and two symmetry related O8w molecules. The 4HB unit consists of two symmetry related O8w–H6 $\cdots$ O4, and two symmetry related O6–H2 $\cdots$ O8w HB interactions. The  $M \cdots M$  distances are 4.3750(2) and 4.417(2) Å for the D2 + HB unit and 5.7323(2) and 5.762(2) Å in the 4HB unit in the RbCA and CsCA complexes, respectively.

Due to the larger interaction distance in the 4HB  $M \cdots M$  interaction, and as in the previous isomorphous pair, it may be more appropriate to describe the point at which the two identical planes meet and interact with one another as an  $M \cdots M$  cluster, as illustrated in Figure 5-85, comprised of the D2 + HB unit above.

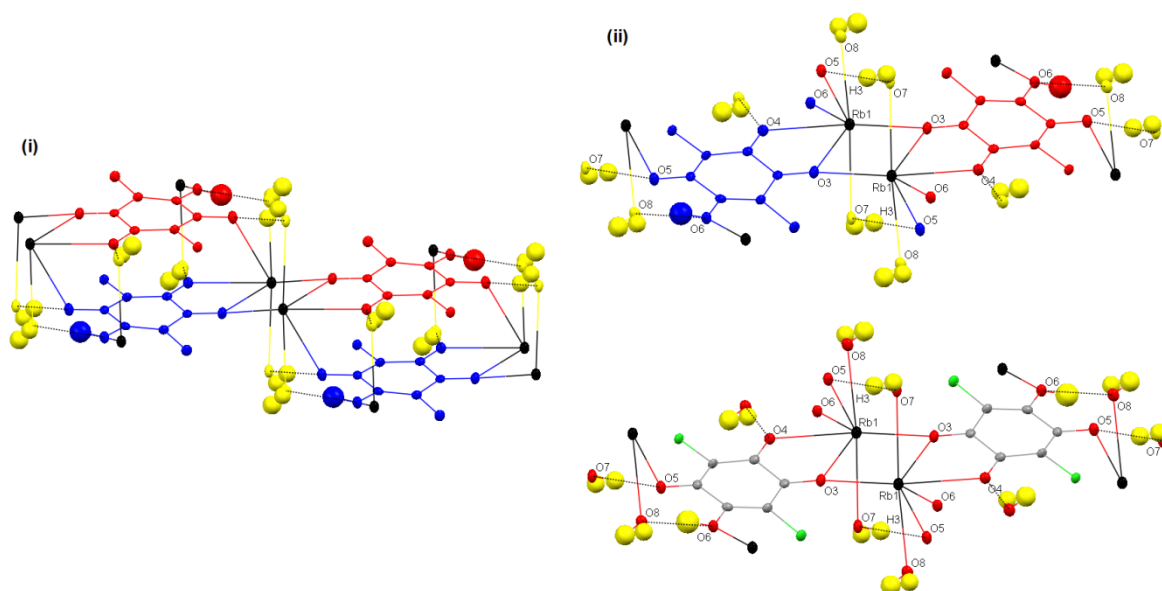


**Figure 5-85.  $2M^+ 2(C_6O_4Cl_2H)^- (C_6O_4Cl_2H_2) 6H_2O$  ( $M = Rb, Cs$ ) isomorphous structures,  $M^+$  and  $HCA^-$  repeating cluster unit (i) point of intersection for two inversely orientated  $HCA^-$  planes (red, blue) (ii) comprised of two  $M^+$  ions and two  $HCA^-$  molecules related by inversion centre.**

This repeating cluster unit can be extended in order to form a layer consisting of the two inversely related  $HCA^-$  planes. This layer is sandwiched between  $H_2CA$  planes, as illustrated previously in Figure 5-83. The green  $H_2CA$  plane is illustrated in Figure 5-86.

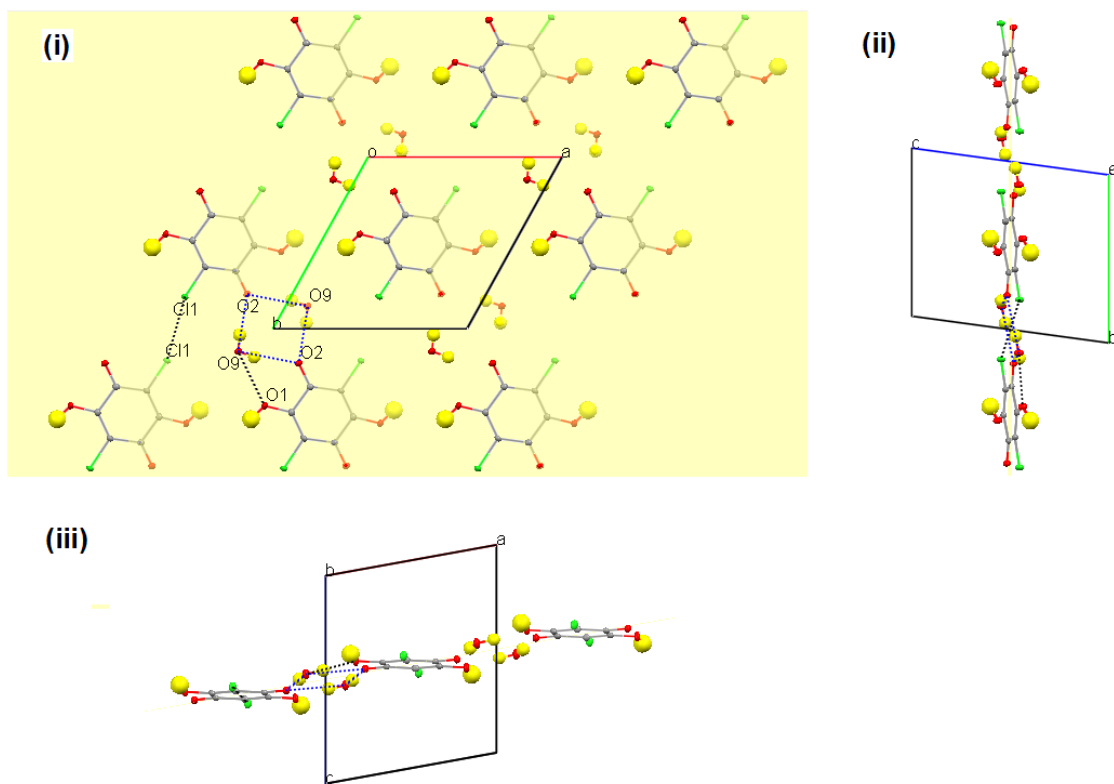


**Figure 5-86**  $2M^+ 2(C_6O_4Cl_2H)^- (C_6O_4Cl_2H_2) 6H_2O$  ( $M= Rb, Cs$ ) isostructures,  $H_2CA$  planes (green) viewed along (i)  $c$ -, (ii)  $a$ - and (iii)  $b$ - axes.

As in the  $HCA^-$  planes, the carbon rings of the  $H_2CA$  molecules also lie on the plane, are arranged in columns and interact directly with one another via  $Cl1 \cdots Cl1$  interactions of 3.1658(1) and 3.276(2) Å in the RbCA and CsCA complexes respectively; these distances are also short in comparison to the average of 3.387 Å obtained from the CSD and the sum of the van der Waals radii of 3.5 Å. The  $H_2CA$  molecules do not interact via  $M^+$  ions, although as they possess an inversion centre they interact with  $H_2CA$  molecules on adjacent columns via two symmetry equivalent water atoms between which there is also an inversion centre. The  $H_2CA$  molecules therefore interact with one another via four HB interactions; two inversely related  $O9w-H7 \cdots O2$  and  $O9w-H8 \cdots O2$  HBs. There is also a significant  $O1 \cdots O9$  interaction distance of 2.9243(1) and 2.932(1) Å in the RbCA and CsCA complexes respectively.

The  $H_2CA$  plane interacts with the inversely related  $HCA^-$  planes above and below in the same manner as illustrated in Figure 5-87.

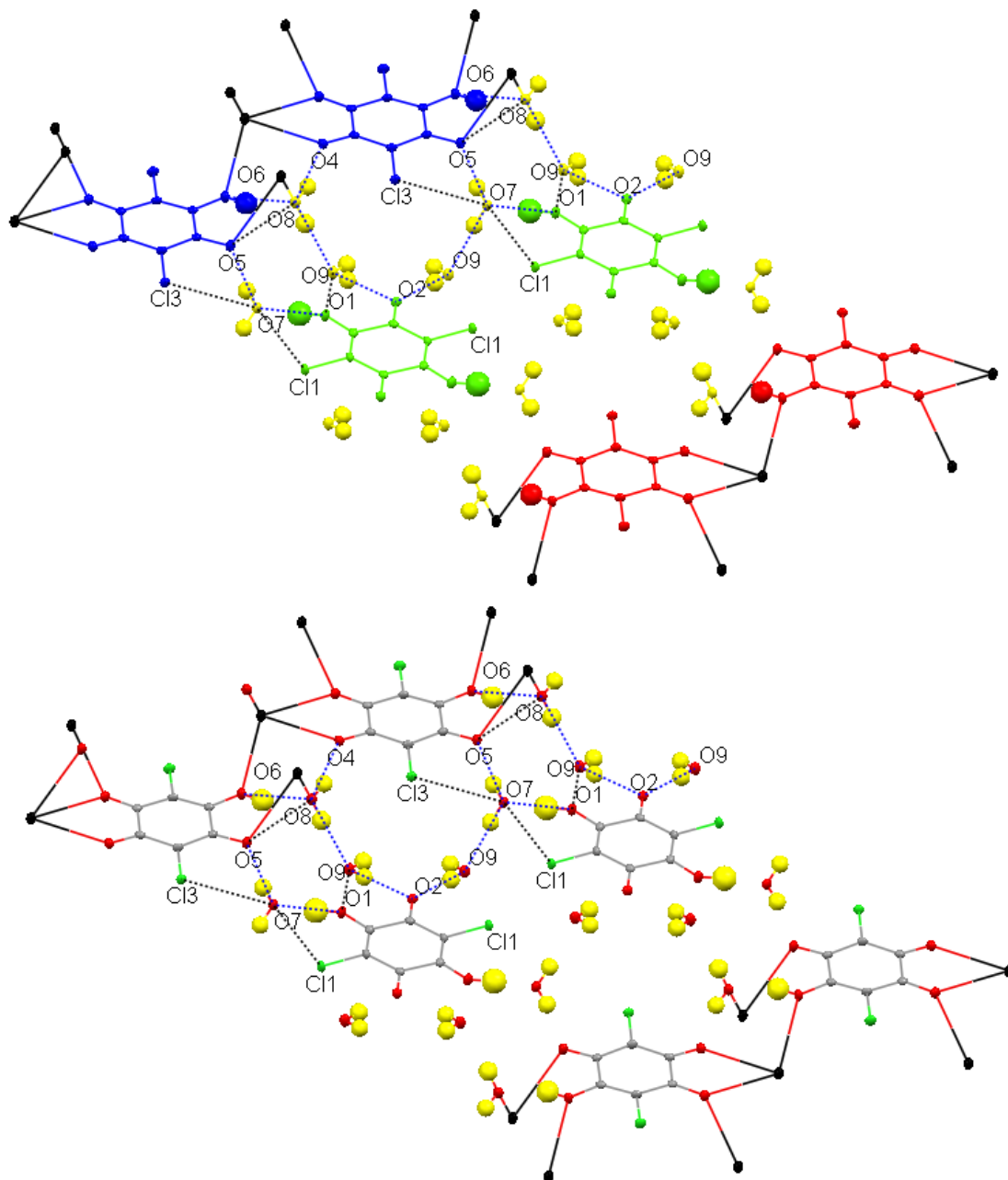


**Figure 5-87**  $2M^+ 2(C_6O_4Cl_2H)^- (C_6O_4Cl_2H_2) 6H_2O$  ( $M = Rb, Cs$ ) isomorphous structures,  $H_2CA$  planes (green) viewed along (i)  $c$ -, (ii)  $a$ - and (iii)  $b$ - axes.

In addition to the interactions mentioned previously, there is an additional HB interaction of the form  $O8w-H5\cdots O9w$ , the parameters of which are the same in both RbCA and CsCA complexes, and an  $O8w\cdots O5$  interaction that increases in length on increased  $M^+$  size. There are also halogen interactions mediated by the  $O7$  water molecule in the form of  $Cl1\cdots O7$  and  $O7\cdots Cl3$  interactions. These interactions are close to the sum of the van der Waals radii and increase in length

with increased  $M^+$  size, Table 5-24. These interactions are also presented as viewed along the  $a$ -,  $b$ -, and  $c$ - axes in Figure 5-88.

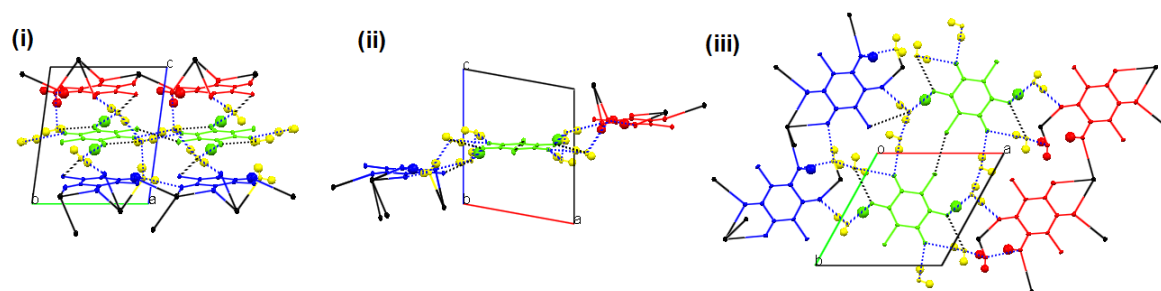


**Figure 5-88**  $2M^+ 2(C_6O_4Cl_2H)^- (C_6O_4Cl_2H_2) 6H_2O$  ( $M = Rb, Cs$ ) isomorphous structures,  $H_2CA$  planes (green) viewed along (i)  $c$ -, (ii)  $a$ - and (iii)  $b$ - axes.

Due to the close proximity of the three CA planes, additional halogen interactions are also present; these can be observed in Figure 5-89.

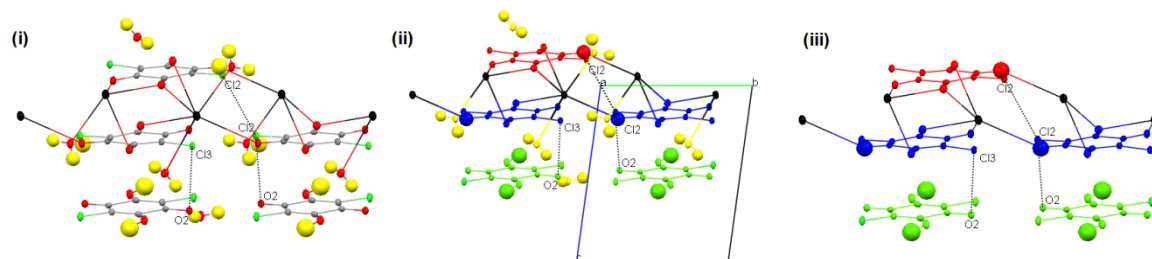


**Figure 5-89**  $2M^+ 2(C_6O_4Cl_2H)^- (C_6O_4Cl_2H_2) 6H_2O$  ( $M = Rb, Cs$ ) isostructures,  $H_2CA$  planes (green) viewed along (i)  $c$ -, (ii)  $a$ - and (iii)  $b$ - axes.

$Cl_2 \cdots Cl_2$  interactions are present between the inversely related  $HCA^-$  planes, of distance 3.3134(1) and 3.381(1) Å in the RbCA and CsCA complexes, respectively. Although these are significant they are not as significant as those within the planes.  $Cl_2 \cdots O_2$  interactions, of length 3.1907(1) and 3.211(2) Å, and  $Cl_3 \cdots O_3$  interactions, of length 3.1849(1) and 3.216(2) Å, in the RbCA and CsCA complexes, respectively, are also present between the  $HCA^-$  and  $H_2CA$  planes.

A comparison of the  $H_2CA$  and the  $HCA^-$  molecules in Table 5-22 shows that the intra-molecular distances are similar to the average values calculated for  $H_2CA$  and  $HCA^-$  molecules in the CSD, presented earlier in chapter one, and there are no significant differences between the values found for RbCA and CsCA complexes.

A comparison of the M interaction distances obtained in the RbCA and CsCA complexes reveals that the  $M\cdots M$  distances are similar in both complexes and the only  $M-O$  distances to show a significant increase on the incorporation of a larger  $M^+$  ion are those around the  $M\cdots M$  cluster. Overall, all HB and significant  $O\cdots O$  interactions either show no change or increase slightly with the incorporation of the larger  $Cs^+$  ion, although not significantly. All  $Cl\cdots Cl$  interactions also increase, the  $Cl1\cdots Cl1$  in particular increases from 3.1658(1) to 3.276(2) Å. Figure 34 shows that the  $Cl1\cdots Cl1$  interaction within the  $H_2CA$  plane is directly above and below the  $M\cdots M$  cluster in the  $HCA^-$  planes, so this is most likely a consequence of the change around the cluster.

This is the first complex in which the  $M^+$  ions are present only within a two dimensional plane. Even in the previous complex, the clusters were more three dimensional. As a result the  $M\cdots M$  distances on the incorporation of a larger ion do not seem to change as significantly. The only distances to increase significantly in comparison to the other were the  $M-O$  interactions around the  $M\cdots M$  cluster and consequently the  $Cl1\cdots Cl1$  interactions in the  $H_2CA$  plane, which was otherwise unaffected.

**Table 5-22 M interaction distances in  $2M^+ 2(C_6O_4Cl_2H)^- (C_6O_4Cl_2H_2) 6H_2O$  (M = Rb, Cs) Isomorphous structures.**

		RbCA	CsCA	$K^+$ Sum of the van der Waals radii / Å	Rb/CsCA M-M change / Å
D2 + 2HB	M1--M1	4.3750(2)	4.417(2)	5.5	0.042
- 4HB	M1--M1	5.7323(2)	5.762(2)	5.5	0.0297
C1 H <sub>2</sub> O	M1--O7	3.119(1)	3.272(2)	3.27	0.153
C1 H <sub>2</sub> O	M1--O8	2.922(1)	3.079(2)	3.27	0.157
C1 HCA <sup>-</sup>	M1--O3	3.0205(8)	3.154(2)	3.27	0.1335
C1 HCA <sup>-</sup>	M1--O5	3.333(1)	3.356(2)	3.27	0.023
C1 HCA <sup>-</sup>	M1--O6	3.1841(8)	3.220(2)	3.27	0.0359
B2 HCA <sup>-</sup>	M1--O3	2.938(1)	3.058(2)	3.27	0.12
	M1--O4	2.930(1)	3.095(2)	3.27	0.165

**Table 5-23 Intra-molecular bond lengths for  $2M^+ 2(C_6O_4Cl_2H)^- (C_6O_4Cl_2H_2) 6H_2O$  (M = Rb, Cs) Isomorphous structures.**

	RbCA	CsCA
H <sub>2</sub> CA		
C-C Distances / Å		
C1-C2	1.3623(17)	1.3485(29)
C2-C3	1.4537(17)	1.4555(23)
C3-C1	1.5134(16)	1.5239(22)
C-O and C-Cl Distances / Å		
C1-O1		
C2-Cl1	1.3041(15)	1.3086(22)
C3-O2	1.7204(12)	1.7260(18)
HCA <sup>-</sup>	1.2270(15)	1.2227(24)
C-C Distances / Å		
C4-C5		
C5-C6		
C6-C7	1.4488(17)	1.4537(23)
C7-C8	1.5451(16)	1.5323(29)
C8-C9	1.4062(17)	1.4148(22)
C9-C4	1.5451(16)	1.4134(24)
C-O and C-Cl Distances / Å	1.5152(17)	1.5068(29)
C4-Cl2	1.3598(17)	1.3594(23)
C5-O3		
C6-O4		
C7-Cl3	1.7234(12)	1.7219(21)
C8-O5	1.2252(15)	1.2254(21)
C9-O6	1.2436(15)	1.2455(22)
	1.7344(12)	1.7291(21)
	1.2485(15)	1.2502(21)
	1.3154(15)	1.3207(22)

**Table 5-24 HBs and significant distances for  $2M^+ 2(C_6O_4Cl_2H)^- (C_6O_4Cl_2H_2) 6H_2O$  (M = Rb, Cs) Isomorphous structures.**

D-----A	RbCA				CsCA				Van der waals radii / Å
	D-H/ Å	H---A/ Å	D---A/ Å	<DHA/ °	D-H/ Å	H---A/ Å	D---A/ Å	<DHA/ °	
O1-H1----O7	0.97(3)	1.52(3)	2.481(1)	174(3)	0.98(4)	1.53(4)	2.484(2)	164(4)	3.04
O1-----O9	-	-	2.9243(1)	-	-	-	2.932(1)	-	3.04
O2-----Cl2	-	-	3.1907(1)	-	-	-	3.211(2)	-	3.27
O2-----Cl3	-	-	3.1849(1)	-	-	-	3.216(2)	-	3.27
O6-H2----O8	0.87(2)	1.75(2)	2.5750(1)	158(2)	0.81(3)	1.80(3)	2.582(2)	161(4)	3.04
O7-H3----O5	0.85(2)	1.89(2)	2.735(1)	170(2)	0.83(3)	1.92(3)	2.741(2)	170(3)	3.04
O7-H4----O9	0.84(2)	1.91(2)	2.752(1)	174(2)	0.83(4)	1.93(4)	2.752(2)	171(3)	3.04
O7-----Cl1	-	-	3.0907(1)	-	-	-	3.113(2)	-	3.27
O7-----Cl3	-	-	3.274(1)	-	-	-	3.350(1)	-	3.27
O8-H5----O9	0.81(2)	2.01(2)	2.816(1)	171(2)	0.77(4)	2.04(4)	2.798(2)	170(4)	3.04
O8-H6----O4	0.81(2)	1.97(2)	2.754(1)	163(2)	0.84(3)	1.93(3)	2.757(3)	168(2)	3.04
O8-----O5	-	-	2.9179(1)	-	-	-	2.964(2)	-	3.04
O9-H7----O2	0.82(2)	2.11(2)	2.903(1)	164(2)	0.76(4)	2.19(4)	2.926(2)	163(3)	3.04
O9-H8----O2	0.82(2)	2.03(2)	2.853(1)	175(2)	0.76(3)	2.10(3)	2.864(2)	176(3)	3.04
Cl1-----Cl1	-	-	3.1658(1)	-	-	-	3.276(2)	-	3.5
Cl2-----Cl2	-	-	3.3134(1)	-	-	-	3.381(1)	-	3.5
Cl2-----Cl3	-	-	3.2150(1)	-	-	-	3.278(1)	-	3.5

**Table 5-25 Crystallographic data for Isomorphous Structures**

	$2M^+(C_6O_4Br_2)^{2-} \cdot 2H_2O$			$2M^+(C_6O_4Cl_2)^{2-} \cdot H_2O$		$M^+(C_6O_4Cl_2H)^- \cdot 2H_2O$		$2M^+ 2(C_6O_4Cl_2H)^-(C_6O_4Cl_2H_2)6H_2O$	
	KBA	RbBA	CsBA	KCA	RbCA	RbCA	CsCA	RbCA	CsCA
Diffractometer	Kappa	Rigaku	Kappa	Rigaku	Kappa	Kappa	Kappa	Kappa	Kappa
Crystal size/mm <sup>3</sup>	0.1 x 0.1 x 0.3	0.1 x 0.3 x 0.3	0.1 x 0.3 x 0.4	0.1 x 0.1 x 0.3	0.2 x 0.2 x 0.5	0.3 x 0.4 x 0.5	0.2 x 0.2 x 0.5	0.4 x 0.4 x 0.5	0.3 x 0.4 x 0.5
M/g mol <sup>-1</sup>	410.11	502.86	597.73	303.16	395.92	329.47	376.91	903.95	998.83
T/K	100	100	100	100	100	100	100	100	100
Space group	P21/c	P21/c	P21/c	C2/c	C2/c	P21/c	P21/c	P-1	P-1
a/Å	3.78850(10)	3.953(5)	4.25820(10)	16.060(4)	16.737(5)	9.084	9.349(5)	9.1681(2)	9.320(5)
b/Å	9.4016(2)	9.518(5)	9.6509(3)	4.7797(10)	4.905(5)	6.867	6.984(5)	9.2064(2)	9.340(5)
c/Å	15.0979(4)	15.219(5)	15.3313(3)	13.669(3)	13.600(5)	17.64	17.670(5)	9.6816(2)	9.764(5)
α/°	90	90	90	90	90	90	90	93.2170(10)	93.485(5)
β/°	97.7420(10)	99.48(2)	101.1980(10)	117.767(16)	117.763(5)	116.66	117.235(17)	97.4810(10)	97.475(5)
γ/°	90	90	90	90	90	90	90	118.1950(10)	118.821(5)
V/Å <sup>3</sup>	532.85(2)	564.8(8)	618.05(3)	928.4(4)	988.0(11)	983.3	1025.8(10)	707.58(3)	730.8(7)
Z	2	2	2	4	4	4	4	1	1
P <sub>calc</sub> /g cm <sup>-3</sup>	2.556	2.933	3.212	2.169	2.662	2.225	2.44	2.121	2.269
μ/mm <sup>-1</sup>	0.8395	1.5745	1.237	1.589	10.441	5.582	4.134	4.108	3.124
θ range/°	2.56 - 27.5	3.46 - 27.48	2.51 - 27.47	3.25 - 27.48	2.75 - 27.55	2.51 - 27.52	2.45 - 27.57	2.53 - 27.5	2.51 - 27.52
Reflections									
Collected	12533	13710	13638	5993	11477	15283	14046	21583	11725
Independent	1197	1273	1427	1061	1131	2252	1464	3211	2058
Observed (>2σ(I))	1175	722	1333	929	1108	2014	1340	3161	2033
Solved using	Sir92	Sir92	Sir92	Sir92	Sir92	Sir92	Sir97		
R <sub>int</sub>	0.021	0.2011	0.077	0.0201	0.0287	0.0287	0.0313	0.0203	0.0190
Completeness/%	98.8	98.8	99.9	99.9	98.3	99.6	61.7	98.8	61.0
Parameters	81	73	81	69	73	122	152	231	231
GOOF	1.189	0.987	1.118	1.303	1.077	1.064	1.058	1.062	1.097
R1 (observed)	0.0146	0.0702	0.0217	0.0196	0.0146	0.0310	0.0204	0.0150	0.0117
R1 (all)	0.0149	0.1134	0.0236	0.0262	0.0151	0.0373	0.0247	0.0155	0.0120
wR2 (all)	0.0374	0.2321	0.0558	0.0583	0.0356	0.0716	0.0448	0.0383	0.0306
ρ <sub>max, min</sub> /eÅ <sup>3</sup>	0.413 -0.662	3.102 -2.488	0.809 -1.552	0.524 -0.393	0.469 -0.390	1.246 -0.731	0.436 -0.618	0.396 -0.244	0.203 -0.228

**Table 5-26 Experimental Details for Isomorphous Structures.**

	K	M <sup>+</sup> Rb	Cs
$2M^+ (C_6O_4Br_2)^{2-} \cdot 2H_2O$	Dark red crystalline needles obtained from a 1:2 molar ratio ( $3.35 \times 10^{-5}$ mol, $6.7 \times 10^{-5}$ mol) of BA (0.01g), and KOH (0.004g), both dissolved in MeOH, combined, and left to evaporate at 50°.	Light pink crystalline plates obtained from a 1:1 molar ratio ( $6.7 \times 10^{-5}$ mol) of BA (0.02g), dissolved in EtOH, and Rb <sub>2</sub> CO <sub>3</sub> (0.016g), dissolved in H <sub>2</sub> O water, combined, and left to evaporate at room temperature.	Light pink crystalline plates obtained from a 1:1 molar ratio ( $6.7 \times 10^{-5}$ mol) of BA (0.02g), dissolved in MeOH and Cs <sub>2</sub> CO <sub>3</sub> (0.022g), dissolved in H <sub>2</sub> O water, combined, and left to evaporate at room temperature.
$2M^+ (C_6O_4Cl_2)^{2-} \cdot H_2O$	Red crystalline needles obtained from a 1:1 molar ratio ( $6.7 \times 10^{-5}$ mol) of CA (0.014g), dissolved in MeOH, and KOH (0.008g), dissolved in H <sub>2</sub> O, combined, and left to evaporate at room temperature.	Dark red crystalline needles obtained from a 1:1 molar ratio ( $6.7 \times 10^{-5}$ mol) of CA (0.014g), dissolved in MeOH, and Rb <sub>2</sub> CO <sub>3</sub> (0.016g), dissolved in H <sub>2</sub> O, combined, and left to evaporate at room temperature.	n/a
$M^+ (C_6O_4Cl_2H)^- \cdot 2H_2O$	n/a	Large red crystalline blocks obtained from a 1:1 molar ratio ( $6.7 \times 10^{-5}$ mol) of CA (0.014g), and Rb <sub>2</sub> CO <sub>3</sub> (0.016g), both dissolved in MeOH, combined, and left to evaporate at 40°.	Large red crystalline blocks obtained from a 1:1 molar ratio ( $6.7 \times 10^{-5}$ mol) of CA (0.014g), and Cs <sub>2</sub> CO <sub>3</sub> (0.022g), both dissolved in MeOH, combined, and left to evaporate at 50°.
$2M^+ 2(C_6O_4Cl_2H)^- (C_6O_4Cl_2H_2) \cdot 6H_2O$	n/a	Large purple crystalline blocks obtained from a 1:1 molar ratio ( $6.7 \times 10^{-5}$ mol) of CA (0.014g), dissolved in HOAc and Rb <sub>2</sub> CO <sub>3</sub> (0.016g), dissolved in MeOH, combined, and left to evaporate at room temperature.	Large purple crystalline blocks obtained from a 1:1 molar ratio ( $6.7 \times 10^{-5}$ mol) of CA (0.014g), dissolved in HOAc, and Cs <sub>2</sub> CO <sub>3</sub> (0.022g), dissolved in MeOH, combined and left to evaporate at 40°.

## 5.4 Additional Group One Metal Complexes

This section contains a description of all the other related group one metal complexes obtained during the investigation and includes two LiCA complexes one of which has undergone a halide substitution reaction, structurally similar NaCA and NaBA complexes differing in the number of incorporated water molecules and an unusual layered KCA complex.

### 5.4.1 Lithium Complexes

Two complexes were obtained upon mixing CA and lithium chloride (LiCl). The crystallographic data and experimental details for each complex are presented in Table 5-36 and Table 5-37, respectively. Attempts to obtain Lithium-BA complexes were unsuccessful as seemingly satisfactory crystals became unstable out of solution and were found to be non crystalline during cell determination.

#### 5.4.1.1 2:1 Lithium-CA Monohydrate Complex: $2\text{Li}^+ (\text{C}_6\text{O}_4\text{Cl}_2)^{2-} \cdot \text{H}_2\text{O}$

The asymmetric unit contains half a  $\text{CA}^{2-}$  molecule, with a centre of inversion, one  $\text{Li}^+$  ion, and half a water molecule.

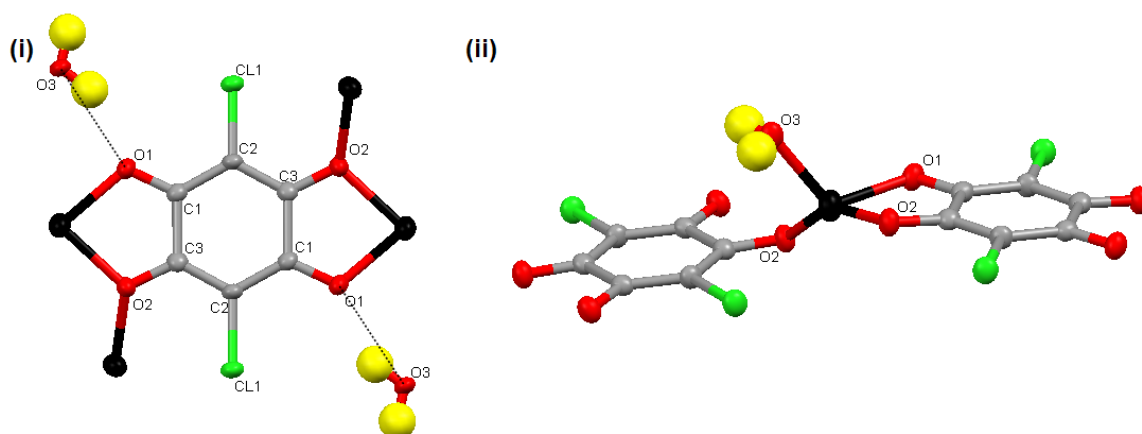


Figure 5-90  $2\text{Li}^+ (\text{C}_6\text{O}_4\text{Cl}_2)^{2-} \cdot \text{H}_2\text{O}$  environment of (i)  $\text{CA}^{2-}$  molecule and (ii)  $\text{Li}^+$  ion.

Due to the inversion centre each identical half of the  $\text{CA}^{2-}$  molecule has the same coordinating unit giving overall 2 (B3) coordination, Figure 5-90. Although there

are no previously identified HB motifs present the deprotonated carbonyl groups, identified by the longest C-O distances in this case, which coordinate to only one  $\text{Li}^+$  ion, act as proton acceptors in the two symmetry equivalent moderate  $\text{O3w-H1}\cdots\text{O1}$  HBs of  $2.6724(11)$  Å, with the nearby water molecule. HB parameters and significant interaction distances are presented in Table 5-29.

Each  $\text{Li}^+$  ion is coordinated to two  $\text{CA}^{2-}$  molecules; one monodentate C1, one bidentate B2, and one water molecule. Each  $\text{Li}^+$  ion is therefore coordinated to four oxygen atoms the bond lengths of which range from  $1.967(3)$  to  $2.004(3)$  Å. The  $\text{Li}^+$  interactions distances are presented in Table 5-27.

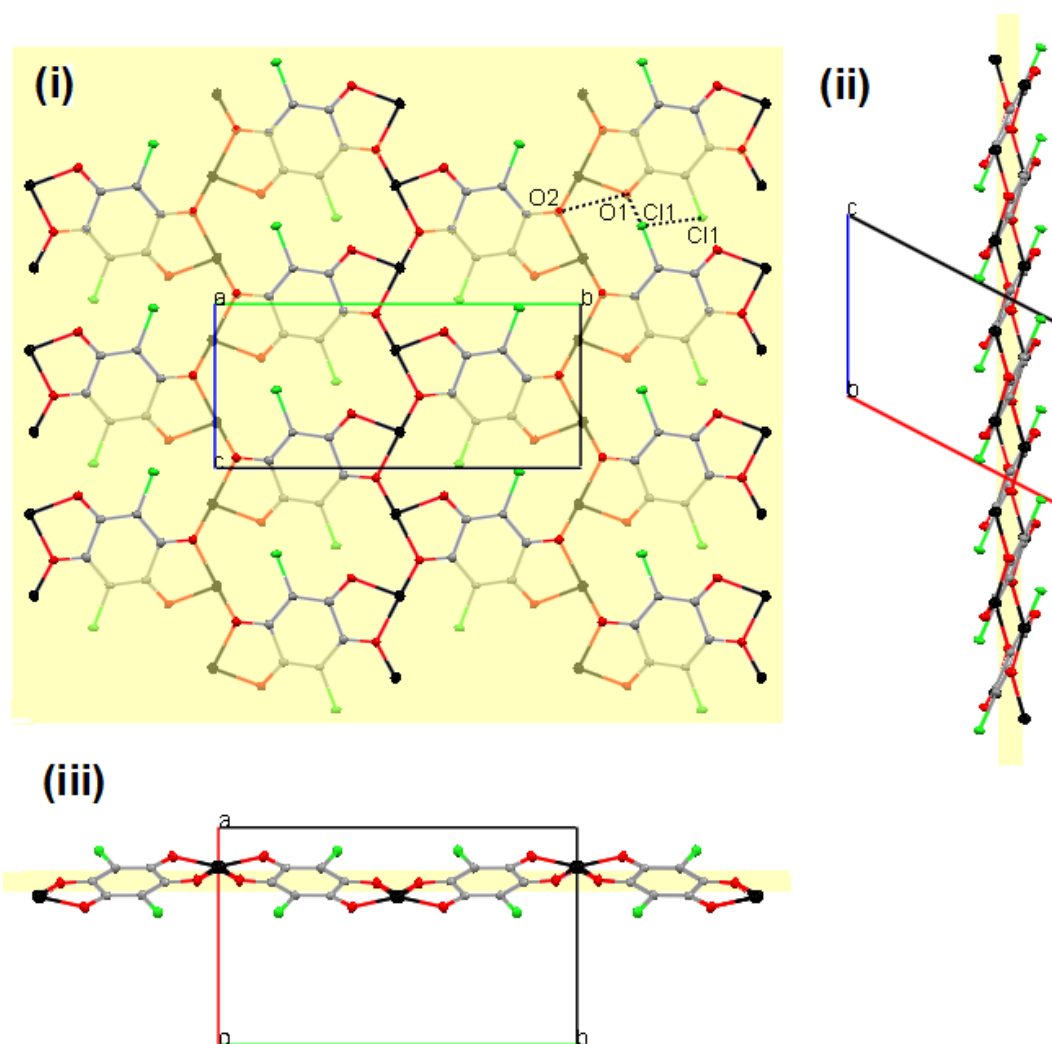
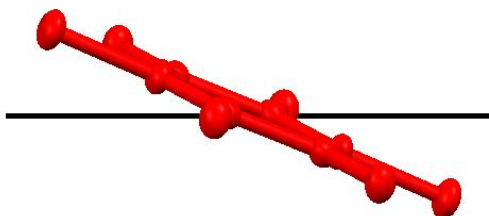


Figure 5-91  $2\text{Li}^+(\text{C}_6\text{O}_4\text{Cl}_2)^{2-}\cdot\text{H}_2\text{O}$  and  $2\text{Li}^+(\text{C}_6\text{O}_4\text{Br}_{1.25}\text{Cl}_{0.75})^{2-}\cdot\text{H}_2\text{O}$   $\text{CA}^{2-}$  planes viewed (i) perpendicular to  $bc$  plane and at angles at which plane cuts the (ii)  $b$ - and (iii)  $c$ - axes.

The resulting structure comprises  $\text{Li}^+$  chains running along the  $c$  axis and  $\text{CA}^{2-}$  planes lying on the  $bc$  plane, the latter of which is illustrated in Figure 5-91.

The way in which the  $\text{CA}^{2-}$  molecules cut the plane is illustrated in Figure 5-92.



**Figure 5-92**  $2\text{Li}^+(\text{C}_6\text{O}_4\text{Cl}_2)^{2-}\text{H}_2\text{O}$  and  $2\text{Li}^+(\text{C}_6\text{O}_4\text{Br}_{1.25}\text{Cl}_{0.75})^{2-}\text{H}_2\text{O}$  angle at which  $\text{CA}^{2-}$  molecules cut the plane.

The  $\text{CA}^{2-}$  planes are composed of rows of  $\text{CA}^{2-}$  molecules joined together by  $\text{Li}^+$  chains by the Li-O interactions mentioned above and an additional  $\text{O1}\cdots\text{O2}$  interaction of  $3.0078(2)$  Å. The Cl atoms do not interact with the  $\text{Li}^+$  ions and due to the way in which the  $\text{CA}^{2-}$  molecules cut the plane the  $\text{Cl1}\cdots\text{Cl1}$  and  $\text{Cl1}\cdots\text{O1}$  interaction distances of  $3.6630(6)$  and  $3.348(1)$  Å, between the  $\text{CA}^{2-}$  molecules within the rows is not significant in comparison to the sum of the van der Waals radii of  $3.5$  and  $3.04$  Å respectively.

The three dimensional structure is composed of two of these planes stacked along the  $a$ - axis in an ABAB manner, as indicated by red and blue in Figure 5-93. The planes are alternating in the sense that each has been rotated at an angle of  $180$  degrees along the  $b$ -axis with respect to the one preceding.

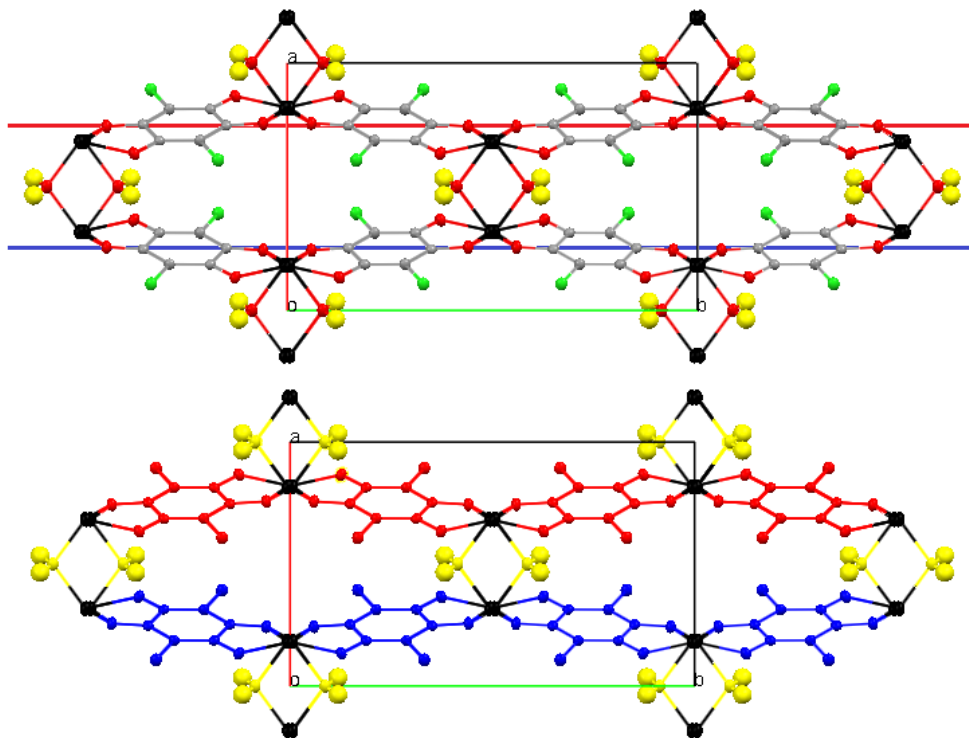
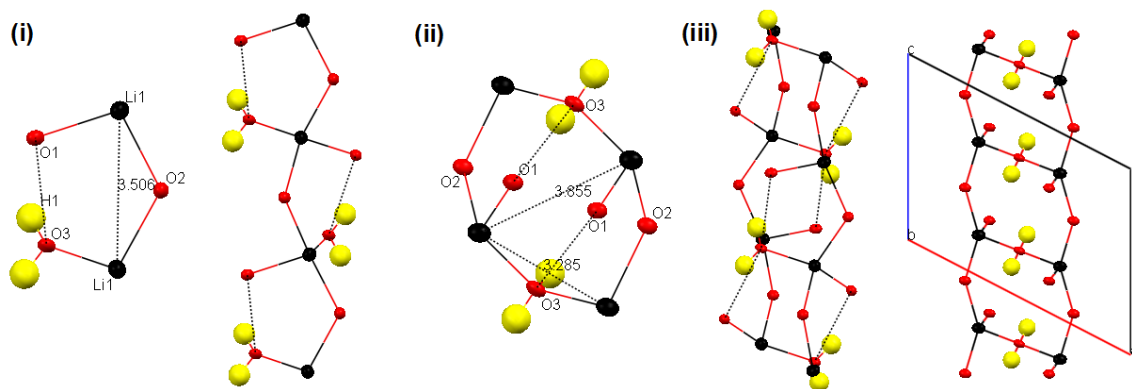


Figure 5-93.  $2\text{Li}^+(\text{C}_6\text{O}_4\text{Cl}_2)^{2-} \cdot \text{H}_2\text{O}$  and  $2\text{Li}^+(\text{C}_6\text{O}_4\text{Br}_{1.25}\text{Cl}_{0.75})^{2-} \cdot \text{H}_2\text{O}$  alternating  $\text{CA}^{2-}$  planes, rotated  $180^\circ$  along b- axis with respect to one another.

The two planes intersect along the  $\text{Li}^+$  chains that run perpendicular to each of the planes. On closer inspection, these  $\text{Li}^+$  chains that coordinate the two  $\text{CA}^{2-}$  planes are actually composed of the two identical individual  $\text{Li}^+$  chains, D1 + HB  $\text{Li}\cdots\text{Li}$  units of  $3.506(4)$  Å. These chains join together, forming the larger chain via a shorter D1 unit of  $3.285(4)$  Å in which the  $\text{Li}^+$  ions from each plane are coordinated by a water molecule. A  $\text{Li}\cdots\text{Li}$  interaction unit of length  $3.855(3)$  Å in which 2 HB interactions also joining the two  $\text{Li}^+$  are also present, although this  $\text{Li}\cdots\text{Li}$  distance is not significant in comparison to the sum of the van der Waals radii ( $3.64$  Å). This is illustrated in Figure 5-94.



**Figure 5-94**  $2\text{Li}^+(\text{C}_6\text{O}_4\text{Cl}_2)^{2-} \cdot \text{H}_2\text{O}$  (i) D1 + HB units (ii)  $\text{Li}^+$  chains in individual  $\text{CA}^{2-}$  planes, joined together via (iii) short D1 unit and 2HB unit to form larger  $\text{Li}^+$  chain that coordinates two alternating  $\text{CA}^{2-}$  planes.

The  $\text{Li}^+$  chains as viewed along the *a*-, *b*-, and *c*- axes is also illustrated in Figure 5-95.

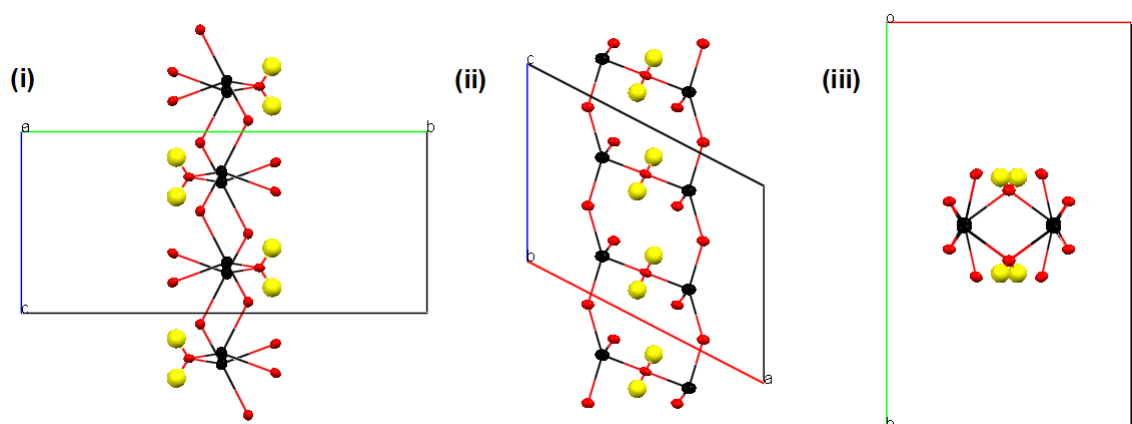


**Figure 5-95**  $2\text{Li}^+(\text{C}_6\text{O}_4\text{Cl}_2)^{2-} \cdot \text{H}_2\text{O}$ . Large  $\text{Li}^+$  chains that coordinate two alternating  $\text{CA}^{2-}$  planes, as viewed along the (i) *a*-, (ii) *b*- and (iii) *c*-axes.

The point at which the two  $\text{CA}^{2-}$  planes and  $\text{Li}^+$  chains intersect is illustrated in Figure 5-96.

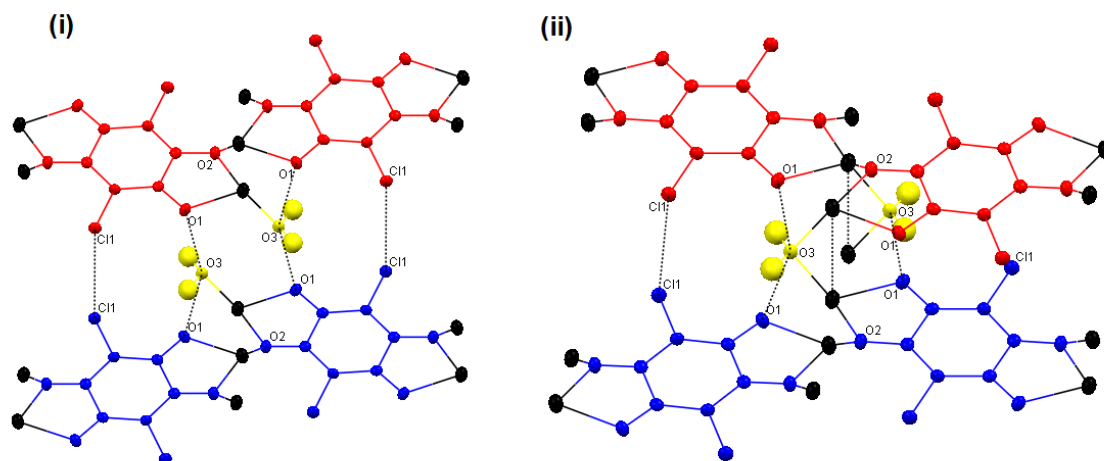


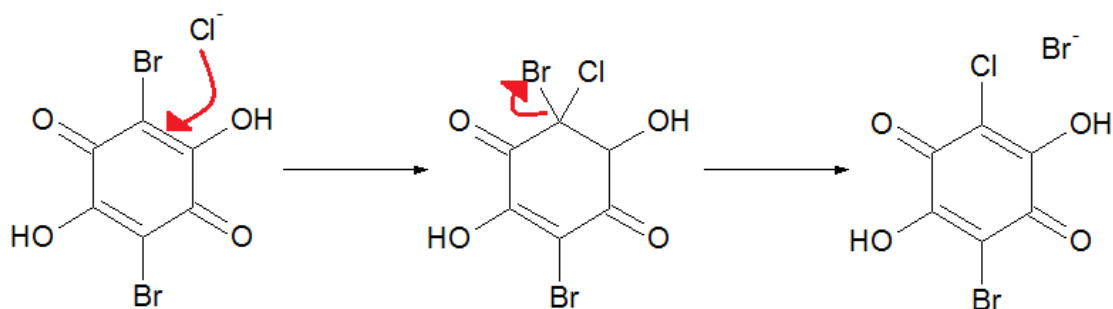
Figure 5-96  $2\text{Li}^+(\text{C}_6\text{O}_4\text{Cl}_2)^{2-} \cdot \text{H}_2\text{O}$ . Point of intersection between  $\text{CA}^{2-}$  planes and  $\text{Li}^+$  chains.

There is a centre of inversion present in the centre of the insignificant 2HB  $\text{Li}\cdots\text{Li}$  interaction unit distance, which is also present in the centre of two separate significant when compared to the sum of the van der Waals radii,  $\text{Li}\cdots\text{Li}$  D1 interactions, so the two planes are inversely related by symmetry. The two symmetry related  $\text{O3w-H1}\cdots\text{O1}$  HB interactions, mentioned previously, between the planes are  $2.6724(11)$  Å in length and the  $\text{Cl1}\cdots\text{Cl1}$  interactions also present at this point of intersection between the two planes are  $3.4263(4)$  Å.

#### 5.4.1.2 2:1 Lithium-CA/BA monohydrate complex: $2\text{Li}^+(\text{C}_6\text{O}_4\text{Br}_{0.25}\text{Cl}_{0.75})^{2-} \cdot \text{H}_2\text{O}$

In addition to the above complex the related 2:1 Lithium-CA/BA monohydrate complex was also obtained from a 1:2 molar ratio of BA and Lithium Chloride in ethanol. Treating the resultant materials as a purely bromanilic acid complex resulted in unreasonable thermal parameters for the Br atoms. The C–Br distances obtained were shorter than those obtained in previous BA molecules. A stable refinement was obtained following the creation of a model representing a solid solution of BA/CA. Restraints were used to fix the C–Cl and C–Br distances and the occupancy of each was allowed to freely refine. The final refinement gave a Cl:Br ratio of 3.25:1. The structure of the complex is identical to the complex above. A substitution reaction is believed to have occurred between the  $\text{Cl}^-$  ion, and the BA molecule in solution (Scheme 5-1).

**Scheme 5-1** Substitution reaction scheme for Cl<sup>-</sup> anion with BA.



A comparison of the intra-molecular bond lengths for the  $2\text{Li}^+ (\text{C}_6\text{O}_4\text{Cl}_2)^{2-} \cdot \text{H}_2\text{O}$  (LiCA) and  $2\text{Li}^+ (\text{C}_6\text{O}_4\text{Br}_{0.25}\text{Cl}_{0.75})^{2-} \cdot \text{H}_2\text{O}$  (LiCABA) complexes, Table 5-28, shows no significant differences apart from the C-Cl distance in the latter which, despite the use of strong restraints, is more characteristic of a C-Br distance.

There is a significant change in the short  $\text{Li}\cdots\text{Li}$  D1 + HB distance and also the  $\text{Cl1}\cdots\text{Cl1}$  distance both of which are interactions between the two interacting planes. The  $\text{Li}\cdots\text{Li}$  distance decreases from 3.285(4) Å in the LiCA complex to 3.254(6) Å in the LiCABA complex, and the  $\text{Cl}\cdots\text{Cl}$  distance of 3.4263(4) Å in the LiCA complex decreases to 3.395(8) Å in the LiCABA complex which, due to the coexistence of the two halogens, also contains related Cl-Br and Br-Br distances of 3.390(6) and 3.385(3) Å in comparison to the sum of the van der Waals radii of 3.6 and 3.7 Å. The effect of incorporating a Br atom in place of a Cl atom in this proportion, has decreased the  $\text{X}\cdots\text{X}$  and  $\text{M}\cdots\text{M}$  distances interaction distances between the  $\text{XA}^{2-}$  planes. Each  $\text{CA}^{2-}$  molecule has an inversion centre and so these interactions also occur at the other side of the molecule, the net result causing the  $\text{O3w-H1}\cdots\text{O1}$  HB interactions to increase in distance from 2.6724(11) to 2.7078(12) Å and decrease in angle from 151(2)° in the LiCA complex to 141(2)° in the LiCABA complex.

Table 5-27 M Distances for  $2\text{Li}^+(\text{C}_6\text{O}_4\text{X}_2)^{2-} \cdot \text{H}_2\text{O}$  (X=Cl, Br)

		X=Cl	X=Cl/Br	Van der waals radii / Å
D1 + HB	Li1-----Li1	3.285(4)	3.254(6)	3.64
D1	Li1-----Li1	3.506(4)	3.532(6)	3.64
- 2HB	Li1-----Li1	3.855(3)	3.829(4)	3.64
C1 H <sub>2</sub> O	Li1-----O3	1.991(3)	2.002(4)	3.34
C1 CA <sup>2-</sup>	Li1-----O2	2.003(3)	2.017(4)	3.34
B2 CA <sup>2-</sup>	Li1-----O1	1.967(3)	1.971(3)	3.34
	Li1-----O2	2.004(3)	2.007(4)	3.34

Table 5-28 Intra-molecular bond lengths for  $2\text{Li}^+(\text{C}_6\text{O}_4\text{X}_2)^{2-} \cdot \text{H}_2\text{O}$  (X=Cl, Br)

	X=Cl	X=Cl/Br
C-C Distances		
C1-C2	1.402(2)	1.400(2)
C2-C3	1.386(2)	1.390(2)
C3-C1	1.537(2)	1.544(2)
C-O and C-X Distances		
C1-O1	1.246(2)	1.264(2)
C3-O2	1.261(2)	1.862(6)
C2-Cl	1.734(1)	1.866(2)
C2-Br	-	-

Table 5-29 HB Parameters and Significant Interactions for  $2\text{Li}^+(\text{C}_6\text{O}_4\text{X}_2)^{2-} \cdot \text{H}_2\text{O}$  (X=Cl, Br)

$2\text{Li}^+(\text{C}_6\text{O}_4\text{X}_2)^{2-} \cdot \text{H}_2\text{O}$	X=Cl				X=Cl/Br				Van der waals radii / Å
	D-H / Å	H---A / Å	D---A / Å	<DHA / °	D-H / Å	H---A / Å	D---A / Å	<DHA / °	
O1-O2	-	-	3.0078(2)	-	-	-	3.035(2)	-	3.04
O1-Cl1	-	-	3.348(1)	-	-	-	3.428(3)	-	3.04
O3-H1---O1	0.81(2)	1.94(2)	2.6724(11)	151(2)	0.86(3)	1.99(3)	2.7078(12)	141(2)	3.04
Cl1-Cl1	-	-	3.4263(4)	-	-	-	3.395(8)	-	3.5
Cl1-Br1	-	-	-	-	-	-	3.390(6)	-	3.6
Br1-Br1	-	-	-	-	-	-	3.385(3)	-	3.7
Cl1-Cl1	-	-	3.6630(6)	-	-	-	3.8790(3)	-	3.5
Cl1-Br1	-	-	-	-	-	-	3.8813(3)	-	3.6
Br1-Br1	-	-	-	-	-	-	3.8790(3)	-	3.7

### 5.4.1.3 1:1 Lithium-CA dihydrate complex: $2\text{Li}^+(\text{C}_6\text{O}_4\text{Cl}_2)^{2-}(\text{C}_6\text{O}_4\text{Cl}_2\text{H}_2) 2\text{H}_2\text{O}$

The Li 1:1 CA monohydrate complex was obtained as described in Table 5-37. The asymmetric unit contains half of a  $\text{CA}^{2-}$  molecule and half of a  $\text{H}_2\text{CA}$  molecule both with an inversion centre, one  $\text{Li}^+$  ion, and one water molecule, Figure 5-97.

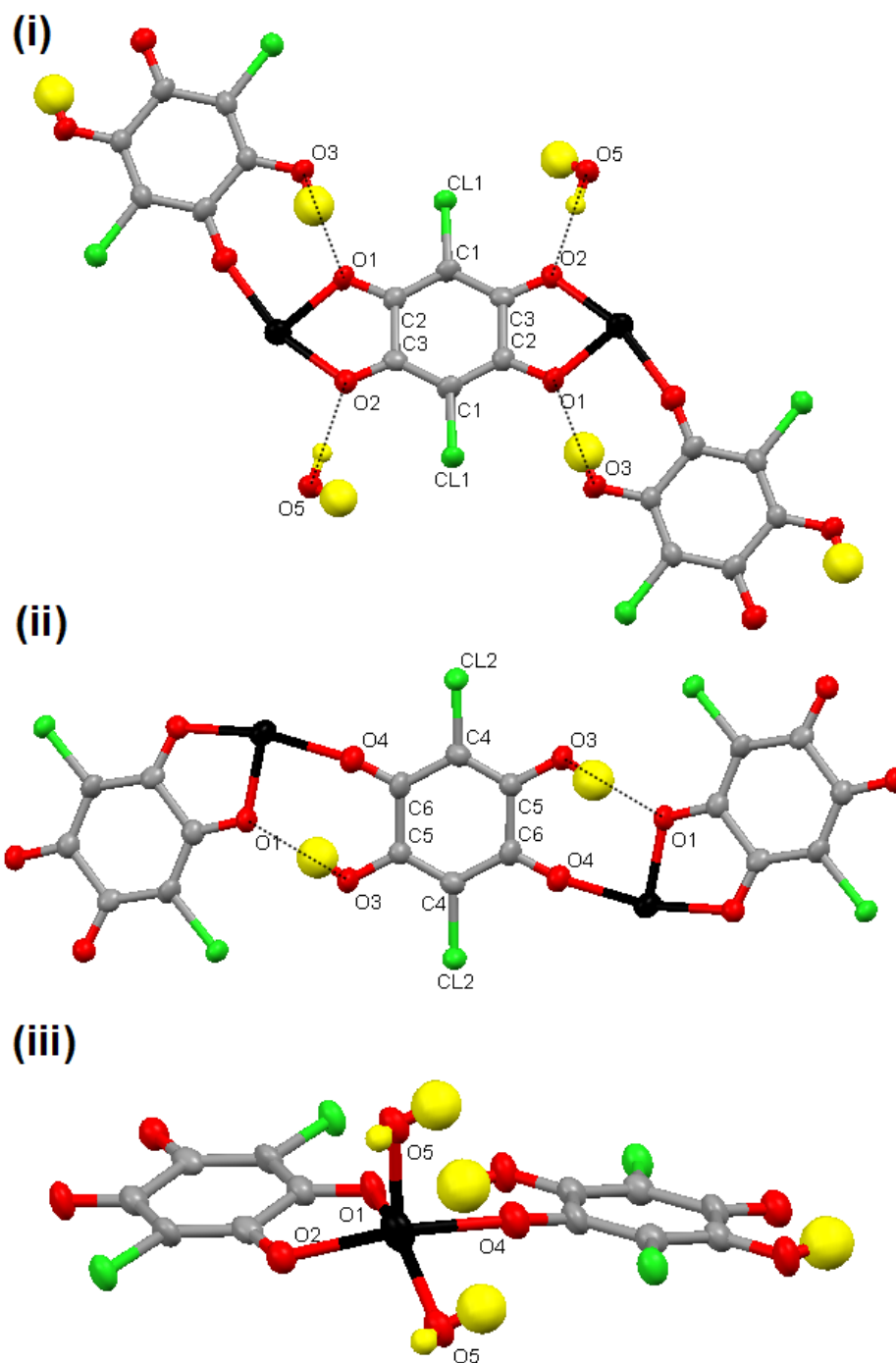


Figure 5-97  $2\text{Li}^+(\text{C}_6\text{O}_4\text{Cl}_2)^{2-}(\text{C}_6\text{O}_4\text{Cl}_2\text{H}_2) 2\text{H}_2\text{O}$  environment of (i)  $\text{CA}^{2-}$  molecule (ii)  $\text{H}_2\text{CA}$  molecule and (iii)  $\text{Li}^+$  ion.

Due to the inversion centre, each identical half of the  $\text{CA}^{2-}$  molecule has the same two metal coordinating units giving overall 2 (B2) coordination. Although there are no previously identified HB motifs present, the O1 carbonyl atoms act as proton acceptors in the two symmetry equivalent O3-H1 $\cdots$ O1 HBs with the coordinating  $\text{HCA}^-$  molecules, and the O2 carbonyl atoms act as proton acceptors in the two symmetry equivalent moderate O5w-H3 $\cdots$ O2 HBs with the nearby water molecules. The HB distances are 2.630(4) and 2.739(5) Å respectively. The  $\text{H}_2\text{CA}$  molecule, due to an inversion centre, has the same two coordinating units giving an overall 2 (C1) coordination, and also 2 (E1) HB motifs with the two symmetry equivalent O5w-H3 $\cdots$ O2 HBs above. All HB parameters and significant interactions are presented in Table 5-30.

Each  $\text{Li}^+$  ion is coordinated to one  $\text{H}_2\text{CA}$  molecule and one  $\text{CA}^{2-}$  molecule by monodentate C1 and bidentate B2 coordination respectively, and two water molecules. Each  $\text{Li}^+$  ion is therefore coordinated to five oxygen atoms the bond lengths of which range from 1.986(9) to 2.08(1) Å. The  $\text{Li}^+$  interaction distances are presented in Table 5-31.

The resulting structure is a three dimensional complex (Figure 5-98), and can be broken down into CA planes and perpendicular  $\text{Li}^+$  chains.

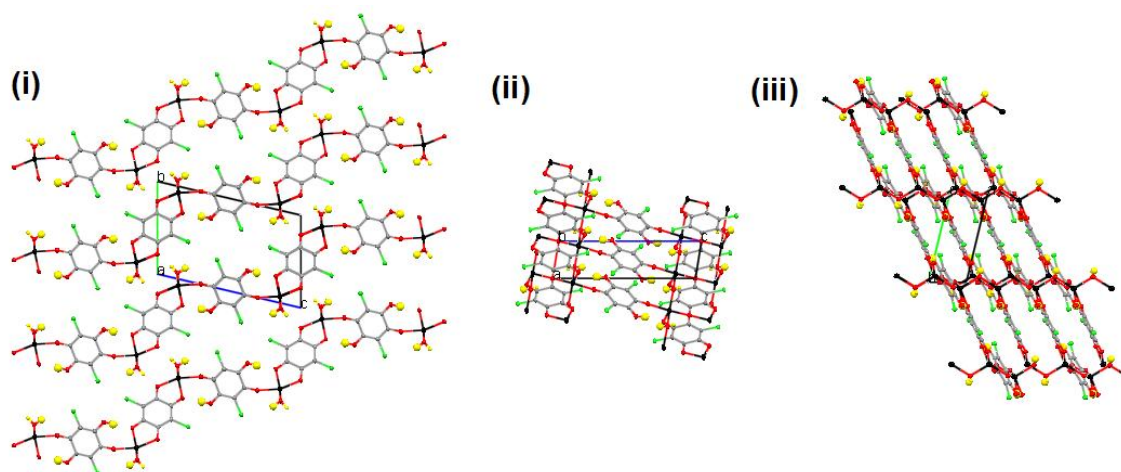


Figure 5-98  $2\text{Li}^+(\text{C}_6\text{O}_4\text{Cl}_2)^{2-}(\text{C}_6\text{O}_4\text{Cl}_2\text{H}_2) 2\text{H}_2\text{O}$  structure viewed along (i) *a*- (ii) *b*- and *c*- axis.

The CA plane, and the angles at which it cuts the *a*-, *b*-, and *c*- axes, is illustrated in Figure 5-99.

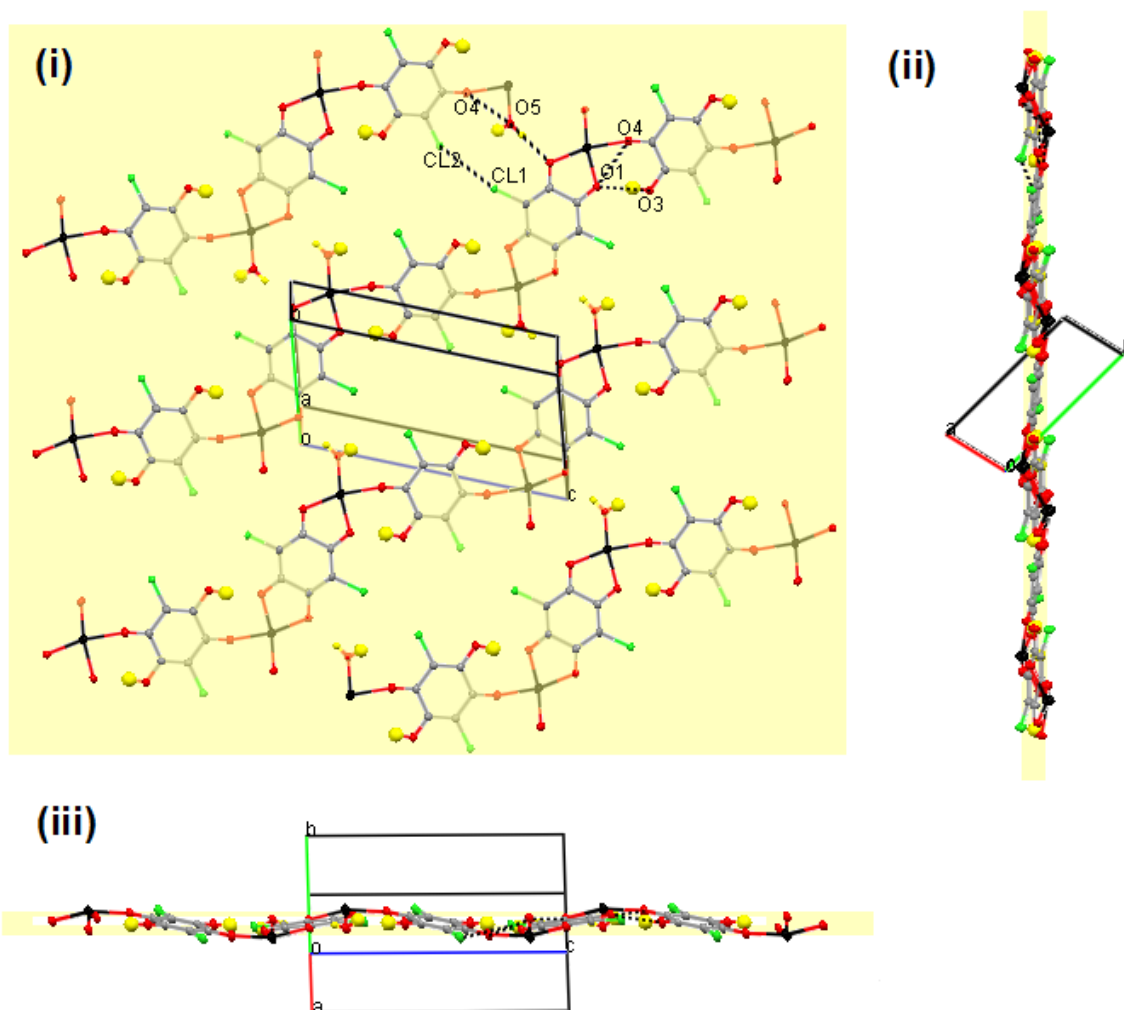


Figure 5-99  $2\text{Li}^+(\text{C}_6\text{O}_4\text{Cl}_2)^{2-}(\text{C}_6\text{O}_4\text{Cl}_2\text{H}_2) 2\text{H}_2\text{O}$  structure viewed (i) perpendicular to plane and as it cuts the (ii) *b*- and (iii) *c*- axes.

The  $\text{CA}^{2-}$  and  $\text{H}_2\text{CA}$  molecules cut the plane as shown in Figure 5-100.

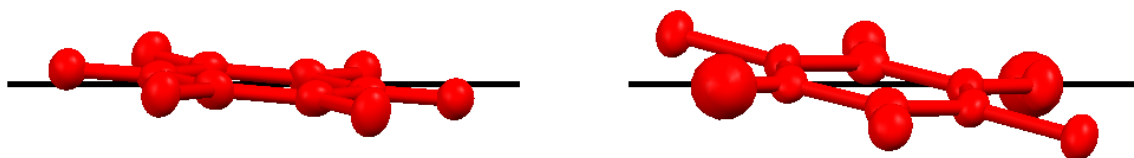


Figure 5-100  $2\text{Li}^+(\text{C}_6\text{O}_4\text{Cl}_2)^{2-}(\text{C}_6\text{O}_4\text{Cl}_2\text{H}_2) 2\text{H}_2\text{O}$  angles at which  $\text{CA}^{2-}$  and  $\text{H}_2\text{CA}$  molecules cut the plane.

The planes are composed of wavy chains of alternating  $\text{CA}^{2-}$  and  $\text{H}_2\text{CA}$  molecules connected by  $\text{Li}^+$  ions. The interconnecting chains are illustrated in Figure 5-101.

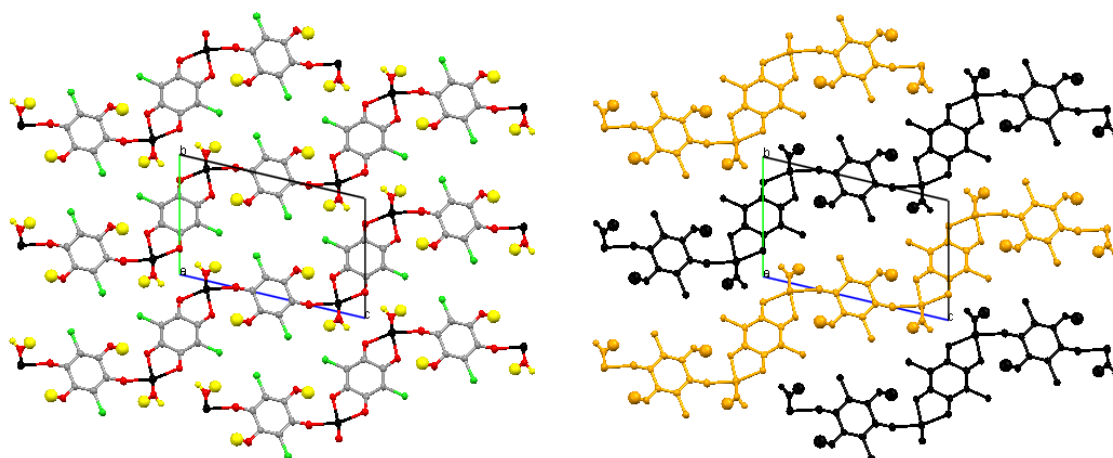


Figure 5-101  $2\text{Li}^+(\text{C}_6\text{O}_4\text{Cl}_2)^{2-}(\text{C}_6\text{O}_4\text{Cl}_2\text{H}_2) \cdot 2\text{H}_2\text{O}$ , CA planes viewed in terms of interconnecting wavy chains (orange and black).

Within the chains, the  $\text{CA}^{2-}$  and  $\text{H}_2\text{CA}$  molecules also coordinate to one another via the  $\text{O3-H1}\cdots\text{O1}$  HB mentioned previously, and an  $\text{O1}\cdots\text{O4}$  interaction of  $2.7412(4)$  Å in comparison to the sum of the van der Waals radii of  $3.04$  Å. The CA chains are connected to one another via the interactions of the O5 water molecule; the  $\text{O5-H3}\cdots\text{O2}$  HBs mentioned previously,  $\text{O5}\cdots\text{O4}$  and  $\text{O5}\cdots\text{Cl1}$  interactions of  $2.7732(5)$  and  $3.3259(5)$  Å, and a  $\text{Cl1}\cdots\text{Cl2}$  interaction of  $3.4994(6)$  Å the latter of which is approximately equal to the sum of the van der Waals radii of  $3.5$  Å and thus is borderline significant. These interactions are illustrated in Figure 5-102.

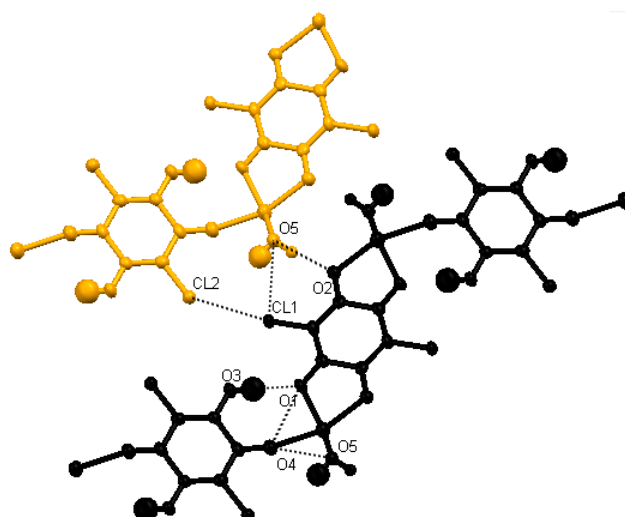


Figure 5-102  $2\text{Li}^+(\text{C}_6\text{O}_4\text{Cl}_2)^{2-}(\text{C}_6\text{O}_4\text{Cl}_2\text{H}_2) 2\text{H}_2\text{O}$ , Interactions within and between interconnecting wavy chains (orange and black) in CA planes.

The CA planes are stacked in an AAA fashion so the molecules in the adjacent planes are in the same position. The CA molecules in adjacent planes do not interact with one another directly although they are held in place by the perpendicular  $\text{Li}^+$  chains and Li-O interactions.

The  $\text{Li}^+$  chains are composed of three  $\text{M}\cdots\text{M}$  interaction units. The most significant is a D1 interaction of  $3.53(2) \text{ \AA}$  that makes up a  $\text{Li}^+$  chain that connects the rows of CA molecules within the CA planes to those directly below, and therefore runs perpendicular to the CA planes, via the O5w atom. Both the CA planes and the CA rows within the planes intersect and interact with one another along these D1 chains. At each point of intersection two of the D1 chains interact via two symmetry equivalent O3-H1 $\cdots$ O1 HBs in the form of two  $\text{M}\cdots\text{M}$  interactions of  $4.37(1)$  and  $5.14(1) \text{ \AA}$  which are not significant when compared to the sum of the van der Waals radii of  $3.64 \text{ \AA}$ . The interacting D1 Li-Li chains and 2HB Li $\cdots$ Li units are illustrated in Figure 5-103.

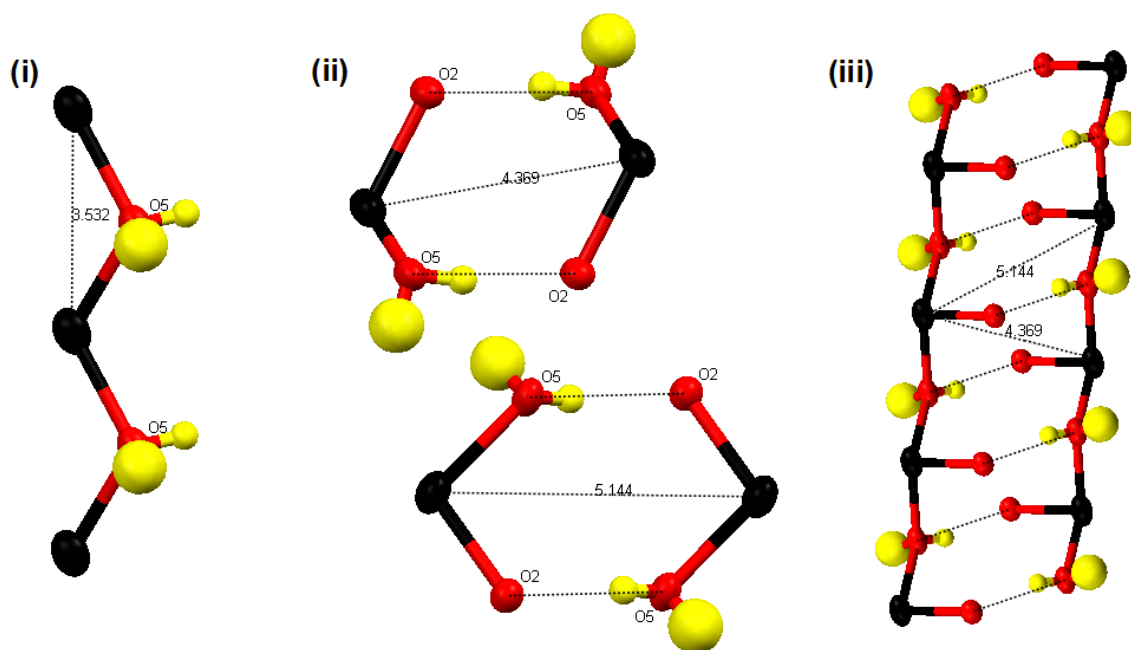
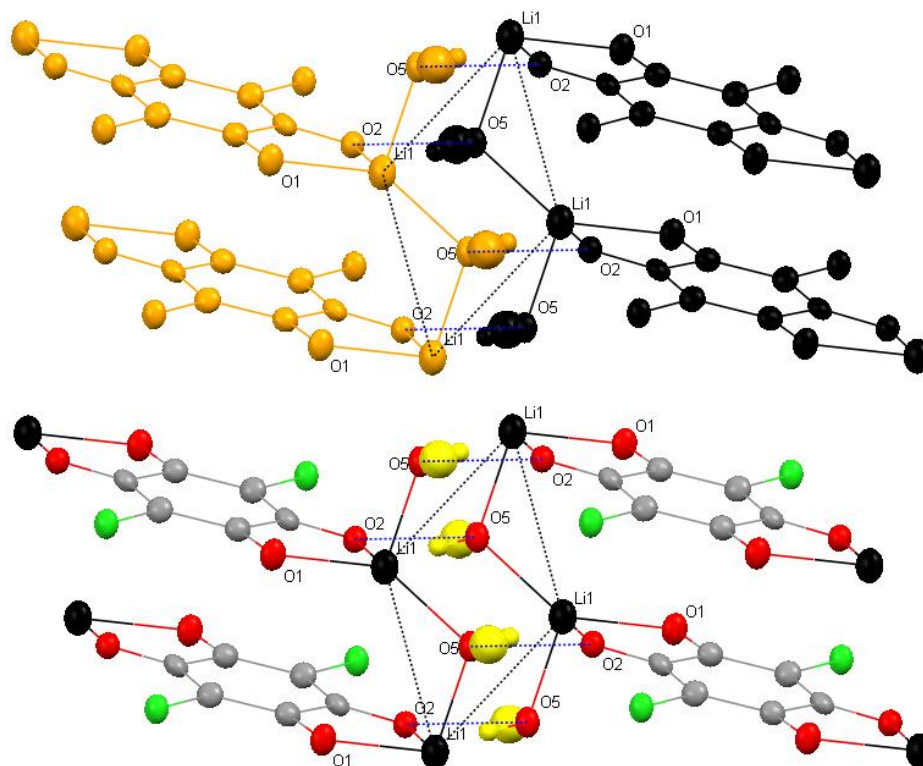


Figure 5-103.  $2\text{Li}^+(\text{C}_6\text{O}_4\text{Cl}_2)^{2-}(\text{C}_6\text{O}_4\text{Cl}_2\text{H}_2) 2\text{H}_2\text{O}$ , (i) D1  $\text{Li}\cdots\text{Li}$  chains and (ii) 2HB  $\text{Li}\cdots\text{Li}$  units comprising (iii) interacting D1 chains.

The way in which the  $\text{CA}^{2-}$  molecules within the CA rows interact with those in adjacent rows and planes via the interacting  $\text{Li}^+$  chains and inversion centres is illustrated in Figure 5-104.



**Figure 5-104**  $2\text{Li}^+(\text{C}_6\text{O}_4\text{Cl}_2)^{2-}(\text{C}_6\text{O}_4\text{Cl}_2\text{H}_2) \cdot 2\text{H}_2\text{O}$ , interaction of  $\text{CA}^{2-}$  molecules within CA rows and adjacent planes via the interacting  $\text{Li}^+$  chains.

The H2CA molecules do not interact with the  $\text{Li}^+$  ions. The intra-molecular distances and arrangement of the single, double and intermediate bond within the carbon rings for both the  $\text{CA}^{2-}$  and H2CA molecules (Table 5-32) are both comparable to the average values obtained from the CSD.

**Table 5-30 HB Parameters and Significant Interactions for  $2\text{Li}^+(\text{C}_6\text{O}_4\text{Cl}_2)^{2-}(\text{C}_6\text{O}_4\text{Cl}_2\text{H}_2) 2\text{H}_2\text{O}$** 

	<i>D-H</i> / Å	<i>H---A</i> / Å	<i>D---A</i> / Å	<i>&lt;DHA</i> / °	<i>Sum of van der Waals radii</i> / Å
O1-O4	-	-	2.7412(4)	-	3.04
O3-H1---O1	0.86(7)	1.79(7)	2.630(4)	167(7)	3.04
O4-O5	-	-	2.7732(5)	-	3.04
O5-H3---O2	0.82(6)	1.94(6)	2.739(5)	163(5)	3.04
O5-Cl1	-	-	3.3259(5)	-	3.27
Cl1-Cl2	-	-	3.4994(6)	-	3.5

**Table 5-31 M interactions for  $2\text{Li}^+(\text{C}_6\text{O}_4\text{Cl}_2)^{2-}(\text{C}_6\text{O}_4\text{Cl}_2\text{H}_2) 2\text{H}_2\text{O}$** 

	<i>M</i>		<i>sum of van der Waals radii</i> / Å
D1	Li1-----Li1	3.53(2)	3.64
2HB	Li1-----Li1	4.37(1)	3.64
2HB	Li1-----Li1	5.14(1)	3.64
C1 H <sub>2</sub> O	Li1-----O5	2.08(1)	3.34
C1 H <sub>2</sub> O	Li1-----O5	2.08(1)	3.34
C1 H <sub>2</sub> CA	Li1-----O4	2.074(8)	3.34
B2 CA <sup>2-</sup>	Li1-----O1	1.986(9)	3.34
	Li1-----O2	2.027(8)	3.34

**Table 5-32 Intra-molecular distances for  $2\text{Li}^+(\text{C}_6\text{O}_4\text{Cl}_2)^{2-}(\text{C}_6\text{O}_4\text{Cl}_2\text{H}_2) 2\text{H}_2\text{O}$** 

	CA <sup>2-</sup>		H <sub>2</sub> CA
C-C Distances		C-C Distances	
C1-C2	1.408(6)	C4-C5	1.349(6)
C2-C3	1.543(6)	C5-C6	1.525(6)
C3-C1	1.395(6)	C6-C4	1.46(6)
C-O and C-Cl Distances		C-O and C-Cl Distances	
C1-Cl1	1.724(4)	C4-Cl2	1.713(5)
C2-O1	1.257(5)	C5-O3	1.300(5)
C3-O2	1.248(6)	C6-O4	1.222(5)

## 5.4.2 Sodium Complexes

Although a large number of conditions were varied in the combination of Na and XA starting materials, only one NaBA and one NaCA complex were identified during crystal screening. The crystallographic data for both complexes are presented in Table 5-36 and although the experimental details for both complexes are also specified in Table 5-37, both complexes were also obtained under a number of other conditions.

### 5.4.2.1 2:1 Sodium-BA tetrahydrate complex: $2\text{Na}^+(\text{C}_6\text{O}_4\text{Br}_2)^{2-} \cdot 4\text{H}_2\text{O}$

The 2:1 Na:BA tetrahydrate complex was obtained as described in Table 5-37. The asymmetric unit of this complex contains one  $\text{BA}^{2-}$  molecule, two  $\text{Na}^+$  ions, and four water molecules, Figure 5-105.

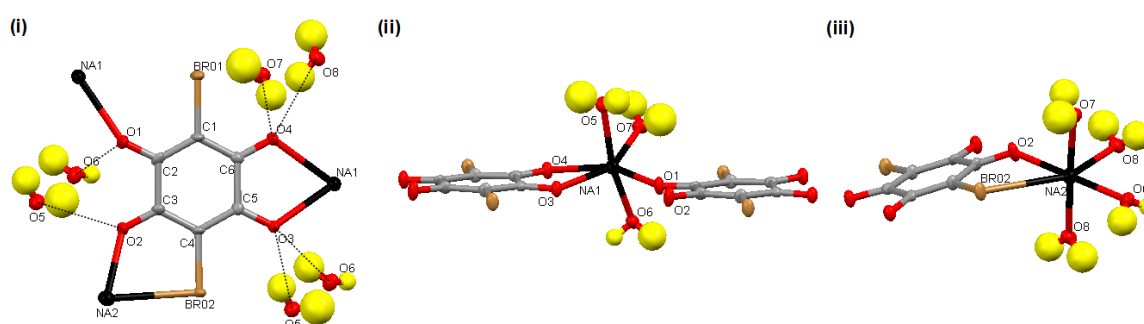


Figure 5-105  $2\text{Na}^+(\text{C}_6\text{O}_4\text{Br}_2)^{2-} \cdot 4\text{H}_2\text{O}$  environment of (i)  $\text{BA}^{2-}$  (ii)  $\text{Na1}^+$  ion and (iii)  $\text{Na2}^+$  ion

The  $\text{BA}^{2-}$  molecule does not have an inversion centre. On one side of the molecule the O3 and O4 carbonyls coordinate to an  $\text{Na1}^+$  ion by a B2 unit, and on the other side of the molecule the O2 and Br2 atoms coordinate to an  $\text{Na2}^+$  ion by an A2 unit and the O1 atom coordinates to another  $\text{Na1}^+$  ion by a C1 unit. This gives an overall (C1 B2 A2) coordination. There are no previously identified HB motifs present, however the O3 and O4 carbonyls both act as proton acceptors in the  $\text{O5w-H2}\cdots\text{O3}$  and  $\text{O6w-H3}\cdots\text{O3}$  HBs of distances 2.973(3) and 2.842(2)Å and the  $\text{O7w-H5}\cdots\text{O4}$  and  $\text{O8w-H8}\cdots\text{O4}$  HBs of distances 2.875(2) 2.905(3)Å. The O1 and O2 atoms also act as proton acceptors in the  $\text{O6w-H4}\cdots\text{O1}$  and  $\text{O5-H1}\cdots\text{O2}$  HBs of

distances 2.908(2) and 2.779(3) Å respectively. All HB parameters and significant interaction distances are presented in Table 5-34.

Each Na<sup>1+</sup> ion is coordinated to two BA<sup>2-</sup> molecules by monodentate C1 and bidentate B2 coordination, and to three water molecules. Each Na<sup>1+</sup> ion is therefore coordinated to six oxygen atoms the bond lengths of which range from 2.342(2) - 2.505(2) Å. Each Na<sup>2+</sup> ion is coordinated one CA<sup>2-</sup> molecule by bidentate A2 coordination, and to four water molecules. Each Na<sup>2+</sup> ion is therefore coordinated to six atoms; five oxygen atoms the bond lengths of which range from 2.325(2) - 2.382(3) Å and one bromine atom of bond length 3.154(1) Å. All Na<sup>+</sup> interaction distances are presented in Table 5-33.

The resulting three dimensional structure, is illustrated as viewed along the *a*-, *b*-, and *c*- axes in Figure 5-106.

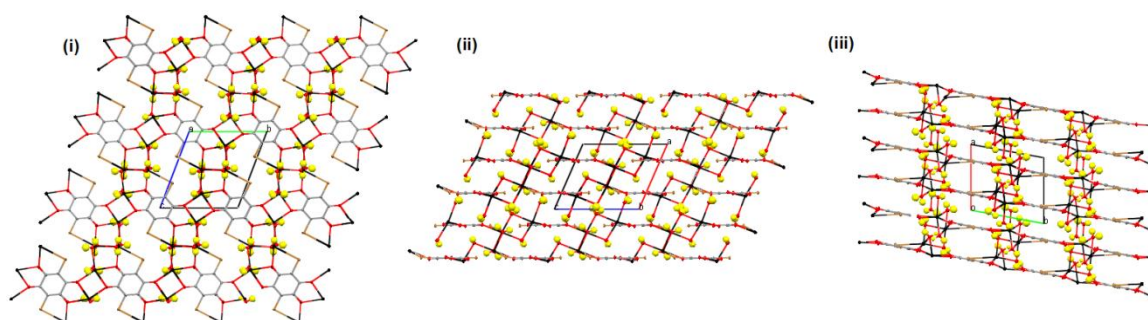


Figure 5-106 2Na<sup>+</sup>(C<sub>6</sub>O<sub>4</sub>Br<sub>2</sub>)<sup>2-</sup>·4H<sub>2</sub>O structure as viewed along the (i) *a*-, (ii) *b*-, and (iii) *c*-axes.

The structure can be broken down into BA<sup>2-</sup> planes that lie along the *bc* plane (Figure 5-107) and Na<sup>+</sup> chains that lie along the *ac* plane (Figure 5-108).

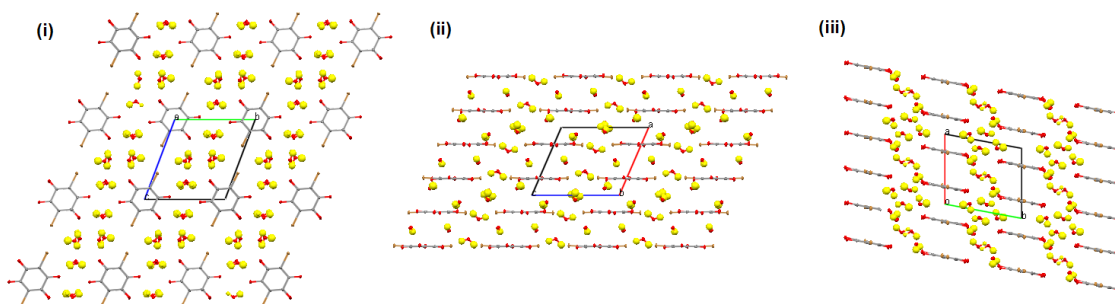


Figure 5-107  $2\text{Na}^+(\text{C}_6\text{O}_4\text{Br}_2)^{2-} \cdot 4\text{H}_2\text{O}$  structure composed of  $\text{BA}^{2-}$  planes that lie along the  $ac$  plane, as viewed along the (i)  $a$ -, (ii)  $b$ -, and (iii)  $c$ -axes.

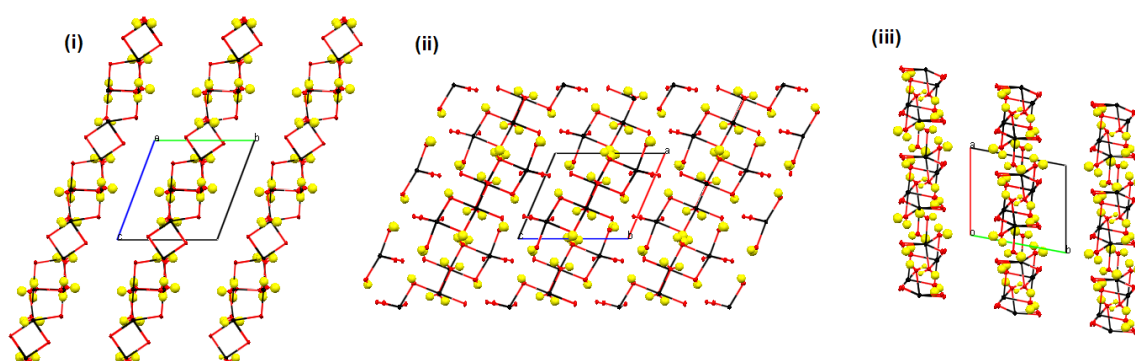


Figure 5-108  $2\text{Na}^+(\text{C}_6\text{O}_4\text{Br}_2)^{2-} \cdot 4\text{H}_2\text{O}$  structure composed of  $\text{Na}^+$  chains that lie along the  $ac$  plane, as viewed along the (i)  $a$ -, (ii)  $b$ -, and (iii)  $c$ -axes.

The  $\text{BA}^{2-}$  planes, illustrated in Figure 5-109, are composed of rows of  $\text{BA}^{2-}$  molecules coordinated to one another via a  $\text{Na}^+$  ion, Figure 5-110.

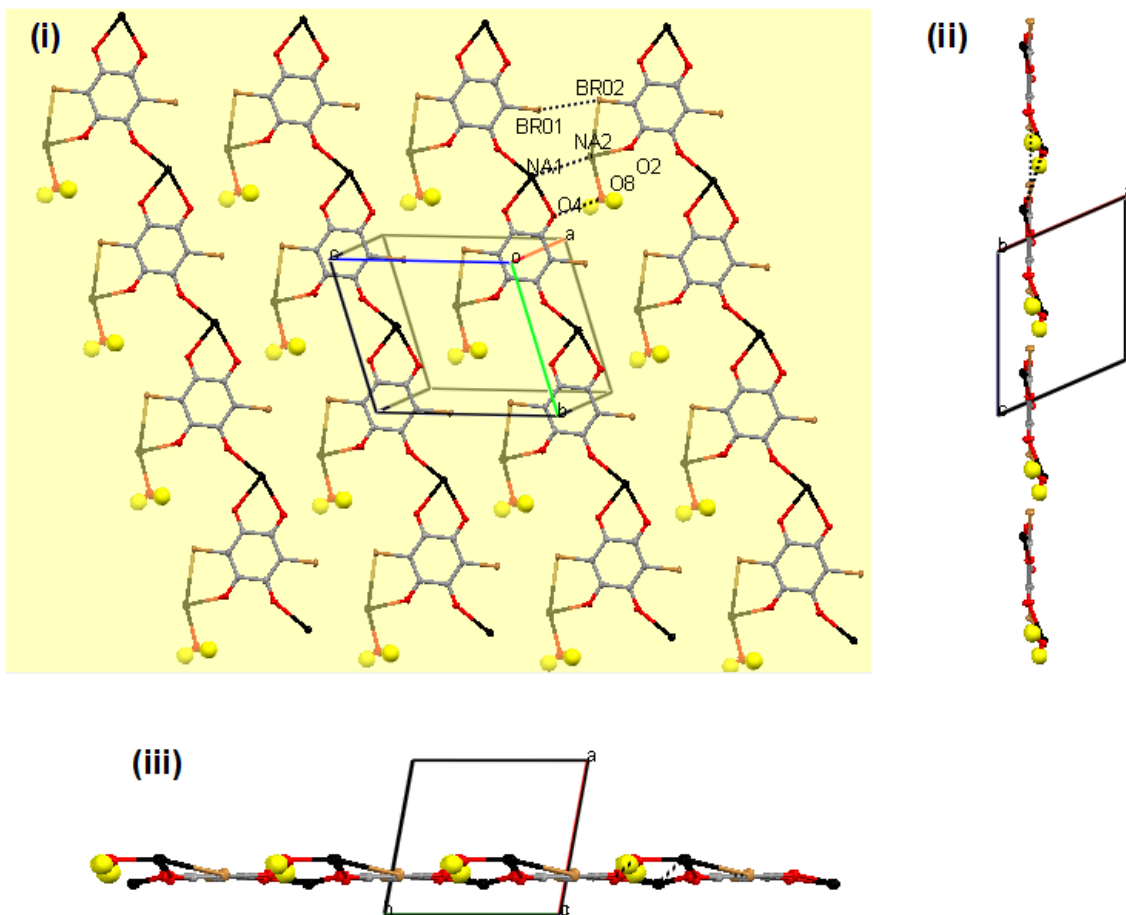


Figure 5-109  $2\text{Na}^+(\text{C}_6\text{O}_4\text{Br}_2)^{2-} \cdot 4\text{H}_2\text{O}$   $\text{BA}^{2-}$  planes viewed (i) perpendicular to the plane and the angle at which the plane cuts the (ii) *b*- and (iii) *c*-axes.

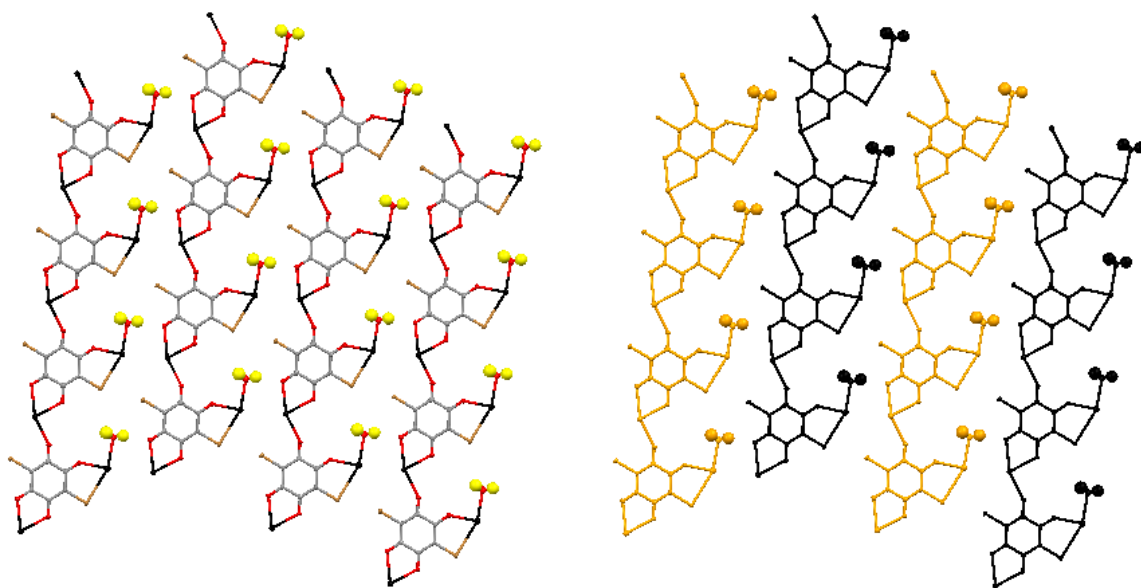
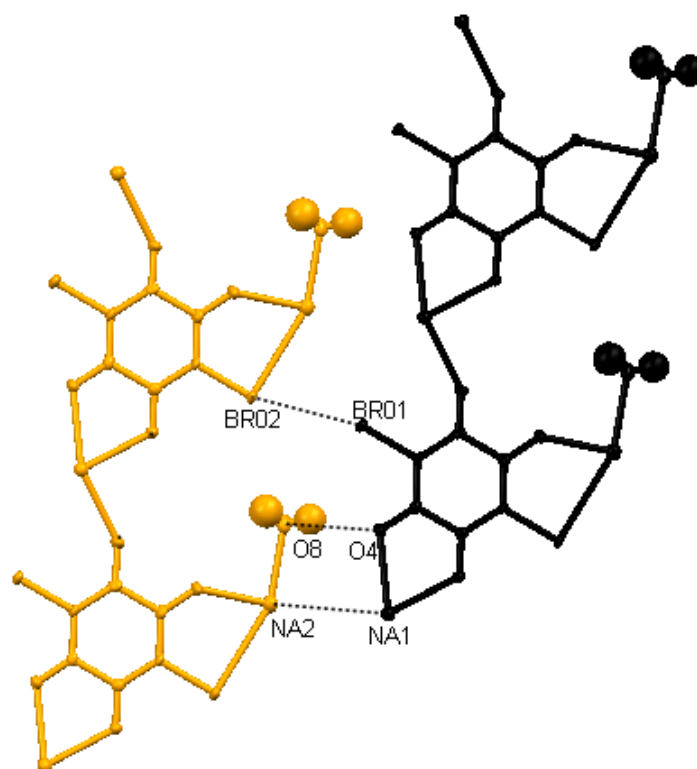


Figure 5-110  $2\text{Na}^+(\text{C}_6\text{O}_4\text{Br}_2)^{2-} \cdot 4\text{H}_2\text{O}$   $\text{BA}^{2-}$  planes composed of rows of  $\text{BA}^{2-}$  molecules (orange and black) connected to one another by  $\text{Na}^+$  ions.

The rows of  $\text{BA}^{2-}$  molecules within the plane are connected by  $\text{O8w-H8}\cdots\text{O4}$  HB interactions, mentioned previously, and  $\text{Br1}\cdots\text{Br2}$  and  $\text{Na1}\cdots\text{Na2}$  interactions of lengths 3.3093(1) and 3.614(2) Å, both significant when compared to the sum of the van der Waals radii of 3.7 and 4.54 Å, and the average interaction distances of 3.570 and 3.695 Å obtained from related complexes in the CSD (Table 5-3). These interactions are illustrated in both Figure 5-109 and Figure 5-111.



**Figure 5-111**  $2\text{Na}^+(\text{C}_6\text{O}_4\text{Br}_2)^{2-} \cdot 4\text{H}_2\text{O}$  Interactions between rows of  $\text{BA}^{2-}$  molecules (orange and black) within  $\text{BA}^{2-}$  planes.

There are no direct interactions between the  $\text{BA}^{2-}$  planes which are stacked in an ABA fashion along the  $a$ -axis, in which the molecules directly above and below in adjacent planes have been rotated by  $180^\circ$  so that the coordinating metals are reversed. The  $\text{BA}^{2-}$  planes are connected by the  $\text{Na}^+$  planes which consist of interacting  $\text{Na}^+$  chains. The  $\text{Na}^+$  chains can be broken down into the three  $\text{Na}\cdots\text{Na}$  units, illustrated in Figure 5-108. This includes a short  $\text{Na2}\cdots\text{Na2}$  D2 unit of length 3.356(2) Å, in which the  $\text{Na}^+$  ions coordinate directly via two O8w atoms and also by two  $\text{O6}\cdots\text{O2}$  interactions of 3.351(3) Å, the latter of which, although illustrated in Figure 5-112, is insignificant in comparison to the sum of the van der Waals radii of

3.04 HBs. There are Na1...Na2 D2 + HB units of length 3.614(2) Å, in which the Na<sup>+</sup> ions coordinate directly via O6w and O7w atoms and also by an O8w–H8...O4 HB, mentioned previously. Also an Na1...Na1 contact distance of 5.648(2) Å which although larger than the sum of the van der Waals radii of 4.54 Å contains an inversion centre in the middle of the two Na<sup>+</sup> ions that coordinate via two symmetry equivalent O5w–H2...O3 HBs, mentioned previously.

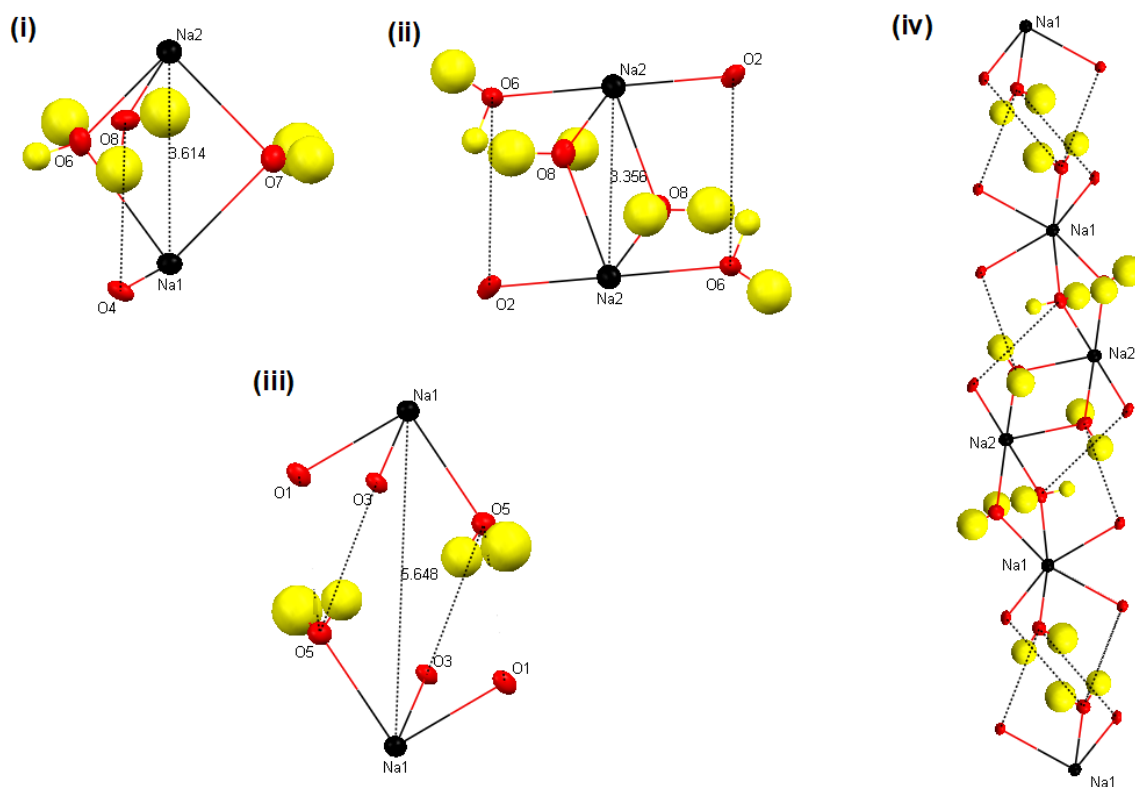


**Figure 5-112**  $2\text{Na}^+(\text{C}_6\text{O}_4\text{Br}_2)^{2-} \cdot 4\text{H}_2\text{O}$  (i) D2 + HB Na1...Na2 (ii) D2 + 2HB Na2...Na2 and (iii) 4HB Na1...Na1 units that comprise (iv) Na<sup>+</sup> chains.

The units alternate in an ABCBA fashion, in which A, B and C are the Na1-Na1, Na1-Na2 and Na2-Na2 units respectively, as illustrated in Figure 5-108. The Na<sup>+</sup> chains also interact with one another to form a Na<sup>+</sup> plane that lies along the ac plane. This is illustrated in Figure 5-113 in which the chains are also shown to stack in an alternate ABA fashion, and each is also flipped 180 degrees with respect to the one beside it.

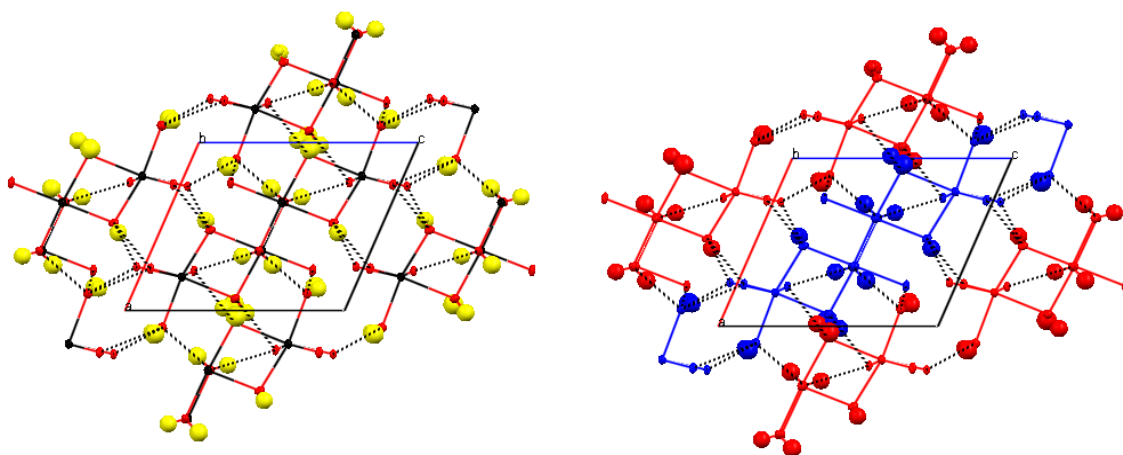


Figure 5-113  $2\text{Na}^+(\text{C}_6\text{O}_4\text{Br}_2)^{2-} \cdot 4\text{H}_2\text{O}$  alternating  $\text{Na}^+$  chains flipped  $180^\circ$  with respect to one another in order to interact and form  $\text{Na}^+$  planes.

The interactions between the reversed interacting chains are illustrated in Figure 5-114.

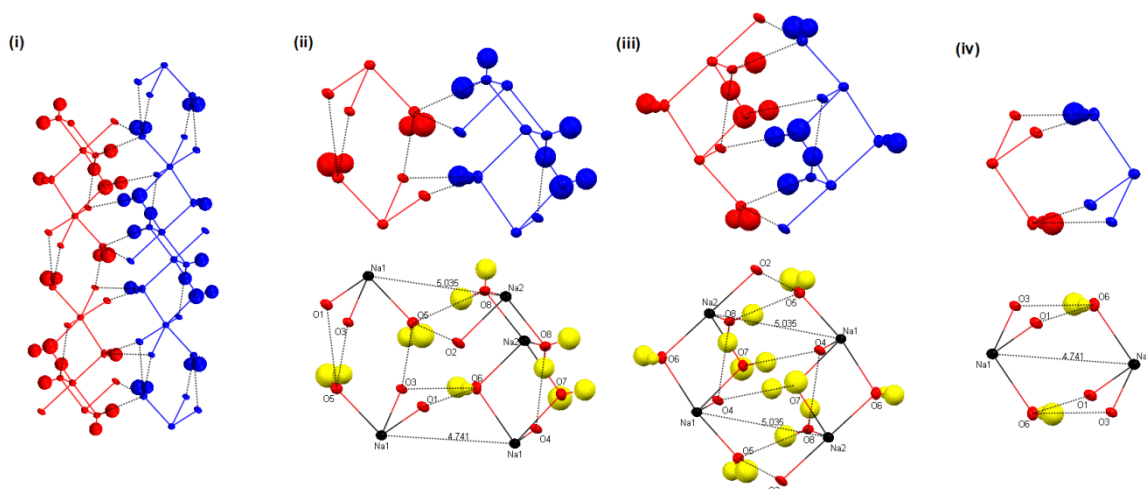


Figure 5-114  $2\text{Na}^+(\text{C}_6\text{O}_4\text{Br}_2)^{2-} \cdot 4\text{H}_2\text{O}$  (i) interaction point of alternating  $\text{Na}^+$  chains (ii) split into repeating units within which are two inversion centres (iii) between two 4HB  $\text{Na1}\cdots\text{Na2}$  units and (iv) and between the  $\text{Na}^+$  ions within a  $\text{Na1}\cdots\text{Na1}$  4HB unit.

All interactions at this point are within the unit presented in Figure 5-114. Within this unit are the additional 4HB  $\text{Na1}\cdots\text{Na1}$  and 4HB  $\text{Na1}\cdots\text{Na2}$  units, of distance 4.741(1) and 5.035(1) Å respectively, also illustrated. There are two centre of inversions present; one in the centre of the  $\text{Na1}\cdots\text{Na1}$  distance and another in the centre of two  $\text{Na1}\cdots\text{Na2}$  interactions as illustrated in figure 5-114(iii).

These inversion centres are also the points at which the alternating  $\text{BA}^{2-}$  planes intersect the  $\text{Na}^+$  planes, Figure 5-115. In addition all water molecules present in the structure coordinate to the  $\text{Na}^+$  ions, and so are condensed in the same regions. An addition HB not yet mentioned is the  $\text{O8w-H2}\cdots\text{O5}$  HB of distance 2.783(3) Å, , also illustrated in Figure 5-115(i).

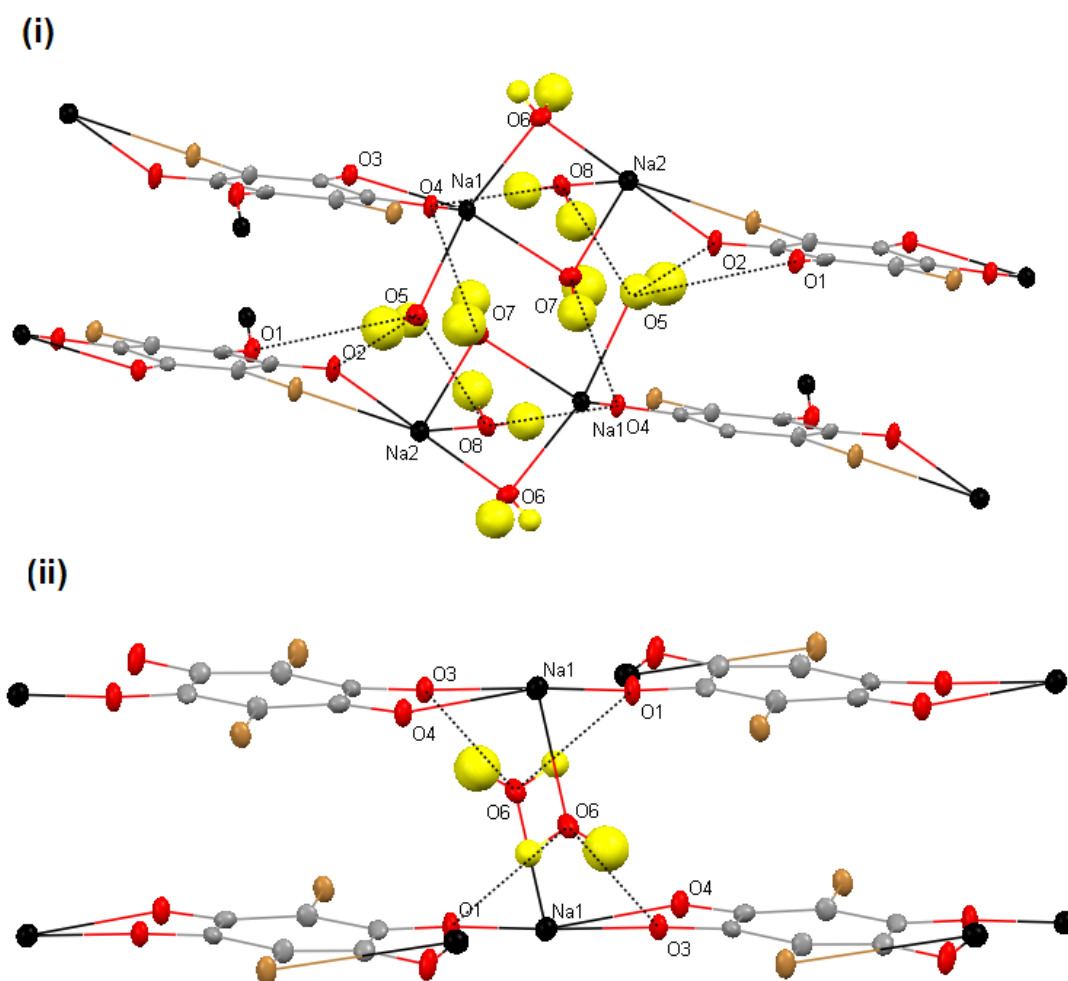


Figure 5-115  $2\text{Na}^+(\text{C}_6\text{O}_4\text{Br}_2)^{2-} \cdot 4\text{H}_2\text{O}$  Planes of  $\text{BA}^{2-}$  molecules connected by (i) the two 4HB  $\text{Na1}\cdots\text{Na2}$  units and (ii) the  $\text{Na}^+$  ions within a  $\text{Na1}\cdots\text{Na1}$  4HB unit

#### 5.4.2.2 2:1 Sodium CA trihydrate complex: $2\text{Na}^+(\text{C}_6\text{O}_4\text{Cl}_2)^{2-} \cdot 3\text{H}_2\text{O}$

The 2:1 Na:CA trihydrate complex was obtained by the method detailed in Table 5-37. The asymmetric unit of this complex contains one  $\text{CA}^{2-}$  molecule and two  $\text{Na}^+$  ion environments, and three water molecules, Figure 5-116.

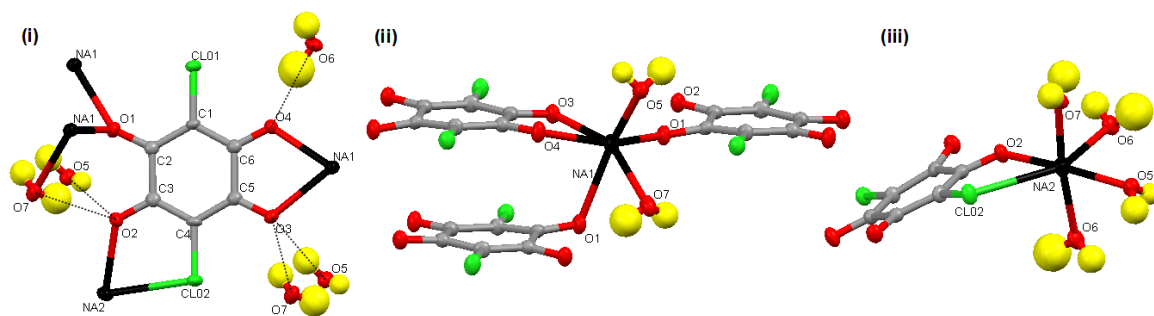


Figure 5-116  $2\text{Na}^+ (\text{C}_6\text{O}_4\text{Cl}_2)^{2-} \cdot 3\text{H}_2\text{O}$  environment of (i)  $\text{CA}^{2-}$  molecule (ii)  $\text{Na}1^+$  ion and (iii)  $\text{Na}2^+$  ion.

The  $\text{CA}^{2-}$  molecule does not have an inversion centre. On one side of the molecule the O3 and O4 carbonyls coordinate to an  $\text{Na}1^+$  ion by a B2 unit, and on the other side of the molecule the O2 and Cl2 atoms coordinate to an  $\text{Na}2^+$  ion by an A2 unit and the O1 atom coordinates to another  $\text{Na}1^+$  ion by a C3 unit. This gives an overall (C3 B2 A2) coordination.

The O2 carbonyl acts as proton acceptor in an E2 HB motif unit in the resulting  $\text{O}7\text{w}-\text{H}6\cdots\text{O}2$  HB, and also acts as a proton acceptor donor in the  $\text{O}5\text{w}-\text{H}1\cdots\text{O}2$  HB with a nearby water molecule. The O3 and O4 carbonyls both act as proton acceptors in the  $\text{O}5\text{w}-\text{H}2\cdots\text{O}3$  and  $\text{O}7\text{w}-\text{H}5\cdots\text{O}3$  HBs with  $\text{O}\cdots\text{O}$  distances 2.778(2) and 3.075(3) Å, and the  $\text{O}6\text{w}-\text{H}4\cdots\text{O}4$  HB of  $\text{O}\cdots\text{O}$  distance 2.750(2) Å respectively.

This is unlike the NaBA complex above in which the O1 carbonyl coordinates to only one  $\text{Na}^+$  ion and thus there is no HB motif and both the O1 and O2 carbonyls act as proton acceptors. Also the  $\text{O}6\text{w}-\text{H}4\cdots\text{O}4$  HB distance of 2.750(2) is slightly shorter than in the NaBA complex in which the equivalent O4 atom acts as proton acceptor for two coordinating Ow molecules, as opposed to one, which may explain the significantly shorter  $\text{O}\cdots\text{O}$  distance of 2.750(2) in this complex in comparison to 2.905(3) Å in the NaBA complex. All HB parameters and significant distances are presented, and can be compared with those of the NaBA complex in Table 5-34.

Each  $\text{Na}1^+$  ion is coordinated to three  $\text{CA}^{2-}$  molecules by two monodentate C1 and one bidentate B2 coordination, and two water molecules. Each  $\text{Na}1^+$  ion is therefore coordinated to six oxygen atoms the bond lengths of which range from

2.297(2) to 2.561(2) Å. Each  $\text{Na}^{2+}$  ion is coordinated one  $\text{CA}^{2-}$  molecule by bidentate A2 coordination, and to four water molecules. Each  $\text{Na}^{2+}$  ion is therefore coordinated to six atoms; five oxygen atoms the bond lengths of which range from 2.331(1) to 2.426(2) Å and one chlorine atom of bond length 2.966(1) Å. All Na interactions are presented, and can be compared with those of the NaBA complex in Table 5-33.

The resulting three dimensional structure, is illustrated as viewed along the *a*-, *b*-, and *c*- axes in Figure 5-117.

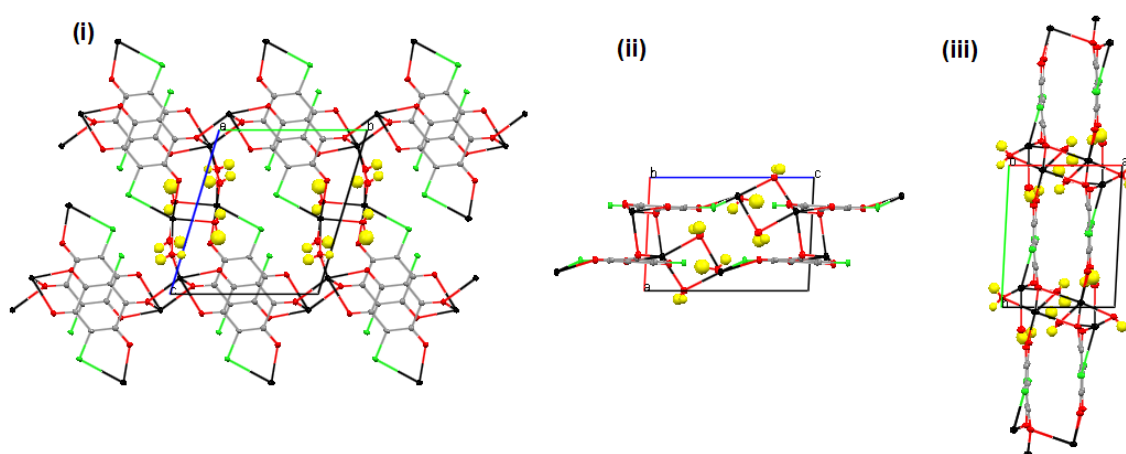


Figure 5-117  $2\text{Na}^+ (\text{C}_6\text{O}_4\text{Cl}_2)^{2-} \cdot 3\text{H}_2\text{O}$  structure as viewed along the (i) *a*- (ii) *b*- and *c*- axes.

The structure can be broken down into  $\text{CA}^{2-}$  planes that lie along the *bc* plane (Figure 5-118) and  $\text{Na}^+$  planes that lie along the *ac* plane (Figure 5-119).

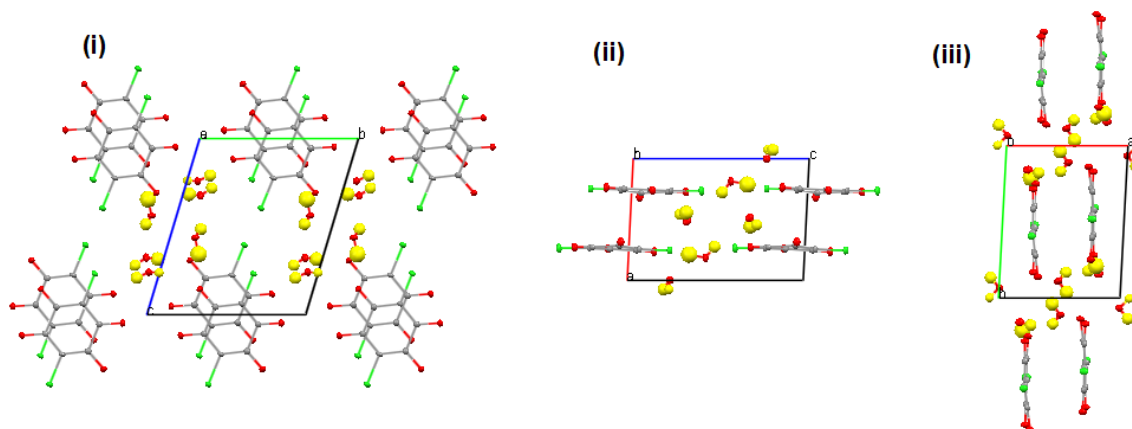


Figure 5-118.  $2\text{Na}^+ (\text{C}_6\text{O}_4\text{Cl}_2)^{2-} \cdot 3\text{H}_2\text{O}$  structure  $\text{CA}^{2-}$  planes as viewed along the (i) *a*- (ii) *b*- and *c*- axes.

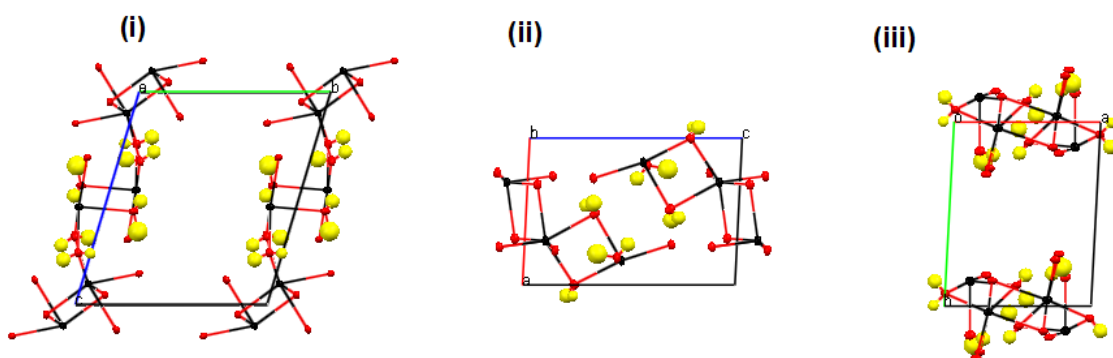


Figure 5-119  $2\text{Na}^+ (\text{C}_6\text{O}_4\text{Cl}_2)^{2-} \cdot 3\text{H}_2\text{O}$  structure  $\text{Na}^+$  planes as viewed along the (i) *a*- (ii) *b*- and *c*- axes.

The  $\text{CA}^{2-}$  planes, illustrated in Figure 5-120, are composed of rows of  $\text{CA}^{2-}$  molecules coordinated to one another via a  $\text{Na}^+$  ion, Figure 5-121.

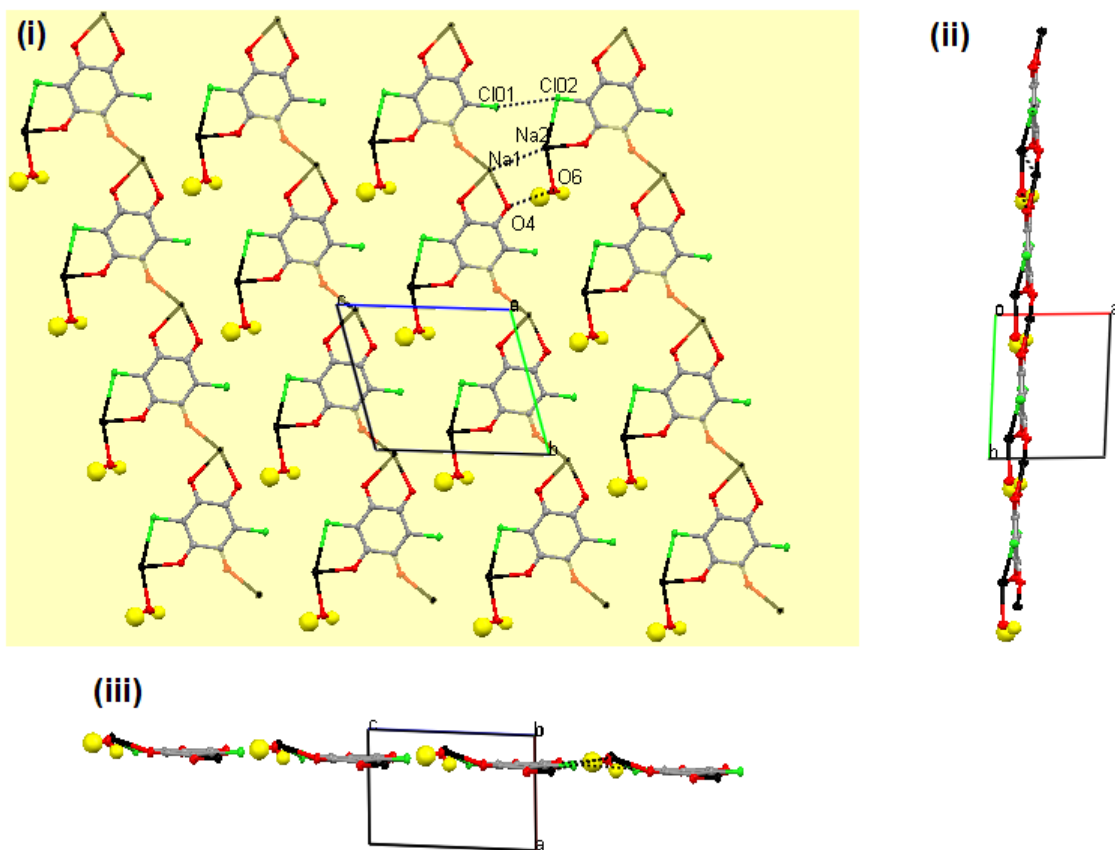


Figure 5-120  $2\text{Na}^+ (\text{C}_6\text{O}_4\text{Cl}_2)^{2-} \cdot 3\text{H}_2\text{O}$   $\text{CA}^{2-}$  planes viewed along (i)  $a$ -axis which is perpendicular to plane and angle at which cuts the (ii)  $b$ - and  $c$ - axes.

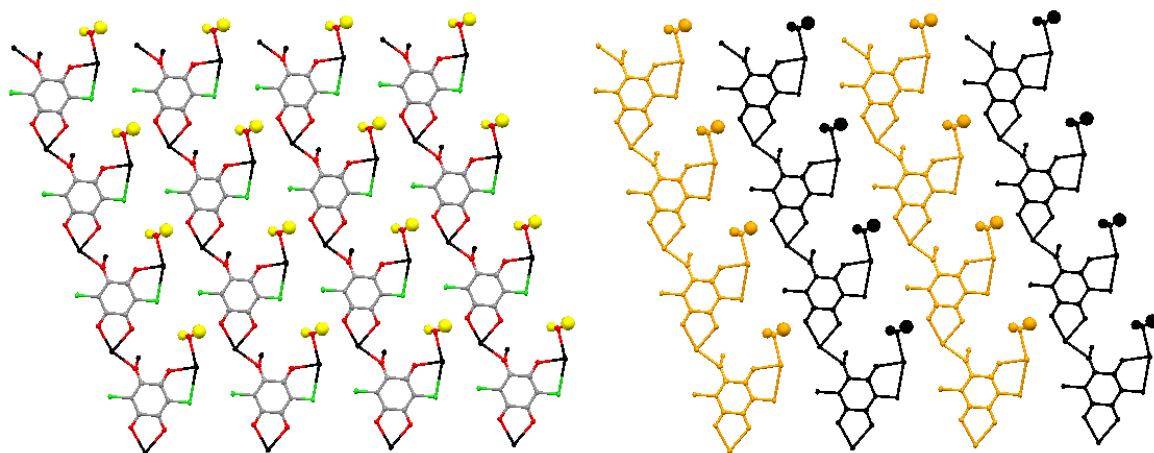
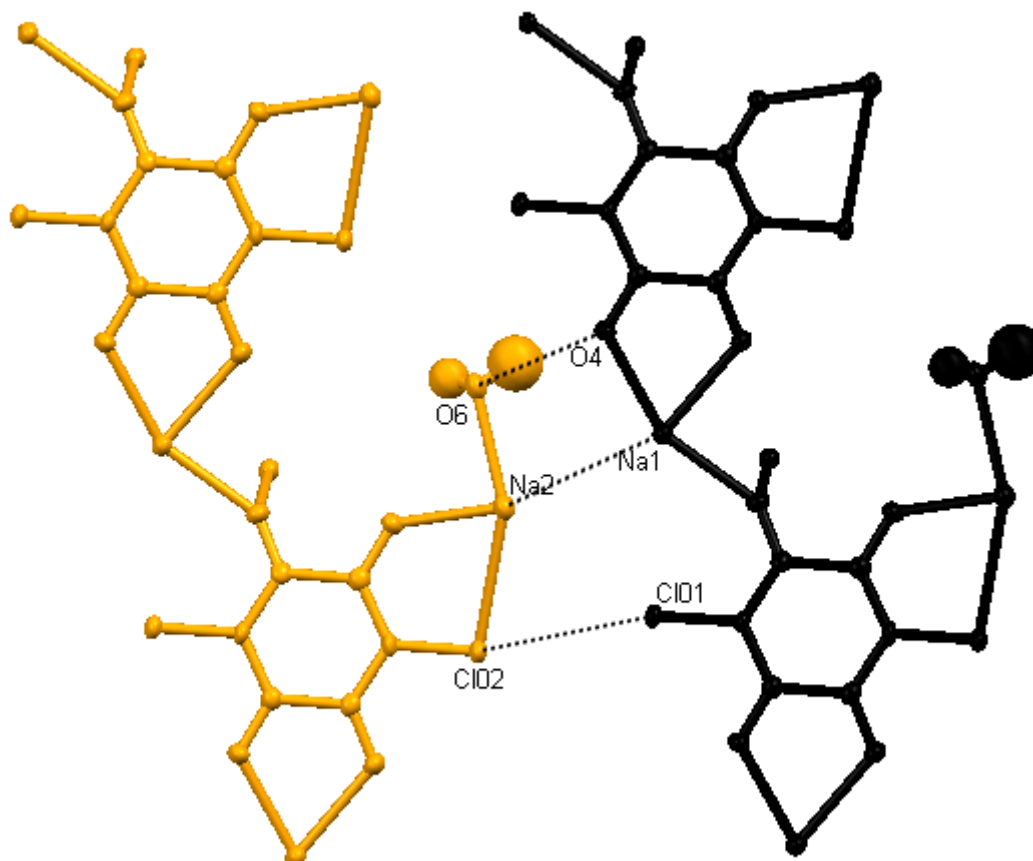


Figure 5-121  $2\text{Na}^+ (\text{C}_6\text{O}_4\text{Cl}_2)^{2-} \cdot 3\text{H}_2\text{O}$  rows of  $\text{CA}^{2-}$  molecules (orange and black) within  $\text{CA}^{2-}$  planes.

The rows of  $\text{CA}^{2-}$  molecules within the plane are connected by  $\text{O6w-H4}\cdots\text{O4}$  HB interactions, mentioned previously, and  $\text{Cl1}\cdots\text{Cl2}$  and  $\text{Na1}\cdots\text{Na2}$  interactions of length 3.4998(4) and 3.477(1) Å both significant when compared to the sum of the

van der Waals radii of 3.5 and 4.54 Å, and the average interaction distances of 3.387 and 3.695 Å obtained from related complexes in the CSD (Table 5-3). These interactions are illustrated in both Figure 5-120 and Figure 5-122.



**Figure 5-122**  $2\text{Na}^+(\text{C}_6\text{O}_4\text{Cl}_2)^{2-} \cdot 3\text{H}_2\text{O}$  interactions between rows of  $\text{CA}^{2-}$  molecules (orange and black) within  $\text{CA}^{2-}$  planes.

The  $\text{XA}^{2-}$  planes are the same in both the BA and CA complexes, however unlike the BA complex there is an additional metal contact from the  $\text{CA}^{2-}$  to one of the  $\text{Na}^+$  ions in the adjacent plane. Like the BA complex, there are no direct interactions between the  $\text{CA}^{2-}$  planes which are also stacked in an ABA fashion along the  $a$ -axis. Each plane has been rotated by  $180^\circ$  and shifted by approximately half a cell along the  $c$  axis. The molecules directly above and below in adjacent planes are therefore out of sync. The  $\text{CA}^{2-}$  planes are connected by the  $\text{Na}^+$  planes which consist of interacting  $\text{Na}^+$  chains.

The Na<sup>+</sup> chains can be broken down into the three Na<sup>+</sup>···Na units, also like the BA complex, illustrated in Figure 5-123. This includes a short Na1···Na1 D2 + HB unit of length 3.309(1) Å, that has an inversion centre in the centre of the two Na<sup>+</sup> ions; the Na<sup>+</sup> ions coordinate directly via two symmetry equivalent O1 atoms and also by two symmetry equivalent O7w–H5···O3 HB interactions, mentioned previously. Also an Na1···Na2 D2 + HB unit of length 3.477(1) Å, in which the Na<sup>+</sup> ions coordinate directly via Ow5 and Ow7 atoms and also by an O6w–H4···O4 HB, mentioned previously. An Na2···Na2 contact distance of 3.433(2) Å is also present that also has an inversion centre in the centre of the two Na<sup>+</sup> ions; the Na<sup>+</sup> ions coordinate via two symmetry equivalent O6w atoms and also by two symmetry equivalent O5w–H1···O2 HB interactions.

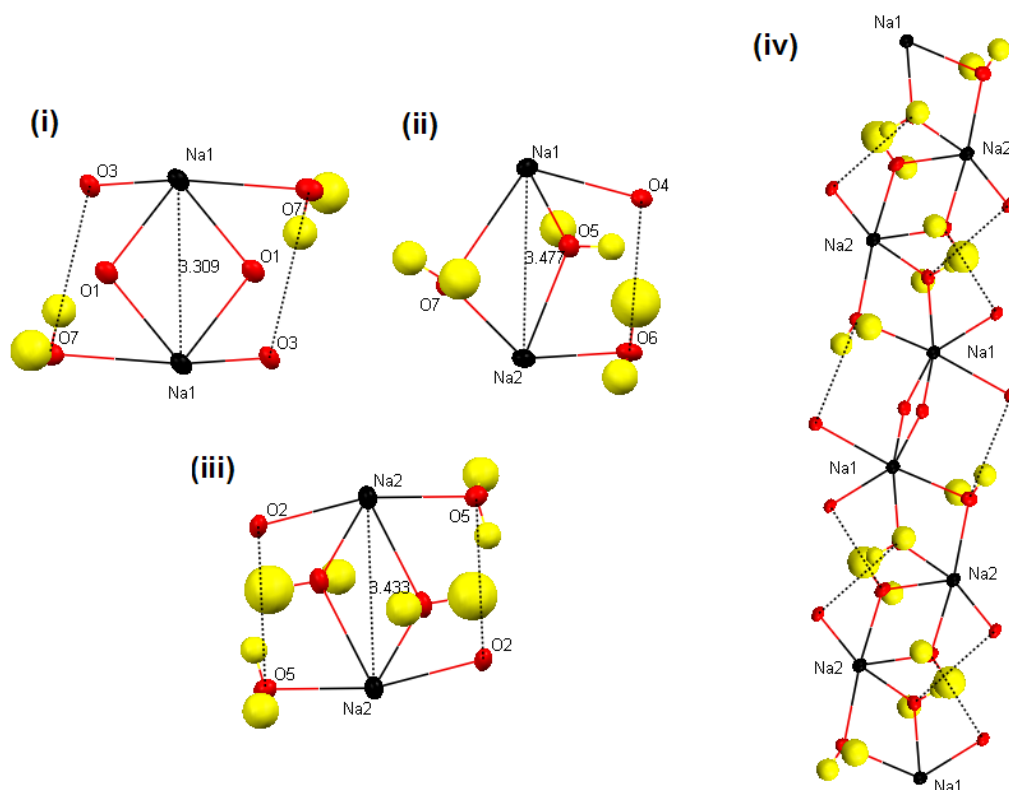


**Figure 5-123** 2Na<sup>+</sup> (C<sub>6</sub>O<sub>4</sub>Cl<sub>2</sub>)<sup>2-</sup> 3H<sub>2</sub>O (i) D2 + 2HB, (ii) D2 + HB (iii) D2 + 2HB Na-Na interaction units arranged in ABACAB fashion to form (iv) Na<sup>+</sup> chains.

The units alternate in an ABACABA fashion, in which the A, B and C correspond to the Na1-Na2, Na2-Na2 and Na1-Na1 interactions as illustrated in Figure 5-123. The Na<sup>+</sup> chains also interact with one another to form a Na<sup>+</sup> plane that lies along the ac plane, as illustrated along the *a*-, *b*- and *c*- axes in Figure 5-124. This is also

illustrated in Figure 5-125 in which the interacting chains (red and blue) are not stacked in an alternate ABA fashion (and flipped 180 degrees with respect to one another as in the BA complex) but instead, are positioned so that each chain periodically coordinates to each adjacent in the same manner.

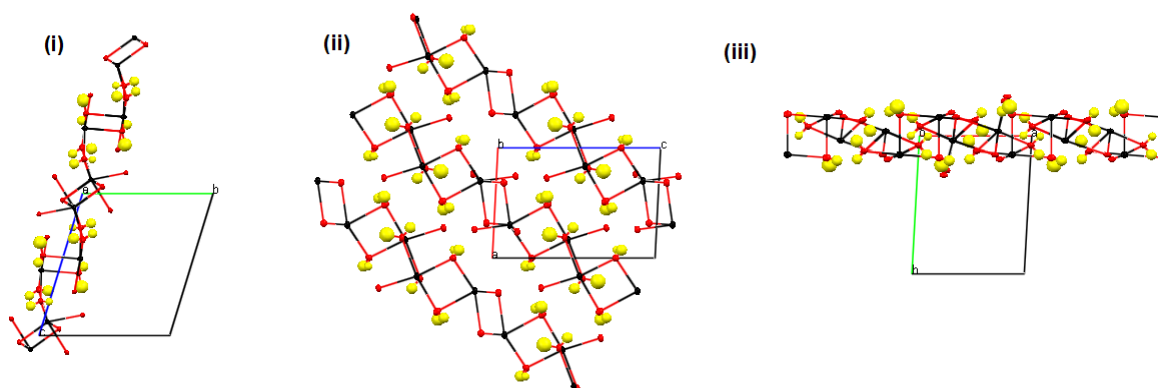


Figure 5-124  $2\text{Na}^+(\text{C}_6\text{O}_4\text{Cl}_2)^{2-} \cdot 3\text{H}_2\text{O}$   $\text{Na}^+$  ion chains interact to form  $\text{Na}^+$  ion planes that run along ac plane, as viewed along (i) a- (ii) b- (iii) and c axes.

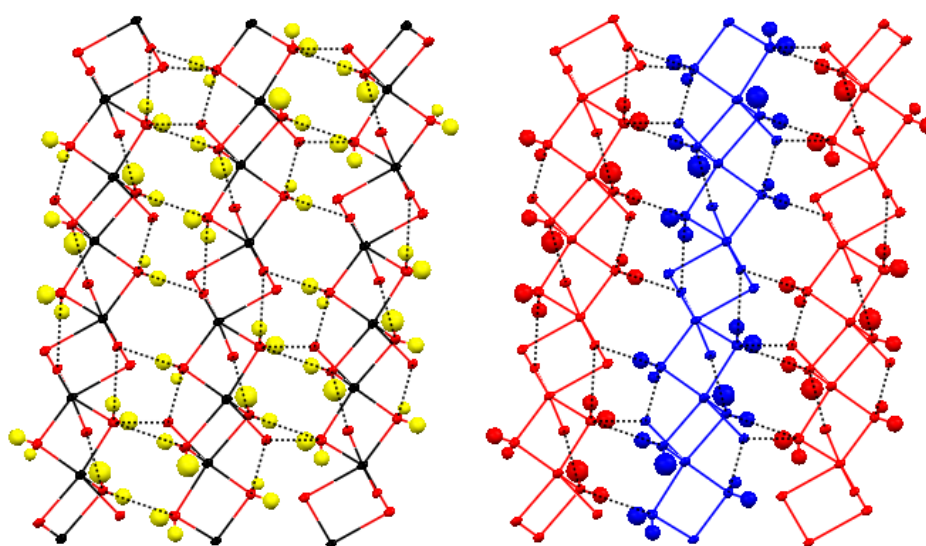
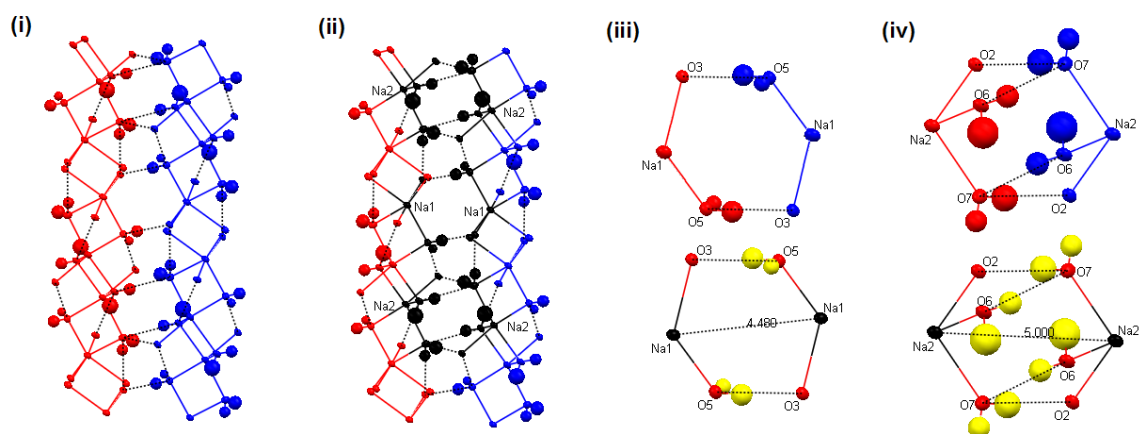


Figure 5-125  $2\text{Na}^+(\text{C}_6\text{O}_4\text{Cl}_2)^{2-} \cdot 3\text{H}_2\text{O}$  interactions between adjacent  $\text{Na}^+$  ion chains (red and blue).

The point at which two adjacent chains meet gives rise to another two repeating  $\text{Na} \cdots \text{Na}$  interaction units, both of which possess inversion centres in the centre of the interacting  $\text{Na}^+$  ions. These units are illustrated in Figure 5-126.



**Figure 5-126**  $2\text{Na}^+ (\text{C}_6\text{O}_4\text{Cl}_2)^{2-} \cdot 3\text{H}_2\text{O}$  (i) Additional Na...Na interactions between adjacent  $\text{Na}^+$  ion chains (ii) highlighted in black (iii)  $\text{Na1}\cdots\text{Na1}$  2HB unit and (iv)  $\text{Na2}\cdots\text{Na2}$  2HB unit. Both units have a centre of inversion in the middle of the Na...Na contact distance.

The 2HB  $\text{Na1}\cdots\text{Na1}$  interaction unit of  $4.480(2) \text{ \AA}$  is composed of two symmetry equivalent  $\text{O5-H2}\cdots\text{O3}$  HB interactions. The 4HB  $\text{Na2}\cdots\text{Na2}$  unit of  $5.000(2) \text{ \AA}$  is composed of two symmetry equivalent  $\text{O7w-H5}\cdots\text{O2}$  HB and two symmetry equivalent  $\text{O6w-H4}\cdots\text{O7}$  HB interactions. In a similar manner to the BA complex, the inversion centre of these two units are the points at which all of the  $\text{CA}^{2-}$  planes, rows of  $\text{CA}^{2-}$  molecules within the  $\text{CA}^{2-}$  planes,  $\text{Na}^+$  planes and  $\text{Na}^+$  chains within the  $\text{Na}^+$  planes intersect via  $\text{Na}^+$  ions and HB interactions due to the surrounding water molecules.

The two points of intersection corresponding to the two halves of the non-symmetric molecule are illustrated in Figure 5-127.

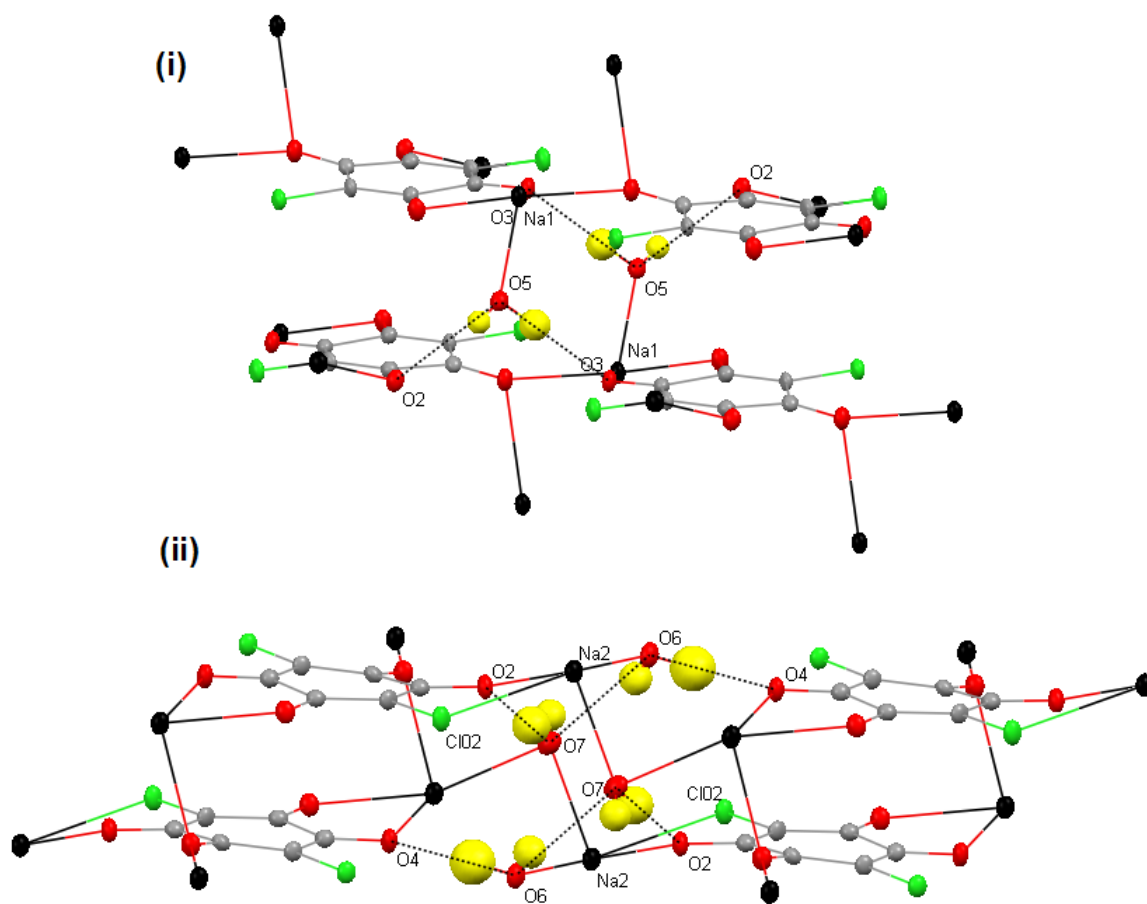


Figure 5-127  $2\text{Na}^+ (\text{C}_6\text{O}_4\text{Cl}_2)^{2-} \cdot 3\text{H}_2\text{O}$  Points of intersection of the alternating/reversed  $\text{CA}^{2-}$  planes and  $\text{Na}^+$  chains at (i)  $\text{Na1}\cdots\text{Na1}$  2HB unit and (ii)  $\text{Na2}\cdots\text{Na2}$  2HB unit.



**Table 5-34 HB and significant interaction distances for  $2\text{Na}^+(\text{C}_6\text{O}_4\text{Br}_2)^{2-} \cdot 4\text{H}_2\text{O}$  and  $2\text{Na}^+(\text{C}_6\text{O}_4\text{Cl}_2)^{2-} \cdot 3\text{H}_2\text{O}$  complexes.**

NaBA	<i>D-H</i> / Å	<i>H...A</i> / Å	<i>D...A</i> / Å	<i>&lt;DHA</i> / °	Van der waals radii / Å	NaCA	<i>D-H</i> / Å	<i>H...A</i> / Å	<i>D...A</i> / Å	<i>&lt;DHA</i> / °	Van der waals radii / Å
O5-H1----O2	0.78(4)	2.07(4)	2.779(3)	150(4)	3.04	O5-H1----O2	0.75(4)	2.21(4)	2.931(3)	160(4)	3.04
O5-H2----O3	0.80(4)	2.20(4)	2.973(3)	161(3)	3.04	O5-H2----O3	0.87(4)	1.91(4)	2.778(2)	171(4)	3.04
O6-H3----O3	0.84(4)	2.04(4)	2.842(2)	158(3)	3.04	O6-H3----O7	0.81(4)	2.41(4)	3.166(3)	155(4)	3.04
O6-H4----O1	0.79(3)	2.18(3)	2.908(2)	153(3)	3.04	O6-H4----O4	0.90(5)	1.86(5)	2.750(2)	168(5)	3.04
O7-H5----O4	0.86(4)	2.06(4)	2.875(2)	159(3)	3.04	O7-H5----O3	0.82(5)	2.28(5)	3.075(3)	162(4)	3.04
O8-H7----O5	0.87(4)	1.94(4)	2.783(3)	162(3)	3.04	O7-H6----O2	0.75(5)	2.00(5)	2.752(3)	174(5)	3.04
O8-H8----O4	0.79(4)	2.14(4)	2.905(3)	161(4)	3.04	O7-----Cl1			3.2265(4)		3.27
Br1-----Br2			3.3093(1)		3.7	Cl1-----Cl2			3.4998(4)		3.5
						Cl1-----Cl2			3.5821(6)		3.5

**Table 5-35 Intra-molecular distances for  $2\text{Na}^+(\text{C}_6\text{O}_4\text{Br}_2)^{2-} \cdot 4\text{H}_2\text{O}$  and  $2\text{Na}^+(\text{C}_6\text{O}_4\text{Cl}_2)^{2-} \cdot 3\text{H}_2\text{O}$  complexes.**

	NaBA	NaCA		NaBA	NaCA
<i>C-C Distances</i>			<i>C-O and C-X Distances</i>		
C1-C2	1.3999(32)	1.4055(32)	C1-X1	1.8955(22)	1.7292(23)
C2-C3	1.5494(31)	1.5367(33)	C2-O1	1.2453(27)	1.2527(29)
C3-C4	1.3993(32)	1.4015(34)	C3-O2	1.2482(27)	1.2639(30)
C4-C5	1.4015(32)	1.3993(32)	C4-X2	1.8950(22)	1.7391(23)
C5-C6	1.5465(31)	1.5409(32)	C5-O3	1.2506(27)	1.2533(29)
C6-C1	1.4075(32)	1.4025(32)	C6-O4	1.2539(27)	1.2520(30)

**Table 5-36 Crystallographic details for additional group one metal complexes**

	2Li <sup>+</sup> (C <sub>6</sub> O <sub>4</sub> Cl <sub>2</sub> ) <sup>2-</sup> H <sub>2</sub> O	2Li <sup>+</sup> (C <sub>6</sub> O <sub>4</sub> Br <sub>1.25</sub> Cl <sub>0.75</sub> ) <sup>2-</sup> H <sub>2</sub> O	2Li <sup>+</sup> (C <sub>6</sub> O <sub>4</sub> Cl <sub>2</sub> ) <sup>2-</sup> ·(C <sub>6</sub> O <sub>4</sub> Cl <sub>2</sub> H <sub>2</sub> ) 2H <sub>2</sub> O	2Na <sup>+</sup> (C <sub>6</sub> O <sub>4</sub> Br <sub>2</sub> ) <sup>2-</sup> 4H <sub>2</sub> O	2Na <sup>+</sup> (C <sub>6</sub> O <sub>4</sub> Cl <sub>2</sub> ) <sup>2-</sup> 3H <sub>2</sub> O
Diffractometer	Rigaku	Rigaku	Rigaku	Kappa	Kappa
Crystal size/mm <sup>3</sup>	0.1x0.2x0.3	0.1x0.1x0.2	0.2x0.2x0.4	0.3x0.4x0.4	0.3x0.3x0.4
M/g mol <sup>-1</sup>	238.86	294.43	465.84	413.92	306.99
T/K	100	100	100	100	100
Space group	C2/c	C2/c	P-1	P-1	P-1
a/Å	9.4545(9)	9.7340(9)	3.5322(5)	7.9387(2)	6.4640(10)
b/Å	13.9297(12)	13.9177(15)	8.5529(15)	8.6885(3)	8.4460(10)
c/Å	7.0034(7)	7.0590(5)	13.446(3)	9.8665(3)	9.7640(10)
α/°	90	90	101.482(5)	108.135(2)	106.588(10)
β/°	117.296(6)	116.433(6)	96.528(5)	111.239(2)	92.039(10)
γ/°	90	90	101.858(4)	92.799(2)	92.336(10)
V/Å <sup>3</sup>	819.63(13)	856.34(14)	384.49(11)	592.70(3)	509.83(11)
Z	4	4	2	2	2
P <sub>calc</sub> /g cm <sup>-3</sup>	1.936	2.284	2.012	2.319	2.000
μ/mm <sup>-1</sup>	0.778	6.187	0.828	6.94	0.741
θ range/°	3.38 - 27.48	3.36 - 27.47	3.13 - 27.48	2.37 - 27.61	2.18 - 27.18
Reflections					
Collected	5233	5334	5392	14000	13927
Independent	943	973	1731	2711	2247
Observed(>2σ(I))	846	893	1424	2206	2008
Solved using				Sir92	
R <sub>int</sub>	0.216	0.0207	0.0479	0.0289	0.0496
Completeness/%	99.8	99.5	97.6	98.6	99.2
Parameters	73	78	139	195	178
GOOF	1.108	1.107	1.176	1.057	1.09
R1 (observed)	0.0234	0.0177	0.0492	0.0226	0.0441
R1 (all)	0.0272	0.0207	0.0603	0.0340	0.0496
wR2 (all)	0.0575	0.0384	0.1573	0.0503	0.1376
ρ <sub>max, min</sub> /eÅ <sup>3</sup>	0.414-0.212	0.499 -0.261	0.609 -0.549	0.795-0.409	1.365-0.462

**Table 5-37 Experimental details for additional M<sup>+</sup> complexes.**

Li <sup>+</sup>	Na <sup>+</sup>
<p>2Li<sup>+</sup> (C<sub>6</sub>O<sub>4</sub>Cl<sub>2</sub>)<sup>2-</sup> · H<sub>2</sub>O</p> <p>Small red crystalline blocks obtained from a 1:1 molar ratio (6.7 × 10<sup>-5</sup> mol) of CA (0.014g), and LiCl (0.004g), both dissolved in MeOH, combined, and left to evaporate at 40°.</p>	<p>2Na<sup>+</sup> (C<sub>6</sub>O<sub>4</sub>Br<sub>2</sub>)<sup>2-</sup> · 4H<sub>2</sub>O</p> <p>Large purple crystalline blocks obtained from a 1:1 molar ratio (6.7 × 10<sup>-5</sup> mol) of BA (0.02g), and NaOH (0.004g), both dissolved in MeOH, combined, and left to evaporate at rt.</p>
<p>2Li<sup>+</sup> (C<sub>6</sub>O<sub>4</sub>Br<sub>1.25</sub>Cl<sub>0.75</sub>)<sup>2-</sup> · H<sub>2</sub>O</p> <p>Small red crystalline blocks obtained from a 1:2 molar ratio (3.35 × 10<sup>-5</sup> mol, 6.7 × 10<sup>-5</sup> mol) of BA (0.01g), and LiCl (0.004g), both dissolved in EtOH, combined, and left to evaporate at rt.</p>	<p>2Na<sup>+</sup> (C<sub>6</sub>O<sub>4</sub>Cl<sub>2</sub>)<sup>-</sup> · 3H<sub>2</sub>O</p> <p>Large purple crystalline blocks obtained from a 1:2 molar ratio (6.7 × 10<sup>-5</sup> mol, 1.34 × 10<sup>-4</sup> mol) of CA (0.014g), and NaOH (0.006g), both dissolved in EtOH, combined, and left to evaporate at rt.</p>
<p>2Li<sup>+</sup> (C<sub>6</sub>O<sub>4</sub>Cl<sub>2</sub>)<sup>2-</sup> (C<sub>6</sub>O<sub>4</sub>Cl<sub>2</sub>H<sub>2</sub>) · 2H<sub>2</sub>O</p> <p>Large purple blocks obtained from a 1:2 molar ratio (6.7 × 10<sup>-5</sup> mol, 1.34 × 10<sup>-4</sup> mol) of CA (0.014g), dissolved in DMF, and LiCl (0.006g), dissolved in MeOH, combined, and left to evaporate at rt.</p>	

## 5.5 Conclusions

A number of related isomorphous BA and CA structures have been obtained and studied, from which it is possible to observe the effects of  $M^+$  identity on structural interactions and packing. No correlation has been found in the conditions under which any of the complexes obtained within this investigation were formed. In cases of the most related isostructural structures the conditions under which they were obtained were very different. In addition structurally very different structures were also obtained under very similar conditions. Therefore more work is required monitoring crystal growing conditions to determine whether it is possible to predict the formation of a structure from a previously obtained isostructure or whether only a finite number of stable crystal arrangements will form irrespective of growth conditions.

Two 1:1 KBA tautomeric anhydrous polymorphs were crystallised within the same vial. One of which contained the  $\text{HBA}^-$  ligand and the other that contained both the  $\text{H}_2\text{BA}$  and  $\text{BA}^{2-}$  forms. In addition the same KBA combination under other conditions resulted in three very different hydrated 2:1 KBA polymorphs with the same isostructural structures with the same formulae. The  $\text{BA}^{2-}$  ligand form was present in all three

As expected, within the isomorphous series, the incorporation of larger  $M^+$  ions results in larger unit cell parameters and an increase in most of the interaction distances. In all complexes the effect of the incorporation of a larger  $M^+$  ion on all other interactions within the structure appears to be a side effect of the strong ionic repulsion interaction between the  $M\cdots M$  ions.

This is particularly true in the complexes with significantly short  $M\cdots M$  distances in comparison to those reported in the CSD. The overall effect of the  $M\cdots M$  repulsion is less apparent in complexes which contained  $M\cdots M$  clusters as opposed to  $M\cdots M$  chains of planes, although the most significant effects can still be traced back to be a consequence of the  $M\cdots M$  cluster.

Although the observed effects on the other interactions within the complex are most likely a consequence of  $M\cdots M$  repulsion, some are interesting and worth acknowledging. For example specific HB distances are decreasing and angles increasing, resulting in significantly stronger interactions, and also switching of the most significant secondary HB interaction within a BHB. In the presence of significantly short  $M\cdots M$  distances, other larger  $M\cdots M$  distances are consequently seen to decrease in spite of their own  $M\cdots M$  repulsion. Other significant  $O\cdots O$ ,  $O\cdots Cl$  interactions are also seen to become insignificant due to an increase in interaction distance due to the incorporation of a larger metal.

The presence of all these subtle consequential effects due to metal identity may allow group 1 metal ions to be used to tune such intermolecular interactions in related systems with potentially useful applications.

## 6 Variable Pressure Neutron Diffraction Study of Potassium Hydrogen Dicrotonate

Neutron diffraction has been used to study the metal organic complex, potassium hydrogen dicrotonate, in an experiment carried out on the SXD instrument at the ISIS neutron source, at 40K and under variable pressure. The complex contains a short, strong HB; such hydrogen bonds have been shown to exhibit interesting H atom behaviour under external perturbations such as temperature and pressure. The importance and interest of the H atom in this case means that neutron diffraction is an obvious technique to utilise.

### 6.1 Potassium Hydrogen Dicrotonate

Previous X-ray and neutron diffraction studies were carried out on the potassium hydrogen dicrotonate complex  $\text{KH}(\text{C}_4\text{H}_5\text{O}_2)_2$  (KHDC) by McGregor and Speakman<sup>195</sup>. The data, obtained at room temperature, revealed a triclinic system of unit cell parameters:  $a=12.465(8)$ ,  $b=6.051(4)$ ,  $c=7.452(2)$  Å, and  $\alpha=65.61(2)$ ,  $\beta=104.05(2)$ , and  $\gamma=97.42(2)^\circ$ . The complex was shown to contain, in the terminology of those authors, a hydrogen dicrotonate anion ( $\text{HDC}^-$ )  $[\text{CH}_3\text{CHCHCO}_2\cdots\text{H}\cdots\text{O}_2\text{CCHCHCH}_3]^-$  which contained a short asymmetrical  $\text{O}_2\text{-H}_1\cdots\text{O}_3$  HB of length  $2.488(2)$  Å composed of the two different  $\text{O}_2\text{-H}_1$  and  $\text{H}_1\cdots\text{O}_3$  distances of  $1.141(2)$  and  $1.348(2)$  Å respectively. Stereoscopic views of the so-called  $\text{HDC}^-$  anion, and the way in which it coordinates to the  $\text{K}^+$  ion is illustrated in Figure 6-1.

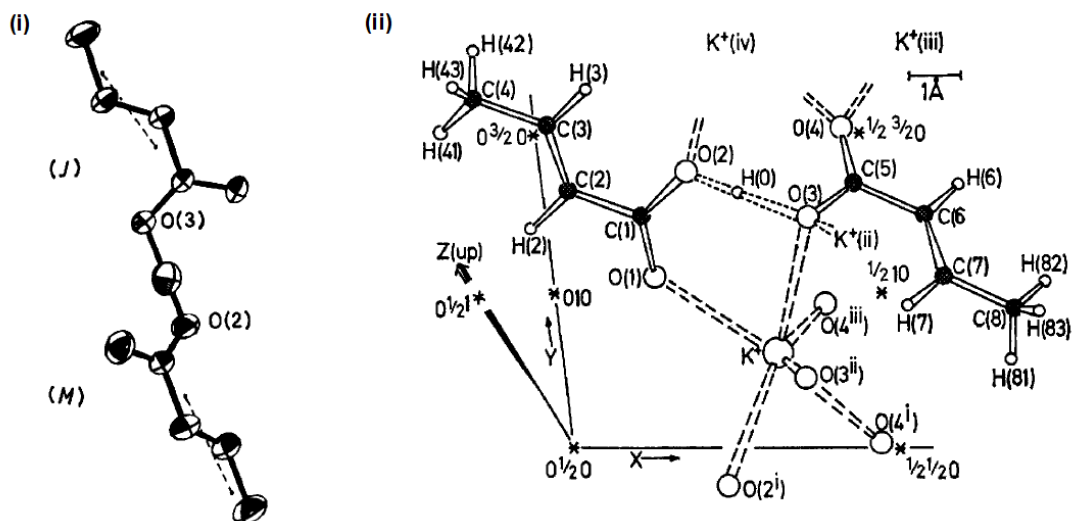


Figure 6-1 (i) Stereoscopic views of the  $\text{HDC}^-$  anion; <sup>195</sup> (J) and (M) refer to the two non equivalent crotonate residues (ii)  $\text{K}^+$  coordination and  $\text{HDC}^-$  contacts: HB (dotted lines) and ionic contacts (broken lines). The authors have identified some centres of inversion by asterisks.

The asymmetry in the arrangement of the crotonate molecules were explained by the differences in the  $\text{O}\cdots\text{K}$  contacts: in the crotonate with the shorter O-H distance, denoted M, each O atom makes one  $\text{K}^+$  contact, whereas in the crotonate with the longer O-H distance, denoted J, each O makes two  $\text{K}^+$  contacts.

## 6.2 Experimental

KHDC crystals of a size suitable for neutron diffraction (ca. 1 mm on a side) were prepared by dissolving a 2:1 mixture of crotonic acid and KOH in water and allowing the solution to evaporate slowly at room temperature. Crotonic acid is very soluble in water and it was necessary to prepare a concentrated solution in order to obtain the neutron sized crystals.

The variable pressure neutron experiment was carried out at ISIS, Oxfordshire, UK on the SXD Single Crystal Diffractometer. A multiple crystal experiment <sup>196</sup> was carried out using three independent and arbitrarily misorientated crystals within a He pressure cell, vertically mounted within a Helium closed-cycle refrigerator. Neutron diffraction data were obtained from this three-crystal sample at a fixed

temperature of 40K and at ambient pressure (0kbar), then at two higher pressures of 2.4 and 4.8 kbar.

### 6.3 The crystal structure of potassium hydrogen dicrotonate

In order to analyse the effects of varied pressure on the KHDC structure, an initial structure analysis will be given for the structure obtained at 40K and ambient pressure. In the nomenclature of McGregor and Speakman, the asymmetric unit contains one  $\text{HDC}^-$  anion and one  $\text{K}^+$  ion (Figure 6-2). It should be noted that the  $\text{HDC}^-$  anion can also be described in terms of two molecules, one crotonate anion and one neutral crotonic acid molecule.

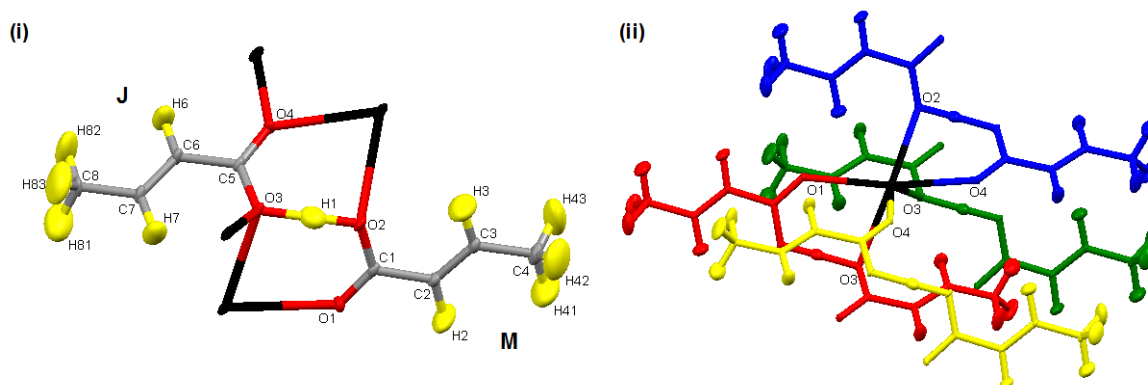
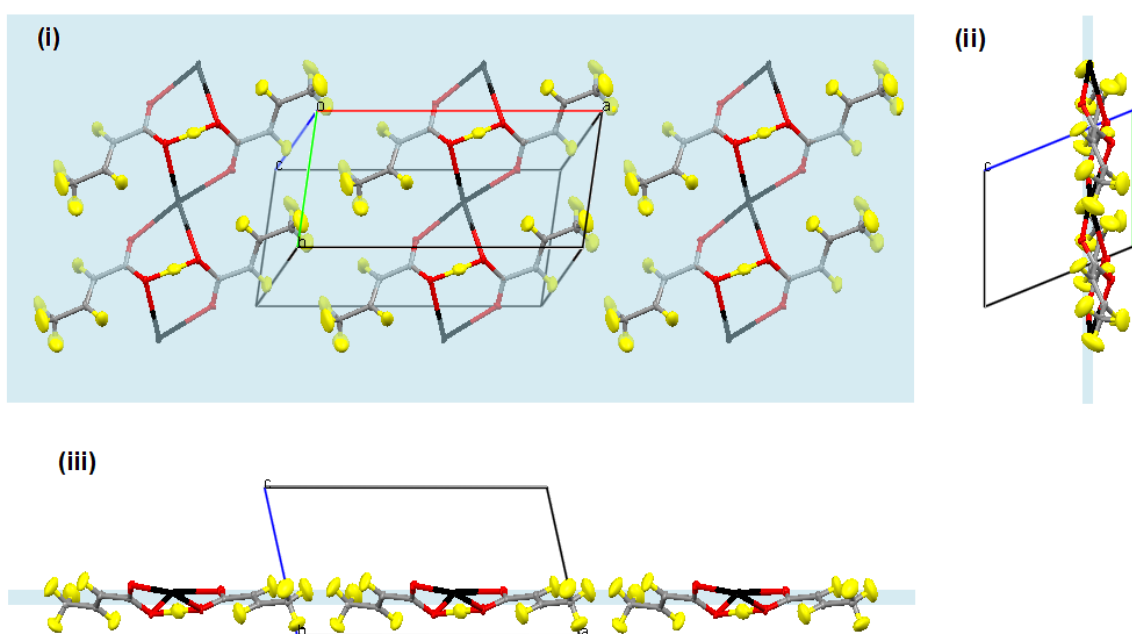


Figure 6-2 KHDC at 40 K and ambient pressure showing (i)  $\text{HDC}^-$  anion and (ii)  $\text{K}^+$  ion coordinated to blue  $\text{HDC}^-$  by O2 and O4, red by O1 and O3, green by O3 and yellow by O4

As described earlier, the  $\text{HDC}^-$  anion consists of two non-equivalent crotonate residues joined via an asymmetric HB. The same atom labels and notation used by McGregor and Speakman has been employed, in which the crotonate residues with the longer, O2–H1, and shorter, O3–H1, distances of 1.144(6) and 1.338(6) Å, above, have been denoted M and J, respectively. Also the O3 and O4 atoms of the J residue both coordinate to two  $\text{K}^+$  ions whereas the O1 and O2 atoms of the M residue only coordinate to one  $\text{K}^+$  ion.

Each  $K^+$  ion is coordinated to four  $HDC^-$  anions, as illustrated by the coloured anions (blue, red, green and yellow) in Figure 6-2, having a total coordination number of 6. The blue  $HDC^-$  is coordinated to the  $K^+$  ion by O2 and O4 atoms at distances of 2.740(5) and 2.691(5) Å respectively, the red by O1 and O3 atoms at 2.712(5) and 2.747(5) Å respectively, the yellow by an O3 atom at 2.933(4) Å and the green by an O4 atom at 2.751(4) Å.

The structure can be said to consist of  $HDC^-$  and  $K^+$  planes. A view of the  $HDC^-$  plane along the  $a$ - and  $b$ - axes and also a view perpendicular to the plane is illustrated in Figure 6-3.



**Figure 6-3** The packing of KHDC at 40 K and ambient pressure, (i) view perpendicular to  $HDC^-$  plane and viewed along (ii)  $a$ - and (iii)  $b$ - axes.

Each plane is composed of columns of  $HDC^-$  anions coordinated to one another via  $K^+$  ions, and stacked in an alternating ABABA... manner along the  $c$ - axis as illustrated in Figure 6-4. The  $HDC^-$  anions within each plane are symmetry related to those in the adjacent planes via inversion centres.

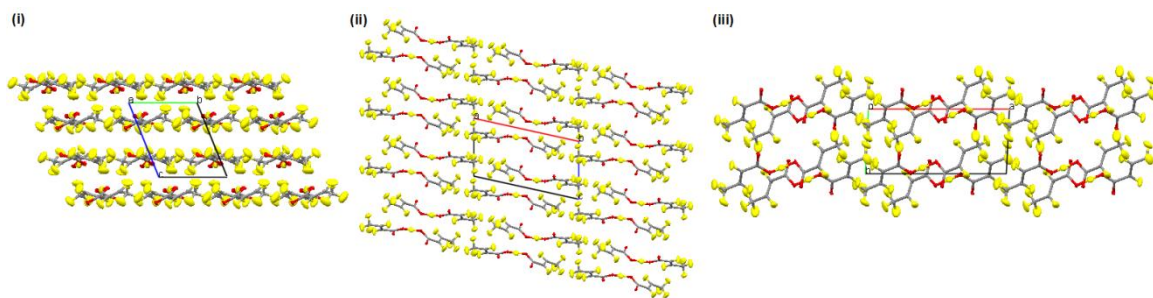


Figure 6-4 KHDC,  $\text{HDC}^-$  planes viewed along the (i) *a*- (ii) *b*- and (iii) *c*-axes.

The inversion centres are placed at the points at which the  $\text{HDC}^-$  anion planes intersect with the  $\text{K}^+$  planes.

Within the  $\text{K}^+$  planes are  $\text{K}^+$  chains composed of two alternating D2  $\text{K}\cdots\text{K}$  interactions of lengths 4.076(6) and 4.436(6) Å compared to the sum of the van der Waals radii of 5.5 Å (Figure 6-5).

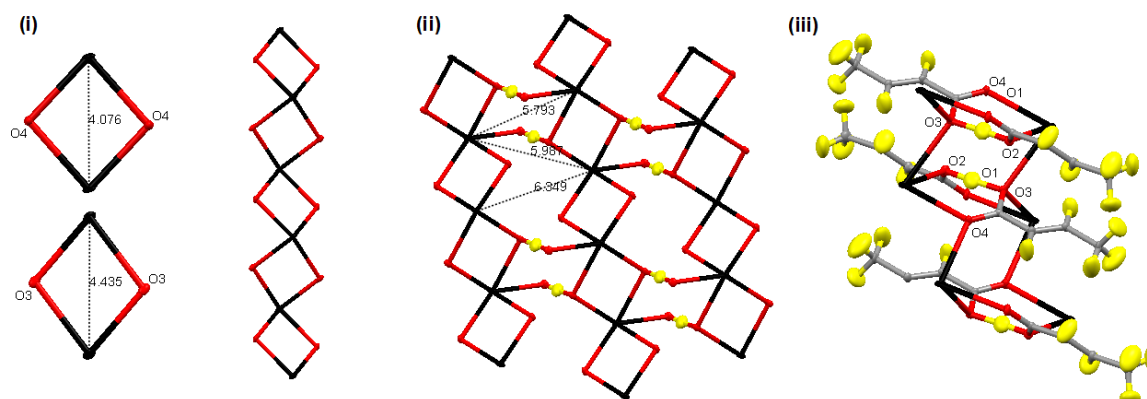


Figure 6-5 The  $\text{K}^+$  ion coordination in KDHC; (i) chains composed of alternating D2 units; (ii) coordination to adjacent chains via the asymmetric  $\text{O2-H1}\cdots\text{O3}$  HB; and (iii) point of intersection of  $\text{HDC}^-$  and  $\text{K}^+$  ion planes.

Each  $\text{K}^+$  chain coordinates to adjacent chains via the  $\text{O2-H1}\cdots\text{O3}$  HB interaction (Figure 6-5). This is the point at which the  $\text{HDC}^-$  and  $\text{K}^+$  planes intersect. The significant interactions present are the six  $\text{K}\cdots\text{O}$  interactions defined earlier. The  $\text{K}\cdots\text{K}$  distances of 5.987(2), 5.793(2), and 6.345(2) Å between adjacent  $\text{K}^+$  chains are significantly larger than the sum of the van der Waals radii. A centre of inversion is present in the centre of the latter two  $\text{K}\cdots\text{K}$  distances. These are the same

centre of inversions between the  $\text{HDC}^-$  anions within alternating planes. As in the previous chapter, this complex has been broken down into planes and chains of the individual components within the system and built up so that these components relate back to one another in the form of key symmetry elements.

The  $\text{HDC}^-$  and  $\text{K}^+$  planes as viewed separately along the  $a$ -,  $b$ -, and  $c$ -axes are presented in Figure 6-4 and Figure 6-6, respectively. The overall structure, presented in Figure 6-7, is the superimposed image of the two sets of planes.

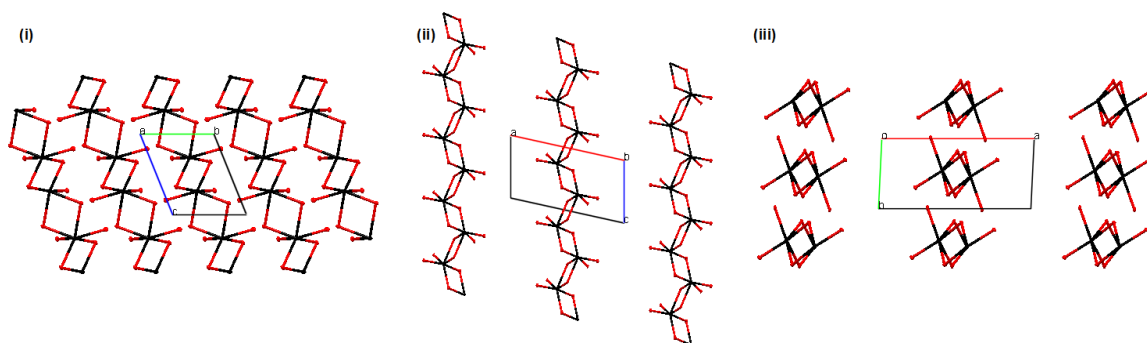


Figure 6-6 KHDC,  $\text{K}^+$  planes viewed along the (i)  $a$ - (ii)  $b$ - and (iii)  $c$ -axes.

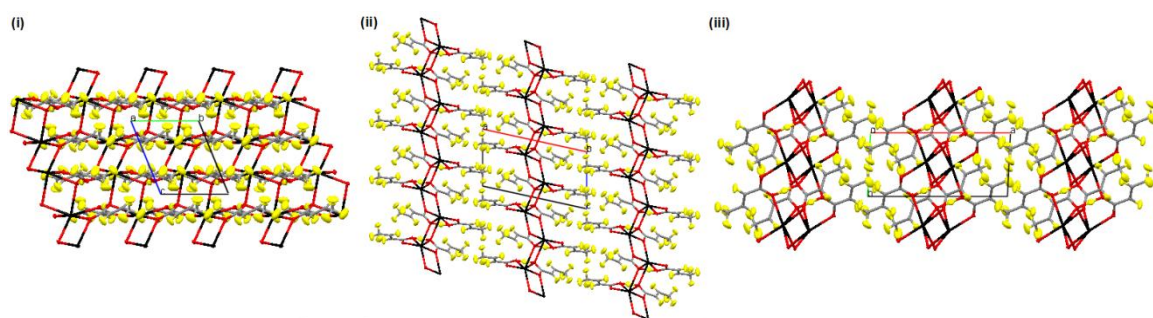


Figure 6-7 KHDC, superimposed  $\text{HDC}^-$  and  $\text{K}^+$  planes viewed along the (i)  $a$ - (ii)  $b$ - and (iii)  $c$ -axes to produce resulting KHDC structure in three dimensions.

## 6.4 The effect of pressure on the crystal structure of potassium hydrogen dicrotonate

The  $K^+$  interaction distances obtained at the three pressures are presented in Table 6-2. Also presented are all intra-molecular  $HDC^-$  distances (Å) and angles (°) in Table 6-1, and crystallographic information in Table 6-3.

As expected, there is a slight decrease in unit cell lattice constants and a slight increase in the unit cell angles with increased pressure. There is also an associated increase in the density as pressure is increased. After the first rise in applied pressure from 0 to 2.4 kbar, the most significant change in lattice constant is in  $c$ , which decreases from 7.200(2) to 7.079(2) Å. This change of 0.121 Å can be compared to changes of 0.066 and 0.036 Å in  $a$  and  $b$  which decrease from 12.398(3) to 12.332(4) Å and 5.9868(2) to 5.951(2) Å, respectively. By further doubling the pressure from 2.4 to 4.8 kbar the  $a$ ,  $b$  and  $c$  lattice constants decrease to 12.282(4), 5.924(2) and 6.991(2) Å respectively, changes of 0.05, 0.027 and 0.088 Å. For each rise in pressure, the effect on the lattice constants is in the order  $c > a > b$ . Also the  $HDC^-$  intra-molecular distances appear to display no significant change during the application of pressure, Table 6-1.

This suggests that the biggest pressure effect is on the  $K^+$  ion chains that run along the  $c$ -axis, and also connect with one another via HBs along the  $b$ -axis to make a  $bc$  plane. Figure 6-4, in which the  $HDC^-$  planes are viewed along the  $a$ ,  $b$  and  $c$  axes shows that the largest free space within the structure is within the  $HDC^-$  planes, along the  $c$ -axis. This makes sense due to the large bulky nature of the anion, and also explains the less significant effect on the  $HDC^-$  anions that lie on the  $ab$  plane, Figure 6-4.

Also observed is the reduction in  $O2-H1\cdots O3$  HB distance from 2.481(4) to 2.469(4) to 2.462(7) Å. In considering the  $O-H$  distances, which are more accurately determined in the neutron diffraction experiment, these are found to vary slightly, though at the margins of significance. Oddly the  $O2-H1$  distance is increased from 1.144(6) to 1.154(8) and is then decreased back to 1.131(11), and the  $O3\cdots H1$

distance is decreased from 1.33(6) to 1.31(8) and then increased back to 1.33(11) Å. The HB is placed between the interacting  $K^+$  chains to make up the  $K^+$  chain, if the main effect of the applied pressure is in the direction of the  $K^+$  chains it would therefore make sense for the HB to be influenced by the applied pressure.

From the previous chapter, the effect of increasing the size of the incorporated metal was most significant on the metal contact distances within the structure, particularly the significantly short  $M\cdots M$  distances. This suggests that the most significant interaction within such metal organic systems in which the  $M^+$  ions are in such close proximity to one another, is the ionic  $M\cdots M$  interactions. The different  $M\cdots M$  distances present in the  $K^+$  planes and the likely effect of pressure on these, i.e. the largest being most likely to compress, may explain the increase, followed by a decrease in HB distance by applying the two steps of pressure.

Overall the HB distance decreased with applied pressure, however the effect was not linear. The effect of increased pressure on the  $HDC^-$  anion and surrounding  $K^+$  ions is illustrated in Figure 6-8.

An overlay of the structures obtained at 0, 2.4 and 4.8 kbar is shown in Figure 6-8 and Figure 6-9. A comparison of the anion at 0 and 2.4 kbar shows very little difference and is also the case on comparing the anion at 2.4 and 4.8 kbar. Again a comparison of the anion at 0 and 4.8 kbar shows very little difference in terms of the intra-molecular positions of the atoms with respect to one another, though a more significance difference between the  $K^+$  and O atom positions is observed.

A comparison of the effects of increased pressure on the  $K^+$  chains is illustrated in Figure 6-9. Comparing the 0 and 4.8 kbar structures again suggests the main discrepancies in atom positions are around the K-O interactions. An examination of the K-O distances presented in Table 6-2 reveals that all changes in distance are of similar magnitude, suggesting the decrease is systematic with respect to the applied pressure. Earlier a total of six K-O interactions from four surrounding  $HDC^-$  anions were defined; those in which the distance decreases the most are the K1-O2 and K-O4 interactions from the same  $HDC^-$  anion and the single K-O3 interaction, Table 6-2. These interactions have been highlighted in Figure 6-10, and seem to be

directed towards one particular side of the  $K^+$  molecule. This may suggest that the  $K^+$  ions move in a particular direction when pressure is applied.

In conclusion, application of pressure to the KHDC structure does have an effect on the short, strong hydrogen bond, which appears to be a consequence of the more significant effect on the anisotropic contraction of the whole structure. The lattice constants are affected in the order  $c > a > b$ , suggesting that the  $HDC^-$  anions, shown to lie on the  $ab$  plane, are less compressible than the  $K^+$  chains which run along the  $c$  axis and form HB bridges with one another along the  $b$  axis. The intra-molecular distances within the crotonate residues of the  $HDC^-$  anions were shown not to change with applied pressure. The HB did not display any significant changes or anomalous behaviour with applied pressure up to 4.8 kbar at 40 K and remained asymmetric. The effects on the K-O interactions were however more pronounced and appear to be directional.

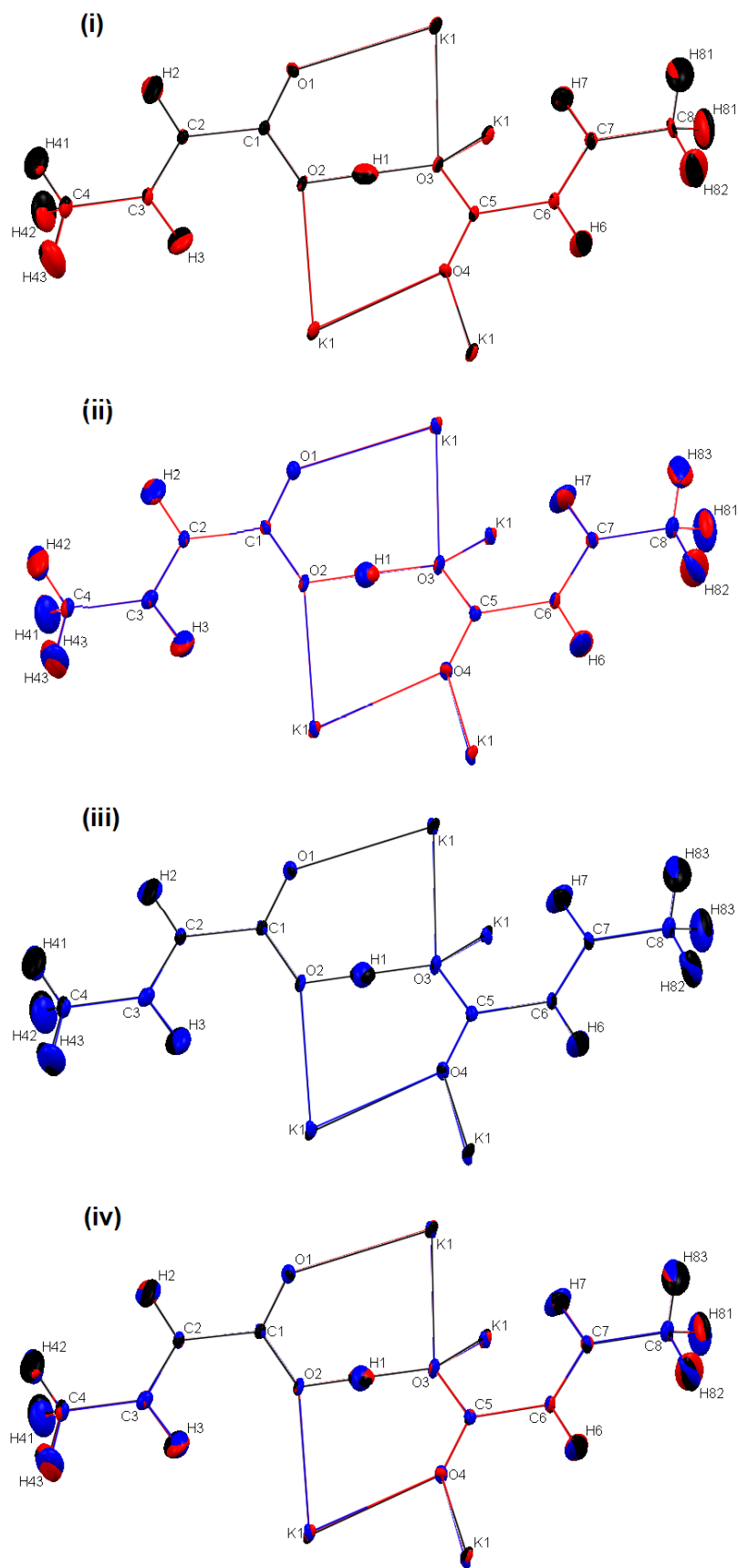


Figure 6-1 Comparison of  $\text{HDC}^-$  anion and surrounding  $\text{K}^+$  ions at 40 K; (i) 0 and 2.4 kbar; (ii) 2.4 and 4.8 kbar; (iii) 0 and 4.8 kbar; and (iv) 0, 2.4 and 4.8 kbar.  
**Key:** 0kbar (black), 2.4kbar (red), 4.8kbar (blue).

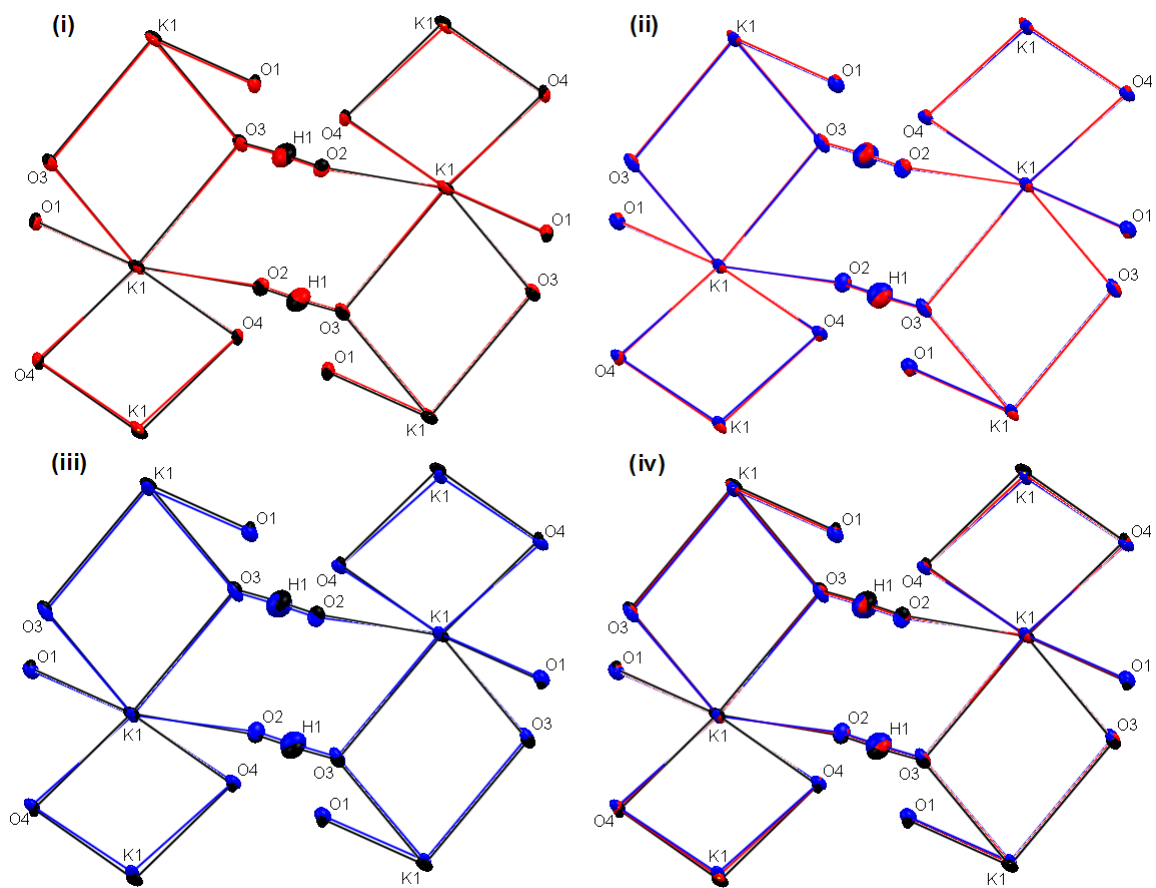


Figure 6-9 Comparison of  $K^+$  ion chains at 40 K; (i) 0 and 2.4 kbar; (ii) 2.4 and 4.8 kbar; (iii) 0 and 4.8 kbar; and (iv) 0, 2.4 and 4.8 kbar. Key: 0 kbar (black), 2.4 kbar (red), 4.8 kbar (blue).

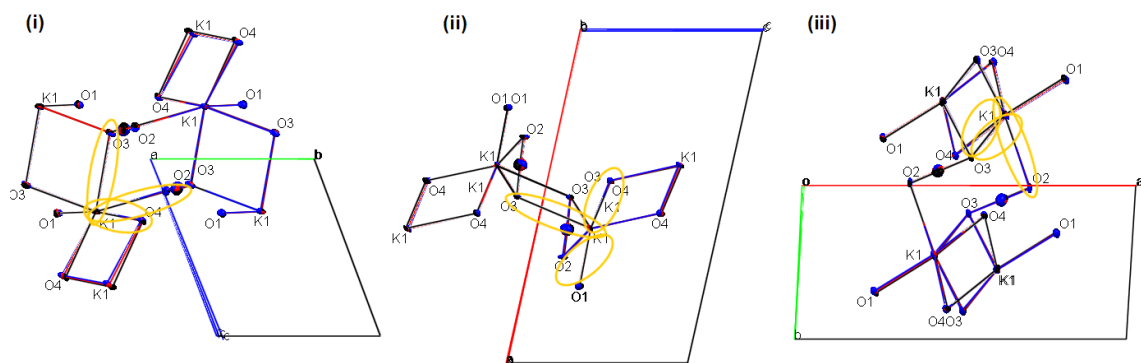


Figure 6-10  $K^+$  ion chains, at 40 K and 0, 2.4 and 4.8 kbar, viewed along (i) *a*- (ii) *b*- and (iii) *c*- axes. Key: 0 kbar (black), 2.4 kbar (red), 4.8 kbar (blue).

**Table 6-1 Distances (Å), angles (°) and standard deviations ( ) in crotonate residues**

		40k			Exp
		0 (kbar)	2.4 (kbar)	4.8 (kbar)	Neutron
M	C1-O1	1.240(4)	1.239(5)	1.234(7)	1.2233(16)
	C1-O2	1.311(2)	1.306(3)	1.310(5)	1.2963(17)
	C1-C2	1.481(3)	1.482(4)	1.485(6)	1.4817(14)
	C2-C3	1.334(4)	1.334(5)	1.332(7)	1.3219(18)
	C3-C4	1.497(3)	1.498(4)	1.494(6)	1.4934(16)
	C2-H2	1.093(4)	1.096(6)	1.086(8)	1.079(4)
	C3-H3	1.086(4)	1.092(5)	1.087(8)	1.059(4)
	C4-H41	1.087(5)	1.086(6)	1.070(9)	1.033(7)
	C4-H42	1.092(5)	1.086(6)	1.070(11)	1.036(5)
	C4-H43	1.087(8)	1.084(10)	1.092(12)	1.031(5)
	O2-H1	1.144(6)	1.154(8)	1.131(11)	1.1407(25)
J	C5-O3	1.296(3)	1.296(3)	1.285(5)	1.2838(15)
	C5-O4	1.243(4)	1.239(5)	1.256(7)	1.2368(14)
	C5-C6	1.492(3)	1.488(4)	1.486(6)	1.4860(13)
	C6-C7	1.335(4)	1.348(5)	1.341(6)	1.3236(14)
	C7-C8	1.498(3)	1.497(4)	1.488(6)	1.4917(17)
	C6-H6	1.080(5)	1.079(5)	1.075(8)	1.078(3)
	C7-H7	1.087(5)	1.078(6)	1.086(8)	1.076(3)
	C8-H81	1.074(7)	1.081(6)	1.087(8)	1.035(6)
	C8-H82	1.081(5)	1.084(6)	1.084(10)	1.045(5)
	C8-H83	1.086(4)	1.083(9)	1.088(13)	1.054(5)
	O3-H1	1.338(6)	1.316(8)	1.331(11)	1.3476(24)
O2—O3	2.481(4)	2.469(4)	2.462(7)	2.4879(15)	
M	O1-C1-O2	123.64(23)	123.95(29)	123.93(43)	123.64(11)
	C2-C1-O1	120.20(17)	119.71(21)	119.73(31)	119.75(10)
	C2-C1-O2	116.16(23)	116.34(29)	116.33(43)	116.51(10)
	C1-C2-C3	123.91(15)	123.61(20)	123.37(30)	124.62(10)
	C2-C3-C4	125.31(17)	125.27(21)	124.81(31)	125.40(12)
J	O3-C5-O4	124.41(22)	124.19(29)	123.23(44)	124.15(11)
	C6-C5-O3	117.39(23)	117.72(29)	118.62(42)	117.83(9)
	C6-C5-O4	118.19(18)	118.07(22)	118.15(33)	118.02(9)
	C5-C6-C7	124.64(17)	124.19(21)	124.20(30)	125.20(10)
	C6-C7-C8	123.85(18)	123.21(22)	123.42(32)	125.03(11)
O2---H1---O3	O2---H1---O3	178.1(4)	177.9(5)	178.9(8)	177.99(26)
	C1-O2---H1	113.89(32)	113.80(42)	114.77(65)	114.0(2)
	C5-O3---H1	112.54(30)	113.54(39)	113.99(55)	113.2(1)

**Table 6-2 KHDC K<sup>+</sup> ion interactions (Å) and associated van der Waals radii (Å).**

	<i>D---A</i>	<i>D---A</i> / Å			Neutron RT (Ref 195)	Sum of the van der Waals radii / Å
		40K 0 kbar	40K 2.8 kbar	40K 4.8 kbar		
D2	K1---K1	4.076(6)	4.027(8)	3.982(13)		5.5
D2	K1---K1	4.436(6)	4.430(7)	4.411(11)		5.5
O2-H1---O3	K1---K1	5.793(2)	5.775(7)	5.77(1)		5.5
O2-H1---O3	K1---K1	5.987(2)	5.951(9)	5.92(1)		5.5
	K1---K1	6.349(6)	6.408(7)	6.42(1)		5.5
HDC <sup>-</sup>	K1---O1	2.712(5)	2.703(7)	2.704(9)	2.737(2)	3.27
	K1---O3	2.747(5)	2.751(6)	2.745(9)	2.784(2)	3.27
HDC <sup>-</sup>	K1---O2	2.740(5)	2.722(6)	2.711(9)	2.580(2)	3.27
	K1---O4	2.691(5)	2.673(7)	2.660(10)	2.693(2)	3.27
HDC <sup>-</sup>	K1---O3	2.933(4)	2.920(5)	2.907(7)	2.996(2)	3.27
HDC <sup>-</sup>	K1---O4	2.751(4)	2.755(5)	2.747(7)	2.789(2)	3.27

**Table 6-3 Crystallographic Information for KHDC at Varied Pressure**

	0 (kbar)	2.4 (kbar)	4.8 (kbar)	Neutron RT (Ref 195)
T /K	40	40	40	room
Diffractometer	SXD ISIS	SXD ISIS	SXD ISIS	
M /g mol <sup>-1</sup>	210.27	210.27	210.27	210.27
Space group	P-1	P-1	P-1	P-1
a /Å	12.398(3)	12.332(4)	12.282(4)	12.453(4)
b /Å	5.9867(17)	5.951(2)	5.924(2)	6.049(2)
c /Å	7.2000(18)	7.079(2)	6.991(2)	7.452(2)
α /°	66.698(16)	67.49(2)	68.00(2)	65.62(2)
β /°	104.559(16)	104.797(19)	105.01(2)	104.04(2)
γ /°	98.143(18)	98.39(2)	98.76(2)	97.44(2)
V /Å <sup>3</sup>	474.5(2)	463.3(2)	454.7(3)	
Z	2	2	2	2
ρ <sub>calc</sub> /g cm <sup>-3</sup>	1.427	1.507	1.536	
μ /mm <sup>-1</sup>	0.159	0.163	0.166	
θ range /°	8.65 – 84.52	9.04 – 84.47	8.3 – 84.11	
Reflections (meas./indep./obs>2σ(I))	5205	3548	3869	
Parameters	219	219	219	
GOOF on F <sup>2</sup>	1.485	1.083	1.643	
R1 (obs/all)	0.0771	0.0766	0.1398	
wR2 (obs/all)	0.1934	0.2036	0.3376	
ρ <sub>max</sub> , min /eÅ <sup>-3</sup>	1.745 -1.638	1.597 -1.769	4.359 -2.411	
RMS /fmÅ <sup>-3</sup>				

## 6 Conclusions and Forward Look

A range of metal containing complexes, ranging from modelled PB and hydrogen bond mediated TM systems to crystalline organometallic systems have been studied in order to investigate the effect of metal identity on the associated electronic, magnetic and structural properties. These investigations have been carried out using both computational quantum chemistry methods and crystallography.

### 6.1 Prussian Blue Analogues

The effect of the metal identity on the band gap in PB and related complexes has been investigated by means of both SCF calculations and density of state plots. The band gap energies obtained from direct SCF calculations using a range of hybrid functionals did not in general compare well with experimental values. The band gap values obtained using the B3LYP functional were significantly lower in comparison to the experimental values. This was also the case when all other hybrid functionals, including HF=100%, were applied.

The values obtained using the uhf functional, usually known to overestimate band gap energies, were as expected, high in comparison to the experimental values, although in comparison to the other functionals, provided values most comparable to experiment. In addition, the means by which the excited electron was modelled had little to no effect on either the band gap energy or the trend of the energies in relation to one another. Slight discrepancies do, however, begin to appear around 20% HF mixing (corresponding to the B3LYP functional) at which it is predicted that the findings from the electronic structure calculations are qualitatively comparable to experiment.

The band gaps calculated from the DOS plots by use of the B3LYP functional were also shown to overestimate the experimentally obtained band gap energies. These did, however, give values significantly better in comparison to those obtained by direct energy differences from SCF calculations. Interestingly, the energy difference between the most populated states in the HOMO and LUMO also

appeared to fit the trend in band gaps with respect to the identity of the metal cation incorporated into the lattice.

A comparison of the PB, PY and PW DOS plots produced some interesting observations, showing the value of these calculations in attempting to understand physical properties that are directly dependent on the electronic structure. As expected the PB HOMO and LUMO were identified as the low spin Fe  $t_{2g}$  orbital and high spin Fe  $t_{2g}$  orbital respectively, in which the  $e^-$  transition was  $\beta$ - $\beta$ . The PY HOMO and LUMO were identified as the low spin Fe  $t_{2g}$  orbital and high spin  $t_{2g}$  orbital respectively, again in which the  $e^-$  transition was  $\beta$ - $\beta$ . Although the energy difference of 1.905 eV between the VB and CB was significantly lower than the expected value for yellow absorption spectra in the 2.89-2.96 eV range, this range was well within the 1.905 - 3.374 eV value spanning the lowest HOMO to lowest LUMO. Also as expected, due to lack of colour in PY, the PW DOS plot produced a band gap in the UV energy range. The associated HOMO and LUMO are both high spin Fe  $t_{2g}$  orbitals suggesting that upon excitation, the  $\beta$  electron in the orbital containing the electron pair moves between the degenerate high spin Fe  $t_{2g}$  orbitals.

A significant effect on band gap resulting from the identity of the included cation has been found. In the PB complexes, a linear relationship was found between the increased lattice constant and decreased band gap upon the incorporation of a larger cation, although the effect was not as significant in group two complexes. In the PW complexes, a linear relationship was also noted between the increased lattice constant and increased band gap upon the incorporation of a larger cation, with the exception of Cs, although again, the effect was not as significant in group two complexes. The effect in group two complexes was, however, more pronounced than that in the PB complexes, suggesting the possibility that the number of metals within the eight available charge balancing sites may also influence the lattice constant and therefore band gap.

In all complexes, an increase in the Fe ion charges are observed with increased cation size, suggesting that the change in band gap is due to both the resulting increase in lattice parameter with the increasing cation size, but also the increase

in the interaction between the Fe ions and the metal cation. This confirms the claim by Wojdeł and Bromley<sup>29-30</sup>. The subtle differences observed suggest that by altering the metal identity it is possible to make small changes in the obtained band gap.

In the future, DOS plots in which the densities of states of the individual *d* orbitals are plotted may provide more information on whether the excitations are specific to any of the degenerate one in for example the case of PW. Also the Kalimori method, outlined in Chapter 2, could also be used to derive expressions for any *d*-electron configuration of the systems in terms of Racah parameters. This may be of use in allowing the order of each state to be visualised in terms of total energy. It is then possible to determine the total energy for all of the excited states by the successful convergence of a limited few.

## 6.2 Transition Metal Hydrogen Halides

The investigation of the effects of a number of parameters on the magnetic coupling interactions borne by FHF, ClHCl and FHCl HBs in TMHH structures produced a number of interesting findings:

- Related work in the literature has shown that the  $F_0=35\%$  hybrid functional yields *J* coupling values in good agreement with experiment. The estimated  $F_0=35\%$   $J_2$  value of  $-0.062$  obtained from our CuFHF material by averaging of the  $F_0 = 30$  and  $40\%$  values was significantly larger than the values of  $-0.03$  and  $0.0190$  quoted for the experimental<sup>82</sup> and theoretical<sup>83</sup>  $[\text{Cu}^{\text{II}}(\text{HF}_2)(\text{pyz})_2]\text{BF}_4$  (pyz = pyrazine) coordination polymers respectively. This could, however, be due to the significantly shorter Cu–Cu, Cu–F, F–H distances in the present material;
- In cases of the very weak couplings along the *z*-axis ( $J_2$ ) in the Cu material, the *nn* Ising Hamiltonian incorporating only  $J_1$  and  $J_2$  couplings did not produce consistent  $J_2$  values when comparing couplings obtained separately from two sets of magnetic energy differences. Interestingly, the average  $J_2$  values computed over the two inconsistent results was identical to the  $J_2$

values calculated using an extended Ising Hamiltonian in which further z-axis *nnn* couplings ( $J_4$ ) were included. It was clear from this that in cases of weak out-of-plane coupling in JT-distorted structures, the additional *nnn* interactions can be as significant as the weak *nn* couplings. However, it is clear that the magnetic interactions in this antiferromagnetic material are highly anisotropic: strong in-plane order (associated with the singly occupied JT split  $x^2-y^2$  orbitals) being anticipated on the basis of the large  $J_1$  couplings, along with a much weaker tendency to form a long-range 3D ordered state at low temperature driven by the small  $J_2$  couplings;

- A number of full atom and geometry optimisation calculations were carried in order to obtain the static ground state structures for materials in which the identity of the TM and X-H-X' ligand, and the  $F_0$  value were altered. This revealed that the magnetic coupling increases with decreased  $F_0$ , and is affected by both the identity of the interacting TM ions and HB halide linkers, the coupling constants emerging in the order Ni >> V > Cu and ClHCl > FHCl > FHF;
- The effect of altering the HB lengths, introduced by expanding and contracting the lattice, and altering the proton position along the one dimensional HB was also examined;
- The HB potential energy and J coupling profiles were then used to obtain quantum mechanical expectation values  $\langle J \rangle$  which incorporated the proton motion.

Due to the 3- charge on the OHO ligand, computational studies using the present structures are not possible, for the reason that a charge neutral cell cannot be easily created. Similar investigations using cluster models are therefore of future interest.

### 6.3 Metal Containing BA and CA complexes

In order to obtain interesting three-dimensional networks the symmetrical halo-anilic acids (XA), and in particular chloranilic (CA) and bromanilic (BA) acid, were selected as ideal starting molecules to act as ligands when combined with metals. The ability for these ligands to take three different forms depending on the degree of protonation or deprotonation gave a large range of possible interactions. A study of the literature revealed a significant amount of work carried out using the CA complex in comparison to the BA complex; almost all of the metal containing complexes contained TM or group 2 metals. In the large majority of the metal CA complexes in the literature, the CA ligand was in the delocalised form and bound to neighbouring metals in an easily identifiable manner such as a bisbidentate ligand in which the XA molecules coordinated to two metals on each side via the four carbonyl groups to make a chain, or in some cases a carbonyl and a halogen to form a wavy chain, or in some cases a plane. By combining group 1 metals with the XA ligands it was anticipated that more extended networks would be formed, due to the single 1+ charge making the ligand more likely to appear in the HXA state within the structure or allow asymmetric units in which different metal coordinations were at the two sides of the XA molecules.

A number of related metal-containing BA and CA complexes were obtained. The structural packing of the molecules were analysed by defining a number of recurring units within the structures in order to identify key similarities. The structures were also broken down in to lower dimensional units composed of the individual XA and  $M^+$  components within the asymmetric unit and built up into higher dimensional units such as clusters, chains and planes that would all intersect with one another in order to produce the overall three-dimensional structures. The interacting planes and chains were used at a point of reference in order to describe the interactions present. In most cases, the point of intersection was on a key symmetry element such as an inversion centre, at which two symmetry-related parts of the structure met.

Among the most interesting findings from this experimental structural work were the following:

- Two 1:1 KBA tautomeric anhydrous polymorphs were synthesised and crystallised within the same sample vial. One of these contained the  $\text{HBA}^-$  ligand and the other that contained both the  $\text{H}_2\text{BA}$  and  $\text{BA}^{2-}$  forms. Although the components within the cell were therefore very different, the structural packing of the two polymorphs could be described in a very similar way. Both consisted of two intersecting planes along the diagonal planes of the unit cells, however at the points of intersection in form I, one  $\text{HBA}^-$  molecule from each plane acts as either the HB donor or the HB acceptor, resulting in two independent  $\text{K}^+$  chains within each plane. This is unlike form II in which the symmetric nature of the  $\text{H}_2\text{BA}$  molecules means that each  $\text{H}_2\text{BA}$  equally contributes a proton at each point of intersection, and the symmetric nature of the  $\text{H}_2\text{BA}$  molecules dictates that the second halves of the molecules also coordinate to another  $\text{K}^+$  ion in the same manner. This results in very different  $\text{K}^+$  chains.
- The same KBA combination synthesised and recrystallised under other conditions resulted in three very different hydrated 2:1 KBA polymorphs with the same isostructural structures with the same formulae. Although the  $\text{BA}^{2-}$  ligand form was present in all three complexes, the result was a varied degree of structures.
- A number of related isomorphous structures were obtained in which different metals occupied the same position in the lattice. The main structural effect in incorporating a larger cation resulted from the increased ionic repulsion between the metal ions. This is particularly true in the complexes with significantly short  $\text{M}\cdots\text{M}$  distances in comparison to those reported in the CSD. The overall effect of the  $\text{M}\cdots\text{M}$  repulsion is less apparent in complexes which contained  $\text{M}\cdots\text{M}$  clusters as opposed to  $\text{M}\cdots\text{M}$  chains of planes, although the most significant effects can still be traced back to be a consequence of the  $\text{M}\cdots\text{M}$  cluster. This was in some cases

found to have a number of interesting effects on the other interactions within the complex particularly those in the proximity of the  $M\cdots M$  contacts. Such effects include specific HB distances decreasing and angles increasing, resulting in significantly stronger interactions, and also switching of the most significant HB interaction within bifurcated hydrogen bonds. In the presence of significantly short  $M\cdots M$  distances, other larger  $M\cdots M$  distances are consequently seen to decrease in spite of their own  $M\cdots M$  repulsion. Other significant  $O\cdots O$  and  $O\cdots Cl$  interactions are also seen to become less significant due to an increase in interaction distance due to the incorporation of a larger metal.

- Lighter group one metal complexes were also obtained although it was not possible to obtain any LiBA complexes, due to their tendency to decompose outside the equilibrium surrounding of the vials in which they were synthesised and recrystallised. Due to the smaller radii of the  $Li^+$  ion in comparison to the other heavier metals, it tended to have a comparably lower coordination number and therefore produced simpler structures. Two LiCA complexes were obtained; the units coordinating to the  $Li^+$  were similar in both complexes, both were coordinated to two CA molecules in the monodentate C1 and bidentate B2 fashion, although one contained an additional two coordinating water molecules the other contained only one. These two complexes were also very different in the sense that one was composed of delocalised  $CA^{2-}$  molecules whereas the other contained both delocalised unprotonated and neutral CA molecules.

The presence of all these subtle consequential effects due to metal identity may allow group 1 metal ions to be used to tune such intermolecular interactions in related systems with potentially useful applications.

## 6.4 Future Potential

The combination of group 1 metals with the BA and CA ligands is still an ongoing project and has also been expanded to include preliminary investigations of

complexes containing group two metals. It is the intention to try and form mixed alkali/TM complexes in order to produce hybrid complexes in which any properties arising from the potential charge transfer of a TM and delocalised XA ligand could be tuned by the incorporated metals.

This is obviously some way down the line at the moment as there are still a number of further systematic studies that should be carried out in order to understand the structural patterns, prior to being able to use these patterns in design of complexes with predictable motifs and hence, ideally, predictable properties.

In terms of the combination of quantum chemical calculations and detailed experimental structural studies, this area again has great future potential. Currently the systems to which each can be applied are not necessarily fully compatible in terms of technique development - some of the computational model systems are difficult to access experimentally, while many of the more complex experimental systems involving larger ligands and extended structures are not easily computed at present. It is to be hoped that the two methods can continue to develop in tandem to provide the ability for chemists to design, synthesise and characterise materials with predictable properties.

## References

- 1 L. Pauling, *J. Am. Chem. Soc.* (1931), **53**, 137-1400.
- 2 W. M. Latimer, W. H. Rodebush, *J. Am. Chem. Soc.* (1920), **42**, 1419-1433.
- 3 M. L. Huggins, *J. Phys. Chem.* (1922), **26**, 601-625.
- 4 G. A. Jeffrey, *An Introduction to Hydrogen Bonding*, Oxford University Press, Oxford, 1997.
- 5 J. Gaultier and C. Hauw, *Acta Cryst.* (1969), **B25**, 546-548.
- 6 M. L. Huggins, *J. Phys. Chem.* (1936), **40**, 723-731.
- 7 M. Ware, *J. Chem. Ed.* (2008), **85**, 612-621.
- 8 A. Dostal, G. Kauschka, S. J. Reddy, F. Scholz, *J. of Electroanal. Chem.* (1996), **406**, 155-163.
- 9 P. A. Christensen, A. Hamnett, and S. J. Higgins, *J. Chem. Soc. Dalton Trans.* (1990), 2233-2238.
- 10 (a) D. R. Rosseinsky, H. Lim, X. Zhang, H. Jiang and J. W. Chai, *Chem. Commun.* (2002), 2988-2989. (b) D. R. Rosseinsky, A. M. Soutara, I. F. Annergrena and A. Glidle, *Proceedings of SPIE* (2001), **4458**, 248-260. (c) D. R. Rosseinsky, H. Lim, H. Jiang, J. W. Chai, *Inorg. Chem.* (2003), **42**, 19, 6015-6023.
- 11 M. Hermes, M. Lovric, M. Hartl, U. Retter, F. Scholz, *J. Electroanal. Chem.* (2001), **501**, 193-204.
- 12 (a) P. J. Kulesza, S. Zamponi, M. Berrettoni, R. Marassi and M. A. Malik, *Electrochimica Acta.* (1995), **40**, 6, 681-688. (b) P. A. Christensen, A. Hamnett, and S. J. Higgins, *J. Chem. Soc. Dalton Trans.* (1990), 2233. (c) K. R. Dunbar and R. A. Heintz, *Prog. Inorg. Chem.* (1997), **45**, 283.

- 13 C. Yang, C. H. Wang, J. S. Wu, X. Xia, *Electrochimica Acta* (2006), **51**, 4019-4023.
- 14 C. M. Pharr and P. R. Griffiths, *Anal. Chem.* (1997), **69**, 22, 4673-4679.
- 15 P. J. Kulesza, *Anal. Chem.* (1996), **68**, 2442-2446.
- 16 J. J. Garcia-Jareno, J. Navarro-Laboulais, A. Sanmatias and F. Vicente, *Electrochimica Acta* (1998), **43**, 9, 1045-1052.
- 17 A. Xidis and V. D. Neff, *J. Electrochem. Soc.* (1991), **138**, 12, 3637-3642.
- 18 A. Roig, J. Navarro, J. J. Garcia and F. Vicente, *Electrochimica Acta* (1994), **39**, 3, 437-442.
- 19 N. Imanishi, T. Morikawa, J. Kondo, Y. Takeda, O. Yamamoto, N. Kinugasa and T. Yamagishi, *J. Power Sources* (1999), **79**, 215-219
- 20 J. F. Keggin and F. D. Miles, *Nature* (1936), **137**, 577-578
- 21 (a) K. M. Jeerage, D. T. Schwartz, *Sep. Sci. Technol.* (2000), **35**, 15, 2375-2392. (b) K. M. Jeerage, W. A. Steen, D. T. Schwartz, *Chem. Mater.* (2002), **14**, 2, 530-535.
- 22 (a) M. Hermes, F. J. Scholz, *Solid State Electrochem.* (1997), **1**, 215. (b) H. Düssel, A. Dostal, F. Scholz, J. Fresenius, *J. Anal. Chem.* (1996), **355**, 21.
- 23 M. Pyrasch, A. Toutianoush, W. Jin, J. Schnepf, B. Tieke, *Chem. Mater.* (2003), **15**, 245-254.
- 24 (a) A. A. Karyakin, E. A. Kotelnikova, L. V. Lukachova, E. E. Karyakina, J. Wang, *Anal. Chem.* (2002), **74**, 1597. (b) F. Ricci, G. Palleschi, *Biosens. Bioelectron.* (2005), **21**, 3, 389-407. (c) Z. J. Song, R. Yuan, Y. Q. Chai, B. Yin, P. Fu, and J. Wang, *Electrochimica Acta.* (2010), **55**, 5, 1778-1784.
- 25 (a) M. Jayalakshimi and F. J. Scholz, *J. Power Sources* (2000), **87**, 212. (b) T. Y. Kinugasa, *J. Power Sources* (1999), **79**, 215. (c) M. Jayalakshmi, F. J. Scholz, *Power Sources*, (2000), **91**, 217-223. (d) L. C. Chen, Y. H. Huang, K.

- S. Tseng and K. C. Ho, *J. New Mater. Electrochem. Syst.* (2002), **5**, 3, 203-212. (e) A. J. Eftekhari, *Power Sources* (2004), **126**, 1-2.
- 26 (a) L. C. Chen, Y. H. Huang and K. C. Ho, *J. Solid State Electrochem.* (2002), **7**, 6. (b) P. R. Somani and S. Radhakrishnan, *Mater. Chem. Phys.* (2003), **77**, 117.
- 27 A. Dostal, G. Kauschka, S. J. Reddy and F. Scholz, *J. Electroanal. Chem.* (1996), **406**, 155-163.
- 28 M. J. D. Low, *Anal. Chem.* (1969), **41**, 97A.
- 29 J. C. Wojdel and S. T. Bromley, *Chem. Phys. Letters* (2004), **397**, 154-159.
- 30 J. C. Wojdel and S. T. Bromley, *J. Mol. Model* (2005), **11**, 288-292. (b) J. C. Wojdel and S. T. Bromley, *J. Phys. Chem. B* (2006), **110**, 48, 24294 - 24298.
- 31 P. J. Kulesza, M. A. Malik, K. Miecznikowski, A. Wolkiewicz, S. Zamponi, M. Berrettoni and R. J. Marassi, *J. Electrochem. Soc.* (1996), **143**, 1, L10-L12.
- 32 (a) P. Zhou, D. Xue, H. Luo and X. Chen, *Nano Lett.* (2002), **2**, 8, 845-847. (b) J. T. Culp, J. H. Park, I. O. Benitez, M. W. Meisel and D. R. Talham, *Polyhedron* (2003), **22**, 2125.
- 33 R. Koncki and O. S. Wolfbeis, *Anal. Chem.* (1998), **70**, 2544.
- 34 (a) S.M. Chen, *J. Electroanal. Chem.* (2002), **521**, p29. (b) K. C. Pan, C. S. Chuang, S. H. Cheng and Y. O. Su, *J. Electroanal. Chem.* (2001), **501**, 160.
- 35 A. Johansson, E. Widenkvist, J. Lu, M. Boman and U. Jansson, *Nano Lett.* (2005), **5**, 8, 1603-1606.
- 36 M. Taguchi, K. Yamada, K. Suzuki, O. Sato and Y. Einaga, *Chem. Mater.* (2005), **17**, 17, 4554-4559.
- 37 D. M. DeLongchamp and P. T. Hammond, *Chem. Mater.* (2004), **16**, 23, 4799-4805.

- 38 (a) S. I. Ohkoshi, Y. Abe, A. Fujishima and K. Hashimoto, *Phys. Rev. Lett.* (1999), **82**, 6, 1285-1288. (b) N. F. Zakharchuk, N. Naumov, R. Stosser, U. Schroder, F. Scholz and H. Mehner, *J. Solid-State Electron. Chem.* (1999), **3**, 264-276. (c) D. Luneau, *Curr. Opin. Solid State Mater. Sci.* (2001), **5**, 123-129. (d) A. Widmann, H. Kahlert, I. Petrovic-Prelevic, H. Wulff, J. V. Yakhmi, N. Bagkar and F. Scholz, *Inorg. Chem.* (2002), **41**, 22, 5706-5715. (e) J. G. Moore, E. J. Lochner, C. Ramsey, N. S. Dalal and A. E. Stiegman, *Angew. Chem. Int. Ed.* (2003), **42**, 24, 2741-2743.
- 39 (a) S. Nakanishi, G. Lu, H. M. Kothari, E. W. Bohannon and J. A. Switzer, *J. Am. Chem. Soc.* (2003), **125**, 14998-14999. (b) D. Schwudke, R. Stosser and F. Scholz, *Electrochem. Commun.* (2000), **2**, 301-306. (c) K. Tennakone and W. G. D. Dharmaratne, *J. Phys. C*, (1983), **16**, 5633-5639.
- 40 M. Verdaguer, A. Bleuzen, V. Marvaud, J. Vaissermann, M. Seuleiman, C. Desplanches, A. Sculler, C. Train, R. Garde, G. Gelly, C. Lomenech, I. Rosenman, P. Veillet, C. Cartier and F. Villain, *Coord. Chem. Rev.* (1999), **190-192**, 1023-1047.
- 41 (a) D. Luneau, *Curr. Opin. Solid-State Mater. Sci.* (2001), **5**, 123. (b) A. Widmann, H. Kahlert, I. Petrovic-Prelevic, H. Wulff, J.V. Yakhmi, N. Bagkar and F. Scholz, *Inorg. Chem.* (2002), **41**, 5706.
- 42 J. G. Moore, E. J. Lochner, C. Ramsey, N. S. Dalal and A. E. Stiegman, *Angew. Chem. Int. Ed.* (2003), 2741.
- 43 (a) M. Pyrasch, A. Toutianoush, W. Jin, J. Schnepf and B. Tieke, *Chem. Mater.* (2003), **15**, 245. (b) N.F. Zakharchuk, N. Naumov, R. Stosser, U. Schroder, F. Scholz and H. Mehner, *J. Solid-State Electrochem.* (1999), **3**, 264.
- 44 D. Luneau, *Curr. Opin. Solid-State Mater. Sci.* (2001), **5**, 123.
- 45 P. Zhou, D. Xue, H. Luo and X. Chen, *Nano Lett.* (2002), **2**, 845.
- 46 K. R. Dunbar and R. A. Heintz, *Prog. Inorg. Chem.* (1997), **45**, 283.

- 47 M. Jayalakshmi and F. Scholz, *J. Power Sources*, (2000), **91**, 217.
- 48 (a) M. Verdager, N. Galvez, R. Garde and C. Desplanches, *Electrochem. Soc. Interface* (2002), **11**, 28. (b) M. Verdager, A. Bleuzen, V. Marvaud, J. Vaissermann, M. Seuleiman, C. Desplanches, A. Sculler, C. Train, R. Garde, G. Gelly, C. Lomenech, I. Rosenman, P. Veillet, C. Cartier and F. Villain, *Coord. Chem. Rev.* (1999), **190-192**, 1023. (c) J. M. Manriquez, G. T. Yee, R. S. McLean, A. J. Epstein and J. S. Miller, *Science* (1991), **252**, 1415.
- 49 S. Ohkoshi, T. Iyoda, A. Fujishima and K. Hashimoto, *Phys. Rev. B* (1997), **56**, 11642.
- 50 S. Ohkoshi, Y. Abe, A. Fujishima and K. Hashimoto, *Phys. Rev. Lett.* (1999), **82**, 1285.
- 51 (a) W.E. Buschmann, J. Ensling, P. Gütlich and J.S. Miller, *Chem. Eur. J.* (1999), **5**, 3019. (b) D.A. Pejakovic, J.L. Manson, J.S. Miller and A.J. Epstein, *Phys. Rev. Lett.* (2000), **85**, 1994.
- 52 (a) S. Ohkoshi, K. Hashimoto, *Electrochem. Soc. Interface* (2002), **11**, 34. (b) S. Ohkoshi, Y. Yorozu, O. Sato, T. Iyoda, A. Fujishima and K Hashimoto, *Appl. Phys. Lett.* (1997), **70**, 1040. (c) O. Sato, Y. Einaga, A. Fujishima and K. Hashimoto, *Inorg. Chem.* (1999), **38**, 4405. (d) T. Kawamoto, Y. Asai and S. Abe, *Phys. Rev. Lett.* (2001), **86**, 348. (e) T. Yokoyama, H. Tokoro, S. Ohkoshi, K. Hashimoto, K. Okamoto and T. Ohta, *Phys. Rev. B.* (2002), **66**, 184111.
- 53 (a) O. Sato, T. Iyoda, A. Fujishima and K. Hashimoto, *Science* (1996), **272**, 704. (b) T. Yokoyama, T. Ohta, O. Sato and K. Hashimoto, *Phys. Rev. B.* (1998), **58**, 8257. (c) T. Yokoyama, M. Kiguchi, T. Ohta, O. Sato, Y. Einaga and K. Hashimoto, *Phys. Rev. B* (1999), **60**, 9340. (d) A. Bleuzen, C. Lomenech, V. Escax, F. Villain, F. Varret, C.C. dit Moulin and M. Verdager, *J. Am. Chem. Soc.* (2000), **122**, 6648. (e) C.C. dit Moulin, F. Villain, A. Bleuzen, M.-A. Arrio, P. Saintavit, C. Lomenech, V. Escax, F. Baudalet, E. Dartyge, J.-J. Gallet and M. Verdager, *J. Am. Chem. Soc.* (2000), **122**,

6653. (f) A. Goujon, F. Varret, V. Escax, A. Bleuzen and M. Verdaguer, *Polyhedron*, (2001), **20**, 1347.
- 54 V. Ksenofontov, G. Levchenko, S. Reiman, P. Gütlich, A. Bleuzen, V. Escax and M. Verdaguer, *Phys. Rev. B*. (2003), **68**, 24415.
- 55 (a) O. Kahn, *Nature* (1995), **378**, 667. (b) S. Ferlay, T. Mallah, R. Ouahes, P. Veillet and M. Verdaguer, *Nature*, (1995), **378**, 701.
- 56 A. Bhattacharjee, S. Saha, S. Koner, V. Ksenofontov, S. Reiman and P. Gütlich, *J. Magnetism Magnetic Materials* (2006), **302**, 173-180.
- 57 (a) O. Sato, T. Iyoda, A. Fujishima and K. Hashimoto, *Science*, (1996), **272**, 704-705. (b) O. Sato, Y. Einaga, A. Fujishima and K. Hashimoto, *Inorg. Chem* (1999), **38**, 4405-4412. (c) A. Bleuzen, C. Lomenech, V. Escax, F. Villain, F. Varret, C. Cartier and M. Verdaguer, *J. Am. Chem. Soc.* (2000), **122**, 6648-6652. (d) V. Ksenofontov, G. Levchenko, S. Reiman, P. Gutlich, A. Bleuzen, V. Escax and M. Verdaguer, *Phys. Rev. B* (2003), **68**, 024415.
- 58 E. Coronado, M. C. G. Lopez, G. Levchenko, F. M. Romero, V. Garcia-Baonza, A. Milner and M. Paz-Pasternak, *J. Am. Chem. Soc.* (2005), **127**, 4580-4581.
- 59 L. Egan, K. Kamenev, D. Papanikolaou, Y. Takabayashi and S. Margadonna, *J. Am. Chem. Soc.* (2006), **128**, 6034-6035.
- 60 G. Girit, A. Harrison, D. R. Allan, K. V. Kamenev, and D. S. Middlemiss, *Phys. Rev. B*, to be published
- 61 (a) S. Ohkoshi, O. Sato, T. Iyoda, A. Fujishima and K. Hashimoto, *Inorg. Chem.* (1997), **36**, 268-269. (b) S. Ohkoshi, T. Iyoda, A. Fujishima and K. Hashimoto, *Phys. Rev. B* (1997), **56**, 18. (c) S. Ohkoshi and K. Hashimoto, *Phys. Rev. B*, (1999), **60**, 18. (d) S. Ohkoshi, Y. Abe, A. Fujishima and K. Hashimoto, *Phys. Rev. Lett.* (1999), **82**, 6. (e) S. Ohkoshi, T. Hozumi, M. Utsunomiya, M. Abe and K. Hashimoto, *Physica B* (2003), **329-333**, 691-692.

- 62 (a) S. Ohkoshi, K. Arai, Y. Sato and K. Hashimoto, *Nat. Mater.* (2004), **3**, 857. (b) S. Ohkoshi, S. Yorozu, O. Sato, T. Iyoda, A. Fujishima and K. Hashimoto, *Appl. Phys. Lett.* (1997), **70**, 1040.
- 63 (a) O. Sato, I. Iyoda, A. Fujishima and K. Hashimoto, *Science* (1996), **271**, 49. (b) O. Sato, I. Iyoda, A. Fujishima and K. Hashimoto, *Science* (1996), **272**, 704. (c) Z. Gu, O. Sato, I. Iyoda, K. Hashimoto and A. Fujishima, *J. Phys. Chem* (1996), **100**, 182-189. (d) S. Ohkoshi, S. Yorozu, O. Sato, I. Iyoda, A. Fujishima and K. Hashimoto, *Appl. Phys. Lett.* (1997), **70**, 1040.
- 64 D. S. Middlemiss, L. M. Lawton and C. C. Wilson, *J. Phys.: Condens. Matter* (2008), **20**, 335231.
- 65 D. S Middlemiss, and C. C. Wilson, *Phys. Rev. B* (2008), **77**, 155129.
- 66 A.D. Becke, *J. Chem. Phys.*(1993), **98**, 1372-1377.
- 67 M. Nishino, Y. Yoshioka and K. Yamaguchi, *Chem. Phys. Lett.* (1998), **297**, 51-59.
- 68 J. A. Chan, B. Montanari, W. L. Chan and N. M. Harrison, *Molecular Physics* (2005), **103**, 18, 2573-2585.
- 69 E. Ruiz, M. Llunell and P. Alemany, *Journal of Solid State Chemistry* (2003), **176**, 400-411.
- 70 E. Ruiz, A. Rodriguez-Forteza, S. Alvarez and M. Verdaguer, *Chem. Eur. J.* (2005), **11**, 2135-2144.
- 71 N.M. Harrison, B.G. Searle, *Chem. Phys. Lett.* (1997), **266**, 507-511.
- 72 X. Feng, N.M. Harrison, *Phys. Rev. B* (2004), **70**, 092402.
- 73 (a) Z. Lu, X. Wang, Z. Liu, F. Liao, S. Gao, R. Xiong, H. Ma, D. Zhang and D. Zhu, *Inorg. Chem.* (2006), **45**, 3, 999. (b) R. Garde, F. Villain and Michel Verdaguer, *J. Am. Chem. Soc.* (2002), **124**, 10531-10538.

- 74 (a) M. Verdaguer and G. Girolami, Magnetic Prussian Blue Analogues, in *Magnetism: Molecules to Materials*, eds. J. S. Miller and M. Drillon (Wiley-VCH: Weinheim), Chapter 9. (b) W. E. Buschmann and J. S. Miller, *Inorgan. Chem.* (2000), **39**, 11, 2411-2421.
- 75 (a) D. Papoutsakis, A. S. Ichimura, V. G. Young, J. E. Jackson and D. G. Nocera, *Dalton Trans.* (2004), 224-228. (b) M. Kajòaková, M. Orendáè, A. Orendáèová, A. Vlèek, J. Èernák, O. V. Kravchyna, A. G. Anders, M. Bałanda, J. H. Park, A. Feher, and M. W. Meisel, *Phys. Rev. B* (2005), **71**, 014435. (c) F. S. Delgado, J. Sanchiz, C. Ruiz-Perez, F. Lloretc and M. Julve, *CrystEngComm* (2004), **6**, 73, 443-450. (d) S. Takeda, A. Watanabe, G. Maruta and T. Matsuo, *Mol. Cryst. Liq. Cryst.* (2002), **376**, 443-448. (e) J. Y. Zhang, Y. Ma, A. L. Cheng, Q. Yue, Q. Sun and E. Q. Gao, *Dalton Trans.* (2008), 2061-2066. (f) M. Sakai, J. Toyoda, M. Mitsumi, K. Nakasuji, K. Furukawa, D. Shiomi, K. Sato and T. Takui, *Synthetic Metals* (2001), **121**, 1776-1777. (g) Y. Q. Liu, Y. G. Wei, Q. Lin, S. W. Zhang and M. C. Shao, *Acta Cryst.* (1999), **C55**, 534-536.
- 76 U. Bentrup, K. Harms, W. Massa and J. Pebler, *Solid State Sciences 2* (2000), 373-376
- 77 C. G. Giribet and M. C. Ruiz de Azua, *J. Phys. Chem. A* (2006), **110**, 11575-11583.
- 78 C. Desplanches, E. Ruiz, A. Rodrí'guez-Fortea, and S. Alvarez, *J. Am. Chem. Soc.* (2002), **124**, 5197-5205.
- 79 J. A. Bertrand, E. Fujita, and D. G. Vanderveer, *Inorg. Chem.* (1980), **19**, 2022.
- 80 (a) W. E. Estes and W. E. Hatfield, *Inorg. Chem.* (1978), **17**, 3226. (b) C. L. Klein, R. J. Majeste, L. M. Trefonas and C. O'Connor, *J. Inorg. Chem.* (1982), **21**, 1891. (c) G. D. Munno, D. Viterbo, A. Caneschi, F. Lloret and M. Julve, *Inorg. Chem.* (1994), **33**, 1585.

- 81 (a) J. A. Bertrand, T. D. Black, P. G. Eller, F. T. Helm and R. Mahmood, *Inorg. Chem.* (1976), **15**, 2965. (b) H. Muhonen, *Inorg. Chem.* (1986), **25**, 4692. (c) W. Plass, A. Pohlmann and J. Rautengarten, *Angew. Chem. Int. Ed.* (2001), **40**, 4207. (d) C. Tuma, A. D. Boese and N. C. Handy, *Phys. Chem. Chem. Phys.* (1999), **1**, 3939.
- 82 (a) J. L. Manson, M. M. Conner, J. A. Schlueter, T. Lancaster, S. J. Blundell, M. L. Brooks, F. L. Pratt, T. Papageorgiou, A. D. Bianchi, J. Wosnitzae and M. Whangbof, *Chem. Commun.* (2006), 4894-4896. (b) J. L. Manson, M. M. Conner, J. A. Schlueter and K. A. Hyzer, *Polyhedron* (2007), **26**, 1912-1916. (c) S. [Brown](#), J. [Cao](#), J. L. [Musfeldt](#), M. M. [Conner](#), A. C. [McConnell](#), H. I. [Southerland](#), J. L. [Manson](#), J. A. [Schlueter](#), M. D. [Phillips](#), M. M. [Turnbull](#) and C. P. [Lande](#), *Inorg. Chem.* (2007), **46**, 21, 8577-8583 (d) M. Conner, A. McConnel, J. Schlueter and J. Manson, *Journal Low Temp. Phys.* (2007). [142, 3-4](#), 273-278.
- 83 Derek S. Middlemiss a, Lorreta M. Lawton a, Carole A. Morrison b, Chick C. Wilson, *Chem. Phys. Letters*, (2008), **459**, 119-123.
- 84 (a) B. Civalleri, F. Napoli, Y. Noël, C. Roetti and R. Dovesi, *CrystEngComm* (2006), **8**, 364. (b) M. Mattesini, J.M. Soler and F. Yndurain, *Phys. Rev. B* (2006), **73**, 094111. (c) W. Zhou and T. Yildirim, *Phys. Rev. B* (2006), **74**, 180301.
- 85 (a) F. Corà, M. Alfredsson, G. Mallia, D. S. Middlemiss, W. C. Mackrodt, R. Dovesi and R. Orlando, *Struct. Bond.* (2004), **113**, 171. (b) X. Feng and N.M. Harrison, *Phys. Rev. B* (2004), **70**, 092402. (c) E. Ruiz, M. Llunell and P. Alemany, *J. Solid State Chem.* (2003), **176**, 400. (d) I. P. R. de Moreira, F. Illas and R. L. Martin, *Phys. Rev. B* (2002), **65**, 155102. (e) J. Muscat, A. Wander and N.M. Harrison, *Chem. Phys. Lett.* (2001), **342**, 397.
- 86 V. J. Murphy, T. Hascall, J. Y. Chen and G. Parkin, *J. Am. Chem. Soc.* (1996), **118**, 7428-7429.
- 87 N. E. Klepeis, A. L. L. East, A. G. Csaszar, W. D. Allen, T. J. Lee and D. W. Schwenke, *J. Chem. Phys.* (1993), **99**, 5, 3865.

- 88 (a) D. C. Roe, W. J. Marshall, F. Davidson, P. D. Soper and V. V. Grushin, *Organometallics* (2000), **19**, 4575-4582. (b) N. A. Jasim and R. N. Perutz, *J. Am. Chem. Soc.* (2000), **122**, 8685-8693.
- 89 D. Guo and J. K. McCusker, *Inorg. Chem.* (2007), **46**, 8, 3257.
- 90 H. Ohtsu and K. Tanaka, *Angew. Chem. Int. Ed.* (2004), **43**, 6301.
- 91 S. Bin-Salomon, S. Brewer, S. Franzen, D. L. Feldheim, S. Lappi and D. A. Shultz, *J. Am. Chem. Soc.* (2005), **127**, 5328.
- 92 (a) S. F. Ye, B. Sarkar, F. Lissner, T. Schleid, J. van Slageren, J. Fiedler, and W. Kaim, *Angew. Chem. Int. Ed.* (2005), **44**, 2103. (b) H.-C. Chang, and S. Kitagawa, *Angew. Chem. Int. Ed.* (2002), **41**, 130.
- 93 E. K. Andersen, *Acta Cryst.* (1967), **22**, 188.
- 94 C. Z. Robl, *Kristallogr.* (1987), **180**, 249.
- 95 E. K. Andersen and I. G. K. Andersen, *Acta Cryst.* (1975), **B31**, 384-387.
- 96 C. Robl and G. M. Sheldrick, *Z. Kristallogr.* (1988), **184**, 295.
- 97 F. H. Allen, *Acta Cryst.* (2002), **B58**, 380-388.
- 98 U. Graebe, *Justus Liebigs Ann. Chem.* (1891), **24**, 263.
- 99 E. K. Andersen, *Acta Cryst.* (1967), **22**, 191.
- 100 E. K. Andersen, *Acta Cryst.* (1967), **22**, 196.
- 101 (a) L. Hostyn and D. Hostynova, *Cesk. Patol.* (1973), **9**, 105. (b) A. J. Chaplin and S. R. Grace, *Histochemistry* (1976), **47**, 263. (c) C. B. Marone and G. Bianchi, *An. Quim.* (1973), **69**, 205. (d) M. Frizanova, A. Reis, L. Hainberger and Z. Fresenius, *Anal. Chem.* (1972), **261**, 400. (e) J. M. Pokier and J. F. Verchere, *Talanta* (1979), **26**, 349. (f) B. Floh, A. Abrao and L. Federgrun, *Inst. Energ. At. (Sao Paulo), Publ. IEA* (1976), 427. (g) V. A. Cortinez and C. B. Marone, *Quim. Anal.* (1976), **30**, 33. (h) O. Baudino, V. A. Cortinez and C. Marone, *Rev. Asoc. Bioquim. Argent.* (1976), **41**, 212.

- 102 D. L. Giokas, E. K. Paleologos, P. G. Veltsistas and M. I. Karayannis, *Talanta* (2002) **56** 415.
- 103 P. G. Veltsistas and M. I. Karayannis, *Analyst* (1987), **112**, 1579.
- 104 P. G. Veltsistas and M. I. Karayannis, *Quim. Anal.* (1996), **15**, 334.
- 105 P. G. Veltsistas and M. I. Karayannis, *Analyst* (1990), **115**, 741.
- 106 (a) Md. Akhtaruzzaman, M. Tomura, K. Takahashi, J. Nishida and Y. Yamashita, *Supramol. Chem.* (2003), **15**, 239. (b) Md. Akhtaruzzaman, Masaaki Tomura, Jun-ichi Nishida, and Yoshiro Yamashita, *J. Org. Chem.* (2004), **69**, 2953. (c) K. Gotoh, R. Ishikawa and H. Ishida, *Acta Cryst.* (2007), **E63**, o4518. (d) H. Ishida and S. Kashino, *Acta Cryst.* (1999), **C55**, 1149-1152. (e) K. Gotoh, H. Nagoshi and H. Ishida, *Acta Cryst.* (2009), **E65**, po614. (f) P. Su, X.-Y. Huang and X. Meng, *Acta Cryst.* (2008), **E64**, o2217-o2218; (g) T. Murata, Y. Morita, Y. Yakiyama, K. Fukui, H. Yamochi, G. Saito, and K. Nakasuji, *J. Am. Chem. Soc.* (2007), **129**, 10837-10846. (h) K. Gotoh, R. Ishikawa and H. Ishida, *Acta Cryst.* (2006), **E62**, o4738-o4740. (i) H. Ishida and S. Kashino, *Acta Cryst.* (2000), **C56**, e202-e204. (j) D.-J. Yang and S.-H. Qu, *Acta Cryst.* (2006), **E62**, o4720-o4722. (k) T. Fukunaga and H. Ishida, *Acta Cryst.* (2003), **E59**, o1793-o1795. (l) H. Ishida, *Acta Cryst.* (2004), **E60**, o1674-o1676. (m) Y. Tabuchi, A. Takahashi, K. Gotoh, H. Akashi and H. Ishida, *Acta Cryst.* (2005), **E61**, o4215-o4217. (n) H. Ishida and S. Kashino, *Acta Cryst.* (2001), **C57**, 476-479. (o) A. S. Gaballa, C. Wagner, S. M. Teleb, E-M. Nour, M. A. F. Elmosallamy, G. N. Kaluđerović, H. Schmidt and D. Steinborn, *J. Mol. Struct.* (2008), **876**, 301-307; (p) S. Horiuchi, R. Kumai, Y. Tokunaga and Y. Tokura, *J. Am. Chem. Soc.* (2008), **130**, 13382-13391. (q) M. Tomura and Y. Yamashita, *Anal. Sci. X-ray Struct. Anal. Online* (2008), **24**, x31. (r) Md. K. Kabir, H. Tobita, H. Matsuo, K. Nagayoshi, K. Yamada, K. Adachi, Y. Sugiyama, S. Kitagawa, and S. Kawata, *Cryst. Growth Des.* (2003), **3**, 5, 791-798. (s) H. Ishida and S. Kashino, *Z. Naturforsch.* (2002), **57**, 829-836. (t) K. Gotoh, Y. Tabuchi, H. Akashi and H. Ishida, *Acta Cryst.* (2006), **E62**, o4420-o4421. (u) K. Gotoh, H. Nagoshi and H. Ishida, *Acta Cryst.* (2009), **C65**, o273-o277.

- 107 (a) Md. B. Zaman, M. Tomura and Y. Yamashita, *Org. Lett.* (2000), **2**, 273. (b) H. Ishida and S. Kashino, *Acta Cryst.* (1999), **C55**, 1923. (c) [K. Gotoh](#) and [H. Ishida](#), *Acta Cryst.* (2008), **E64**, o2095. (d) S.-X. Liu, S. Dolder, A. Neels, G. Labat, H. Stoeckli-Evans and S. Decurtins, *J. Phys. IV France* (2004), **114**, 679. (e) [K. Gotoh](#), [T. Asaji](#) and [H. Ishida](#), *Acta Cryst.* (2007), **C63**, o17-o20.
- 108 M. B. Zaman, M. Tomura, Y. Yamashita, M. Sayaduzzaman and A. M. S. Chowdhury, *CrystEngCom* (1999), **1**, 36
- 109 S. Liu, S. N. Shaikh and J. Zubieta, *J. Chem. Soc. Chem. Commun.* (1988), 1017-1019.
- 110 *Vista - A Program for the Analysis and Display of Data Retrieved from the CSD*, Cambridge Crystallographic Data Centre (1994).
- 111 M. Kawahara, K. Kabir, K. Yamada, K. Adachi, H. Kumagai, Y. Narumi, K. Kindo, S. Kitagawa and S. Kawata, *Inorg. Chem.* (2004), **43**, 1, 92.
- 112 P. E. Riley, S. F. Haddad, and K. N. Raymond, *Inorg. Chem.* (1983), **22**, 3090-3096.
- 113 [S. Reinoso](#), [P. Vitoria](#), [L. San Felices](#), [L. Lezama](#) and [J. M. Gutiérrez-Zorrilla](#), *Acta Cryst.* (2005), **E61**, m1925-m1927.
- 114 K. S. Min, A. G. DiPasquale, J. A. Golen, A. L. Rheingold, and J. S. Miller, *J. Am. Chem. Soc.* (2007), **129**, 2360-2368.
- 115 (a) C. Janiak, *J. Chem. Soc. Dalton Trans.* (2000), 3885-3896. (b) T. Kawase and H. Kurata, *Chem. Rev.* (2006), **106**, 5250-5273.
- 116 [S. Kashino](#), [H. Ishida](#), [T. Fukunaga](#) and [S. Oishi](#), *Acta Cryst.* (2001), **C57**, 18-19.
- 117 (a) P. Metrangolo, H. Neukirch, T. Pilati and G. Resnati, *Acc. Chem. Res.* (2005), **38**, 386-395. (b) R. B. Walsh, C. W. Padgett, P. Metrangolo, G. Resnati, T. W. Hanks and W. T. Pennington, *Cryst. Growth Des.* (2001), **1**, 165-175. (c) B. K. Saha, A. Nangia and M. Jaskolski, *CrystEngComm* (2005),

- 7, 355-358. (d) P. Metrangolo and G. Resnati, *Chem.-Eur. J.* (2001), **7**, 2511-2519. (e) T. Caronna, R. Liantonio, T. A. Logothetis, P. Metrangolo, T. Pilati and G. Resnati, *J. Am. Chem. Soc.* (2004), **126**, 4500-4501.
- 118 (a) D. B. Leznoff, B.-Y. Xue, R. J. Batchelor, F. W. B. Einstein and B. O. Patrick, *Inorg. Chem.* (2001), **40**, 6026-6034. (b) E. J. Fernandez, M. C. Gimeno, A. Laguna, J. M. Lopez-de-Luzuriaga, M. Monge, P. Pyykko and D. Sundholm, *J. Am. Chem. Soc.* (2000), **122**, 7287-7293 (c) M. A. Rawashdeh-Omary, M. A. Omary, H. H. Patterson and J. P. Fackler Jr., *J. Am. Chem. Soc.* (2001), **123**, 11237-11247.
- 119 (a) F. Corbellini, R. Fiammengo, P. Timmerman, M. Crego-Calama, K. Versluis, A. J. R. Heck, I. Luyten and D. N. Reinhoudt, *J. Am. Chem. Soc.* (2002), **124**, 6569-6575. (b) F. Corbellini, L. D. Costanzo, M. Crego-Calama, S. Geremia and D. N. Reinhoudt, *J. Am. Chem. Soc.* (2003), **125**, 9946-9947. (c) Y. Chi and S. H. Gellman, *J. Am. Chem. Soc.* (2006), **128**, 6804-6805.
- 120 L.-S. Long, *CrystEngComm* (2010), **12**, 1354-1365.
- 121 (a) G. R. Desiraju, *Acc. Chem. Res.* (2002), **35**, 565-573. (b) G. R. Desiraju, *Chem. Commun.* (2005), 2995-3001. (c) D. Braga and F. Grepioni, *Acc. Chem. Res.* (2000), **33**, 601-608; L. Brammer, *Chem. Soc. Rev.* (2004), **33**, 476-489. (d) B. Moulton and M. J. Zaworotko, *Chem. Rev.* (2001), **101**, 1629-1658. (e) H. W. Roesky and M. Andruh, *Coord. Chem. Rev.* (2003), **236**, 91-119.
- 122 [S. Cueto](#), [H.-P. Straumann](#), [P. Rys](#), [W. Petter](#), [V. Gramlich](#) and [F. S. Rys](#), *Acta Cryst.* (1992), **C48**, 458-460.
- 123 S. Kawata, S. Kitagawa, M. Kondo, M. Katada, *Synthetic Metals*, (1995), **71**, 1917-1918.
- 124 J. V. Folgado, R. Ibanez, E. Coronado, D. Beltran, J. M. Savariault, J. Galy, *Inorg. Chem.* (1988), **27**, 1, 19.
- 125 S. Kawata, H. Kumagai, K. Adachi and S. Kitagawa, *J. Chem. Soc. Dalton Trans.* (2000), 2409.

- 126 S. Kawata, S. Kitagawa, H. Kumagai, C. Kudo, H. Kamesaki, T. Ishiyama, R. Suzuki, M. Kondo, and M. Katada, *Inorg. Chem.* (1996), **35**, 4449-4461.
- 127 (a) H. Kumagai, S. Kawata, S. Kitagawa, *Inorganica Chimica Acta* (2002), **337**, 387-392. (b) S. Kawata, H. Kumagai, K. Adachi and S. Kitagawa, *J. Chem. Soc. Dalton Trans.* (2000), 2409. (c) S. Kawata, H. Kumagai, S. Kitagawa, K. Honda, M. Enomoto and M. Katada, *Mol. Cryst. Liq. Cryst.* (1996), **286**, 51. (d) S. Kawata, S. Kitagawa, M. Kondo, I. Furuchi and M. Munakata, *Angew. Chem. Int. Ed.* (1994), **33**, 1759. (e) M. K. Kabir, M. Kawahara, H. Kumagai, K. Adachi, S. Kawata, T. Ishii and S. Kitagawa, *Polyhedron* (2001), **20**, 1417.
- 128 S. Kawata, S. Kitagawa, H. Kumagai, T. Ishiyama, K. Honda, H. Tobita, K. Adachi and M. Katada, *Chem. Mater.* (1998), **10**, 12, 3902-3912.
- 129 M. K. Kabir, N. Miyazaki, S. Kawata, K. Adachi, H. Kumagai, K. Inoue, S. Kitagawa, K. Iijima and M. Katada, *Coord. Chem. Rev.* (2000), **198**, 157-169.
- 130 L.-M. Zheng, H. W. Schmalke, R. Huber and S. Decurtins, *Polyhedron* (1996), **15**, 24, 4399-4405.
- 131 B. F. Abrahams, K. D. Lu, B. Moubaraki, K. S. Murray and R. Robson, *J. Chem. Soc. Dalton Trans.* (2000), 1793.
- 132 K. S. Min, A. L. Rheingold, A. DiPasquale and J. S. Miller, *Inorg. Chem.* (2006), **45**, 16, 6135-6137.
- 133 S. Liu, S. N. Shaikh and J. Zubieta, *Inorg. Chem.* (1989), **28**, 4, 723-732.
- 134 S. Liu, S. N. Shaikh and J. Zubieta, *Inorg. Chem.* (1988), **27**, 3064-3066.
- 135 D. F. Xiang, C. Y. Duan, X. S. Tan, Y. J. Liu and W. X. Tang, *Polyhedron* (1998), **17**, 2647.
- 136 M. K Kabir, M. Kawahara, H. Kumagai, K. Adachi, S. Kawata, T. Ishii and S. Kitagawa, *Polyhedron* (2001), **20**, 1417-1422

- 137 R.-T. Liao, W.-C. Yang, P. Thanasekaran, C.-C. Tsai, M. Sathiyendiran, Y.-H. Liu, T. Rajendran, H.-M. Lin, T.-W. Tseng and K.-L. Lu, *Chem. Commun.* (2008), 3175-3177.
- 138 (a) Y.-F. Han, Y.-J. Lin, W.-G. Jia and G.-X. Jin, *Organometallics* (2008), **27**, 4088-4097. (b) Y.-F. Han, W.-G. Jia, Y.-J. Lin and G.-X. Jin, *Organometallics* (2008), **27**, 5002-5008.
- 139 (a) P. S. Mukherjee, N. Das, Y. K. Kryschenko, A. M. Arif and P. J. Stang, *J. Am. Chem. Soc.* (2004), **126**, 2464-2473. (b) Y. K. Kryschenko, S. R. Seidel, D. C. Muddiman, A. I. Nepomuceno and P. J. Stang, *J. Am. Chem. Soc.* (2003), **125**, 9647-9652. (c) K. Kumazawa, K. Biradha, T. Kusukawa, T. Okano and M. Fujita, *Angew. Chem. Int. Ed.* (2003), **42**, 3909-3913. (d) M. Yoshizawa, J. Nagakawa, K. Kumazawa, M. Nagao, M. Kawano, T. Ozeki and M. Fujita, *Angew. Chem. Int. Ed.* (2005), **44**, 1810-1813. (e) L. Gomez, A. Company, X. Fontrodona, X. Ribas and M. Costas, *Chem. Commun.* (2007), 4410-4412, and references therein. (f) S. M. Woessner, J. B. Helms, Y. Shen and B. P. Sullivan, *Inorg. Chem.* (1998), **37**, 5406-5407. (g) J. Taraba and Z. Zak, *Inorg. Chem.* (2003), **42**, 3591-3594; For reviews, see: (h) P. H. Dinolfo and J. T. Hupp, *Chem. Mater.* (2001), **13**, 3113-3125. (i) P. Thanasekaran, R. T. Liao, Y. H. Liu, T. Rajendran, S. Rajagopal and K. L. Lu, *Coord. Chem. Rev.* (2005), **249**, 1085-1110. (j) S. S. Sun and A. J. Lees, *Coord. Chem. Rev.* (2002), **230**, 170-192.
- 140 C. Robl, *Mat. Res. Bull.* (1987), **22**, 11, 1483-1491.
- 141 A. Michaelides, C. D. Papadimitriou, J. C. Plakatouras, S. Skoulika, P. G. Veltsistas, *Polyhedron* (2004), **23**, 2587-2593.
- 142 B. F. Abrahams, J. Coleiro, K. Ha, B. F. Hoskins, S. D. Orchard and R. Robson, *J. Chem. Soc. Dalton Trans.* (2002), 1586.
- 143 A. Elduque, Y. Garcés, F. J. Lahoz, J. A. López, L. A. Oro, T. Pinillos and C. Tejel, *Inorg. Chem. Comm.* (1999), **2**, 9, 414-418.
- 144 S. N. Shaikh and J. Zubieta, *Inorganica Chimica Acta* (1988), **146**, 149-150.

- 145 C. Robl and A. Weiss, *Mat. Res. Bull.* (1987), **22**, 497-504.
- 146 C. Robl and A. Weiss, *Z. Naturforsch. B: Chem.Sci* (1986), **31**, 1495.
- 147 F. H. Herbstein and M. Kaftory, *J. Appl. Cryst.* (1972), **5**, 51
- 148 R. Benchekroun and J.-M. Savariault, *Acta Cryst.* (1995), **C51**, 186-188.
- 149 C. Papadimitriou, P. Veltsistas, J. Marek, J. Novosad, A. M. Z. Slawin and J. D. Woollins, *Inorg. Chem. Comm.* (1998), **1**, 418-420.
- 150 R. Dovesi, V.R. Saunders, C. Roetti, R. Orlando, C. M. Zicovich-Wilson, F. Pascale, B. Civalleri, K. Doll, N.M. Harrison, I.J. Bush, Ph. D'Arco and M. Llunell, *CRYSTAL06 User's Manual*, University of Torino, Torino, (2006).
- 151 C. C. Wilson, *Single Crystal Neutron Diffraction From Molecular Crystals*, World Scientific, (2000).
- 152 W. Massa, *Crystal structure Determination*, Second Edition, Springer, (2004).
- 153 A. D. Becke, *Phys. Rev. A* (1988), **38**, 3098.
- 154 C. Lee, W. Yang, and R. G. Parr, *Phys. Rev. B* (1988), **37**, 785.
- 155 S. H. Vosko, L. Wilk, and M. Nusair, *Can. J. Phys.* (1980), **58**, 1200.
- 156 F. Corà, M. Alfredsson, G. Mallia, D. S. Middlemiss, W. C. Mackrodt, R. Dovesi, and R. Orlando, *Struct. Bond.* (2004), **113**, 171.
- 157 J. Muscat, A. Wander, and N. M. Harrison, *Chem. Phys. Lett.* (2001), **342**, 397.
- 158 F. Corà, M. Alfredsson, G. Mallia, D. S. Middlemiss, W. C. Mackrodt, R. Dovesi and R. Orlando, *Struct. Bond.* (2004), **113**, 171.
- 159 X. Feng and N. M. Harrison, *Phys. Rev. B* (2004), **70**, 092402.
- 160 R. M. Martin, *Electronic Structure: basic theory and practical methods*, Cambridge University Press, (2004).

- 170 J. Kanamori, *J. Phys. Chem. Solids* (1959), **10**, 87.
- 171 M. Gerloch and R. C. Slade, *Ligand Field Parameters*, Cambridge University Press, Cambridge, (1973).
- 172 D. S. Middlemiss and W. C. Mackrodt, *J. Phys.: Condens. Matter* (2008), **20**, 015207.
- 173 W. C. Mackrodt, D. S. Middlemiss, and T. G. Owens, *Phys. Rev. B* (2004), **69**, 115119.
- 174 J. S. Griffith, *The Theory of Transition Metal Ions*, Cambridge University Press, Cambridge, (1964).
- 175 S. Sugano, Y. Tanabe and H. Kamimura, *Multiplets of Transition-Metal Ions in Crystals*, Academic Press, New York, (1970).
- 176 N.W. Ashcroft and N. D. Mermin, *Solid State Physics*, Saunders College Publishing, U.S.A., 1976, First Edition
- 177 E. Ruiz, A. Rodriguez-Forteza, S. Alvarez and M. Verdaguer *Chem. Eur. J.* (2005), **11**, 2135.
- 178 L. Neel, *Ann. Phys. Fr.* (1948), **3**, 137.
- 179 F. Herren, P. Fischer, A. Ludi, and W. Halg, *Inorg. Chem.* (1980), **19**, 956.
- 180 M. Verdaguer and G. Girolami, in *Magnetism: Molecules to Materials V*, edited by J. S. Miller and M. Drillon. Wiley-VCH, Weinheim, 2004
- 181 Crystal web page: <http://www.crystal.unito.it>
- 182 R. D. Shannon, *Acta Cryst.* (1976), **A32**, 751.
- 183 N. E. Klepeis, A. L. L. East, A. G. Csaszar, W. D. Allen, T. J. Lee and D. W. Schwenke, *J. Chem. Phys* (1993), **99**, 5, 3865-3897.
- 184 F. Corà, M. Alfredsson, G. Mallia, D. S. Middlemiss, W. C. Mackrodt, R. Dovesi and R. Orlando, *Struct. Bonding* (Berlin) (2004), **113**, 171.

- 185 L. J. de Jongh and A. R. Miedema, *Adv. Phys.* (1974), **23**, 1.
- 186 O. Kahn, *Molecular Magnetism*, VCH, Weinheim, 1993.
- 187 M. Verdaguer and G. Girolami, *Magnetism : Molecules to Materials*, Chapter 9: Magnetic Prussian Blue Analogues, Wiley, (2004).
- 188 (a) B. Zheng, H. Dong, J. F. Bai, Y. Z. Li, S. H. Li and M. Scheer, *J. Am. Chem. Soc.* (2008), **130**, 7778-7779. (b) S. Khatua, T. Harada, R. Kurodabc and M. Bhattacharjee, *Chem. Commun.* (2007), 3927-3929. (c) R. Yamasaki, A. Tanatani, I. Azumaya, H. Masu, K. Yamaguchi and H. Kagechika, *Cryst. Growth Des.* (2006), **6**, 2007-2010. (d) V. R. Pedireddi and S. Varughese, *Inorg. Chem.* (2004), **43**, 450-457. (e) T. Wu, D. Li and S. W. Ng, *CrystEngComm* (2005), **7**, 514-518.
- 189 (a) M.-L. Tong, S. Hu, J. Wang, S. Kitagawa and S. W. Ng, *Cryst. Growth Des.* (2005), **5**, 837-839. (b) J. X. Chen, M. Ohba, D. Zhao, W. Kaneko and S. Kitagawa, *Cryst. Growth Des.* (2006), **6**, 664-668. (c) D. F. Sun, Y. X. Ke, T. M. Mattox, B. A. Ooro and H.-C. Zhou, *Chem. Commun.* (2005), 5447-5449. (d) Y.-B. Dong, Y.-Y. Jiang, J. Li, J.-P. Ma, F.-L. Liu, B. Tang, R.-Q. Huang and S. R. Batten, *J. Am. Chem. Soc.* (2007), **129**, 4520-4521.
- 190 (a) M. Tsaramyrsi, M. Kaliva, A. Salifoglou, C. P. Raptopoulou, A. Terzis, V. Tangoulis and J. Giapintzakis, *Inorg. Chem.* (2001), **40**, 5772-5779. (b) S. Faulkner and B. P. Burton-Pye, *Chem. Commun.* (2005), 259-261.
- 191 K. Molcanov and B. Kojic-Prodic, *CrystEngComm* (2010), **12**, 925-939.
- 192 C. F. Macrae, I. J. Bruno, J. A. Chisholm, P. R. Edgington, P. McCabe, E. Pidcock, L. Rodriguez-Monge, R. Taylor, J. van de Streek and P. A. Wood, *J. Appl. Cryst.* (2008), **41**, 466-470.
- 193 WebElements database: <http://www.webelements.com/>.
- 194 M. R. Chierotti, L. Ferrero, N. Garino, R. Gobetto, L. Pellegrino, D. Braga, F. Grepioni, L. Maini, *Chem. Eur. J.* (2010), **16**, 4347.

- 195 D. R. McGregor, J. C. Speakman and M. S. Lehmann, *J. Chem. Soc., Perkin Trans. 2*, 1977, 1740-1745.
- 196 C C Wilson (1997) *J Appl Cryst*, 30, 184-189.